The University of Sheffield

Electromagnetic Performance of Consequent Pole Permanent Magnet Machines, with Particular Reference to Analysis and Minimization of Torque Ripples

Ji Qi

A thesis submitted for the degree of Doctor of Philosophy

Department of Electronic and Electrical Engineering
The University of Sheffield
Mappin Street, Sheffield, S1 3JD, UK

November 2022

ABSTRACT

Consequent pole permanent magnet (CPPM) machines can save the amount of permanent magnet (PM) while produce comparable torque as conventional surface-mounted PM (SPM) machines. However, due to the unbalanced features between north and south poles, i.e. PM and iron poles, the presence of a large torque ripple can hinder their adoption in some applications. Unfortunately, the basic characteristics and generalized principles have not been fully established. This thesis investigates the electromagnetic performances of CPPM machines, with particular reference to the analysis and minimization of torque ripples.

A general analytical model is developed for the first time to analyze the cogging torque accounting for unequal north and south pole widths as well as pole shifting. It can be applied to CPPM machines and other rotor PM machines. Based on the analytical expression, optimal design parameters for minimum cogging torque with/without pole shifting, including slot opening and pole-arc to pole-pitch ratio, are analytically derived and verified by finite element method (FEM).

By selecting appropriate design parameters, the cogging torque and torque ripple under light load conditions can be suppressed effectively but little torque ripple reduction can be achieved at high currents. To solve this problem, symmetrical and asymmetric pole shaping methods with different PM and iron pole shapes are proposed. It is confirmed that the symmetrical pole shaping methods can only reduce the PM torque ripple while the asymmetric pole shaping method can minimize the overall torque ripple since it can adjust the amplitudes and phasors of torque ripple components, i.e. PM, reluctance, and cogging torques, to make them counteract each other. It is also the first time that the contribution of reluctance torque ripple is revealed and utilized to minimize the overall torque ripple in CPPM machines.

However, the effect of proposed methods will be affected by different slot/pole number combinations and different load conditions. For CPPM and SPM machines with odd number of coils per phase per submachine, the influences of unbalanced pole characteristics can cause additional torque ripple harmonics due to additive effects in windings, but can be canceled in other machines. Compared with symmetrical pole shaping method, asymmetric pole shaping method can achieve lower torque ripple for CPPM machines with odd number of coils per phase per submachine, while these two pole shapes have similar effects on torque ripple reduction for other CPPM machines and all the SPM machines. It also confirms that for all the CPPM machines, the armature reaction will lead to variations of fundamentals and harmonics in performances, including flux density, flux linkage, back electromotive force, inductance, and torque ripple, as well as significant magnetic saturation and limited overload capability.

All the investigations have been carried out by analytical analyses or FEM and experimental verification.

ACKNOWLEDGEMENTS

Foremost, I would like to express my sincerest gratitude to my supervisor Professor Zi-Qiang Zhu. He gave me the chance to study in the UK and receive the best guidance in the world. During my Ph.D. study, he offered his best efforts to help me, support me, and encourage me in both academic and life. His insightful comments and invaluable advice not only gave me knowledge, but are also valuable assets for my future life.

I would express my thanks to Professor Geraint Wyn Jewell for his great effort in supervising my Ph.D. research and offering valuable comments to complete my thesis. His guidance and speeches expanded my knowledge and inspired my thinking.

I would like to thank Protean Electric Ltd. and the UK EPSRC Future Electrical Machines Manufacturing (FEMM) Hub for the financial support to allow me to complete my fantastic research. Particularly, I wish to thank Dr. Simon Brockway, Dr. Chris Hilton, Dr. Chengwei Gan, Dr. Yuan Ran, Ms. Chathurika Mahanama, Mr. Dave Withers, Dr. Glynn Atkinson for their helpful supervision and advice as well as for their support and assistance with prototypes.

I would like to thank Dr. Panos Lazari at the University of Sheffield for his help in educating engineering students. He also encourages me to face difficulties. I would like to thank JAMG and Media for allowing me to communicate the latest research achievements. I learned a lot from them.

I would like to thank Dr. Luocheng Yan, Dr. Yue Liu, Dr. Yanxin Li, Dr. Shun Cai, Dr. Yafeng Zhang, Dr. Yu Wang, Dr. Fangrui Wei, Dr. Dawei Liang, Dr. Tianran He, Dr. Huan Qu, Mr. Shensheng Wang, Mr. Yinzhao Zheng, Mr. Hai Xu, and all my colleagues in the Electrical Machines and Drives Research Group of the University of Sheffield for their technical discussions and support. I will never forget the time we spent together.

I would also like to thank my family for their unconditional love.

Finally, I would like to acknowledge everyone who has knowingly and unknowingly helped me and wished me the best in successfully accomplishing this research.

CONTENTS

NOMENCLATURES

Symbol	Description	Unit
A_{Aci}	Amplitude of the i-th harmonic in flux density for symmetrical shape machines	T
A_{Bcj}, A_{Bsj}	Amplitude of the j-th harmonic in flux density for asymmetric shape machines	T
A_{icb}	Amplitudes of cos components for L'_{ip} for the b-th harmonic	mm
A_{isb}	Amplitudes of sin components for L'_{ip} for the b-th harmonic	mm
A_{mca}	Amplitudes of cos components for L'_{mp} for the a-th harmonic	mm
A_{msa}	Amplitudes of sin components for L'_{mp} for the a-th harmonic	mm
A_t	Cross-sectional area of tooth tips at air-gap	mm^2
B	Air-gap flux density	T
$B(\theta, \alpha)$	Flux density function	-
B_{a0}, B_{aqp}, B_{bqp}	Fourier coefficients of $B^2(\theta)$	-
B_{fA}	Flux density for symmetrical shape machines	T
B_{fB}	Flux density for asymmetric shape machines	T
B_{iron}	Flux densities under iron pole	T
B_{PM}	Flux densities under PM pole	T
$\boldsymbol{C}$, $\boldsymbol{P}$	Transformation matrices	-
Fc_{PM}	Magnetic potential of PMs	AT

F_s	Magnetic potential in stator	AT
$G(\theta)$	Relative air-gap permeance function	-
G_{a0}, G_{akNs}, G_{bkNs}	Fourier coefficients of $G^2(\theta)$	-
H_c	Coercivity of magnet	A/m
$\boldsymbol{I}_{abc}$	Current matrix in *abc*-axes	A
$\boldsymbol{I}_{dq}$	Current matrix in *dq*-axes	A
I_{ch}	Characteristic current	A
i_d	*d*-axis current	A
i_q	*q*-axis current	A
I_{unit}	Unit current	A
k_{north}, k_{south}	Ratios of north and south pole-arcs to pole-pitch	-
k_{PM}, k_{iron}	Ratios of PM and iron pole-arcs to pole-pitch	-
k_{so}	Slot opening ratio	-
L_{2n-1}	Amplitude of 2*n*-order harmonic in inductances	mH
L^i_{2n-1}, L^j_{2n-1}	2*n*-order harmonics in inductances of the *i*-th and the *j*-th coils	-
L'_{ip}	Rotor outline functions for iron pole	mm
L'_{mp}	Rotor outline functions for PM pole	mm
l_0	Average value of self-inductance	mH
l_2	Amplitude of self-inductance harmonic	mH

L_{aa}	Self-inductance of phase A	mH
$\boldsymbol{L}_{abc}$	Inductance matrices in *abc*-axes	H
L_{ag}	Air-gap length	mm
L_{bb}	Self-inductance of phase B	mH
L_{cc}	Self-inductance of phase C	mH
L_d	*d*-axis inductances	mH
L_{dq}	*dq*-axes inductances	mH
$\boldsymbol{L}_{dq}$	Inductance matrixes in *dq*-axes	H
L_{PM}	Thickness of magnet	mm
L_q	*q*-axis inductances	mH
L_s	Stack length	mm
m	Phase number	-
N_c	Least common multiple between slot number pole-pair number	-
N_{ps}	Point number in half pole	-
N_s	Slot number	-
N_{TPC}	Number of turns per coil	-
N_{TPW}	Number of turns of a winding	-
p	Rotor pole-pair number	-
R_{AG}	Flux reluctance in air-gap under one pole	H^{-1}

R_{PMi}	Flux reluctance in magnets	H^{-1}
R_{ik}	Radius of *k*-th point in iron pole for determining the pole shape	mm
R_{iron}	Flux reluctances in air-gap under iron pole	H^{-1}
R_m	Flux reluctance along the flux circuit	H^{-1}
R_{mk}	Radius of *k*-th point in PM pole for determining the pole shape	mm
R_{PM}	Flux reluctances in air-gap under PM pole	H^{-1}
R_s	Stator inner radius	mm
R_{si}	Stator inner radius	mm
S_m	Number of submachine	-
S_{p1}	Cross areas under PM pole	mm^2
S_{p2}	Cross areas under iron pole	mm^2
$Sq(\theta)$	Standard square wave function	-
T_{avg}	Average torque	Nm
T_{avg}	Average torque	Nm
T_{cog}	Cogging torque	Nm
T_e	Total output torque	Nm
T_{PM}	PM excitation torque	Nm
T_r	Ratio of peak to peak torque value to average torque	-
T_r	Reluctance torque	Nm

T_{ripple}	Ratio of the peak to peak value to average torque	-
U_s	Back EMF	V
V_{PM}	Magnet volume	mm^3
W	Magnetic energy	J
W_r'	Magnetic co-energies due to PM flux	J
W_s'	Magnetic co-energies due to armature current	J
W_{sr}'	Magnetic co-energies due to armature current and PM flux	J
α	Rotational angle of the rotor	rad
α_{ij}	Phasor angle between the *i*-th and the *j*-th coils	rad
β	Pole shifting angle	rad
γ_0	Slot opening angle	rad
η_{PM}	Torque per magnet volume	-
η_{PM}	Ratio of average torque to PM volume	-
θ	Circumferential angle	rad
θ_{2n}^{L}	Initial position angle of 2*n*-order harmonic in inductance	rad
θ_{2n}^{ψ}	Initial position angle of the 2*n*-order harmonic in flux linkages	rad
θ_{ik}	Angle of *k*-th point in iron pole for determining the pole shape	rad
θ_{mk}	Angle of *k*-th point in PM pole for determining the pole shape	rad
θ_{pi}	Iron pole arc span	rad

θ_{pm}	PM pole arc span	rad
θ_r	Rotor position	rad
μ	Magnetic permeability of air	H/m
φ_{CPPM}	Magnet flux for CPPM machine	Wb
φ_{SPM}	Magnet flux for SPM machine	Wb
ψ_{2n}	Amplitude of the 2n-order harmonic in flux linkage	Wb
$\psi_{2n}^{i},\ \psi_{2n}^{j}$	2n-order harmonics in flux linkage of the i-th and the j-th coils	-
$\boldsymbol{\Psi}_{abc}^{PM}$	PM flux matrixes in abc-axes	Wb
$\boldsymbol{\Psi}_{dq}^{PM}$	PM flux matrixes in dq-axes	Wb
ψ_d^{PM}	d-axis PM flux linkage	Wb
ψ_q^{PM}	q-axis PM flux linkage	Wb
ψ_f	PM flux linkage	Wb

ABBREVIATIONS

AC	Alternating current
CCPPM	Conventional CPPM
CP	Consequent pole
CPPM	Consequent pole permanent magnet
CW	Concentrated winding
DC	Direct current
DL	Double layer
DS	Dual stator
DW	Distributed winding
EMF	Electromotive force
EV	Electric vehicle
FEM	Finite element method
FP	Frozen permeability
FRPM	Flux reversal permanent magnet
FS	Fractional slot
FSCW	Fractional slot concentrated winding
GA	Genetic algorithm
GCD	Greatest common divisor
IPM	Interior PM
IS	Integer slot

LCM	Least common multiple
MMF	Magnetomotive force
Non-OW	Non-overlapping winding
OW	Overlapping winding
PM	Permanent magnet
PSCPPM	Pole-shaped CPPM
PWM	Pulse width modulation
SFPM	Switched flux permanent magnet
SL	Single layer
SPM	Surface-mounted PM
UMF	Unbalanced magnetic force

CHAPTER 1
GENERAL INTRODUCTION

1.1 Introduction

In 1820, the magnetic effect of current was discovered by Oersted, based on which the first primitive electric motor was developed in 1821 [Edw91]. By 1900, the main types of electrical machines, including induction machine, reluctance machine, permanent magnet machine, and so on, had been proposed and followed by a rapid development over the next century. In 1930s, the industrial application of permanent magnet (PM) machines started with the availability of Alnico. In the 1950s, ferrite permanent magnets appeared and were used in motors for small appliances. It was not until the 1960s (SmCo magnets) and 1980s (NdFeB magnets), rare earth based PMs were introduced with significant improvement in magnetic performance. With the decrease in manufacturing cost of rare earth PM material, a large variety of rare earth based PM synchronous machines were invented and widely used in industrial and domestic applications until today, which benefit from their advantages of high torque density, high efficiency, simplicity, and easy control. In recent years, machine drives took the largest part of electricity consumption and play a significant role in economy and industry [EIA20]. Additionally, in order to solve the problem of fossil energy and environmental pollution caused by fuel engines, rare earth based PM electrical machines have attracted considerable attention in many areas.

Generally, electrical machines can be divided into two groups, i.e. brushed and brushless machines. For brushed machines, such as direct current (DC) machines, the windings are located in the rotor, and thereby, commutator/brushes are necessary for the power supply. Although the control of a brushed machine is relatively simple, the mechanical friction of the commutator/brushes and the sparks caused by the mechanical commutator limit the lifetime and application of this type of machine.

With advances in semiconductor technology, such problems can be solved by brushless machines with the mechanical commutator replaced by a DC link converter, Fig. 1.1. Although

the voltage waveforms generated from the converter circuit tend to be a rectangular shape, the switching technique called pulse width modulation (PWM) can produce the current in nearly sinusoidal. The converter makes it possible to provide controllable alternating current (AC) from a DC source to the stator armature winding, which inherently avoids the drawbacks caused by commutator/brushes in brushed machines. Besides, since the frequency of output current from the converter is adjustable, speed control is, therefore, possible for electrical machines.

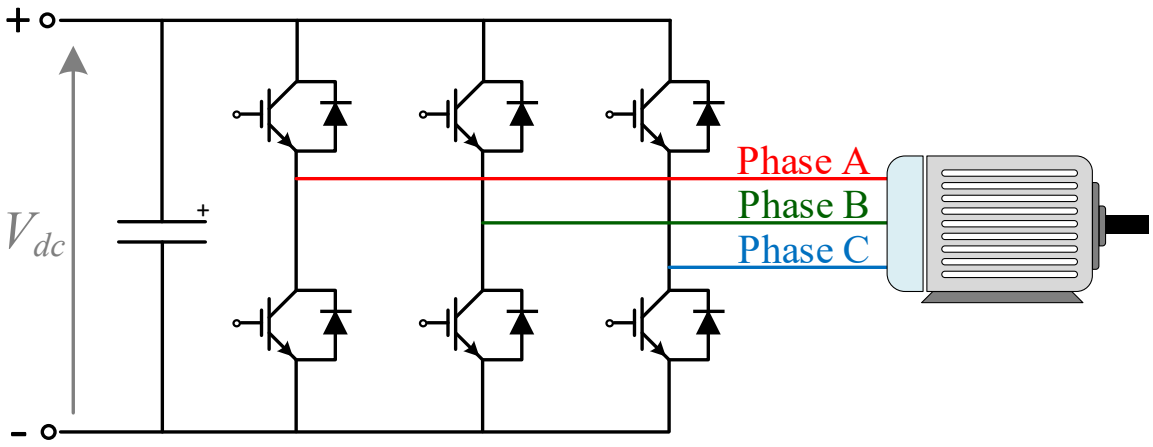

Fig. 1.1 Three-phase converter circuit.

Depending on whether the mechanical speed of the rotor is synchronized with the stator magnetic field, the brushless machine can be divided into two categories as illustrated in Fig. 1.2.

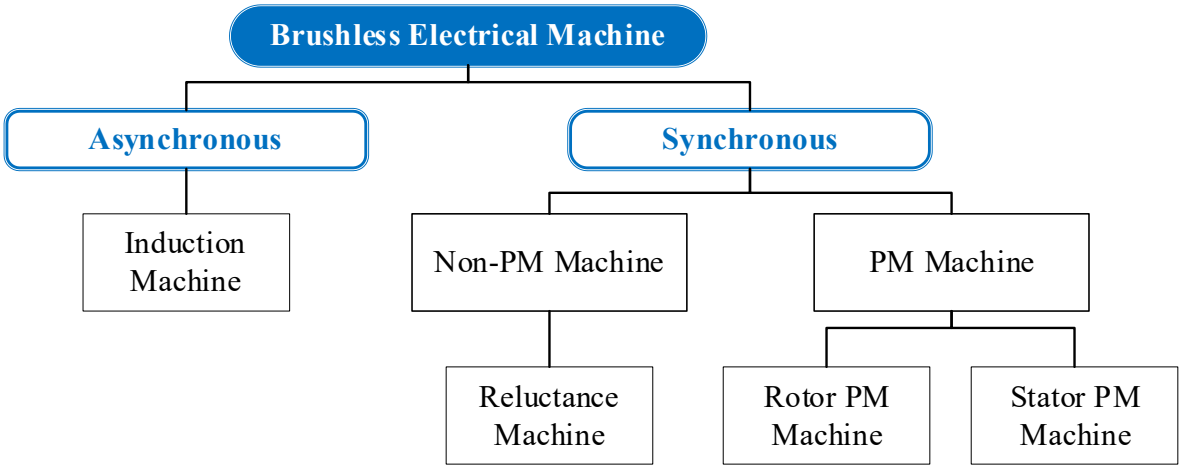

Fig. 1.2 Classification of brushless machines.

Induction machine, Fig. 1.3 (a), is a typical asynchronous machine that has the advantages of robust, reliable, and low cost. However, the control of induction machines is relatively complex due to asynchronous magnetic field rotation in stator and mechanical rotation in rotor.

A very different type of machine is synchronous machine, which includes non-PM machines and PM machines. Reluctance machine shown in Fig. 1.3 (b) is a kind of non-PM machine. Due to simple structure, reluctance machines can be used in harsh working environments. Nevertheless, the power density, i.e. power per unit volume or per unit weight, for the non-PM machines tends to be relatively low.

With the requirement of higher power density, PM machines, especially rare earth PM machines, are a competitive candidate. PM machines can be classified into two categories: rotor PM machines and stator PM machines. The two most common types of rotor PM machines are surface-mounted PM (SPM) machines and interior PM (IPM) machines shown in Fig. 1.3 (c) and Fig. 1.3 (d), while the two typical types of stator PM machines are flux reversal permanent magnet (FRPM) machines and switched flux permanent magnet (SFPM) machines illustrated in Fig. 1.3 (e) and Fig. 1.3 (f). Due to the limitation of complex stator and the relatively poor overload capability of stator PM machines, rotor PM machines are more popular in wide applications. In consequence, the rotor PM synchronous machine is the focus of this thesis.

However, due to high cost and some volatility in the supply of rare-earth PM materials, there is continual pressure to reduce the volume of PM material required to achieve a given torque/power rating of PM machine. The torque density will be greatly diminished if very low-cost PM materials, such as ferrites, are used for substituting rare-earth material. In an attempt to realize a cost-effective solution, magnet arrangement in PM machines has been optimized to improve the utilization of magnet material. Consequent pole (CP) PM machines, Fig. 1.4, in which only alternate poles are equipped with PMs, have been identified as one excellent means of reducing PM volume in machines, albeit there are several challenges to overcome in their design to remain competitive in terms of overall machine performance. It has been reported that approximately 33% saving in the quantity of PM can be realized for fractional slot concentrated winding (FSCW) consequent pole permanent magnet (CPPM) machines while

maintaining similar output torque as its conventional SPM machine counterpart [Chu15]. Besides, the CPPM machines are also found to have better flux weakening performance. Therefore, CPPM machine has been widely investigated in recent years and it is also the object of this thesis. However, due to the large armature reaction, CPPM machines suffer from poor overload capability and large iron loss. In addition, the torque ripple for CPPM machines tends to be large. With the higher and higher requirements of torque density, torque quality, and efficiency, the application of CPPM machines is limited. At present, the CPPM machines are claimed to have application prospects in electric vehicles (EVs) [Chu16], downhole electric drilling systems [Che21], ceiling fan [Sha21], industrial cooling fan [Liu22], rope-less elevator [Xu20], injection pumps [Gha19] [Asa13], refrigerant compressor [Hu18], and so on. These PM topologies will be introduced in detail in the following section.

This chapter will review the state of art of CPPM machines. Section 1.2 will introduce the PM machine topologies and demonstrate the relationship of CPPM machines with other machines. After that, the various topologies of CPPM machines will be reviewed in Section 1.3. Focusing on the rotor PM consequent pole machines, the achievements in solving or mitigating the problems in CPPM machines are overviewed in Section 1.4. Finally, in Section 1.5, the research scope and contributions of this thesis will be illustrated.

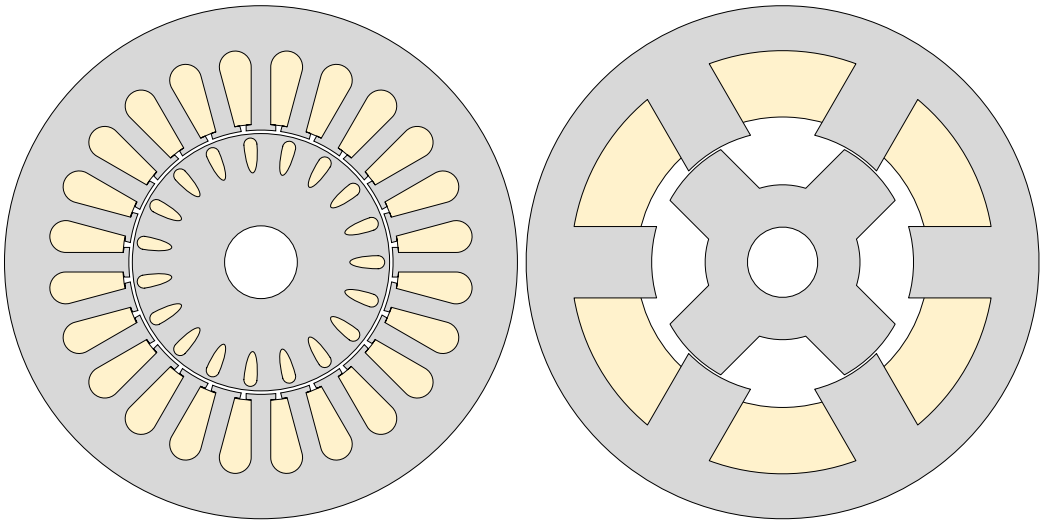

(a) Induction machine (b) Reluctance machine

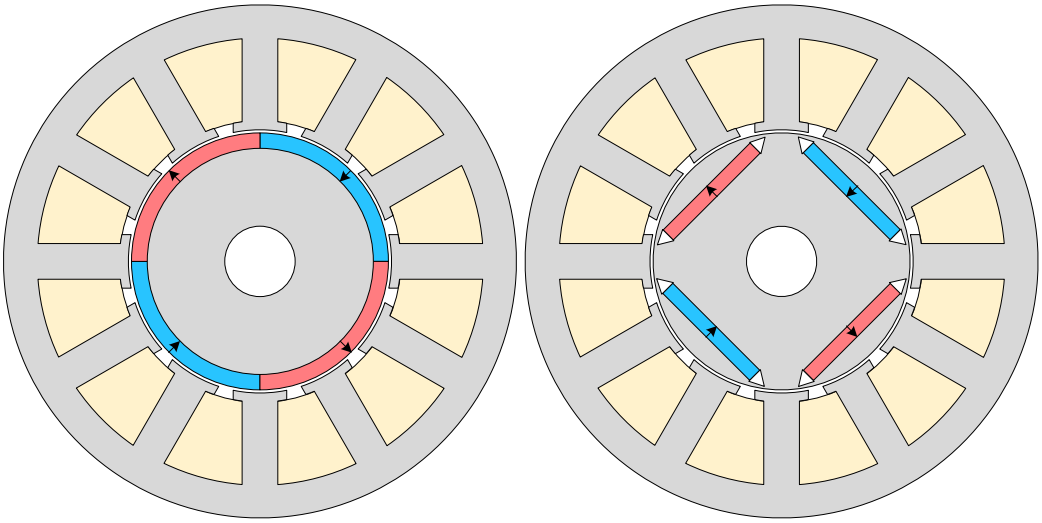

(c) SPM (d) IPM

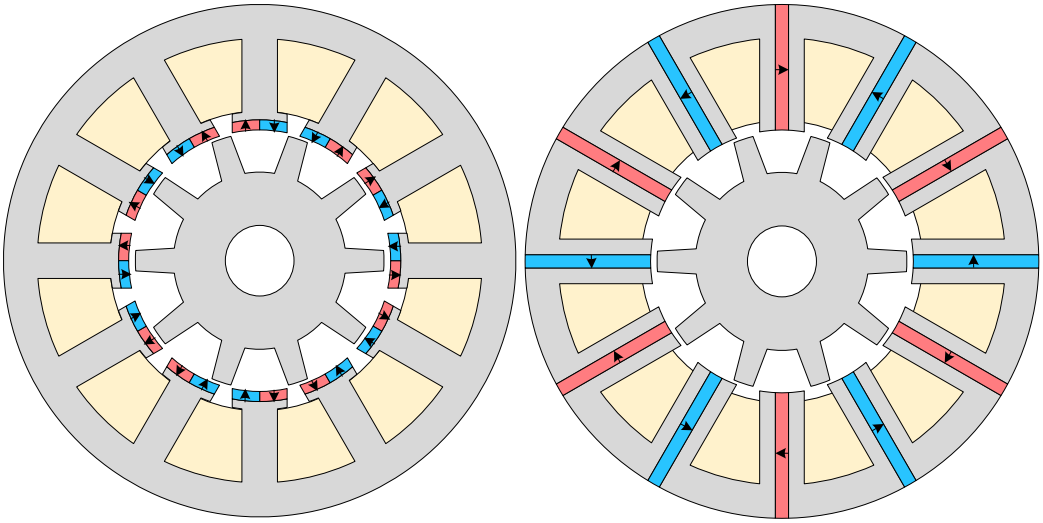

(e) FRPM (f) SFPM

Fig. 1.3 Typical brushless electrical machines.

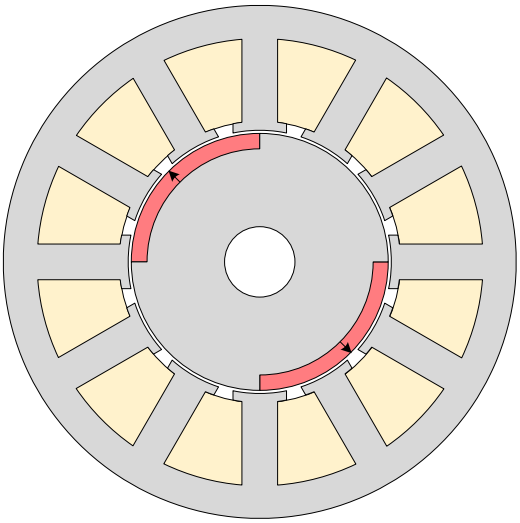

Fig. 1.4 Structure of CPPM machine.

1.2 Permanent Magnet Synchronous Machines

In this section, the winding topologies and the PM topologies will be introduced. The classification of PM synchronous machines is presented in Fig. 1.5.

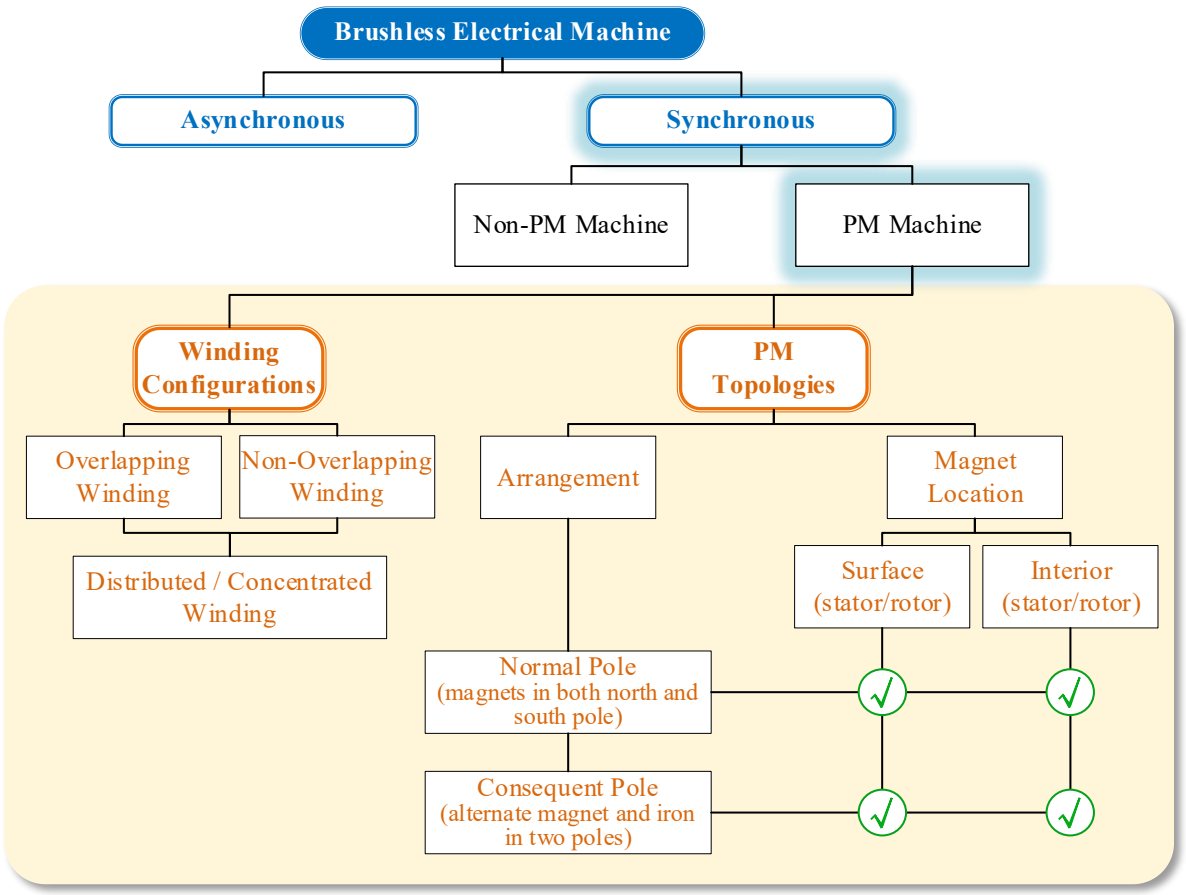

Fig. 1.5 Classification of PM synchronous machines.

1.2.1 Winding Topologies

There are mainly two types of winding configurations, namely overlapping winding (OW) and non-overlapping winding (non-OW).

As shown in Fig. 1.6 (a) and Fig. 1.6 (b), OW is usually employed in the machine with the slot per pole per phase equal to or larger than 1, including distributed winding (DW) and concentrated winding (CW) machines. The benefits of OW are a relatively high winding factor and fewer magnetomotive force (MMF) harmonics as shown in Fig. 1.7 (a) and Fig. 1.7 (b). Normally, the lowest order harmonic in MMF with the highest amplitude is the working harmonic in machines with OW. Further, the reluctance torque can be utilized in OW machines.

However, the end winding is relatively long, which results in a high copper loss and a low power density. It should be mentioned that for 12s2p machine, Fig. 1.6 (a), the coil pitch is usually 5 in application to reduce the end winding length but with the same MMF waveform as shown in Fig. 1.7 (a).

On the contrary, when non-OW is equipped in a machine, the end winding can be reduced significantly. The typical configurations for non-OW are shown in Fig. 1.6 (c) with tooth wound windings. Therefore, the efficiency and power density of non-OW machines tend to be improved compared with OW machines. It is worth noting that tooth wound winding is always a CW. In order to achieve a higher winding factor, this configuration is generally used in fractional slot machines with the slot per pole per phase smaller than 1. The MMF generated by this configuration contains more harmonics as presented in Fig. 1.7 (c) and Fig. 1.7 (d). Thus, with concentrated winding, the working harmonic may not be the lowest one. For example, the working harmonic for 12-slot/10-pole (12s10p) machine is the 5th harmonic while the lowest harmonic is the 1st.

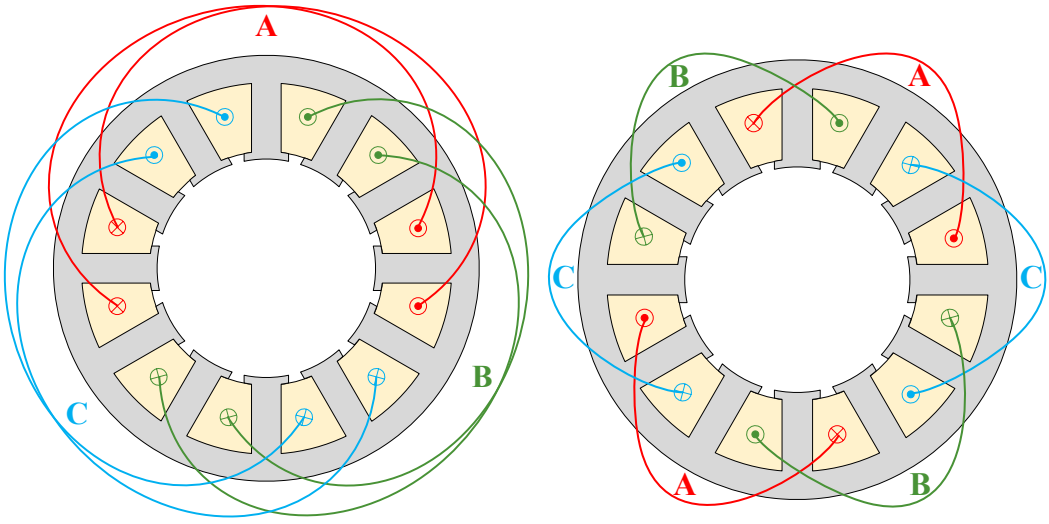

(a) OW (DW) (12s2p)

(b) OW (CW) (12s4p)

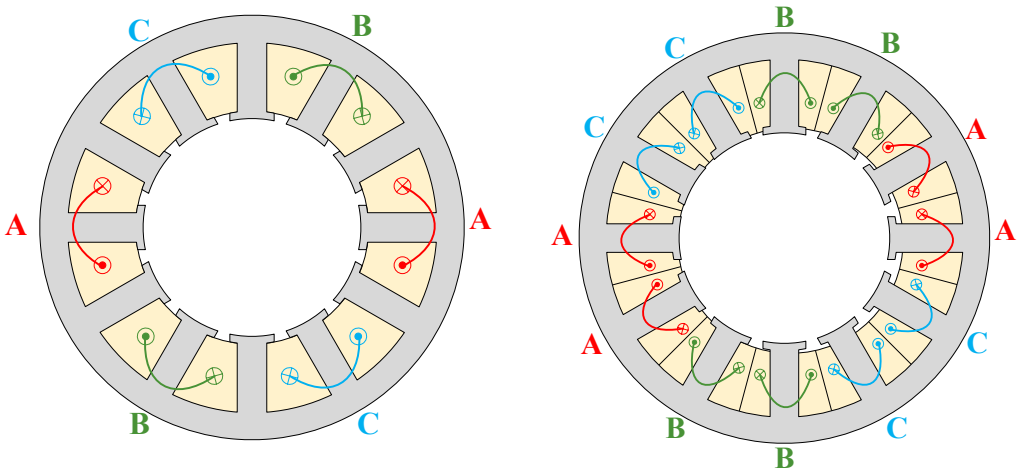

(c) Non-OW (CW) with single/double layer (12s10p)

Fig. 1.6 Winding configurations in PM machines.

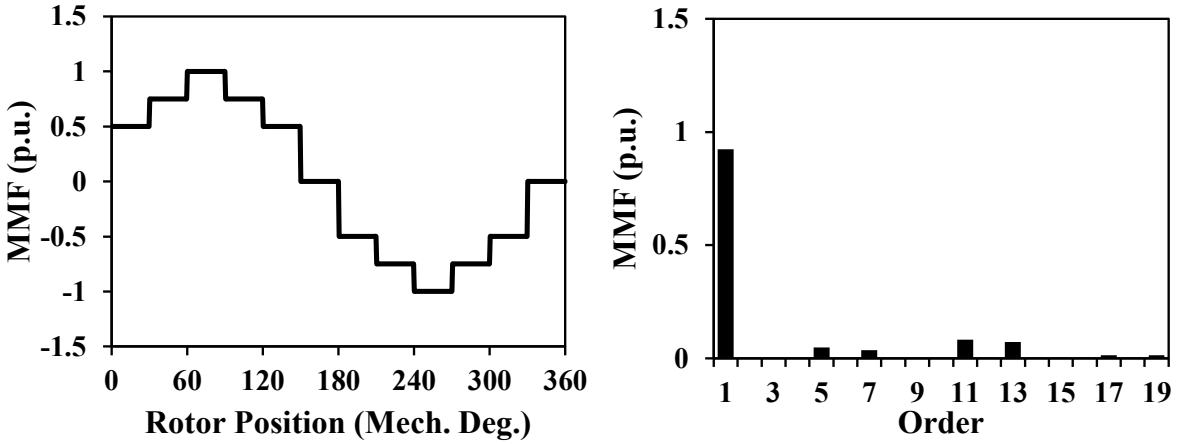

(a) MMF of the OW (DW) machine (12s2p)

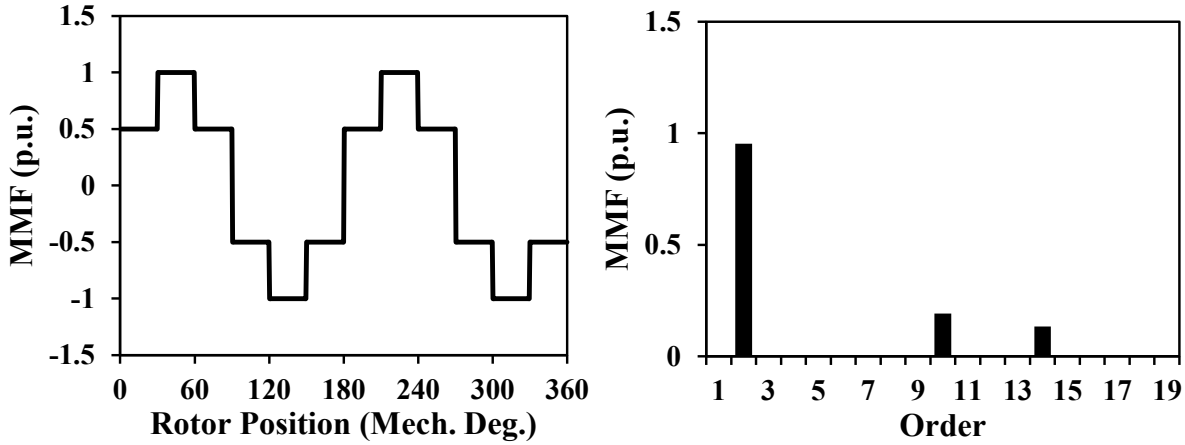

(b) MMF of the OW (CW) machine (12s4p)

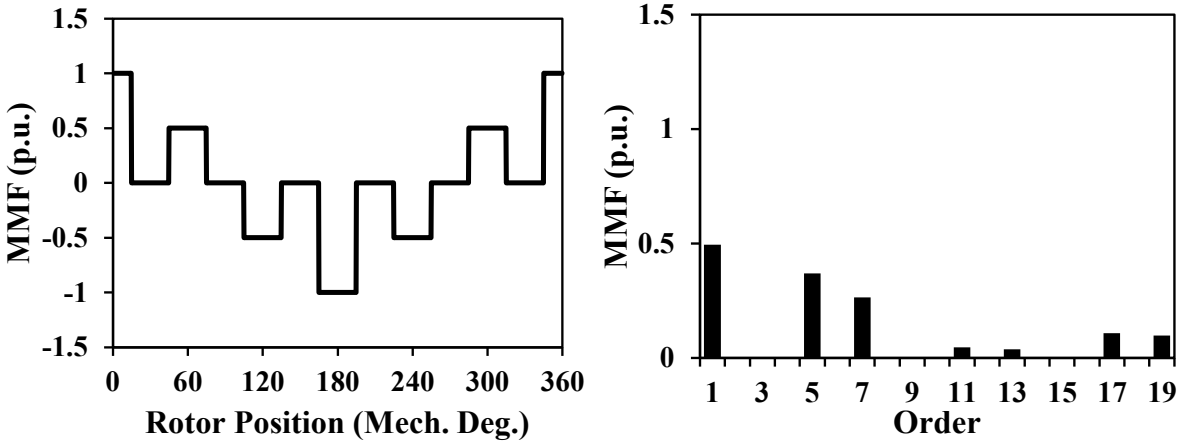

(c) MMF of the Non-OW (CW) machine with single layer (12s10p)

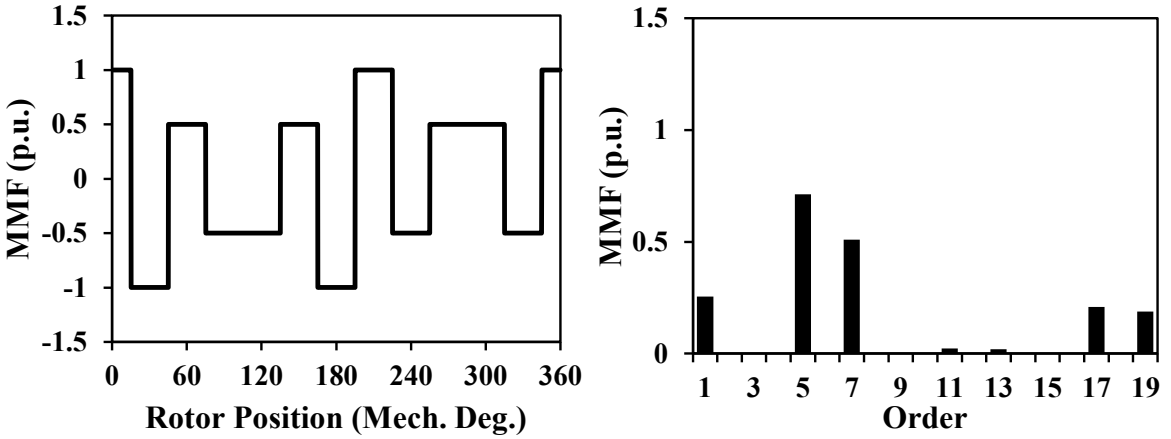

(d) MMF of the Non-OW (CW) machine with single layer (12s10p)

Fig. 1.7 MMF waveforms and spectra of OW and Non-OW machines.

1.2.2 PM Topologies

Generally, the magnets can be placed on the surface or the inside of the iron, including rotor iron and stator iron. When the magnets are placed on the rotor, two common structures shown in Fig. 1.8 and Fig. 1.9 are normally denoted as surface PM and interior PM rotors, respectively. When the magnets are placed on the stator, two common structures shown in Fig. 1.10 (a) and Fig. 1.10 (b) are normally denoted as FRPM and SFPM stators, respectively.

The structures with magnets on the rotor surface can be categorized into three main types as shown in Fig. 1.8, namely surface-mounted PM, surface inset PM, and Halbach PM. The SPM structure is simple for the manufacturer but there is no reluctance torque, which to some extent weakens the torque capabilities and particularly the ratio of torque per PM volume. Due to the

iron saliences between magnets, the surface inset PM has reluctance torque and the structure makes it easier to fix the PMs. However, since the magnetic pole arc width is reduced as well as the larger flux leakage, the average torque of the machine with surface inset PM structure will be relatively reduced. To improve the PM flux and PM torque, the magnets can be magnetized along the direction of the flux path, which forms the Halbach structure. However, a large number of magnets and a complex magnetization process diminish its advantages.

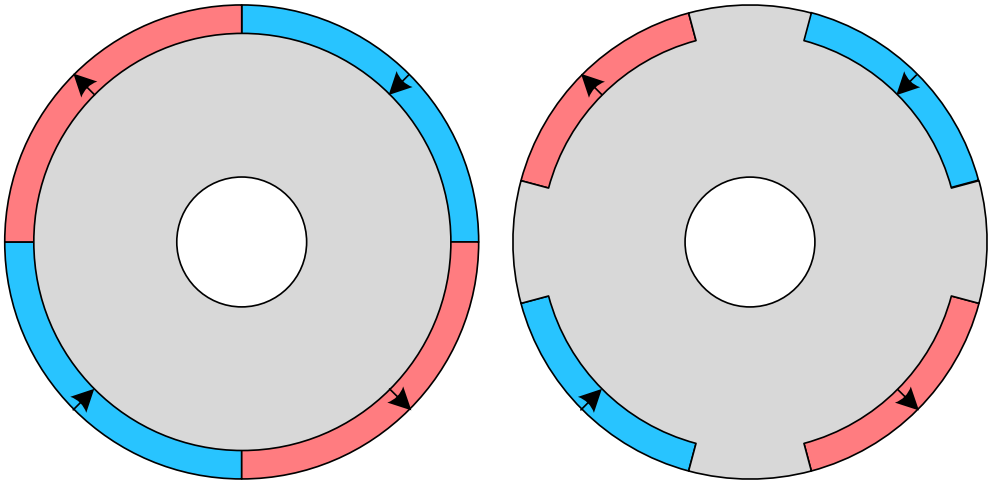

(a) SPM (b) Surface inset PM

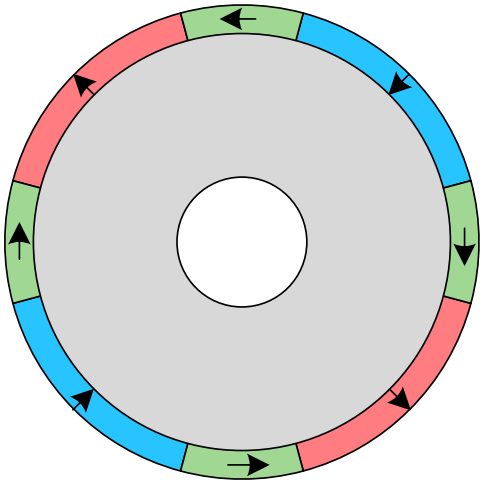

(c) Halbach PM

Fig. 1.8 Rotor surface PM structures.

Rotor interior PM topologies can be divided into five types as illustrated in Fig. 1.9, i.e. I-type, V-type, Δ-type, hybrid-type, and spoke-type. Reluctance torque for machines with interior PM

rotors can be utilized to improve the torque capabilities, especially under flux weakening conditions. The air spaces adjacent to magnets are working as flux barriers and can reduce flux leakages. The thin iron bridge is used for maintaining the mechanical strength of the rotor. Compared with the I-type IPM structure, the V-type and spoke-type structures can take advantage of the flux focusing effect thus enhancing the torque performance. By combining the features of I-type and V-type IPM structures, a hybrid-type rotor, which is usually called Δ-type, can be achieved. Hybrid-type rotors can be more flexible as another example is shown in Fig. 1.9 (d), which can provide even higher PM flux but with a relatively complex structure, which leads to high cost and manufacturing difficulties.

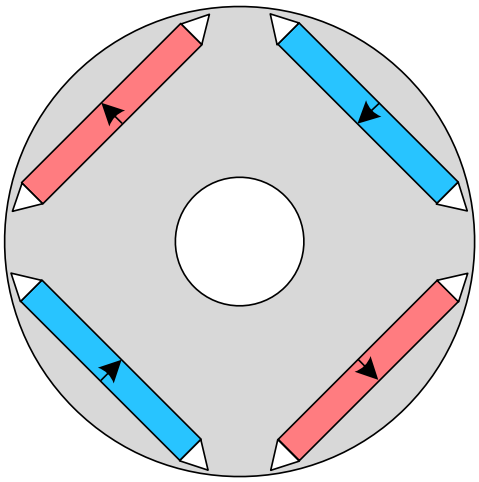

(a) I-type

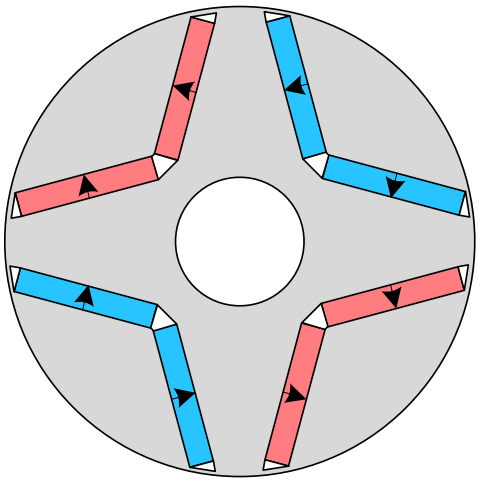

(b) V-type

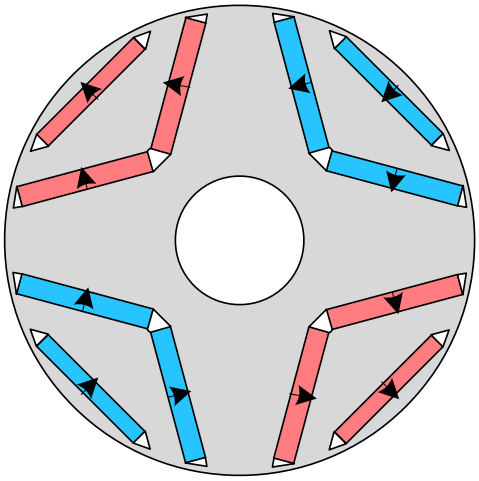

(c) Δ-type

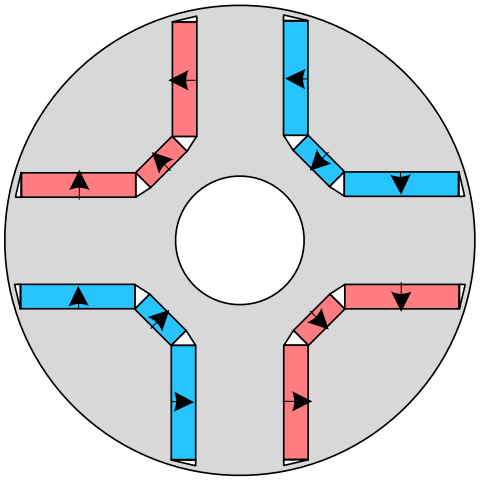

(d) Hybrid-type

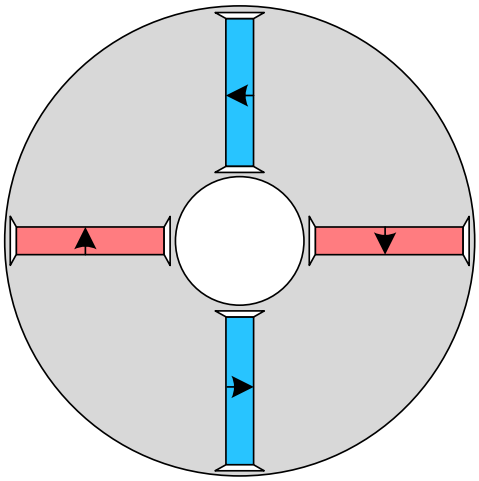

(e) Spoke-type

Fig. 1.9 Rotor interior PM structures.

The surface and interior PM structures can also be applied to the stator as two typical stator machines are shown in Fig. 1.10. The stator PM machines usually use the principle of magnetic gear effect thus owning the benefit of high torque density. Due to the magnet located on the stator, this kind of machine has comparatively simple thermal management. However, the overload capability is low and the stator is much more complicated, which limit their applications.

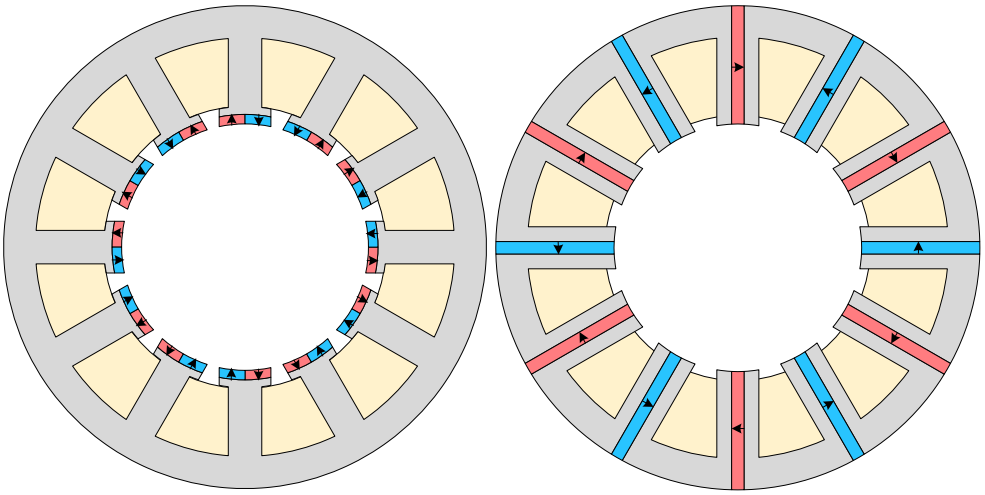

(a) FRPM stator (b) SFPM stator

Fig. 1.10 Stator PM topologies.

Normally, the north pole and the south pole are both formed by magnets as aforementioned PM topologies. However, to reduce the manufacturing cost, the arrangement of poles can be

changed to consequent pole arrangement, where alternate magnet poles are replaced by iron poles to form virtual poles. Thus, only unipolar magnetized PMs are necessary for the CPPM rotor. Take SPM-CP machine, Fig. 1.11 (a), as an example, for the CPPM machine with the same pole pair number as the SPM counterpart, the magnet number can be halved. Such behavior can be applied to almost all the surface and interior PM topologies, including both stator and rotor as demonstrated in Fig. 1.11 - Fig. 1.13. It is worth mentioning that the spoke-type is also a special kind of CPPM arrangement, which can be treated as the V-type IPM-CP arrangement with parallel magnets for one pole. But from the perspective of CPPM, the pole arc spans for north and south poles can be unequal for spoke-type IPM-CP arrangement [Li19h] as shown in Fig. 1.12 (e).

As a dominant part of the material cost, the number of magnets and the amount of magnet for the machines with CPPM arrangement can be reduced compared to the normal poles [Chu15] [Gha19]. Simultaneously, it is also found that the average torque for CPPM machines can be almost unchanged [Chu15] [Zha19a]. Consequently, CPPM arrangement has drawn more and more attention in recent years. However, the different features between north and south poles also inevitably introduce many problems, such as even order harmonics in air-gap flux density, odd order torque ripple harmonics, and so on. Therefore, much research has been developed to solve or mitigate those problems.

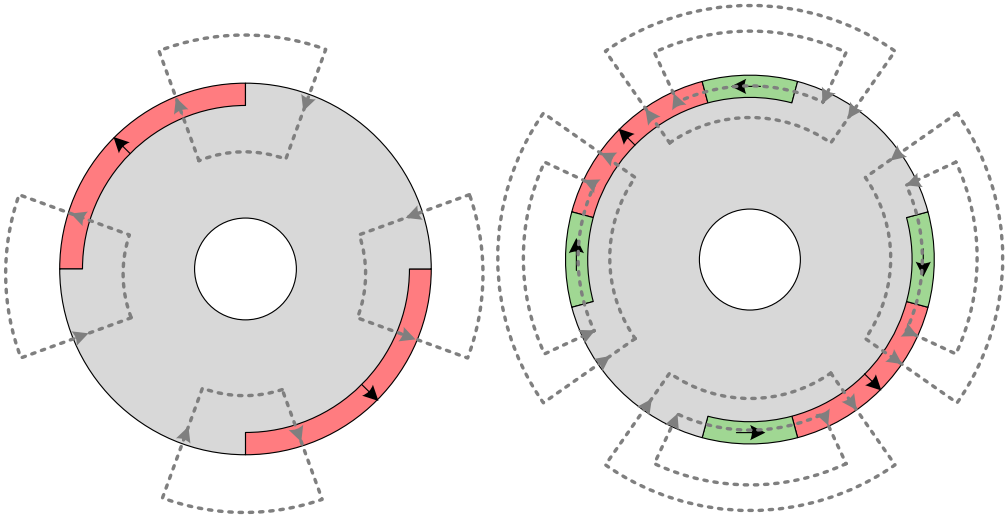

(a) SPM-CP (b) Halbach PM-CP

Fig. 1.11 CPPM arrangements with rotor surface PM topologies.

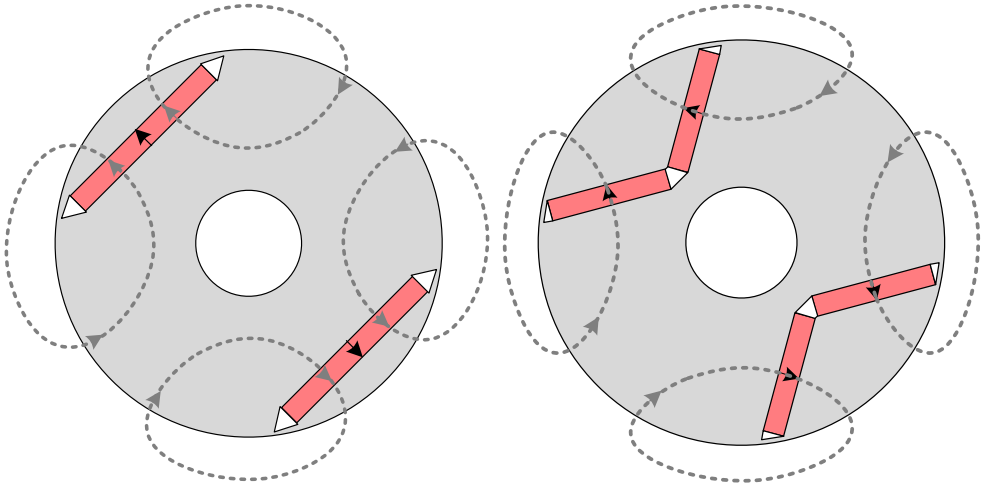

(a) I-type IPM-CP (b) V-type IPM-CP

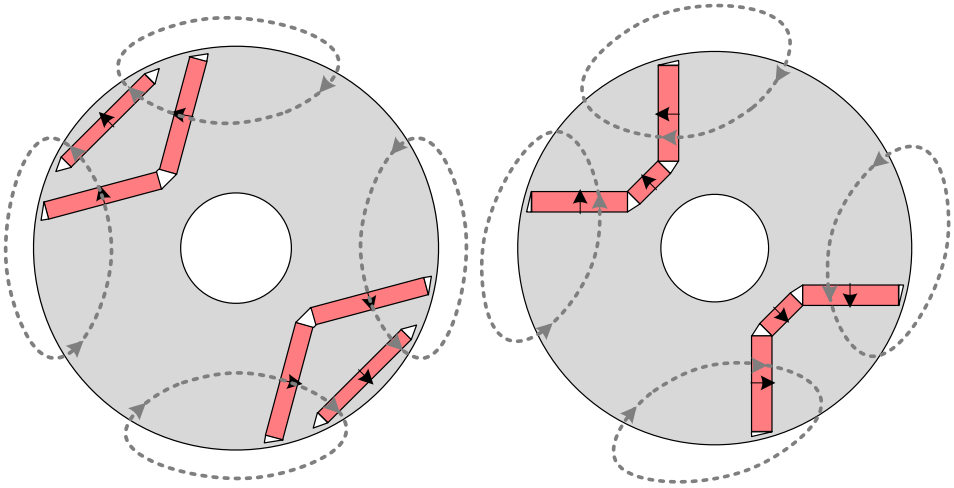

(c) Δ-type IPM-CP (d) Hybrid-type IPM-CP

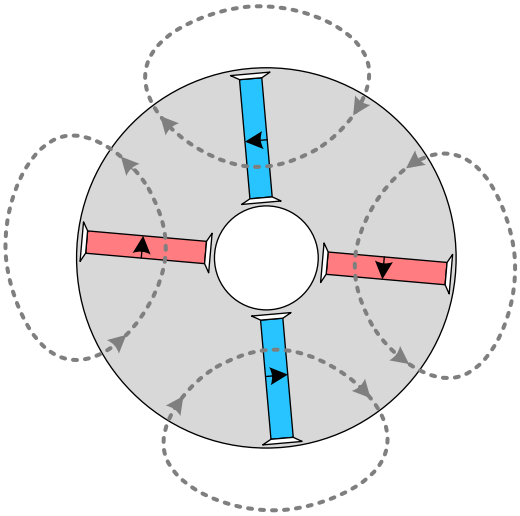

(e) Spoke-type IPM-CP

Fig. 1.12 CPPM arrangements with rotor interior PM topologies.

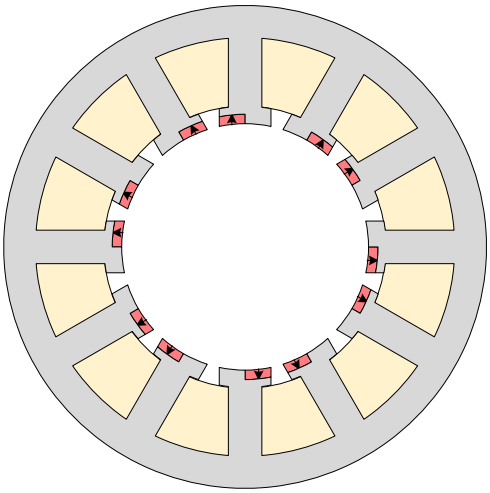

Fig. 1.13 CP arrangement with stator PM topologies.

Although there are various topologies of CPPM arrangement, the scope of this thesis focuses on the CPPM arrangement with rotor surface-mounted PM topologies but the findings are equally applicable to other rotor topologies. The state of art for CPPM arrangement will be reviewed in detail in the next section.

1.3 Consequent Pole Permanent Magnet Machines

1.3.1 Basic Introduction of CPPM Machines

It was reported in 1978 that machines with CPPM arrangements can save half of the PM material with only a 20% decrease in average torque [Kol78]. In 1986, the consequent pole rotor was pointed out to have the capability to reduce the susceptibility of the magnet to thermal degradation caused by the heat-shrinking operation [Mcc86]. Similar conclusions are also drawn in 1994 [Hen94]. It has been verified in the subsequence research that the CPPM machine can increase PM material utilization, i.e. ratio of torque to PM volume, in cost-sensitive applications. This is mainly due to almost unchanged PM flux for CPPM machines with less PM amount compared with SPM counterparts. To aid the understanding of this behavior, conventional SPM and SPM CPPM machines are selected as examples in this section and their flux paths are illustrated in Fig. 1.14. Supposing the permeability for stator and rotor irons are infinite and for the magnet is the same as air, the magnet fluxes for SPM machine φ_{SPM} and CPPM machine φ_{CPPM} can be obtained.

$$\varphi_{SPM} = \frac{2Fc_{PM}}{2R_{PMi} + 2R_{AG}} \tag{1.1}$$

$$\varphi_{CPPM} = \frac{Fc_{PM}}{R_{PMi} + 2R_{AG}} \tag{1.2}$$

where Fc_{PM} is the magnetic potential of PMs, R_{AG} is the flux reluctance in air-gap, R_{PMi} and *is* the flux reluctance in magnets for SPM and CPPM machines. When neglecting R_{AG}, the PM flux for CPPM machines can be the same as that for SPM machines. However, due to the exists of R_{AG}, the PM flux and hence the output torque for CPPM machines tend to be lower than those for SPM machines.

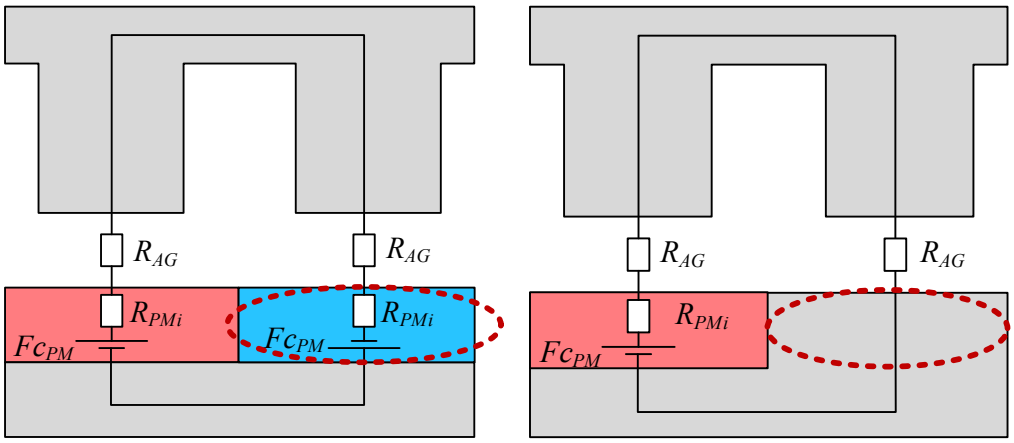

(a) SPM (b) SPM CPPM

Fig. 1.14 Flux path in one pole pair.

As shown in Fig. 1.14, since one magnet has been replaced by iron, the air-gap flux density will be reduced and hence the thickness of the remaining one magnet should be increased. Further, the reluctance for armature reaction field has been significantly reduced (since the permeability of the magnet is equivalent to the air for the armature reaction), the armature reaction field will be significantly increased. Consequently, the winding inductance in CPPM machine is much larger than that in SPM machine. Similarly, the overload capability of CPPM machine is much lower than that in SPM machine due to magnetic saturation. It is unsurprising that compared with SPM machines, CPPM machines tend to show better performances under light load conditions.

It is important to select proper parameters in CPPM machines, such as PM pole thickness and arc width, as well as split ratio, in order to achieve similar output torque as that of the SPM machine [Chu15] [Li18a] [Li18b] [Bai18].

Apart from high torque per PM volume, CPPM machines also possess better flux weakening capability compared to conventional SPM machines [Zho19b]. This is due to the larger inductance L, whose definition of winding inductance can be derived as:

$$L = \frac{{N_{TPW}}^2}{R_m} \tag{1.3}$$

where N_{TPW} is the number of turns of a winding and R_m is the flux reluctance along the flux circuit. Clearly, due to the reduced R_m for CPPM machine, the inductance L can be improved, including both d- and q-axes inductances, which means that the armature reaction is significant.

As is well known, when the phase current reaches the characteristic current, the optimal flux weakening condition can be achieved. The characteristic current I_{ch} can be expressed as:

$$I_{ch} = \frac{\psi_d^{PM}}{L_d} \tag{1.4}$$

where ψ_d^{PM} and L_d are the d-axis PM flux linkage and inductance, respectively. It is clear that for CPPM machine, the relatively larger inductance and smaller PM flux linkage can result in lower characteristic current thus realizing better flux weakening performance.

Additionally, benefitting from the smaller PM area for CPPM machines, the PM eddy current loss can also be reduced in CPPM machines [Gha19].

From the above discussions, the advantages of CPPM can be summarized as follows:

1. The lower amount of PM leads to cost reduction, including both fabrication and maintenance.

2. Flux weakening performance is better [Zho19b].

3. The eddy current losses in the magnet can be reduced [Gha19].

Apart from the aforementioned advantages, there are also many other special characteristics of CPPM arrangement, such as special flux paths for rotor suspension force in bearingless machines and flux modulation effect in magnetically-geared machines. Therefore, CPPM arrangement is also widely used in many other novel structure machines, including the bearing-less machine, hybrid excited machine, vernier machine, stator PM machine, and so on. Given their potentials and in particular the scope for marked reductions in the quantity of magnet required to meet a given specification, CPPM machines have been employed in many applications, such as EVs [Chu16], downhole electric drilling systems [Che21], ceiling fan [Sha21], industrial cooling fan [Liu22], rope-less elevator [Xu20], injection pumps [Gha19] [Asa13], refrigerant compressor [Hu18], and so on.

The arrangement of this chapter is shown in Fig. 1.15 and a detailed description of literature review in this chapter is summarized in Table 1.1. From three aspects: rotor PM, stator PM, and other CPPM machines, the works of literature will be reviewed in this section.

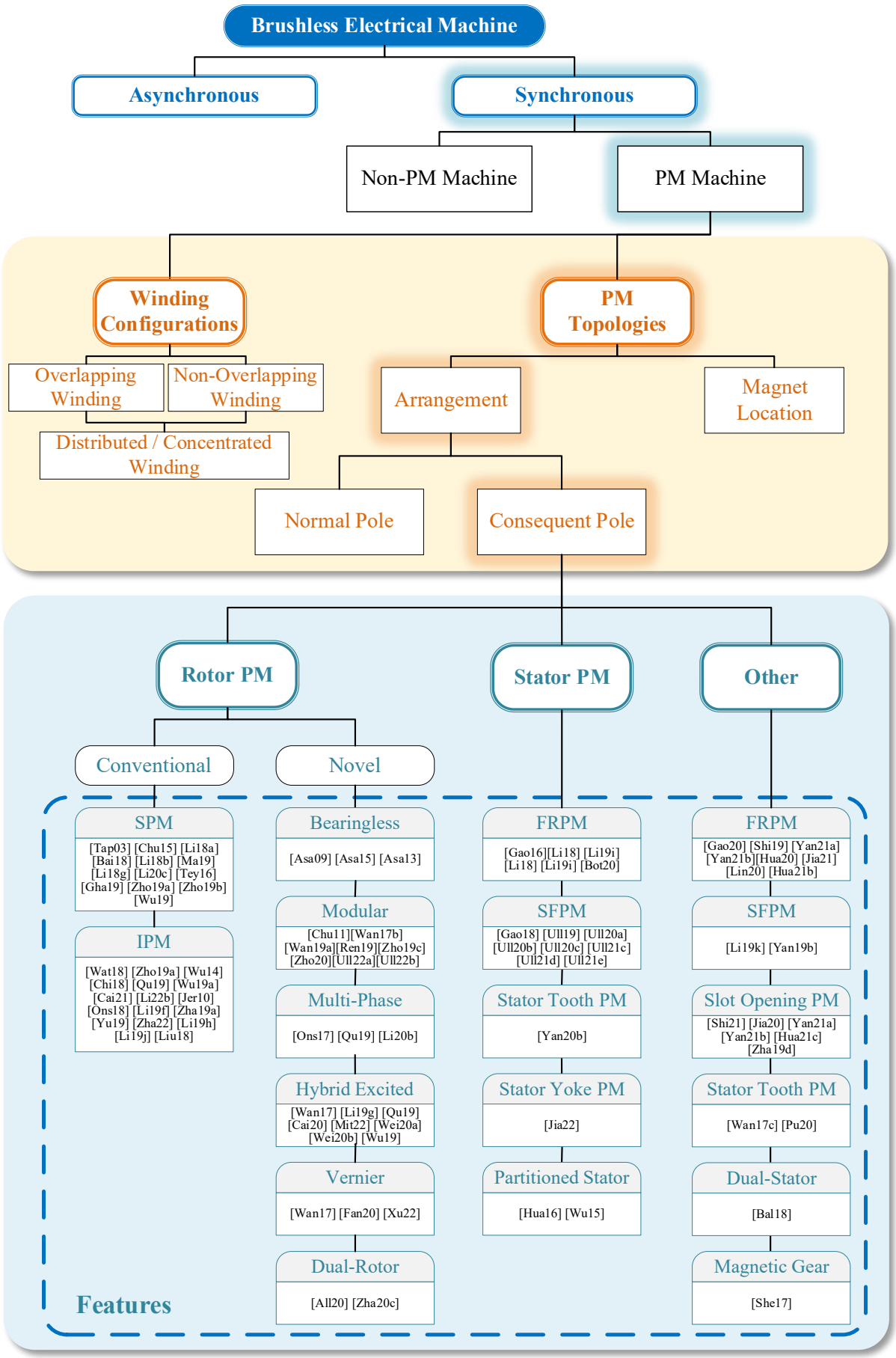

Fig. 1.15 Arrangement of section 1.3.

Table 1.1 Review of literature for CPPM machines.

Reference	Feature	Remark
Rotor PM - Conventional		
[Kol78] [Mcc86] [Hen94]	SPM-CP	Found the potential of reducing magnet amount and saving cost for CPPM machines in last century.
[Tap03]		Axially staggered CPPM rotor was proposed to enhance flux weakening capability
[Li18b] [Bai18]		Analytical method was developed to find out the optimum PM pole arc ratio which can achieve the largest average torque.
[Li18a]		Analytical method was developed to obtain the optimal split ratio.
[Ma19]		Investigated the inductance characteristics.
[Li18g] [Li20c]		Double-side field modulation effect was developed to demonstrate the torque mechanism.
[Tey16] [Gha19]		Subdomain method was utilized in SPM-CPM machines
[Zho19a] [Zho19b] [Wu19a] [Li19h]		Comparisons of SPM-CP and IPM-CP machines.
[Wat18] [Zho19a]	IPM-CP	Analyses of I-type IPM-CP machines.
[Wu14] [Chi18] [Qu19] [Wu19a] [Cai21] [Li22b]		Analyses of V-type IPM-CP machines.
[Jer10] [Ons18] [Li19f] [Zha19a] [Yu19] [Zha22]		Analyses of hybrid-type IPM-CP machines.
[Li19h] [Li19j] [Liu18]		Analyses of spoke-type IPM-CP machines.
Rotor PM - Novel		
[Asa09] [Asa13] [Asa15]	Bearingless	CPPM rotors can provide a special flux path and can ease the active magnetic suspension control in bearingless machines.
[Chu11]	Modular	Proposed a modular vernier machine to suppress the magnetic unbalance.
[Ren19] [Zho19c] [Zho20]		E-core and C-core stator CPPM machines.
[Ull22a] [Ull22b]		Performance and pole shaping are analyzed for H-core stator CPPM machines.

[Ons17] [Qu19] [Li20b]	Multi-phase	9-phase, 5-phase, and dual-3-phase CPPM machines are analyzed.
[Wan17a]	Hybrid excited	Adjust flux easily and can extend the speed range.
[Li19g] [Qu19]		Use the iron pole of CPPM rotor to provide field excitation flux path.
[Cai20] [Mit22]		Use the flux modulation effect of iron pole in CPPM rotor to provide extra output torque.
[Wei20a] [Wei20b]		Dual-stator machines are proposed.
[Fan20] [Xu22] [Wan17a]	Vernier	Vernier CPPM machines are proposed.
Stator PM		
[Gao16] [Li18f] [Li19i] [Qu21] [Wei22a] [Wei22b] [Bot20]	Flux reversal PM	Flux reversal machines with CPPM arrangement are proposed.
[Gao18] [Ull19] [Ull20a] [Ull20b] [Ull20c] [Ull21c] [Ull21d] [Ull21e]	Switched flux PM	Performances, including C-core/E-core stator shapes, coupled electromagnetic-thermal analysis, subdomain modeling, and so on are analyzed.
[Yan20b]	Stator tooth PM	Alternate teeth have PMs with the same magnetization direction.
[Jia22]	Stator yoke PM	PMs are set between stator yoke and teeth with the same magnetization direction.
[Hua16] [Wu15]	Partitioned stator	Partitioned stator structures with CPPM arrangement can improve torque density and efficiency.
Stator and rotor dual-PM		
[Gao20] [Hua20] [Jia21] [Lin20] [Hua21b]	Flux reversal PM	Combining the flux reversal CPPM stator and the SPM-CP rotor.
[Li19k] [Yan19b]	Switched flux PM	Combining the switched flux stator and CPPM stator and the SPM-CP rotor.
[Zha19d] [Shi21] [Hua21c] [Jia20] [Yan21a] [Yan21b]	Slot opening PM	Combining the stator with slot opening PM and SPM-CP rotor.
[Pu20] [Pu21] [Wan17c]	Stator tooth PM	Combining the stator with tooth PM and SPM-CP rotor.
[Bal18] [All20] [Zha20c]	Dual-stator/rotor	Dual-stator/rotor topologies are proposed with conventional or toroidal windings.
Magnetic gear		
[She17]	CPPM arrangement	By replacing SPM arrangement with SPM-CP arrangement, it was validated to have improved pull-out torque and offer additional reluctance torque.

1.3.2 Rotor Permanent Magnet CP Machines

1.3.2.1 Conventional CPPM machine

Although the CPPM arrangement was proposed in the last century, it has not been widely analyzed until the last two decades. Recently, more and more researchers paid attention to the special characteristics of CPPM arrangement.

SPM-CP machine is one of the most popular types among all CPPM machines. It has been found that machines with CPPM arrangements can improve the ratio of torque to magnet volume [Kol78]. Staggered CPPM rotor was proposed, which can extended field-weakening capability and enhance power density [Mai87] [Tap03]. [Chu15] analyzed the FSCW machines for low-speed direct drive and found that the CPPM rotor uses 33% less PM material than the conventional SPM rotor topology while maintaining almost equivalent rated output power. [Li18b] and [Bai18] used analytical methods to calculate the optimal PM pole arc ratio, namely the ratio of PM pole width to pole pitch, to obtain maximum torque and found that the optimum ratio is around 1.2-1.3. As a consequence, the wider PM pole and narrower iron pole for CPPM machines are widely used. Equivalent magnetic circuit method was adopted in [Li18a] to obtain the optimal split ratio of CPPM machines. The results showed that the optimal PM pole arc ratio is determined by the ratio of the air-gap length to the PM thickness. [Ma19] analyzed the variation trend of the winding self-inductance by equivalent magnetic circuit method. The results showed that the 36-slot/32-pole (36s32p) machine has large first order harmonic in self-inductance over one electrical cycle, while the 48s40p machine only has even order harmonics as is the same as conventional normal pole PM machines. However, the resultant reluctance torque characters were not mentioned and the relationship between inductance characteristics and pole/slot number combinations was not summarized. A double-side field modulation effect was developed in CW CPPM machines to demonstrate the torque production mechanism [Li18g] [Li20c] [Li22a]. It was reported that with the increase of gear ratio (ratio of the difference between slot number and rotor pole pair number to rotor pole pair number), the torque proportion produced by the field modulation effect firstly increases and then decreases. The critical point is the when the number of rotor pole pairs equals the number of slots. In 2016, A. Rahideh et al. applied the subdomain method on inner-rotor CPPM machines, Fig. 1.16 (a),

with both surface mounted and Halbach structures [Tey16]. Then, they analyzed the outer-rotor nonoverlapping-winding CPPM machine, Fig. 1.16 (b), with the subdomain method in 2019 [Gha19]. However, the subdomain model is quite complex and hard to analyze irregular shapes in pole-shaped machines. Besides, only linear material was taken into consideration in all the analytical models while CPPM is easy to be saturated.

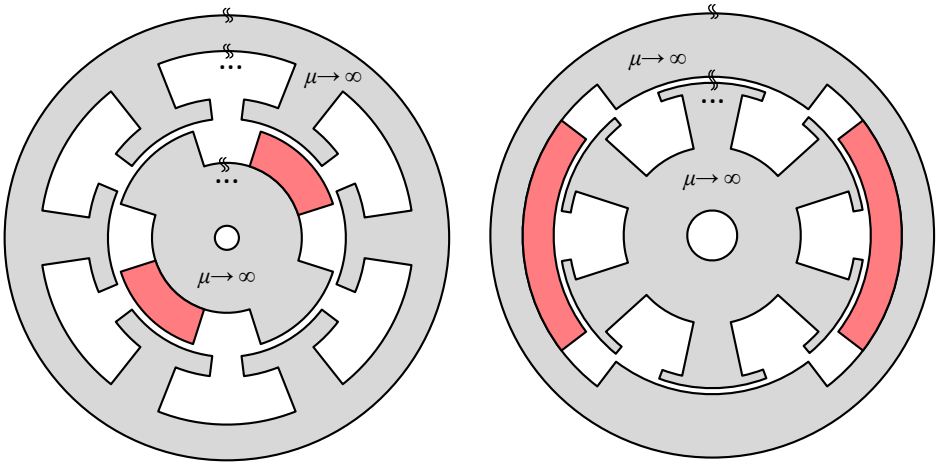

(a) Inner Rotor (b) Outer rotor

Fig. 1.16 Inner and outer rotor CPPM machines in [Tey16] and [Gha19]

[Zho19a] [Zho19b] compared the characteristics of SPM-CP, I-type IPM-CP, and V-type IPM-CP machines with integer slot (IS) and fractional slot (FS) windings. Results illustrated that the IS CPPM machines have lower PM loss than FS CPPM machines, while the FS CPPM machines have better flux weakening capability. Additionally, SPM-CP machines have higher average torque than IPM machines. But compared with the IS SPM-CP machine, the FS SPM-CP machine has a larger torque ripple, which can be reduced by some methods. A similar conclusion was drawn in [Wu19a] where a V-type IPM-CP machine was compared with an SPM-CP machine.

For CPPM machines with interior PM topologies, various IPM-CP machines with I-type [Wat18] [Zho19a], V-type [Wu14] [Chi18] [Qu19] [Wu19a] [Cai21] [Li22b], Hybrid-type [Jer10] [Ons18] [Li19f] [Zha19a] [Yu19] [Zha22], and spoke-type [Li19h] [Li19j] [Liu18] PM structures are extensively developed and studied. Compared with SPM and SPM-CP machines, IPM-CP machine shows that a better demagnetization withstand capability compared with their

SPM and SPM-CPM counterparts [Zho19a]. L. Wu, and R. Qu compared the performances, including back electromotive force (EMF), torque density, overload capacity, losses, and speed range between V-type IPM machines and V-type IPM CPPM machines in 2014 [Wu14]. It showed that the V-type IPM CPPM machines have larger torque density and lower torque ripple than conventional pole IPM machines at rated conditions but the CPPM machine has lower overload capacity than the conventional pole IPM machine. Hybrid-type IPM-CP machines were investigated and compared with their conventional counterparts in [Yu19] [Zha22] and found that although the salient pole ratio of the consequent pole IPM machine is smaller compared with the conventional IPM machine, the flux-weakening coefficient is larger than the conventional one. The spoke-type CPPM machine was compared with SPM-CP, V-type IPM-CP machines in [Li19h] and the results showed that the spoke-type CPPM machine presents higher average torque than the SPM-CP machine. But the mechanical strength of spoke-type CP machines is relatively low.

1.3.2.2 Novel CPPM machine

CPPM structures are also widely used in many novel structure machines.

Due to the special flux path of the iron pole in the CPPM rotor, the angular detection of the rotor in bearing-less motor is not required for active magnetic suspension control, and there is no tradeoff problem between the torque and the suspension force [Asa09] [Asa15]. Only x-axis controlled bearing-less machines and both x- and y-axes controlled bearing-less machines were proposed in [Asa09] and [Asa15], respectively. To relieve the high saturation problem in rotor iron, the magnet shape was changed in [Asa09], Fig. 1.17 (a). A two-axes actively regulated consequent pole bearing-less motor with passive stable axial and tilting motions was proposed in [Asa13] but the 3-dimension structure is quite complex.

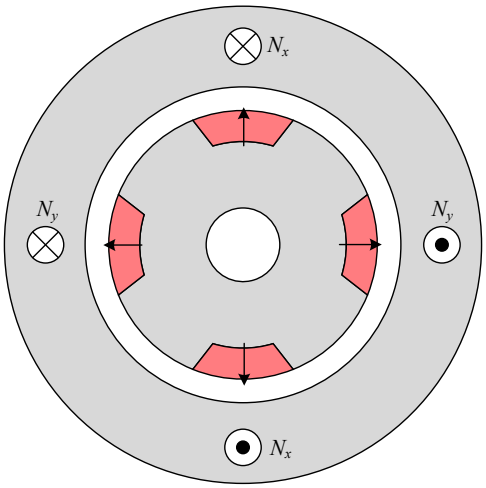

Fig. 1.17 Bearing-less CPPM structures.

CPPM structure is also widely used in hybrid excited machines, which is firstly proposed by E. Spooner in 1994 [Miz94]. In [Wan17a], a hybrid excited vernier CPPM machine, Fig. 1.18 (a), for EV application with DC field windings located between flux modulation poles was proposed which can adjust flux easily. A parallel hybrid excited CPPM machine was proposed in [Li19g], which used the iron pole to provide field excitation flux path. A similar idea was also used in [Qu19] where a hybrid-excited CPPM machine with unequal teeth was proposed and analyzed. As shown in Fig. 1.18 (b), [Cai20] used the flux modulation effect of iron pole in CPPM rotor to provide extra output torque on a 12s14p machine where the DC field coils are located on alternate tooth of the stator. With the same structure, [Mit22] analyzed the 12s16p and 12s20p hybrid excited CPPM machines. More complex, dual stator (DS) hybrid excited CPPM machines are proposed in [Wei20a] [Wei20b] where SPM-CP and Halbach PM-CP structures are placed on the rotor, respectively. Results demonstrated that the proposed machines can enhance the torque density and have good flux-regulating capability with field winding. Besides, the Halbach PM-CP structures can achieve a relatively high power factor. In [Wu19b], the subdomain method was developed on a dual stator CPPM machine but only open-circuit field was predicted. The dual stator machines with SPM-CP and Halbach PM-CP structures are demonstrated in Fig. 1.18 (c) and Fig. 1.18 (d). In general, the dual stator structures are too complex to be used.

Apart from the aforementioned hybrid excited vernier machines, normal vernier machines were also investigated [Fan20] [Xu22]. The rotor axially segmented method was utilized in [Fan20]

to reduce the torque ripple. However, two axially placed rotors need to be separated by a flux barrier but it was not mentioned in the paper. In [Xu22], the end windings of vernier CPPM machines were considered and the machines with CW have the potential to produce larger torque than those with DW.

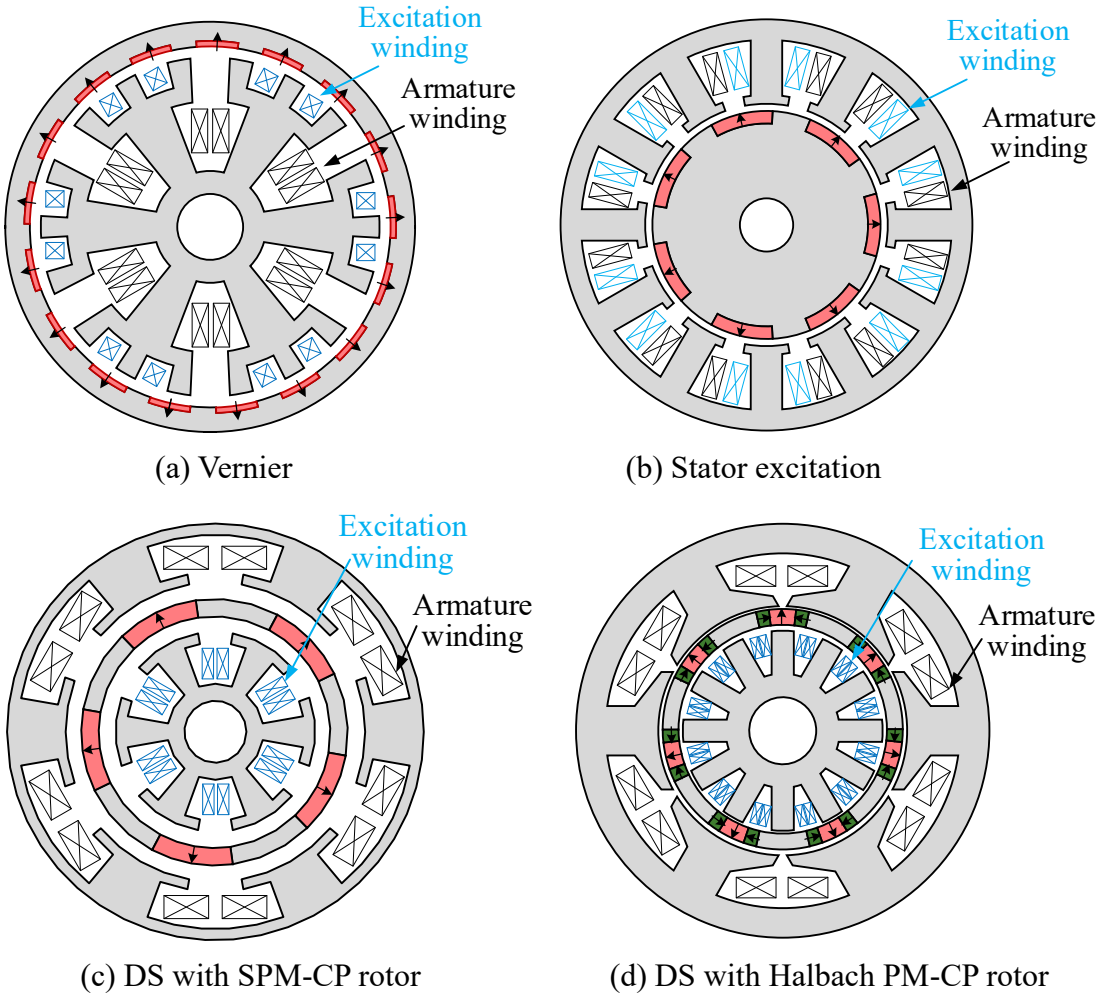

(a) Vernier (b) Stator excitation

(c) DS with SPM-CP rotor (d) DS with Halbach PM-CP rotor

Fig. 1.18 Hybrid-excited CPPM machine structures.

Modular structure has been widely studied for electrical machines. [Zhu18a] provides an overview of modularity techniques in PM machines, with both mechanical and electromagnetic aspects in the fields of domestic appliances, electric vehicles, aircrafts, and wind power generators being analyzed. The modular stator can also be applied to CPPM machines to achieve some goals. [Chu11] proposed a modular vernier machine that can suppress the magnetic unbalance caused by the CP rotor. In [Ren19], it was found that the output torques of the consequent pole modular machines are always higher than those of the inset modular machines. E-core and C-core stator, Fig. 1.19 (a) and Fig. 1.19 (b), with 12s10p and 12s14p

CPPM machines are analyzed in [Zho19c]. It was found that the E-core stator modules can improve the average torque of the 12s14p CPPM machines, while C-core structure can be a better candidate when relatively low torque ripple is desirable. Based on the E-core modular CPPM machines, the air spaces between stator modules are ideal for use as cooling channels and the influences of mechanical dimensions on the cooling effect were analyzed in [Zho20]. By extending the stator tooth for both E-core and C-core modular structures to the outer side, the H-shape modular machines can be achieved as shown in Fig. 1.19 (c), which have similar performances as the E-core and C-core modular machines [Ull22a]. The rotor pole shaping method with third order harmonic utilization was applied to the H-shape modular machines in [Ull22b] and shows good capabilities in torque ripple reduction and average torque enhancement. However, since the magnetic flux path is open, the outer windings, which are wound on extended teeth, are useless in [Ull22a] and [Ull22b]. This can be solved by adopting toroidal windings.

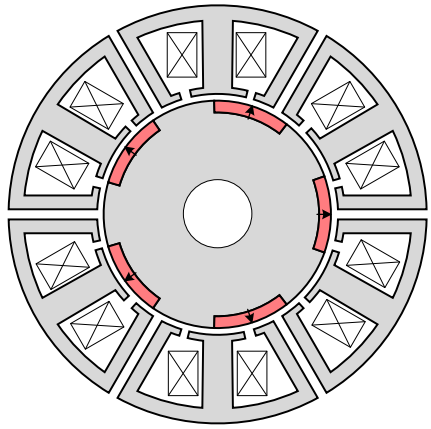

(a) E-core

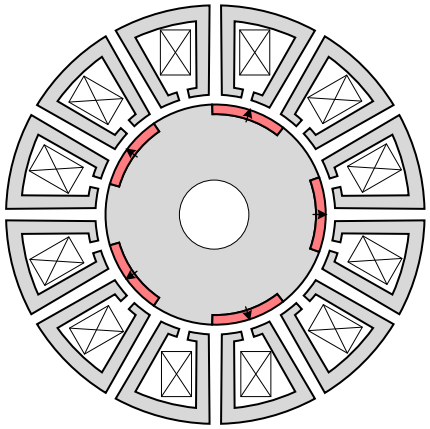

(b) C-core

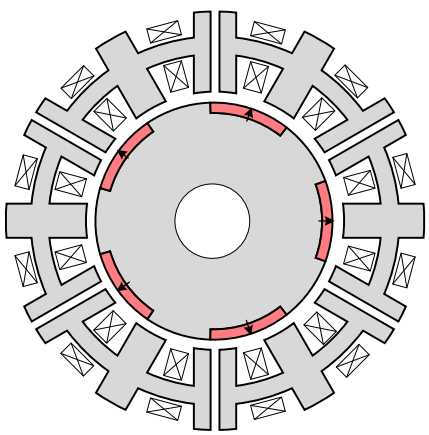

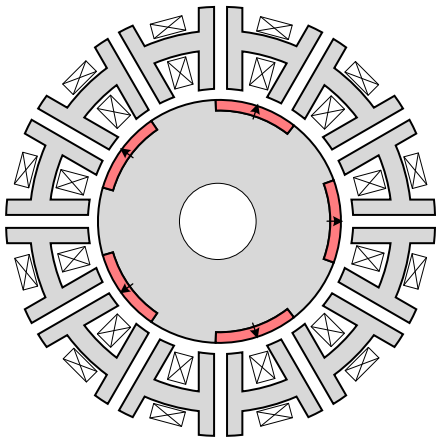

(c) H-core

Fig. 1.19 Modular CPPM structures.

Two dual-rotor CPPM machines were proposed in [All20] with the same pole numbers for inner and outer rotors where two sets of 3-phase windings are located on the inner and outer sides of the stator. It is easy to come up with the toroidal stator winding with the same structure as demonstrated in [Zha20c] and the structure was optimized to improve torque performance. The structure is demonstrated in Fig. 1.20.

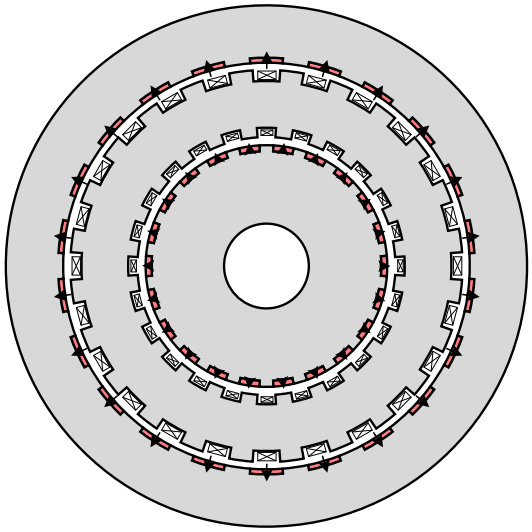

Fig. 1.20 Dual-rotor CPPM machine.

Multi-phase CPPM machines are also investigated in [Ons17] [Qu19] [Li20b]. A nine-phase CPPM synchronous motor is proposed, analyzed, and designed in [Ons17] where lower magnet cost, demagnetization risk, and temperatures can be achieved with the proposed machine. In [Li20b], four dual 3-phase winding topologies, i.e. two sets of 3-phase windings with 0°, 15°, 30°, and 60° displacements are analyzed. It is validated that the 30° displacement exhibits the highest average torque and better demagnetization withstand capability. Nevertheless, for CPPM machines, compared with single 3-phase machines, the multi-phase machines are rarely analyzed.

1.3.3 Stator Permanent Magnet CP Machines

Compared with rotor PM machines, stator PM machine structures are more flexible.

As illustrated in Fig. 1.21 (a), it was reported in [Gao16] that the flux reversal machine with CPPM structure can produce higher output torque. With a similar structure, the key design parameters were parametrically investigated and the impact on machine performance was

revealed in [Li18f] [Li19i]. After that, various types of flux reversal CPPM machines with or without field winding excitations were proposed and analyzed, including rotation machines [Qu21] [Wei22a] [Wei22b] and linear machines [Bot20].

CPPM structure in switched flux PM machine, Fig. 1.21 (b), can also achieve high torque capability [Gao18]. This structure is further comprehensively analyzed by W. Ullah, F. Khan, et al. [Ull19] [Ull20a] [Ull20b] [Ull20c] [Ull21c] [Ull21d] [Ull21e], including performances of C-core/E-core stator shapes, multi-objective optimization, coupled electromagnetic-thermal analysis, subdomain modeling, and so on. However, the complexity and the stator strength are the main problems of this structure.

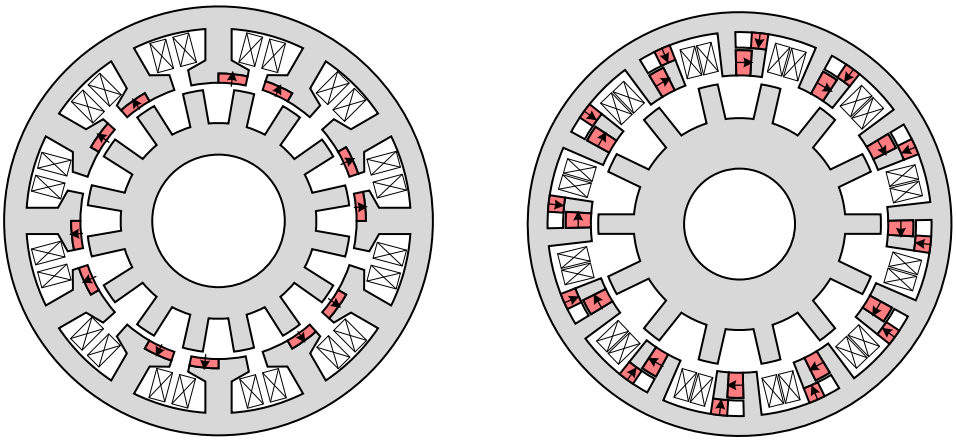

(a) Flux reversal CPPM machine (b) switched flux CPPM machine

Fig. 1.21 Flux reversal and switched flux machines with CPPM arrangement.

CPPM arrangement can also be placed on the stator tooth and stator yoke as shown in Fig. 1.22. [Yan20b] proposed a stator tooth CPPM reluctance machine. Axial segmented stators and rotors were also adopted in [Yan20b], which can eliminate even harmonics and thus lower cogging torque amplitude and torque ripple. [Jia22] used the ferrite PM to form CP arrangement in the stator yoke part to enhance the PM utilization ratio, while maintaining a relatively large torque density.

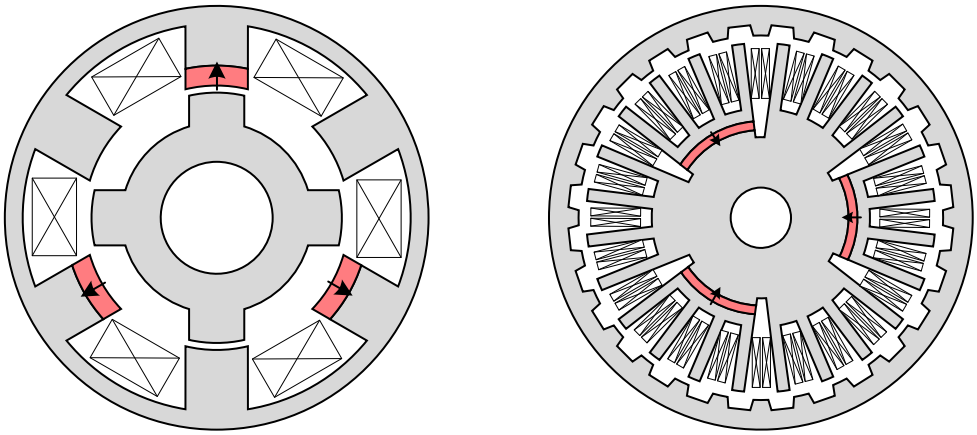

(a) Stator tooth PM machine [Yan20b] (b) Stator yoke PM machine [Jia22]

Fig. 1.22 Other stator CPPM structure machines.

Partitioned stator machines with CPPM structures are shown in Fig. 1.23 [Hua16] [Wu15]. The machine in [Hua16] exhibits a wide flux regulation range as well as good torque density. In [Wu15], a partitioned stator flux reversal CPPM machine was proposed with similar torque density and efficiency to the SPM counterpart.

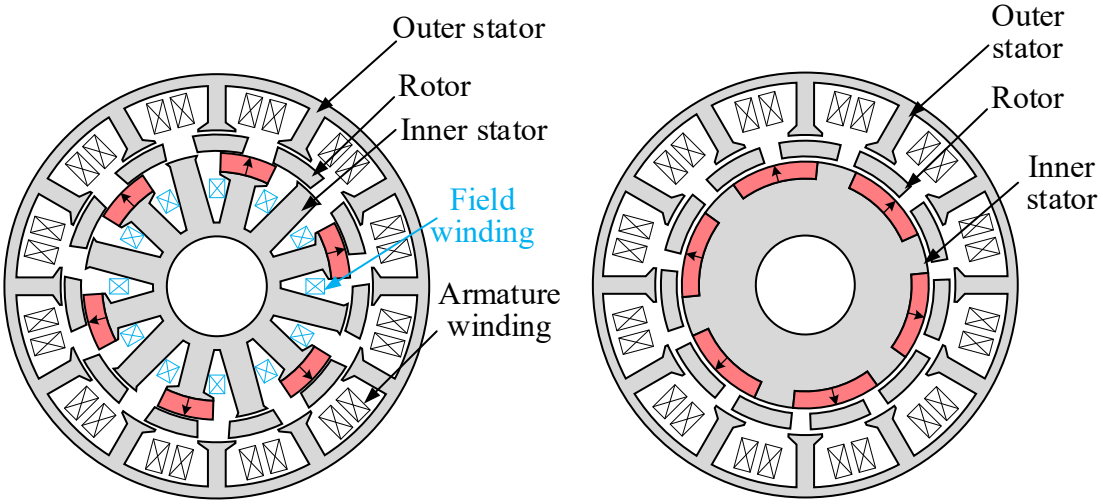

(a) Hybrid excited CPPM machine [Hua16] (b) FR CPPM machine [Wu15]

Fig. 1.23 Partitioned stator machines with CPPM arrangement.

1.3.4 Other CPPM Machines

CPPM structure can also be used in some special constructions, including stator and rotor dual-PM machines and magnetic gear machines.

By combining the flux reversal CPPM stator and the SPM-CP rotor, a double flux modulation flux reversal machine is obtained as demonstrated in Fig. 1.24. This structure was extensively studied and there are many variants [Gao20] [Hua20] [Jia21] [Lin20] [Hua21b]. A similar structure can also be applied in the linear machine to improve the thrust density as analyzed in [Shi19].

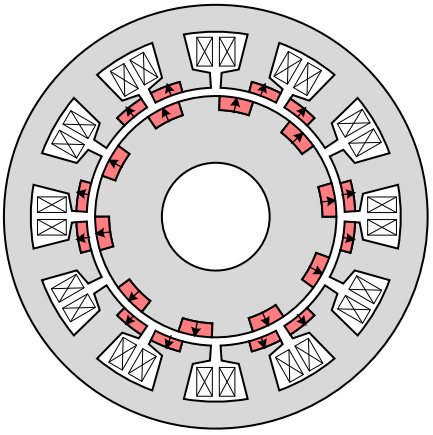

Fig. 1.24 Flux reversal machine with CPPM structure.

SPM-CP rotor combined with switched flux stator, Fig. 1.25, was analyzed in [Li19k] and [Yan19b]. With the help of the finite element method (FEM), some design guidance is concluded in [Yan19b].

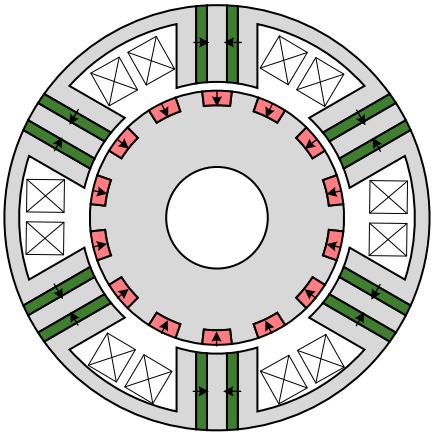

Fig. 1.25 Switched flux machine with CPPM structure.

With the same CPPM rotor structure, stator slot opening PM machines shown in Fig. 1.26 (a) can also enhance the torque capacity due to the bi-directional field modulation effect [Ish95] [Zha19d] [Shi21]. In [Hua21c] and [Jia20], the stator slot opening PMs were replaced by

Halbach array, which can enhance flux modulation harmonics and further improve the torque density. For the same aim, the Halbach array was moved to the rotor slot from the stator slot in [Yan21a] [Yan21b], Fig. 1.26 (b), to guide the flux into the rotor teeth and reduce the leakage flux, while a flux reversal CPPM stator was adopted. However, the demagnetization performances for those Halbach arrays tend to be a big challenge.

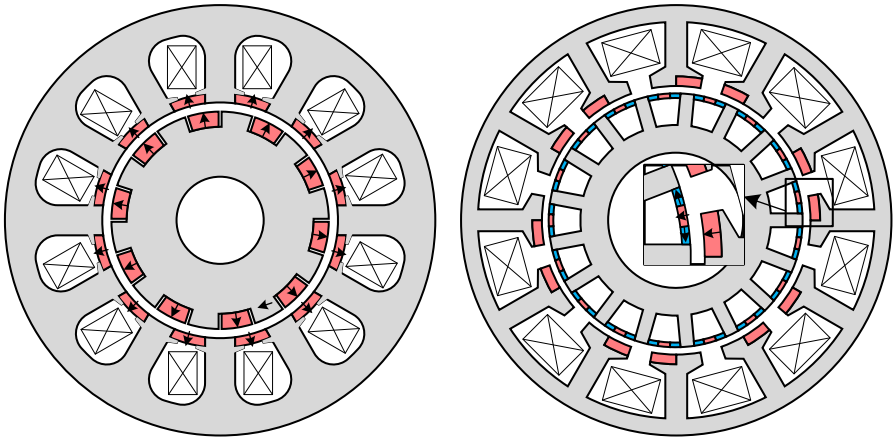

(a) Slot PM in stator (b) Slot PM in rotor

Fig. 1.26 Slot opening PM machine with CPPM structure.

As presented in Fig. 1.27, stator tooth PM stator and SPM-CP rotor can also be combined which has been studied in [Pu20] and [Pu21]. By introducing the field excitation winding in this structure, a hybrid excited machine was proposed in [Wan17c], which can achieve flexible flux adjustment.

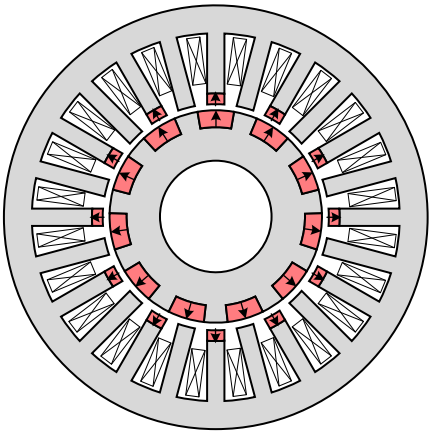

Fig. 1.27 Stator tooth PM machine with CPPM structure.

[Bal18] proposed a dual-stator consequent pole permanent magnet vernier machine that can realize high torque and PM utilization with the structure illustrated in Fig. 1.28 (a).

In addition, CPPM arrangement can also be utilized in coaxial magnetic gear, Fig. 1.28 (b), which was validated to have improved pull-out torque and offer additional reluctance torque [She17].

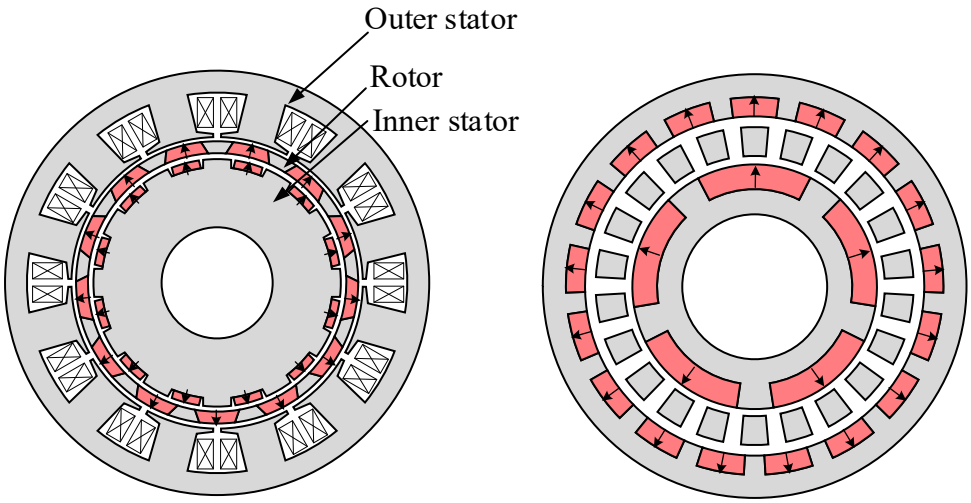

(a) Dual-stator (b) Coaxial magnetic gear with CPPM structures

Fig. 1.28 Structures of dual-stator machine and magnetic gear.

1.4 Challenges of Rotor PM CP Machines

Although various CPPM machines are introduced in section 1.3, the scope of this thesis is restricted to the rotor PM consequent pole machines. It has been found that there are many different characteristics of this kind of CPPM machine, including

- Unipolar axial flux leakage;
- Even order harmonics in back EMF;
- Higher torque ripple;
- Potential lower average output torque and overload torque capabilities than SPM counterpart; and
- Unbalanced magnetic force (UMF).

Therefore, many studies have been carried out to address these issues and they will be introduced in this section. The arrangement of this chapter is shown in Fig. 1.29 and the detailed descriptions are summarized in Table 1.2.

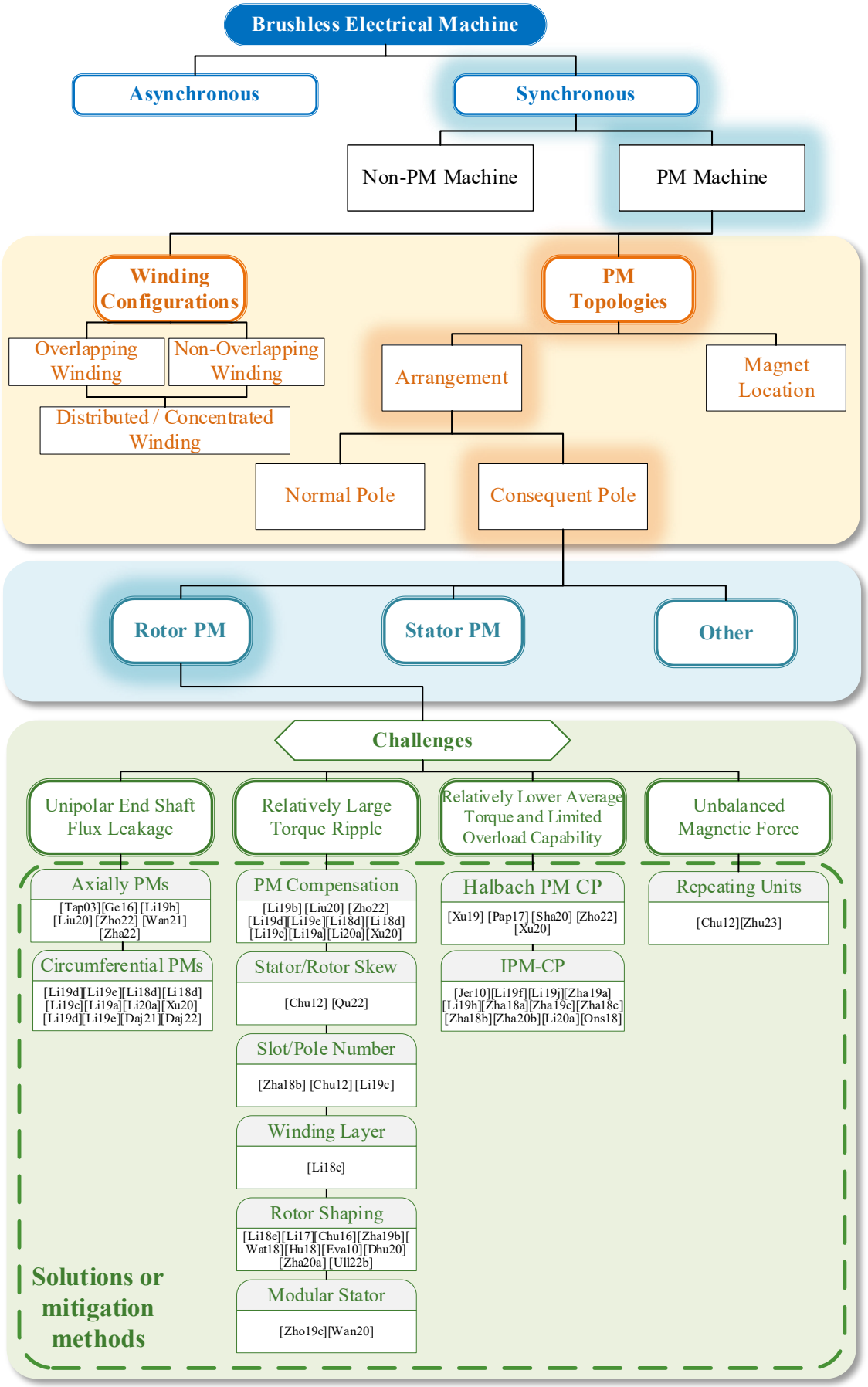

Fig. 1.29 Arrangement of section 1.4.

Table 1.2 Review of literature about the challenges for rotor CPPM machines

Reference	Feature	Remark
Unipolar End Shaft Flux Leakage		
[Ge16]		Axially staggered structure was, for the first time, utilized to eliminate the end shaft flux leakage with spoke-type PM and SPM-CP machines.
[Li19b] [Liu20] [Zho22]		The staggered rotor was adopted in SPM-CP machines.
[Wan21] [Zha22]		Analytical methods were developed to calculate the 3-D electromagnetic performances.
[Li19d] [Li19e]	Circumferential bipolar magnets	N-S-N-iron sequence rotor structure was proposed and can realize smaller end shaft flux leakage. But the unipolar flux leakage still exists due to the amount of north-pole and south-pole magnets were not equal.
[Li18d] [Li19c] [Li19a] [Li20a] [Xu20a] [Daj18] [Daj19] [Daj20]		Same amount of north and south pole PMs in radial magnetization direction are set in rotor and spoke-type PMs are set to improve the average torque.
Relatively Large Torque Ripple		
[Tap03] [Ge16] [Li19b] [Liu20] [Zho22] [Wan21] [Zha22][Li19d] [Li19e] [Li18d] [Li19c] [Li19a] [Li20a] [Xu20a] [Daj18] [Daj19] [Daj20]	Bipolar magnet compensation	Rotor structures with same amount of north and south pole magnets in radial magnetization direction can eliminate the even order harmonics in phase back EMF due to the compensation effect of two kinds of rotor segments and have the capability to reduce the torque ripple.
[Chu12] [Qu22]	Stator/rotor skew	Rotor skew can eliminate a series of harmonics in torque ripple but also has a negative influence on average torque.
[Chu12] [Li19c] [Zha18b]	Slot pole number combination	CPPM machine with even number slots for one phase in a submachine can eliminate the even order harmonics in phase back EMF and the torque ripple can be reduced.

[Li18c]	Changing winding layer	A four-layer winding was proposed to reduce even order harmonics and torque ripple.
[Li18e] [Li17] [Chu16]	Rotor shaping	Magnet shaping methods.
[Zha19b] [Hu18] [Wat18] [Eva10]		Rotor iron shaping methods.
[Dhu21] [Zha20a] [Ull22b]		Both PM and iron shaping for SPM-CP rotor.
[Zho19c] [Wan20]	Modular stator	Both separated stator and integrated stator modular machines can reduce torque ripple.
Relatively Lower Average Torque		
[Xu19] [Pap17] [Sha20] [Zho22] [Xu20]	Halbach PM-CP	Halbach PM-CP structure combines the advantages of high PM utilization in CPPM machines and high air-gap flux density in Halbach machines.
[Li19f] [Li19j] [Zha19a] [Jer10]	IPM-CP	IPM-CP structures can place more magnets in the rotor and form a flux focusing effect to enhance average torque.
[Li19h] [Zha18a] [Zha19c] [Zha18c] [Zha18b] [Zha20b]		Spoke-type machine can be treated as a special CPPM machine and has been analyzed with various topologies.
Unbalanced Magnetic Force		
[Che21] [Dor10]	UMF analysis	Pointed out that the CPPM machines can generate high UMF under some circumstances.
[Chu12] [Zhu23]	Symmetrical repeating units	Using symmetrical repeating units can eliminate UMF.

1.4.1 Suppression of Unipolar End Shaft Flux Leakage

The unipolar end shaft flux leakage is caused by the unipolar PMs set in the rotor and it will lead to the magnetization risks of the mechanical components in the end region [Ge16]. Therefore, in order to suppress or eliminate the unipolar end shaft flux leakage, the main idea is to set bipolar magnets, i.e. north pole and south pole magnets with radial magnetization direction in the rotor where the magnetic flux still forms a circuit through the iron poles. There are mainly two methods:

1. Axially bipolar magnets [Ge16] [Li19b] [Liu20] [Zho22] [Wan21] [Zha22].

2. Circumferential bipolar magnets [Li19d] [Li19e] [Li18d] [Li19c] [Li19a] [Li20a] [Xu20a] [Daj18] [Daj19] [Daj20].

As for the first one, the staggered CPPM rotor was utilized, for the first time, to eliminate the end shaft flux leakage for CPPM rotor and IPM rotor with consequent pole style in [Ge16] as shown in Fig. 1.30 (a) and Fig. 1.30 (b). The staggered rotor was then adopted in IPM-CP [Wat18] and SPM-CP [Li19b], [Liu20], [Zho22]. Analytical methods, such as the lumped parameter magnetic circuit method, were developed in [Wan21] [Zha22] to calculate the 3-D electromagnetic performances. It is worth noting that the staggered rotor in [Zho22] was divided into three steps but with the same amount of north and south pole magnets to reduce the unipolar flux leakage. It should be noted that the flux barriers are necessary between stages to ensure that the PM fluxes go through the iron poles in each stage. However, the flux barriers will decrease the torque density and the inevitable flux leakage between stages will diminish the torque performance. Therefore, the axially magnetized PM was employed in [Li19b] to replace the flux barriers and can enhance the output torque, which is presented in Fig. 1.30 (c).

Axially bipolar magnet structures can eliminate the unipolar end shaft flux leakage effectively. But 3-D FEM is necessary for the simulation process and the complex structure causes difficulties in both design and manufacturing.

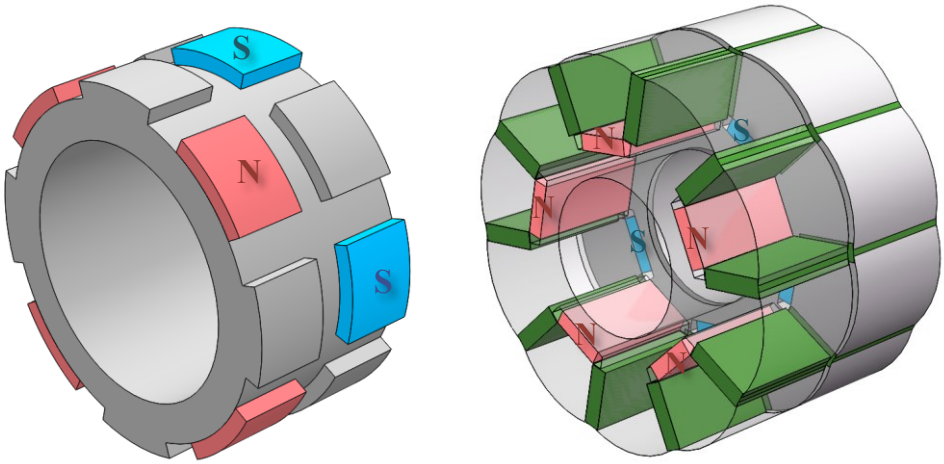

(a) Staggered CPPM rotor [Ge16]　　(b) Staggered spoke-type machine [Ge16]

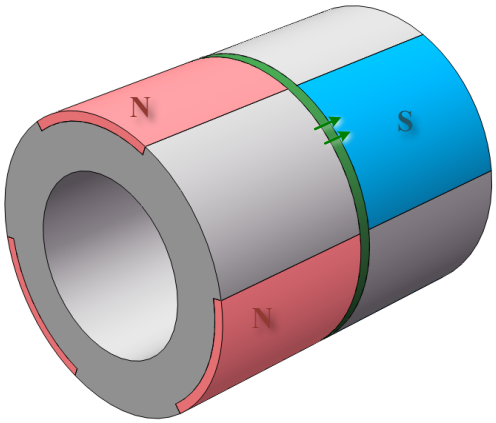

(c) Staggered CPPM rotor with axially magnetized PM [Li19b]

Fig. 1.30　Structures of the staggered rotors.

The second method is circumferentially set bipolar magnet. By adopting both north pole and south pole PMs in the rotor, the unipolar axial flux leakage can be suppressed or be changed into bipolar, which eliminates the magnetization risks of the mechanical components, such as the shaft, in the end region.

In [Li19d] and [Li19e], the N-S-N-iron sequence rotor structure shown in Fig. 1.31 was proposed and analyzed which can realize smaller end shaft flux leakage. However, the unipolar flux leakage still exists due to the amount of north and south pole magnets were not equal.

To eliminate the unipolar end shaft flux leakage, the same amount of two polar magnets is necessary. However, to make sure that the PM fluxes go through the iron pole and form the

required pole number, the air space is necessary to separate the rotor segments. But it will inevitably affect the torque capability. Consequently, the tangentially magnetized magnets were used in the rotor air space to improve the average output torque. The rotor structures which combine the CPPM and spoke-type PM were mainly investigated by K. Wang in these years. Based on this idea, there were many variants proposed and the corresponding structures are illustrated in Fig. 1.32 (a)-(e) [Li18d] [Li19c] [Li19a] [Li20a]. However, the structures are relatively complex and to some extent have the constraint of pole numbers.

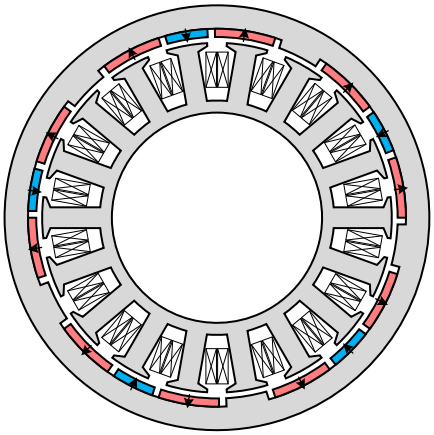

Fig. 1.31 N-S-N-iron sequence CPPM rotor [Li19d] [Li19e].

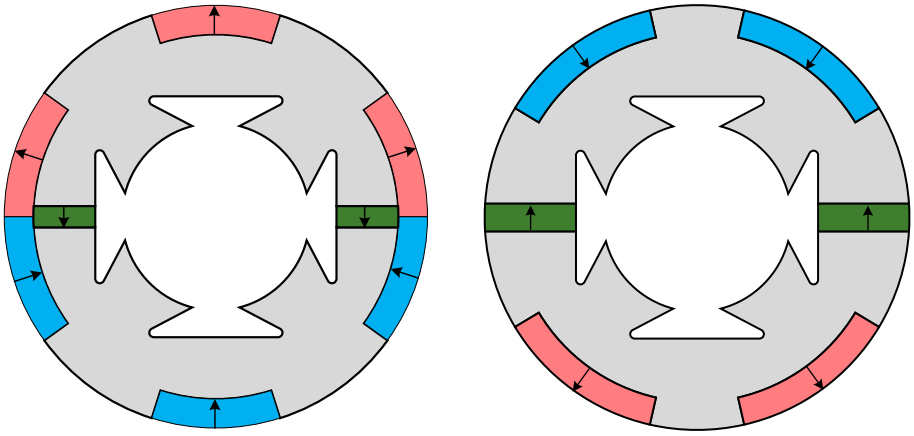

(a) N-iron-N-iron-N sequence [Li18d] (b) Iron-N-iron-N-iron sequence [Li18d]

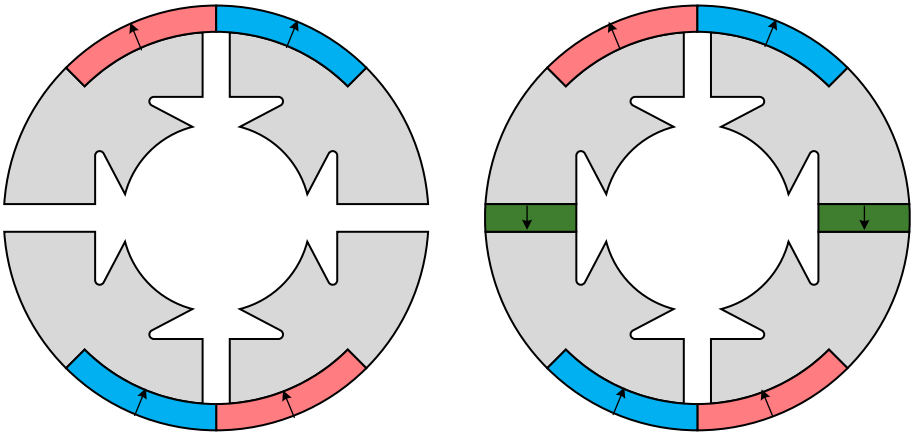

(c) N-iron-iron-S sequences [Li19a]

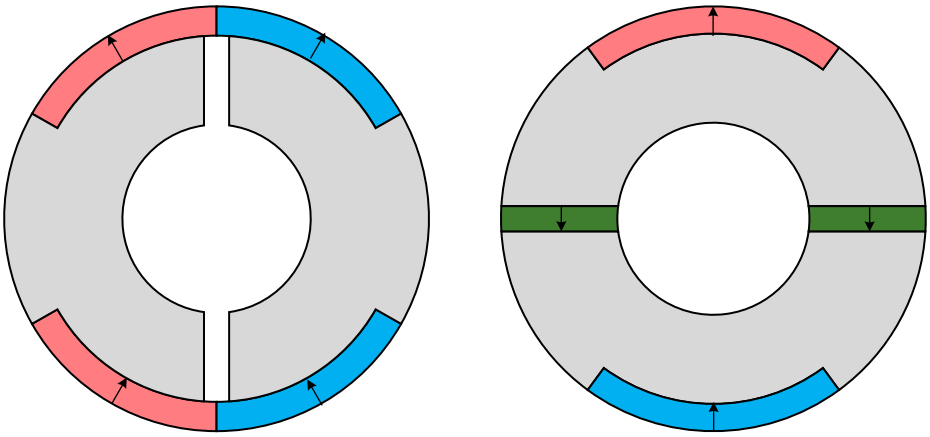

(d) N-iron-N sequence [Li19c]

(e) Iron-N-iron [Li20a]

Fig. 1.32 Structures proposed by K. Wang to eliminate the unipolar end shaft flux leakage.

In [Xu20a], a variant of this structure, Fig. 1.33, was proposed for a five-phase machine to enhance torque performances which also has the potential to reduce the unipolar end shaft flux leakage. It is worth mentioning that the similar structure in [Li20a] was also proposed previously and independently by G. Dajaku and Gerling et al. as shown in Fig. 1.34 (a) in a patent [Daj18] in 2018 and analyzed in two papers [Daj19] [Daj20]. But it was only proposed to improve the PM utilization ratio, namely the ratio of average torque to PM amount, and end shaft flux leakage was not mentioned. It can be found that this structure can only be utilized in machines with a multiple of 6 poles. To make this structure more flexible, the 4-pole structure was proposed and analyzed in [Daj21] [Daj22] as presented in Fig. 1.34 (b). However, the

amount of north pole and south pole surface-mounted magnets is unequal, which means it cannot eliminate the unipolar flux leakage.

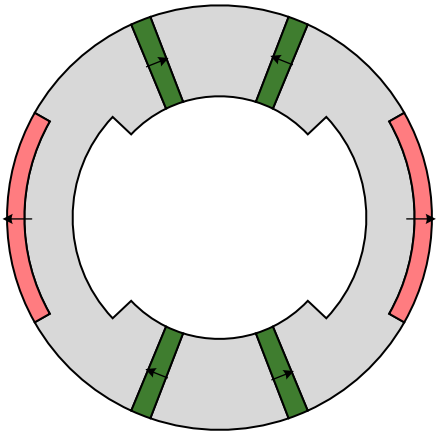

Fig. 1.33 Structures proposed in [Xu20].

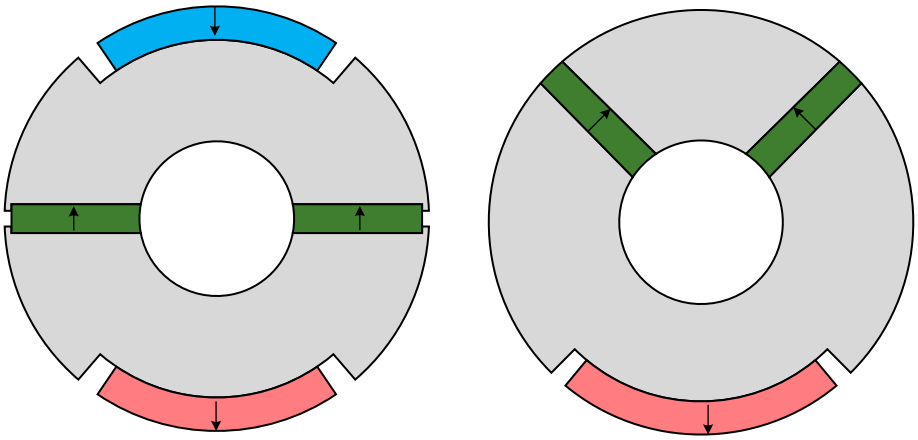

(a) [Daj18] [Daj19] [Daj20] (b) [Daj21] [Daj22]

Fig. 1.34 Structures proposed by G. Dajaku and Gerling et al.

1.4.2 Suppression of Torque Ripple

The unbalanced north and south poles in CPPM rotor can produce unbalanced air-gap flux density, which will lead to the even order harmonics in coil flux linkage and coil back EMF. Such even order harmonics, which normally do not exist in conventional SPM machines, tend to interact with fundamental current and were commonly regarded as the sources of 3^{rd}, 9^{th}, and so on order torque ripples thus leading to the large overall torque ripple for CPPM machines. Therefore, suppression of even order harmonics in air-gap flux density and back EMF is an effective way to reduce the overall on-load torque ripple.

The main methods to suppress the torque ripple for CPPM machines can be summarized as follows:

1. Bipolar magnet compensation [Ge16] [Li19b] [Liu20] [Zho22] [Wan21] [Zha22] [Li19d] [Li19e] [Li18d] [Li19c] [Li19a] [Li20a] [Xu20a] [Daj18] [Daj19] [Daj20].

2. Stator/rotor skew [Chu12] [Qu22].

3. Slot pole number combination [Chu12] [Li19c] [Zha18b].

4. Changing the winding layer [Li18c].

5. Rotor shaping [Li18e] [Li17] [Chu16] [Zha19b] [Hu18] [Wat18] [Eva10] [Dhu21] [Zha20a] [Ull22b].

6. Modular stator [Zho19c] [Wan20].

It has been found that all the structures in section 1.4.1 can suppress torque ripple, which forms the first method. It was reported that those rotor structures with the same amount of north and south pole magnets can eliminate the even order harmonics in phase back EMF due to the compensation effect of two kinds of rotor segments and have the capability to reduce the torque ripple. Nevertheless, as demonstrated in section 1.4.1, the rotor structures always need to be changed and are relatively complex. Besides, to a certain extent, the structures are limited by the slot/pole number combinations.

Step skew in rotor [Chu12] and stator [Qu22] can also reduce the torque ripple. But the structures are also quite complex which will lead to an increase in cost, while the low cost is one of the main advantages of CPPM machines.

An easier method is by selecting some specific slot/pole number combinations to achieve a compensation effect that can eliminate the additional odd order torque harmonics for CPPM machines. In this way, the rotor can be a conventional CPPM structure. Supposing a fractional slot machine can be divided into S_m submachines, where S_m is the greatest common divisor (GCD) between slot number N_s and pole-pair number p, it has been reported that the CPPM machine with an even number of slots for one phase in a submachine, (1.5), can eliminate the

even order harmonics in phase back EMF and the torque ripple can be reduced a lot [Chu12] [Li19c].

$$\begin{cases} N_s/mS_m = 2n, n \in N^+ \\ S_m = \mathrm{GCD}(Q,p) \end{cases} \tag{1.5}$$

where m is the phase number and n is an arbitrary positive integer.

In [Zha18b], this phenomenon was explained by the fact that with this slot/pole number combination, even number slots with 180° electrical degree differences will be allocated into the same phase to achieve a high winding factor. Then, the even-order harmonics in the back EMFs of two slots will be eliminated, without affecting the odd number harmonics. However, this can only explain the reduction of PM torque ripple while the reluctance torque ripple is always neglected for CPPM machines. In addition, this method cannot be applied to all slot/pole number combinations.

Therefore, other methods are proposed to solve the problem. A four-layer winding, Fig. 1.35, was proposed in [Li18c] to reduce even order harmonics and torque ripple. However, by this method, the even order harmonics can only be suppressed, but not eliminated.

Rotor shaping, including both PM shaping and iron shaping, has been widely used in conventional PM machines to reduce torque ripple, which can also be used in CPPM machines. [Li18e] proposed a dovetailed rotor PM shape as presented in Fig. 1.36 (a), which can improve both output torque and PM utilization ratio but reduce torque ripple. Using a similar PM shape with thin sides and a thick center, an outer-rotor CPPM machine in [Li17] was reported to obtain an even lower torque ripple than that of the SPM counterpart but with slightly lower output torque. The nonuniform air-gap PM shape shown in Fig. 1.36 (b) was applied to a CPPM machine for in-wheel direct drive to reduce cogging torque and torque ripple [Chu16]. However, it will also lead to a drop in output torque.

Apart from PM shaping, rotor iron shaping is also investigated. As illustrated in Fig. 1.36 (c), the magnet shifting method was adopted in [Zha19b] to reduce the torque ripple but the assisted flux barrier was introduced to compensate for the average torque loss. [Wat18] tried to optimize the pole-end angle to obtain a large torque and low torque ripple, which is demonstrated in Fig.

1.36 (d). As shown in Fig. 1.36 (e), a normalized Gaussian network was utilized to optimize the shape of rotor iron flux barriers to reduce torque ripple [Hu18]. Two rotor iron surface shaping methods, i.e. inverse cosine and center offset arc pole, for IPM-CP machine were introduced to reduce harmonics in air-gap flux density [Eva10] with the former one shown in Fig. 1.36 (f). Both of these two shaping methods have the potential to reduce torque ripple although the torque ripple was not calculated in [Eva10].

Both PM and iron shaping for SPM-CP rotor was reported in [Dhu21] [Zha20a] [Ull22b]. In [Dhu21], the center offset arc pole, Fig. 1.36 (g), was optimized for a 6-phase machine. But the ripple of optimized machines is still larger than that of its SPM counterpart. The rotor pole shaping method with third harmonic utilization, which has been comprehensively analyzed by Z. Q. Zhu and K. Wang in [Wan17b] [Wan19a] for conventional SPM and IPM machines, can also be applied to the CPPM machines [Zha20a] [Ull22b]. Both PM pole and iron pole adopted the same pole shaping method in [Ull22b], while the iron poles still have a rectangular shape with variable pole arc width in [Zha20a] as shown in Fig. 1.36 (h). Unsurprisingly, the pole shaping method in [Zha20a] [Ull22b] can suppress the torque ripple and enhance the average torque effectively. Nevertheless, all of these pole shaping methods are limited by given shapes which means that they may not reach the optimal conditions.

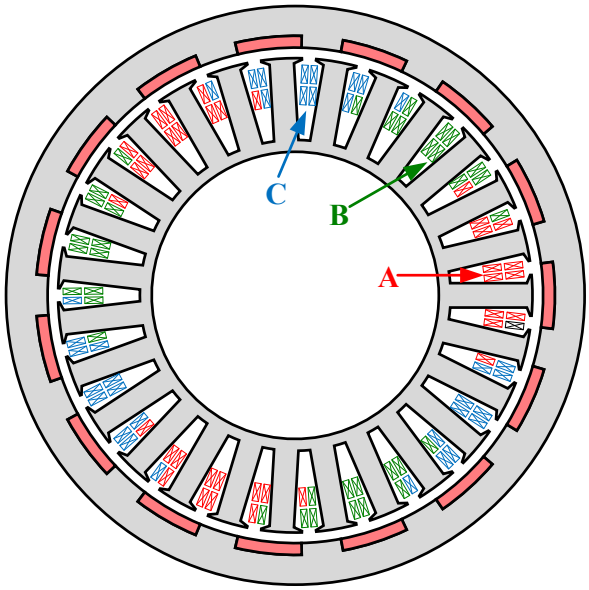

Fig. 1.35 4-layer winding [Li18c]

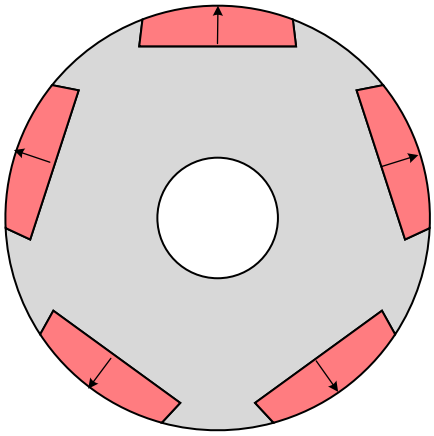

(a) Dovetailed rotor [Li18e]

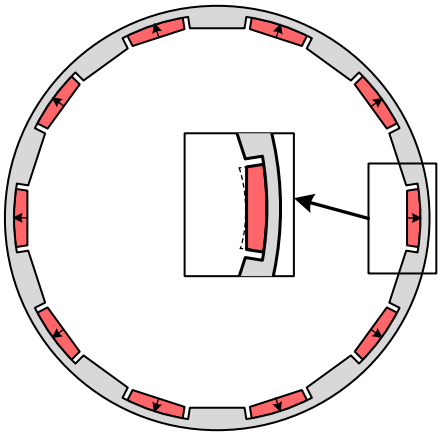

(b) Nonuniform air-gap [Chu16]

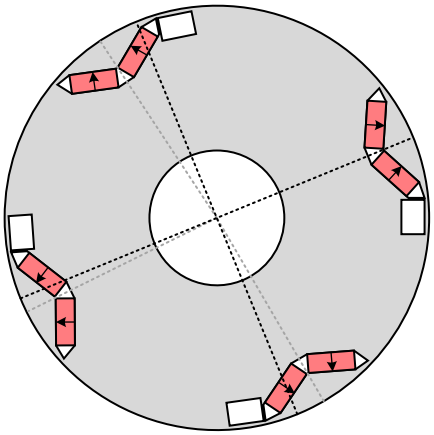

(c) Magnet shifting [Zha19b]

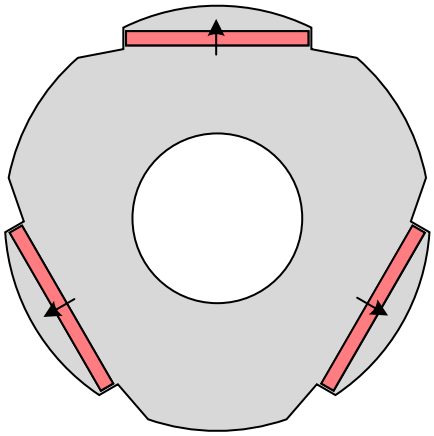

(d) Pole-end angle [Wat18]

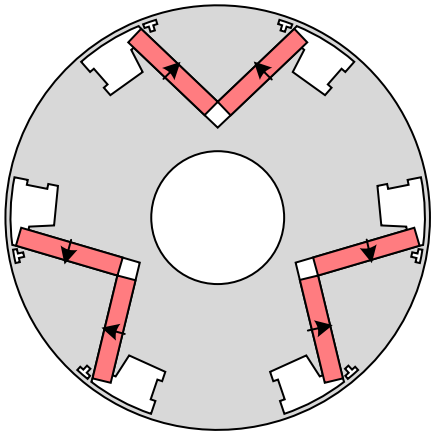

(e) Barrier shape optimization [Hu18]

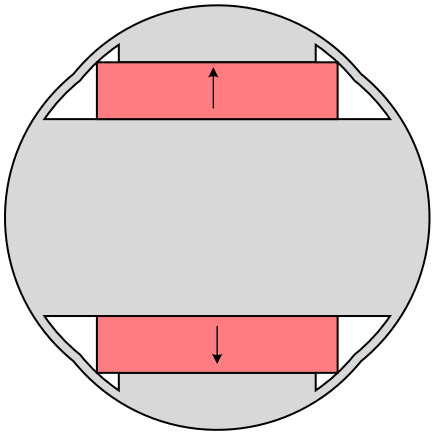

(f) Inverse cosine air-gap [Eva10]

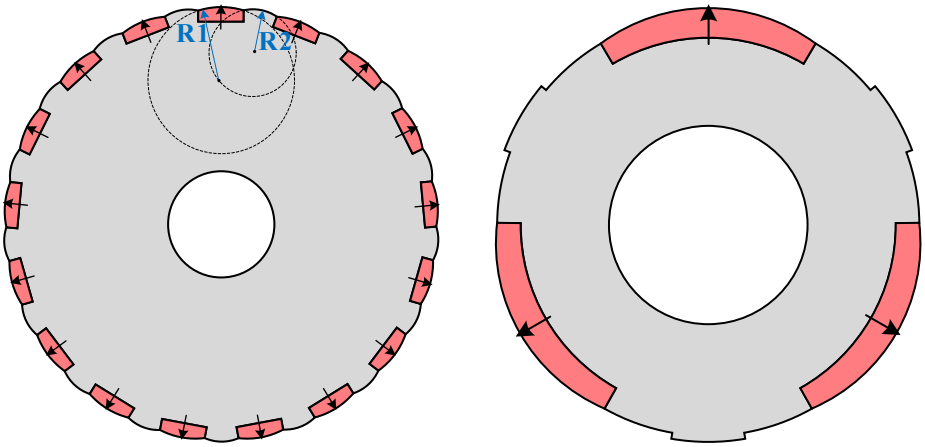

(g) Center offset arc pole [Dhu21] (h) 3rd order harmonic injected shape [Zha20a]

Fig. 1.36 Structures to reduce torque ripple.

Modular stators can also be utilized to reduce torque ripple. It has been noticed that by selecting the proper width of flux barrier for E-core and C-core, torque ripple for CPPM machines can be reduced slightly [Zho19c], but without in-depth analysis. In [Wan20], several modular stator structures as shown in Fig. 1.37 were proposed to reduce the even order harmonics in back EMF and thus the reduction in torque ripple. The results showed that the modular stator with auxiliary tooth illustrated in Fig. 1.37 (b) can achieve better performance in a balance between higher torque density and reduced torque ripple.

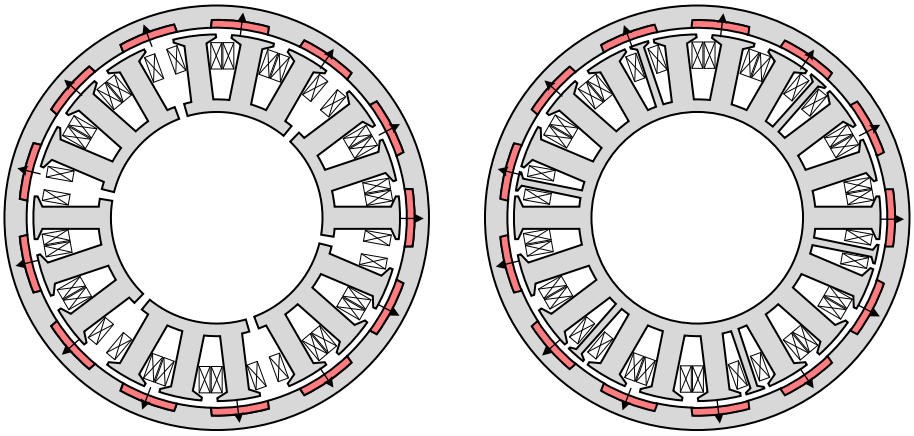

(a) Modular stator without auxiliary tooth (b) Modular stator with auxiliary tooth

Fig. 1.37 Modular stator for reducing torque ripple.

1.4.3 Average Torque Enhancement

Although the magnet utilization can be improved for CPPM arrangement, the SPM-CP machines tend to have slightly lower output torque than that of their SPM counterparts,

especially under overload working conditions. Therefore, some methods are proposed to enhance the torque capability of CPPM machine:

1. Halbach PM-CP structure [Xu19] [Pap17] [Sha20] [Zho22] [Xu20].

2. IPM-CP structure [Li19f] [Li19j] [Zha19a] [Jer10] [Li19h] [Zha18a] [Zha19c] [Zha18c] [Zha18b] [Zha20b].

Halbach PM-CP, Fig. 1.38, combines both the characteristics of high PM utilization in CPPM machines and high air-gap flux density in Halbach machines [Xu19]. [Pap17] compared the performances of SPM-CP rotor and Halbach PM-CP rotor, which shows that the latter can improve the average output torque but is still lower than that of SPM counterpart. However, the Halbach arrays were not fully optimized in the analysis. [Sha20] optimized a Halbach PM-CP machine for a ceiling fan. Compared with conventional SPM and SPM-CP machines, the Halbach PM-CP machine can achieve higher average torque with relatively low torque ripple. The magnetization angles of side PMs for Halbach PM-CP machines were optimized in [Zho22] and [Xu20] to enhance torque performances. Due to the mitigation of the saturation problem in rotor back iron, Halbach PM-CP can also improve the overload capability compared to the conventional SPM-CP counterpart [Zho22]. Nevertheless, Halbach structures will result in difficulties in manufacturing. Besides, the demagnetization performances are not analyzed in these papers while a weak demagnetization withstand capability is a common issue in Halbach arrays.

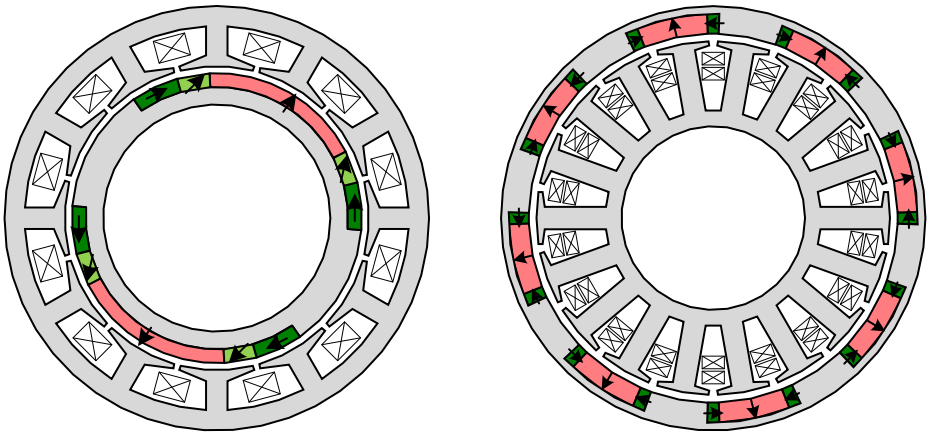

(a) Inner rotor [Pap17] (b) Outer rotor [sha20]

Fig. 1.38 Halbach PM-CP structures.

Another method is to use IPM-CP structures to place more magnets in the rotor and form a flux focusing effect to enhance average torque. Dovetail-shaped rotor structure with consequent pole topology, presented in Fig. 1.39 (a) was proposed in [Jer10], which can increase the strength of the rotor under high-speed conditions. This structure was compared with V-type IPM machines and conventional SPM machine in [Li19f] and the results showed that this structure can obtain the largest output torque and much lower UMF. Similarly, an asymmetric CPPM rotor shown in Fig. 1.39 (b) was proposed by [Li19j] to gain large average torque and high rotor strength. However, the complex structure causes difficulties in manufacturing. In [Zha19a], VI-IPM and VI-IPM-CP machines were compared and the average torque of CPPM machine, Fig. 1.39 (c), can increase by 2.76% with much less PM usage. However, the current density in comparison was small while under heavy load conditions the results may be different.

As an IPM machine, the spoke-type machine can be treated as a special CPPM machine that comes from the V-IPM CPPM machine with parallel magnets for one pole. Torque performances of outer-rotor SPM, surface-mounted CPPM, V-IPM CPPM, and spoke-type machines were compared in [Li19h], as can be seen in Fig. 1.40 (a). It shows that the spoke-type machine possesses the highest average torque and lowest torque ripple. Spoke-type machines with equal north and south pole widths are widely analyzed since they can overcome many problems caused by the unbalanced features between two poles [Zha18a] [Zha19c]. By removing alternate PMs of spoke-type rotor, modular structure shown in Fig. 1.40 (b) and Fig. 1.40 (c) was investigated for radial flux machine [Zha18c] [Zha18b] and axial flux machine [Zha20b]. Since the pole number and magnet number are the same in one rotor module, this structure is more similar to CPPM structure. It was reported that this construction shows better flux weakening performance and higher PM utilization, whereas the problems of CPPM machines, including even order harmonics in back EMF, also exist.

In addition, the spoke-type PM can also be combined with other structures to improve output torque. In Fig. 1.32 (e), the structure that combines the SPM-CP with spoke-type PM is presented to improve output torque [Li20a]. [Ons18] combined the IPM-CP with modular spoke-type PM to improve torque as shown in Fig. 1.40 (d).

Unfortunately, the overload capabilities for these IPM-CP machines are hardly discussed in literatures.

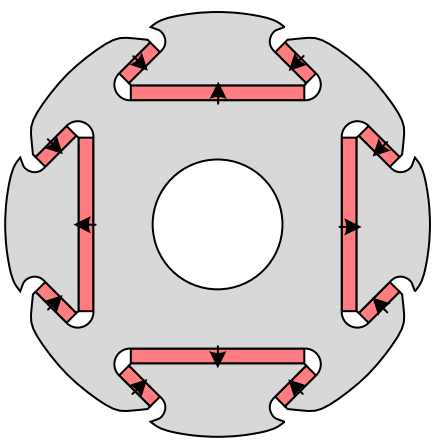

(a) Dovetail-shaped rotor

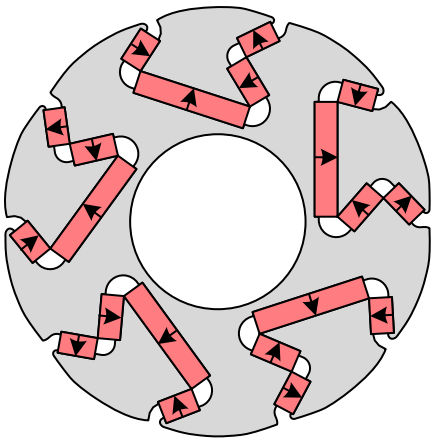

(b) Asymmetric rotor

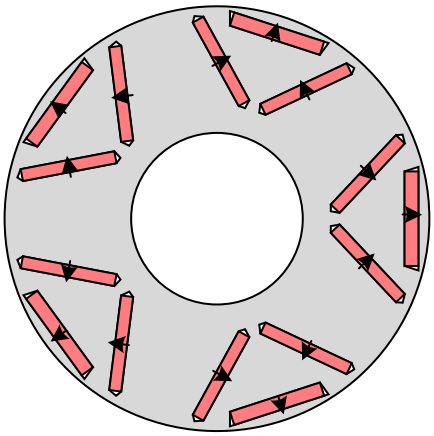

(c) VI-IPM

Fig. 1.39 IPM CPPM structures.

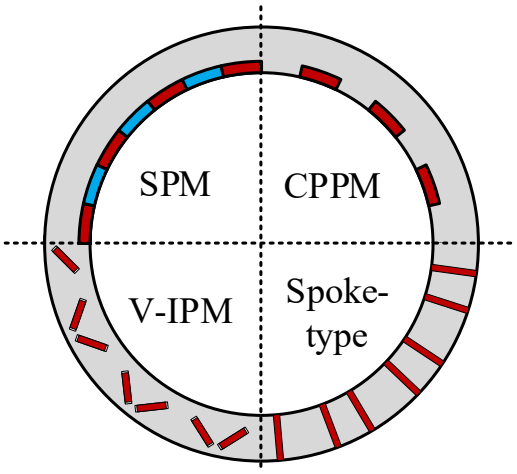

(a) 4 types of rotor in [Li19h]

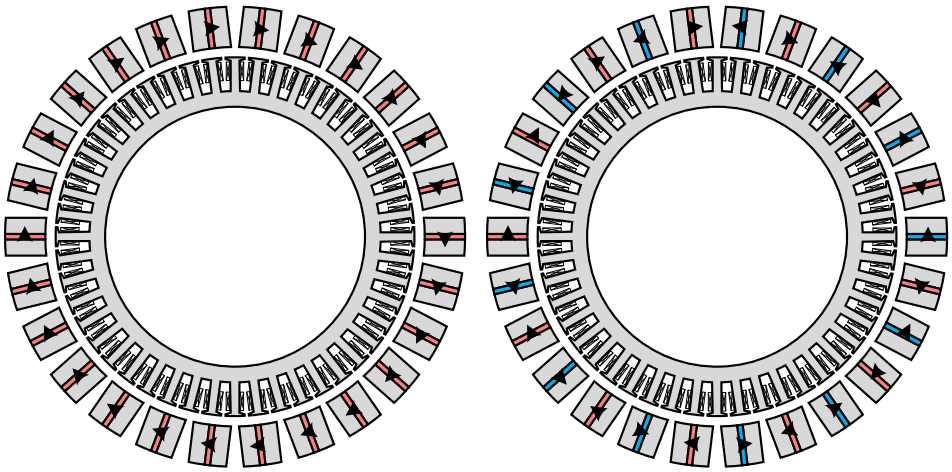

(b) Radial flux modular spoke-type

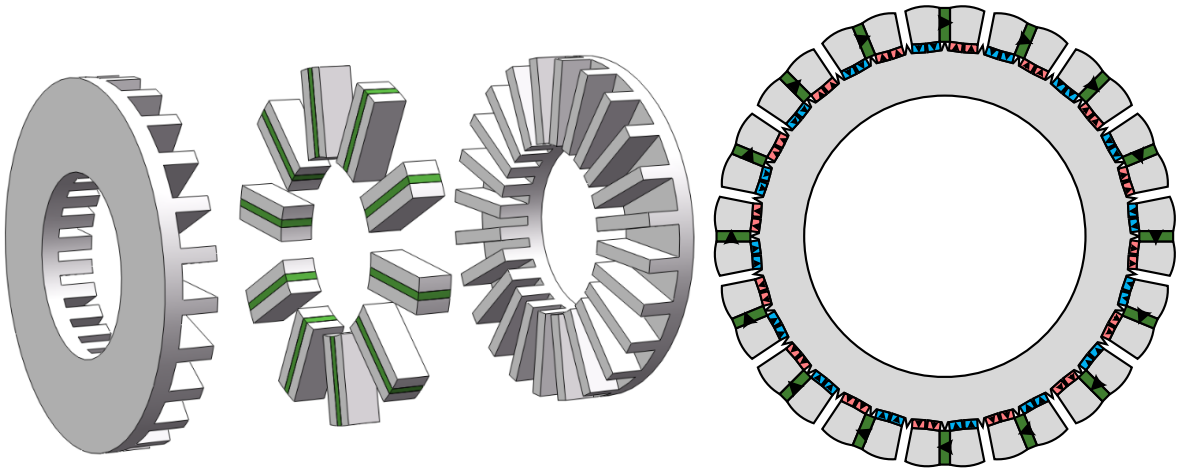

(c) Axial flux modular spoke-type (d) IPM-CP and modular spoke-type PM combined

Fig. 1.40 IPM spoke-type structures.

1.4.4 Reduction of Unbalanced Magnetic Force (UMF)

With the analysis of an 18s12p and an 18s16p CPPM machines, [Dor10] pointed out that the CPPM machines can generate high UMF regardless of whether with or without rotor eccentricity. But no further investigations have been carried out on the principles. The slot/pole number combinations for CPPM machines that will lead to UMF are summarized in [Che21] where the radial force for CPPM machines is comprehensively analyzed and compared with conventional SPM machines. One way to eliminate UMF is to use symmetrical repeating units which were adopted in [Chu12] and [Zhu23]. A 48s40p CPPM machine was proposed in [Chu12], which can be divided into 8 submachines. Besides, in [Zhu23], a novel rotor structure

with two symmetries, which was the same as the one proposed in [Li18d] as shown in Fig. 1.41, was proposed.

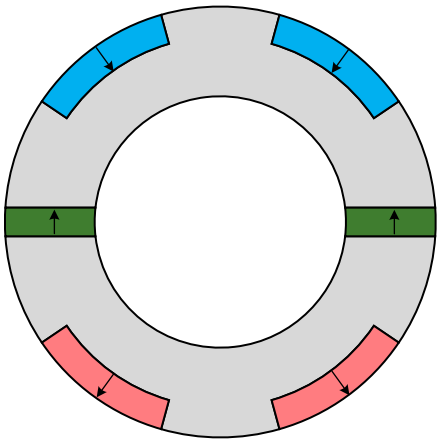

Fig. 1.41 Rotor structure with two symmetries to reduce UMF.

1.5 Research Scope and Major Contributions

1.5.1 Research Scope

This thesis focuses on the suppression of torque ripple, including both no-load cogging torque and on-load torque ripple for SPM-CP machines. The arrangements of each chapter are demonstrated in Fig. 1.42 with the detailed contents described as follows:

Chapter 1

PM machine topologies, including both normal pole and consequent pole arrangements, are introduced. With particular attention paid to the CPPM machines, the basic principles as well as the topologies are reviewed. For rotor CPPM machines, the challenges and corresponding mitigation methods are reviewed for further investigation.

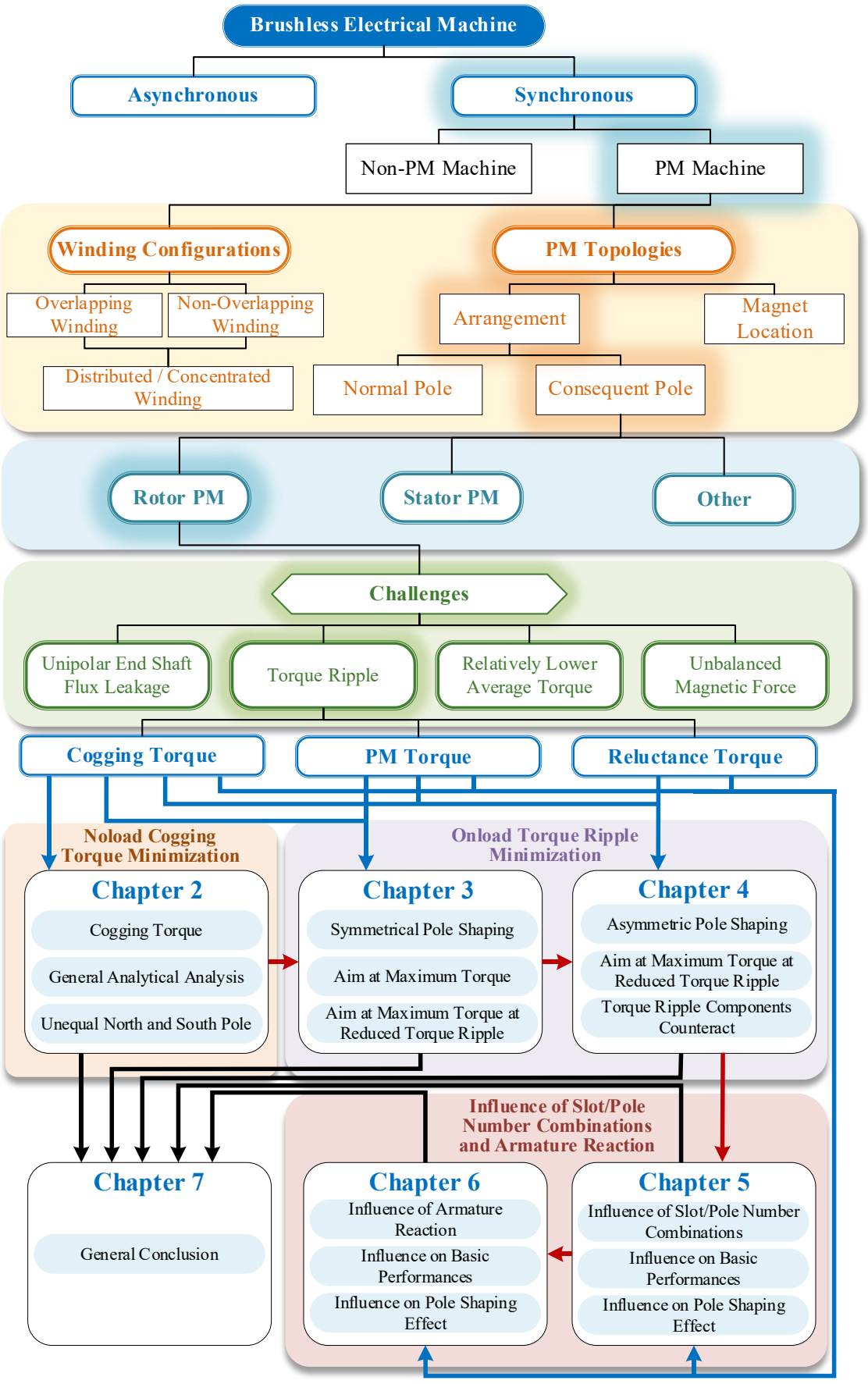

Fig. 1.42 Research scope and chapter arrangements.

Chapter 2

Since the PM pole arcs for CPPM machines are always extended to enhance the average torque, the general cogging torque expressions for machines with different north and south pole arc widths are derived, which can be applied to both CPPM and SPM machines. Three CPPM machines and three SPM machines with 9s8p, 12s8p, and 12s10p machines are selected to verify the results.

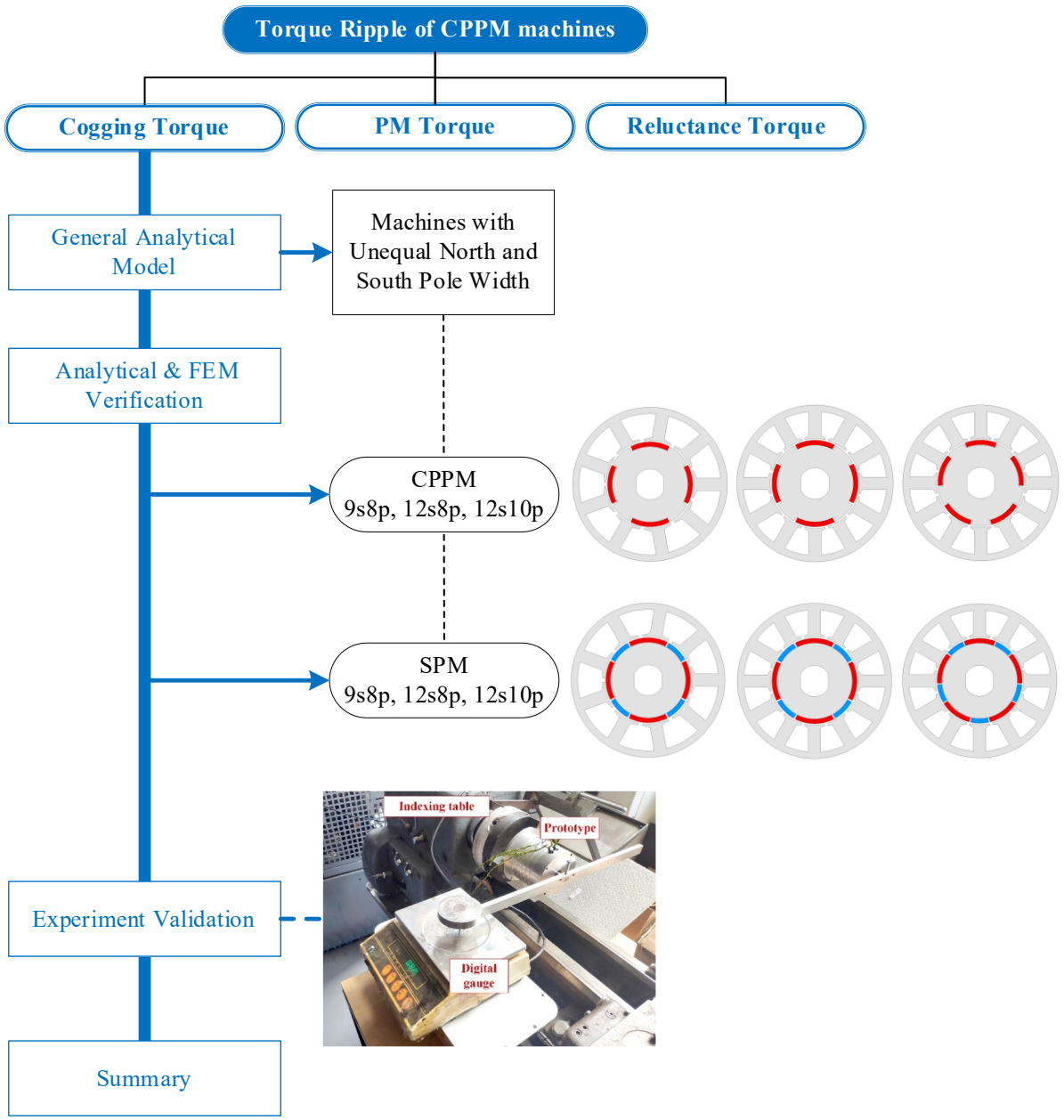

Fig. 1.43 Main content of chapter 2.

Chapter 3

It has been found that the unbalanced characteristics in PM and iron poles for CPPM machines can lead to not only large cogging torque, but also even order harmonics in back EMF, which will inevitably lead to large overall on-load torque ripple. Thus, in this chapter, the symmetrical pole shaping method was developed to reduce the on-load torque ripple for a 12s8p CPPM machine. Besides, a CPPM machine was optimized for maximum torque to investigate the effect of such a pole shaping method. Finally, the FEM and experiments are conducted to validate the analysis.

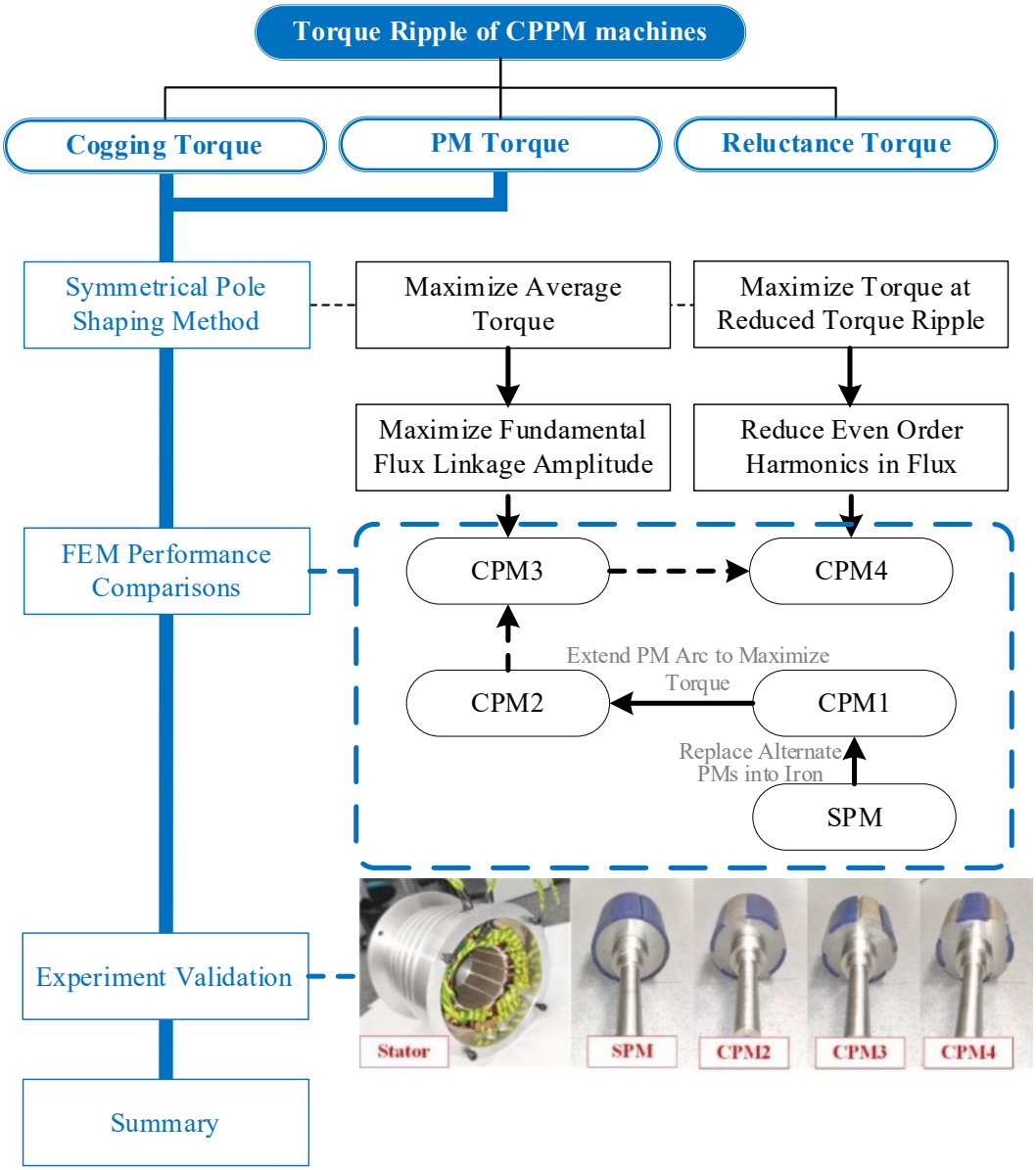

Fig. 1.44 Main content of chapter 3.

Chapter 4

Since the reluctance torque ripple is not considered, the torque ripple for CPPM machines in Chapter 2 cannot be reduced any further. Thus, in this chapter, the asymmetric pole shaping method is proposed to make each torque ripple component, including cogging torque, PM torque, and reluctance torque, counteract each other to reduce the overall torque ripple. The analyses are verified by three 12s8p CPPM machines with FEM and experiments.

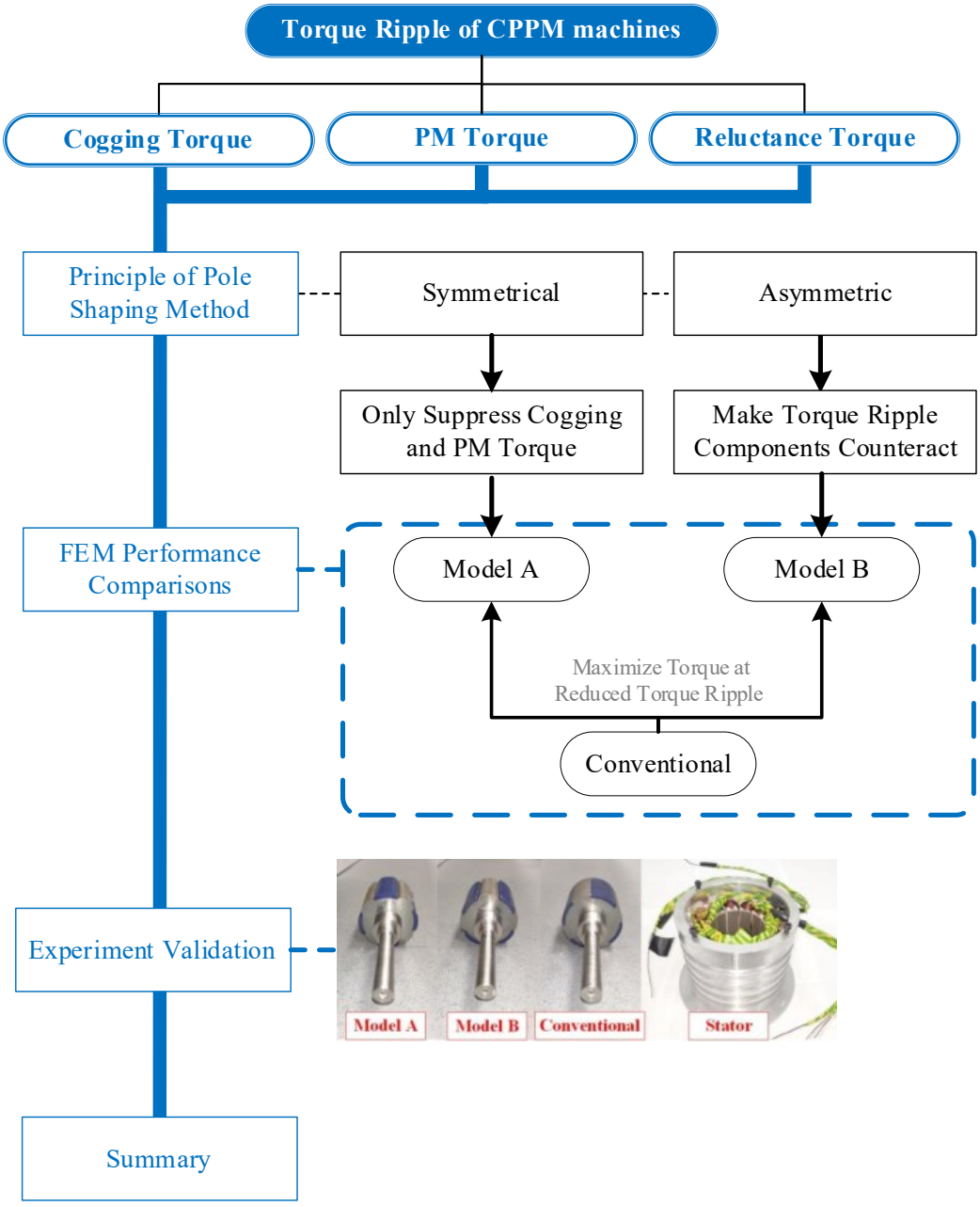

Fig. 1.45 Main content of chapter 4.

Chapter 5

Although asymmetric pole shaping method can reduce torque ripple for the 12s8p machine significantly, it is not always so effective in other CPPM machines that have even slot numbers for one phase in a submachine. Besides, for all the SPM machines, symmetrical and asymmetric pole shaping methods have a similar capability in torque ripple reduction. Consequently, in this chapter, the influences of slot/pole number combinations on performances, such as flux linkage, inductance, and so on, are investigated for both CPPM and SPM machines. Based on these characteristics, the effects of symmetrical and asymmetric pole shaping methods with different slot/pole number combinations are comprehensively analyzed and validated.

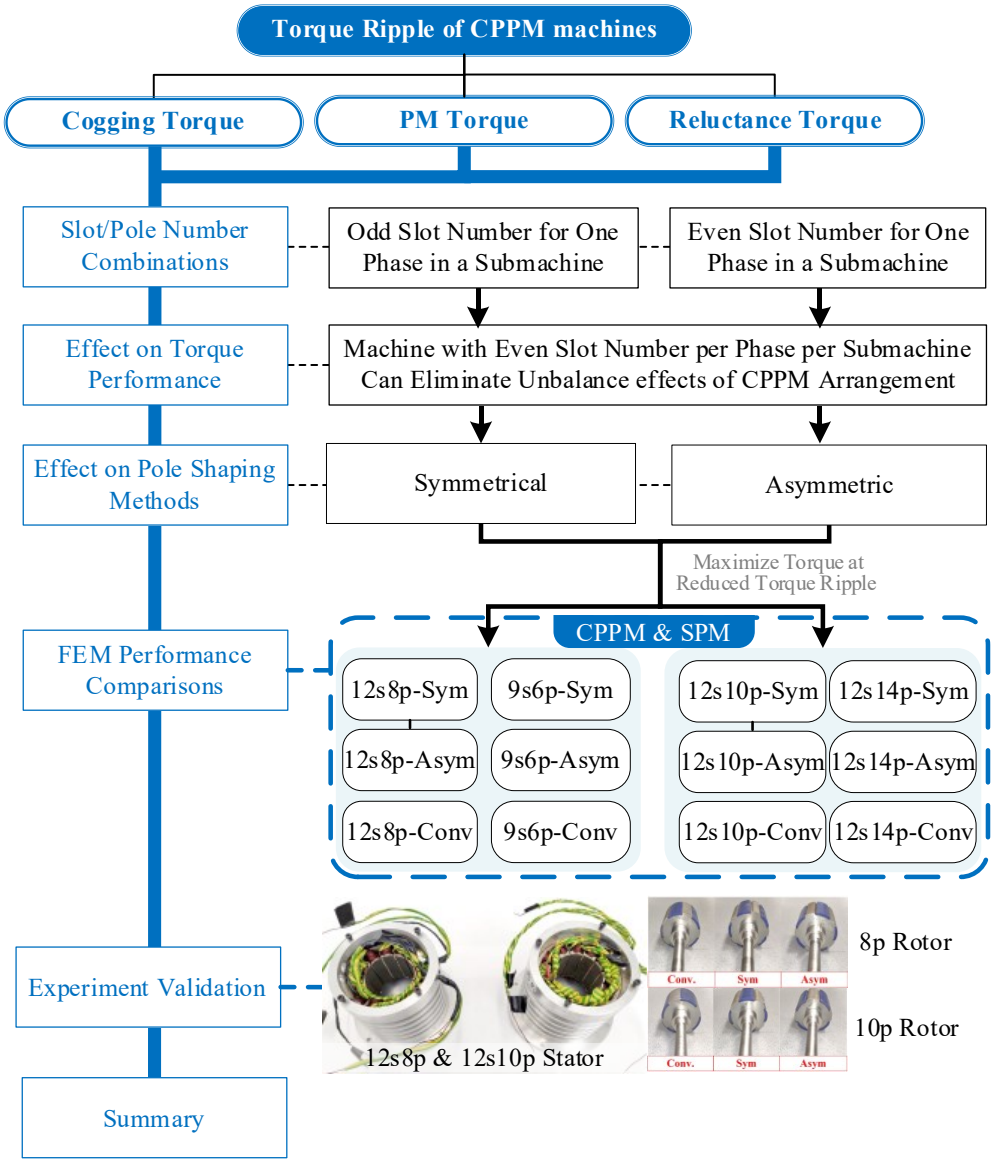

Fig. 1.46 Main content of chapter 5.

Chapter 6

Since the CPPM machines have larger inductance than their SPM counterparts, the large armature reaction has a greater influence on performances, including flux density, flux linkage, back EMF, inductance, torque ripple, demagnetization withstand capability, and so on. Therefore, in this chapter, the effects of armature reaction on CPPM machines are analyzed and compared.

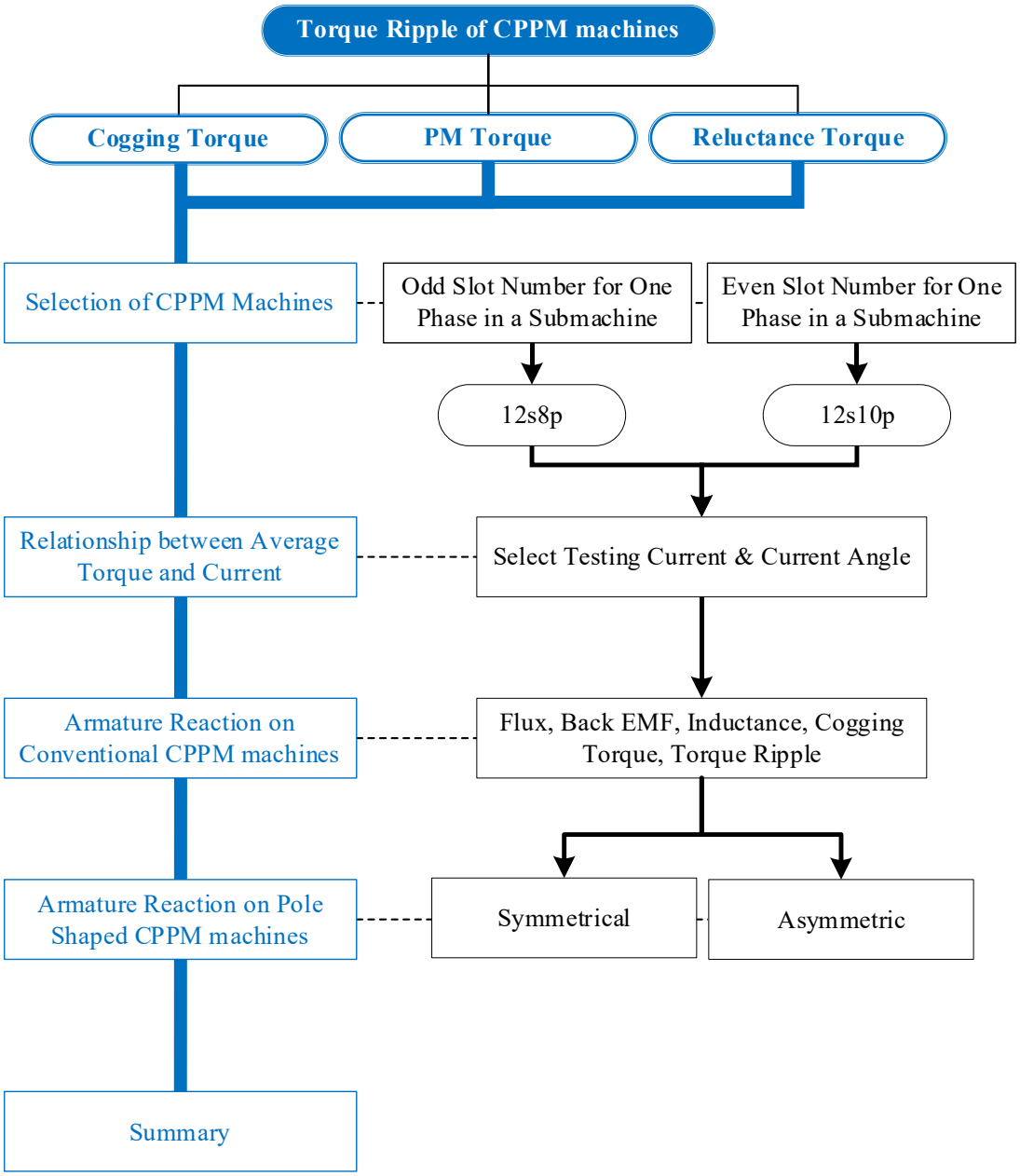

Fig. 1.47 Main content of chapter 6.

Chapter 7

General conclusions are drawn based on the previous chapters. Also, potential future works will be proposed.

1.5.2 Contributions

The contributions of this thesis can be summarized as follows:

1. A general cogging torque analytical model, which considers unequal north pole and south pole widths as well as pole shifting, is derived based on the energy method. The model can be applied to all the machines with unequal pole widths, including rotor CPPM, SPM, and IPM machines. The guidelines for minimizing cogging torque are given based on the general model.

2. The torque ripple sources for SPM-CP machines are revealed for the first time, which include cogging torque, PM torque, and reluctance torque. In addition, an asymmetric pole shaping method is proposed to minimize the overall torque ripple by making torque ripple components counteract each other.

3. The effects of slot/pole number combinations on the basic performances of CPPM machines, SPM machines with equal north and south pole widths, and SPM machines with unequal pole widths, are investigated, which include flux density, flux linkage, inductance, and torque ripple. Based on this, the effects of slot/pole number combinations on symmetrical and asymmetric pole shaping methods are also derived for both CPPM and SPM machines.

4. The effects of armature reaction on CPPM machines with/without pole shaping are analyzed. It confirms that the armature reaction will lead to variations of fundamentals and harmonics in performances, including flux density, flux linkage, back EMF, inductance, and torque ripple for all the CPPM machines. Besides, CPPM machines suffer from weaker demagnetization withstand capabilities.

The publications originated from this PhD research work are listed below.

Journal Papers Published:

[1] J. Qi, Z.Q. Zhu, L. Yan, G.W. Jewell, C.W. Gan, Y. Ren, S. Brockway, and C. Hilton, "Effect of pole shaping on torque characteristics of consequent pole PM machines," *IEEE Trans. Ind. Appl.*, vol. 58, no. 3, pp. 3511-3521, May-June 2022.

[2] J. Qi, Z.Q. Zhu, L. Yan, G.W. Jewell, C.W. Gan, Y. Ren, S. Brockway, and C. Hilton, "Suppression of torque ripple for consequent pole PM machine by asymmetric pole shaping method," *IEEE Trans. Ind. Appl.*, vol. 58, no. 3, pp. 3545-3557, May-June 2022.

[3] J. Qi, Z.Q. Zhu, L. Yan, G.W. Jewell, C.W. Gan, Y. Ren, S. Brockway, and C. Hilton, "Analytical analysis of cogging torque in permanent magnet machines with unequal north and south poles, with particular reference to consequent pole machines," *IEEE Trans. Energy Convers.*, 2022. (Early Access)

[4] J. Qi, Z.Q. Zhu, G.W. Jewell, L. Yan, C.W. Gan, Y. Ren, S. Brockway, and C. Hilton, "Influence of slot/pole number combinations and pole shaping on electromagnetic performance of permanent magnet machines with unbalanced north and south poles," *IET Electr.* Power Appl., pp. 1–28, 2023. DOI: https://doi.org/10.1049/elp2.12293

[5] J. Qi, Z.Q. Zhu, L. Yan, G.W. Jewell, C.W. Gan, Y. Ren, S. Brockway, and C. Hilton, "Influence of armature reaction on electromagnetic performance and pole shaping effect in consequent pole PM machines," *Energies*, vol. 16, no. 4, pp. 1982, Jan. 2023.

Other Journal Papers:

[6] L. C. Yan, Z. Q. Zhu, J. Qi, Y. Ren, C. W. Gan, S. Brockway, and C. Hilton, "Enhancement of disturbance rejection capability in dual three phase PMSM system by using virtual impedance," *IEEE Trans. Ind. Appl.*, vol.57, no.5, pp. 4901-4912, Sept./Oct. 2021.

[7] L. C. Yan, Z.Q. Zhu, J. Qi, Y. Ren, C. Gan, S. Brockway, and C. Hilton, "Suppression of major current harmonics for dual three phase PMSMs by virtual multi three phase systems," *IEEE Trans. Ind. Electron.*, vol.69, no.6, pp.5478-5490, June 2022.

[8] L. C. Yan, Z. Q. Zhu, J. Qi, Y. Ren, C. Gan, S. Brockway, and C. Hilton, “Multiple synchronous reference frame current harmonic regulation of dual three phase PMSM with enhanced dynamic performance and system stability,” *IEEE Trans. Ind. Electron.*, vol.69, no.9, pp. 8825-8838, Sept. 2022.

[9] L.C. Yan, Z. Q. Zhu, B. Shao, J. Qi, Y. Ran, C.W. Gan, S. Brockway, and C. Hilton, “Arbitrary current harmonic decomposition and regulation for permanent magnet synchronous machines," *IEEE Trans. Ind. Electron*. (Early Access)

[10] F. R. Wei, Z. Q. Zhu, X. Y. Sun, L.C. Yan, and J. Qi, "Investigation of asymmetric consequent-pole hybrid excited flux reversal machines," *IEEE Trans. Ind. Appl.*, vol.58, no.3, pp. 3434-3446, May/June 2022.

[11] F.R. Wei, Z.Q. Zhu, L.C. Yan, and J. Qi, "Investigation of stator/rotor pole number combinations and PM numbers in consequent-pole hybrid excited flux reversal machine,” *IEEE Trans. Energy Convers.*, vol.37, no.3, pp.2092-2106, Sept.2022.

[12] F.R. Wei, Z.Q. Zhu, L.C. Yan, and J. Qi, "New dual-PM spoke-type flux-reversal machines for direct-drive applications,” *IEEE Trans. Ind. Appl.*, vol.58, no.5, pp.6190-6202, Sept/Oct. 2022.

Conference Papers:

[13] J. Qi, Z. Q. Zhu, L. Yan, G.W. Jewell, C.W. Gan, Y. Ren, S. Brockway, and C. Hilton, “Effect of pole shaping on the torque characteristics of consequent pole PM machines,” *IEEE Int. Electr. Mach. Drives Conf. (IEMDC)*, Mohegan Sun, May 17-20, 2021.

[14] J. Qi, Z. Q. Zhu, L. Yan, G.W. Jewell, C.W. Gan, Y. Ren, S. Brockway, and C. Hilton, “Suppression of torque ripple for consequent pole PM machine by asymmetric pole shaping,” *IEEE Int. Electr. Mach. Drives Conf. (IEMDC)*, Mohegan Sun, May 17-20, 2021.

[15] L. Yan, Z. Q. Zhu, J. Qi, Y. Ren, C.W. Gan, S. Brockway, and C. Hilton, “Enhancement of disturbance rejection capability in dual three phase PMSM system by using virtual impedance,” *IEEE Energy Convers. Congr. Expo. (ECCE)*, Detroit, USA, OCT 10-15, 2020.

CHAPTER 2
ANALYTICAL ANALYSIS OF COGGING TORQUE IN PERMANENT MAGNET MACHINES WITH UNEQUAL NORTH AND SOUTH POLES, WITH PARTICULAR REFERENCE TO CONSEQUENT POLE MACHINES

As a result of unbalanced features between north and south poles, i.e. PM and iron poles in CPPM machines, relatively high cogging torque tends to cause high torque ripple, especially under light load conditions. Therefore, to improve the torque performance, it is important to suppress the cogging torque. The easiest way is to adjust basic design parameters, including slot opening width, north and south pole arc widths, and so on. Therefore, in this chapter, a general analytical model is developed to analyze the cogging torque accounting for unequal north and south poles as well as pole shifting, which can be applied to both CPPM machines and SPM machines. The optimal slot opening and optimal pole-arc to pole-pitch ratio with/without pole shifting for minimum cogging torque are then analytically derived and verified by finite element analyses and experiments. It shows that in contrast to conventional PM machines with equal north and south poles, of which the fundamental cogging torque order is the least common multiple (LCM) between slot number Ns and pole number $2p$, the fundamental cogging torque order for the PM machines with unequal north and south poles (as often the case in CPPM machines), is the LCM between Ns and p, which has been derived analytically. However, in the special case when the slot number in one submachine is even, the LCM between Ns and $2p$ has the same value as the LCM between Ns and p.

This chapter has been accepted by IEEE Transactions on Energy Conversion [Qi22c]:

[Qi22c] J. Qi, Z.Q. Zhu, L. Yan, G.W. Jewell, C.W. Gan, Y. Ren, S. Brockway, and C. Hilton, "Analytical analysis of cogging torque in permanent magnet machines with unequal north and south poles, with particular reference to consequent pole machines," *IEEE Trans. Energy Convers.*, 2022. (Early Access)

2.1 Introduction

PM machines are widely investigated and utilized in electric vehicles, wind power generators, electric aircrafts, industrial drives, and domestic appliances, etc. [Zhu07] [Hwa14] [Zhu09a] [Hen94]. To reduce cogging torque, pole shifting and unequal PM pole widths were often adopted in conventional PM machines [Bia02] [Bre00] [Wan10] [Liu13] [Wan13] [Wan06] [Liu21]. However, for the pole shifting method, the even order harmonics resulting from pole shifting are not fully analyzed [Liu13] and the influence of pole shifting on optimum pole widths for minimum cogging torque has not been investigated. Additionally, the unequal PM pole width method will increase the cost of magnets with different sizes and introduce many other problems such as even order harmonics in air-gap flux density [Bia02]. Consequently, it has not been investigated in-depth and is rarely used in conventional PM machines.

One of the major concerns of PM machines is rare-earth materials, which face continual challenges of volatile supply, high cost, and price fluctuation. Therefore, CPPM machines have drawn considerable attention in these years as a promising candidate for reducing the usage of PMs and improving the torque per PM volume [Hen94] [Chu15] [Li18b] [Gha19] [Sha20].

Compared with the SPM counterpart, Fig. 2.1 (a), larger PM pole width than iron pole width can produce higher average output torque and the optimum ratio of PM pole-arc to pole-pitch (average angle of each pole-arc, i.e. the ratio of 360^{o} to pole number $2p$) is around 1.2 [Li18b] [Bai18]. Noting that the unequal PM and iron pole widths will not introduce any additional cost, this technique is widely used in CPPM machines, Fig. 2.1 (b). Consequently, in this chapter, focusing on the effect of unbalanced features between the north and south poles, a general analytical model is developed to analyze the cogging torque and the influences of design parameters on cogging torque are analyzed with particular reference to CPPM machines. All the developed theories can also be applied to SPM machines with unequal or equal north and south pole widths.

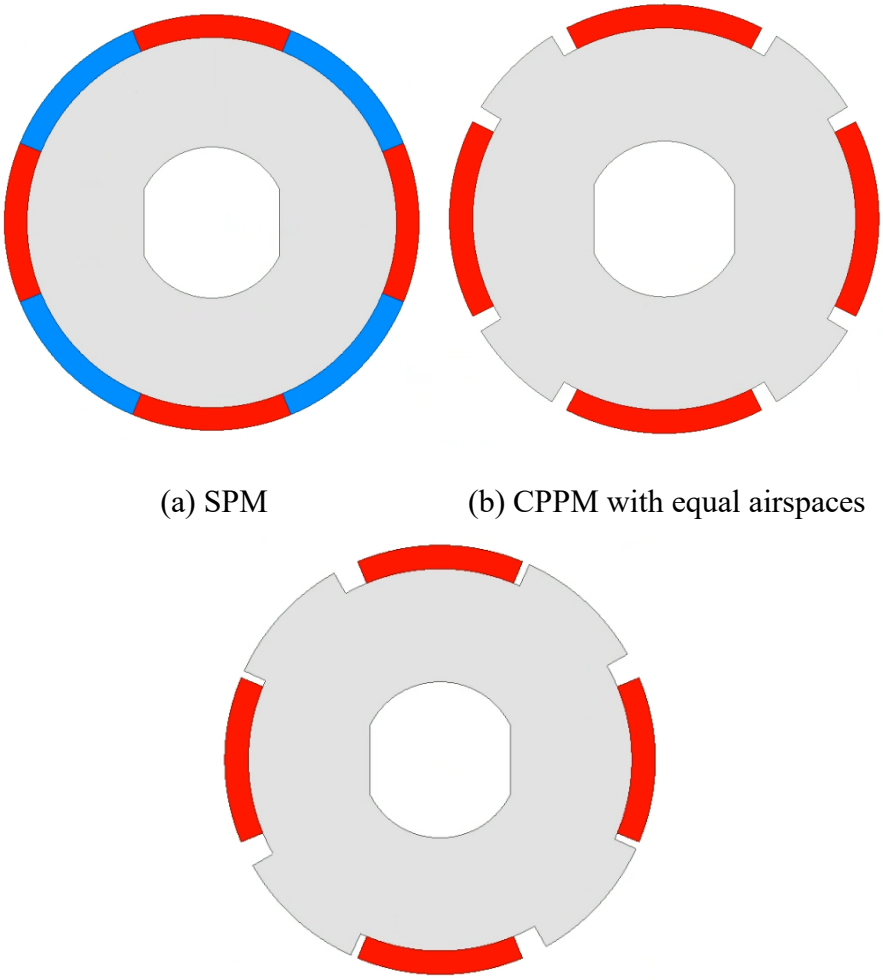

(a) SPM (b) CPPM with equal airspaces

(c) CPPM with pole shifting and unequal airspaces

Fig. 2.1 SPM and CPPM rotor structures.

The unbalanced PM and iron poles in CPPM machines will result in asymmetric flux density distributions under PM and iron poles, which will also lead to different characteristics of cogging torque from the conventional SPM machines with equal pole widths. It has been reported in [Li18c] [Qi22a] that the harmonics in cogging torque for CPPM machines are prone to be more than those of SPM machines. In addition, it is widely reported that CPPM machines tend to exhibit larger cogging torque than SPM counterparts [Li18c] [Cha20] [Ma18], which may exacerbate the torque performance. Staggered rotor [Li19b] and special magnet-iron arrangements [Li19c] [Li18d] [Wan19b] [Li19a] [Daj19] are reported to have the ability to reduce the cogging torque.

Unfortunately, the basic characteristics of cogging torque in CPPM machines with unequal pole widths are still not well understood in literature. Firstly, the formula for calculating the

fundamental order of the cogging torque waveform for a CPPM machine has conflict in various papers and without any detailed explanation [Li18c] [Ma18] [Zha19a]. In [Ma18] and [Zha19a], it is the LCM of slot number N_s and pole number $2p$, while it is the LCM of N_s and p in [Li18c].

In addition, the influences of design parameters on cogging torque of CPPM machines have not been thoroughly studied and some researchers report that the cogging torque cannot be optimized by changing pole-arc width [Ma18]. However, as will be shown in this chapter, optimal pole-arc widths exist for minimum cogging torque.

In this chapter, a general analytical model will be developed first to analyze the cogging torque and to identify the differences and relations in the formulae of fundamental orders between CPPM and SPM machines. Compared with the analytical model of cogging torque developed for SPM machines in [Zhu09a], this chapter accounts for the special characteristics, namely unequal PM and iron pole-arc ratios and pole shifting, to obtain different general methodologies for minimizing the cogging torque of both CPPM and SPM machines. The developed analytical model is then used to investigate the influences of design parameters in CPPM machines, including slot opening, rotor PM and iron pole-arc ratios, and pole shifting, Fig. 2.1 (c), as verified by FEM on three CPPM machines and three SPM machines with 9-slot/8-pole (9s8p), 12s8p, and 12s10p, respectively. The conclusions can also be applied to other PM machines with unequal north and south poles.

The main contributions of this chapter can be summarized as follows:

1. A general analytical model is developed for the first time to analyze the cogging torque accounting for unequal north and south pole widths as well as pole shifting, which can be applied to CPPM machines and other rotor PM machines.

2. It is validated by both analytical methods and FEM that the optimum pole-arc widths for CPPM machines to minimize the cogging torque are derived by the analytical method with/without considering pole shifting.

3. The relationships of cogging torque harmonics between CPPM machines and SPM machines with/without equal north and south pole-arc widths are revealed for the first time.

This chapter is organized as follows. Firstly, a general analytical method for analyzing the cogging torque in CPPM machines is developed in section 2.2 based on the energy method [Zhu09a] [Hwa01] [Hwa00]. The optimal slot opening and optimal pole-arc to pole-pitch ratio with/without pole shifting for minimum cogging torque are then analytically derived and verified by FEM on three CPPM machines and three SPM machines in section 2.3 and section 2.4, respectively. In section 2.5, 12s8p and 12s10p CPPM machines are prototyped and their cogging torques are measured to validate the FEM predicted results. In section 2.6, the effects of saturation on cogging torque are analyzed. The conclusions are summarized in section 2.7.

2.2 Cogging Torque Analysis by Energy Method

In this section, the general analytical expression of cogging torque with unequal north and south poles and pole shifting is firstly developed with CPPM machine as an example. Then, this model is applied to CPPM and SPM machines and the characteristics are analyzed.

2.2.1 General Analytical Expression of Cogging Torque for Machine with Unequal Pole Widths

To obtain the analytical expression of cogging torque in machines with unequal north and south pole widths, the following assumptions are made:

1) The permeabilities of stator and rotor irons are set as infinite, i.e. magnetic saturation is neglected.

2) End effect and flux leakage are neglected.

Cogging torque T_{cog} can be estimated from the energy method [Hwa00] [Hwa01] [Zhu09a]:

$$\begin{aligned} T_{cog}(\alpha) &= -\frac{\partial W(\alpha)}{\partial \alpha} \\ W(\alpha) &= \frac{1}{2\mu}\frac{L_s}{2}({R_s}^2 - {R_m}^2)\int_0^{2\pi} G^2(\theta)B^2(\theta,\alpha)d\theta \end{aligned} \tag{2.1}$$

where α, θ, $W(\alpha)$, μ, L_s, R_s, R_m, $G(\theta)$, and $B(\theta, \alpha)$ are the rotational angle of the rotor, the circumferential angle, the magnetic energy, the permeability, the stack length, the stator inner

radius, the rotor outer radius, the relative air-gap permeance function, and the flux density function, respectively.

It should be noted that it is the stator slot rather than the rotor iron saliency that causes the permeability fluctuation, which interacts with rotor flux density to generate cogging torque. Consequently, the waveform of $G^2(\theta)$ only accounts for the effect of stator slots. Take CPPM machine as an example, as illustrated in Fig. 2.2 (a), the waveform of $G^2(\theta)$ for this kind of machine with infinite slot depth is the same as that of conventional PM machines. However, different from conventional PM machines which usually have equal north and south poles, Fig. 2.3, this kind of machine exhibits unbalanced features between PM and iron poles, Fig. 2.2 (b). Consequently, there exist even order harmonics in air-gap flux density B over one pole-pair. Thus, in an electric cycle, the waveform of B^2 consists of all the harmonics with the order from 0 to infinite. The functions of $G^2(\theta)$ and $B^2(\theta, \alpha)$ can be expressed as:

$$G^2(\theta) = G_{a0} + \sum_{k=1}^{\infty}\left[G_{akN_s}\cos(kN_s\theta) + G_{bkN_s}\sin(kN_s\theta)\right] \tag{2.2}$$

$$B^2(\theta,\alpha) = B_{a0} + \sum_{q=1}^{\infty}\left[B_{aqp}\cos(qp(\theta-\alpha)) + B_{bqp}\sin(qp(\theta-\alpha))\right] \tag{2.3}$$

where N_s is the slot number, p is the pole-pair number, G_{a0}, G_{akNs}, G_{bkNs} and B_{a0}, B_{aqp}, B_{bqp} are the Fourier coefficients of $G^2(\theta)$ and $B^2(\theta, \alpha)$, respectively, and will be given in the appendix. It is worth mentioning that the unequal airspace widths at the sides of a magnet can be simply treated as the south pole shifting and only one more parameter β in electrical degree is enough to describe it, as shown in Fig. 2.2 (b). Besides, due to the circumferential distribution of north and south poles, the south pole shifting can also be equivalent to the north pole shifting.

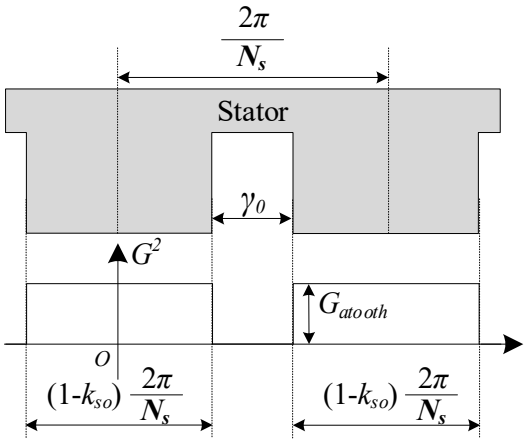

(a) $G^2(\theta)$, a square of permeance function, due to stator slotting

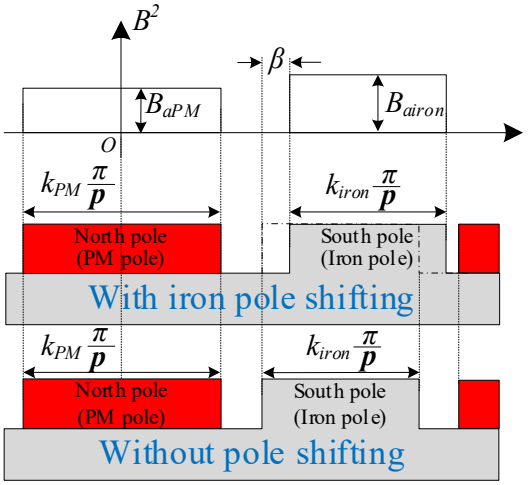

(b) $B^2(\theta,\alpha)$, square of flux density distribution, due to PMs in an equivalent slotless model

Fig. 2.2 Waveforms of $G^2(\theta)$ and $B^2(\theta,\alpha)$ in CPPM machines.

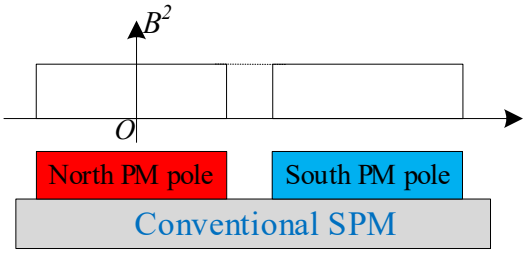

Fig. 2.3 Waveforms of $B^2(\theta,\alpha)$ in conventional SPM machines with equal north and south pole widths.

Substituting (2.2) and (2.3) into (2.1), the cogging torque in machines with unequal north and south pole widths becomes:

$$
\begin{aligned}
T_{cog}(\alpha) &= \frac{\pi L_s}{4\mu_0} N_C \left({R_s}^2 - {R_m}^2\right) \sum_{n=1}^{\infty} nG_{akN_s} \begin{bmatrix} B_{aqp}\sin(nN_C\alpha) \\ +B_{bqp}\cos(nN_C\alpha) \end{bmatrix} \\
&= \frac{\pi L_s}{\mu_0} N_C \left({R_s}^2 \right. \\
&\left. - {R_m}^2\right) \sum_{n=1}^{\infty} \frac{N_s G_{atooth} p B_{aN}}{n(N_C\pi)^2} \sin\left((1-k_{so})\frac{nN_C}{N_s}\pi\right) \left[\left(\sin\left(\frac{nN_C k_{north}}{2p}\pi\right)\right.\right. \\
&+ (-1)^{\frac{nN_C}{p}} \left(\frac{k_{north}}{k_{south}}\right)^2 \sin\left(\frac{nN_C k_{south}}{2p}\pi\right) \cos\left(\frac{nN_C}{p}\beta\right)\Bigg) \cdot \sin(nN_C\alpha) \\
&\left. + (-1)^{\frac{nN_C}{p}} \left(\frac{k_{north}}{k_{south}}\right)^2 \sin\left(\frac{nN_C k_{south}}{2p}\pi\right) \cdot \sin\left(\frac{nN_C}{p}\beta\right)\cos(nN_C\alpha)\right]
\end{aligned}
\tag{2.4}
$$

where G_{atooth} is the amplitude of $G^2(\theta)$, k_{so} is the slot opening ratio, i.e. the ratio of slot opening width to slot-pitch, k_{north} and k_{south} are the ratios of north and south pole-arcs to pole-pitch, respectively, and B_{aN} is the amplitudes of $B^2(\theta,\alpha)$ waveform for north poles. The restraints for k_{north} and k_{south} for machines are as follows:

$$
\begin{cases}
0 < k_{north} < 2 - 2\beta/\pi \\
0 < k_{south} < 2 - 2\beta/\pi \\
k_{north} + k_{south} \leq 2 - 2\beta/\pi
\end{cases}
\tag{2.5}
$$

It is worth mentioning that according to (2.1), the torque can be produced only when the harmonic orders in $G^2(\theta)$ and $B^2(\theta, \alpha)$, i.e. (2.2) and (2.3), are the same. Therefore, the orders, nN_c, in (2.4) must satisfy:

$$
nN_C = kN_s = qp \tag{2.6}
$$

For (2.6), N_c must be the multiple of both N_s and p when n=1. Consequently, N_C is the LCM between slot number N_s and rotor pole-pair number p.

$$
N_C = \mathrm{LCM}(N_s, p) \tag{2.7}
$$

2.2.2 Cogging Torque for CPPM Machine

In CPPM machines, the PM pole width is always extended to achieve higher average torque, which results in unequal north and south pole widths. Therefore, the above analytical model can be directly applied to CPPM machines. According to (2.4), fundamental order, i.e. the cycle number of cogging torque in a mechanical rotation cycle, is N_C, the LCM between N_s and p in this kind of machine according to (2.7).

Supposing CPPM machines can be divided into *Sm* submachines, where:

$$Sm = \mathrm{GCD}(N_s, p) \tag{2.8}$$

Since

$$\mathrm{GCD}(N_s, p)\mathrm{LCM}(N_s, p) = N_s p \tag{2.9}$$

i.e.

$$S_m N_C = N_s p \tag{2.10}$$

the corresponding order of cogging torque can be obtained from (2.7) and (2.10):

$$N_C = \mathrm{LCM}(N_s, p) = jp \tag{2.11}$$

where j is the slot number in one submachine:

$$j = \frac{N_s}{S_m} \tag{2.12}$$

For the first scenario, when j is an odd number, jp is not the multiple of $2p$. Consequently, the order of cogging torque for the CPPM machine is different from that for the conventional SPM counterpart which is given by:

$$\mathrm{LCM}(N_s, 2p) = 2jp \tag{2.13}$$

The analysis confirms the results in [Li18c] and [Qi22a] with 27s30p and 12s8p CPPM machines, which have 9 slots and 3 slots in one submachine, respectively. Take 12s8p machines for instance, according to (2.7), the fundamental order of cogging torque is LCM(N_s, p) = 12 for CPPM, but is 24 for conventional SPM machines since LCM(N_s, 2p) = 24. This means that the additional harmonics, including the 12th and the 36th, will exist in the cogging torque for 12s8p CPPM machine. Further, a higher cogging torque in the CPPM machine is likely to be generated due to additional harmonics.

However, for the second scenario, when j is even, jp is also the multiple of 2p:

$$\mathrm{LCM}(N_s, 2p) = \mathrm{LCM}(N_s, p) = jp \tag{2.14}$$

Consequently, it can be concluded that when the slot number in one submachine is even, the order of cogging torque of the CPPM machine is the same as that of the conventional SPM counterpart. Take 12s10p machines as an example, which have 6 slots in one submachine, the fundamental orders of cogging torque for both CPPM and SPM machines are 60, which underpins the results in [Zha19a].

The north and south pole characteristics in CPPM machines are generally unequal even if the PM pole width and iron pole width are the same, and thus, the fundamental order of cogging torque in CPPM machines, N_c, is usually the LCM between N_s and p.

2.2.3 Cogging Torque for SPM Machine

When the north and south pole widths are different in conventional SPM machines, the cogging torque characteristics have already been derived in section A, i.e., they are identical to those of the CPPM machines as discussed in part B.

However, if the north and south poles are equal and without pole shifting, as shown in Fig. 2.3, the waveform of B^2 over one pole-pair only consists of even order harmonics:

$$B^2(\theta, \alpha) = B_{a0} + \sum_{q=1}^{\infty} \left[B_{aq2p} \cos(2qp(\theta - \alpha)) + B_{bq2p} \sin(2qp(\theta - \alpha)) \right] \tag{2.15}$$

Therefore, the orders, nN_c, in (2.15) must satisfy:

$$nN_C = kN_s = 2qp \tag{2.16}$$

Consequently, under this condition, N_C is the LCM between slot number N_s and rotor pole number $2p$ as is the same case for conventional SPM machines [Zhu00] [Zhu09a].

$$N_C = \mathrm{LCM}(N_s, 2p) \tag{2.17}$$

As is well known, (2.17) is the fundamental order of cogging torque N_c for conventional SPM machines with equal north and south pole widths [Zhu00] [Zhu09a].

2.3 Cogging Torque Minimization for CPPM Machine

As can be seen from (2.4), for a specific order harmonic in cogging torque, the amplitude can be zero when B_{aqp}=B_{bqp}=0 or G_{akNs}=0, which are determined by the rotor and stator design parameters, respectively. In this section, focusing on CPPM machines, the influences of slot opening ratio, PM and iron pole-arc ratios, and pole shifting angle are analyzed by FEM parametric sweep to verify the analytical expression (2.4). Both the analytical method and the FEM are applied to 3 CPPM machines with 9s8p, 12s8p, and 12s10p, respectively. ANSYS Maxwell package was used throughout the paper for FEM.

The common design parameters of three analyzed CPPM machines with internal rotors are listed in Table 2.1. It is worth noting that the method and discussions can be equally applicable to other types of PM machines with unequal north and south poles, including interior PM machines.

2.3.1 Stator Slot Opening

According to (2.4), the amplitude of the n-th order harmonic of cogging torque can be minimized when the slot opening ratio satisfies:

$$k_{so} = \frac{iN_s}{nN_C}\left(i = 0,1,2,3\cdots\frac{nN_C}{N_s}\right) \tag{2.18}$$

It can be seen from (2.18) that a larger n can result in more optimum values of k_{so} for minimum cogging torque. Additionally, since the amplitudes of lower order harmonics tend to be larger,

the dominant order harmonics (n=1, 2, 3) are analyzed based on (2.18) and the results are shown in Table 2.2.

The results obtained from FEM are demonstrated in Fig. 2.4 where the ratio of slot opening to slot pitch k_{so} varies from 0.05 to 0.95. It can be found that the numbers of optimum values and the trends for the overall cogging torque and each harmonic agree well with the analytical analysis although the optimum ratio values in Fig. 2.4 are a little higher than those from (2.18), i.e. Table 2.2. This is because the leakage fluxes in slots are neglected in the analytical model. In addition, due to the low amplitudes of high order harmonics (n=2 and 3) for 9s8p and 12s10p CPPM machines, the overall cogging torques for these two machines are largely related to the variation of fundamental harmonic amplitudes, which makes them different from that for 12s8p CPPM machine.

Table 2.1 Key Design Parameters of Analyzed Machines

Parameter	**Value**	**Unit**
Number of stator slots	9, 12	-
Number of rotor poles	8, 10	-
Stator outer diameter	100	mm
Stator inner diameter	57	mm
Stator stack length	50	mm
Air-gap	1	mm
Yoke width	4.2	mm
Rotor inner diameter	36	mm
Magnet thickness	3	mm
Remanence of magnet	1.2	T
Ratio of PM pole-arc to pole-pitch	0.1~1.9	-
Ratio of iron pole-arc to pole-pitch	0.1~1.9	-
Ratio of slot opening to slot-pitch	0.05~0.95	-

Table 2.2 Optimum k_{SO} of Three Machines for the Dominant 1st, 2nd, and 3rd Order Harmonics

Machine	Harmonic Order	Optimum k_{so}
9s8p	n=1	0, 0.25, 0.5, 0.75, 1
	n=2	0, 0.125, 0.25, 0.375, 0.5, 0.625, 0.75, 0.875, 1
	n=3	0, 0.083, 0.17, 0.25, 0.337, 0.42, 0.5, 0.58, 0.67, 0.75, 0.83, 0.92, 1
12s8p	n=1	0, 1
	n=2	0, 0.5, 1
	n=3	0, 0.33, 0.67, 1
12s10p	n=1	0, 0.2, 0.4, 0.6, 0.8, 1
	n=2	0, 0.1, 0.2, 0.3, 0.4, 0.5, 0.6, 0.7, 0.8, 0.9, 1
	n=3	0, 0.067, 0.13, 0.20, 0.27, 0.33, 0.40, 0.47, 0.53, 0.60, 0.67, 0.73, 0.80, 0.87, 0.93, 1

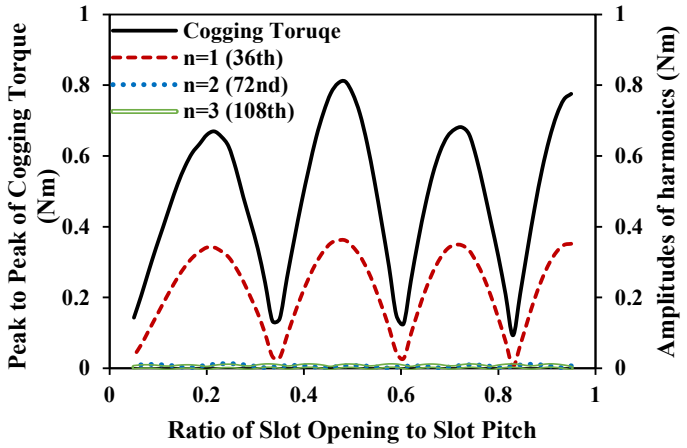

(a) 9s8p

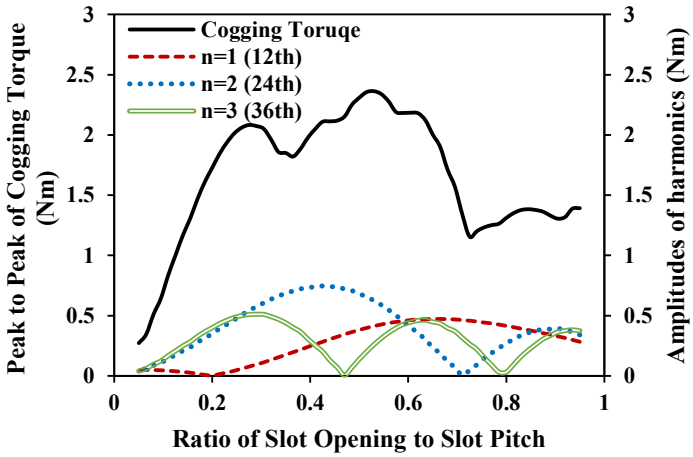

(b) 12s8p

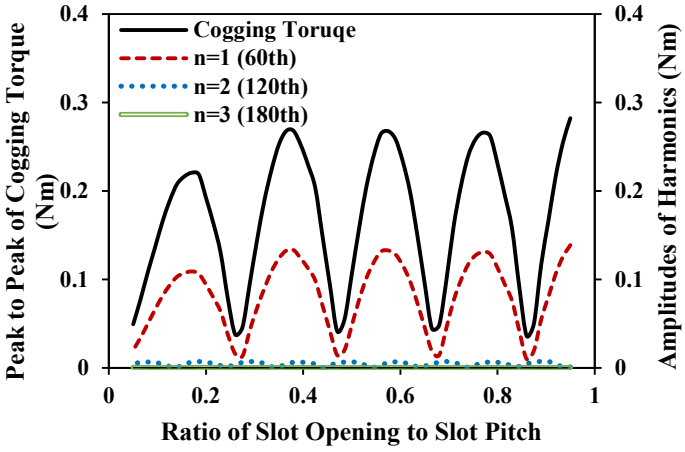

(c) 12s10p

Fig. 2.4 FEM predicted peak cogging torque variations and amplitudes of harmonics under different slot opening ratios.

2.3.2 Pole-Arc to Pole-Pitch Ratio without Pole Shifting

In this section, the cogging torques of 12s8p, 9s8p, and 12s10p CPPM machines are analyzed for various pole-arc to pole-pitch ratios without pole shifting. Since β=0, the Fourier coefficient B_{bqp} = 0, and only B_{aqp} needs to be considered. To make it clear for CPPM machines, in this section, k_{north} and k_{south} will be replaced by k_{PM} and k_{iron}, i.e., the ratios of PM and iron pole arcs to pole pitch, respectively.

According to (2.4), the cogging torque will be minimum if the PM and the iron pole-arc to pole-pitch ratios satisfy:

$$B_{aqp} = 0 \tag{2.19}$$

which can be rewritten as:

$$\sin\left(\frac{nN_C k_{PM}}{2p}\pi\right) + (-1)^{\frac{nN_C}{p}}\left(\frac{k_{PM}}{k_{iron}}\right)^2 \sin\left(\frac{nN_C k_{iron}}{2p}\pi\right) = 0 \tag{2.20}$$

from which the optimal k_{PM} and k_{iron} for minimum cogging torque of each order harmonic can be derived.

2.3.2.1 9s8p

From the previous analysis, the fundamental order of cogging torque N_c is 36 for 9s8p CPPM machine. In this section, the dominant 36th and 72nd order harmonics are investigated, which correspond to n=1 and 2 according to (2.4). Substituting N_c and n into (2.20), the optimal k_{PM} and k_{iron} combinations can be plotted in black lines in the left column of Fig. 2.5, which means the cogging torque harmonics can be minimum under these PM and iron pole-arc ratio combinations. For comparison, the FEM results by ANSYS Maxwell parametric sweep are shown in the right column of Fig. 2.5, where dark blue means the minimum cogging torque. It is worth mentioning that the figures are all plotted in MATLAB and adjusted in Microsoft Visio. Clearly, the analytical results are in good agreement with the simulation results. It can also be found that the trends of the optimal k_{PM} and k_{iron} are slightly deformed, as a consequence of the unbalanced characteristics between the PM and iron poles as well as the magnet fringing effect.

To seek the minimum overall cogging torque, the optimum k_{PM}/k_{iron} combinations for the dominant components, i.e. both the 36th and the 72nd cogging torques, should be taken into account simultaneously. Thus, by plotting the analytical optimal k_{PM}/k_{iron} for each harmonic in the same figure, Fig. 2.6 (a), the corresponding k_{PM}/k_{iron} of cross points between black and red lines, which are shown within the blue points and lines, can contribute to the minimum overall cogging torque. The analytically predicted results are compared with the peak-to-peak values obtained by FEM shown in Fig. 2.6 (b). It is clear that the optimum points in Fig. 2.6 (a) and Fig. 2.6 (b) are almost the same, which validates the analytical analysis.

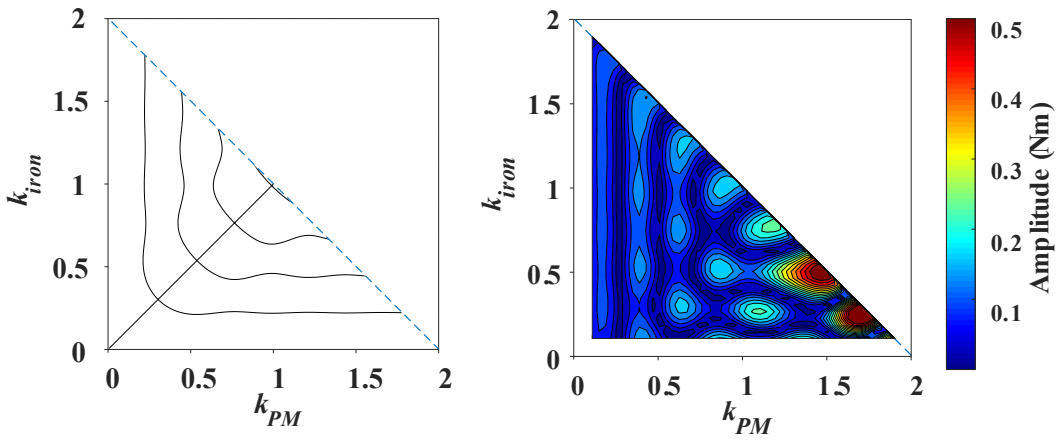

(a) 36th

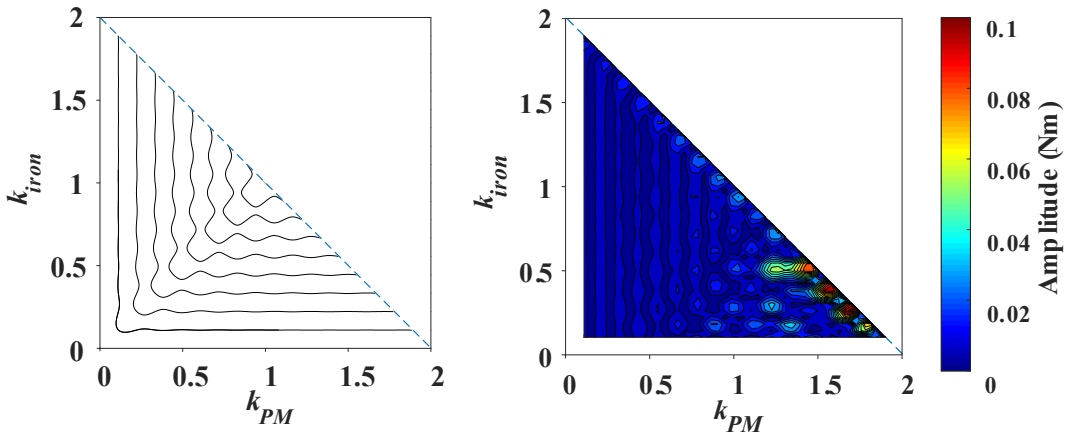

(b) 72nd

Fig. 2.5 Cogging torque harmonics for 9s8p CPPM machine with various PM and iron pole-arc ratios. (left: optimal k_{PM}/k_{iron} combinations for minimum cogging torque harmonics from analytical method, right: harmonic amplitudes from FEM).

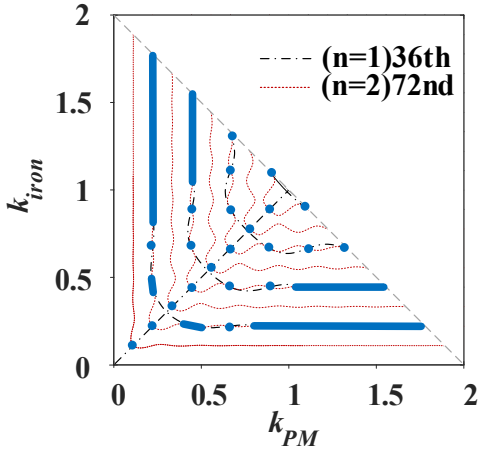

(a) Analytical results (cross points between black and red lines shown in blue points and lines)

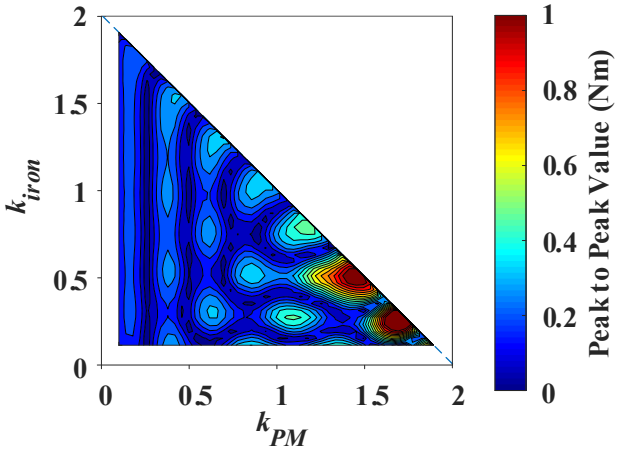

(b) FEM results (dark blue parts)

Fig. 2.6 Optimal k_{PM}/k_{iron} combinations for minimum overall cogging torque of 9s8p CPPM machine with various PM and iron pole-arc ratios.

2.3.2.2 12s8p

The fundamental order of cogging torque N_c is 12 for 12s8p CPPM machine. The dominant 12th, 24th, and 36th order harmonics (n=1, 2, 3) are analyzed in this section. The analytical results are compared with the FEM results in Fig. 2.7 in which good agreement can be seen. It is worth noting that with more harmonics in cogging torque taken into account, the predicted pole-arc ratios will be more accurate.

Similarly, based on the harmonic analysis, the overall minimum cogging torque points can be obtained and compared with the FEM results in Fig. 2.8. Clearly, the analytical results can predict the optimal points of optimal points accurately albeit the values of k_{PM} are a little larger than those from the analytical method.

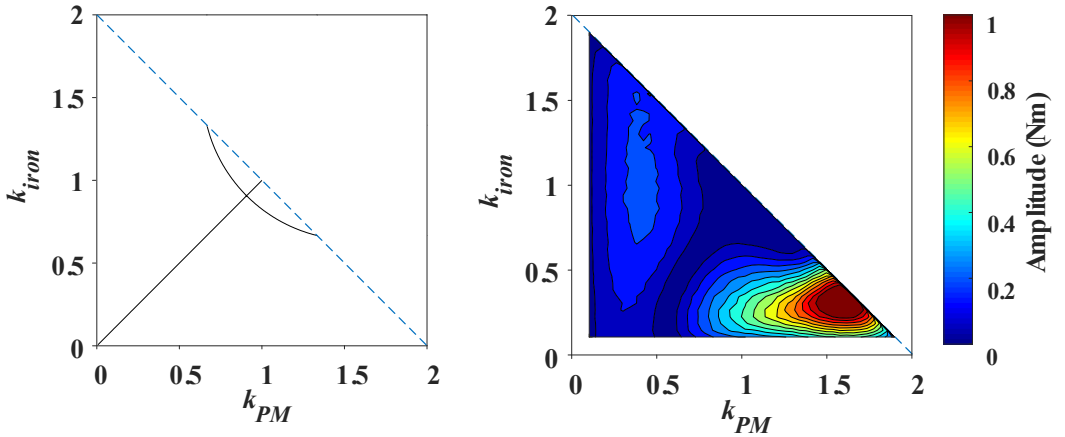

(a) 12th

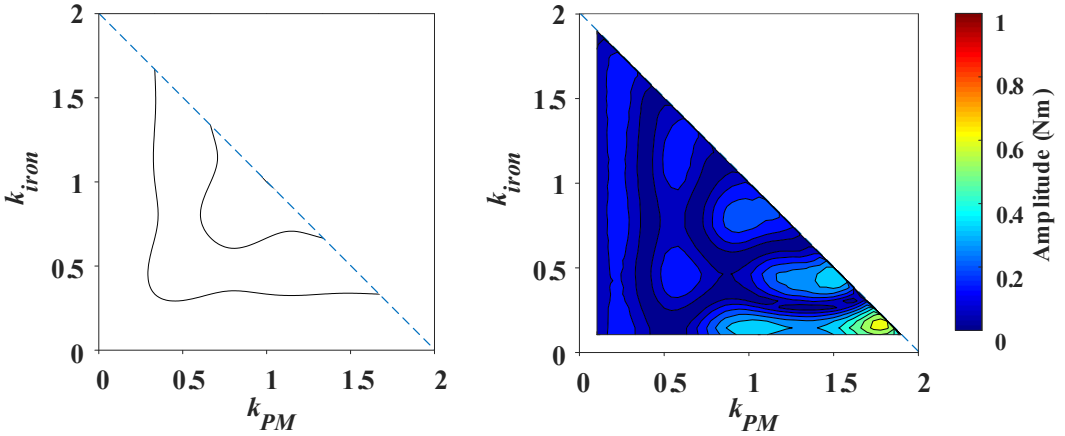

(b) 24th

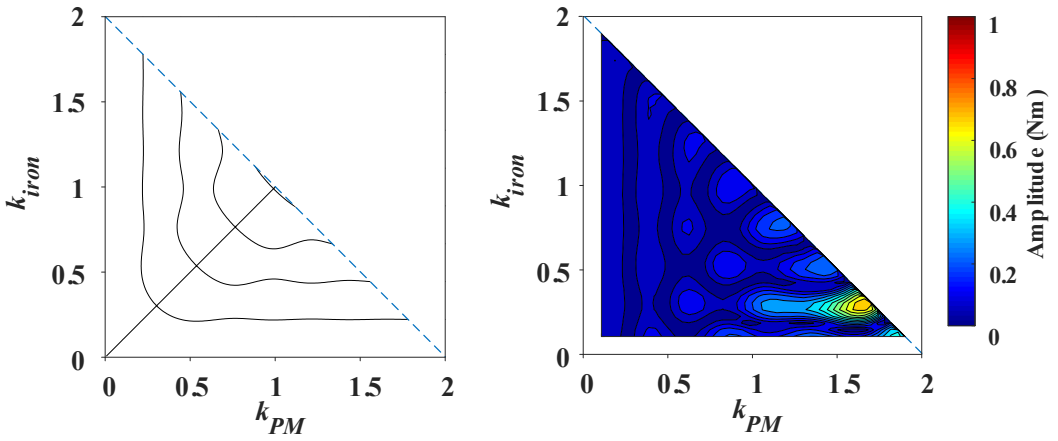

(c) 36th

Fig. 2.7 Cogging torque harmonics of 12s8p CPPM machine with various PM and iron pole-arc ratios. (left: optimal k_{PM}/k_{iron} combinations for minimum cogging torque harmonics from analytical method, right: harmonic amplitudes from FEM).

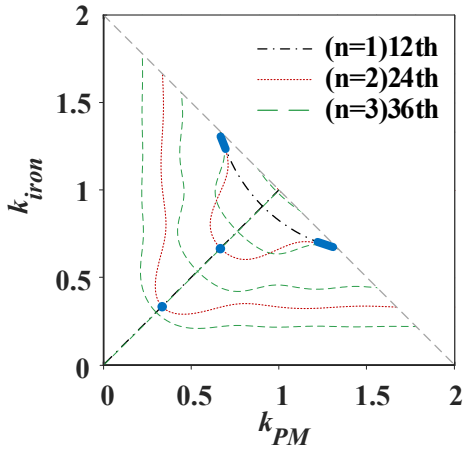

(a) Analytical results (cross points among black, red, and green lines shown in blue points and lines)

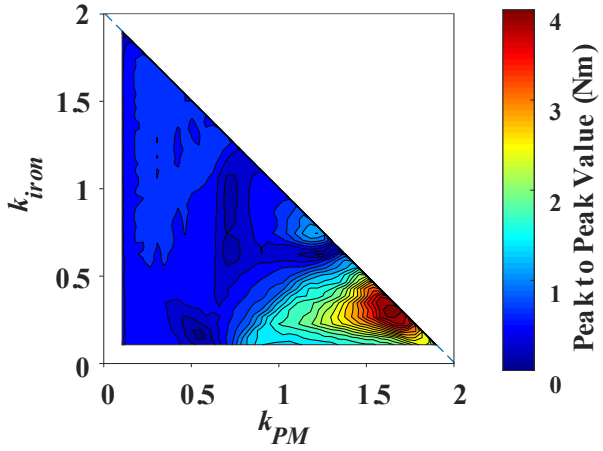

(b) FEM results (dark blue parts)

Fig. 2.8 Optimal k_{PM}/k_{iron} combinations for minimum overall cogging torque of 12s8p CPPM machine with various PM and iron pole-arc ratios.

2.3.2.3 12s10p

The value of the fundamental cogging torque order for 12s10p CPPM machine is identical to that of the SPM counterpart since N_c=LCM(N_s, p)=LCM(N_s, 2p)=60. For the 12s10p CPPM machine, the major harmonic orders of cogging torque are the 60th and 120th (n=1, 2), which are analyzed and compared in Fig. 2.9. The overall cogging torque is illustrated in Fig. 2.10. The results show good agreement with the FEM ones.

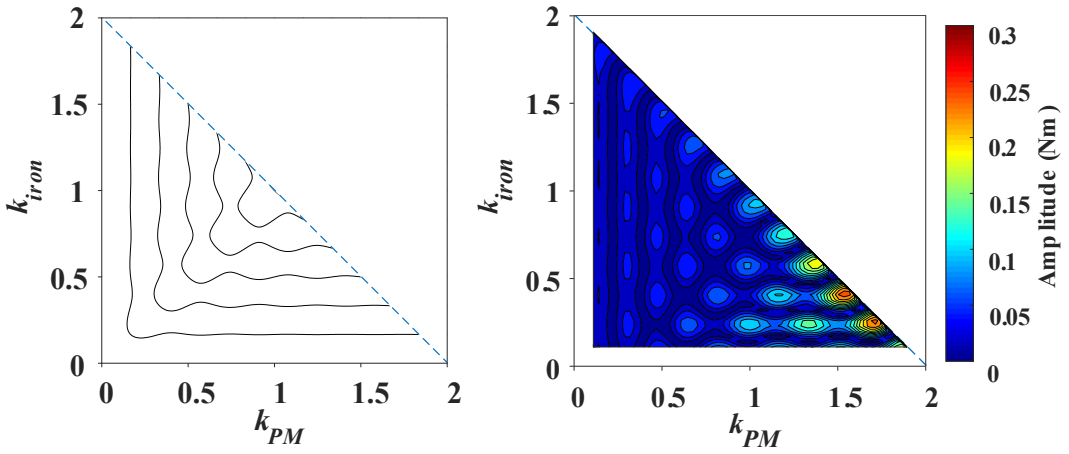

(a) 60th

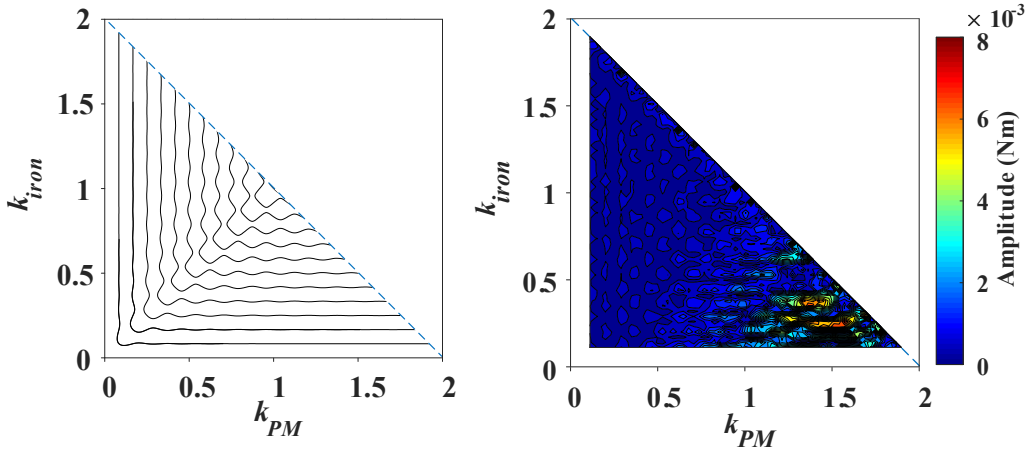

(b) 120th

Fig. 2.9 Cogging torque harmonics for 12s10p CPPM machine with various PM and iron pole-arc ratios. (left: optimal k_{PM}/k_{iron} combinations for minimum cogging torque harmonics from analytical method, right: harmonic amplitudes from FEM).

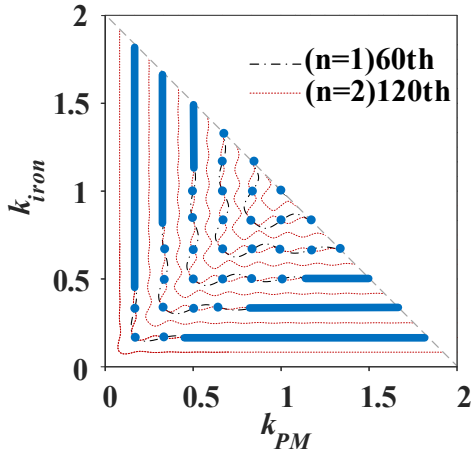

(a) Analytical results (cross points between black and red lines shown in blue points and lines)

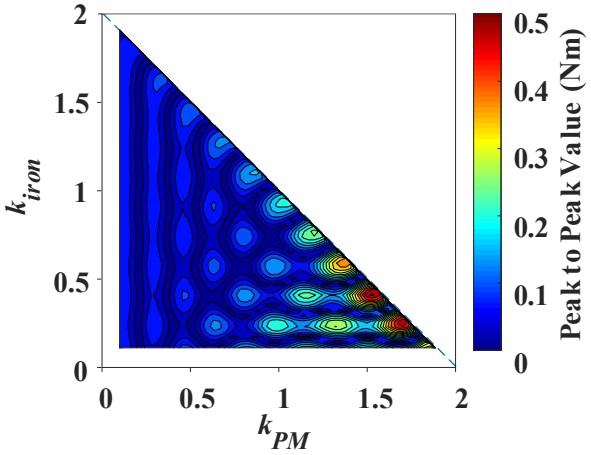

(b) FEM results (dark blue parts)

Fig. 2.10 Optimal k_{PM}/k_{iron} combinations for minimum overall cogging torque of 12s10p CPPM machine with various PM and iron pole-arc ratios.

2.3.3 Pole-Arc to Pole-Pitch Ratio with Pole Shifting

In this section, the cogging torque performances with unbalanced airspace width, i.e. pole shifting, are illustrated.

It can be found from (2.4) that the optimum stator slot opening ratios will not be affected by β, which is the same as the analysis in section III. A. However, for the rotor part, when β is not 0, the Fourier coefficient B_{bqp} is not zero anymore, which introduces the $\cos(nN_c\alpha)$ components in the cogging torque equation (2.4), apart from the $\sin(nN_c\alpha)$ components. Therefore, the introduced additional quadrature components, i.e. $\cos(nN_c\alpha)$, in the cogging torque harmonics tend to reduce the selection range of optimal PM and iron pole-arc ratio combinations. But it can also be found that there will be some specific pole-arc ratios that can lead to the minimum cogging torque and will not change with the shifting angle β.

When

$$\begin{cases} k_{PM} = \dfrac{2lp}{N_c}, l = 1,2,\cdots,2\cdot\left(\dfrac{N_c}{p}-1\right) \\ k_{iron} = \dfrac{2lp}{N_c}, l = 1,2,\cdots,2\cdot\left(\dfrac{N_c}{p}-1\right) \\ k_{PM} + k_{iron} \le 2 - 2\beta/\pi \end{cases} \tag{2.21}$$

the lowest cogging torque can be obtained no matter what the pole shifting angle β is. Clearly, larger N_c will contribute to more feasible optimum k_{PM}/k_{iron} combinations. The third formula in (2.21) is the limitation of structure geometry under pole shifting conditions.

In this section, focusing on the rotor side, β is set as $\pi/18$ electrical degree for three machines to verify the analysis.

2.3.3.1 9s8p

When $\beta=\pi/18$, N_c =36, according to (2.21), the feasible combinations of k_{PM} and k_{iron} are:

$$\begin{cases} k_{PM} = \dfrac{2}{9},\dfrac{4}{9},\dfrac{6}{9},\dfrac{8}{9},\dfrac{10}{9},\dfrac{12}{9},\dfrac{14}{9},\dfrac{16}{9} \\ k_{iron} = \dfrac{2}{9},\dfrac{4}{9},\dfrac{6}{9},\dfrac{8}{9},\dfrac{10}{9},\dfrac{12}{9},\dfrac{14}{9},\dfrac{16}{9} \\ k_{PM} + k_{iron} \le 17/9 \end{cases} \tag{2.22}$$

which are shown in blue points in Fig. 2.11 (a) where the grey points are the points that cannot be selected due to the structure geometric constraint. Compared with the simulation results shown in Fig. 2.11 (b), good agreement verifies the above analysis.

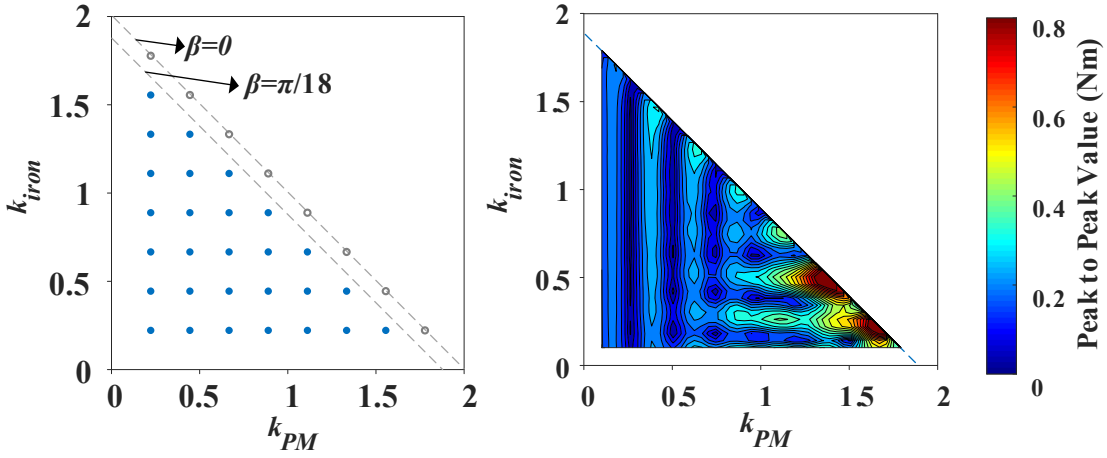

(a) Analytical results (b) FEM results

Fig. 2.11 Optimal k_{PM}/k_{iron} combinations for minimum cogging torque of 9s8p CPPM machine with $\beta=\pi/18$.

2.3.3.2 12s8p

According to (2.21), for 12s8p CPPM machine, N_c is 12 and the minimum pole-arc ratios are:

$$\begin{cases} k_{PM} = \frac{2}{3}, \frac{4}{3} \\ k_{iron} = \frac{2}{3}, \frac{4}{3} \\ k_{PM} + k_{iron} \leq 17/9 \end{cases} \tag{2.23}$$

which are illustrated in Fig. 2.12 (a) and are compared with the FEM results, Fig. 2.12 (b). Obviously, the FEM results agree well with the analytical prediction. Additionally, compared with Fig. 2.8, it is apparent that the iron pole shifting leads to a reduction in the selection range for the optimum PM and iron pole-arc ratios, including both the structure geometric constraint as shown in Fig. 2.12 (a) grey points and also the harmonic constraint according to (2.4).

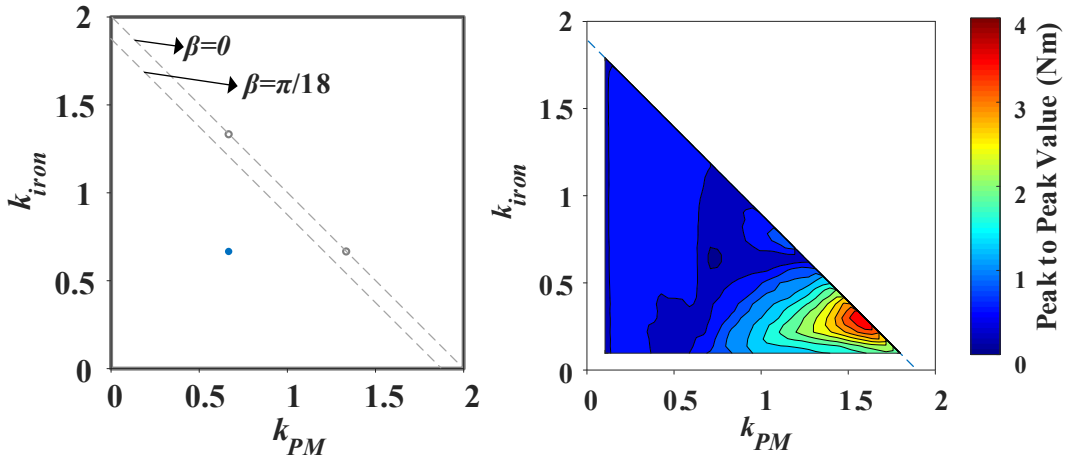

(a) Analytical results (b) FEM results

Fig. 2.12 Optimal k_{PM}/k_{iron} combinations for minimum cogging torque of 12s8p CPPM machine with β=π/18.

2.3.3.3 12s10p

For 12s10p CPPM machine, N_c is 60. Consequently, the feasible optimum pole-arc ratio combinations can be derived accordingly:

$$\begin{cases} k_{PM} = \frac{2}{12}, \frac{4}{12}, \frac{6}{12}, \frac{8}{12}, \frac{10}{12}, \frac{12}{12}, \frac{14}{12}, \frac{16}{12}, \frac{18}{12}, \frac{20}{12}, \frac{22}{12} \\ k_{iron} = \frac{2}{12}, \frac{4}{12}, \frac{6}{12}, \frac{8}{12}, \frac{10}{12}, \frac{12}{12}, \frac{14}{12}, \frac{16}{12}, \frac{18}{12}, \frac{20}{12}, \frac{22}{12} \\ k_{PM} + k_{iron} \leq 17/9 \end{cases} \tag{2.24}$$

The results obtained from the analytical method and FEM method are compared in Fig. 2.13. Under pole shifting conditions, the PM and iron pole-arc ratio cannot be extended to 1 due to the structure geometry constraint as demonstrated in (2.21), thus leading to the grey points in Fig. 2.13 (a). Clearly, larger N_c results in a higher number of optimum pole-arc ratio combinations (more blue points). In addition, simulation results validate the analytical results.

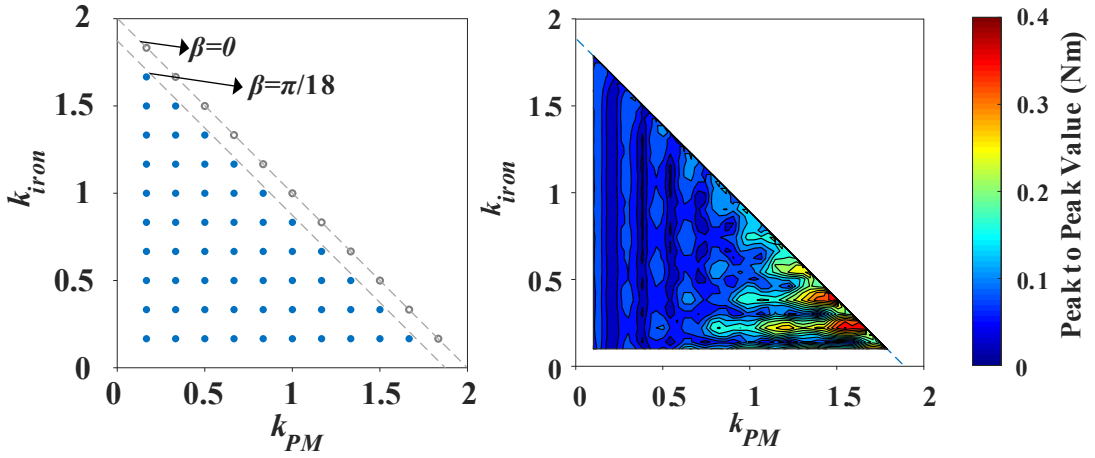

(a) Analytical results (b) FEM results

Fig. 2.13 Optimal k_{PM}/k_{iron} combinations for minimum cogging torque of 12s10p CPPM machine with β=π/18.

2.4 Cogging Torque Minimization for SPM Machine

Similar to section III, the optimum slot opening and pole widths for minimum cogging torque of SPM machines should be the same as those of CPPM machines. It should be noted that in this section, k_{north} and k_{south} denote the ratios of north and south pole arcs to pole pitch, respectively. Since the variation of cogging torque with slot opening for SPM machines has been analyzed comprehensively in [Zhu00] [Zhu09a], only the influences from the rotor side will be analyzed in this section.

2.4.1 Pole-Arc to Pole-Pitch Ratio without Pole Shifting

Without pole shifting, the optimum north and south pole widths are compared in Fig. 2.14 - Fig. 2.19 for 9s8p, 12s8p, and 12s10p SPM machines. It is clear that the FEM results of optimum points for three SPM machines agree well with the analytical results, which validates its effectiveness. It should be noted that due to the balanced characteristics between north and south poles for SPM machines, the agreement of FEM results and analytical results for SPM machines is even better than that for CPPM machines.

2.4.1.1 9s8p

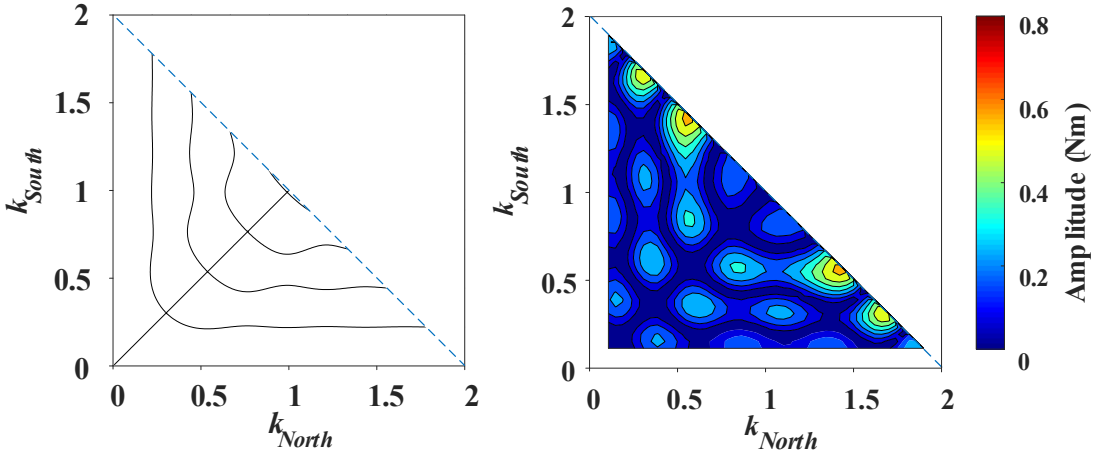

(a) 36th

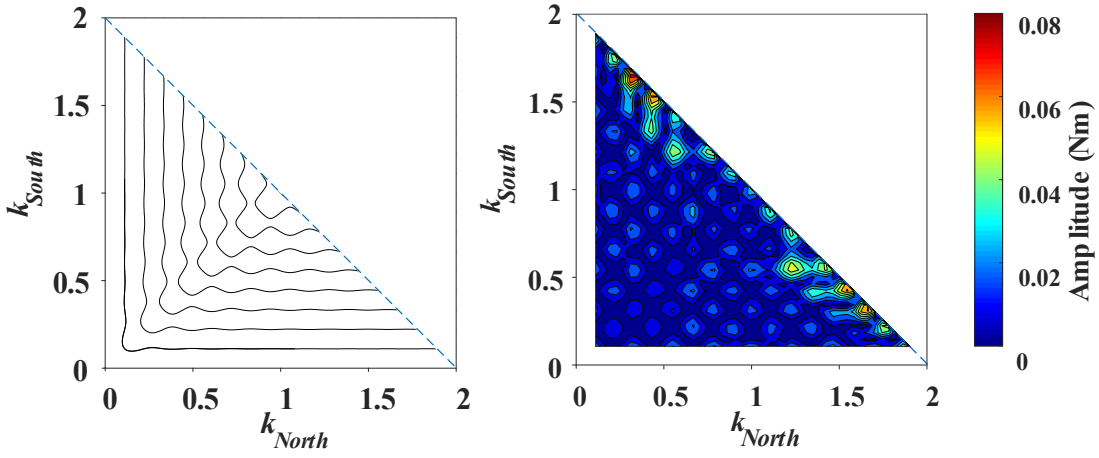

(b) 72nd

Fig. 2.14 Cogging torque harmonics for 9s8p CPPM machine with various PM and iron pole-arc ratios. (left: optimal k_{PM}/k_{iron} combinations for minimum cogging torque harmonics from analytical method, right: harmonic amplitudes from FEM).

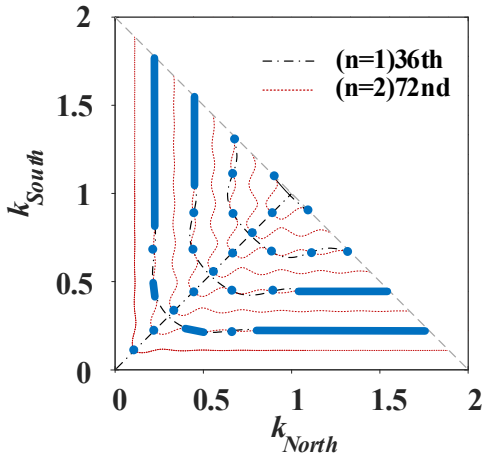

(a) Analytical results (cross points between black and red lines shown in blue points and lines)

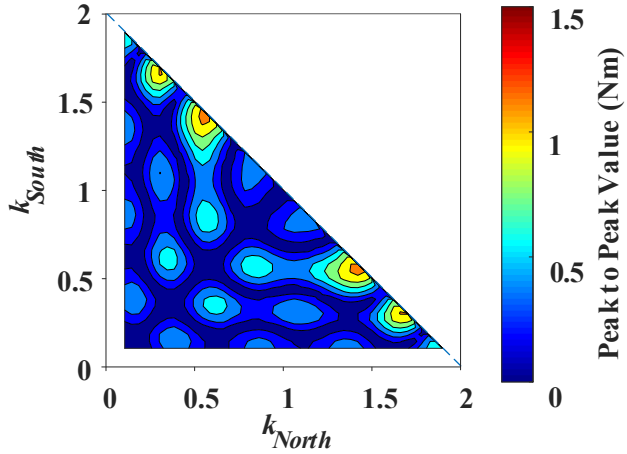

(b) FEM results (dark blue parts)

Fig. 2.15 Optimal k_{PM}/k_{iron} combinations for minimum overall cogging torque of 9s8p CPPM machine with various PM and iron pole-arc ratios. (a) Analytical results (cross points between black and red lines shown in blue points and lines).

2.4.1.2 12s8p

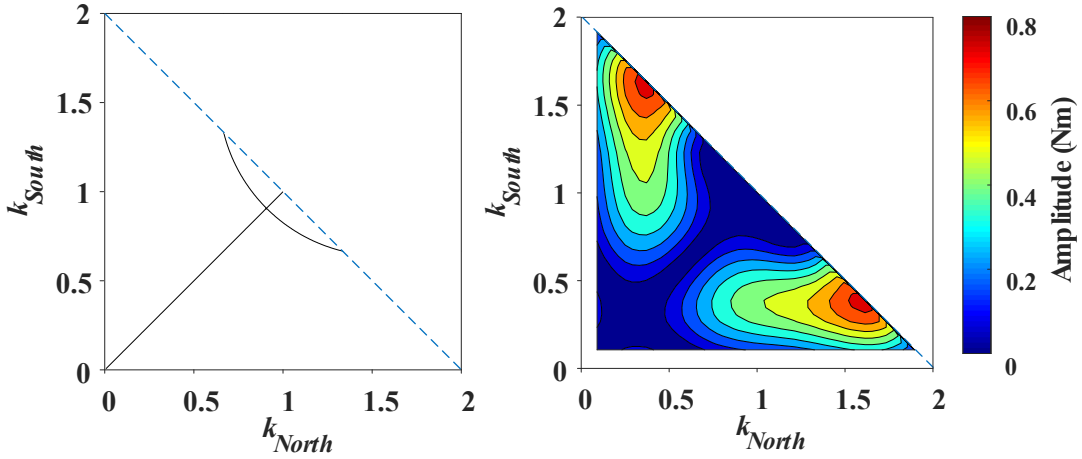

(a) 12th

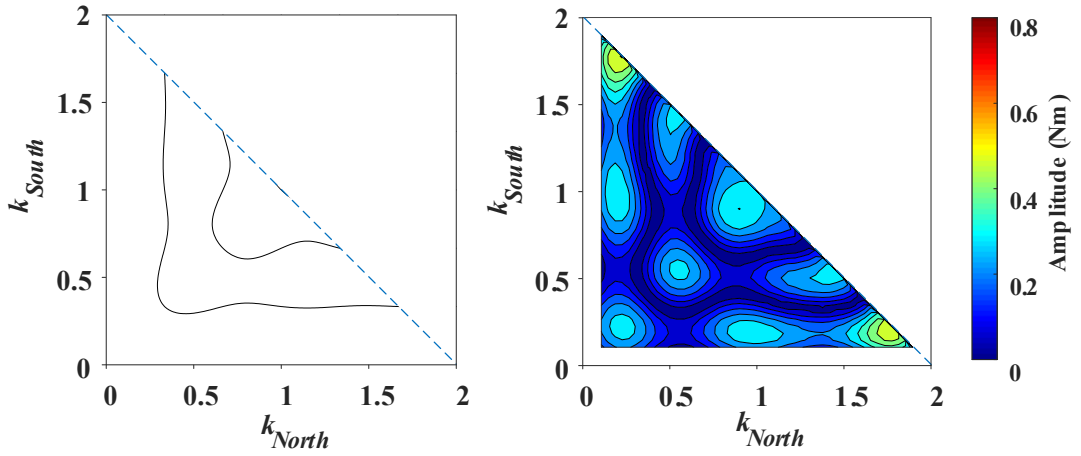

(b) 24th

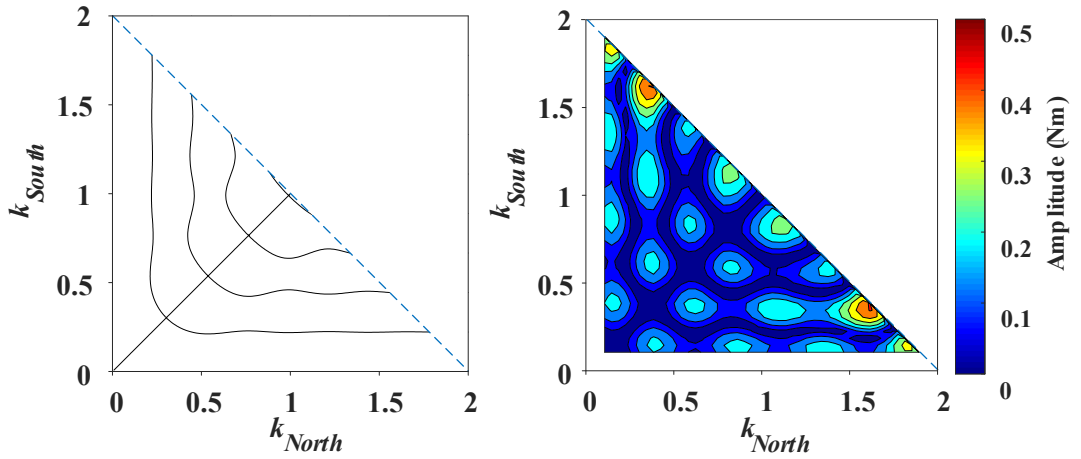

(c) 36th

Fig. 2.16 Cogging torque harmonics of 12s8p CPPM machine with various PM and iron pole-arc ratios. (left: optimal k_{PM}/k_{iron} combinations for minimum cogging torque harmonics from analytical method, right: harmonic amplitudes from FEM).

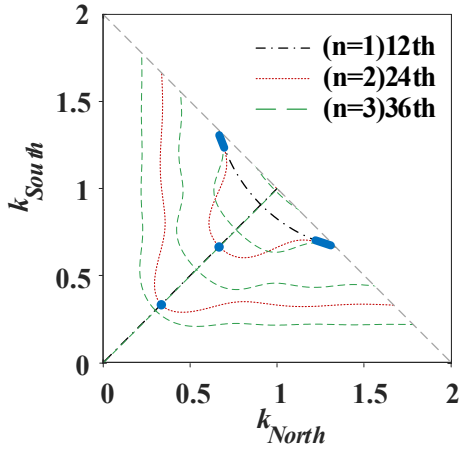

(a) Analytical results (cross points among black, red, and green lines shown in blue points and lines)

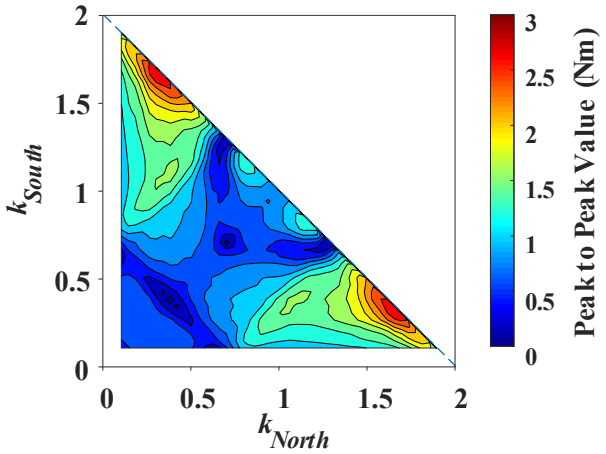

(b) FEM results (dark blue parts)

Fig. 2.17 Optimal k_{PM}/k_{iron} combinations for minimum overall cogging torque of 12s8p CPPM machine with various PM and iron pole-arc ratios.

2.4.1.3 12s10p

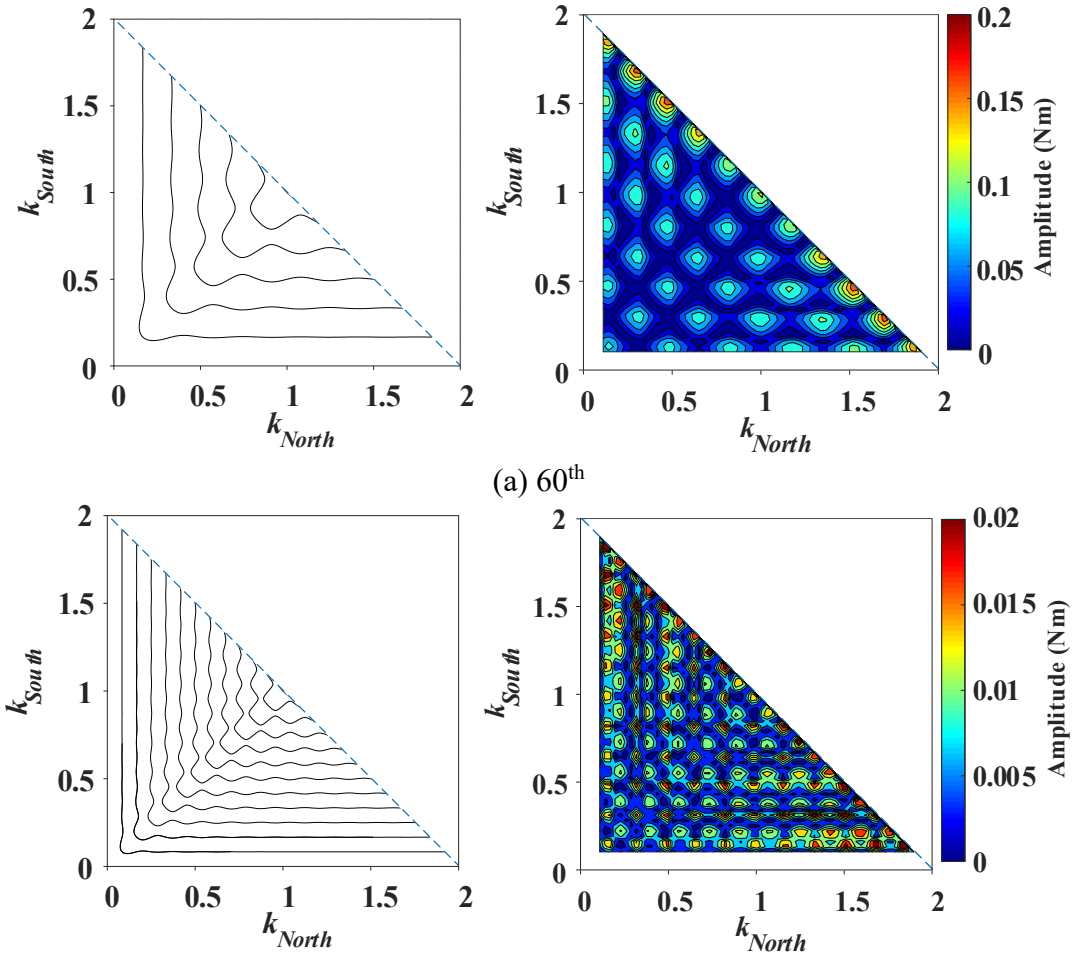

(a) 60th

(b) 120th

Fig. 2.18 Cogging torque harmonics for 12s10p CPPM machine with various PM and iron pole-arc ratios. (left: optimal k_{PM}/k_{iron} combinations for minimum cogging torque harmonics from analytical method, right: harmonic amplitudes from FEM).

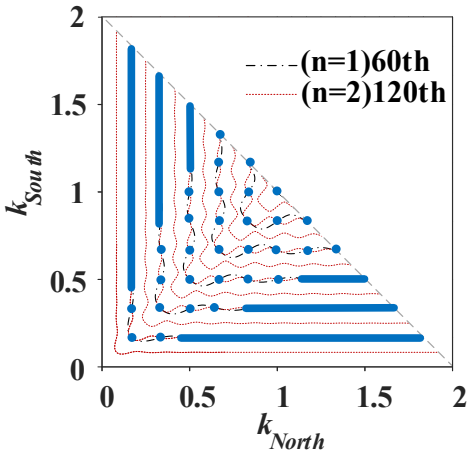

(a) Analytical results (cross points between black and red lines shown in blue points and lines)

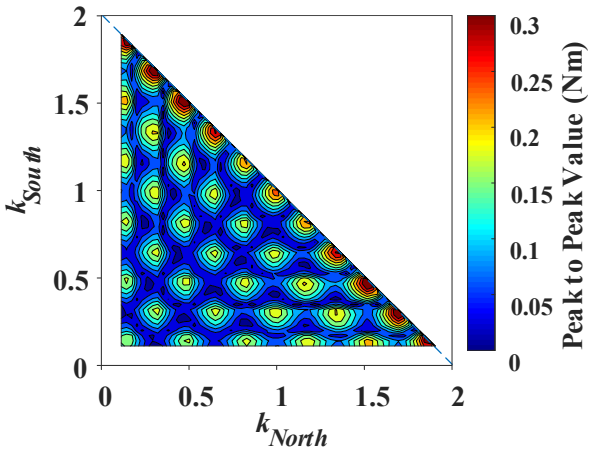

(b) FEM results (dark blue parts)

Fig. 2.19 Optimal k_{PM}/k_{iron} combinations for minimum overall cogging torque of 12s10p CPPM machine with various PM and iron pole-arc ratios.

2.4.2 Pole-Arc to Pole-Pitch Ratio with Pole Shifting

When the pole shifting angle $\beta=\pi/18$, the cogging torque performances for these three SPM machines are analyzed and compared with FEM results in this section.

2.4.2.1 9s8p

For 9s8p machine, N_c =36. According to (2.21), the feasible combinations of k_{PM} and k_{iron} are:

$$\begin{cases} k_{PM} = \frac{2}{9}, \frac{4}{9}, \frac{6}{9}, \frac{8}{9}, \frac{10}{9}, \frac{12}{9}, \frac{14}{9}, \frac{16}{9} \\ k_{iron} = \frac{2}{9}, \frac{4}{9}, \frac{6}{9}, \frac{8}{9}, \frac{10}{9}, \frac{12}{9}, \frac{14}{9}, \frac{16}{9} \\ k_{PM} + k_{iron} \leq 17/9 \end{cases} \tag{2.25}$$

which are shown in blue points in Fig. 2.20 (a) where the grey points are the points that cannot be selected due to the structure geometric constraint. It has a good agreement with the FEM results, Fig. 2.20 (b).

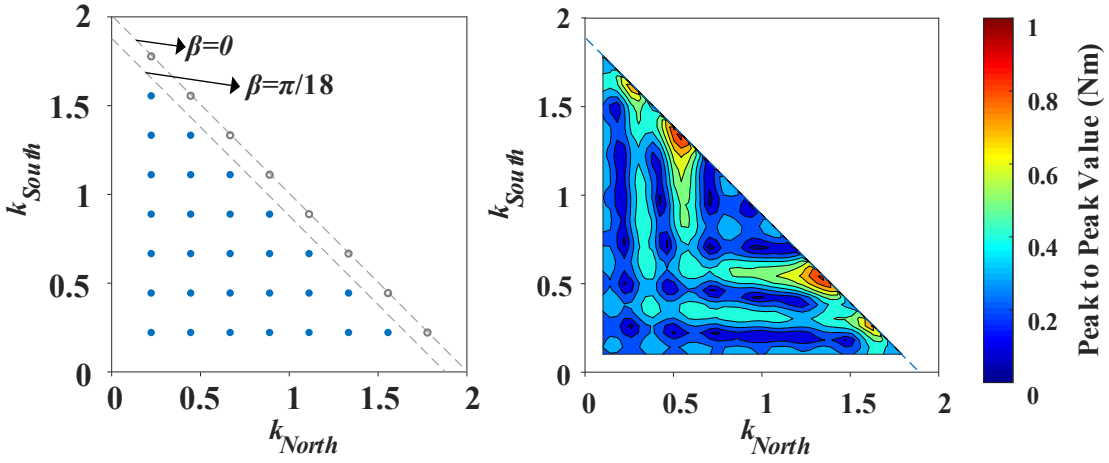

(a) Analytical results (b) FEM results

Fig. 2.20 Optimal k_{PM}/k_{iron} combinations for minimum cogging torque of 9s8p SPM machine with $\beta=\pi/18$.

2.4.2.2 12s8p

According to (2.21), for 12s8p SPM machine, N_c is 12 and the minimum pole-arc ratios are:

$$\begin{cases} k_{PM} = \frac{2}{3}, \frac{4}{3} \\ k_{iron} = \frac{2}{3}, \frac{4}{3} \\ k_{PM} + k_{iron} \leq 17/9 \end{cases} \tag{2.26}$$

which are illustrated in Fig. 2.21 (a) and are compared with the FEM results, Fig. 2.21 (b). Again, a good agreement has been achieved.

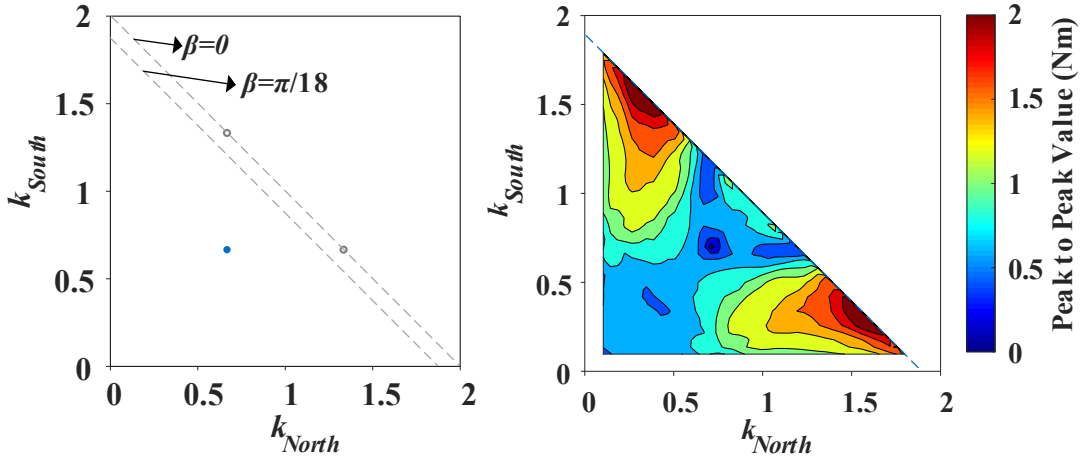

(a) Analytical results (b) FEM results

Fig. 2.21 Optimal k_{PM}/k_{iron} combinations for minimum cogging torque of 12s8p SPM machine with $\beta=\pi/18$.

2.4.2.3 12s10p

For 12s10p SPM machine, N_c is 60. Consequently, the feasible optimum pole-arc ratio combinations can be derived accordingly:

$$\begin{cases} k_{PM} = \frac{2}{12}, \frac{4}{12}, \frac{6}{12}, \frac{8}{12}, \frac{10}{12}, \frac{12}{12}, \frac{14}{12}, \frac{16}{12}, \frac{18}{12}, \frac{20}{12}, \frac{22}{12} \\ k_{iron} = \frac{2}{12}, \frac{4}{12}, \frac{6}{12}, \frac{8}{12}, \frac{10}{12}, \frac{12}{12}, \frac{14}{12}, \frac{16}{12}, \frac{18}{12}, \frac{20}{12}, \frac{22}{12} \\ k_{PM} + k_{iron} \leq 17/9 \end{cases} \tag{2.27}$$

The results obtained from the analytical method and FEM method are compared in Fig. 2.22. The good agreement has verified the analyses.

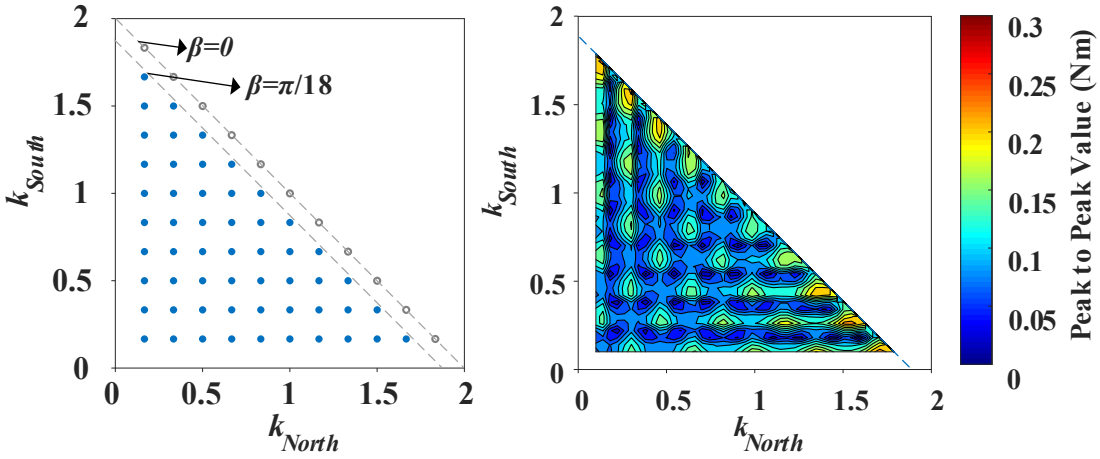

(a) Analytical results (b) FEM results

Fig. 2.22 Optimal k_{PM}/k_{iron} combinations for minimum cogging torque of 12s10p SPM machine with $\beta=\pi/18$.

2.5 Experimental Verification

The cogging torque waveforms of 12s8p and 12s10p CPPM machines, Fig. 2.23, are prototyped and measured to verify the FEM results with the PM and the iron pole-arc ratios of 1.2 and 0.8, respectively. Other key parameters are the same as those listed in Table 2.1.

A dynamic test platform, Fig. 2.24 (a), is used to test the back EMFs and on-load torques. To test the cogging torque, the method proposed in [Zhu09b] is employed with the experimental setup shown in Fig. 2.24 (b). It is worth mentioning that although the cogging torque can also be read from the torque transducer when the prototype is driven by the DC motor at a very low speed, the measured results are the superposition of the cogging torques of the prototype and the DC motor, and tend to be affected by the platform assembly error. To avoid these problems, the static platform is used in this chapter. As shown in Fig. 2.24 (b), the stator is clamped by a three-jaw chuck and a beam is fixed to the rotor shaft. A weight is set on one side of the beam with a scale below it, thus allowing the torque of the rotor always positive to be transferred to the beam and act on the scale. The chuck and stator can rotate to various positions so that the force acting on the scale can be read at any rotor position. The cogging torque can be obtained by removing the offset from the product of the force on the scale and the length of the force arm.

Fig. 2.25 and Fig. 2.26 show the measured and FEM predicted results for 12s8p and 12s10p CPPM machines, respectively, including back EMFs, rated torques under peak current of $10A_{pk}$, and cogging torques. In Fig. 2.25 (c) and Fig. 2.26 (c), the analytically predicted are also compared with the measured and FEM results. It is obvious that the fundamental orders for 12s8p and 12s10p CPPM machines are 12 and 60, respectively, which verifies the analytical analysis (the LCM between N_s and p). Good agreements have been achieved and validated the effectiveness of FEM. The slight difference is mainly due to the manufacturing error and the measurement error. For the cogging torques, the analytically predicted results match well with the FEM and measured results, which confirms the accuracy of the analytical model. The main reason for the errors is that the flux leakage is neglected in the analytical model. It also confirms that the fundamental order in cogging torque of CPPM machine is LCM between N_s and p,

which is the same as obtained by the analytical analysis. The 12s10p machine has 6 slots (even number) in one submachine where the value of the fundamental order of cogging torque in CPPM machine is 60, the same as that of SPM counterpart. However, the 12s8p machine has 3 slots (odd number) in one submachine where the fundamental order of cogging torque in CPPM machine is 12, different from 24 for SPM counterpart.

To evaluate the working points for 12s8p and 12s10p CPPM machines, five positions for each machine are selected which represent stator tooth, stator yoke, rotor tooth, rotor yoke, and magnet, respectively. The maximum flux densities for these positions are illustrated in Table 2.3. Based on the flux densities at these positions, the working points over one electrical cycle in time at the maximum values on B-H curves are shown in Fig. 2.27 (c) and Fig. 2.27 (d) for 12s8p machine, and Fig. 2.28 (c) and Fig. 2.28 (d) for 12s10p machine, where the iron model is 35WW300 and the magnet model is N35. Clearly, the saturation levels are not serious for both of these two machines.

It is worth mentioning that reducing cogging torque is a good method for reducing the no load torque ripples or onload torque ripples for CPPM machines under light load if cogging torque is the dominant torque ripples. However, it is well-known that under load conditions, apart from the cogging torque, reluctance and PM torque ripples may be very large and need to be considered for CPPM machines [Qi22b]. One of the effective solutions is pole shaping method [Qi22b].

(a) 12s8p and 12s10p stators

(b) 8 pole and 10 pole CPPM rotors

Fig. 2.23 Manufactured prototypes.

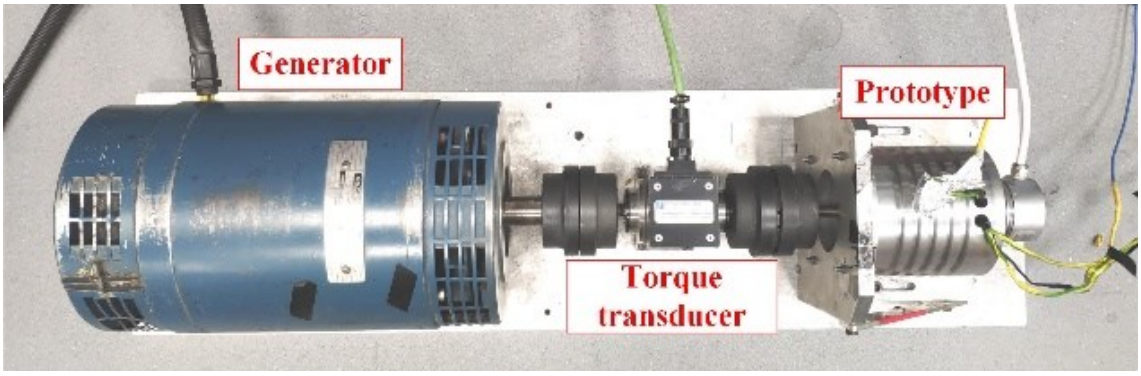

(a) Dynamic test platform for testing back EMF and on-load torque waveform

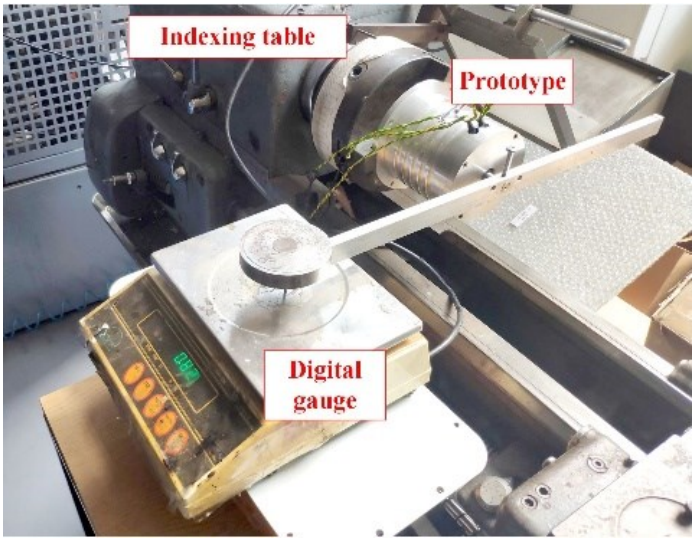

(b) Static test platform for testing cogging torque

Fig. 2.24 Experiment test rigs.

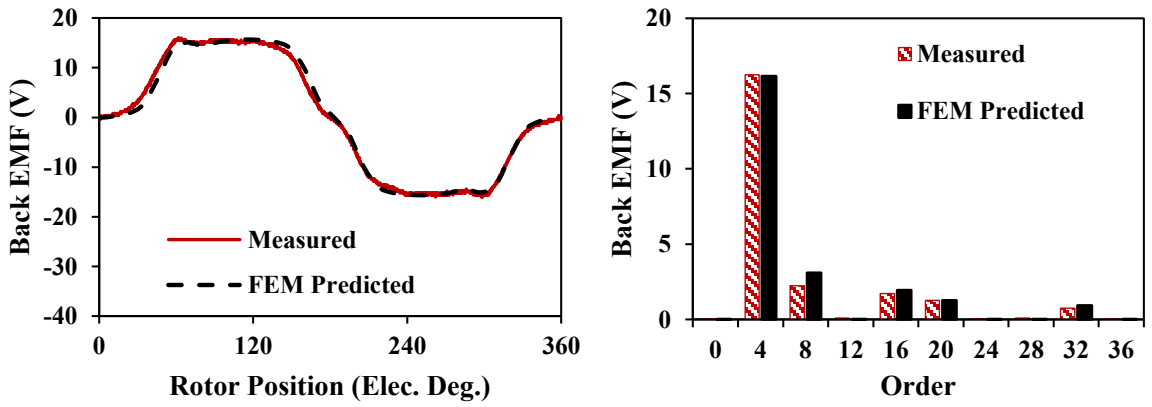

(a) Back EMF

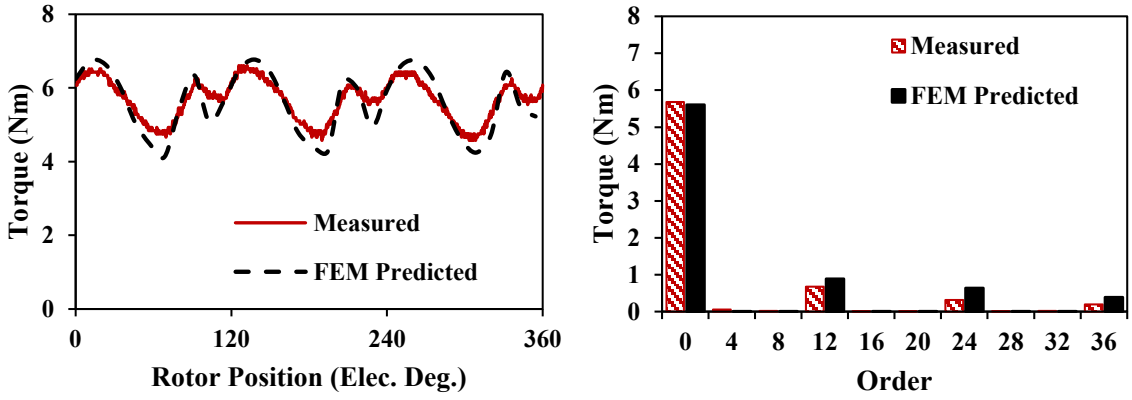

(b) Rated torque (I=10A_{pk})

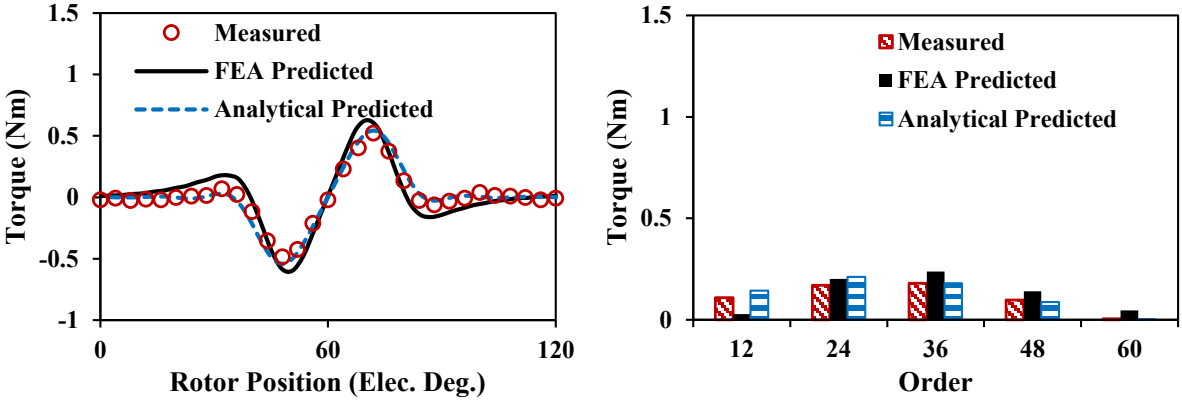

(c) Cogging torque (Order is the cycle number in a mechanical rotation cycle)

Fig. 2.25 Measured and FEM predicted performances for 12s8p CPPM prototype with k_{PM}=1.2 and k_{iron}=0.8. (Order is the cycle number in a mechanical rotation cycle)

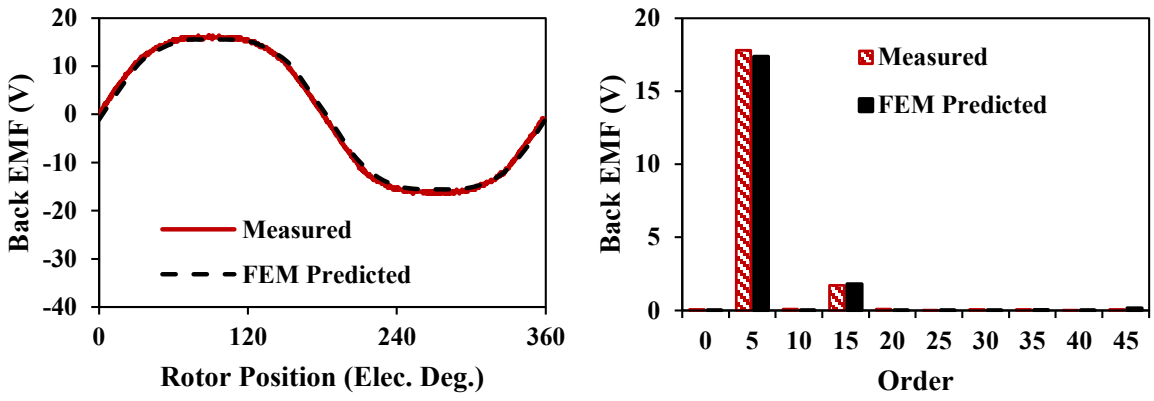

(a) Back EMF

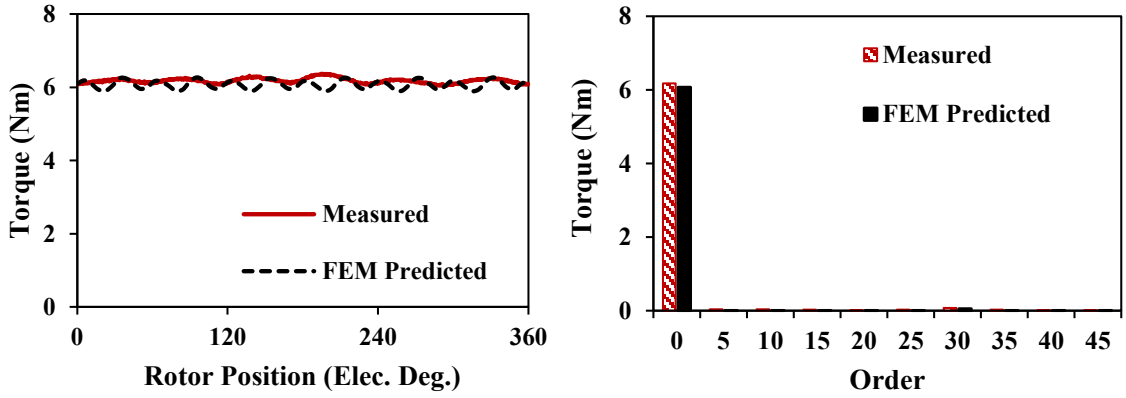

(b) Rated torque (I_{pk}=10A_{pk})

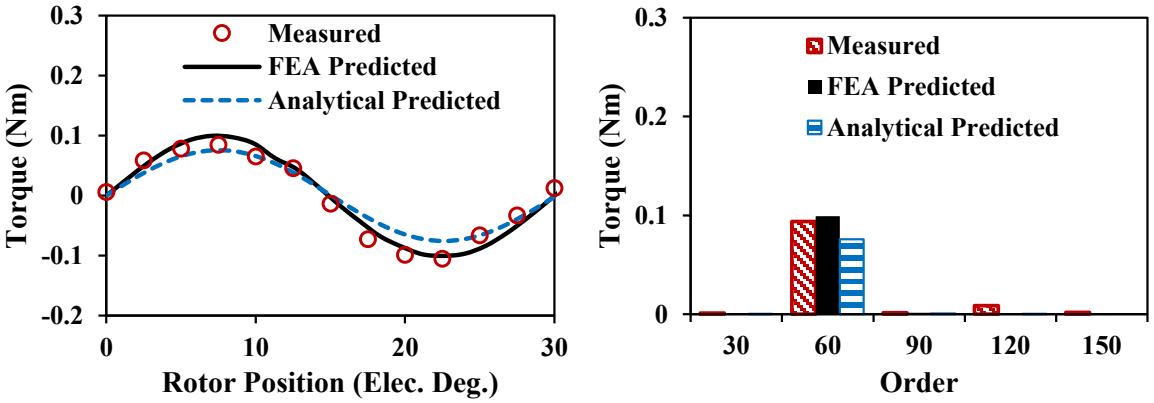

(c) Cogging torque (Order is the cycle number in a mechanical rotation cycle)

Fig. 2.26 Measured and FEM predicted cogging torques for 12s10p CPPM prototype with k_{PM}=1.2 and k_{iron}=0.8. (Order is the cycle number in a mechanical rotation cycle)

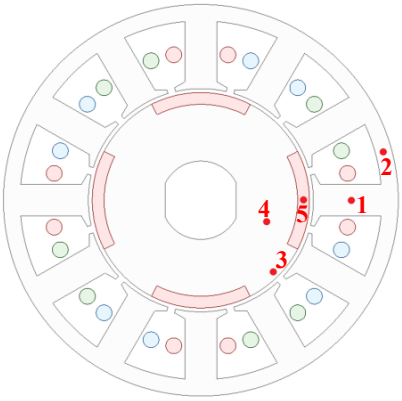

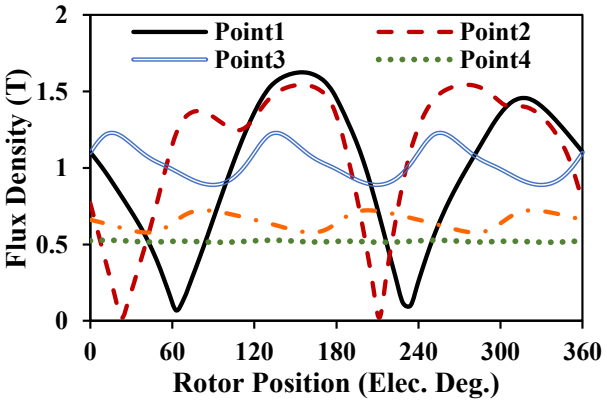

(a) Selected 5 positions (b) Flux density waveforms under one electrical cycle in time

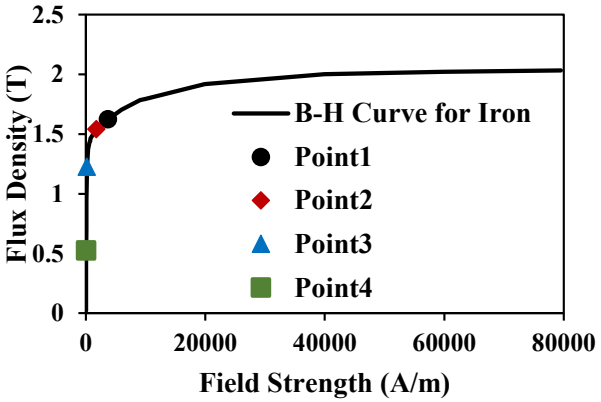

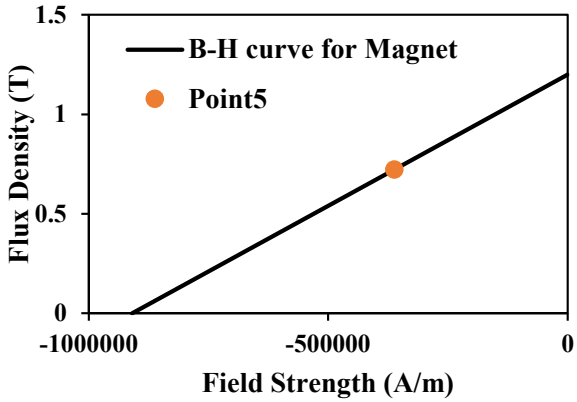

(c) Working points for stator and rotor irons (d) Working point for magnet

Fig. 2.27 Working points for five positions in 12s8p CPPM machine at the highest flux density values.

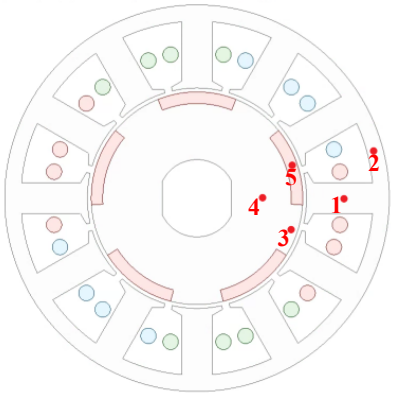

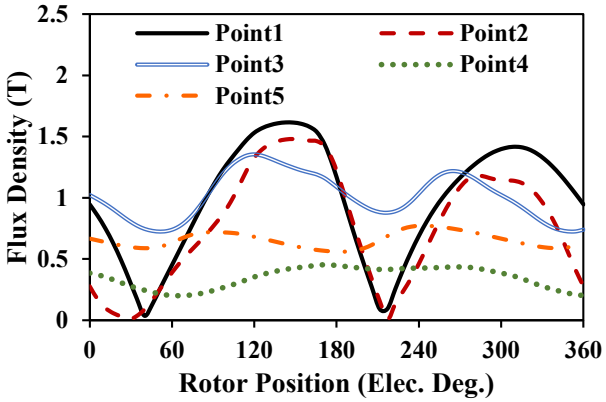

(a) Selected 5 positions (b) Flux density waveforms under one electrical cycle in time

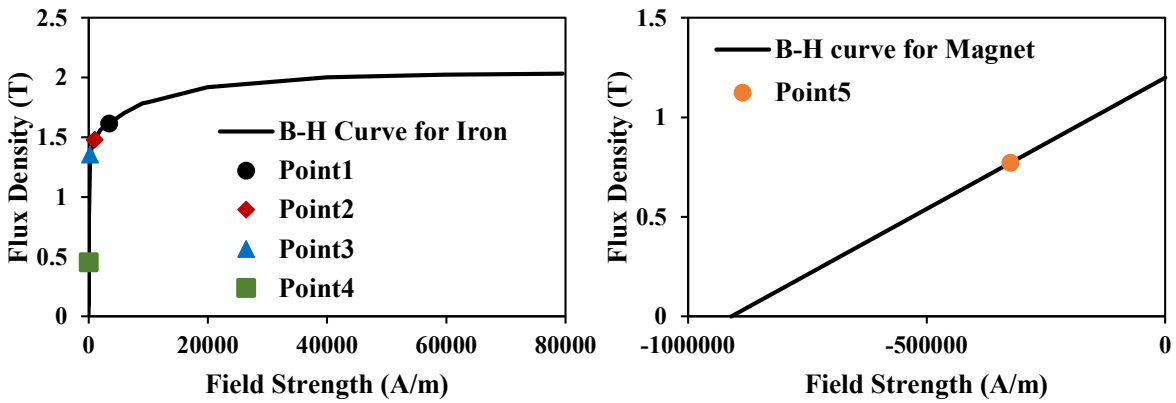

(c) Working points for stator and rotor irons (d) Working point for magnet

Fig. 2.28 Working points for five positions in 12s10p CPPM machine at the highest flux density values.

TABLE 2.3 Maximum Flux Densities for Five Positions over One Electrical Cycle

	12s8p CPPM		12s10p CPPM	
	Peak value (T)	Average value (T)	Peak value (T)	Average value (T)
Point1	1.62	0.98	1.61	0.98
Point2	1.54	1.12	1.48	0.77
Point3	1.23	1.04	1.36	1.01
Point4	0.53	0.52	0.45	0.35
Point5	0.72	0.65	0.77	0.65

2.6 Effect of Magnetic Saturation

The impact of magnetic saturation can be divided into two aspects: overall uniform magnetic saturation and local magnetic saturation.

When the machine suffers from overall uniform magnetic saturation, the increased flux reluctance in iron will lead to the amplitude decrease of the function $G^2(\theta)$, which will result in a larger fringing effect. At the same time, the flux leakage of magnets will also be affected. Therefore, this will inevitably result in a variation of amplitudes of cogging torque harmonics. By setting the relative permeability μ_r of iron as 10000, 500, and 100 with linear material, the cogging torques obtained from FEM for 12s8p and 12s10p CPPM machine with a pole-arc to pole-pitch ratio of 1.2 are shown in Fig. 2.29. Evidently, the amplitudes of harmonics in cogging torques are changed for both machines.

When the machine suffers from local magnetic saturation, it will lead to more complex characteristics in cogging torque harmonics since the function $G^2(\theta)$ varies at each rotor position. Because the magnetic saturation tends to happen under load conditions, the effect of on-load saturation on cogging torque is deeply analyzed in [Aza12] and [Chu13]. With the help of the frozen permeability method, it was found that the saturation will not only affect the amplitude of cogging torque harmonics but also has the potential to change the harmonic order content [Aza12].

However, the magnetic saturation needs to be considered in the design process. However, the magnetic saturation is usually neglected in analytical prediction of cogging torque.

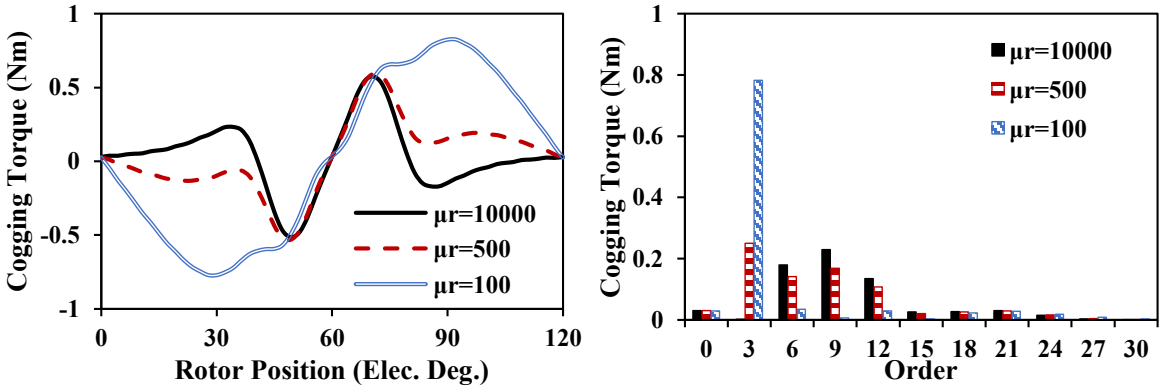

(a) 12s8p CPPM

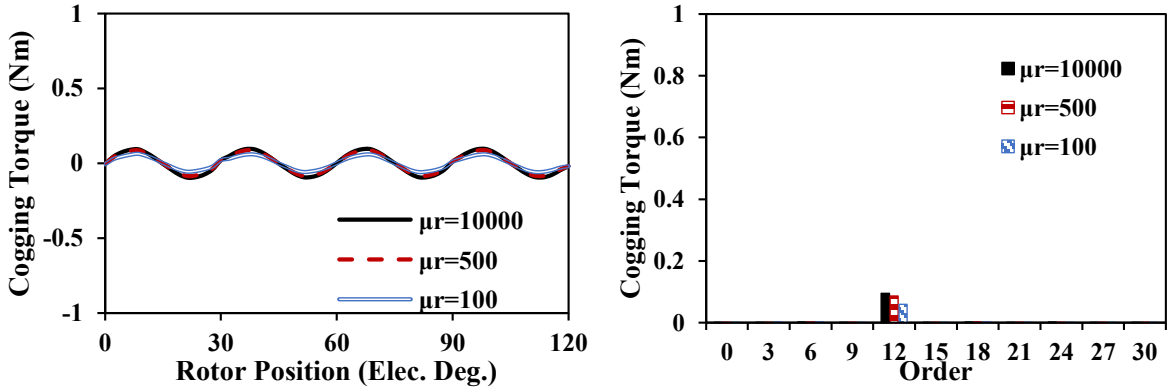

(b) 12s10p CPPM

Fig. 2.29 Cogging torques with different permeability of iron.

2.7 Summary

In this chapter, a general analytical expression of cogging torque accounting for unequal north and south poles as well as pole shifting has been developed, which can be applied to both CPPM and SPM machines. Based on the developed analytical model, the characteristics of cogging torque in the machines with unequal north and south pole widths, particularly the fundamental cogging torque order, are analytically derived and general methodologies for minimizing the cogging torque are obtained, accounting for the influences of design parameters, including the slot opening ratio, the rotor pole ratio, and the rotor pole shifting, etc. The cogging torques of CPPM and SPM machines with 9s8p, 12s8p, and 12s10p slot/pole number combinations are used for analyses as illustration and two CPPM prototypes with 12s8p and 12s10p are measured to validate the FEM predicted results. The conclusions can be summarized as follows:

1) When the north and south pole widths are unequal, no matter whether they are CPPM machines or SPM machines, the fundamental cogging torque order is the LCM between N_s and p, while it is the LCM between N_s and $2p$ when the machine has equal north and south pole widths.

2) Even if the north and south pole widths are equal, as long as the north and south poles are physically not identical, as is often the case in CPPM machines, the fundamental cogging torque order is the LCM between N_s and p.

3) When there is an even number of slots in one submachine, LCM(N_s, p)=LCM(N_s, $2p$). On the contrary, when there is an odd number of slots in one submachine, LCM(N_s, p)=LCM(N_s, $2p$)/2.

4) It is possible to minimize the cogging torque in CPPM machines by selecting proper slot opening width, PM and iron pole widths.

5) North or south pole shifting is prone to changing the optimum PM and iron pole widths combinations. However, it is verified that the pole shifting will not affect the minimum cogging torque under some specific pole-arc widths combinations.

6) The magnetic saturation will affect the harmonic amplitudes of cogging torques and thus peak to peak value of overall cogging torques.

7) All the conclusions obtained for CPPM and SPM machines in this chapter can be equally applied to other types of PM machines, such as IPM CPPM and conventional IPM machines with equal or unequal north and south poles.

CHAPTER 3
EFFECT OF POLE SHAPING ON THE TORQUE CHARACTERISTICS OF CPPM MACHINES

It has been found in chapter 2 that although the cogging torque can be reduced by adjusting the PM and iron pole arc widths, the on-load torque ripple is still relatively large due to torque ripples caused by armature reaction effect. Besides, since the average torque is also sensitive to the pole arc widths, the minimization of cogging torque by this method will inevitably affect the average torque. In fact, in consequent pole machines, the rotor pole arc is usually optimized to realize the largest output torque with pole shaping methods used to reduce torque ripple. However, such approaches tend to be limited by constraints imposed on the pole shapes. It is a common practice to adopt similar PM and iron pole shapes, an approach that does not fully account for the different characteristics of PM and iron poles in CPPM machines, often leading to large even order harmonics in the air-gap flux density. This chapter proposes a shaping method with a variable rotor profile and pole arc span being established by means of optimization by Genetic Algorithm (GA). Actually, any optimization method, including Simulated Annealing (SA), GA, and so on, can be used to find out the optimum pole shape and verify the analyses. However, GA, as a random search method, is often applied as an approach to solving global optimization problems and is integrated with ANSYS Maxwell package, which makes it suitable and convenient to be used. Thus, it is adopted in this thesis. It is demonstrated that for a fixed quantity of PM material, different PM and iron pole shapes in combination with optimal PM and iron pole arc spans are essential for ensuring both maximum output torque and lower torque ripple when due account is taken of flux leakage. It also demonstrates that since the flux density in the region under a PM pole is governed by the magnetic potential produced by magnets while it is governed by magnetic reluctance under iron pole, different PM pole and iron pole shapes are necessary to reduce the even order harmonics in a CPPM machine and consequently to reduce torque ripple. The performances of optimized and more conventional CPPM machines are compared by the finite element method on 12-slot/8-pole prototype motors.

This chapter is published on IEEE Transactions on Industry Applications [Qi22a]:

[Qi22a] J. Qi, Z.Q. Zhu, L. Yan, G.W. Jewell, C.W. Gan, Y. Ren, S. Brockway, and C. Hilton, "Effect of pole shaping on torque characteristics of consequent pole PM machines," *IEEE Trans. Ind. Appl.*, vol. 58, no. 3, pp. 3511-3521, May-June 2022.

3.1 Introduction

Commonly, the PM pole arc span of CPPM machines is extended beyond that employed in a conventional PM machine in an attempt to increase the output torque [Li18b] [Bai18]. However, the flux leakage at sides of each magnet is neglected in such considerations and the additional material in this wider pole can lead to only a modest increase in torque which does not commensurately trade favorably within the increased PM volume and hence fails to fully optimize the potential cost savings of adopting a CP arrangement. In this chapter, pole shapes are optimized to maximize output torque with full consideration of flux leakage with an imposed fixed PM volume design constraint.

Another feature of many CPPM machines is that unbalanced flux density distributions caused by the different nature of PM and iron poles give rise to even order harmonics in the air-gap field and hence induced EMF, and tend to lead to large cogging torque and torque ripple, in turn contributing to increased vibration and acoustic noise [Chu10] [Zha19b] [Li19c].

Rotor pole shaping is an effective means to reduce the unique even-order back EMF harmonics and hence torque ripple. This technique has been widely used and many specific shapes have been employed in various types of machines, including CPPM machines, to achieve low torque ripple [Jah96] [Wan14a] [Wan14b] [Wan19a] [Wat18] [Eva10] [Li18e] [Chu16]. For CPPM machines, pole-end angle optimization [Wat18], inverse cosine air-gap [Eva10], dovetailed rotors [Li18e], non-uniform air-gaps [Chu16], different PM and iron pole shape [Zha20a] have been investigated.

However, the fundamentally different natures of PM and iron poles are not meaningfully taken into account in these previous design studies. The flux density waveform under the PM pole is

governed largely by the magnetic potential of PMs, while under the iron pole it is mainly governed by the air-gap magnetic reluctance. Therefore, it is unsurprising that the adoption of different shapes for these two pole types is likely to yield some performance dividend.

Taking the specific case of a 12-slot/8-pole CPPM machine as an example, the unbalance between PM and iron poles for consequent pole machine is considered in pole shaping process, where the even order harmonics in flux will be induced by the unbalanced characters. The arrangement of this chapter is as follows: Firstly, the principles will be demonstrated in section 3.2. Then, the pole shaping methods will be introduced and optimized with the FEM in section 3.3. In section 3.4, the FEM predicted performance and experiments will be analyzed and compared. Finally, conclusions are highlighted in section 3.5.

3.2 Principles of Shaping in CPPM Machines

3.2.1 Air-Gap Flux Density for CPPM Machines

The flux path under one pole pair is adopted to demonstrate the principle of pole shaping in a CPPM machines can be illustrated using the simplified representation of the air-gap shown in Fig. 3.1. Clearly, the air-gap region can be divided into two parts, viz. the section under the PM pole and that under the iron pole. Supposing the magnetic permeabilities of stator and rotor laminations are sufficiently high that being approximately treated as infinitely permeable is a reasonable assumption. Then, the magnetic field strength in the idealized rotor core can, by definition, be obtained from:

$$H_c L'_{mp} = B_{PM} S_{p1} R_{PM} + F_s \tag{3.1}$$

$$F_s = B_{iron} S_{p2} R_{iron} \tag{3.2}$$

$$R_{iron} = (L_{ag} + L_{PM} - L'_{ip})/\mu S_{p2} \tag{3.3}$$

where B_{PM} and B_{iron} are the flux densities under PM pole and iron pole, S_{p1} and S_{p2} are the corresponding cross areas, H_c is the coercivity of magnet, L_{PM} is the thickness of magnet, μ is the magnetic permeability of air, L'_{mp} and L'_{ip} are the rotor outline functions, R_{PM} and R_{iron} are the flux reluctances in air-gap under PM and iron poles, respectively, and F_s is the magnetic

potential in stator. R_{PM} can be treated as a constant value when the permeability of permanent magnet is considered to be the same as that of air.

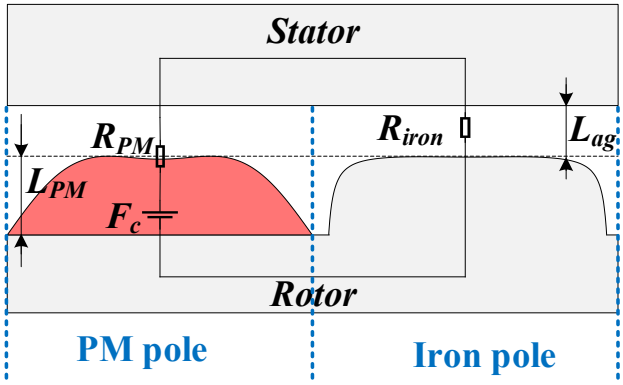

Fig. 3.1 Idealized flux path of one pole pair.

In pole shaping, only the rotor profile functions L'_{mp} and L'_{ip} vary with the rotor position θ_r, and can be expressed by harmonic series:

$$\begin{cases} L'_{mp} = \sum_{a}^{\infty} [A_{msa} sin(a\theta_r) + A_{mca} \cos(a\theta_r)] \\ L'_{ip} = \sum_{b}^{\infty} [A_{isb} sin(b\theta_r) + A_{icb} cos(b\theta_r)] \end{cases} \tag{3.4}$$

where A_{msa} and A_{mca} are the amplitudes of sin and cos components for L'_{mp} for the a-th harmonic and A_{isb} and A_{icb} are the amplitudes of sin and cos components for L'_{ip} for the b-th harmonic.

Consequently, the resultant air-gap flux density due to the rotor shaping effects can be expressed as the product of (3.1)-(3.3):

$$\begin{cases} B_{PM} = \dfrac{HL'_{mp} - F_s}{R_{PM} S_{p1}} \\ B_{iron} = \dfrac{\mu F_s}{L_{ag} + L_{PM} - L'_{ip}} \end{cases} \tag{3.5}$$

Based on (3.5), the fundamental air-gap flux density is derived in [Li18b] with the fixed PM thickness and neglecting flux leakage at the sides of each magnet. However, subject to the

constraint of a fixed quantity of PM and introducing the flux gap at the end of each magnet segment as a feature to reduce the flux leakage, the optimum pole arc ratio tends to decrease slightly from that established in [Li18b].

It can also be seen that (3.5) provides a relationship between flux density in air-gap and the rotor shape. As will be apparent from (3.4) and (3.5), smaller values of L'_{mp} and L'_{ip} can lead to larger flux density under two poles, which tends to enhance the average torque. Besides, L'_{mp} is in the numerator while L'_{ip} is in the denominator, which means the flux density under the PM pole is driven by the magnetic potential produced by magnets while it is driven by magnetic reluctance under the iron pole. Therefore, it can be found that for the identical PM pole and iron pole shapes, the flux densities under two poles are unbalanced, which will lead to large even order harmonics in spatial variation of flux density in the air-gap. As will be apparent, different PM pole and iron pole shapes are necessary for low even order harmonics and hence torque ripple.

3.2.2 Effect on EMF and Torque Performance

The no-load, open-circuit, back EMF U_s can be derived by:

$$U_s = \frac{d\psi_f}{dt}$$
$$\psi_f = N_{TPC} \int B(t) d\, A_t \tag{3.6}$$

where ψ_f is the PM flux linkage, B(t) is the air-gap flux density at time t, A_t is the cross-sectional area of tooth tips at the air-gap and N_{TPC} is the number of turns per coil.

The unbalanced positive and negative waveforms in air-gap flux density will lead to the spatial even order harmonics, which will in turn contribute to the even order harmonics in phase flux linkage and hence the even order harmonics in back EMF. Therefore, a balanced flux density in air-gap can result in the suppression of even order harmonics in flux linkage and back EMF. Furthermore, the dominant third order torque ripple can also be reduced when injecting sinusoidal current.

As for the cogging torque, it has been calculated from the energy method in chapter 2:

$$T_{cog}(\alpha) = \frac{\pi L_s}{4\mu} N_C ({R_s}^2 - {R_m}^2) \sum_{n=1}^{\infty} \begin{bmatrix} n\left(G_{akN_s} B_{aqp} + G_{bkN_s} B_{bqp}\right) sin(nN_C\alpha) \\ +n\left(G_{akN_s} B_{bqp} - G_{bkN_s} B_{aqp}\right) cos(nN_C\alpha) \end{bmatrix} \quad (3.7)$$

where N_C is the least common multiple between N_s and p:

$$N_C = LCM(N_s, p) \quad (3.8)$$

Therefore, the cycle number of the cogging torque waveform over 360° electrical angle for conventional CPPMs is the multiple of N_C/p, which is different from that of SPM machines when there are odd number of slots in one submachine, including the 12-slot/8-pole CPPM machine as analyzed in this chapter.

Apart from the established pole arc widths optimization methods to minimize cogging torque in chapter 2, decreasing the amplitudes of field harmonics in air-gap is generally effective in reducing the cogging torque amplitude.

3.3 Proposed Optimization Method and Results

3.3.1 Proposed Model

In order to optimize the rotor dimensions to achieve the highest possible output torque while also reducing torque ripple, a GA based shaping method with variable rotor outline and pole arc span has been employed. To predict the performance accurately, FEM is utilized in this section and the GA optimizer is adopted. Fig. 3.2 shows a schematic of the model, in which the outer profiles of the PM and iron poles are different and represented respectively by spline curves which pass through several discrete points uniformly distributed over each half pole pitch to form a smooth surface, noting that each pole exhibits mirror symmetry within that pole. The key parameters for these machines are listed in Table 3.1. Due to the feature of spline curve, the rotor surface sometimes extends outside the rotor area R_{max}, which makes the smallest air-gap length smaller than 1mm. To avoid this, a boolean operation called “intersect” is applied to rotor poles and a circle with radius R_{max}. In other words, the outside part of both PM and iron poles can be removed by this operation.

Table 3.1 Key Design Parameters of Analyzed Machines

Parameter	Value	Unit
Stator outer diameter	100	mm
Stator inner diameter	57	mm
Stator stack length	50	mm
Air-gap	1	mm
Yoke width	4.2	mm
Tooth width	8	mm
Rotor inner diameter	36	mm
Magnet volume	14700	mm^3
Remanence of magnet	1.2	T
Number of rotor poles	8	-
Number of stator slots	12	-
Stator turns per coil	46	-
Rated current	10	A_{pk}
Rated speed	400	rpm

As shown in Fig. 3.2, for the *k*-th point in iron pole, the position can be defined by:

$$\begin{cases} \theta_{ik} = \dfrac{k-1}{2(N_{ps}-1)}\theta_{pi}, k \in N^+ \\ R_{si} - L_{ag} - L_{PM} < R_{ik} < R_{si} - L_{ag} \end{cases} \tag{3.9}$$

where N_{ps} is the number of points over the half pole, θ_{ik} and R_{ik} determine the angle and radius, respectively, θ_{pi} is the pole arc span of iron pole, R_{si} is the stator inner radius, L_{ag} is the air-gap length and L_{PM} is the PM thickness.

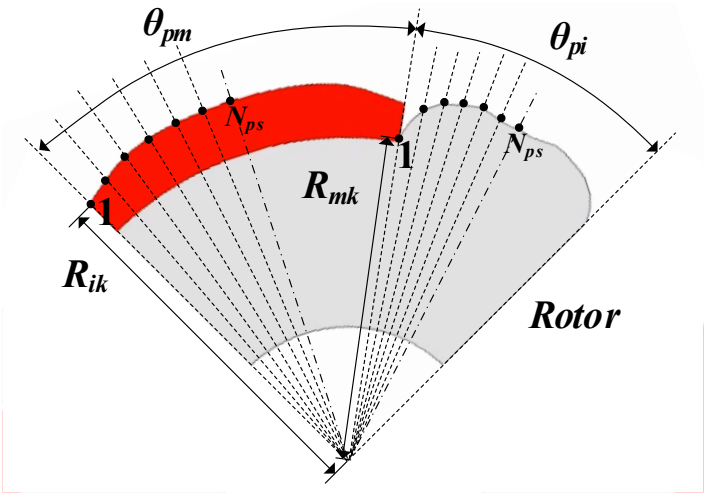

Fig. 3.2 Proposed shaping method.

Similarly, as for the k-th point in PM pole, the angle and radius can be defined by θ_{mk} and R_{mk} and expressed by:

$$\begin{cases} \theta_{mk} = \dfrac{k-1}{2(N_{ps}-1)}\theta_{pm}, k \in N^{+} \\ R_{si} - L_{ag} - L_{PM} < R_{mk} < R_{si} - L_{ag} \end{cases} \tag{3.10}$$

where θ_{pm} is the pole arc span of PM pole.

3.3.2 Determination of Point Number for Defining Rotor Profile

Any integer number can be selected for the number of points over each half pole pitch. However, small number of points will inevitably affect the torque performances of optimization models, while large number of points will cause large computational consumption and is easy to fall into local optimum results. Consequently, to find out the suitable number, 2 points, 4 points, and 7 points in half pole arc as shown in Fig. 3.3 are analyzed. To avoid falling into local optimum, the GA optimization process is always run a few times. For each time, weighting factors, initial values, and variable ranges are adjusted according to the obtained results. The results can be plotted into the same figure. When the Pareto Frontier for each time basically does not move, the results can be treated as globally optimized. The optimization routine is run on a computer with Intel Xeon W-2135 CPU and 16GB memory, which always takes around one week for each model. The time can be reduced with a specialist computer. For the optimization goal being maximum torque only and maximum torque at reduced torque ripple, the optimization results are shown in Fig. 3.4 and Fig. 3.5 with the torque performances of optimized models compared in Fig. 3.6, respectively. It should be noted that in Fig. 3.5 and Fig. 3.6, Pareto frontier, which is a line that gives optimal feasible combinations between average torque and torque ripple, is used to find out the optimum result. In Fig. 3.6, it is clear that the torque ripples and average torques for the models with 4 points and 7 points are almost the same, which means that both the models with N_{ps}=4 and with N_{ps}=7 can be selected. For accuracy, N_{ps}=7 is chosen for example in this chapter.

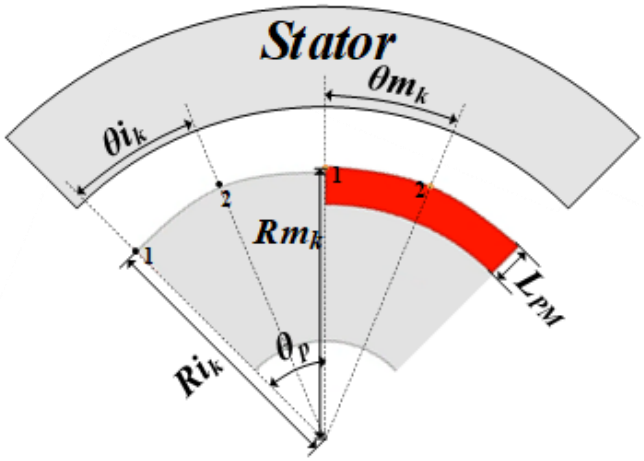

(a) 2-points in half pole

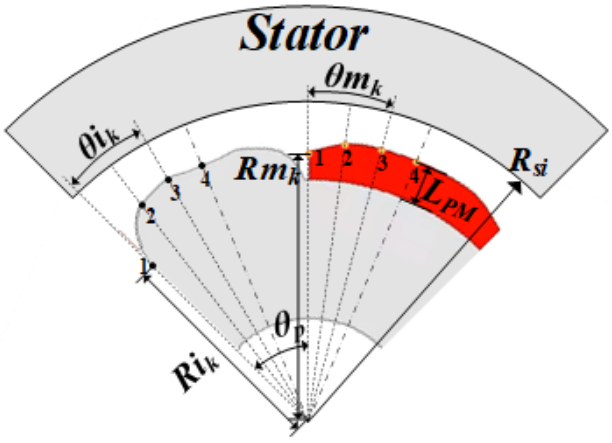

(b) 4-points in half pole

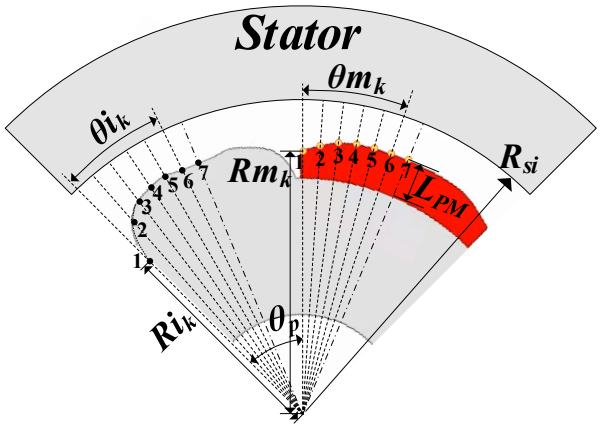

(c) 7-points in half pole

Fig. 3.3 Models with different point number for defining rotor profile.

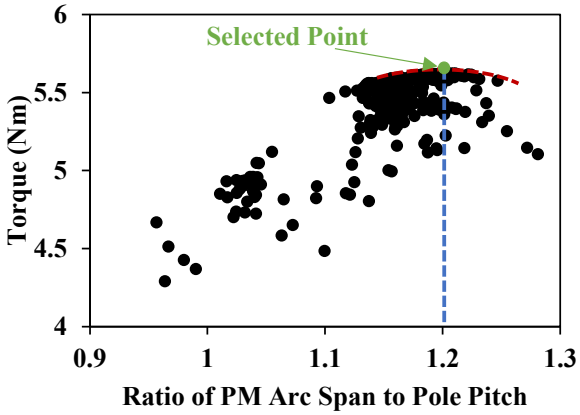

(a) 2 points in half-pole

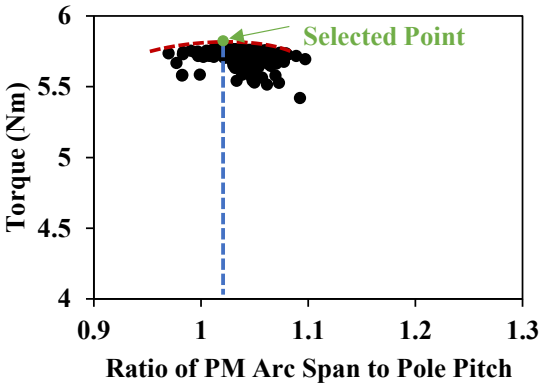

(b) 4 points in half-pole

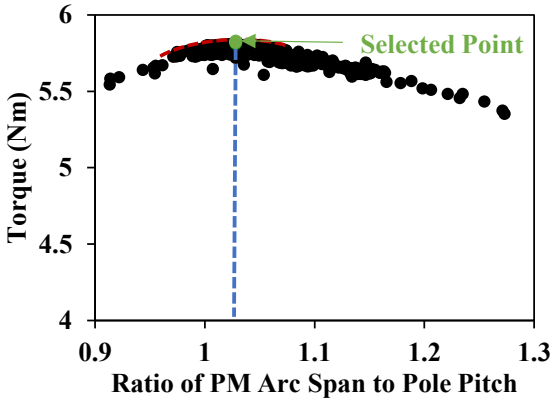

(c) 7 points in half-pole

Fig. 3.4 Optimization results for maximum torque.

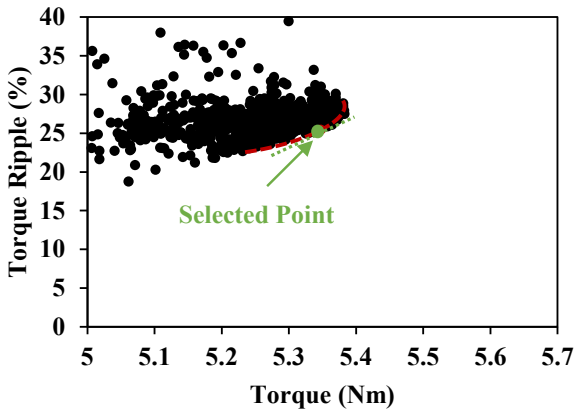

(a) 2 points in half-pole

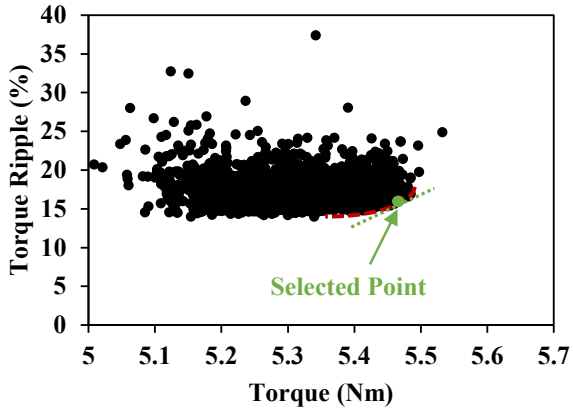

(b) 4 points in half-pole

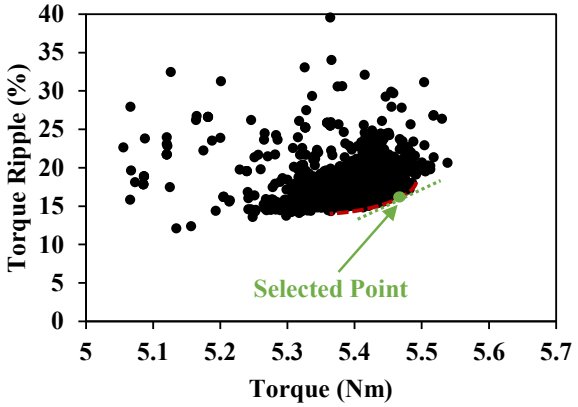

(c) 7 points in half-pole

Fig. 3.5 Optimization results for maximum torque at reduced torque ripple.

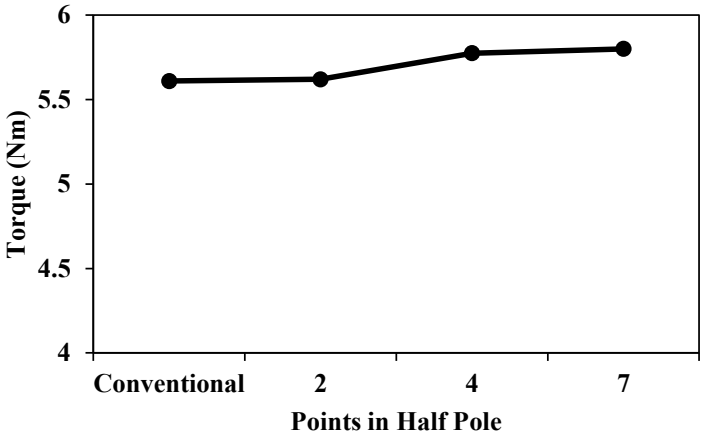

(a) Comparison of results for optimized models with maximum torque

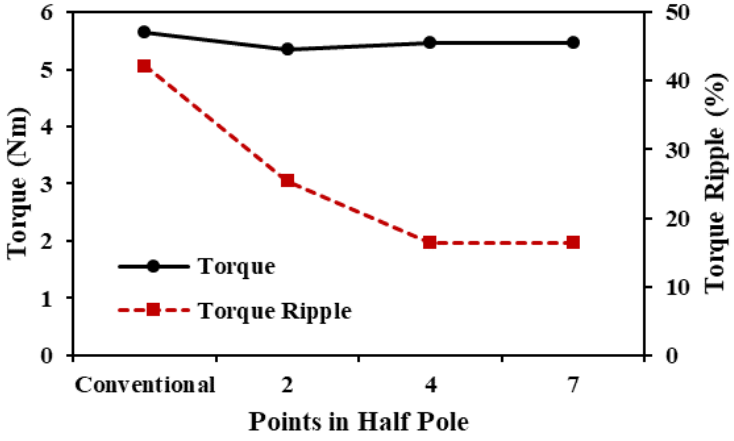

(b) Comparison of results for optimized models with maximum torque at reduced torque ripple

Fig. 3.6 Torque performances comparison for optimized models.

3.3.3 Optimization

The stator parameters are kept constant for all the design variants considered and the key parameters for these machines are listed in Table 3.1. R_{ik}, R_{mk} and pole arc spans are optimized to obtain the optimal model. Since the contribution to the overall torque from the reluctance torque is very modest in these machines, an I_d=0 control strategy is applied. The optimization results are illustrated in Fig. 3.7 and Fig. 3.8. A conventional SPM rotor with 180° (electrical) pole arc span is illustrated in Fig. 3.7 (a). By directly replacing the alternate PMs in SPM machines with iron poles, the conventional CPPM machine with equal pole arc span can be obtained, which serves as a useful baseline as shown in Fig. 3.7 (b). In this particular case, which is designated as CPM1, the PM pole and iron pole shapes are the same and the PM magnet volume is exactly half of that of the SPM. Subject to a constraint of same amount of magnet as CPM1, the iron pole arc span is optimized, Fig. 3.8 (a), to obtain the maximum output torque as shown in Fig. 3.7 (c), which is designated as CPM2. This rotor retains the same circular outer profile on each pole with no pole shaping, with the increased pole arc being realized by a corresponding reduction in the magnet radial thickness. The proposed combined variable pole arc and pole shaping model is optimized to obtain CPM3 with consideration of maximum torque only, and CPM4 with maximum torque at reduced torque ripple, respectively. The blue points shown in Fig. 3.8 (b) and (c) are selected and the models are shown in Fig. 3.7 (d) and (e), respectively.

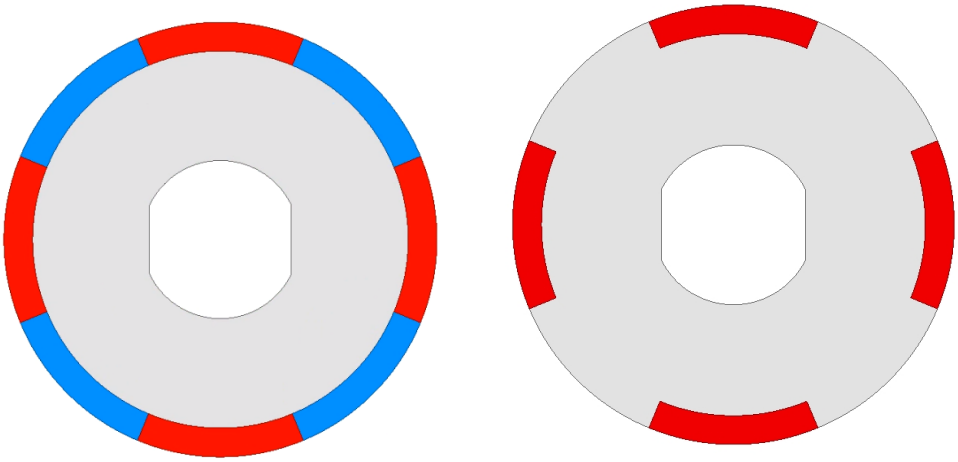

(a) SPM (b) CPM1

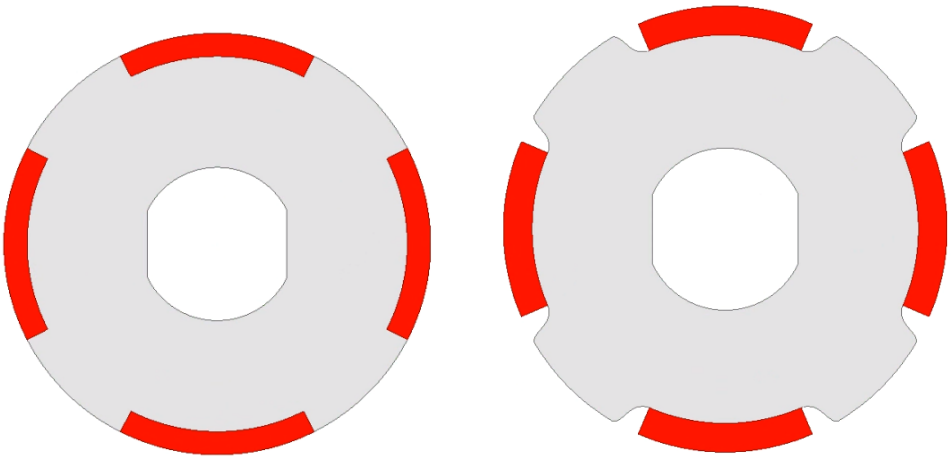

(c) CPM2 (d) CPM3

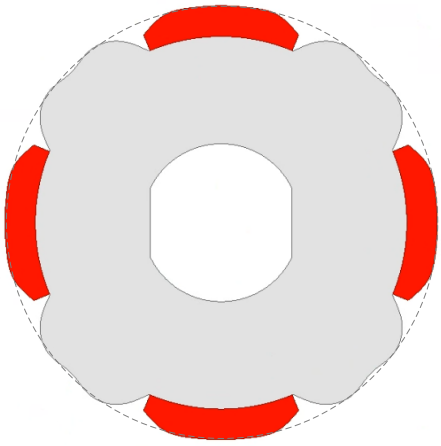

(d) CPM4

Fig. 3.7 Optimized models.

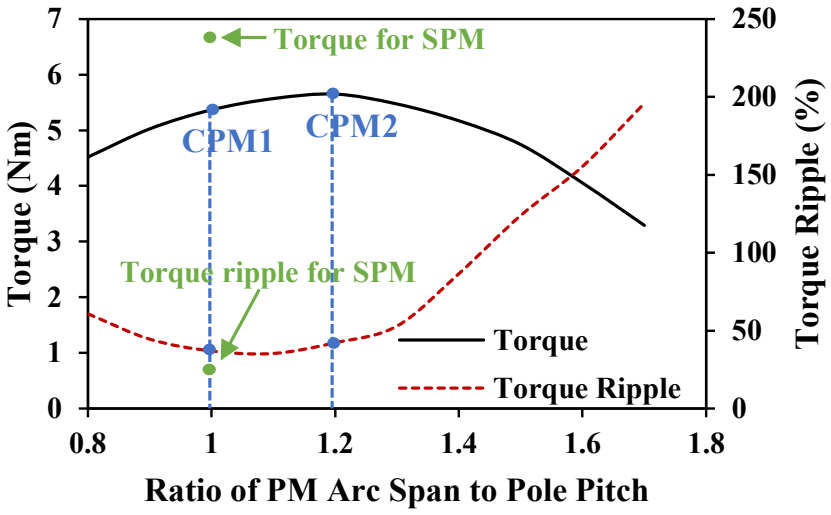

(a) CPM1 and CPM2

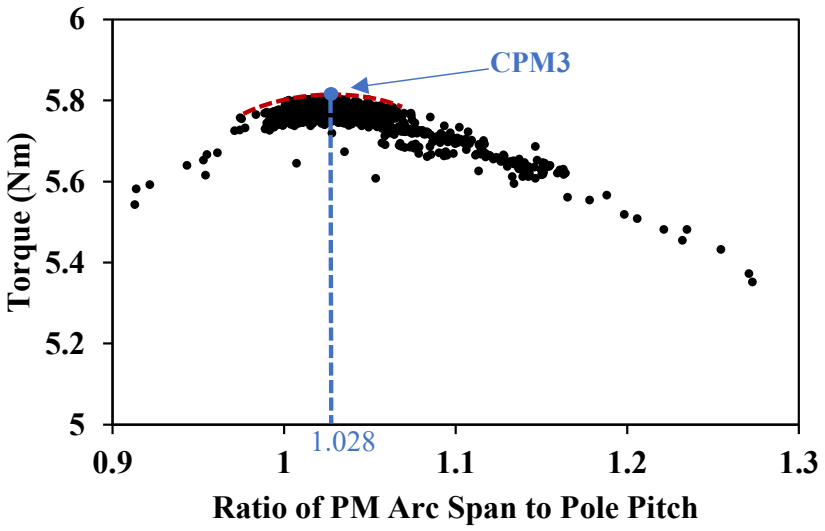

(b) CPM3

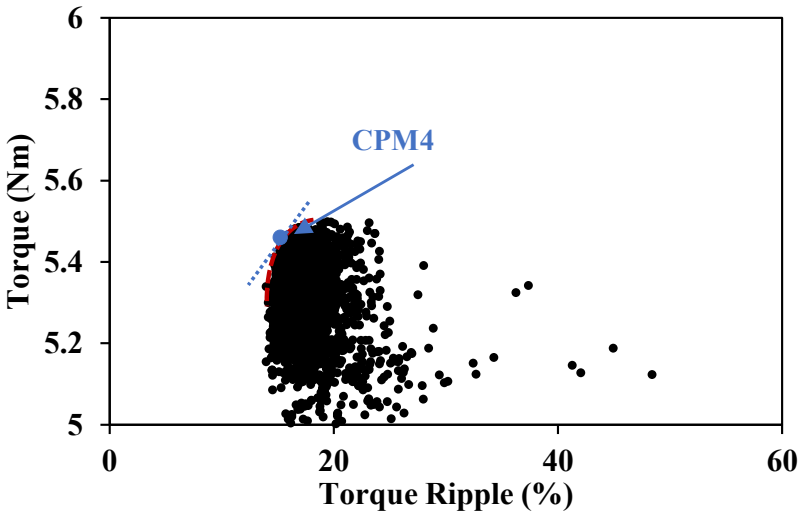

(c) CPM4

Fig. 3.8 Optimization results.

It can be seen that when only the PM arc is optimized, the CPM2 design achieves the maximum output torque and has a larger PM arc span than the pole pitch, i.e. >180°(electrical). This is also observed in [Li18b].

However, when introducing the flux gap at the end of each magnet segment as a feature to reduce the flux leakage, the optimum pole arc ratio tends to drop slightly, which can be seen in Fig. 3.8 (b) for CPM3. It is evident that for CPM3 which is optimized with the sole objective of maximum torque, the optimized PM pole arc is only slightly increased as compared with CPM1, but remains very close to the pole pitch. Meanwhile, the optimization process has led to only a modest degree of shaping of the PM pole, retaining an almost uniform radial thickness.

For CPM4, which is optimized for maximum torque in combination with reduced torque ripple, the PM pole arc and iron pole arc have almost the same spans but significant different shapes. Because similar air-gap flux density distributions under PM and iron poles can eliminate even order harmonics, resulting in low torque ripple, which can only be achieved by almost equal PM pole arc and iron pole. Furthermore, as noted previously, since the flux density under PM pole is governed by the magnetic potential produced by magnets while it is governed by reluctance under the iron pole, it is unsurprising that different PM pole and iron pole shapes are required to achieve a low torque ripple for CPM4. It is worth noting that the optimized rotor profile of CPM4 inevitably leads to a larger equivalent air-gap length than CPM3, and hence the reduction in output torque in Fig. 3.8 is expected.

3.3.4 Torque Performance Comparison

As one of the components of on-load torque ripple, the lower cogging torque tends to result in lower torque ripple. Apart from the rotor side, the stator slot width also has an effect on the cogging torque [Zhu00] [Zhu09a]. But only the rotor is optimized and analyzed in this chapter. It is expected that the number of cycles of the cogging torque waveform in an electrical cycle for the analyzed 12-slot/8-pole CPPM machine is 3, while it is 6 for SPM machine as can be seen in Fig. 3.9 and Table 3.2. For CPM4, a lower cogging torque can be achieved by suppressing the amplitudes of harmonics in flux density of CPPM machines. As the cogging torque for CPM4 is already small enough, it is not an effective way to reduce the on-load torque ripple further by adjusting the slot opening width.

The rated torque performances for analyzed machines are compared in Table 3.3 and Fig. 3.10, where torque ripple T_{ripple} is the ratio of peak to peak torque value to average torque T_{avg} and PM utilization ratio η_{PM} is defined as the torque per unit magnet volume:

$$\eta_{PM} = T_{avg}/V_{PM} \tag{3.11}$$

where V_{PM} is the magnet volume.

Clearly, CPM3 has the largest output torque amongst all the CPPM machines due to its flux gap in the rotor and relatively smaller equivalent air-gap length, which can reduce the flux leakage and improve the flux density. Although the average torque is smaller for all the CPPM machines in comparison with the SPM, they all exhibit significantly higher PM utilization ratios.

The on-load torque ripple for CPM4 is the smallest among all CPPM machines. This is resulted from the smaller harmonics of flux density for CPM4, especially for the lower even order harmonics, which leads to the smaller odd number torque such as the 3rd and 9th order torque ripples as shown in Fig. 3.10 (b). It is worth mentioning that the total output torque T_e consists of three components: PM excitation torque T_{PM}, reluctance torque T_r, and cogging torque T_{cog} [Liu05] [Chu98] [Yan19a]. Both PM torque ripple and reluctance torque ripple will contribute to the 3rd order total torque ripple. Consequently, by suppressing the even order harmonics in the back EMF can only eliminate the 3rd order PM torque ripple. This is the reason the total 3rd order torque ripple is still evident.

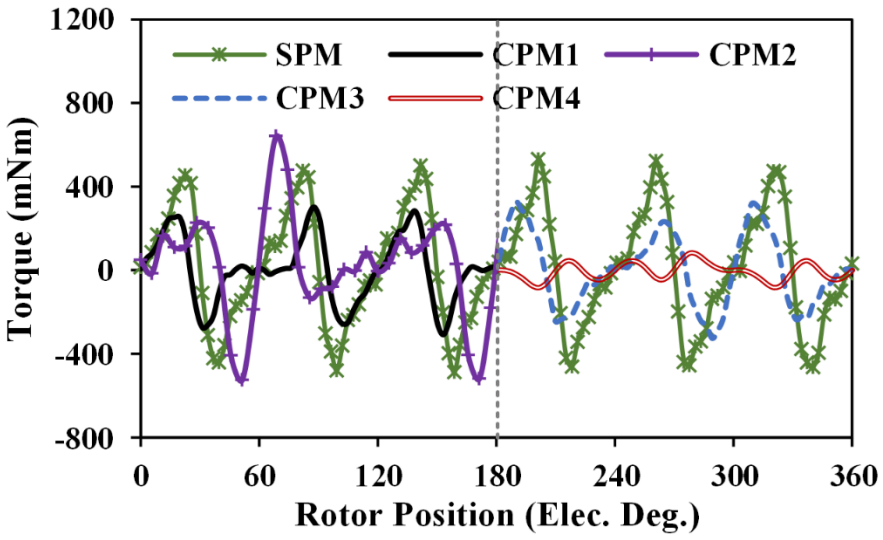

(a) Waveforms

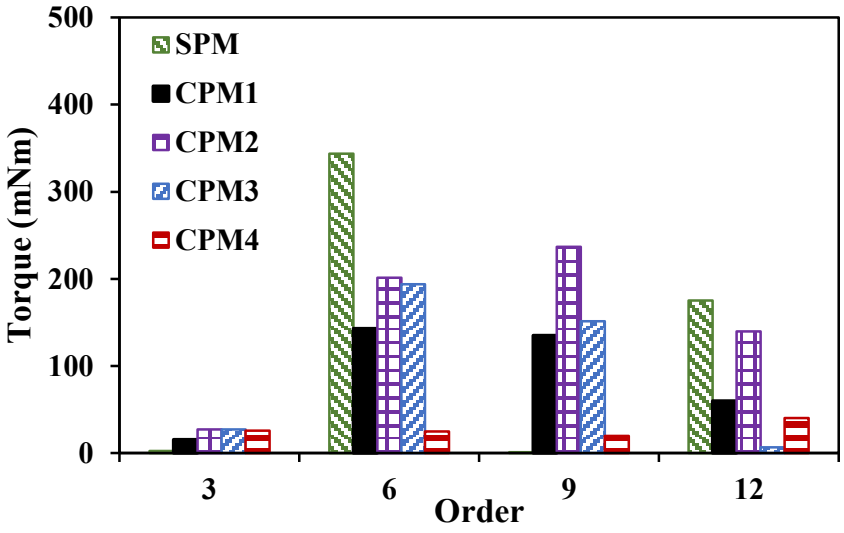

(b) Spectra

Fig. 3.9 Cogging torque.

Table 3.2 Cogging Torque of Analyzed Machines

Machine	SPM	CPM1	CPM2	CPM3	CPM4
T_{cog} (mNm)	988	613	1166	653	164

Table 3.3 Torque Ripples of Analyzed Machines

Machine	SPM	CPM1	CPM2	CPM3	CPM4
T_{avg} (Nm)	6.7	5.44	5.61	5.83	5.45
η_{PM} (Nm/m^3)	228×10^3	370×10^3	381×10^3	397×10^3	373×10^3
T_{ripple} (%)	24.9	38.2	47.1	37.9	16.4

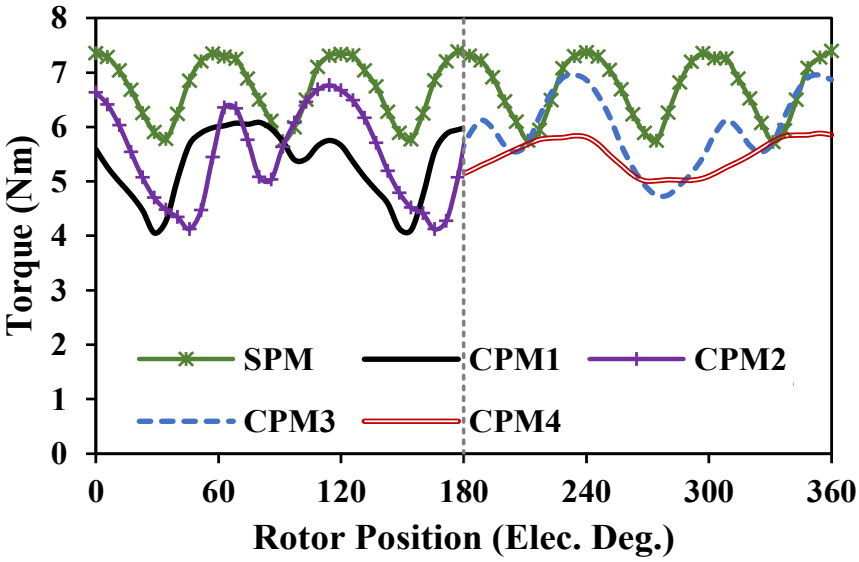

(a) Waveforms

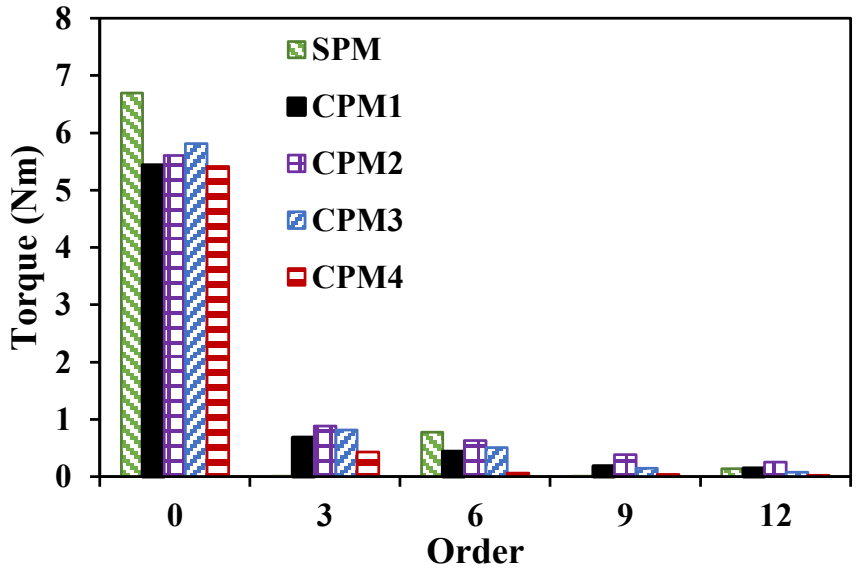

(b) Spectra

Fig. 3.10 Rated torque.

From Fig. 3.11, it can be seen that CPM4 can achieve the lowest torque ripple among all the working conditions. It is also clear that CPM3 can achieve the highest output torque. In addition, under overload condition, the output torque of CPM4 is higher than that of CPM1, which mainly results from the larger equivalent air-gap length due to the pole shapes.

The variation of average torque with current angle is shown in Fig. 3.12. It can be found that only CPM1 has a relatively obvious improvement of average torque due to the second order

harmonic in self-inductance but the contribution of reluctance torque to overall average torque is less than 0.08Nm. It is clear that the contribution of reluctance torques are too small to be used for all the machines, which is caused by the close average values of *d*-/*q*-axis inductances.

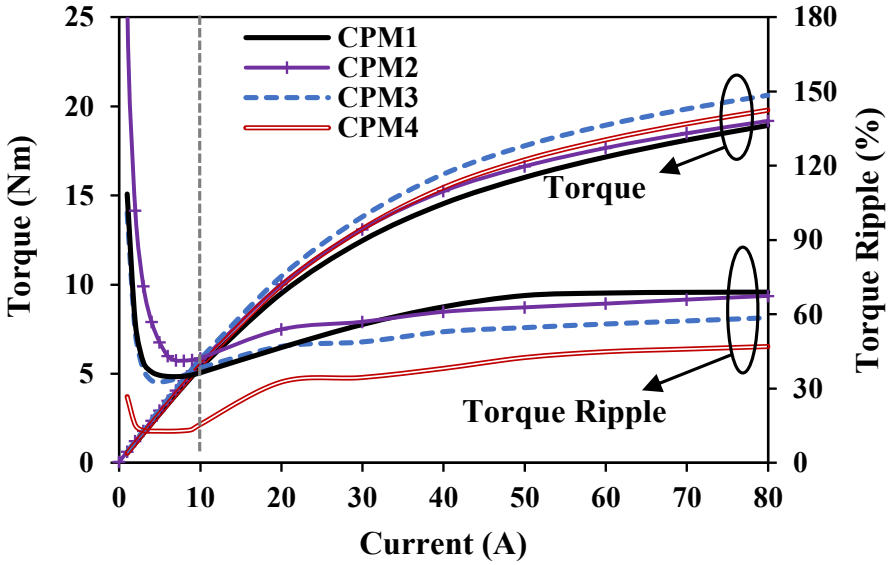

Fig. 3.11 Torque performance under different load.

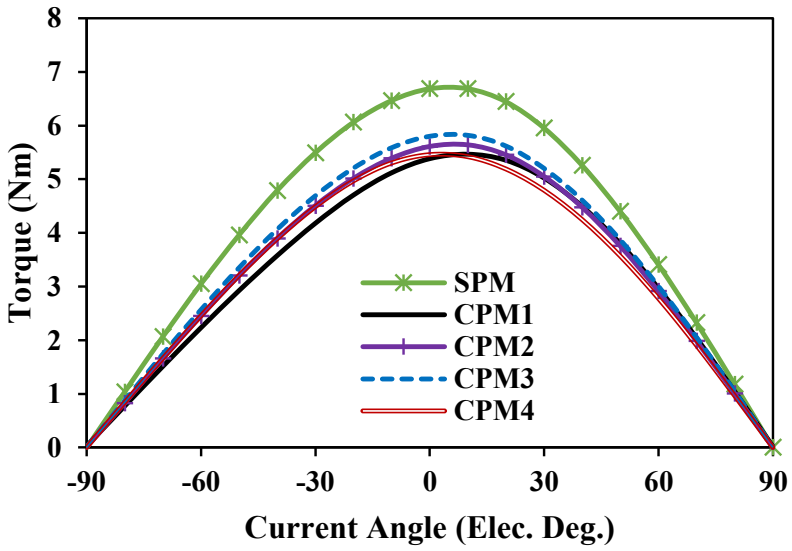

Fig. 3.12 Variation of average torque with current angle.

3.4 Results of FEM and Experiment

The no-load and on-load performances of these machines are analyzed and compared with both FEM and experiments in this section. Both waveforms and corresponding spectra are shown for key quantities.

3.4.1 FEM Analysis

3.4.1.1 Open-Circuit Flux Density Distribution

Neglecting the slot opening in stator, the no-load flux density distributions around the air-gap periphery for all the CPPM machine designs and SPM are compared in Fig. 3.13 along with the corresponding harmonic spectra. In comparison to other CPPM machines, the optimized CPM4 can reduce the even order harmonics in flux density very effectively, especially for the dominant 8th and 16th order harmonics, which verifies the utility of the proposed optimization method model. It is worth noting that the amplitude of fundamental waveform for SPM is the highest, which contributes to the highest output torque. The 12th order harmonic which is the source of the 3th order harmonic in back EMF will not contribute to the torque ripple.

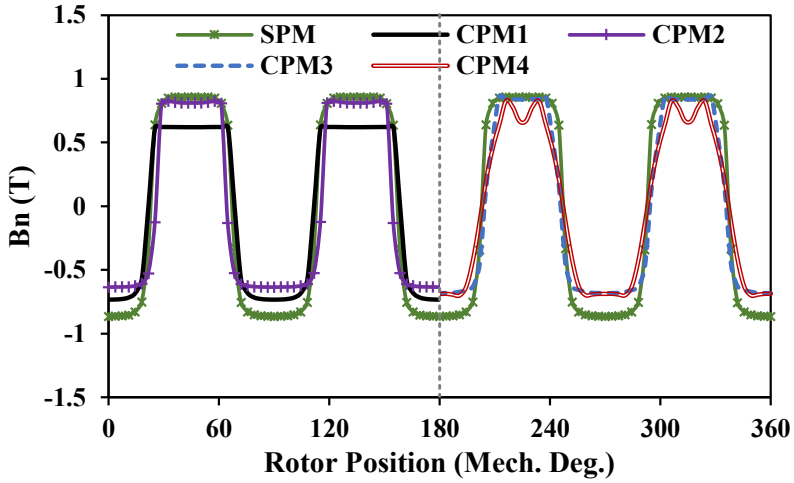

(a) Waveforms

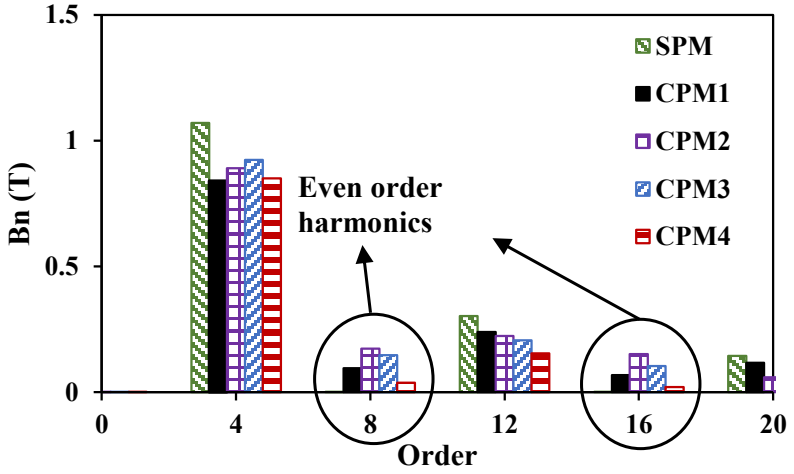

(b) Spectra

Fig. 3.13 Air-gap flux density.

3.4.1.2 Axial Flux Leakage

For CPPM rotors, the unipolar magnets in the rotor core will inevitably lead to the unipolar axial end shaft flux leakage, while that for SPM rotor does not exist due to the closed flux path resulted from bipolar magnets in the rotor core of SPM rotor. The axial flux leakage is analyzed by 3D FEM and the end shaft flux density vectors of five topologies under open circuit condition are shown in Fig. 3.14. It is obvious that the end shaft flux density of SPM machine is extremely small, while that of CPPM machines is relatively larger. Additionally, it is clear that CPM4 has the largest axial flux leakage, which is because end shaft flux path is parallel to the air-gap flux path so that larger flux reluctance in air-gap will lead to higher axial flux leakage.

Radial flux densities of the end shaft surface at different shaft positions for five machines are illustrated in Fig. 3.15. Obviously, SPM machine can achieve bipolar end shaft flux, while that for CPPM machines are unipolar which will cause magnetization risks for mechanical components. This can be solved by using axially staggered rotor structure [Ge16] [Li19b].

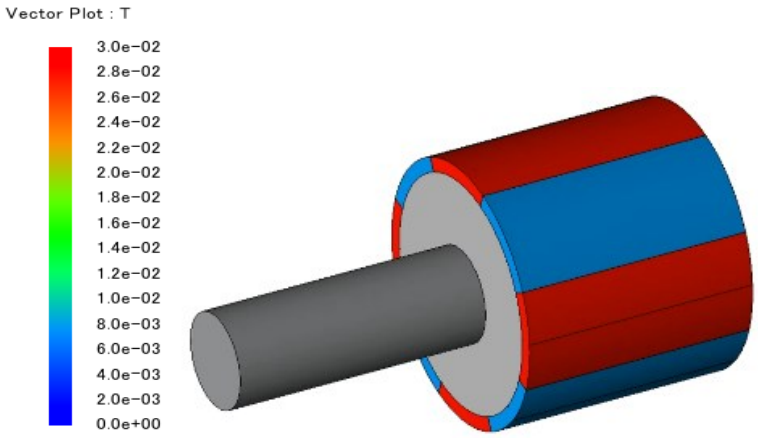

(a) SPM

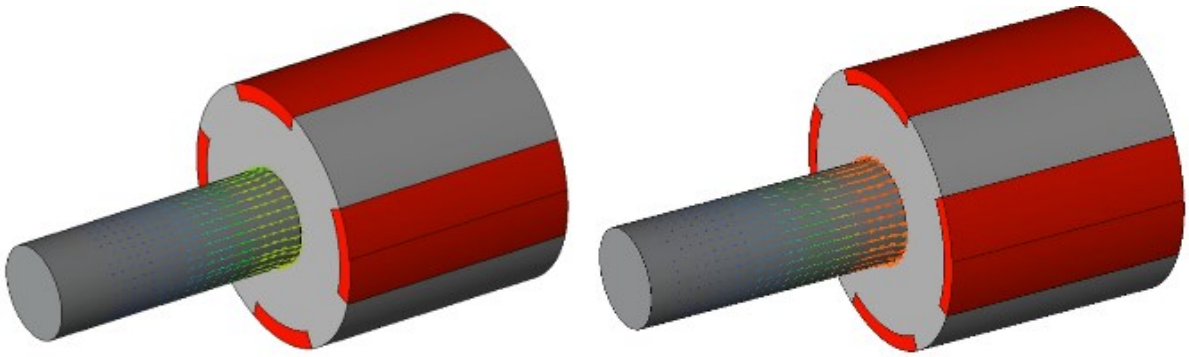

(b) CPM1 (c) CPM2

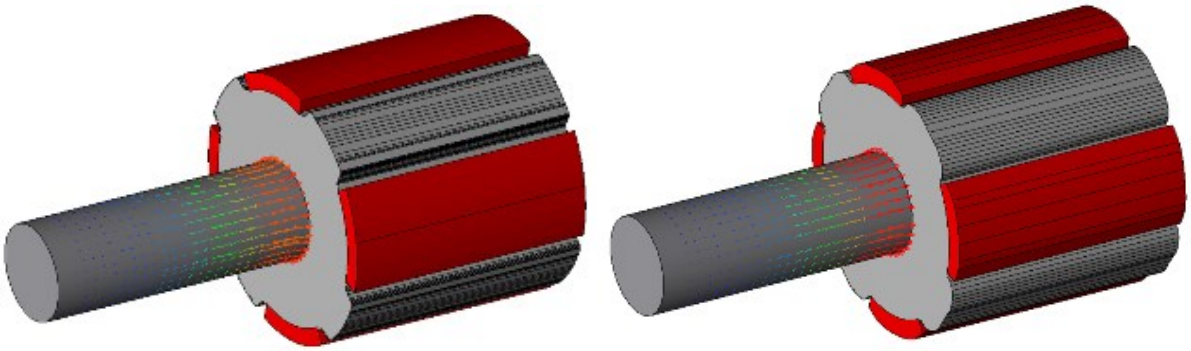

(d) CPM3 (e) CPM4

Fig. 3.14 Open-circuit flux density vectors on the end shaft.

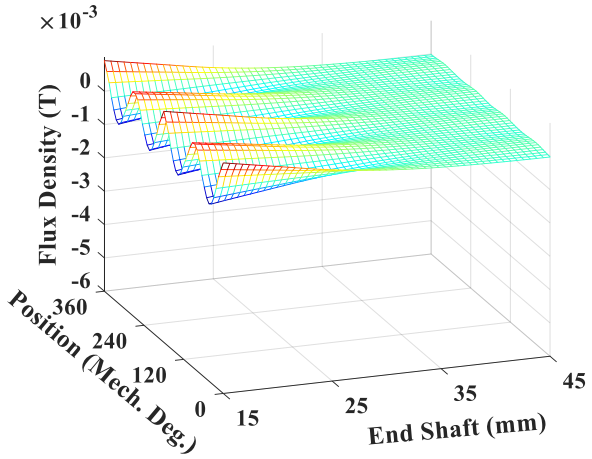

(a) SPM

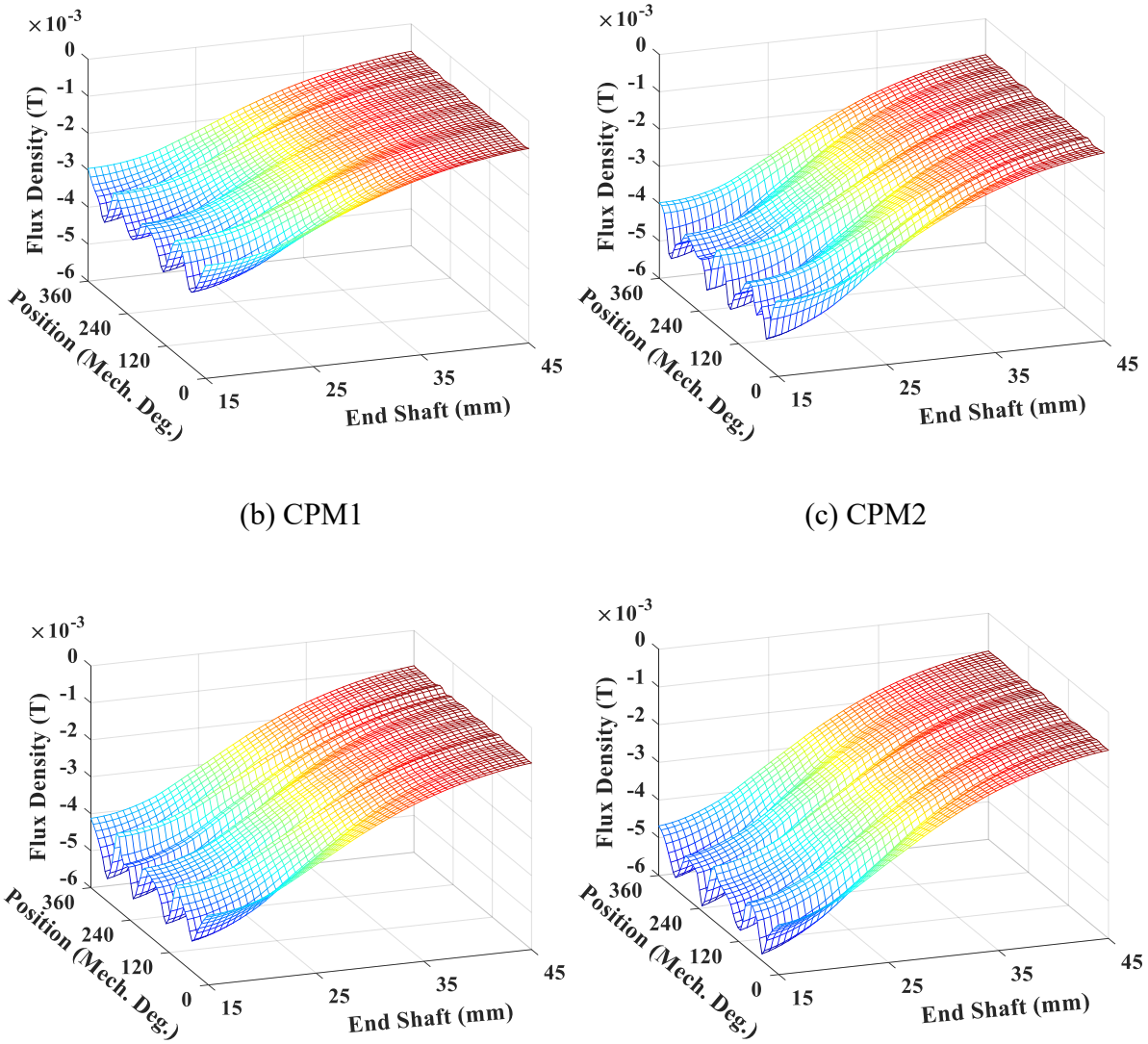

(b) CPM1 (c) CPM2

(d) CPM3 (e) CPM4

Fig. 3.15 Radial flux density of the end shaft surface at different shaft position.

3.4.1.3 Losses and Flux Density Distribution Under Rated Condition

Under the rated current, the losses of three analyzed machines are compared in Table 3.4. Clearly, CPM1, CPM2 and CPM3 exhibit similar losses, while CPM4 shows the lowest value for both core loss and PM eddy current loss. The decrease of the dominant core loss is because of the smaller high order harmonics and the lower saturation levels in stator and rotor cores as shown in Fig. 3.16. Thicker permanent magnets of CPM1, CPM3 and CPM4 increase the capability to resist the armature flux and thus lead to lower PM eddy current loss.

Table 3.4 Losses under Rated Condition

	SPM	CPM1	CPM2	CPM3	CPM4
Total core loss (W)	1.5866	1.4859	1.4865	1.4613	1.2931
(Percentage)	(100%)	(93.6%)	(93.7%)	(92.1%)	(81.5%)
PM loss (W)	0.0616	0.0392	0.0511	0.0382	0.0263
(Percentage)	(100%)	(63.6%)	(83.0%)	(62.0%)	(42.7%)

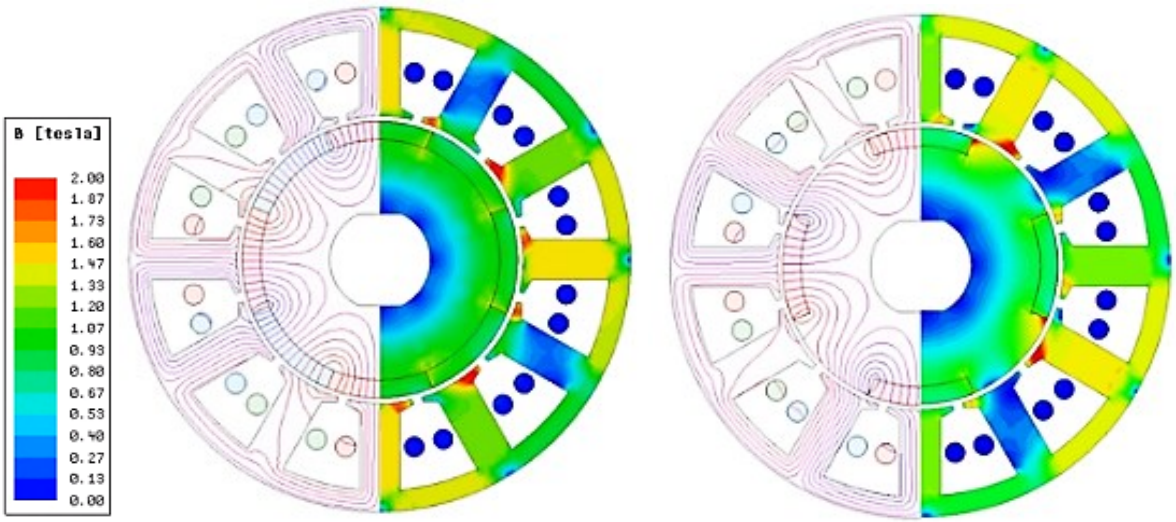

(a) SPM (b) CPM1

(c) CPM2 (d) CPM3

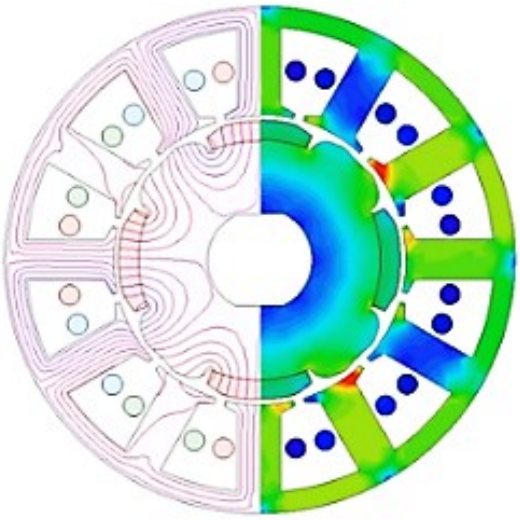

(e) CPM4

Fig. 3.16 Equal potential distributions and flux contours.

3.4.2 Experiments

Experiments are performed to validate the analysis with a 12-slot/8-pole machine prototyped as shown in Fig. 3.17. One stator and four rotors are manufactured. The measured phase resistance is 917mΩ, which is close to the predicted value, 852mΩ. The main reasons for the differences are the inaccuracy prediction model and the manufacturing tolerance of winding.

Fig. 3.17 12-slot/8-pole stator and rotors with and without shaping method.

3.4.2.1 No-Load Back EMF

At first, the back EMFs of the prototype machine with different rotors are tested at 400 rpm by the DC machine with dynamic platform as shown in Fig. 3.18.

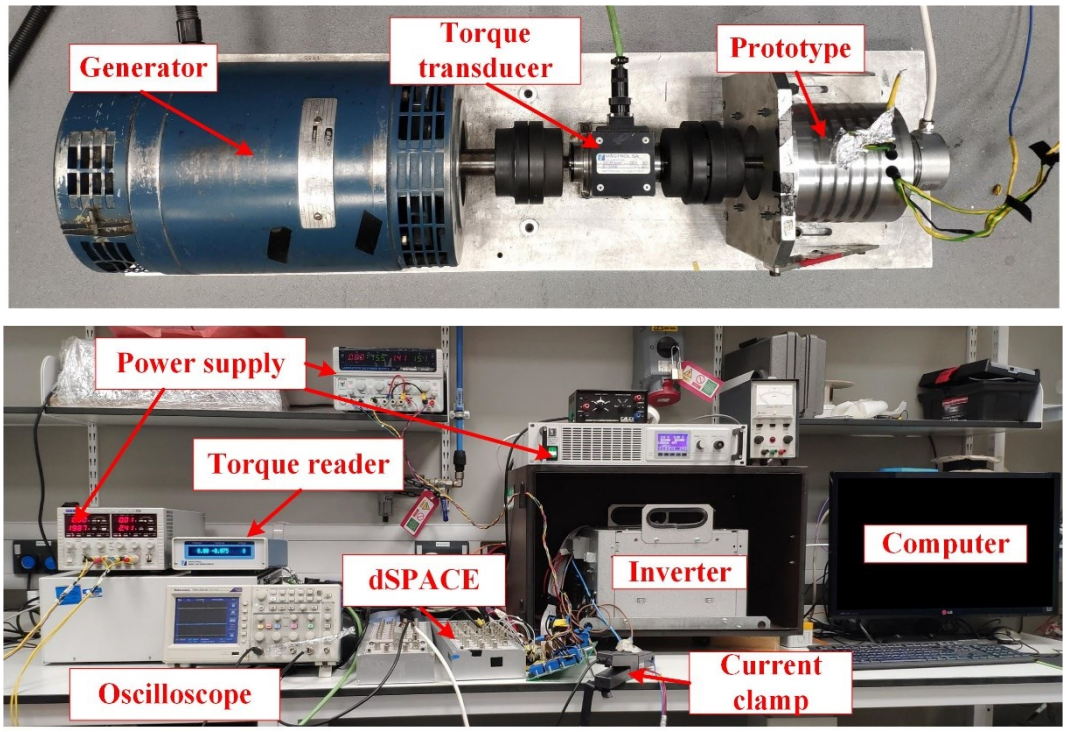

Fig. 3.18 Dynamic platform.

The measured waveforms and their spectra are demonstrated in Fig. 3.19. It is apparent that the measured waveforms agree well with the FEM results, albeit with minor distortions caused by the measurement errors, including device errors, noise of probe, temperature, motor speed error, and so on. The even order harmonics in flux density of CPPM machines will result in corresponding harmonics in the back EMF waveform. Clearly, with the optimization objectives used to establish CPM4, the even order back EMF harmonics are significantly smaller, while CPM2 possess the highest harmonics, which in turn will result in appreciable torque ripple.

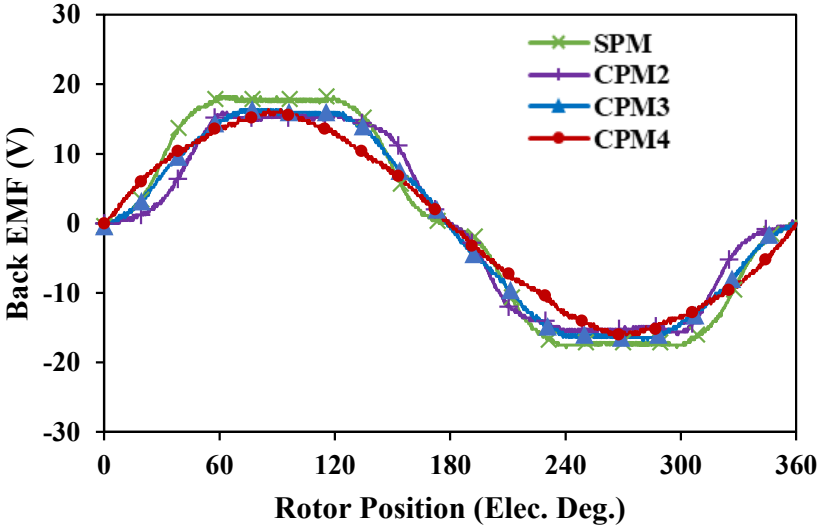

(a) Measured waveforms

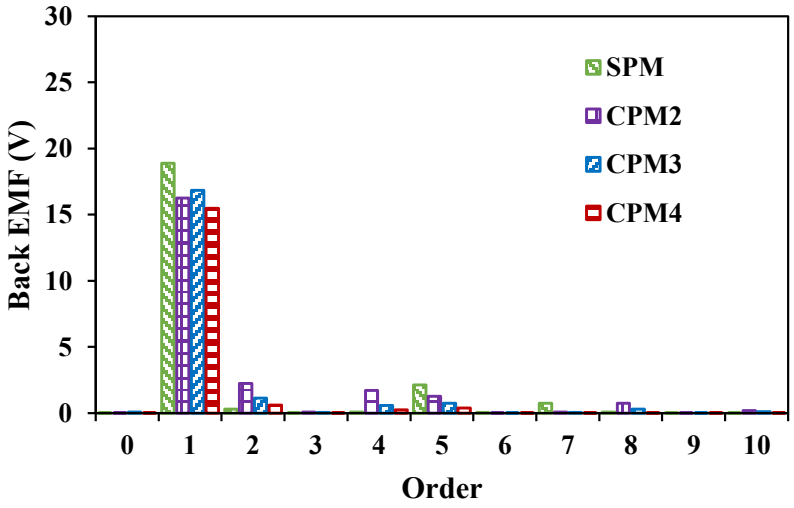

(b) Spectra of measured waveforms

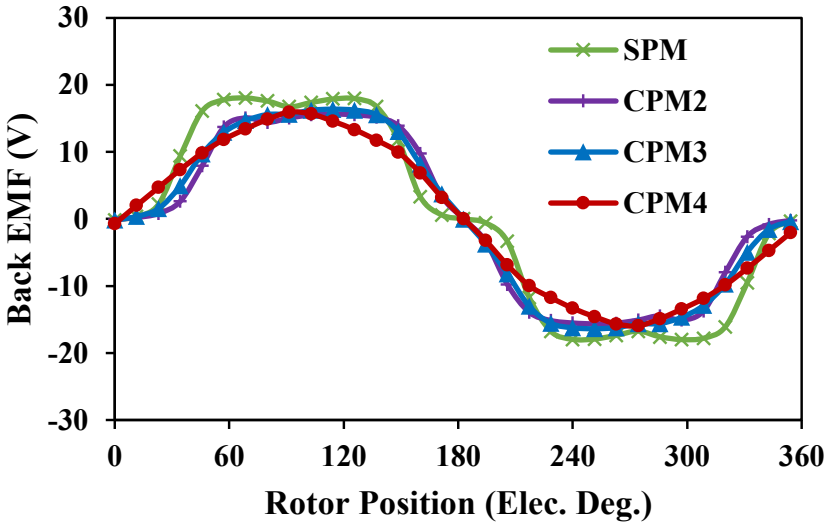

(c) FEM predicted waveforms

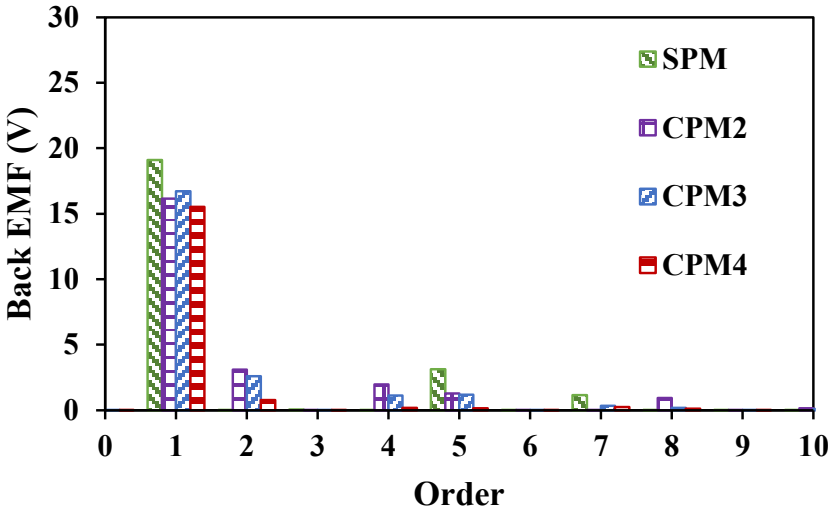

(d) Spectra of FEM predicted waveforms

Fig. 3.19 Measured and FEM predicted back EMF (400 rpm).

3.4.2.2 Torque Performance

The static torque test platform is adopted to measure the cogging torque as shown in Fig. 2.24. Under no-load condition, the measured and simulated cogging torques are compared in Fig. 3.20. The amplitudes of measurement results are slightly lower than the predicted values. It confirms that CPM4 has the lowest cogging torque due to the lowest harmonic amplitudes among all the CPPM machines.

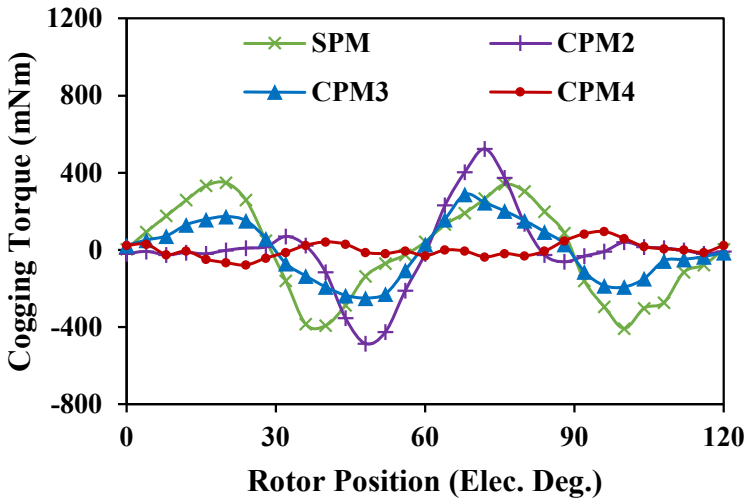

(a) Measured waveforms

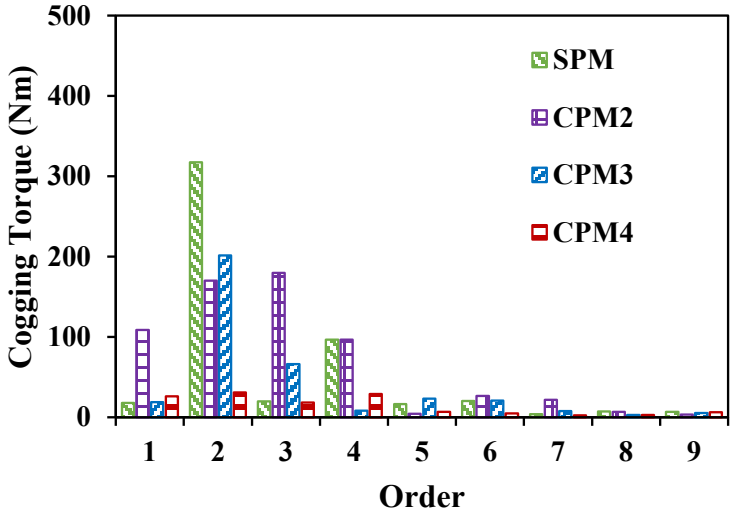

(b) Spectra of measured waveforms

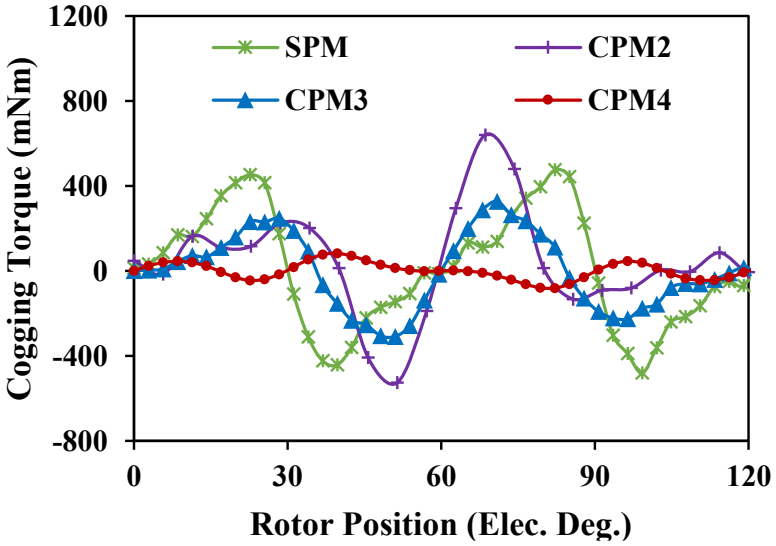

(c) FEM predicted waveforms

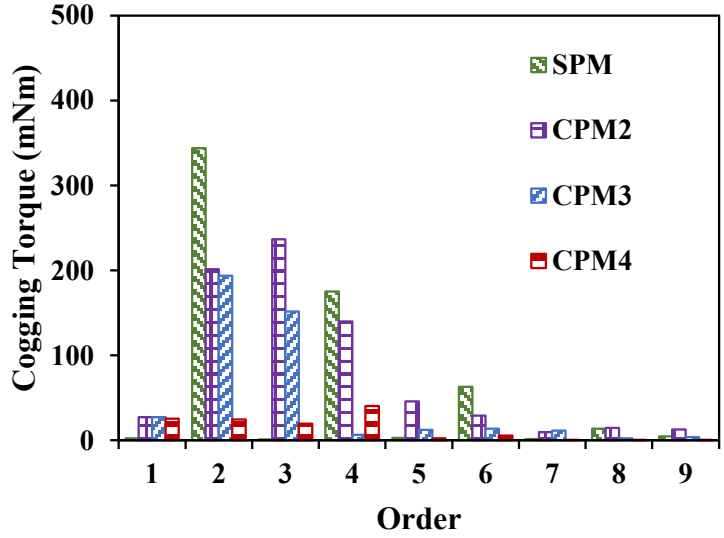

(d) Spectra of FEM predicted waveforms

Fig. 3.20 Measured and FEM predicted cogging torques for prototypes.

By utilizing the torque transducer and the torque reader in dynamic platform, the transient torque waveforms of the prototype machine with different rotors can be measured, Fig. 3.21 (a). It should be noted that dSPACE is used to control the prototypes, which can reduce the difficulty and time of conducting experiments significantly. The predicted results of 2D-FEM and 3D-FEM are compared in Fig. 3.21 (b) and (c). The mesh quality leads to the difference between the waveforms of 2D and 3D models. It is obvious that the torque ripple reduction trend for CPPM machines agrees well, which means the axial flux linkage has limited impact on the torque ripple. During the experiment, the phase peak current is fixed as 10A. It can be observed that the measured results agree well with the simulation results. It confirms that the CPM3 with the flux gap at the sides of each magnet segment can improve the average torque for CPM machine. Additionally, it is also verified that the torque ripple for pole shaped CPM4 is much smaller than those of other machines.

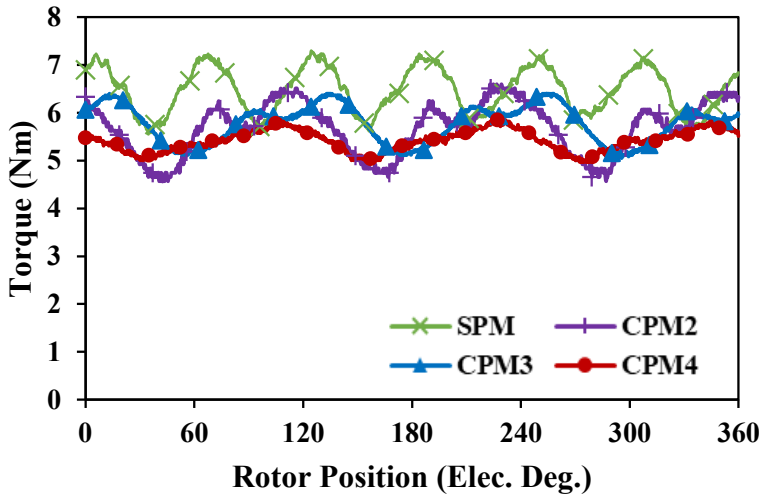

(a) Measured waveforms

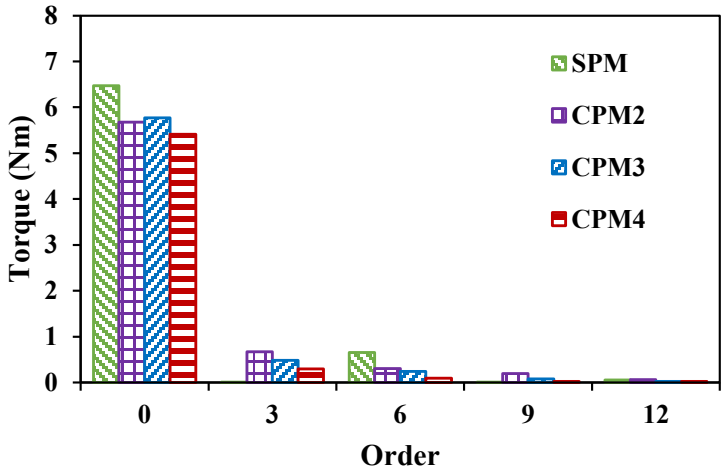

(b) Spectra of measured waveforms

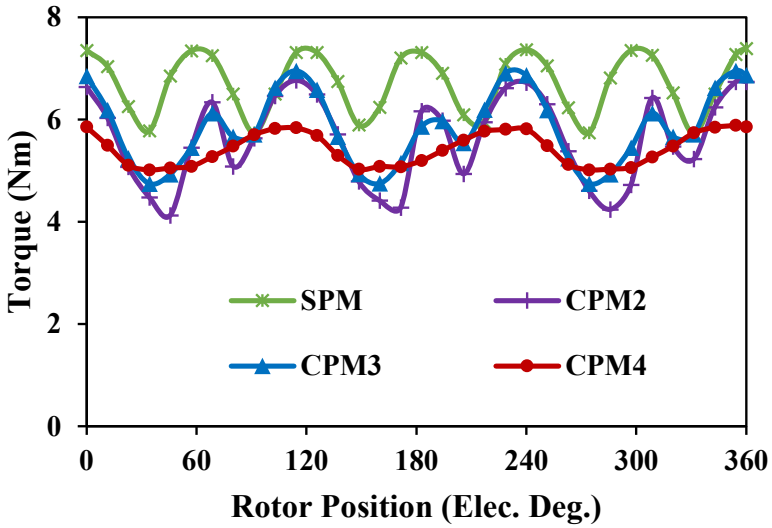

(c) 2D-FEM predicted waveforms

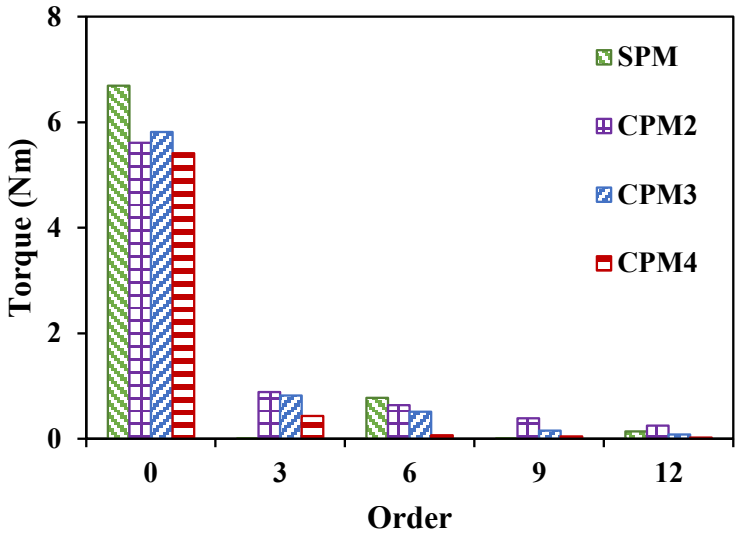

(d) Spectra of 2D-FEM predicted waveforms

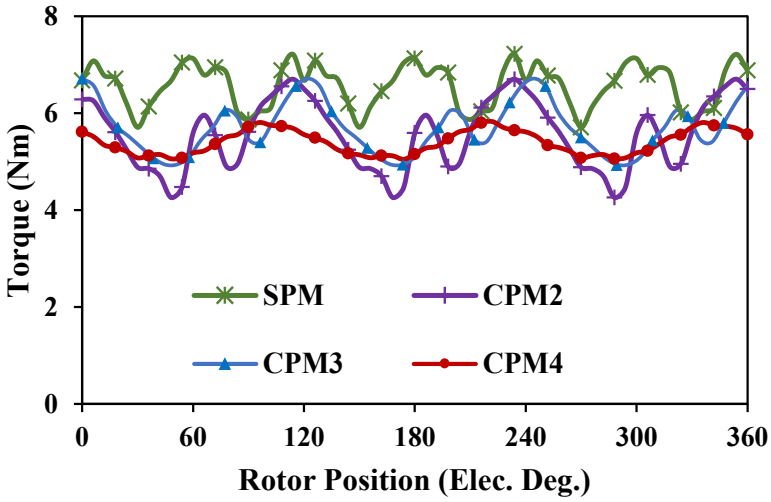

(e) 3D-FEM predicted waveforms

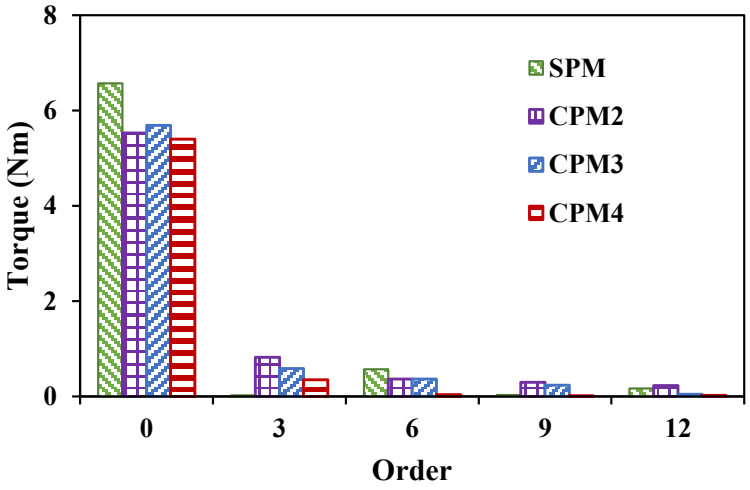

(f) Spectra of 3D-FEM predicted waveforms

Fig. 3.21 Measured and FEM predicted torque performances for prototypes (I = 10A).

Fig. 3.22 compares the variation of torque ripple against current. Limited by the test rig, the machine can only be tested up to a maximum current of $10A_{pk}$. It can be seen that compared with the predicted results, the measured average torques have slight differences. What is more, the measured torque ripples are slightly larger than those predicted by FEM. This is mainly due to noise in the transient torque caused by the test rig and assembly deficiencies. However, the torque ripples are largely reduced with the proposed rotor shaping methods as expected. Regarding the variation of torque ripple with load, CPM4 maintains the lowest among all the machines including both rated and light load conditions. The good agreement in Fig. 3.22 verifies that the symmetrical pole shape can suppress the torque ripple within a certain current range.

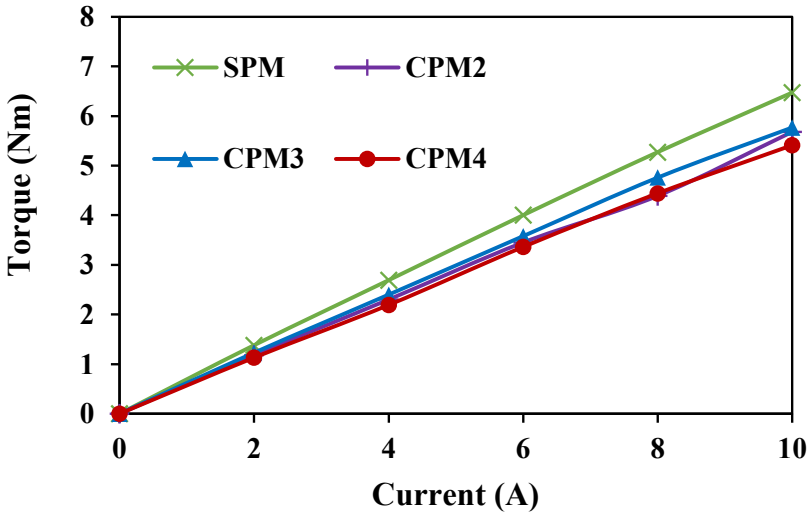

(a) Measured average torques

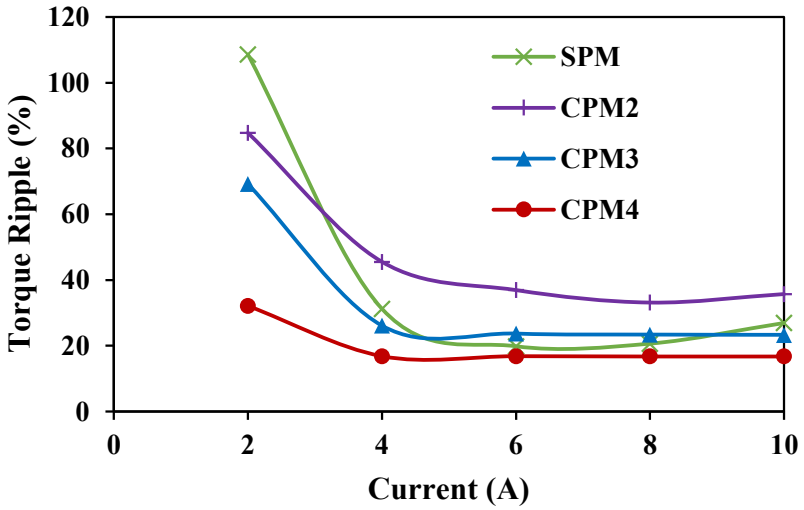

(b) Measured torque ripples

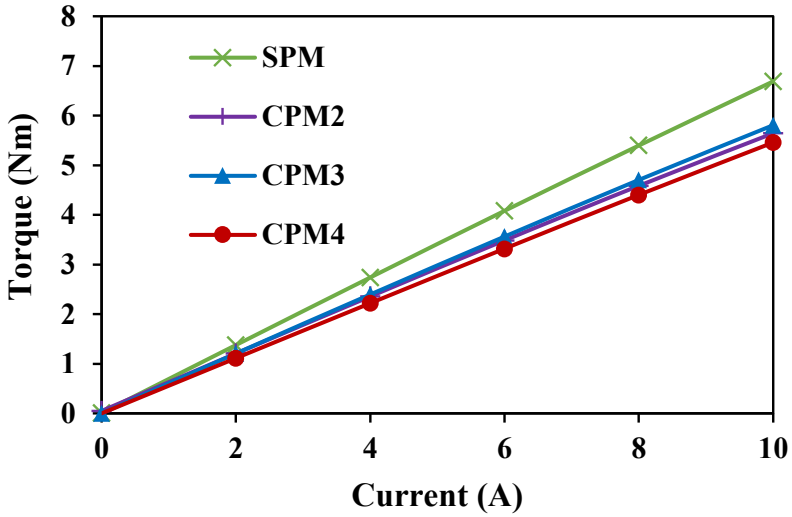

(c) FEM predicted average torques

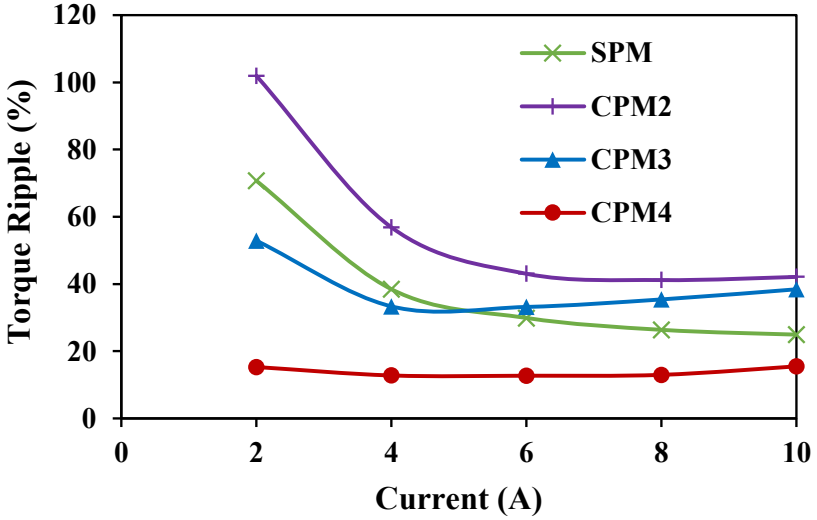

(d) FEM predicted torque ripples

Fig. 3.22 Measured and FEM predicted torque performances under different loads.

3.5 Summary

To achieve the largest output torque and reduce the large torque ripple in CPPM machines, the rotor PM and iron pole shapes were optimized by GA in this chapter. It has been demonstrated that different PM and iron pole shapes and approximately equal PM pole arc span and pole pitch are necessary to achieve both the largest output torque and low torque ripple for a fixed amount of magnet. For CPM3, the approximate square shape of PMs can increase the fundamental air-gap flux density and the flux gaps adjacent to the sides of the magnet are effective in reducing flux leakage. For CPM4, modified different PM and iron pole shapes can achieve lower harmonics in flux density, especially for the even order harmonics, and consequently cogging torque, torque ripples and losses can be reduced. However, the torque ripple cannot be reduced further with this design mainly due to the existence of the reluctance torque ripple, which means that some other techniques are necessary to make it lower [44]. In addition, the cycle numbers of cogging torque and axial flux leakage for CPPM machines are different from that of conventional SPM machines which is also demonstrated. The principle of the shaping method is explained and verified by FEM.

CHAPTER 4
ASYMMETRIC POLE SHAPING METHOD IN TORQUE RIPPLE SUPPRESSION FOR CONSEQUENT POLE PM MACHINES

It has been verified in chapter 3 that by applying different PM pole and iron pole shapes can reduce the torque ripple of CPPM machines. But the torque ripple cannot be reduced further as shown in Fig. 3.9 (c). Besides, although several design-specific modifications have been proposed to ameliorate torque ripple, arguably the generalized principles underpinning this behavior have not been fully established. In this chapter, it will be illustrated that an aggregation of the fluctuations in inductance, back EMF and cogging torque contributes to increased torque ripple. Meanwhile, an asymmetric pole shaping method is proposed to reduce the torque ripple, taking the dominant third order torque ripple as example. Both simulated and experimental results of the 12-slot/8-pole prototypes show that compared to symmetrical pole shaping model and the plain pole model, the proposed asymmetric shaping method is effective in reducing torque ripple.

This chapter is published on IEEE Transactions on Industry Applications [Qi22b]:

[Qi22b] J. Qi, Z.Q. Zhu, L. Yan, G.W. Jewell, C.W. Gan, Y. Ren, S. Brockway, and C. Hilton, " Suppression of torque ripple for consequent pole PM machine by asymmetric pole shaping method," *IEEE Trans. Ind. Appl*, vol. 58, no. 3, pp. 3545-3557, May-June 2022.

4.1 Introduction

To reduce torque ripple in CPPM machines, many different pole shaping methods have been proposed in literature. Despite previous investigations into the role of harmonics in the back EMF, the role of reluctance torque ripple has hitherto not been addressed. The inductance characteristics of CPPM machines are analyzed in [Ma19] from which it can be found that for machines with an odd ratio of $N_s/(mS_m)$, the fundamental fluctuations of the self-inductances tend to be large, which in turn produce large reluctance torque ripple to compound the overall

torque ripple. Therefore, the symmetrical pole shaping method only have the capability of minimizing the PM torque ripple in CPPM machines, while having little effect on the reluctance contribution to the torque ripple. Consequently, in this chapter, the asymmetric pole shaping method is proposed and the results show that the proposed pole shaping method can reduce the torque ripple effectively due to the counteraction of harmonic components in the torque ripple.

Noting that although the 12-slot/8-pole CPPM machine is selected as an example for demonstration, such behavior can be applied to all the CPPM machines with $N_s/(mS_m)$ being odd.

This chapter is arranged as follows: At first, the symmetrical and asymmetric shaping methods are introduced and optimized in section 4.2. In section 4.3, the principles are demonstrated. Then, the performances of these machines will be compared and discussed in section 4.4. This is followed by the experimental verification in section 4.5. Finally, important conclusions will be highlighted in section 4.6.

4.2 Shaping Methods and Optimization

In this section, symmetrical and asymmetric shaping methods are introduced and optimized with 12-slot/8-pole CPPM machines as example.

4.2.1 Shaping Methods

Many pole shaping methods have been investigated, including, inter-alia, eccentric circular shaping [Xu01], sine/cosine with or without 3rd order harmonic shaping [Wan19a] [Eva10], trapezoidal shaping [Too16], multi-step shaping [Hua18]. But such approaches tend to be limited by constraints imposed on the pole shapes. In order to determine the influence symmetrical or asymmetric, two different models are illustrated as Model A and Model B, respectively. Serval discrete radii points for both of these two models which are uniformly distributed across the pole-pair face are defined as shown in Fig. 4.1. For both models, the radial distances from these discrete points to the center of the rotor define the nature of the profile. Clearly, for Model A, the shapes of left side and right side for both the north pole (PM

pole) and south pole (iron pole) are identical, which leads to fewer variables in optimization. It should be noted that a boolean operation is applied to rotor poles and a circle with radius R_{max}, which can remove the outside part of both PM and iron poles caused by spline curve. A random search method is then employed to establish optimal combination of radii at these discrete points with a spline curve adopted in the models to connect the discrete points.

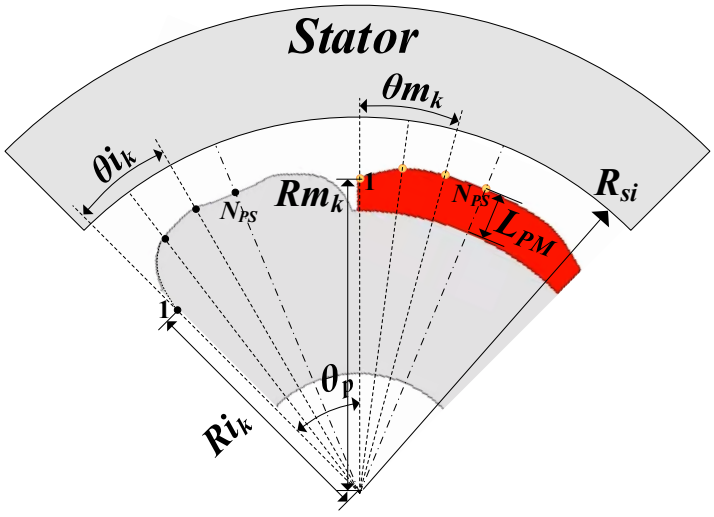

(a) Model A with symmetrical poles

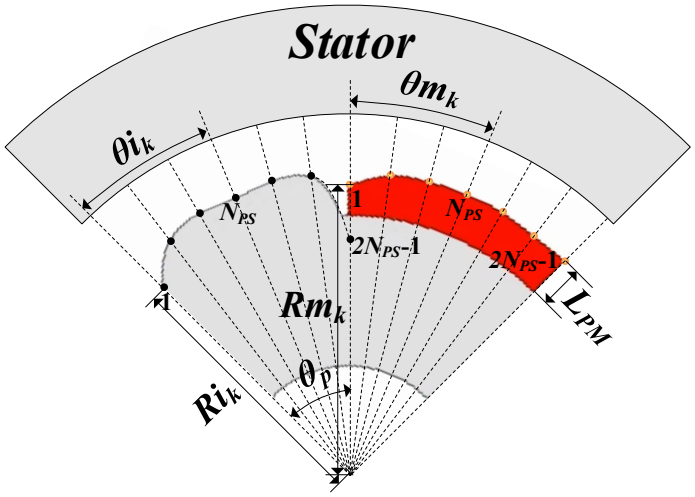

(b) Model B with asymmetric poles

Fig. 4.1 Proposed shaping methods.

The rotor outline can be determined by adjusting the point radius and the position for *k*-th point in two models can be defined by:

$$\begin{cases} \theta_{ik} = \dfrac{k-1}{2(N_{ps}-1)}\theta_{pi}, k \in N^{+} \\ \theta_{mk} = \dfrac{k-1}{2(N_{ps}-1)}\theta_{pm}, k \in N^{+} \\ R_{si} - L_{ag} - L_{PM} < R_{ik} < R_{si} - L_{ag} \\ R_{si} - L_{ag} - L_{PM} < R_{mk} < R_{si} - L_{ag} \end{cases} \tag{4.1}$$

where θ_{ik} and R_{ik} determine the angle and distance between the points in iron pole and stator inner circle, respectively, θ_{mk} and R_{mk} determine the angle and distance between the points in PM pole and stator inner circle, respectively, θ_{pi} and θ_{pm} means the pole arc for iron and PM pole, respectively, L_{ag} means the air-gap length, R_{si} is the stator inner radius.

4.2.2 Determination of Point Number for Defining Rotor Profile

It has been validated in chapter 3 that both 4 points and 7 points over half pole is enough to minimize torque ripple for symmetrical model. Therefore, in this section, the torque performances with different point numbers for asymmetric model are analyzed in Fig. 4.3 and compared in Fig. 4.4. Clearly, the torque ripple and average torque for optimized models with both 4 points and 7 points are almost the same, which means that these two models are all acceptable. Consequently, 7 points in half pole is used in this chapter and offer sufficient degrees of freedom to exercise precise control over the profile and demonstrate the utility of the method in this chapter.

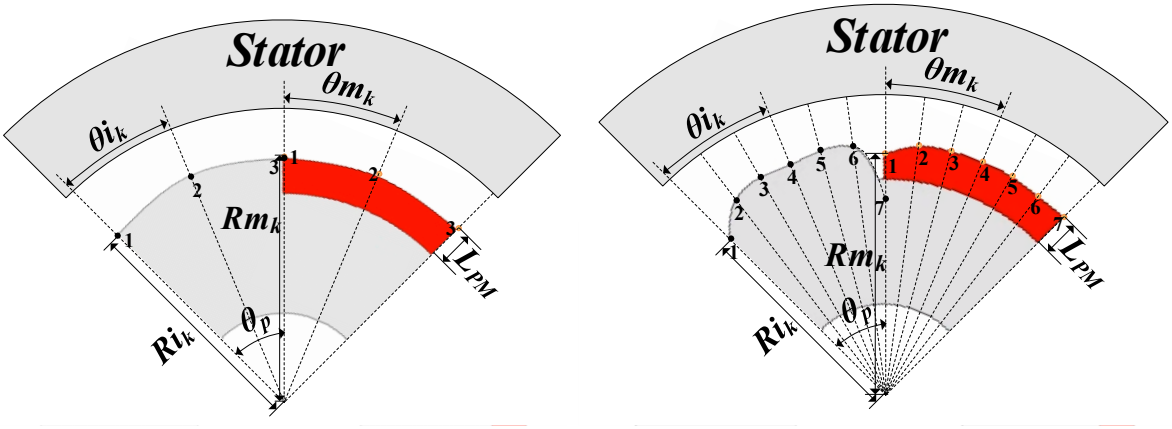

(a) 2-points in half pole (b) 4-points in half pole

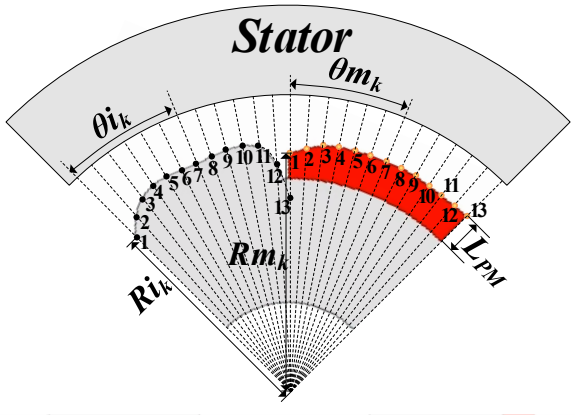

(c) 7-points in half pole

Fig. 4.2 Asymmetric models with different point number for defining rotor profile.

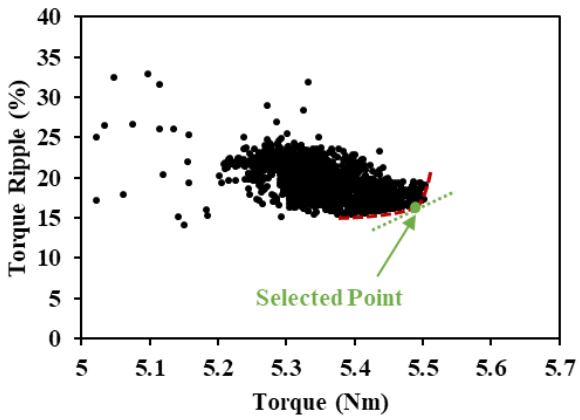

(a) 2 points in half-pole

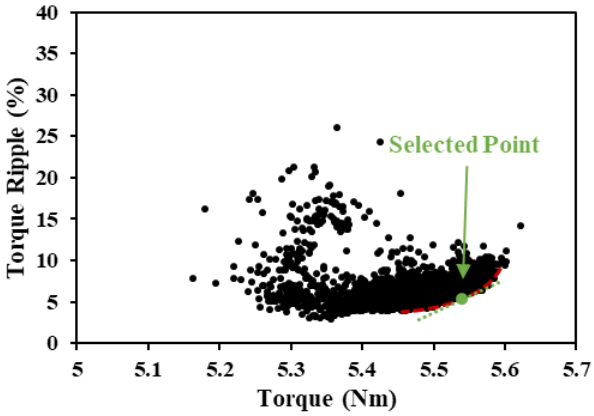

(b) 4 points in half-pole

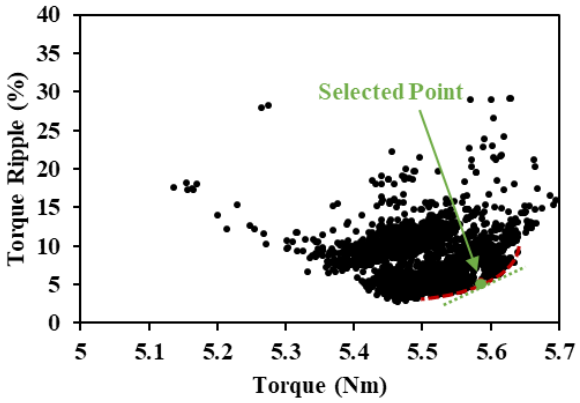

(c) 7 points in half-pole

Fig. 4.3 Optimization results for asymmetric models.

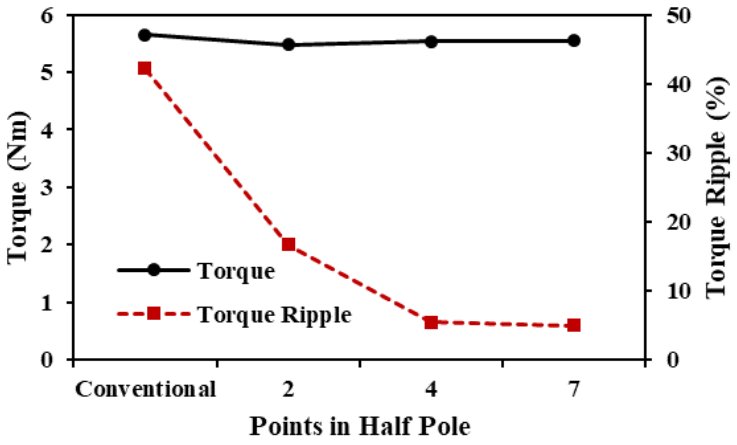

Fig. 4.4 Torque performances comparison for optimized asymmetric models.

4.2.3 Maintaining the Integrity of the Specifications

GA was adopted to obtain the optimal structure, specifically the GA optimizer available within the ANSYS Maxwell package. The stator geometry was fixed as constant throughout the optimization, and the stator slotting effects are accounted for at this stage of the analysis. Although significant harmonics due to reluctance torque can be present in these machines, the average reluctance torque is insufficient to warrant exploitation, and hence the current advanced angle is set as 0°in all predictions of on-load torque (i.e. zero *d*-axis current $I_d = 0$ control). The radial positions of the 14 points and the span of the PM pole arc are regarded as the variables in the optimization. The key parameters for these machines are listed in Table 3.1. It is worth mentioning that all the current units are peak value based on the sinewave in this chapter. For each combination of fixed and variable dimensions, the resulting average torque and torque ripple under rated $10A_{pk}$ current were calculated by two-dimensional finite element analysis. The resulting optimization results are illustrated in Fig. 4.5, in which the inevitable trade-off between torque and torque ripple is evident. Two specific designs, identified by green points, are selected and these designs are shown in Fig. 4.6 (a) and Fig. 4.6 (b). It should be mentioned that the different stator slot shape may result in different optimum pole shape. For the purpose of comparison, a conventional CPPM machine with un-shaped arc segments with a ratio of PM arc span to pole pitch of 1.2 was also considered and is shown in red dot in Fig. 4.5 and Fig. 4.6 (c), which can achieve the maximum average torque for a fixed amount of magnet. The PM thickness in this conventional design was set to 3mm to provide a similar PM volume as the optimized machines.

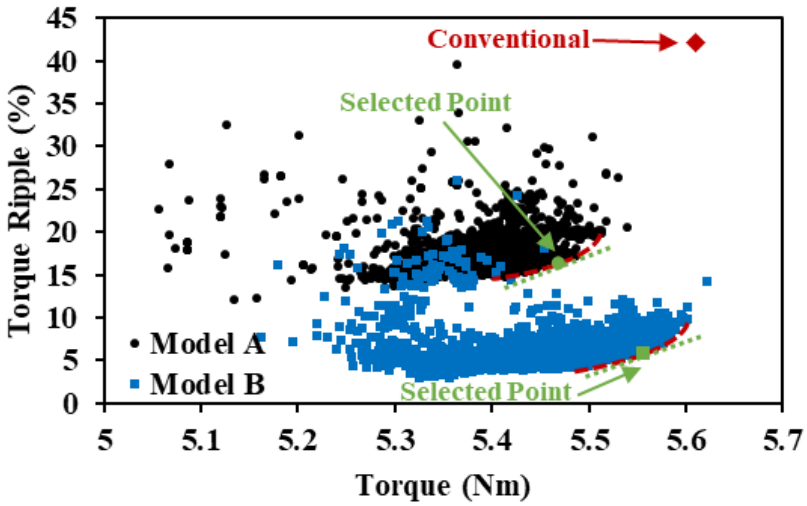

Fig. 4.5 Optimization results under rated condition of Model A and Model B.

In comparison to the conventional rotor, some specific characteristics of optimized machines can be observed:

1) Unequal North and South pole arc span can be seen in the conventional machine, which is set to improve the output torque. However, almost identical pole arc span can be seen in shaped machines.

2) Equivalent air-gap lengths for optimized machines are inevitably larger than that of conventional machine, which will lead to the drop in output torque and improvement of overload capability.

3) Gaps adjacent to the sides of the magnet in shaped machines can contribute to the reduction of PM flux leakage and improvement of the PM utilization ratio.

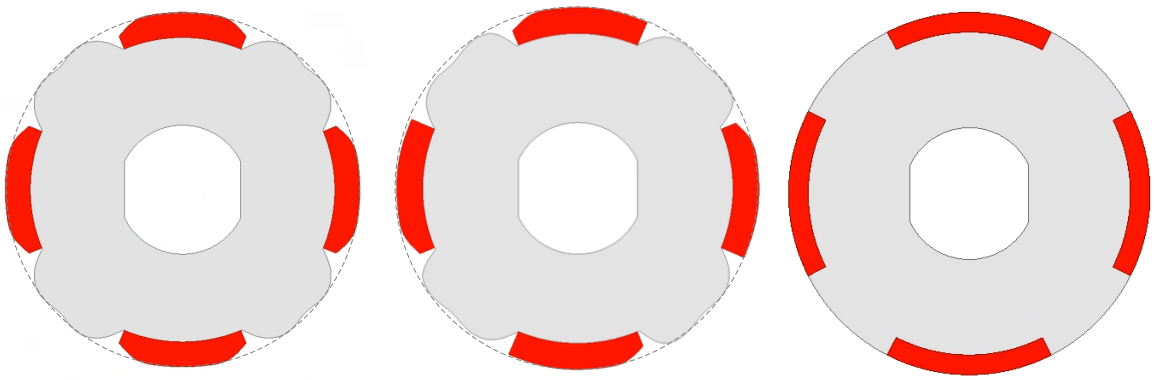

(a) Model A (b) Model B (c) Conventional

Fig. 4.6 Optimized rotor shapes.

4.3 Principles of Shaping

The overall output torque T_e can be considered as being made up of three components: PM excitation torque T_{PM}, reluctance torque T_r and cogging torque T_{cog}. The total torque ripple is the sum of the ripples contributed by these three components. Recalling that suppression of the torque ripple with the dominant third order as example is the focus in this chapter.

Using magnetic co-energy method, the overall torque can be expressed as:

$$T_e = p\frac{\partial W'_{sr}}{\partial \theta_e} + p\frac{\partial W'_s}{\partial \theta_e} + \frac{\partial W'_r}{\partial \theta_e} \tag{4.2}$$

where θ_e is the rotor position in electric angle, p is the pole pair number, W_s', W_{sr}', and W_r' are the magnetic co-energies due to armature current, armature current and PM flux, and PM flux, respectively.

The first item in (4.2) is the PM excitation torque T_{PM}, and the second item is the reluctance torque T_r.

$$
\begin{aligned}
T_{PM} &= p\frac{\partial W'_{sr}}{\partial \theta_e} \\
&= p\boldsymbol{I}_{abc}^{T}\frac{d\boldsymbol{\psi}_{abc}^{PM}}{d\theta_e} \\
&= p\left(\boldsymbol{C}\boldsymbol{I}_{dq}\right)^{T}\frac{d\left(\boldsymbol{C}\boldsymbol{\psi}_{dq}^{PM}\right)}{d\theta_e} \\
&= p\boldsymbol{I}_{dq}^{T}\boldsymbol{C}^{T}\frac{d\boldsymbol{C}}{d\theta_e}\boldsymbol{\psi}_{dq}^{PM} + p\boldsymbol{I}_{dq}^{T}\boldsymbol{C}^{T}\boldsymbol{C}\frac{d\boldsymbol{\psi}_{dq}^{PM}}{d\theta_e} \\
&= \frac{3}{2}p\boldsymbol{I}_{dq}^{T}\boldsymbol{Q}\boldsymbol{\psi}_{dq}^{PM} + \frac{3}{2}p\boldsymbol{I}_{dq}^{T}\frac{d\boldsymbol{\psi}_{dq}^{PM}}{d\theta_e}
\end{aligned}
\tag{4.3}
$$

$$
\begin{aligned}
T_r &= p\frac{\partial W'_{s}}{\partial \theta_e} \\
&= p\frac{1}{2}\boldsymbol{I}_{abc}^{T}\frac{d\boldsymbol{L}_{abc}}{d\theta_e}\boldsymbol{I}_{abc} \\
&= \frac{1}{2}p\left(\boldsymbol{C}\boldsymbol{I}_{dq}\right)^{T}\frac{d\left(\frac{2}{3}\boldsymbol{C}\boldsymbol{L}_{dq}\boldsymbol{C}^{T}\right)}{d\theta_e}\left(\boldsymbol{C}\boldsymbol{I}_{dq}\right) \\
&= \frac{p}{3}\boldsymbol{I}_{dq}^{T}\boldsymbol{C}^{T}\frac{d\boldsymbol{C}}{d\theta_e}\boldsymbol{L}_{dq}\boldsymbol{C}^{T}\boldsymbol{C}\boldsymbol{I}_{dq} + \frac{p}{3}\boldsymbol{I}_{dq}^{T}\boldsymbol{C}^{T}\boldsymbol{C}\frac{d\boldsymbol{L}_{dq}}{d\theta_e}\boldsymbol{C}^{T}\boldsymbol{C}\boldsymbol{I}_{dq} + \frac{p}{3}\boldsymbol{I}_{dq}^{T}\boldsymbol{C}^{T}\boldsymbol{C}\boldsymbol{L}_{dq}\frac{d\boldsymbol{C}^{T}}{d\theta_e}\boldsymbol{C}\boldsymbol{I}_{dq} \\
&= \frac{3}{4}p\boldsymbol{I}_{dq}^{T}\frac{d\boldsymbol{L}_{dq}}{d\theta_e}\boldsymbol{I}_{dq} + \frac{3}{2}p\boldsymbol{I}_{dq}^{T}\boldsymbol{Q}\boldsymbol{L}_{dq}\boldsymbol{I}_{dq}
\end{aligned}
\tag{4.4}
$$

where $\boldsymbol{I}_{abc}$ and $\boldsymbol{I}_{dq}$ are current matrixes, $\boldsymbol{L}_{abc}$ and $\boldsymbol{L}_{dq}$ are the inductance matrixes, $\boldsymbol{\Psi}_{abc}{}^{PM}$ and $\boldsymbol{\Psi}_{dq}{}^{PM}$ are the PM flux matrixes, $\boldsymbol{C}$ is the transformation matrix.

$$
\begin{aligned}
&\boldsymbol{\psi}_{abc}^{PM} = \begin{bmatrix}\psi_a^{PM}\\ \psi_b^{PM}\\ \psi_c^{PM}\end{bmatrix}, \boldsymbol{I}_{abc} = \begin{bmatrix}I_a\\ I_b\\ I_c\end{bmatrix}, \boldsymbol{L}_{abc} = \begin{bmatrix}L_{aa} & L_{ab} & L_{ac}\\ L_{ba} & L_{bb} & L_{bc}\\ L_{ca} & L_{cb} & L_{cc}\end{bmatrix}, \\
&\boldsymbol{\psi}_{dq}^{PM} = \begin{bmatrix}\psi_d^{PM}\\ \psi_q^{PM}\end{bmatrix}, \boldsymbol{I}_{dq} = \begin{bmatrix}I_d\\ I_q\end{bmatrix}, \boldsymbol{L}_{dq} = \begin{bmatrix}L_d & 0\\ 0 & L_q\end{bmatrix}, \mathbf{Q} = \begin{bmatrix}0 & -1\\ 1 & 0\end{bmatrix}, \\
&\boldsymbol{C} = \begin{bmatrix}\cos(\theta) & \cos(\theta-2\pi/3) & \cos(\theta+2\pi/3)\\ -\sin(\theta) & -\sin(\theta-2\pi/3) & -\sin(\theta+2\pi/3)\end{bmatrix}^{T}
\end{aligned}
\tag{4.5}
$$

Consequently, T_{PM} and T_r can be expressed by [Liu05] [Chu98] [Yan19a]:

$$\begin{cases} T_e = T_{PM} + T_r + T_{cog} \\ T_{PM} = \dfrac{3}{2} p i_q \left(\psi_d^{PM} + \dfrac{d\psi_q^{PM}}{d\theta} \right) - \dfrac{3}{2} p i_d \left(\psi_q^{PM} - \dfrac{d\psi_d^{PM}}{d\theta} \right) \\ T_r = \dfrac{3}{2} p i_q i_d (L_d - L_q) + \dfrac{3}{4} p {i_d}^2 \dfrac{dL_d}{d\theta} + {i_q}^2 \dfrac{dL_q}{d\theta} \end{cases} \tag{4.6}$$

where ψ_d^{PM} and ψ_q^{PM} are the dq-axes PM fluxes, i_d and i_q are the dq-axes currents, L_d and L_q are the dq-axes inductances and p is the pole pair number.

It can be seen from (4.6) that the PM torque is produced by the interaction between input current and PM flux. As shown in (4.7), the even order harmonics in flux linkage are a result of the flux density in air-gap, which can be modified by the pole shaping method.

$$\psi_f = N_c \int B(t) d\, A_t \tag{4.7}$$

where B(t) is the air-gap flux density at time t, A_t is the face area of tooth tips at air-gap and N_{TPC} is the number of turns per coil. Due to the unbalanced flux density in CPPM machine, even order harmonics exist in the flux linkage. Take the dominant third order torque ripple as example, this will be produced by an interaction between the fundamental current and the dominant 2nd and 4th harmonics in the flux linkage. Thus, it is feasible to change the phasor of 3rd order PM torque ripple by changing the phasors of 2nd and 4th flux linkage harmonics.

According to (4.6), the fluctuations in L_d and L_q will also lead to large reluctance torque ripple. From the CP structure, it is clear that there is only one iron pole in an electrical cycle, which means that due to the saliency effect the first order harmonic in phase inductance is the largest [Ma19]. Assuming the mutual inductance for concentrated winding machine is negligible, the inductance matrix can be expressed by:

$$\boldsymbol{L}_{abc} = \begin{bmatrix} L_{aa} & 0 & 0 \\ 0 & L_{bb} & 0 \\ 0 & 0 & L_{cc} \end{bmatrix} \tag{4.8}$$

where L_{aa} L_{bb} L_{cc} are the self-inductance of each phase and can be defined by:

$$\begin{cases} L_{aa} = l_0 + l_2\cos(\theta_r) \\ L_{bb} = l_0 + l_2\cos(\theta_r - 2\pi/3) \\ L_{cc} = l_0 + l_2\cos(\theta_r + 2\pi/3) \end{cases} \tag{4.9}$$

where θ_r is the rotor position in electrical degree, l_0 and l_2 are the average value and harmonic amplitude, respectively.

The d-axis and q-axis inductance matrix $\boldsymbol{L}_{dq}$ can be calculated by:

$$\boldsymbol{L}_{dq} = \boldsymbol{P}\boldsymbol{L}_{abc}\boldsymbol{P}^{-1} \tag{4.10}$$

where

$$\boldsymbol{P} = \frac{2}{3}\begin{bmatrix} \cos(\theta) & \cos(\theta - 2\pi/3) & \cos(\theta + 2\pi/3) \\ -\sin(\theta) & -\sin(\theta - 2\pi/3) & -\sin(\theta + 2\pi/3) \\ 0.5 & 0.5 & 0.5 \end{bmatrix} \tag{4.11}$$

Therefore, L_d and L_q can be written as:

$$\begin{cases} L_d = l_0 + \dfrac{l_2}{2}\cos(3\theta) \\ L_q = l_0 - \dfrac{l_2}{2}\cos(3\theta) \end{cases} \tag{4.12}$$

According to (4.6) and (4.10), the fluctuation in inductance will lead to a large third order harmonic in reluctance torque even under an i_d=0 control strategy.

From (4.6)-(4.10), the phasor of the third order reluctance torque ripple is determined by that of inductance, which is limited by the saliency of iron pole in CP structure. Due to almost fixed position of iron poles, the phasor of third order harmonic inductance is nearly constant, which leads to the fact that the phasors of reluctance torque ripple remain fairly consistent in the pole shaping process.

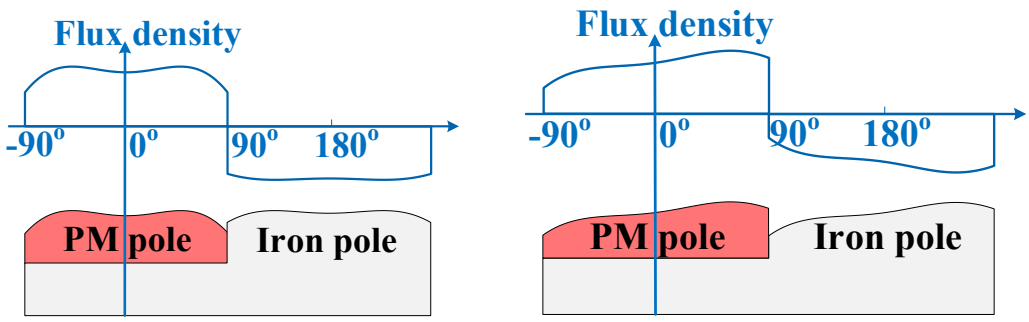

(a) Model A (b) Model B

Fig. 4.7 Illustration of flux density distributions of one pole pair.

From Fig. 4.7 (a), it is clear that the balanced rotor outline of Model A produces symmetrical flux density, which means that the waveform is symmetrical at 0°. Therefore, the flux density B_{fA} can be written as:

$$B_{fA} = \sum_{i=0}^{\infty} A_{Aci} \cos(i\theta) \tag{4.13}$$

where A_{Aci} is the amplitude of the i-th harmonic for Model A.

However, in the case of the asymmetric rotor shape, there is no symmetry axis in the flux density waveform in Model B. Consequently, the flux density B_{fB} can be written as:

$$B_{fB} = \sum_{j=0}^{\infty} [A_{Bcj} \cos(j\theta) + A_{Bsj} \sin(j\theta)] \tag{4.14}$$

where A_{Bcj} and A_{Bsj} are the amplitudes of j-th harmonic for Model B.

Comparing (4.11) and (4.12), it is evident that the phases of harmonics, including even order harmonics are fixed in Model A, while those in Model B are flexible. Therefore, the asymmetric shape in Model B has the potential to reduce the total torque ripple by manipulating the phasors of PM torque ripple and cogging torque.

As is the case of the symmetrically shaped pole in Model A, the flux density of conventional CPPM machine with constant profile poles and different PM pole arc span is also symmetrical and the PM third order torque ripple similarly cannot be manipulated.

As for the CPPM machine with $N_s/(mS_m)$ being even, it is reported that the torque ripple can be decreased to the level of SPM counterpart (without third order harmonic) [Chu10] [Zha19b] [Li19c]. This is because of the elimination of both PM torque ripple and reluctance ripple. When using this slot/pole number combination, even number slots with opposite phasors will be allocated into the same phase to achieve a high winding factor. In such cases, the even-order harmonics in the back EMFs of two slots will be eliminated, which leads itself to the reduction of the third order PM torque ripple. The teeth with opposite phasor also lead to the elimination of first order self-inductance [Ma19], which removes the third order reluctance torque ripple. Consequently, there is no 3rd order torque ripple in the superposition of PM torque and reluctance torque.

4.4 Performance Comparison and Analysis

4.4.1 Open-Circuit Flux Density

Finite element predicted PM flux densities in the air-gap under open-circuit condition of these three machines are compared in Fig. 4.8. It is clear that the amplitudes of these even order harmonics in Model B are larger than those in Model A, which is because of the asymmetric waveform between the flux density under PM pole and iron pole in Model B.

To aid the understanding of this behaviour, Table 4.1 shows the amplitudes and associated phase angles of the 8^{th} order and 16^{th} order flux density harmonics. As will be apparent, the angles associated with the even order harmonics for symmetrically shaped poles of Model A and conventional model are the same, while for the asymmetrically shaped poles in Model B they exhibit the different angles, which illustrates the principles that the harmonic phasors are fixed for symmetrical pole-shaped CP rotors.

4.4.2 Flux Linkage and Back EMF

The finite element predicted flux linkages and back EMFs under open-circuit condition are compared in Fig. 4.9 and Fig. 4.10. It can be seen that Model B tends to have larger even order harmonics in flux linkage than those of Model A, which leads to the same trend in the back EMF performances as illustrated in Fig. 4.10.

In addition, the features of the harmonics in back EMF are quantified in Table 4.2. As was the case with Table 4.1, Model A and conventional model share the same phasors in back EMF. Under I_d=0 control, the fixed phasors in back EMF will limit the corresponding phasors of PM torque harmonics.

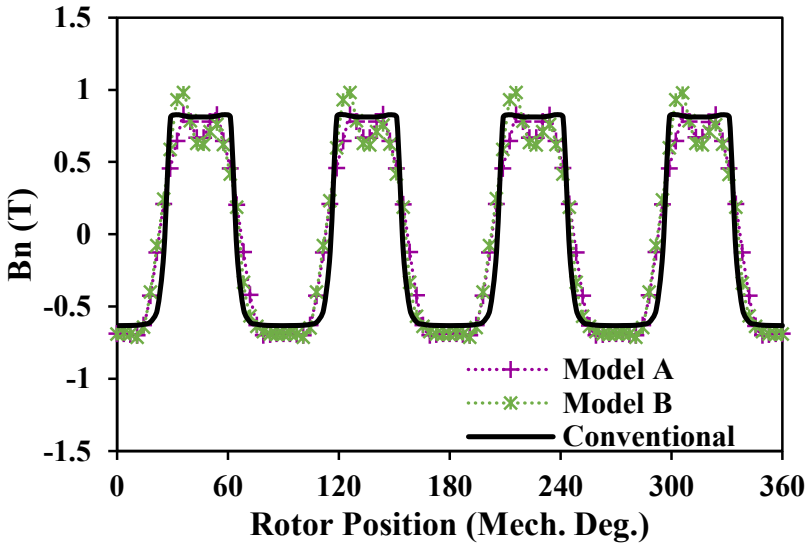

(a) Waveforms

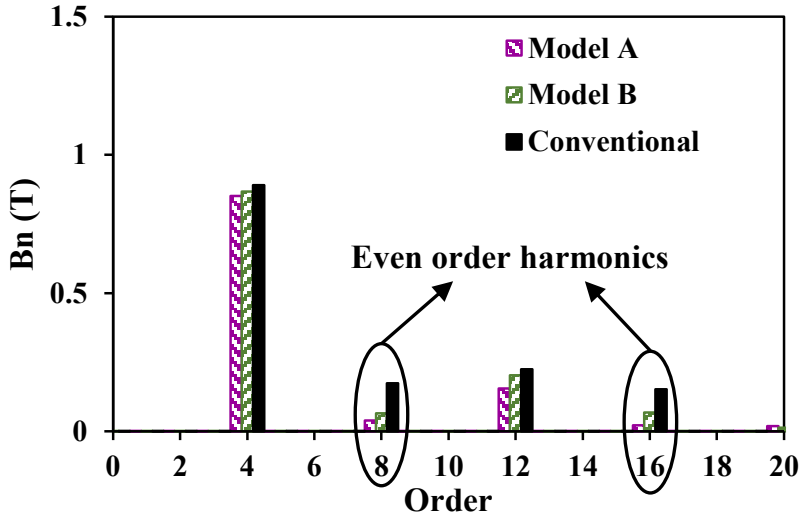

(b) Spectra

Fig. 4.8 Open-circuit flux density in air-gap.

Table 4.1. Amplitudes and Angles of Flux Density Harmonics

Harmonic		Model A	Model B	Conventional
8th	Amplitude (T)	0.038	0.064	0.173
	Angle (°)	0.0	52.6	0.0
16th	Amplitude (T)	0.021	0.068	0.151
	Angle (°)	180.0	172.6	180.0

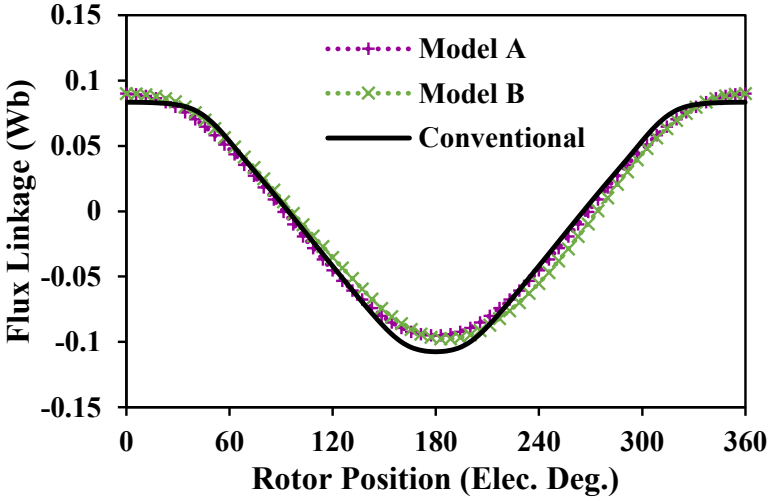

(a) Waveforms

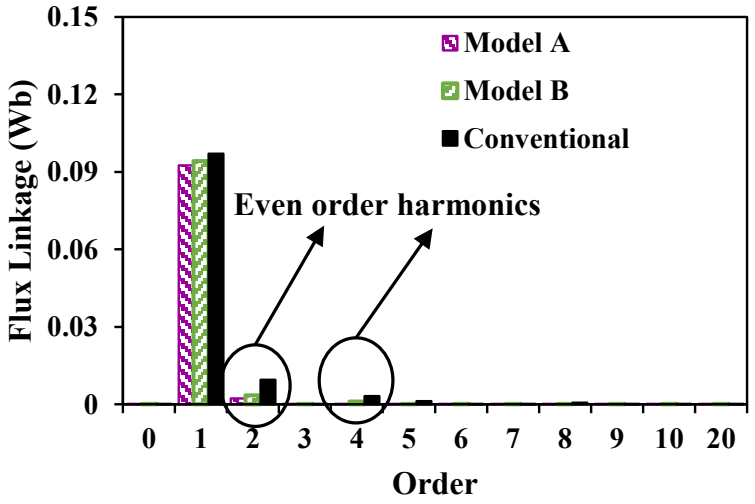

(b) Spectra

Fig. 4.9 Open-circuit flux linkage of three machines.

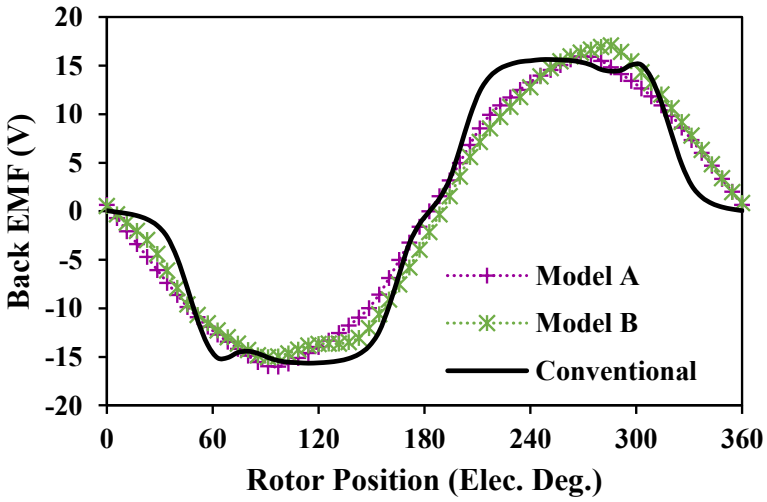

(a) Waveforms

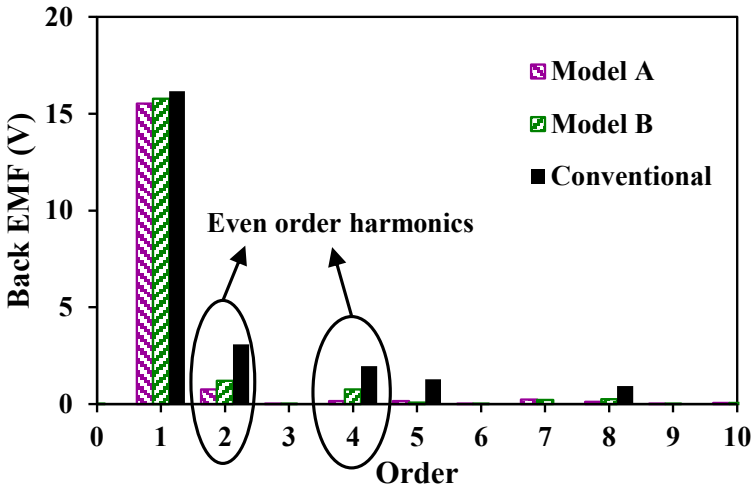

(b) Spectra

Fig. 4.10 Open-circuit back EMF of three machines.

Table 4.2. Amplitudes and Angles of Back EMF Harmonics

Harmonic		Model A	Model B	Conventional
2th	Amplitude (V)	0.768	1.208	3.093
	Angle (º)	-95.7	-144.9	-95.7
4th	Amplitude (V)	0.165	0.757	1.957
	Angle (º)	-101.3	-89.0	-101.4

4.4.3 Shaft Flux Leakage

As shown in Fig. 4.11, consequent pole topology will lead to axial end shaft flux leakage due to the unipolar magnets in rotor. It can be seen that under the open-circuit condition, the pole shaped two models have a little higher end shaft flux density than that of the conventional model, which is largely a consequence of the larger equivalent air-gap length. Due to the parallel end shaft flux path and the air-gap flux path, larger air-gap flux reluctance caused by larger equivalent air-gap length will inevitably result in the larger flux density in axial end shaft. The unipolar end shaft flux leakage will cause magnetization risks of the mechanical components and reduce the reliability and safety. This can be solved by axially staggered structure as introduced in [Ge16] and [Li19b].

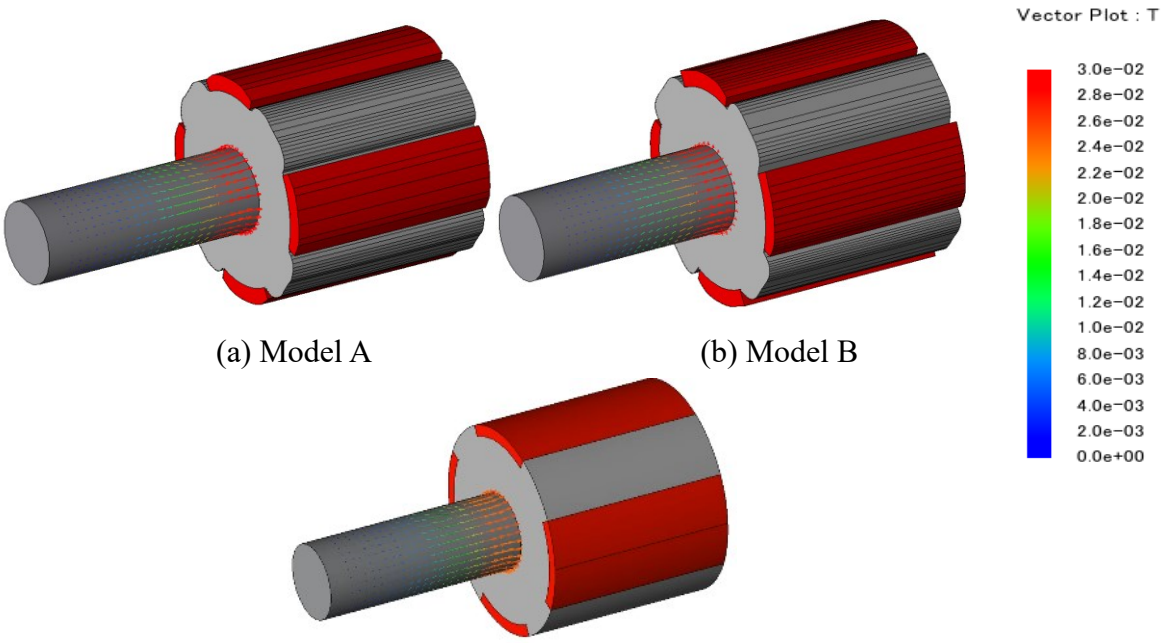

(a) Model A (b) Model B

(c) Conventional

Fig. 4.11 Open-circuit flux density vectors on the end shaft.

4.4.4 On-load Inductance

The variation of inductance directly relates to the reluctance torque ripple. Frozen permeability method [Zhu16] is adopted in this section to analyze the on-load inductance characteristics. Before injecting unit DC current in one phase winding, the permeability of iron part at each step in each grid under the load condition is applied to the model. By utilizing the flux linkage in each phase and the injected current, the inductances can be obtained.

Different from the conventional inset rotor, the saliency of the iron pole in CPPM structures can contribute to large odd order harmonics in self-inductances as shown in Fig. 4.12, which results from the single salient iron in an electrical cycle of CPPM structures.

The *d*-/*q*-axis inductances for analyzed machines are shown in Fig. 4.13. As can be seen, there are large third order harmonics resulted from the odd order harmonics in self-inductance. According to (4.6), these third order harmonics in *d*-/*q*-axis inductances will inevitably contribute to large third order reluctance torque ripple even under i_d=0 control. Besides, similar average *d*-/*q*-axis inductance values can be seen for three CPPM machines, which means the reluctance torque is very small.

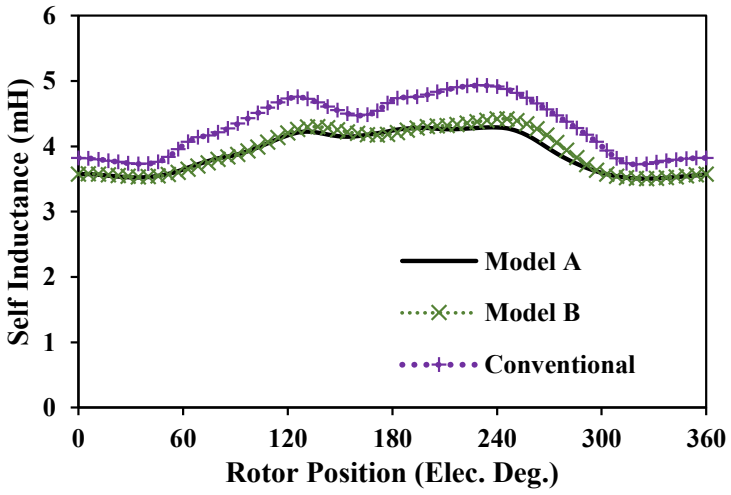

(a) Waveforms

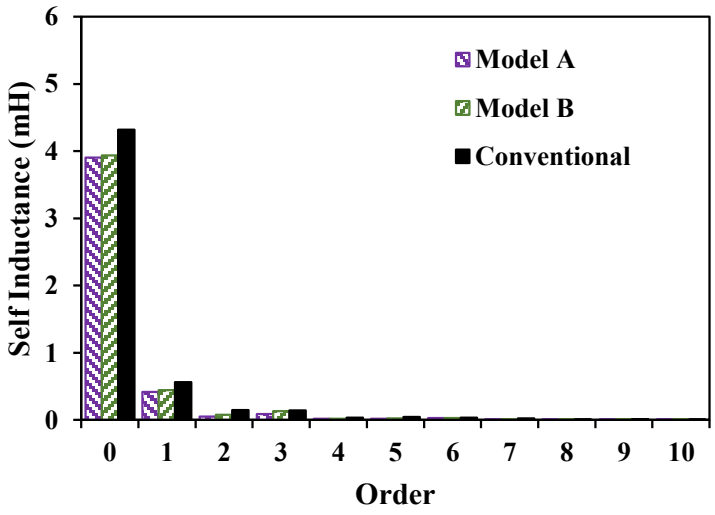

(b) Spectra

Fig. 4.12 Rated-load self-inductances.

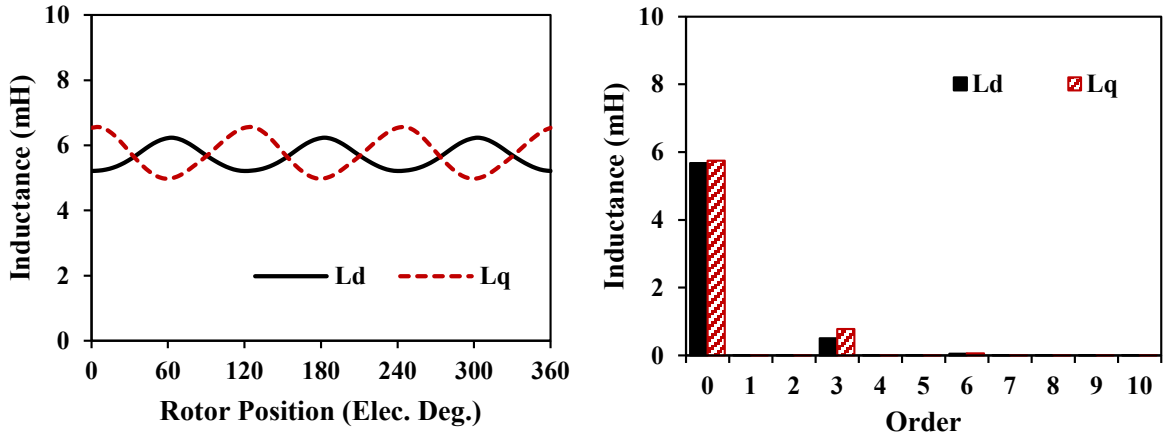

(a) Model A

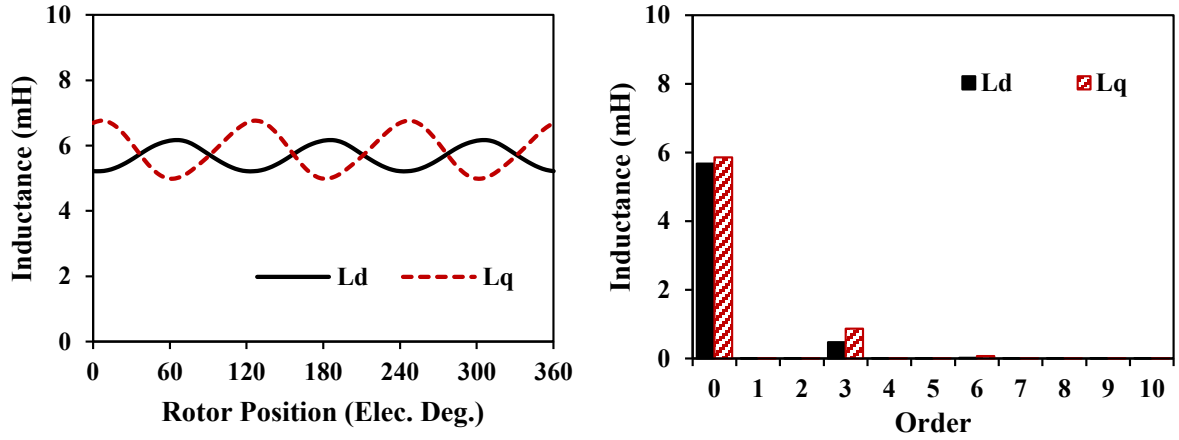

(b) Model B

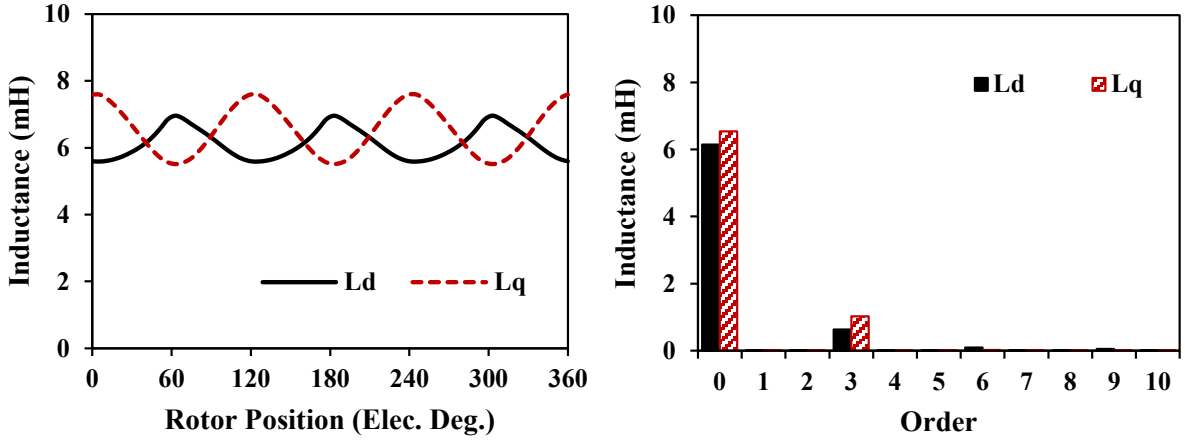

(c) Conventional

Fig. 4.13 Rated-load *d*-/*q*-axis inductances.

4.4.5 Torque Characteristics at Rated Condition

The average torques versus current advanced angle are shown in Fig. 4.14. It can be found that for the three machines, the optimum current angle is very close to 0, which is mainly caused

by the small reluctance torque as mentioned before. The maximum output torque points for three machines are adopted in the following analysis.

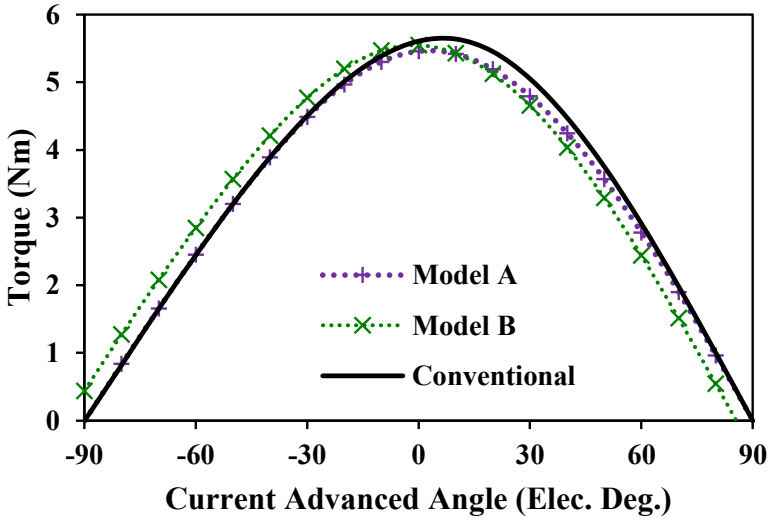

Fig. 4.14 Rated-load average torque versus current advanced angle.

Fig. 4.15 and Table 4.3 compare the output torque waveforms of the two machine designs with shaped magnets with that produced by the conventional CPPM machine. The frozen permeability method [Zhu16] was adopted in order to disaggregate the individual torque components. Firstly, the model runs under the load condition, and the permeability of iron part at each step in each grid is recorded. Then, the material with those recorded permeabilities can be treated as linear at each step and the model will be run again without current or without magnet to obtain the on-load cogging torque and the on-load reluctance torque, respectively. After that, the on-load PM torque can be obtained by making the difference between the total torque and the other two components. The torque ripple index T_{ripple} is the ratio of the peak to peak value to average torque T_{avg} and η_{PM} is the ratio of average torque to PM volume. It can be seen that the third order harmonic in total torque ripple is still clearly evident for Model A while it is much reduced in Model B. This is mainly because of the approximately opposite phasors of the third order PM torque ripple and reluctance torque ripple.

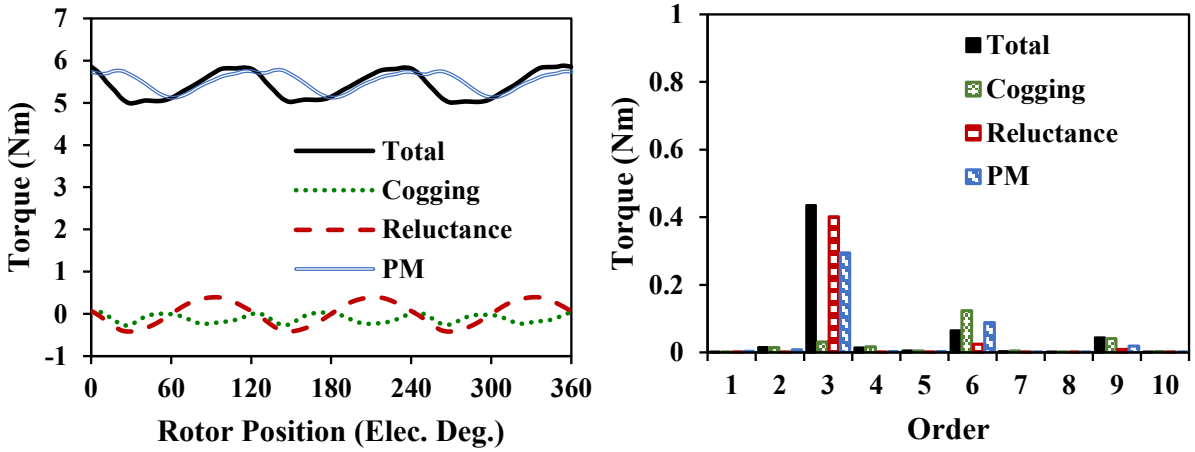

(a) Model A (T_{avg}=5.42Nm, T_{ripple}=16.4%, η_{PM}=3.7×10^{5}Nm/m^3)

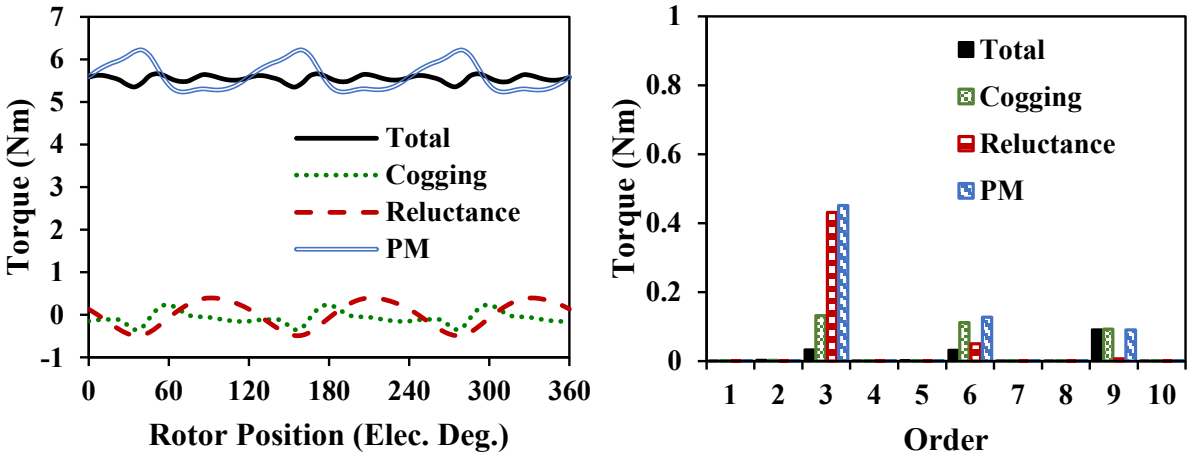

(b) Model B (T_{avg}=5.54Nm, T_{ripple}=5.9%, η_{PM}=3.7×10^{5}Nm/m^3)

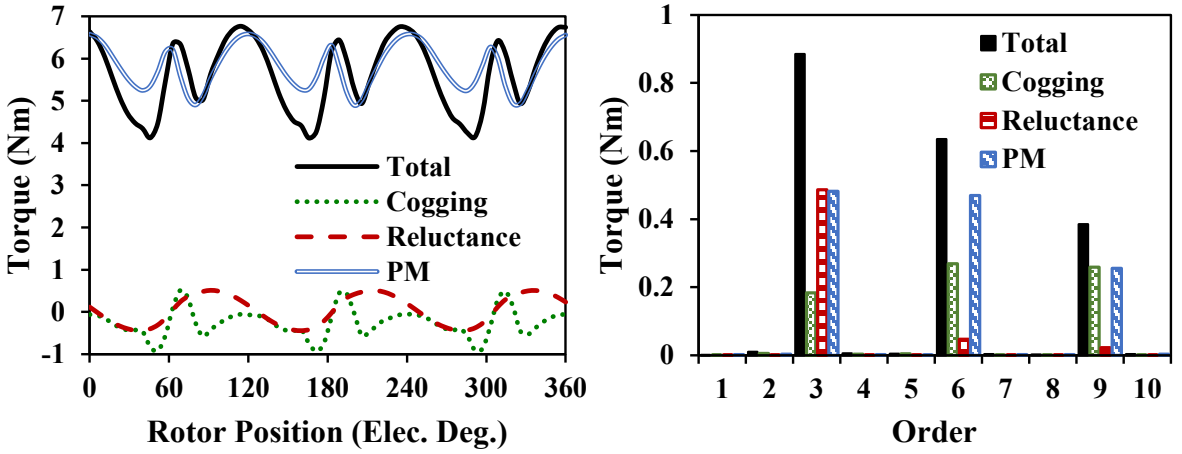

(c) Conventional (T_{avg}=5.61Nm, T_{ripple}=42.1%, η_{PM}=3.8×10^{5}Nm/m^3)

Fig. 4.15 Rated torque waveforms and torque ripple spectra.

Table 4.3. Third Order Torque Harmonics of Machines

Harmonic		Model A	Model B	Conventional
Total	Amplitude (Nm)	0.435	0.034	0.885
	Angle (°)	45.3	76.6	45.0
Reluctance	Amplitude (Nm)	0.401	0.431	0.486
	Angle (°)	85.8	75.9	81.9
PM	Amplitude (Nm)	0.295	0.451	0.482
	Angle (°)	-12.0	-87.8	-2.5
Cogging	Amplitude (Nm)	0.031	0.132	0.184
	Angle (°)	-111.8	150.4	65.4

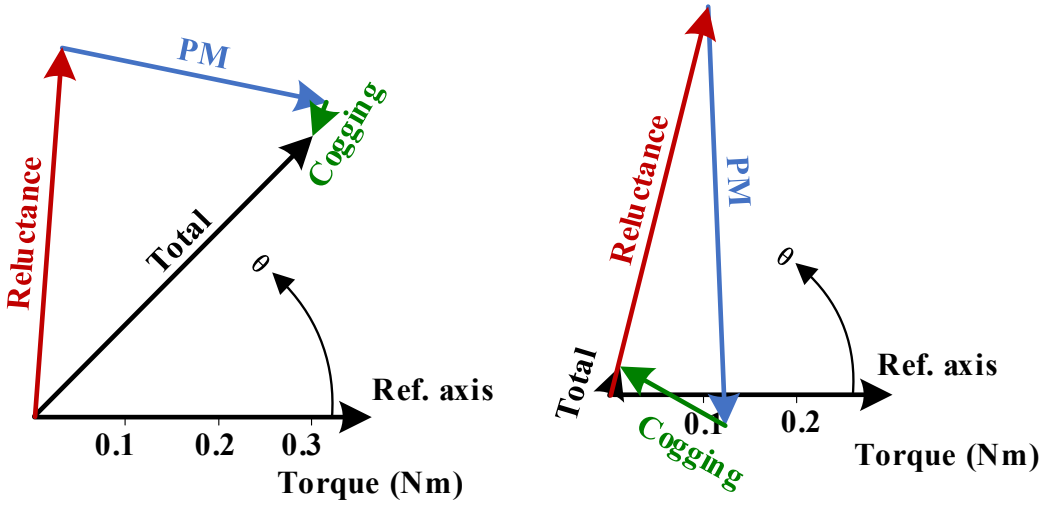

(a) Model A (b) Model B

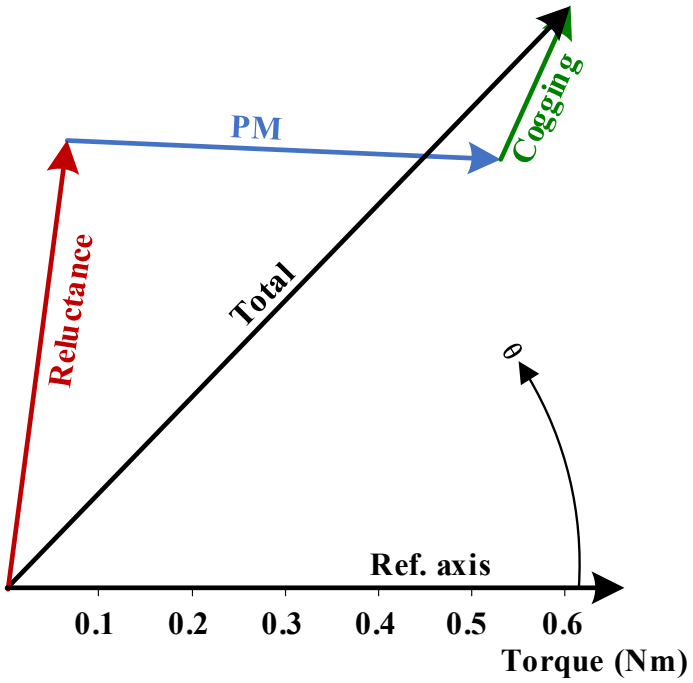

(c) Conventional

Fig. 4.16 Phasor diagrams of 3rd torque ripple.

Adopting the convention that angular position 0 in Fig. 4.15 is the reference axis, phasor diagrams of the 3rd order torque ripple can be plotted, as shown in Fig. 4.16. It is clear that the amplitudes of PM torque ripple and cogging torque for Model A are the smallest and have almost the same phase as the conventional model. Therefore, large third order total torque ripple is produced by these two symmetrical models. However, for Model B with the asymmetrically shaped magnets, the angle between the phasors of PM torque ripple and reluctance torque ripple is close to 180° resulting in near cancellation. Once the contribution of the cogging torque phase is added in, an extremely small third order total torque ripple is achieved.

4.4.6 Torque Characteristics under Reversed Rotation Direction

The torque characteristics in reversed rotation direction for these machines are analyzed as illustrated in Fig. 4.17. It can be seen that the average torques for three machines are almost the same as before with the differences less than 1%. Also, it is clear that the conventional model and Model A with symmetrical pole shapes have almost same torque waveform as before. However, the torque waveform of Model B deformed significantly and the corresponding

torque ripple is increased from 5.9% to 36.4% but it is still lower than that of conventional model.

To aid the understanding of the performance, the torque components for Model B with asymmetric pole shape are demonstrated in Fig. 4.18 and the phasor diagram of the dominant 3rd order torque ripple is presented in Fig. 4.19. It is obvious that when rotating in a reverse direction, the harmonic phases are shifted and are superimposed to form a larger amplitude. Consequently, the asymmetric pole shape can only reduce the torque ripple in one rotation direction.

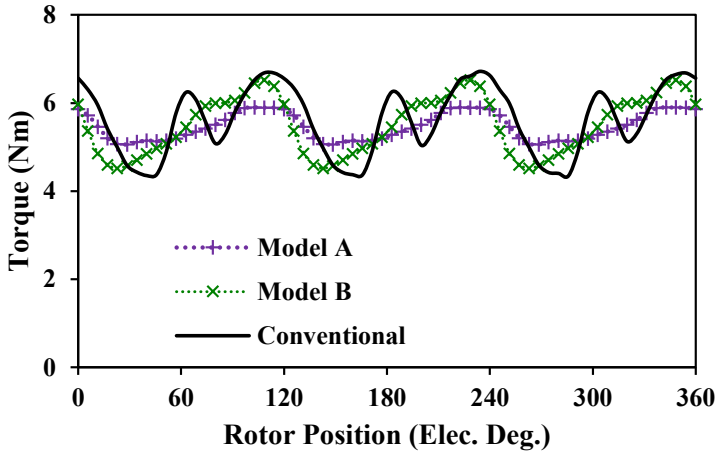

(a) Waveforms

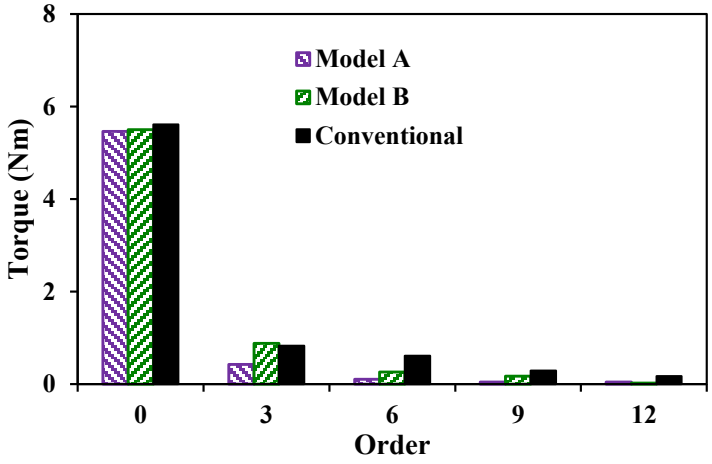

(b) Spectra

Fig. 4.17 Rated torque characteristics in reversed rotation direction for three machines (Model A: T_{avg}=5.46Nm, T_{ripple}=15.5%. Model B: T_{avg}=5.50Nm, T_{ripple}=36.4%. Conventional: T_{avg}=5.61Nm, T_{ripple}=42.3%).

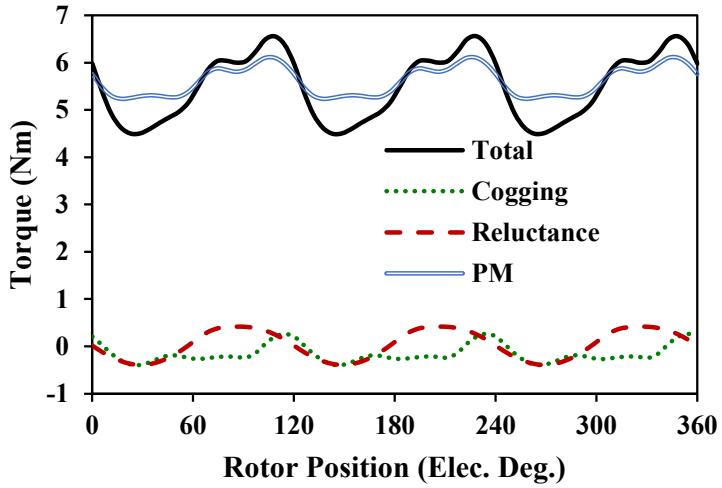

(a) Waveforms

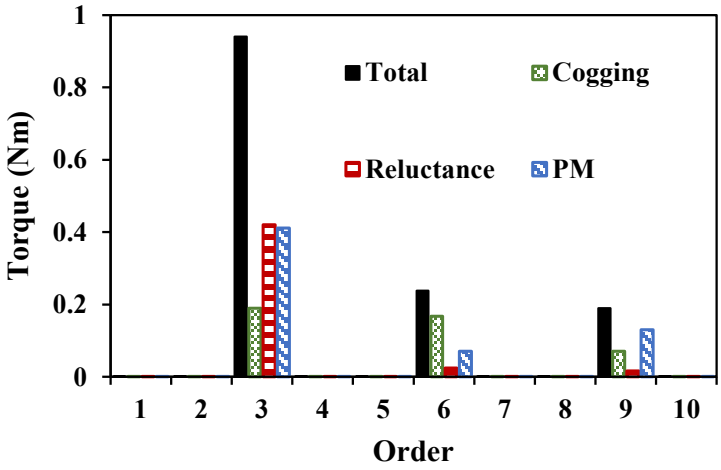

(b) Spectra

Fig. 4.18 Rated torque components for Model B in reversed rotation direction.

For the application of automotive drive system, large torque ripple will inevitably affect the driving experience. But the reverse state is rarely used in EV traction and the Model B still has reduced torque ripple than that of the conventional CPPM machine. Besides, the automotive drive system is only one of the application scenarios of CPPM machines. This behavior can be more suitable for other applications, such as electric fan, which only work in one direction and fixed load.

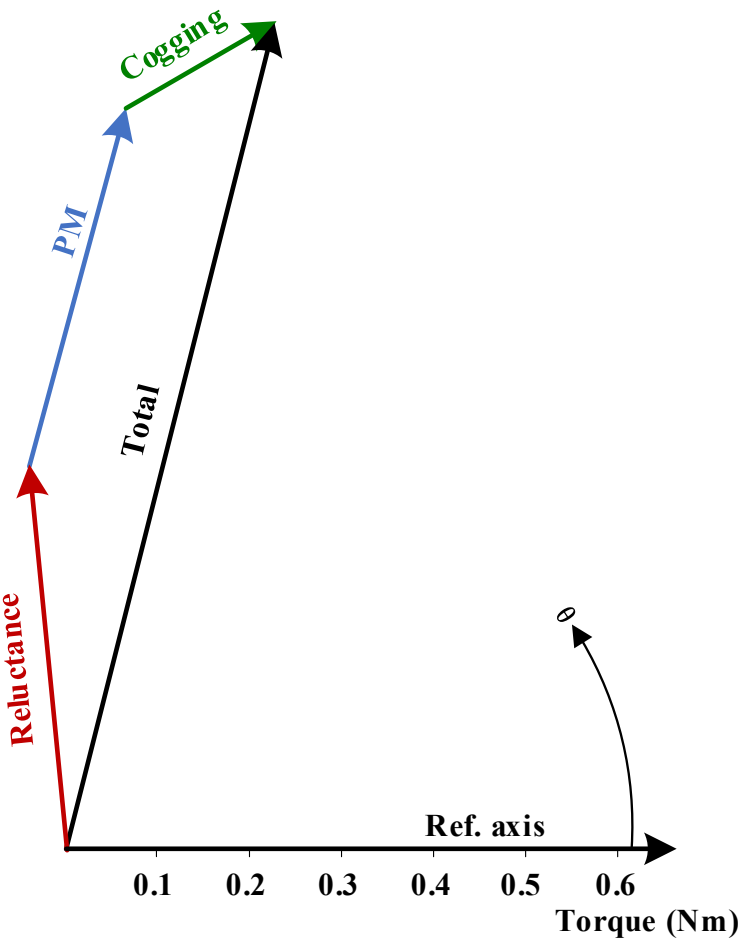

Fig. 4.19 Phasor diagrams of the 3rd order torque ripple for Model B in reversed rotation direction.

4.4.7 Effect of Load

Whereas the phases of the various contributing components of ripple torque can be set by design features, their relative magnitudes are determined by the magnitude of the stator current. Hence, the degree to which cancellation of the harmonics occurs will be a function of the load imposed on the machine. As shown in Fig. 4.20, Model A with the symmetrical magnet shaping produced the smallest peak to peak value of cogging torque. This is largely a consequence of Model A having the most balanced flux density in air-gap.

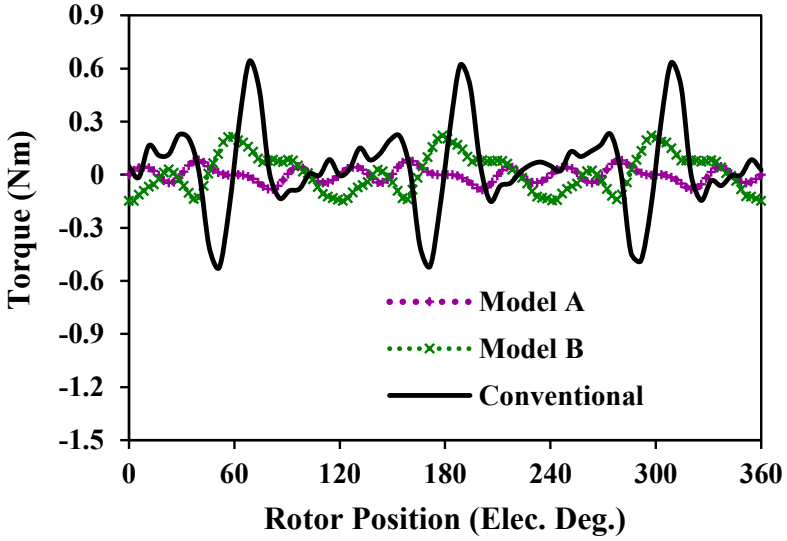

(a) Waveforms

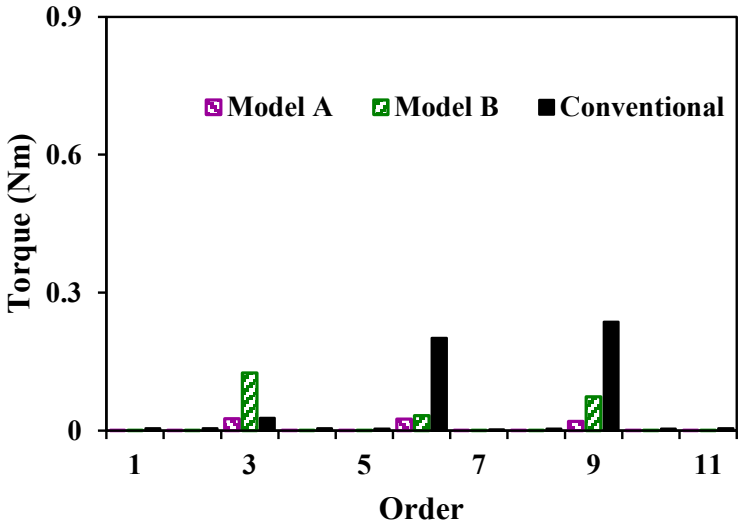

(b) Spectra

Fig. 4.20 Open circuit cogging torque comparison.

The relatively larger cogging torque of Model B leads to a marginally higher torque ripple under light load condition as demonstrated in Fig. 4.21. It is worth noting that by reducing the cogging torque with changing geometry [Zhu00] [Zhu09a], the torque ripples at different loads tend to be reduced further. But the optimization of cogging torque is not the focus of this chapter. The torque performances for the three machine designs under different load conditions are illustrated in Fig. 4.21. Clearly, both two optimized machines have a slightly enhanced over-load capability compared to the conventional machine, which can be explained by the slightly larger equivalent air-gaps for two shaped machines. In addition, the torque ripples of Models

A and B improve significantly with the increase in current, which is because reluctance torque is proportional to the square of the current while PM torque is proportional to current. This will also happen in light load condition, which means that under other conditions, the torque ripple tends to diminish the usefulness of this technique. Despite this variation in the effectiveness of the torque ripple elimination, under all the working conditions considered, the torque ripple of Model B with asymmetric magnet shaping is always lower than that of its conventional CPPM counterpart.

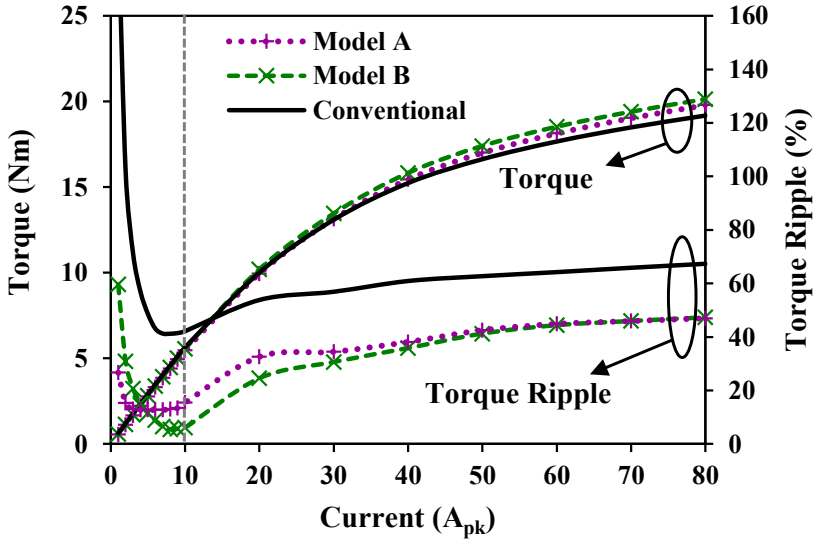

Fig. 4.21 Torque performance under different load (Rated current is $10A_{pk}$ shown by a vertical grey dash line).

4.4.8 Iron Loss and Flux Distribution

As illustrated in Table 4.4, the predicted iron losses of two optimized machines are lower than that of conventional machine under rated condition, which can be attributed to the larger equivalent air-gaps and reduced air-gap field harmonics for two shaped machines and consequently the lower armature effect and relatively lower flux density distribution as shown in Fig. 4.22.

Table 4.4. Losses for Three Machines under Rated Condition

	Model A	Model B	Conventional
Stator iron loss (W)	1.2814	1.2387	1.4618
Rotor iron loss (W)	0.0117	0.0118	0.0247
PM loss (W)	0.0263	0.0278	0.0511
Total loss (W)	1.3194	1.2783	1.5376

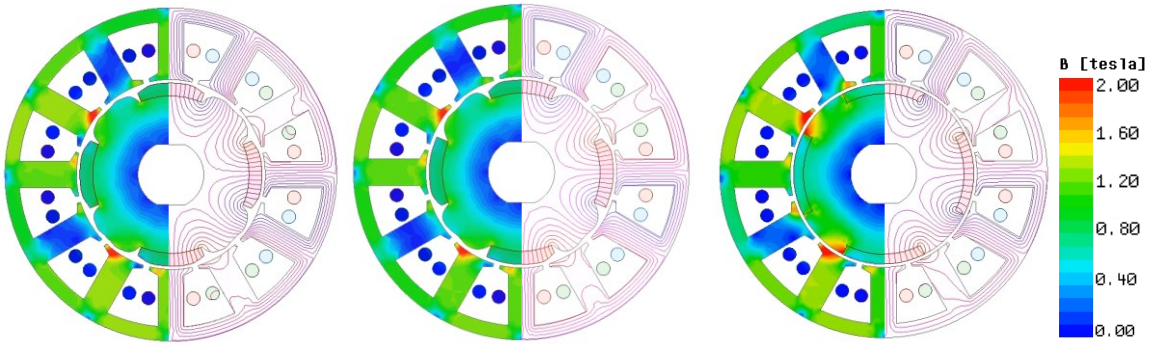

(a) Model A (b) Model B (c) Conventional

Fig. 4.22 Rated-load flux density distributions and flux lines.

4.5 Experimental Results

As shown in Fig. 4.23, three analyzed CPPM rotors and a 12-slot stator are prototyped to validate the foregoing analysis. The iron cores and the magnets are produced in China and assembled in UK. With the test rigs presented in Fig. 3.18, Fig. 2.24 (b), and Fig. 4.24, dynamic and static experiments are carried out to test the on-load torque, cogging torque, and inductance waveform.

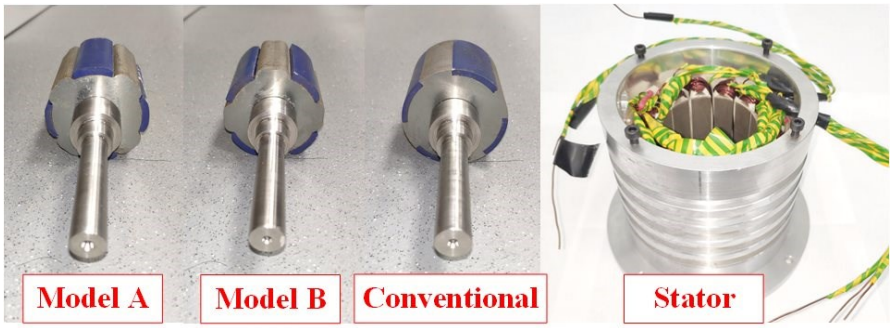

Fig. 4.23 12-slot/8-pole stator and rotors with and without shaping method.

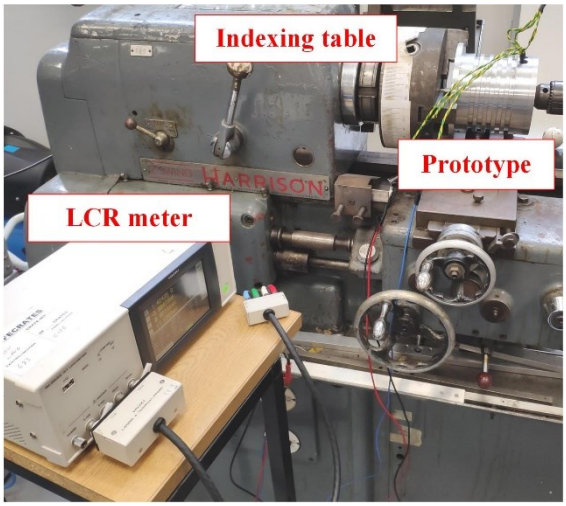

Fig. 4.24 Static test rig for inductance measurement.

4.5.1 Back EMF

Fig. 4.25 shows the measured and FEM predicted results of back EMF under no-load condition and 400 rpm for the 12-slot/8-pole CPPM machines with and without pole shaping. It is obvious that both waveforms and their spectra show good agreement, which confirms that the Model A has the lowest even order harmonics while the conventional CPPM machine has the highest.

4.5.2 No-load Inductance

The no-load inductance is measured with an IM 3533-01 LCR meter and a static platform as shown in Fig. 4.24 left figure. The rotor is fixed on a gauge and the stator can rotate with an indexing table. Then, the inductance value can be read from the LCR meter at different stator positions which can be read from the indexing table. Fig. 4.26 shows the comparison between the measured and predicted self-inductances of these machines under no-load condition. The measured results shown in Fig. 4.26 agree with the FEM predicted results quite well, except a little reduction for the average value, which is caused by the axial flux leakage and assembly deficiencies in the manufacture. Overall, it validates that the inductance of conventional CPPM machine is larger than those of other CPPM machines due to the relatively smaller equivalent air-gap. Furthermore, it shows that all the CPPM machines have odd order harmonics which in turn results in odd order torque ripples.

4.5.3 Cogging Torque

The measured and FEM predicted cogging torques for these machines are compared in Fig. 4.27. A good agreement can be witnessed, indicating that the cogging torques of pole shaped CPPM machines are both lower than that of conventional one. In addition, Model A has lower cogging torque due to the lower harmonic amplitudes in the flux density.

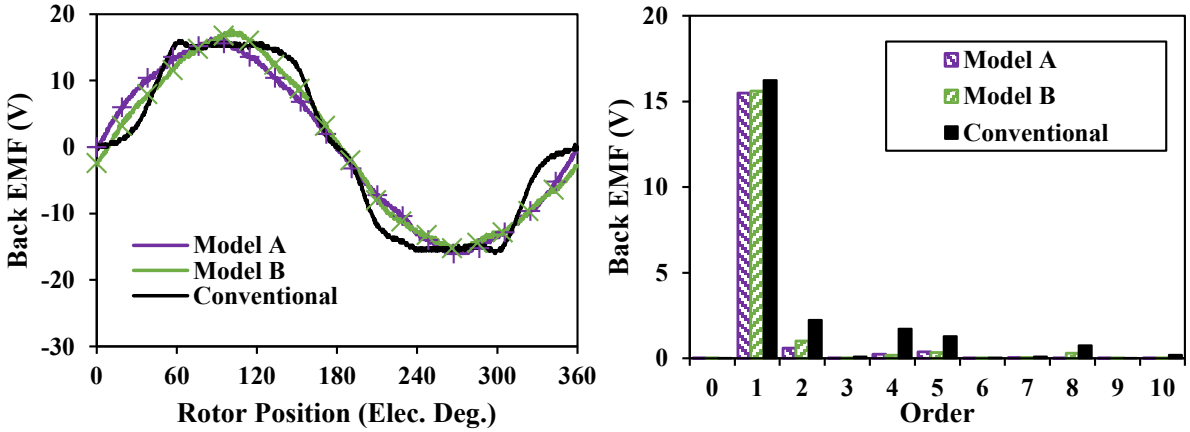

(a) Measured

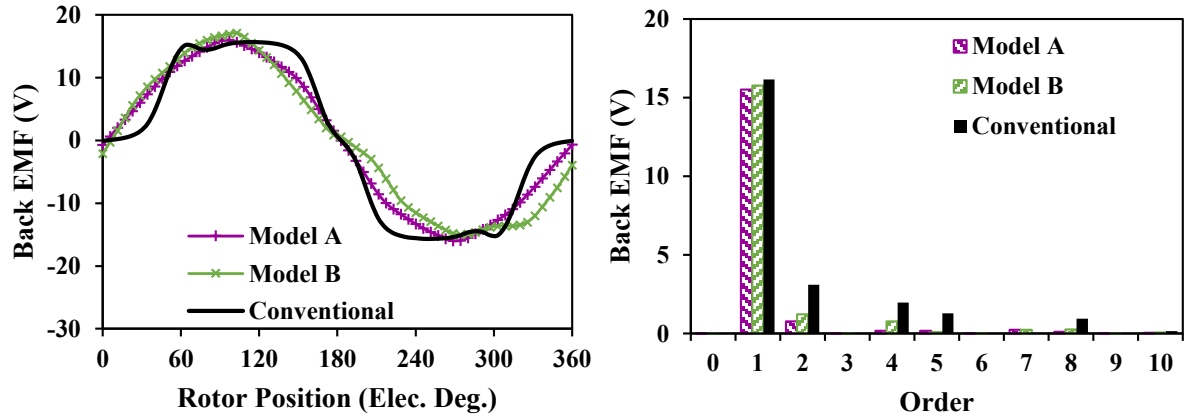

(b) FEM predicted

Fig. 4.25 Open-circuit back EMFs at 400 rpm.

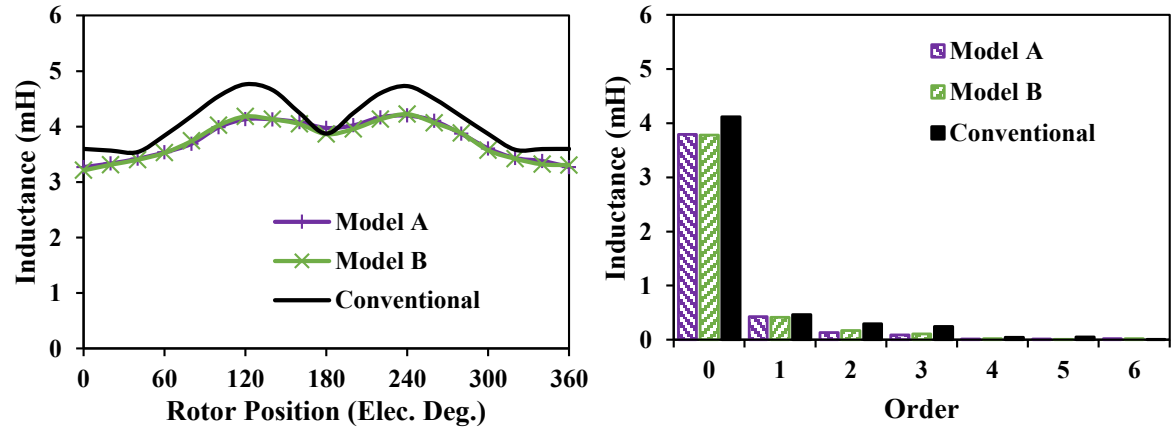

(a) Measured

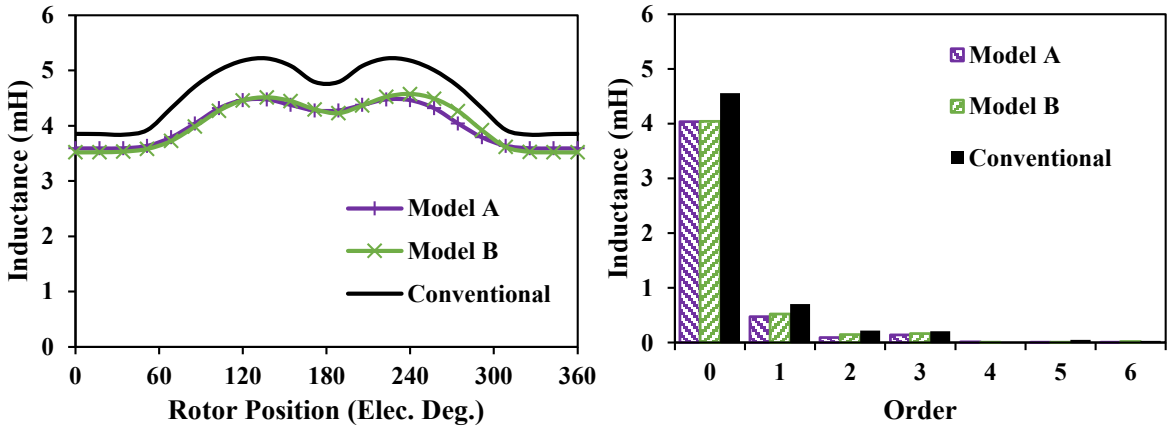

(b) FEM predicted

Fig. 4.26 Open-circuit self-inductance.

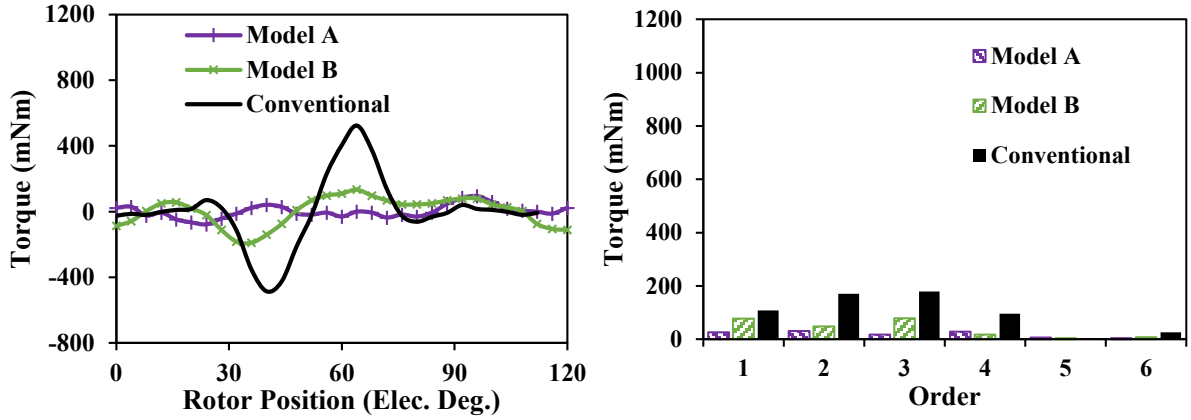

(a) Measured

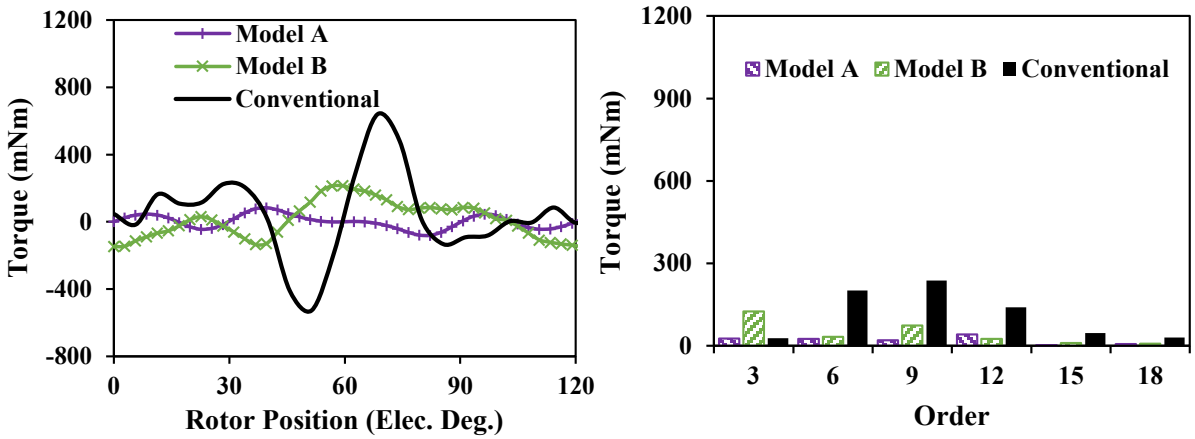

(b) FEM predicted

Fig. 4.27 Open-circuit cogging torque waveforms for prototypes.

4.5.4 Rated Torque

Under I=10A_{pk}, the torque waveforms of CPPM prototype with three rotors are demonstrated in Fig. 4.28 with the torque ripple compared in Table 4.5. Apparently, Model B has the lowest torque ripple, which agrees with the foregoing analysis. However, the torque ripple for Model B is larger than the predicted value, which is largely a consequence of the existence of the third order harmonic as shown in Fig. 4.28. To achieve the low torque ripple for the optimized Model B, accurate coordination of each torque component is required. In other words, the back EMF and inductance need to be accurate. However, the prototype is handmade, which means both the back EMF and inductance have some errors as shown in Fig. 4.25 and Fig. 4.26. Consequently, the small third order torque ripple for Model B can be seen in Fig. 4.28. Additionally, the torque waveforms for Model B in reverse direction are compared in Fig. 4.29. Good agreement validates the above analysis.

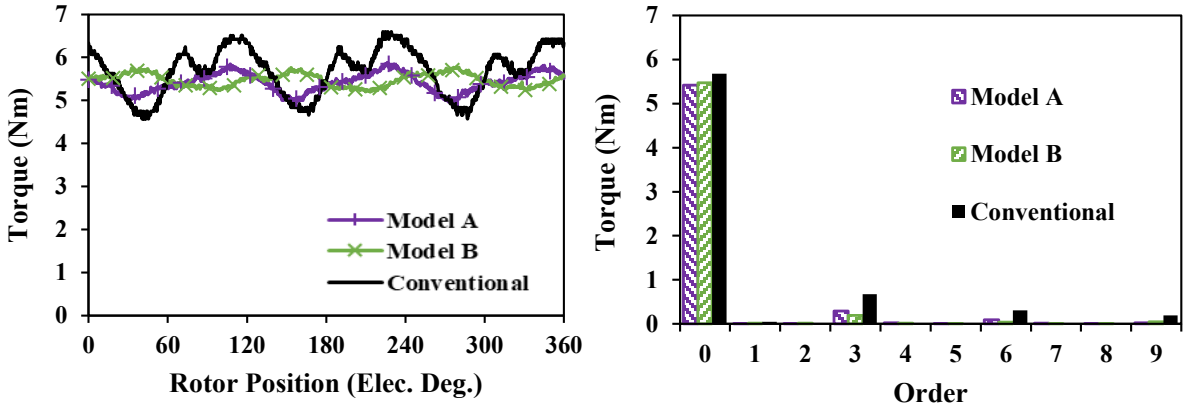

(a) Measured

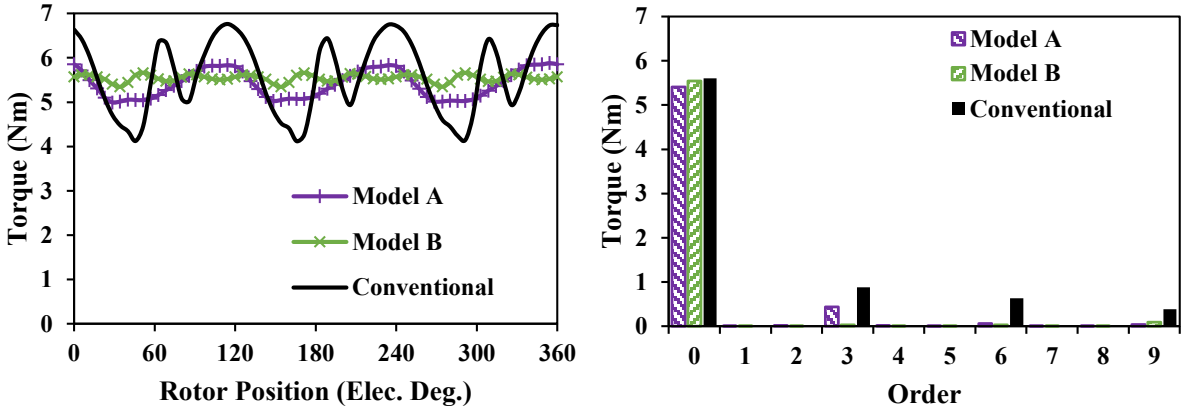

(b) FEM predicted

Fig. 4.28 Rated torque waveforms and spectra for prototypes ($I = 10A_{pk}$).

Table 4.5. Comparison of Measured and Predicted Torque Ripples Under Rated Current

	Model A	Model B	Conventional
Measured	16.8%	10.4%	35.7%
Predicted	16.4%	5.9%	42.1%

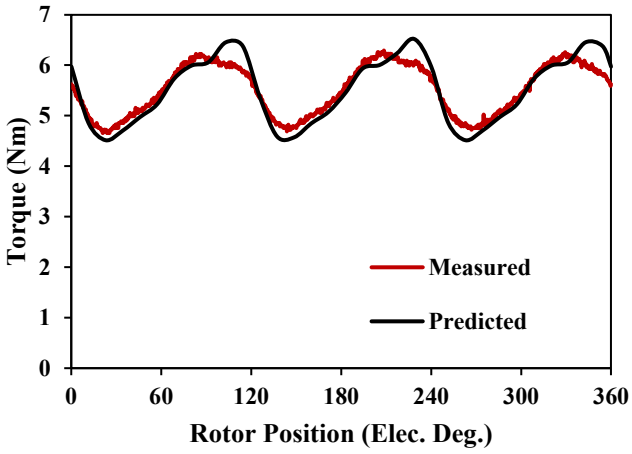

(a) Waveforms

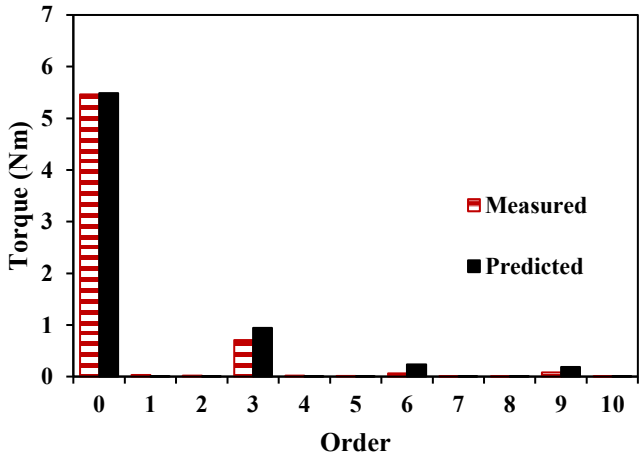

(b) Spectra

Fig. 4.29 Rated torque waveforms and spectra for Model B in reverse direction ($I = 10A_{pk}$).

4.5.5 Torque under Different Currents

Additionally, the measured and predicted torque performances under different currents are compared in Fig. 4.30 and show good agreement. The results verify that the asymmetric pole shape can only suppress the torque ripple within a certain current range.

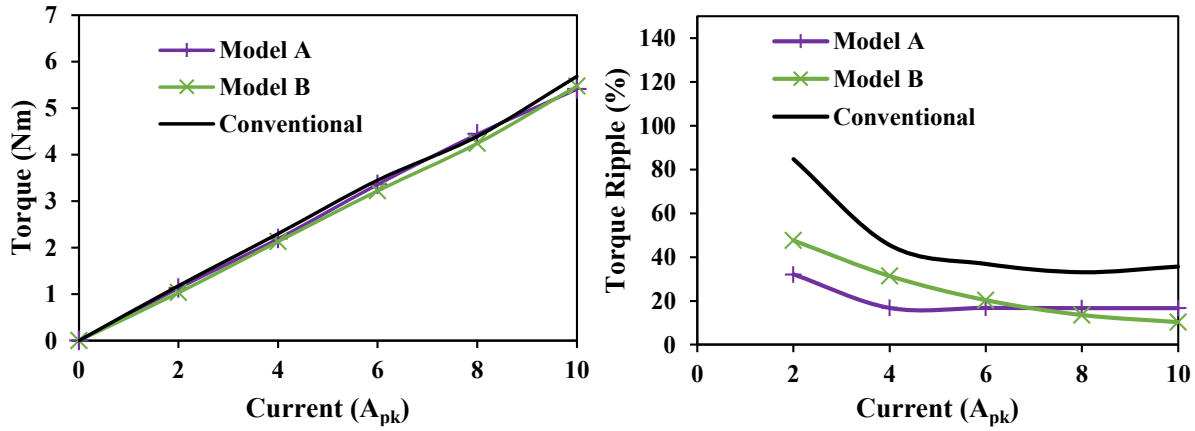

(a) Measured

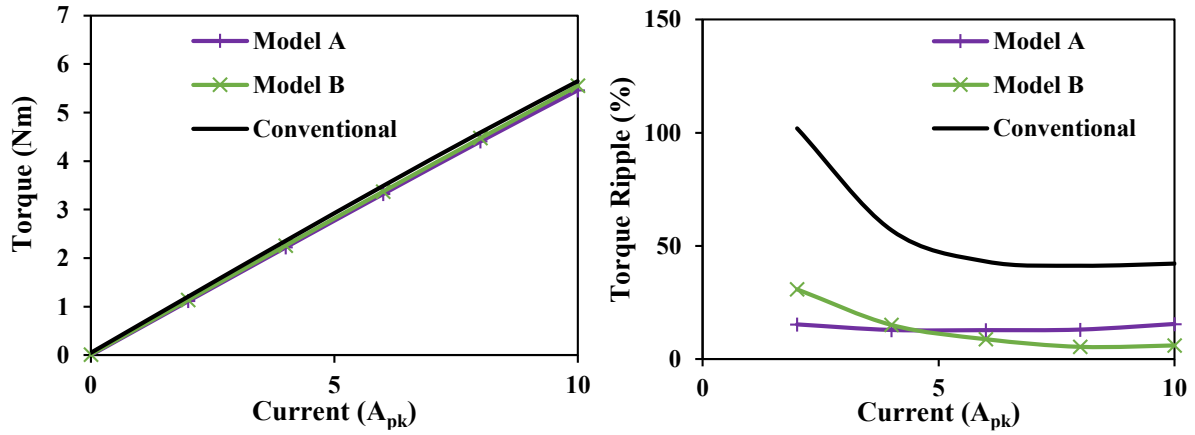

(b) FEM predicted

Fig. 4.30 Average torque and torque ripple under different load.

4.6 Summary

In this chapter, the dominant 3rd order torque ripple for a 12-slot/8-pole CPPM machine is illustrated as example to be suppressed effectively by asymmetric pole shaping method (Model B). The principle of manipulating harmonic phasors of even order flux density in air-gap is demonstrated in this chapter, which results in the phasor movements of corresponding PM torque ripple and cogging torque harmonics, leading to a high degree of torque ripple cancellation, albeit with a variation of the effectiveness with the load. It is found that this technique is more practical around the rated condition and in one rotation direction. FEM results demonstrate that a symmetrical shaped pole, including a conventional machine and Model A with the symmetrically shaped magnet, cannot eliminate the 3rd order torque ripple effectively due to the presence of reluctance torque ripple, while the proposed asymmetric magnet shaping can almost entirely cancel the 3rd order torque ripple by introducing even order

harmonic in back EMF. Lower cogging torque and lower iron loss can also be achieved by the proposed machine. Such behavior will also work for other CPPM machines with $N_s/(mS_m)$ being odd.

CHAPTER 5
INFLUENCE OF SLOT/POLE NUMBER COMBINATIONS AND POLE SHAPING ON ELECTROMAGNETIC PERFORMANCE OF PERMANENT MAGNET MACHINES WITH UNBALANCED NORTH AND SOUTH POLES

The unbalanced features in PM and iron poles in CPPM machines can cause problematic levels of torque ripple, which can be mitigated by the pole shaping method as has been analyzed in the previous chapters. However, it has been noticed that the effects of unbalanced features in PM and iron poles are highly dependent on the slot/pole number combinations, which means that the torque ripple characteristics and the effects of pole shaping methods can be different accordingly. Therefore, in this chapter, the influences of slot/pole number combinations on electromagnetic performances, including flux linkage, inductance, and torque ripple harmonic components, etc., resulting from unbalanced characteristics between north and south poles in concentrated winding PM machines with symmetrical and asymmetric rotor pole shaping methods are theoretically analyzed and experimentally validated in this chapter. It shows that for the PM machines with odd number of coils per phase per submachine, including CPPM and SPM machines, the influences of unbalanced pole characteristics can lead to additional torque ripple harmonics due to additive effects in windings, but can be cancelled in other machines. Compared with symmetrical pole shaping method, asymmetric pole shaping method can result in lower torque ripple for CPPM machines with odd number of coils per phase per submachine, while symmetrical and asymmetric pole shapes have similar effects on torque ripple reduction for other CPPM machines and all the SPM machines. The findings have been validated by finite element analyses on 12-slot/8-pole, 12-slot/10-pole, 9-slot/6-pole, and 12-slot/14-pole machines, and by experiments with 12-slot/8-pole and 12-slot/10-pole CPPM prototypes.

This chapter has been published on IET Electric Power Applications [Qi22d]:

[Qi22d] J. Qi, Z.Q. Zhu, G.W. Jewell, L. Yan, C.W. Gan, Y. Ren, S. Brockway, and C. Hilton, "Influence of slot/pole number combinations and pole shaping on electromagnetic performance of permanent magnet machines with unbalanced north and south poles," *IET Electr. Power Appl.*, pp.1–28, 2023. DOI: https://doi.org/10.1049/elp2.12293

5.1 Introduction

Even when CPPM machines are competitive in terms of torque density and/or magnet volume, they also have drawbacks. Arguably the foremost of these is the large torque ripple in the CPPM structures [Li18c] [Li19b]. It has been found that additional harmonics in back EMF, inductance, and cogging torque resulting from the unbalanced features between iron and PM poles will contribute to the overall torque ripples [Qi22a] [Qi22b], which in turn gives rise to significant vibration and noise.

To reduce torque ripples, several pole shaping methods have been proposed for CPPM structures, such as non-uniform air-gap profile [Chu16], pole-end barrier shape optimization [Wat18] [Hu18], inverse cosine shape air-gap [Eva10], etc. Investigations reported in [Qi22a] and [Qi22b] demonstrated that different pole shapes between PMs and iron poles as well as asymmetric pole shaping are effective in suppressing the torque ripple for a 12-slot/8-pole (12s8p) CPPM machine.

At a more general level, it has been noticed that the torque ripple and back EMF of CPPM machines are comparable to an SPM counterpart when $N_s/m/\mathrm{GCD}(N_s, p)$ is even, where N_s and m are the slot number and the phase number, respectively, and $\mathrm{GCD}(N_s, p)$ is the GCD of slot number and rotor pole-pairs number p [Li19b] [Li19c]. This includes the machine with 48s44p [Chu15], and 24s20p [Chu16]. However, the basic principle of this phenomenon for CPPM machines is still not revealed and analyzed in depth. Further, the flux linkage and inductance will also be affected, of which the basic principles have hitherto not been fully investigated. It is unsurprising that such influences will lead to differences in torque ripple components, which will inevitably result in dissimilar torque ripple reduction capabilities of symmetrical and asymmetric pole shaping methods.

In this chapter, for general CPPM machines, the effects of slot/pole number combinations on flux linkage, back EMF, and inductance are investigated theoretically, based on which different characteristics of symmetrical and asymmetric pole shaping methods are revealed and validated by the FEM with FSCW 12s8p, 9s6p, 12s10p, and 12s14p CPPM machines as examples. Experiments with 12s8p and 12s10p CPPM prototypes further confirm the analyses.

Such analysis can also be applied to SPM machines with unequal north and south pole widths. Actually, unequal pole widths are commonly utilized to suppress the cogging torque for SPM machines [Bia02] [Wan06] but the performances and pole shaping effects with different slot/pole number combinations have not been investigated. Consequently, the SPM machines will also be analyzed in this chapter. It will be revealed that similar to CPPM machines, the harmonics in winding flux linkage will be affected by slot/pole number combinations. However, different from CPPM machines, both symmetrical and asymmetric pole shaping methods have a similar effect on torque ripple reduction for SPM machines due to absence of reluctance torque ripple.

The contributions and new findings of this chapter can be summarized from two aspects:

1) When $N_s/m/$ GCD(N_s,p) is an odd number, the unbalanced pole behaviors will result in additional harmonics in various performances, including flux linkage, back EMF, inductance, cogging torque, and torque ripples for CPPM machine as well as flux linkage, back EMF, cogging torque, and torque ripple for SPM machine. However, such influences can be eliminated in other machines with an even number of $N_s/m/$GCD(N_s,p).

2) Asymmetric pole shaping method shows a better capability in torque ripple reduction for CPPM machines with $N_s/m/$GCD(N_s,p) being an odd number. However, for other machines with an even number of $N_s/m/$GCD(N_s,p), including CPPM and SPM machines, the symmetrical pole shaping method has advantages in reducing both torque ripple and optimization complexity simultaneously.

This chapter is organized as follows. Firstly, the influences of slot/pole number combinations on electromagnetic performances of CPPM machines are investigated theoretically in section 5.2. Symmetrical and asymmetric pole shaping models and finite element optimization method

for torque ripple reduction are described in section 5.3, and applied to the 12s8p, 9s6p, 12s10p, and 12s14p CPPM and SPM machines in section 5.4 and section 5.5, respectively. The performances of CPPM and SPM machines are compared in section 5.6. This is followed by experimental verification in section 5.7 and the conclusions in section 5.8.

5.2 Topologies and Effect of Slot/Pole Number Combinations on Electromagnetic Performances

5.2.1 Slot/Pole Number Combinations for CPPM Machines

An FSCW machine with balanced phase windings can be divided into S_m identical submachines:

$$S_m = \mathrm{GCD}(N_s, p)/v \tag{5.1}$$

where N_s is the slot number, p is the pole-pair number, and v is 1 or 2 for double layer (DL) or single layer (SL) windings.

The FSCW machines can be separated into two groups according to the coil number for one phase in a submachine, $N_s/v/m/N_{sp}$, i.e. $N_s/m/\mathrm{GCD}(N_s,p)$, equal to an odd number (5.2), or an even number (5.3):

Group 1
$$\frac{N_s}{m\mathrm{GCD}(N_s, p)} = 2k - 1, (k = 1,2,3\cdots) \tag{5.2}$$

Group 2
$$\frac{N_s}{m\mathrm{GCD}(N_s, p)} = 2k, (k = 1,2,3\cdots) \tag{5.3}$$

For 3-phase FSCW machines (m=3), the machines with 12s8p-DL, 9s6p-DL, and 12s8p-SL, Fig. 5.1 (a), belong to the first group. In this group, the number of coils that are allocated to the same phase in one submachine is an odd number as demonstrated in Fig. 5.2 (a) and Table 5.1. As will be seen later, for the first group machines, unbalanced features between north and south poles can produce winding flux linkage harmonics for both SPM and CPPM machines and inductance harmonics for CPPM machines.

On the other hand, the machines with 12s10p-DL, 12s14p-DL, and 12s10p-SL belong to the second group, Fig. 5.1 (b), and the number of coils that are allocated to the same phase in one submachine is an even number as demonstrated in Fig. 5.2 (b) and Table 5.1. As shown in Fig.

5.2 (b), there exist the coils with a 180-electrical-degree difference and they are allocated into the same phase to achieve a high winding factor, as is the same case in [Zha18b]. Consequently, for the second group machines, harmonics in winding flux linkage and inductance caused by unbalanced features between north and south poles can be canceled. This will be analyzed in detail in the following parts.

This classification can be applied to both SPM and CPPM machines, and their rotor structures are illustrated in Fig. 5.3. It is worth noting that the unbalanced north and south poles are more common in CPPM machines. Therefore, the following analysis will particularly refer to CPPM machines.

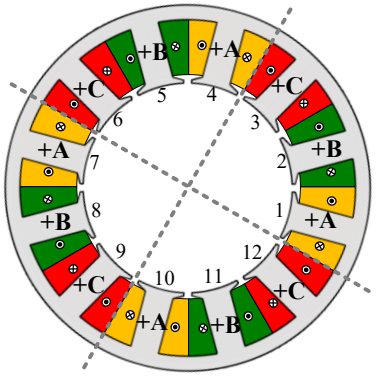

12s8p-DL

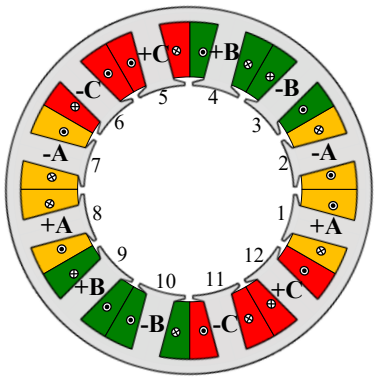

12s10p-DL

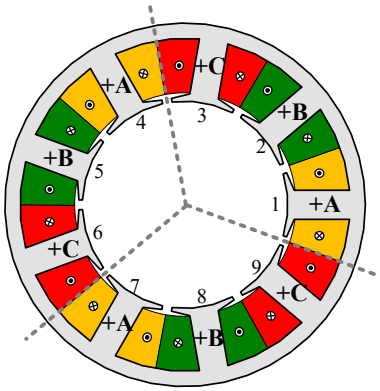

9s6p-DL

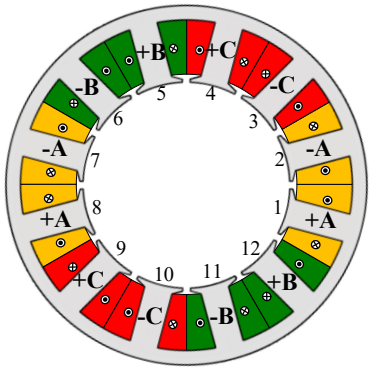

12s14p-DL

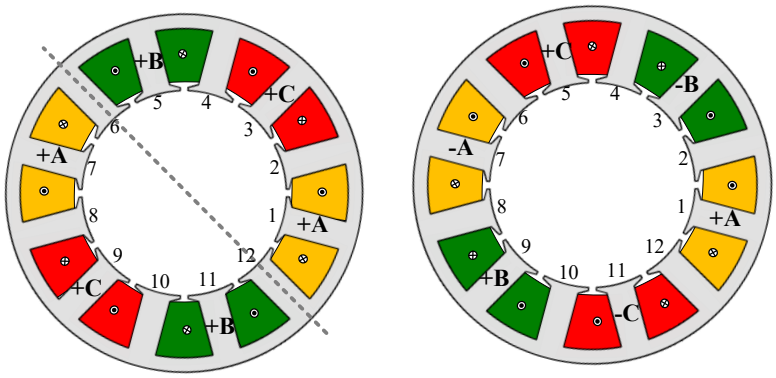

12s8p-SL　　12s10p-SL

(a)　　(b)

Fig. 5.1　Stator winding layouts. (a) Group 1. (b) Group 2.

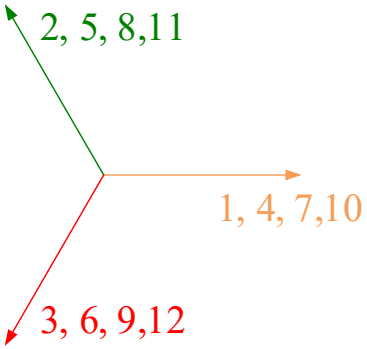

12s8p-DL

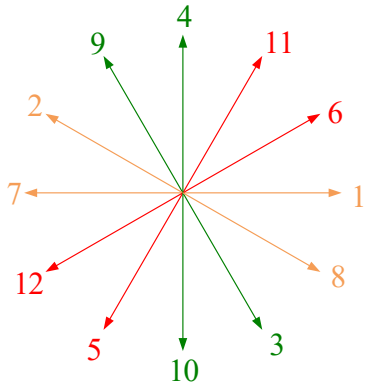

12s10p-DL

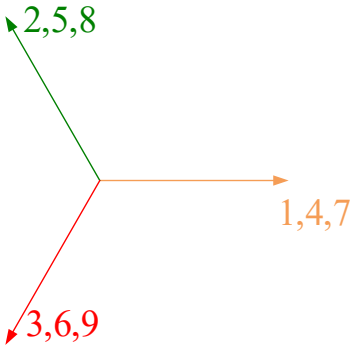

9s8p-DL

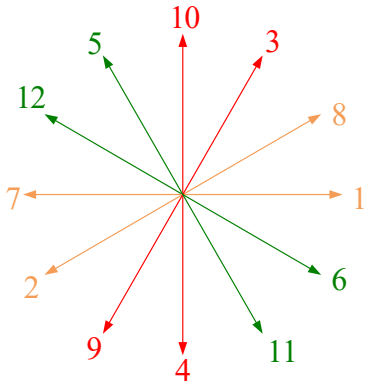

12s14p-DL

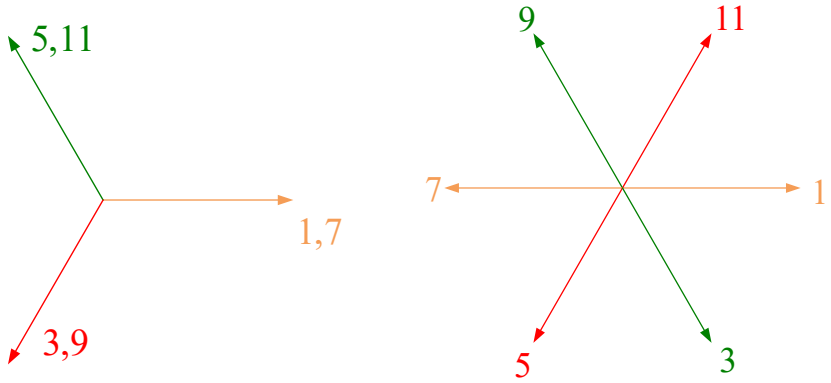

12s8p-SL 12s10p-SL

(a) (b)

Fig. 5.2 Back EMF phasors of coils. (a) Group 1. (b) Group 2.

Table 5.1. Number of Submachine and Coils per Phase in a Submachine for Machines in Two Groups

	Group 1			Group 2		
Slot/pole	12s8p-DL	9s6p-DL	12s8p-SL	12s10p-DL	12s14p-DL	12s10p-SL
N_{sp}	4	3	2	1	1	1
$N_s/m/\mathrm{GCD}(N_s,p)$	1	1	1	4	4	2

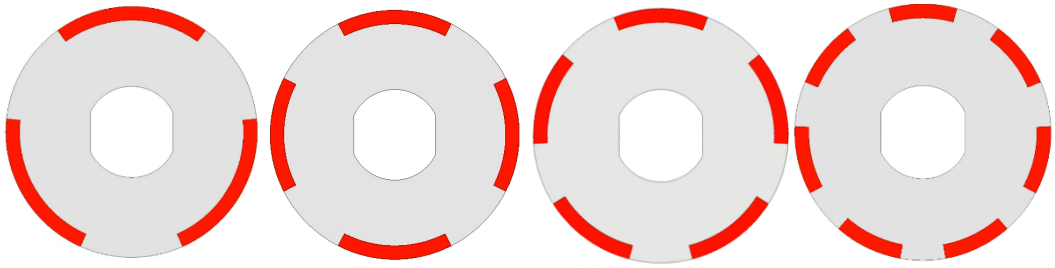

(a)

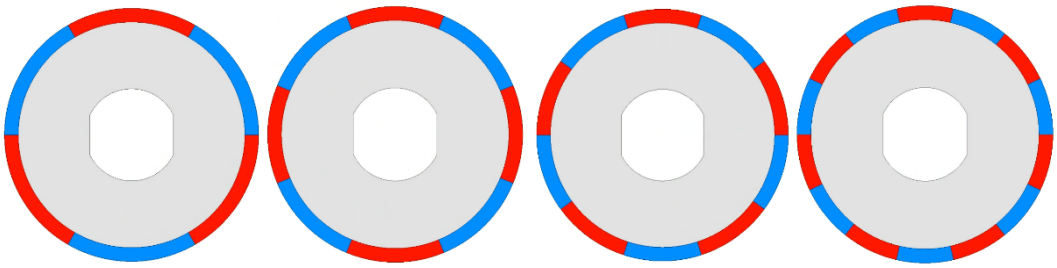

(b)

Fig. 5.3 Rotor topologies (from left to right: 6p, 8p, 10p, and 14p). (a) CPPM. (b) SPM.

5.2.2 Analysis of Flux Linkage and Inductance Harmonics and Torque Ripple for CPPM Machines

5.2.2.1 Harmonics in Flux Linkage and Inductance

The double layer winding machines are demonstrated as example in the following analysis, while the phenomenon, principles, and conclusions of double layer machines can be equally applied to the single layer winding machines.

The features of north and south poles in CPPM machines are unequal even if the PM and iron pole widths are the same and it will inevitably result in even order harmonics in air-gap flux density [Li19b] and odd order harmonics in the inductance of a coil [Ma19]. However, additional harmonics do not always exist in winding flux linkage and winding inductance. This is affected by the coil connection that is determined by slot/pole number combinations.

For the first group CPPM machines, the even order harmonics in winding flux linkage and odd order harmonics in winding inductance can be produced due to additive effect of phase coils, while those for the second group CPPM machines can be eliminated due to cancellation effect of phase coils. The derivation process can be explained below.

The phasor angle α_{ij} between the *i*-th and the *j*-th coils can be written as:

$$\alpha_{ij} = (i-j)p\frac{2\pi}{N_s} \tag{5.4}$$

For the second group CPPM machines, supposing the *i*-th and the *j*-th coils are in the same phase and a submachine, the relation between the numbers of the *i*-th and the *j*-th coils can be expressed by:

$$(i-j) = \frac{N_s}{2\mathrm{GCD}(N_s, p)} \tag{5.5}$$

Because the coil number for one phase in a submachine is an even number for both double and single layer winding machines, each *i*-th coil has its corresponding *j*-th coil in the same phase, which has 180-electrical-degree difference to achieve high winding factors, as illustrated in Fig. 5.2 (b). Consequently, the even order harmonics in flux linkages of *i*-th and *j*-th coils will be eliminated, which can be expressed as:

$$\psi_{2n}^{i} - \psi_{2n}^{j} = \psi_{2n}\left[\sin\left(2nip\frac{2\pi}{N_s} + \theta_{2n}^{\psi}\right) - \sin\left(2nip\frac{2\pi}{N_s} + 2n\pi\frac{p}{\mathrm{GCD}(N_s,p)} + \theta_{2n}^{\psi}\right)\right] = 0 \tag{5.6}$$

where ψ_{2n}^{i} and ψ_{2n}^{j} are the $2n$-order harmonics in flux linkages of the i-th and the j-th coils, respectively, ψ_{2n} and θ_{2n}^{ψ} are the amplitude and the initial position angle of the $2n$-order harmonic. It is worth noting that the item p/GCD(N_s,p) in (5.6) is an odd number when (5.3) is satisfied.

For the odd order harmonics in flux densities, including the fundamental order harmonic, they will not be affected by the winding connection since:

$$\begin{aligned}\psi_{2n-1}^{i} - \psi_{2n-1}^{j} &= \psi_{2n-1}\left[sin\left((2n-1)ip\frac{2\pi}{N_s} + \theta_{2n}^{\psi}\right)\right. \\ &\left. - \sin\left((2n-1)ip\frac{2\pi}{N_s} + (2n-1)\pi\frac{p}{\mathrm{GCD}(N_s,p)} + \theta_{2n}^{\psi}\right)\right] \\ &= 2\psi_{2n-1}\sin\left((2n-1)ip\frac{2\pi}{N_s} + \theta_{2n}^{\psi}\right)\end{aligned} \tag{5.7}$$

The inductance harmonics can also be derived similarly. It has been found that the inductance in one coil consists of all orders of harmonics in CPPM machines due to only one salient pole in an electrical cycle for a CPPM rotor [Ma19]. However, when the coil number for one phase in a submachine is an even number, namely the second group CPPM machines, the odd order harmonics in inductances of the i-th and j-th coils will be eliminated since

$$L_{2n-1}^{i} + L_{2n-1}^{j} = L_{2n-1}\left[\sin\left((2n-1)ip\frac{2\pi}{N_s} + \theta_{2n}^{L}\right) + \sin\left((2n-1)ip\frac{2\pi}{N_s} + (2n-1)\pi\frac{p}{\mathrm{GCD}(N_s,p)} + \theta_{2n}^{L}\right)\right] = 0 \tag{5.8}$$

where L_{2n-1}^{i}, L_{2n-1}^{j} are the $2n$-order harmonics in inductances of the i-th and the j-th coils, respectively, L_{2n-1} and θ_{2n}^{L} are the amplitude and the initial position angle of $2n$-order harmonic.

Since each i-th coil has its corresponding j-th coil, the odd order harmonics in inductance can be eliminated. However, the even order harmonics still exist:

$$\begin{aligned} L_{2n}^{i} + L_{2n}^{j} &= L_{2n}\left[\sin\left(2nip\frac{2\pi}{N_s} + \theta_{2n}^{L}\right)\right. \\ &\left. + \sin\left(2nip\frac{2\pi}{N_s} + 2n\pi\frac{p}{\mathrm{GCD}(N_s,p)} + \theta_{2n}^{L}\right)\right] \\ &= 2L_{2n}\sin\left(2nip\frac{2\pi}{N_s} + \theta_{2n}^{L}\right) \end{aligned} \tag{5.9}$$

From the above analyses, it can be concluded that for the second group CPPM machines, the even order harmonics in flux linkage and odd order harmonics in winding inductance can be eliminated, which makes it similar to the SPM counterparts.

However, for the first group CP, whose slot/pole numbers can be expressed by (5.2), there will be no coupling between the i-th and j-th coils which have the opposite phasors allocated in the same phase, as can be seen in in Fig. 5.2 (a). Therefore, (5.6) and (5.8) cannot be 0 anymore, which will lead to the additional even order harmonics in flux linkage and the odd order harmonics in inductance. The different electromagnetic characteristics found in specific CPPM machines in [Chu15] [Li19b] [Qi22a] [Chu16] [Ma19] underpin the above theoretic analysis and the general conclusions.

5.2.2.2 Torque Ripple Production

The even order harmonics in flux linkage and the odd order harmonics in inductance of CPPM machines will inevitably lead to torque ripples. To make it clear, the output torque T_e can be divided into three constituent components: PM torque T_{PM}, reluctance torque T_r, and cogging torque T_{cog}. These can be expressed as [Liu05] [Yan19a]:

$$\begin{cases} T_e = T_{PM} + T_r + T_{cog} \\ T_{PM} = \dfrac{3}{2} p i_q \left(\psi_d^{PM} + \dfrac{d\psi_q^{PM}}{d\theta} \right) - \dfrac{3}{2} p i_d \left(\psi_q^{PM} - \dfrac{d\psi_d^{PM}}{d\theta} \right) \\ T_r = \dfrac{3}{2} p \left(i_q i_d \left(L_d - L_q \right) + {i_d}^2 \dfrac{dL_d}{d\theta} + {i_q}^2 \dfrac{dL_q}{d\theta} \right) \\ T_{cog} = -\dfrac{dW_r(\theta)}{d\theta} \end{cases} \tag{5.10}$$

where L_d and L_q are the dq-axes inductances, i_d and i_q are the dq-axes currents, ${\psi_d}^{PM}$ and ${\psi_q}^{PM}$ are the dq-axes PM flux linkages, p is the pole-pair number, θ is the rotor position in electrical degree, and $W_r(\theta)$ is the magnetic co-energy solely due to PM flux linkage. Evidently, the variations in dq-axes PM flux linkages, dq-axes inductances, and $W_r(\theta)$ will lead to the total torque ripple.

A detailed analysis has been developed in [Qi22b] that the odd order harmonics in inductance can contribute to the dominant 3rd and high order ripple in reluctance torque T_r. Therefore, the elimination of odd order harmonics in inductance will result in the cancellation of those additional reluctance torque ripples. Since the production of torque ripple in T_r has been demonstrated in [Qi22b], in this chapter, with a similar method adopted, only the production of torque ripple in T_{PM} and cogging torque will be derived as follows.

The even order harmonics in flux linkage $\boldsymbol{\Psi}_{abc}^{PM}$ for CPPM machines can be expressed as:

$$\boldsymbol{\Psi}_{abc}^{PM} = \begin{bmatrix} \sum_{n=2,4,6\cdots} \psi_{an} \cos(n\theta) \\ \sum_{n=2,4,6\cdots} \psi_{an} \cos\left(n(\theta - \frac{2\pi}{3}) \right) \\ \sum_{n=2,4,6\cdots} \psi_{an} \cos\left(n(\theta + \frac{2\pi}{3}) \right) \end{bmatrix} \tag{5.11}$$

where ψ_{an} is the amplitude of the n-order harmonic. Then, the d-axis and q-axis flux linkages $\boldsymbol{\Psi}_{dq}^{PM}$ can be derived as:

$$\boldsymbol{\Psi}_{dq}^{PM} = \boldsymbol{P}\boldsymbol{\Psi}_{abc}^{PM} \tag{5.12}$$

where

$$\boldsymbol{P} = \frac{2}{3}\begin{bmatrix} \cos(\theta) & \cos(\theta - 2\pi/3) & \cos(\theta + 2\pi/3) \\ -\sin(\theta) & -\sin(\theta - 2\pi/3) & -\sin(\theta + 2\pi/3) \\ 0.5 & 0.5 & 0.5 \end{bmatrix} \tag{5.13}$$

Therefore, the harmonics in ψ_d^{PM} and ψ_q^{PM} resulted from the even order harmonics in $\boldsymbol{\Psi}_{abc}^{PM}$ can be written as:

$$\begin{cases} \psi_d^{PM} = \sum_{j=1,3,5\cdots} \psi_{adj} \cos(3j\theta) \\ \psi_q^{PM} = \sum_{j=1,3,5\cdots} \psi_{aqj} \sin(3j\theta) \end{cases} \tag{5.14}$$

where ψ_{adj} and ψ_{aqj} are the corresponding amplitudes of 3j-order harmonics. Obviously, the even order harmonics will lead to the additional 3j-th order harmonics in ψ_d^{PM} and ψ_q^{PM}, which will inevitably result in the corresponding harmonics in PM torque ripple according to (5.10). Therefore, the first group CPPM machines will suffer from the triplet order harmonics in T_{PM}. However, for the second group CPPM machines, the elimination of even order harmonics in flux linkages will contribute to the same harmonic orders, i.e., the multiple of 6, as SPM machines in T_{PM}.

Due to the effect of even order harmonics in flux density, the cogging torque cycle number in a mechanical rotation cycle for CPPM machines is the LCM between slot number N_s and pole-pair number p. Based on the relation between LCM and GCD:

$$\mathrm{LCM}(N_s, p)\mathrm{GCD}(N_s, p) = N_s p \tag{5.15}$$

(5.3) can be rewritten as:

$$\mathrm{LCM}(N_s, p) = 2kmp, (\, k = 1,2,3,\cdots) \tag{5.16}$$

It is obvious that 2kmp is also multiple of 2p:

$$\mathrm{LCM}(N_s, 2p) = \mathrm{LCM}(N_s, p) = 2kmp, (k = 1,2,3,\cdots) \tag{5.17}$$

Since LCM(N_s, $2p$) is the fundamental order of cogging torque for the conventional SPM machines with equal north and south pole arc widths [Zhu00] [Zhu09a], the fundamental cogging torque cycle number for CPPM machines is the same as that for SPM counterparts. In other words, the influence of even order harmonics in flux density on the cogging torque harmonics can be eliminated for the CPPM machines in the second group. In contrast, for CPPM machines in the first group, the fundamental order for cogging torque is halved and there exist additional harmonics.

5.2.3 Analysis of Flux Linkage and Inductance Harmonics and Torque Ripples for SPM Machines

Similar to CPPM machines, when north and south pole arc widths are different for SPM machines, the even order harmonics in air-gap flux density can produce corresponding harmonics in winding flux linkages for the first group SPM machines. Therefore, it will lead to additional odd order PM torque ripples according to (5.10). However, such harmonics can be canceled in the second group SPM machines as has been explained in (5.6) and (5.7). It is worth noting that when the SPM machines have equal north and south pole arc widths, the even order harmonics in air-gap flux density can be eliminated and thus even order harmonics in winding flux linkage are eliminated.

When machine geometries are fixed, the cogging torque is determined by the air-gap flux density [Zhu00] [Zhu09a]. Thus, for SPM machines with unequal north and south pole arc widths, the characteristic of cogging torque harmonics are the same as that for CPPM machines, i.e. the first group of SPM machines has lower fundamental harmonic LCM(N_s,p), while that for the second group SPM machines is LCM(N_s,$2p$). The latter one is the same as conventional SPM machines with equal north and south pole arc widths.

Nevertheless, different from CPPM machines, the inductance for SPM machines can be treated as constant since there is no iron saliency in the rotor. Consequently, SPM machines are inherently free of inductance harmonics, and thus, there are no ripples in reluctance torque not matter whether the north and south poles have equal or unequal arc widths.

To validate the analysis, CPPM and SPM machines for the first group (12s8p and 9s6p as examples) and the second group (12s10p and 12s14p as examples) machines are analyzed by FEM. The SPM machines with both equal and unequal north and south pole arc widths are analyzed and the names of the latter ones are suffixed with "-un" in Fig. 5.4 and Fig. 5.5. For all SPM machines with unequal pole widths and CPPM machines, the ratios of PM pole arc to pole pitch are set as 1.2. As shown in Fig. 5.4 and Fig. 5.5, the harmonics in flux densities, winding flux linkages, coil inductances, winding inductances, cogging torques, on-load PM torque, on-load reluctance torque, and rated torques are illustrated, where the frozen permeability method in [Zhu16] is adopted to obtain the on-load reluctance torques and on-load PM torques.

For the first group machines, Fig. 5.4, it can be found that the even order harmonics in air-gap flux densities can produce corresponding harmonics in winding flux linkages regardless of whether they are SPM or CPPM machines. Only the SPM machine with equal pole arc widths can eliminate those even order harmonics, Fig. 5.4 (a) and Fig. 5.4 (b). Such harmonics can lead to odd order PM torque ripples as illustrated in Fig. 5.4 (f). However, differently, there are no odd order harmonics in inductances for all SPM machines while such harmonics are obvious for CPPM machines, Fig. 5.4 (c) and Fig. 5.4 (d), thus leading to the significant odd order reluctance torque ripple for CPPM machines, Fig. 5.4 (g). As can be seen in Fig. 5.4 (h), the overall torque ripple harmonic orders are the multiple of 3 for SPM machines with unequal pole widths and CPPM machines, while they are the multiple of 6 for conventional SPM machines with equal pole widths.

For the second group machines, Fig. 5.5, it is obvious that the even order harmonics in winding flux linkage and the odd order harmonics in winding inductances can be eliminated for all the CPPM and SPM machines with equal and unequal pole arc widths. Therefore, for all the machines, the PM torque ripple harmonic orders are the multiple of 6 and the reluctance torque ripples are nearly 0. As can be seen in Fig. 5.5 (h), the overall torque ripple harmonic orders are the multiple of 6. The FEM results prove the analyses very well.

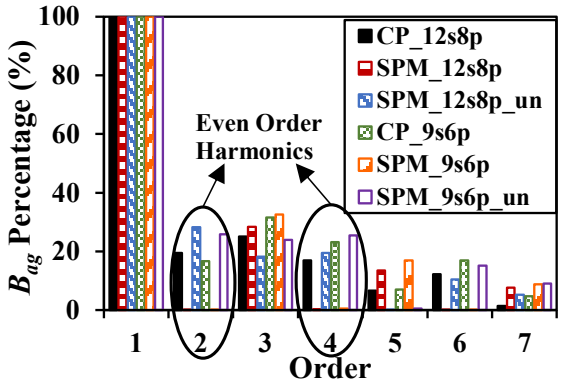

(a) Air-gap flux density B_{ag}

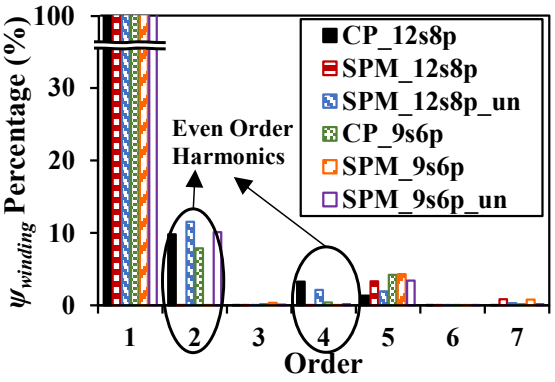

(b) Winding flux linkage $\psi_{winding}$

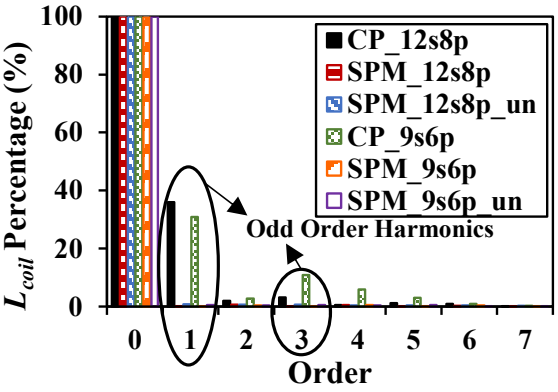

(c) Coil inductance L_{coil}

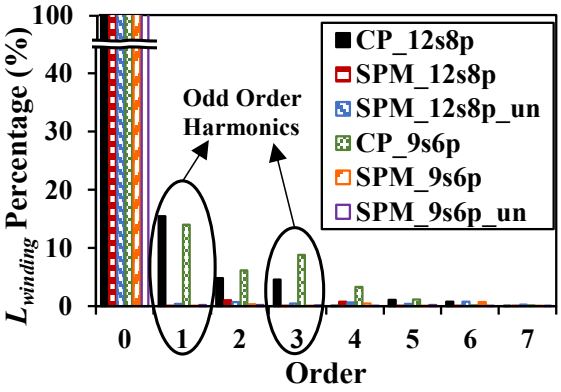

(d) Winding inductance $L_{winding}$

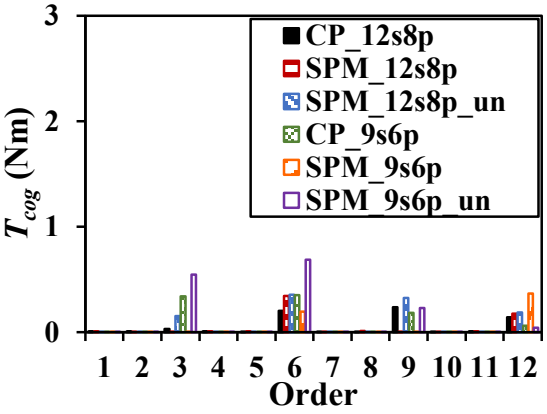

(e) No-load cogging torque T_{cog}

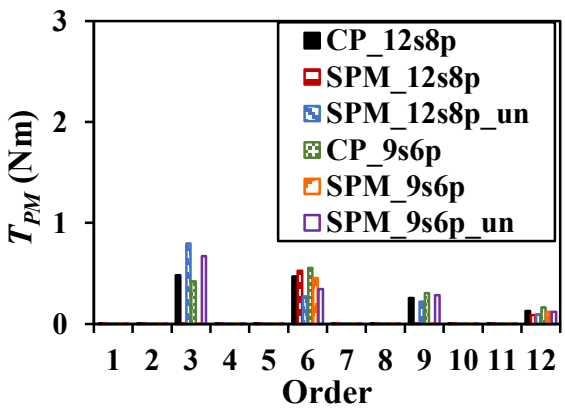

(f) On-load PM torque T_{PM}

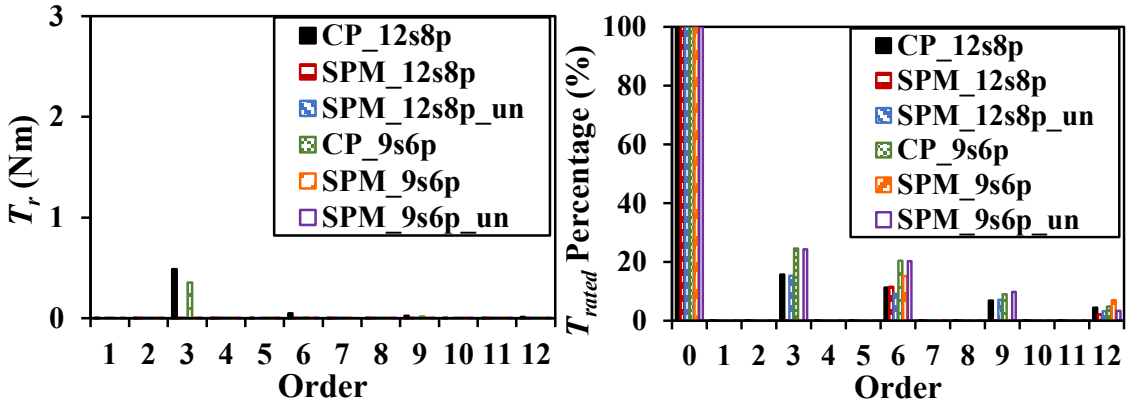

(g) On-load reluctance torque T_r (h) Rated torque T_{rated}

Fig. 5.4 Harmonics in one electrical cycle for Group 1 machines.

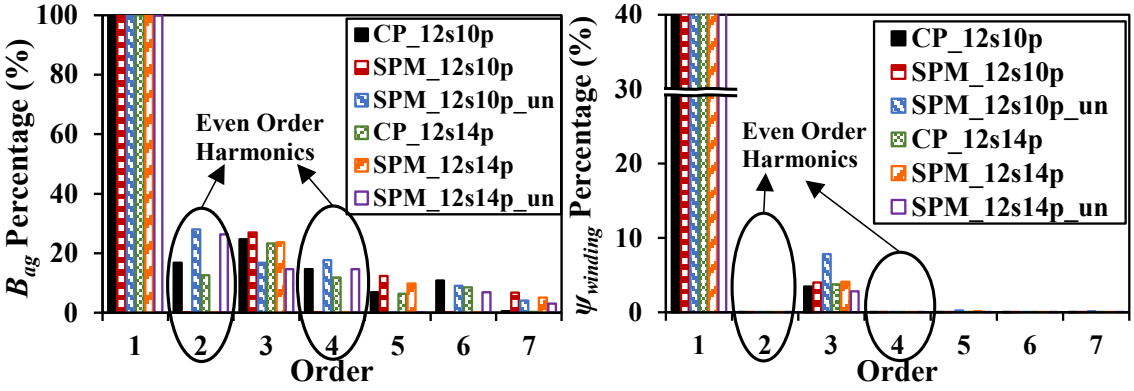

(a) Air-gap flux density B_{ag} (b) Winding flux linkage $\psi_{winding}$

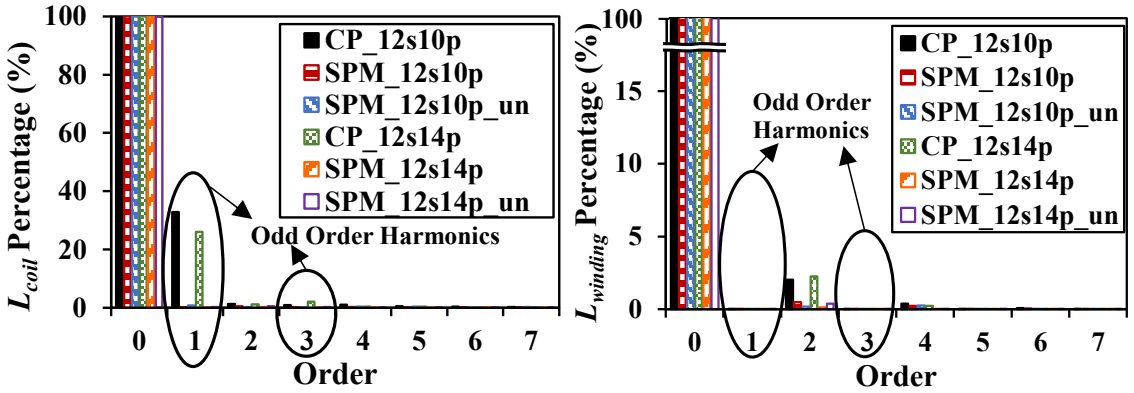

(c) Coil inductance L_{coil} (d) Winding inductance $L_{winding}$

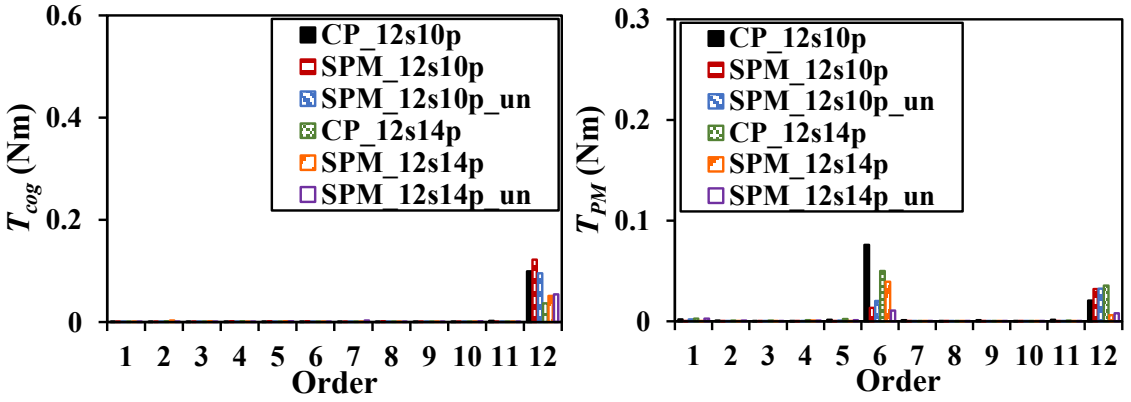

(e) No-load cogging torque T_{cog} (f) On-load PM torque T_{PM}

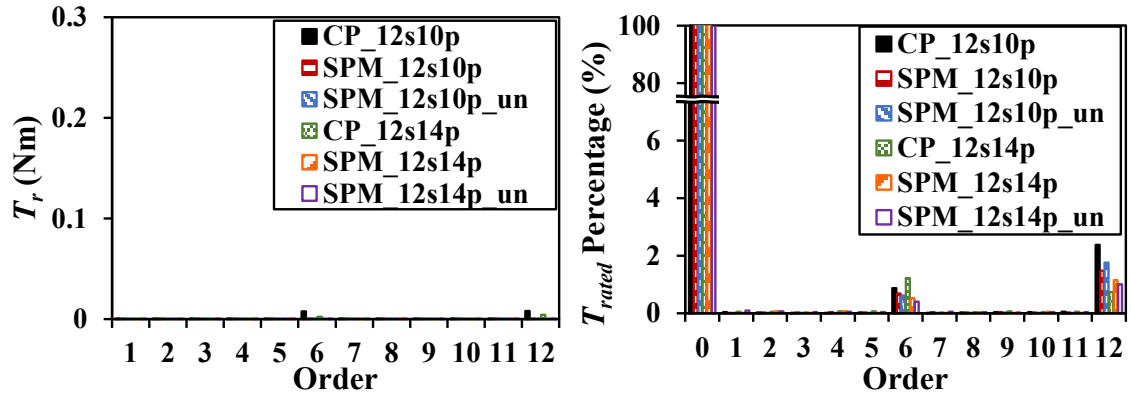

(g) On-load reluctance torque T_r (h) Rated torque T_{rated}

Fig. 5.5 Harmonics in one electrical cycle for Group 2 machines.

5.3 Torque Ripple Reduction with Symmetrical and Asymmetric Pole Shaping Methods and Optimization Result Analysis

5.3.1 Symmetrical and Asymmetric Pole Shaping Methods

Based on the above analysis, from the perspective of torque ripple, it can be concluded that the first group CPPM machines will be affected by the unbalanced features and suffer from the additional torque ripples, including the 3rd and the 9th. However, the second group CPPM machines have the same torque ripple harmonics as SPM machines, which means the CPPM machines in the second group can overcome the unbalanced features caused by PM and iron poles due to cancellation effect by the arrangement of coils. Therefore, the pole shaping methods for these two types of CPPM machines should be different.

The pole shaping methods largely modify the harmonics of PM flux density, including amplitudes and phases, which have little effect on the fundamental self-inductance since there is only one salient pole in one pole-pair of the CPPM rotor. Consequently, for the first group CPPM machines, introducing the unbalance in flux density (even order harmonics) and manipulating the phases of harmonics to make torque ripple components cancel with each other is an effective means of eliminating the triplet order total torque ripple.

As shown in Fig. 5.6, the symmetrical flux density B_{fA} and the asymmetric flux density B_{fB} can be written as:

$$B_{fA} = \sum_{i=0}^{\infty} A_{si} \cos\left(\frac{p}{2} i\theta\right) \tag{5.18}$$

$$B_{fB} = \sum_{i=0}^{\infty} A_{aci} \cos\left(\frac{p}{2} i\theta + \theta_{i0}\right) \tag{5.19}$$

where A_{si} and A_{acj} are the amplitudes of the i-th harmonics for symmetrical and asymmetric models, respectively, and θ_{i0} is the phase angle for each harmonic.

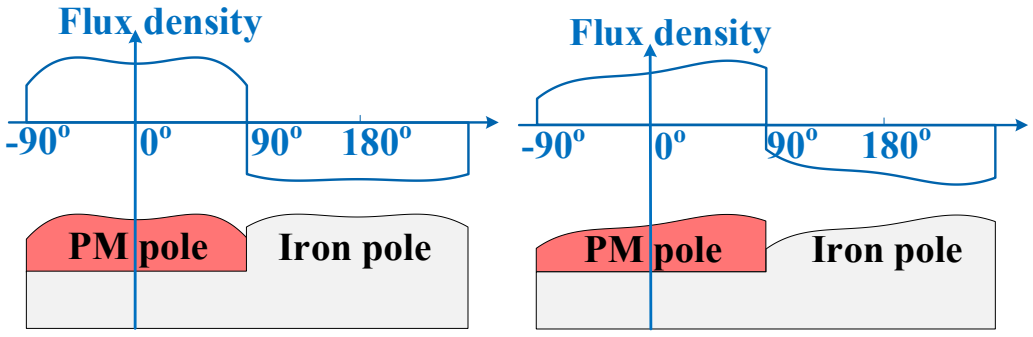

(a) Symmetrical (b) Asymmetric

Fig. 5.6 Flux density distributions under one pole-pair.

Obviously, the phase angle for each harmonic in B_{fA} is fixed, while it is variable in B_{fB}. It can be found that by shifting the phases of flux density harmonics, it is possible to shift the phase of winding flux linkage and thus the torque ripple harmonics in T_{PM} and T_{cog}. Consequently, these torque ripple harmonics can be manipulated to counteract the torque ripple in T_r to reduce

the overall torque ripple. Therefore, the asymmetric pole shaping method for CPPM machines in the first group CPPM machines, e.g. 12s8p machines [Qi22b], can reduce torque ripple effectively.

Nevertheless, the torque ripple characteristics of CPPM machines in the second group, e.g. 12s10p, are close to those of their SPM counterparts and can overcome the unbalanced features resulting from the CPPM rotor. Therefore, the PM pole arc can be extended to maximize the output torque without introducing additional torque ripple harmonics. Furthermore, asymmetric pole shape is not necessary since it is just used for overcoming the effects of unbalance in pole behaviors for the CPPM machines in the first group. It is unsurprising that the adoptions of symmetrical and asymmetric pole shapes tend to exhibit similar capacities in torque ripple reduction since the phase shift resulting from asymmetric pole shape has little effect on the PM torque ripple amplitudes and it has almost no reluctance torque component to be counteracted.

The characteristics of torque ripples and their reduction methods for two groups of CPPM machines are summarized in Table 5.2.

It is worth mentioning that the pole shaping effects on SPM machines are similar to those of the second group CPPM machines. Since there is no reluctance torque ripple, it is impossible to make PM torque ripple and reluctance torque ripple counteract each other by the asymmetric pole shaping method. Consequently, the adoptions of symmetrical and asymmetric pole shapes tend to exhibit similar capabilities in torque ripple reduction. The characteristics of torque ripples and their reduction methods for two groups of SPM machines are summarized in Table 5.3.

Table 5.2. Summaries of Torque Ripple Characteristics and Reduction Methods for CPPM Machines in Two Groups

		Group 1 CPPM machines e.g. 12s8p, 9s6p, 9s8p etc.	Group 2 CPPM machines e.g. 12s10p, 12s14p, 6s10p etc.
Sources of torque ripple	T_{PM}	Even order harmonics in air-gap flux density can produce even order harmonics in winding flux linkage, which will lead to triplen ripples in T_{PM}.	Even order harmonics in air-gap flux density cannot produce even order harmonics in winding flux linkage, which makes the ripple orders of T_{PM} a multiple of 6 regardless of whether PM and iron poles are equal or unequal in width.
	T_r	The odd order harmonics in winding inductance will lead to triplen ripples in T_r.	The odd order harmonics in winding inductance can be canceled and torque ripple orders of T_r are the multiple of 6 which are the same as those of conventional SPM machines with equal north and south pole widths.
	T_{cog}	The fundamental cycle number is half of that of conventional SPM counterpart with equal pole widths.	The fundamental cycle number is the same as that of conventional SPM counterpart with equal pole widths.
Torque ripple reduction		Different from symmetrical pole shaping method, asymmetric pole shaping method can make the torque ripple components counteract each other and lead to a smaller overall torque ripple.	Asymmetric and symmetrical profiles have a similar capacity in torque ripple reduction.

Table 5.3. Summaries of Torque Ripple Characteristics and Reduction Methods for SPM Machines in Two Groups

		Group 1 - SPM machines e.g. 12s8p, 9s6p, 9s8p etc.	Group 2 - SPM machines e.g. 12s10p, 12s14p, 6s10p etc.
Sources of torque ripple	T_{PM}	Even order harmonics in air-gap flux density can produce even order harmonics in winding flux linkage, which will lead to triplen ripples in T_{PM}.	Even order harmonics in air-gap flux density cannot produce even order harmonics in winding flux linkage, which makes the ripple orders of T_{PM} a multiple of 6 regardless of whether north and south poles are equal or unequal in width.
	T_r	There are no harmonics in winding inductance and thus no reluctance torque ripple.	
	T_{cog}	The fundamental cycle number is half of that of conventional SPM counterpart with equal pole widths.	The fundamental cycle number is the same as that of conventional SPM counterpart with equal pole widths.
Torque ripple reduction		Asymmetric and symmetrical profiles have a similar capacity in torque ripple reduction.	

Fig. 5.7 (a) and Fig. 5.7 (b) illustrate the modeling method of symmetrical and asymmetric pole shapes in ANSYS Maxwell, respectively. Clearly, both poles (PM and iron poles for CPPM machines, north and south poles for SPM machines) are shaped and the rotor pole profiles are determined by the corresponding pole arc spans as well as the radius of k-th point in north pole Rm_k and in south pole Ri_k for CPPM machines, which are distributed uniformly along the circumferential angle. As has been proven effective in [Qi22b], 14 variable points over one pole-pair are adopted in this chapter, which are connected by spline curves for each pole. Supposing θm_p and θi_p are the arc span angle of north and south pole as demonstrated in Fig. 5.7, the position for the k-th point in the two models is determined by:

$$\begin{cases} \theta m_k = \dfrac{k-1}{6}\theta m_p, k \in [1,7]\ or\ k \in [1,4] \\ \theta i_k = \dfrac{k-1}{6}\theta i_p, k \in [1,7]\ or\ k \in [1,4] \\ R_{ri} < Ri_k < R_{ro},\ R_{ri} < Rm_k < R_{ro} \end{cases} \tag{5.20}$$

where R_{ro} and R_{ri} are the outer and inner radii of the rotor, respectively, θm_k and θi_k determine the angle of each point in north and south poles to the left side of each pole. It is worth noting that for symmetrical model, there are only 4 points, which formed as equivalent 7 points over one pole. The reduced variable number can, to some extent, lead to the benefits of time saving in the design process.

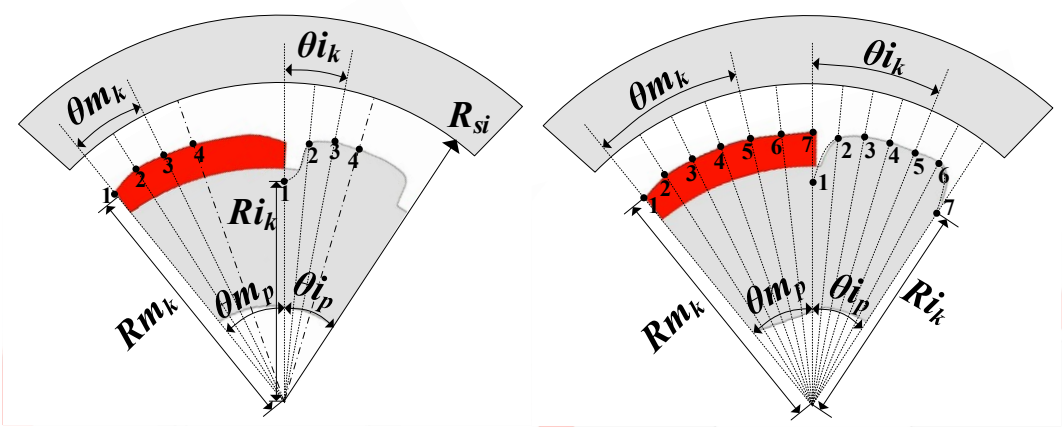

(a) Symmetrical (b) Asymmetric

Fig. 5.7 Models of two shaping methods.

5.3.2 Optimization Results and Analysis

CPPM and SPM machines with 12s8p and 9s6p as well as 12s10p and 12s14p are selected for demonstration, where the first two slot/pole number combinations belong to the first group and the last two slot/pole number combinations belong to the second group. The performances of CPPM and SPM models with symmetrical and asymmetric pole shapes, which will be denoted as Sym and Asym in the following text, are optimized for a combined objective of maximum torque and reduced torque ripple, as shown in Fig. 5.8 to Fig. 5.11. The shaping optimization with flexible rotor outline and pole arc span employ a GA to explore rotor design parameters while the stator geometry remains fixed in the optimization process with the key parameters listed in Table 5.4.

Table 5.4. Key Design Parameters of Analyzed Machines

Parameter	Value	Unit
Slot/pole number combinations in Group 1	12s8p 9s6p	
Slot/pole number combinations in Group 2	12s10p, 12s14p	
Stator outer radius	50	mm
Stator inner radius	28.5	mm
Axial length	50	mm
Air-gap length	1	mm
Stator yoke width	4.2	mm
Stator tooth width	8	mm
Stator turns per coil	46	-
Rated current	10	A_{pk}
Rated speed	400	r/min
Remanence of magnet	1.2	T

The optimization results for two group machines produced by the GA are shown in Fig. 5.8 to Fig. 5.11. To discover the potential of each shape of PM and iron poles, GA optimization aims to obtain the Pareto frontiers rather than just finding an optimal case for each shape of the model. A total of over 40000 combinations of rotor parameters are considered in GA optimization to form the delicate Pareto frontiers, in each case by performing a two-dimensional FEM across one electrical cycle.

Fig. 5.8 and Fig. 5.9 demonstrate the results for CPPM machines. Obviously, for the first group machines, the frontiers of asymmetric models are much lower than those of symmetrical models in Fig. 5.9, which means that the asymmetric pole shaping can result in a lower torque ripple. However, the frontiers for the second group machines in Fig. 5.9 are almost the same line, which means that the two pole shaping methods have a similar effect on torque ripple reduction. The results have validated the previous analyses.

Fig. 5.10 and Fig. 5.11 demonstrate the results for SPM machines. It is clear that the frontiers of symmetrical and asymmetric models are almost the same line, which means that the two pole shaping methods have a similar effect on torque ripple reduction. The results also have validated the previous analyses.

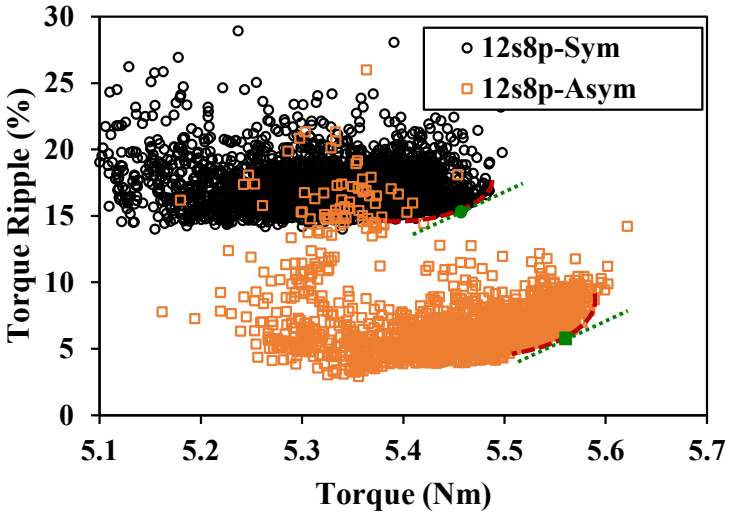

(a) 12s8p

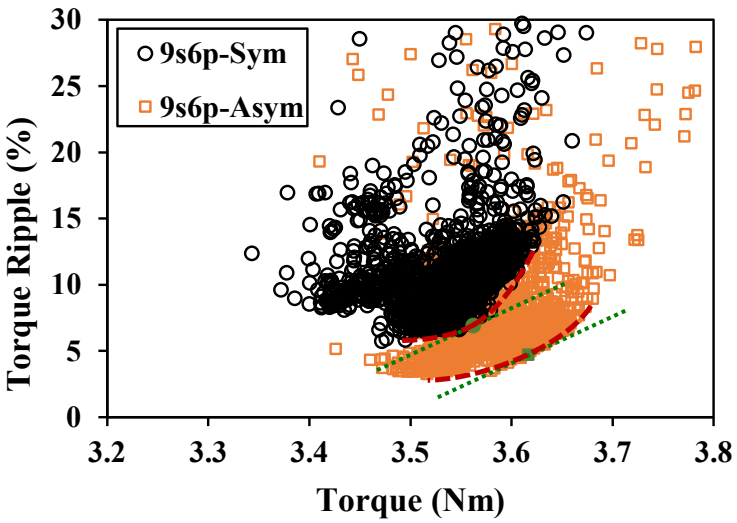

(b) 9s6p

Fig. 5.8 Pareto frontiers form multi-objective optimization for Group 1 CPPM machines.

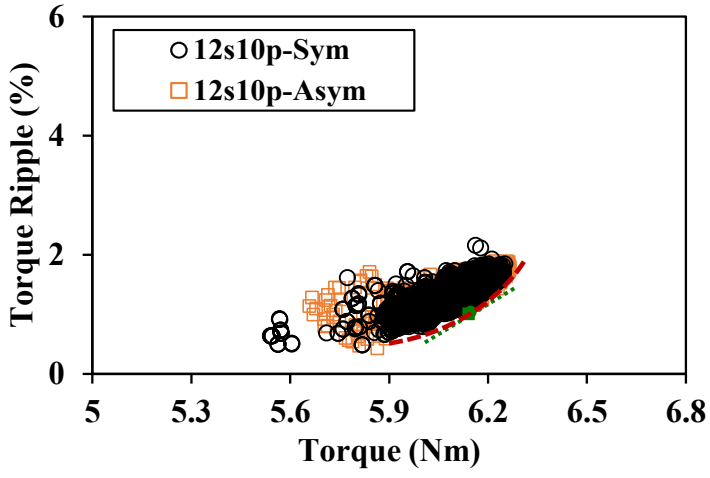

(a) 12s10p

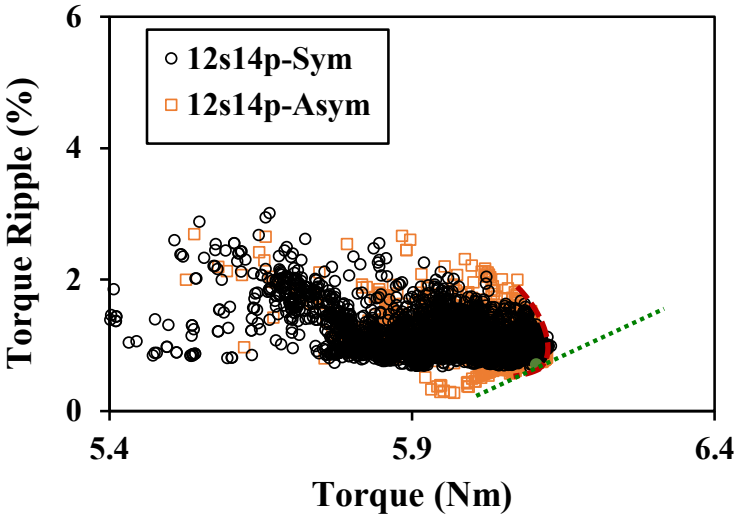

(b) 12s14p

Fig. 5.9 Pareto frontiers form multi-objective optimization for Group 2 CPPM machines.

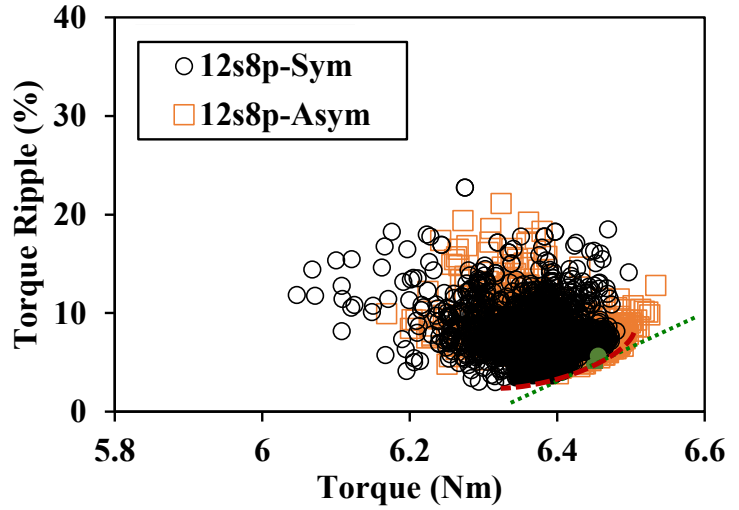

(a) 12s8p

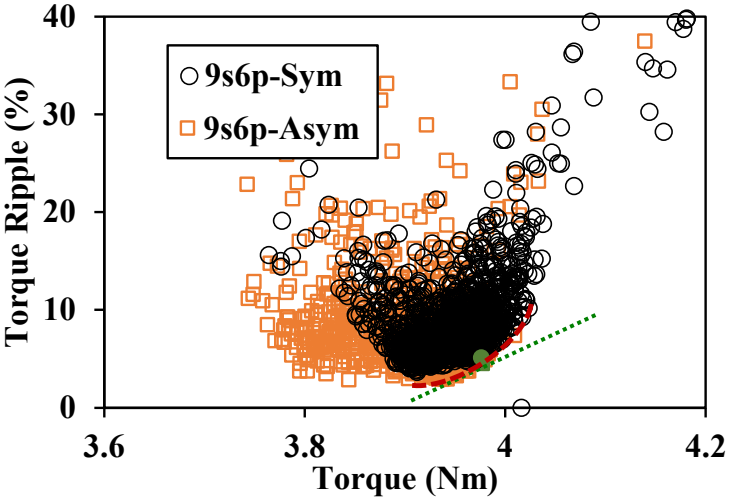

(b) 9s6p

Fig. 5.10 Pareto frontiers form multi-objective optimization for Group 1 SPM machines.

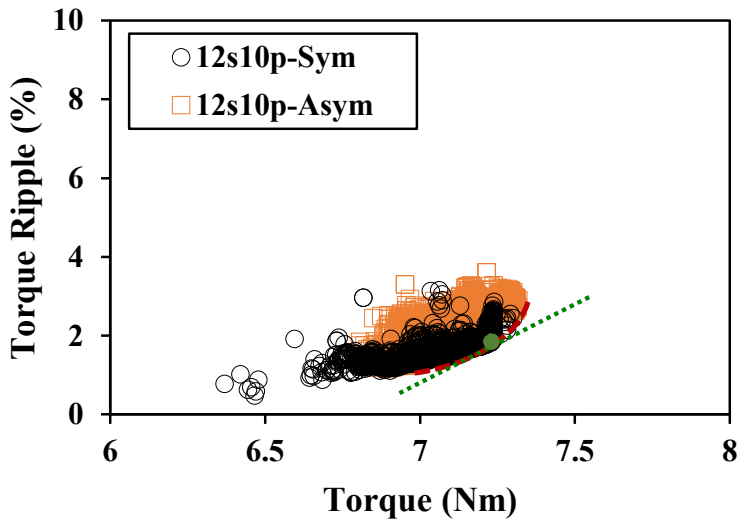

(a) 12s10p

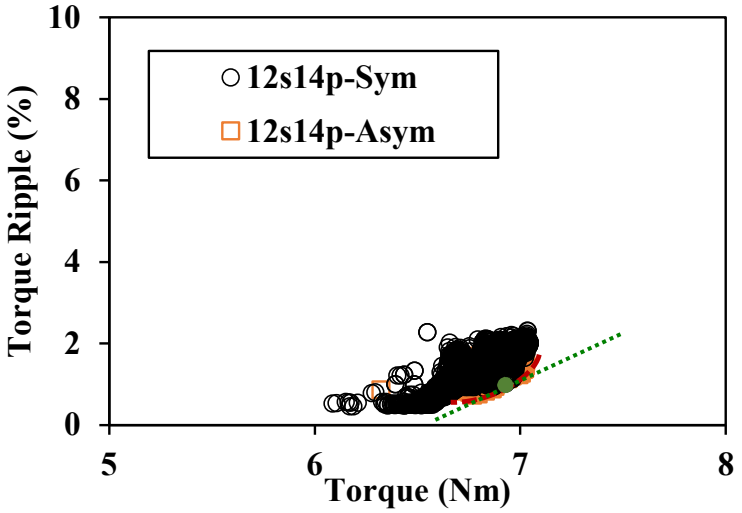

(b) 12s14p

Fig. 5.11 Pareto frontiers form multi-objective optimization for Group 2 SPM machines.

To further investigate the specific electromagnetic performances of these pole-shaped models, some typical machines shown in the green points in Fig. 5.8 to Fig. 5.11 are selected, which will be analyzed in the following sections.

5.4 Comparison and Analysis of Performances of CPPM Machines

5.4.1 Comparison and Analysis of Performances in Group 1 - CPPM Machines Having Odd Coil Number per Phase per Submachine

For the first CPPM group machines, four typical machines that cover two pole shapes and two slot/pole number combinations as shown in green points in Fig. 5.8 are identified and ultimately selected as representatives in the following analysis, where inevitable tradeoffs between

average torque and torque ripple are necessary. The selected 4 machines will be denoted as 12s8p-Sym, 12s8p-Asym, 9s6p-Sym, and 9s6p-Asym, respectively, in the following parts. The rotor parameters for four selected models are listed in Table 5.5.

To provide useful baselines for comparison purposes, conventional CPPM machines which have plain magnet profiles without shaping are also considered. The PM pole arc to pole pitch ratios of conventional models are set as 1.2 to maximize the average torque. The schematics of the optimized profiles together with their conventional CPPM counterparts are illustrated in Fig. 5.12 (a)-(f).

In the following part, FEM predicted performances of the CPPM machines detailed in Table 5.5 and Fig. 5.12 under no-load and on-load conditions are analyzed and compared.

Table 5.5. Rotor Parameters for 4 Optimized CPPM Models

12s8p-Sym (mm)		12s8p-Asym (mm)				9s6p-Sym (mm)		9s6p-Asym (mm)			
Rm_1	25.93	Rm_1	25.93	Ri_1	23.55	Rm_1	25.06	Rm_1	25.97	Ri_1	21.27
Rm_2	27.28	Rm_2	27.35	Ri_2	26.54	Rm_2	26.11	Rm_2	24.66	Ri_2	25.27
Rm_3	27.49	Rm_3	27.50	Ri_3	27.25	Rm_3	27.47	Rm_3	27.49	Ri_3	27.11
Rm_4	27.44	Rm_4	27.49	Ri_4	26.89	Rm_4	27.45	Rm_4	27.30	Ri_4	27.46
Ri_1	23.94	Rm_5	27.49	Ri_5	27.45	Ri_1	24.95	Rm_5	27.32	Ri_5	27.49
Ri_2	26.62	Rm_6	27.39	Ri_6	27.15	Ri_2	25.66	Rm_6	26.71	Ri_6	27.08
Ri_3	27.41	Rm_7	27.32	Ri_7	22.97	Ri_3	27.09	Rm_7	27.23	Ri_7	20.70
Ri_4	27.08	θm_p	45.2°			Ri_4	27.43	θm_p	60.6°		
θm_p	44.9					θm_p	59.5°				

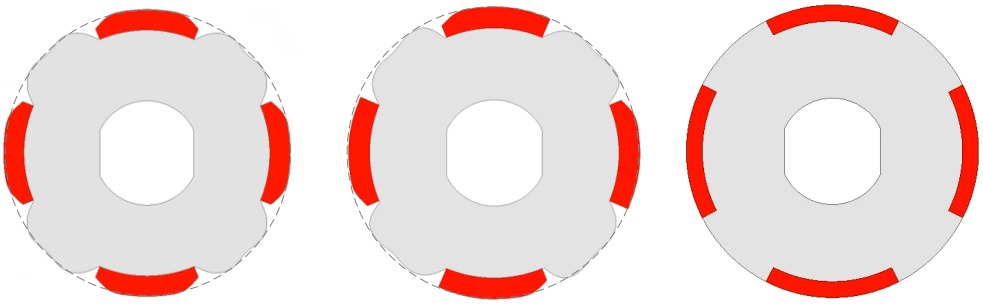

(a) 12s8p-Sym (b) 12s8p-Asym (c) 12s8p-Conv

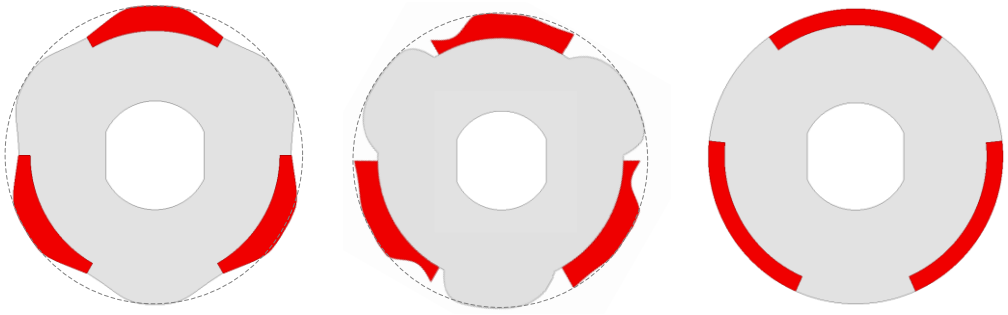

(d) 9s6p-Sym (e) 9s6p-Asym (f) 9s6p-Conv

Fig. 5.12 Optimized models for Group 1 CPPM machines.

5.4.1.1 Open-circuit Flux Density and Flux Linkage

Neglecting the effect of slot openings for the time being, the no-load flux density distribution in air-gap for these CPPM machines and corresponding spectra are compared in Fig. 5.13. It can be seen that the even order harmonics are evident in both 12s8p and 9s6p CPPM machines due to unbalanced features between PM and iron poles. Clearly, they can lead to the corresponding harmonics in coil flux linkages and phase winding flux linkages as shown in Fig. 5.14 and Fig. 5.15. It can also be found that these pole-shaped models which have low torque ripples tend to exhibit lower amplitudes of harmonics in both flux density and flux linkage.

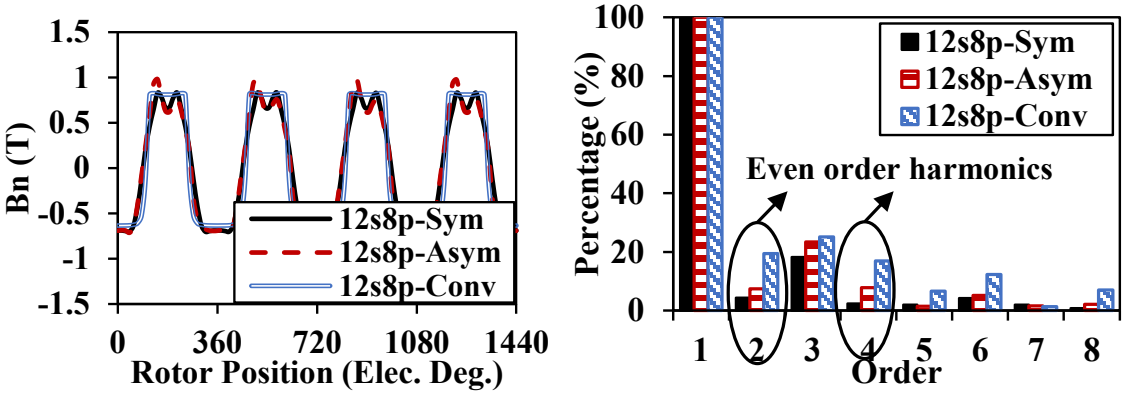

(a) 12s8p

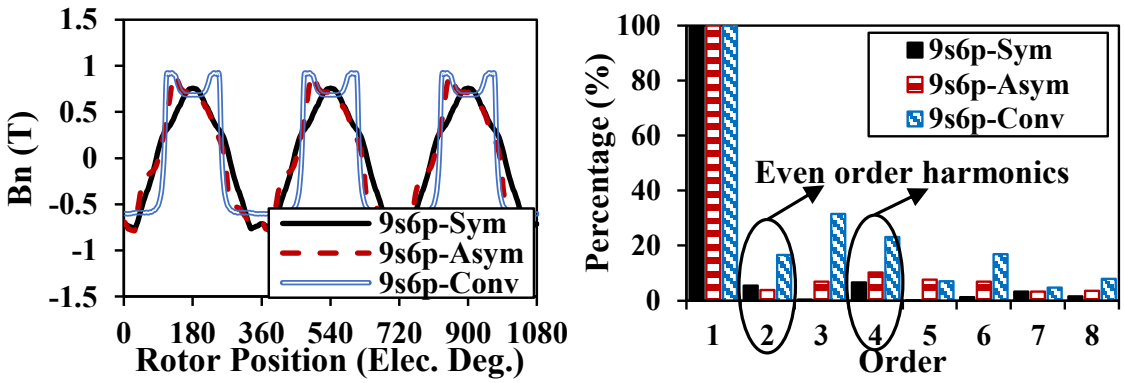

(b) 9s6p

Fig. 5.13 Air-gap flux density.

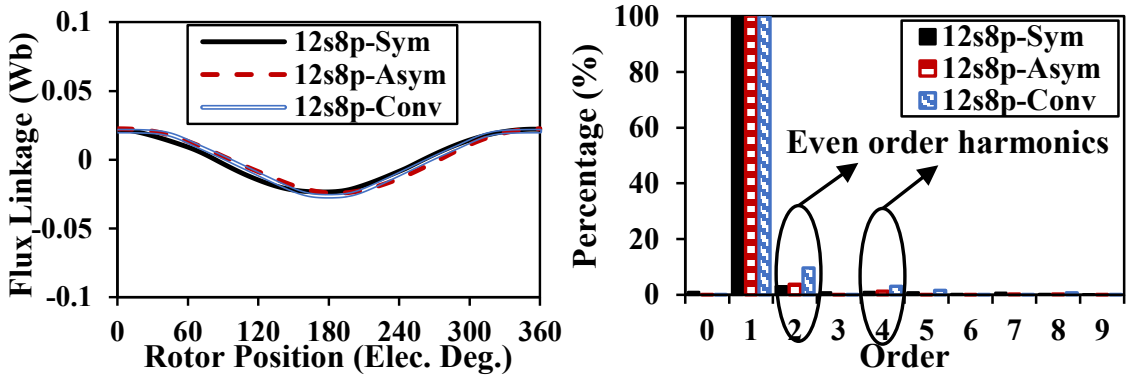

(a) 12s8p

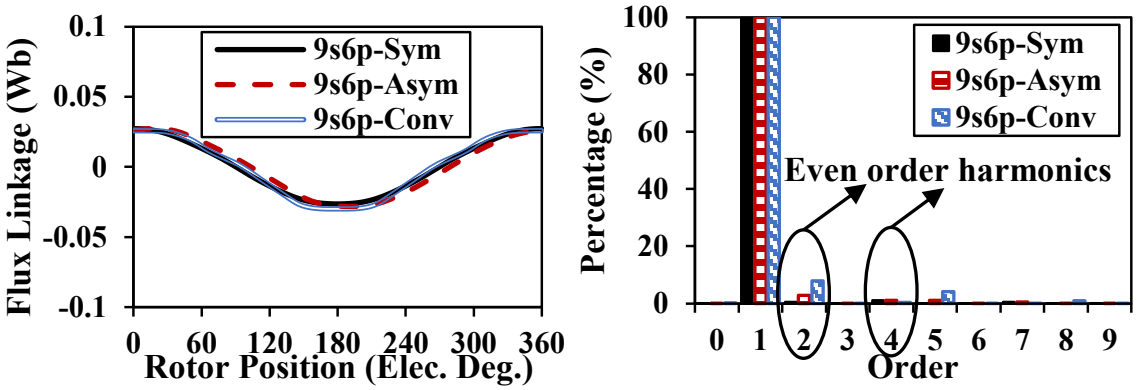

(b) 9s6p

Fig. 5.14 Open-circuit flux linkages for one coil.

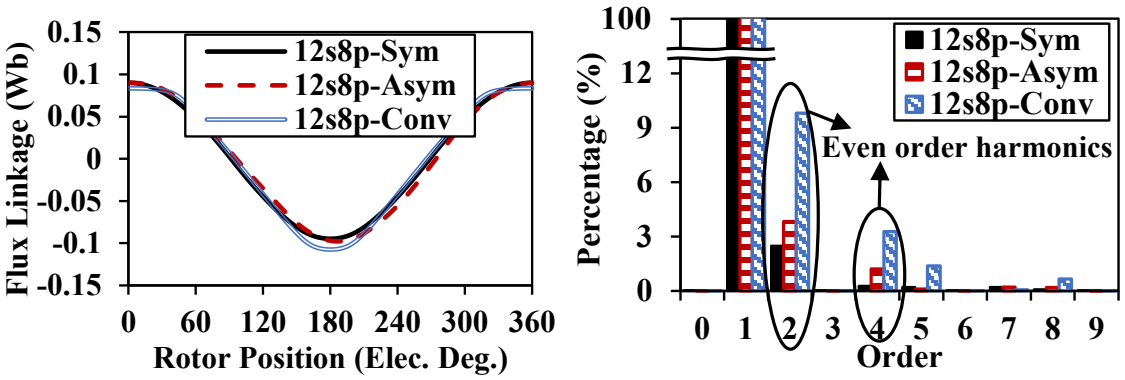

(a) 12s8p

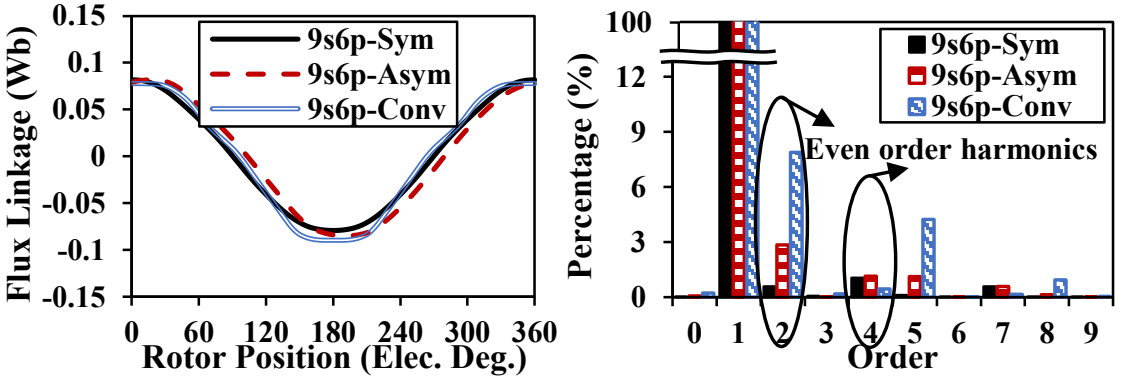

(b) 9s6p

Fig. 5.15 Open-circuit flux linkages for one phase winding.

5.4.1.2 Inductance

Fig. 5.16 and Fig. 5.17 show the inductances for one coil and one phase winding, respectively. Obviously, due to iron saliency in CPPM rotor, the odd order harmonics exist in all the coil inductances and winding inductances for all machines, which confirms the foregoing analyses.

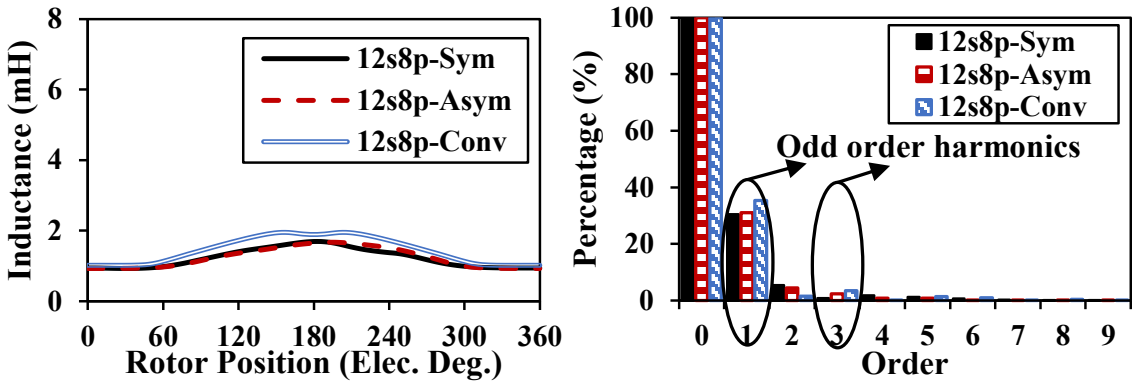

(a) 12s8p

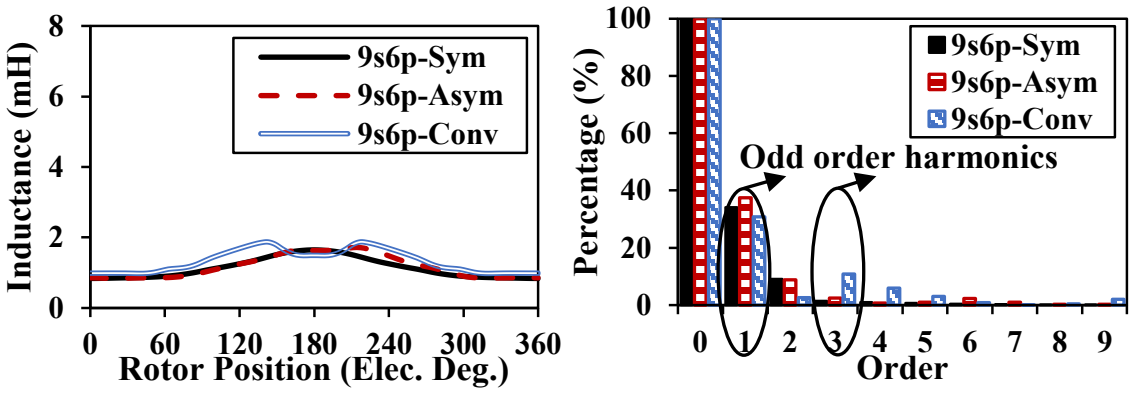

(b) 9s6p

Fig. 5.16 Inductances for one coil.

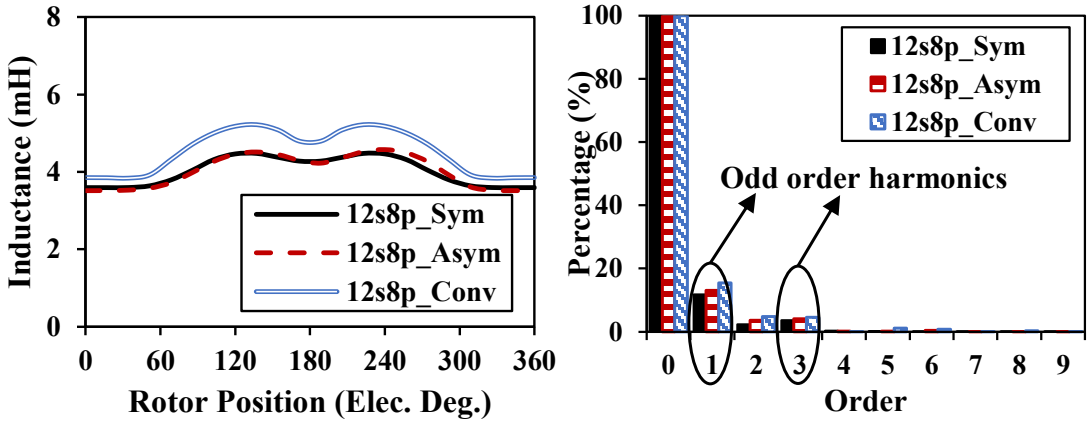

(a) 12s8p

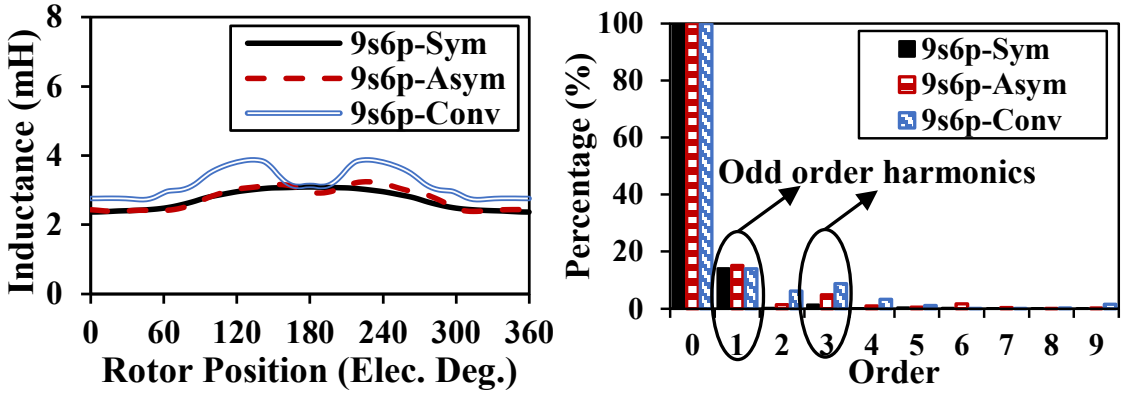

(b) 9s6p

Fig. 5.17 Inductances for one phase winding.

5.4.1.3 Cogging Torque

Fig. 5.18 shows the cogging torques for 12s8p and 9s6p machines. Supposing T_{ripple} is the peak-to-peak value for the cogging torques, as shown in Table 5.6, the pole-shaped CPPM machines

tend to show lower cogging torques than those of their conventional counterparts. This can be attributed to the reduction in flux density harmonics for pole-shaped machines.

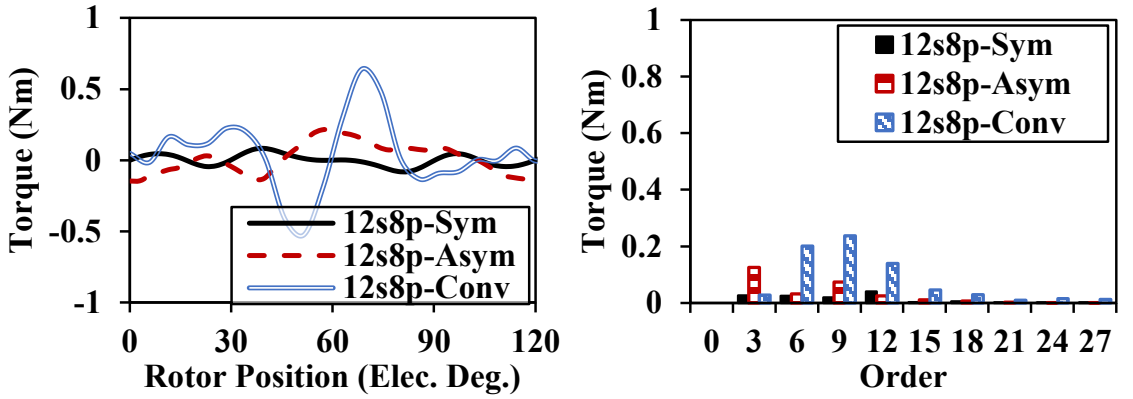

(a) 12s8p

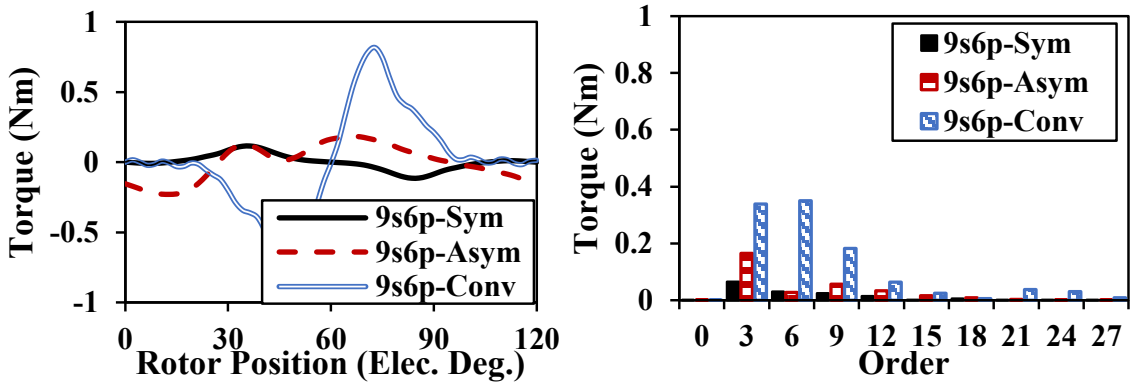

(b) 9s6p

Fig. 5.18 Cogging torque.

Table 5.6. Summary of Cogging Torque of Analyzed Machines

Machine	12s8p			9s6p		
	Sym	Asym	Conv.	Sym	Asym	Conv.
$T_{cogging}$ (mNm)	252	369	1166	228	413	1612

5.4.1.4 Torque Characteristics at Rated Load Condition

Based on the average torque T_{avg}, the peak-to-peak torque T_{pp} and the volume of PM V_{PM}, the PM utilization ratio η_{PM} and torque ripple T_{ripple} can be defined by:

$$\begin{aligned} \eta_{PM} &= T_{avg}/V_{PM} \\ T_{ripple} &= T_{pp}/T_{avg} \end{aligned} \tag{5.21}$$

The torque performances are compared in Table 5.7 and the torque waveforms are shown in Fig. 5.19.

Table 5.7. Torque Characteristics and PM Utilization Ratio Comparison

Parameters	12s8p			9s6p		
	Sym.	Asym.	Conv.	Sym.	Asym.	Conv.
3rd (Nm)	0.435	0.034	0.885	0.1126	0.047	0.9252
6th (Nm)	0.066	0.032	0.635	0.0187	0.0414	0.7708
9th (Nm)	0.044	0.092	0.385	0.0111	0.0438	0.3411
12th (Nm)	0.023	0.031	0.253	0.0145	0.0122	0.1849
T_{pp} (Nm)	0.89	0.33	2.36	0.25	0.18	2.70
T_{avg} (Nm)	5.42	5.54	5.61	3.57	3.63	3.79
η_{PM} (Nm/m^3)	3.7×10^5	3.7×10^5	3.8×10^5	2.5×10^5	2.5×10^5	2.6×10^5
T_{ripple} (%)	16.4	5.9	42.1	7.0	4.9	71.4

For these CPPM machines, the pole-shaped machines tend to have lower average torque than the conventional CPPM machine, which is largely a consequence of the almost same PM and iron pole arc spans for reduced even order harmonics.

In the case of torque ripple, it is evident that all machines have torque harmonic orders that are multiples of three and the asymmetric models have the lowest torque ripples among these machines. This is mainly because the harmonic torque components can be almost entirely counteracted, resulting in a reduced total torque ripple [Qi22b]. The results are consistent with the theoretical discussion in section III.

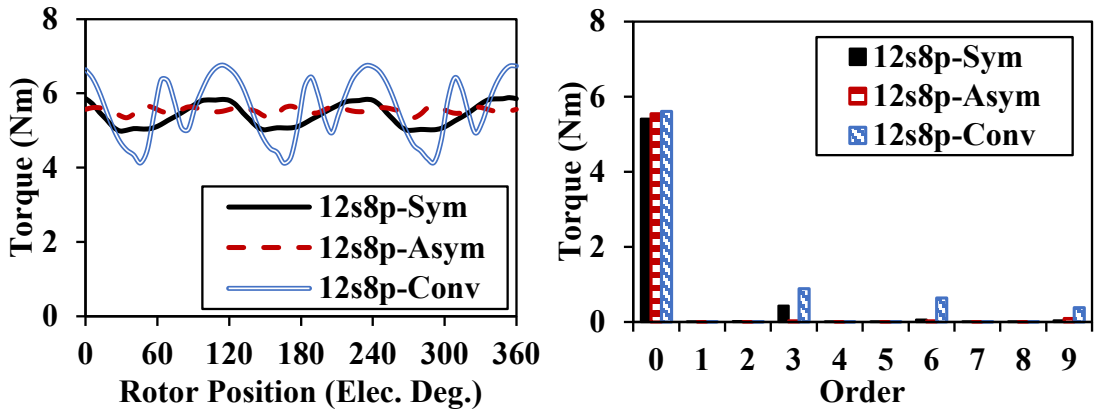

(a) 12s8p

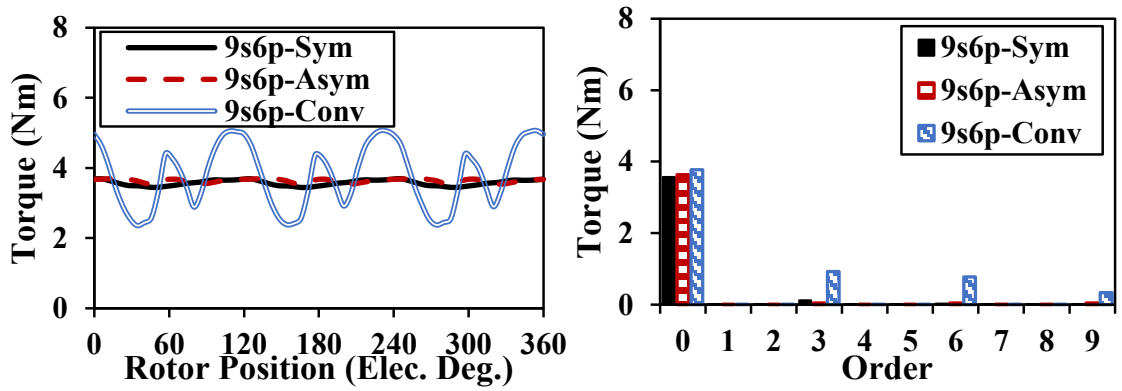

(b) 9s6p

Fig. 5.19 Rated torque.

5.4.1.5 Effect of Load

Both average torques and torque ripples under different operating conditions are presented in Fig. 5.20 where the grey dash line means the rated current condition. It can be observed that with increasing current (particularly beyond 10A), the torque ripples of all the pole-shaped designs tend to increase but remain lower than those of their conventional counterparts. This is mainly because the relative magnitudes of components of torque ripples are determined by the magnitude of the stator current.

When the injected current reduces from 10A to 0, the torque ripples for pole-shaped machines show the rising trends. This is largely a consequence of the relatively large contribution from cogging torque caused by flux density harmonics.

The average torques are very similar for all three machines, and as a consequence of larger equivalent air-gap lengths, the lower armature effect of pole-shaped machines exhibits slightly enhanced overload capability.

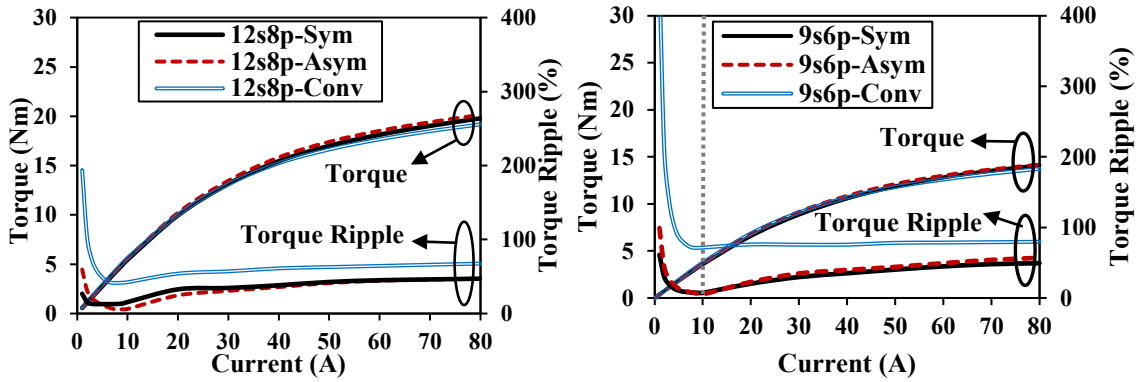

(a) 12s8p (b) 9s6p

Fig. 5.20 Torque characteristics under different loads.

5.4.2 Comparison and Analysis of Performances in Group 2 - CPPM Machines Having Even Coil Number per Phase per Submachine

For the second group CPPM machines, four typical machines, which are denoted as 12s10p-Sym, 12s10p-Asym, 12s14p-Sym, and 12s14p-Asym, are selected as illustrated in green points in Fig. 5.9. For comparison, conventional CPPM machines with plain PM and iron profiles without shaping are also analyzed, which are denoted as 9s6p-Conv and 12s14p-Conv. The pole arc ratios of conventional models are set as 1.2 to maximize the average torque. The structures for these machines are presented in Fig. 5.21 and the rotor geometry parameters are listed in Table 5.8. It is evident that the GA optimization process has led to a larger PM pole arc span for optimized CPPM machines.

In the following part, FEM predicted performance of the CPPM machines detailed in Table 5.8 and Fig. 5.21 under no-load and on-load conditions are analyzed and compared.

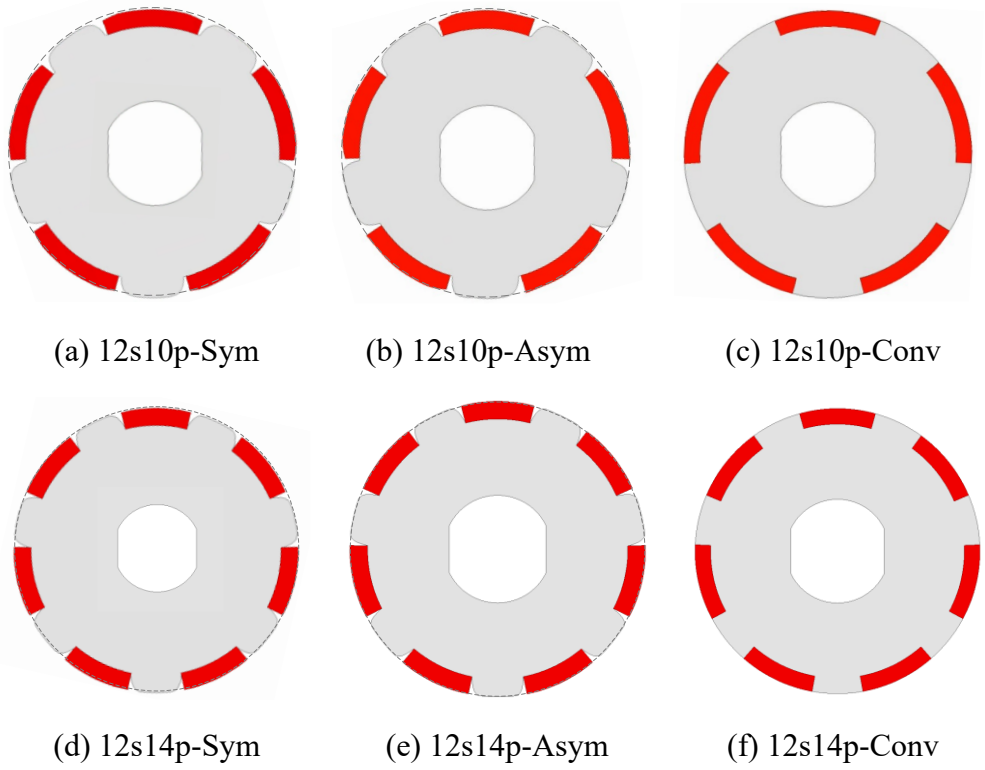

(a) 12s10p-Sym (b) 12s10p-Asym (c) 12s10p-Conv

(d) 12s14p-Sym (e) 12s14p-Asym (f) 12s14p-Conv

Fig. 5.21 Optimized models for Group 2 CPPM machines.

Table 5.8. Rotor Parameters for 4 Optimized CPPM Models

12s10p-Sym (mm)		12s10p-Asym (mm)				12s14p-Sym (mm)		12s14p-Asym (mm)			
Rm_1	21.77	Rm_1	22.25	Ri_1	26.79	Rm_1	27.45	Rm_1	27.44	Ri_1	23.95
Rm_2	27.15	Rm_2	27.02	Ri_2	27.38	Rm_2	27.49	Rm_2	27.49	Ri_2	27.43
Rm_3	27.50	Rm_3	27.45	Ri_3	27.45	Rm_3	27.47	Rm_3	27.48	Ri_3	27.47
Rm_4	27.49	Rm_4	27.49	Ri_4	27.50	Rm_4	27.50	Rm_4	27.49	Ri_4	27.47
Ri_1	27.08	Rm_5	27.43	Ri_5	27.46	Ri_1	24.66	Rm_5	27.48	Ri_5	27.48
Ri_2	27.50	Rm_6	27.46	Ri_6	27.32	Ri_2	27.34	Rm_6	27.49	Ri_6	27.42
Ri_3	27.49	Rm_7	21.84	Ri_7	27.48	Ri_3	27.50	Rm_7	27.47	Ri_7	24.31
Ri_4	27.50	θm_p	39.4°			Ri_4	27.49	θm_p	28.5°		
θm_p	41.2°					θm_p	28.4°				

5.4.2.1 Open-circuit Flux Density and Flux Linkage

Neglecting the effect of slot openings for the time being, the open-circuit flux density distribution in air-gap for these CPPM machines and corresponding spectra are compared in Fig. 5.22. Obviously, even order harmonics exist, leading to the corresponding harmonics in coil flux linkages as shown in Fig. 5.23. However, in the phase winding flux linkages, even order harmonics are eliminated as shown in Fig. 5.24.

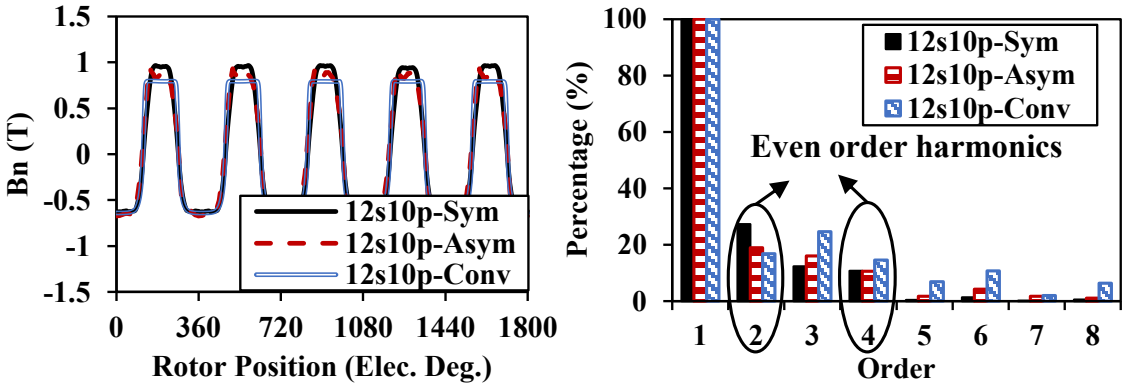

(a) 12s10p

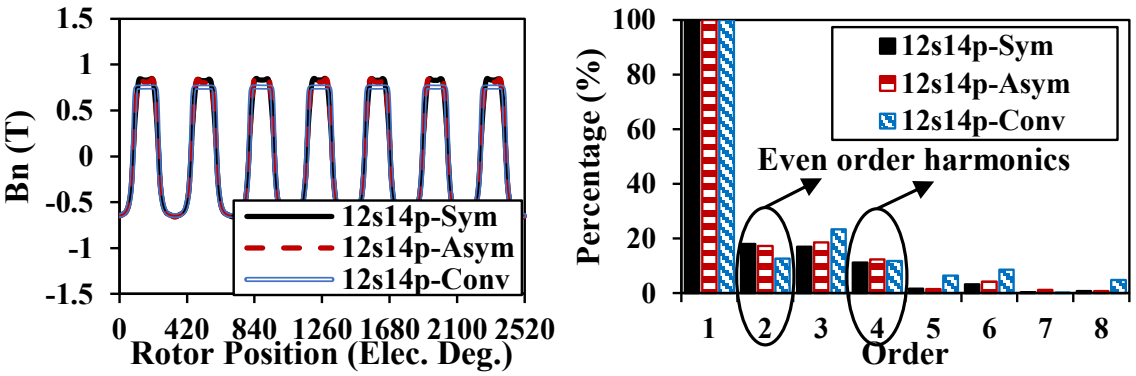

(b) 12s14p

Fig. 5.22 Air-gap flux density.

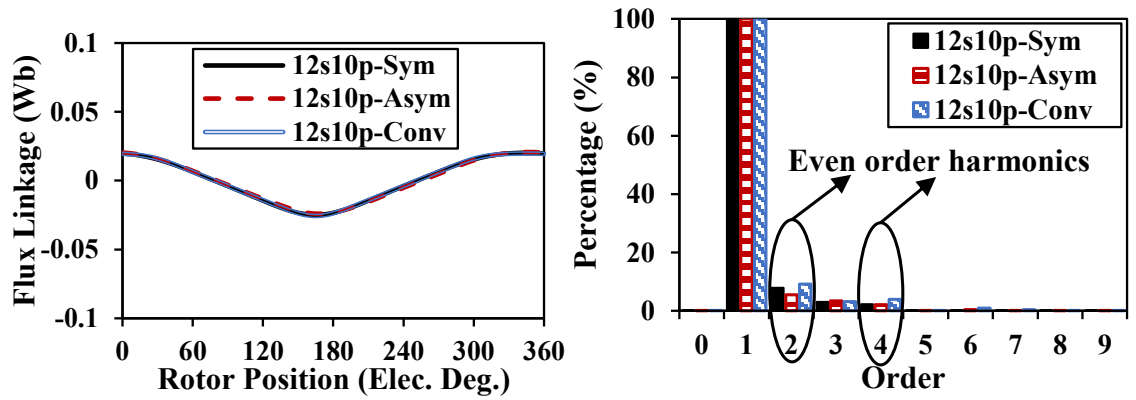

(a) 12s10p

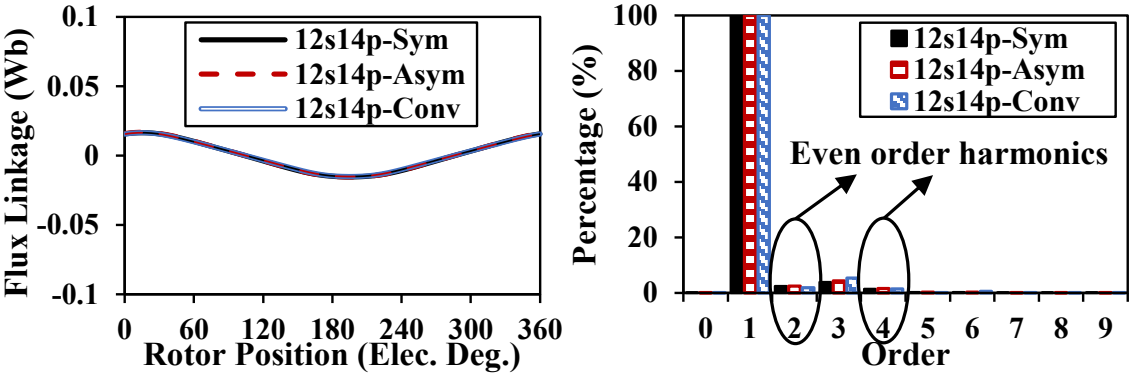

(b) 12s14p

Fig. 5.23 Open-circuit flux linkages for one coil.

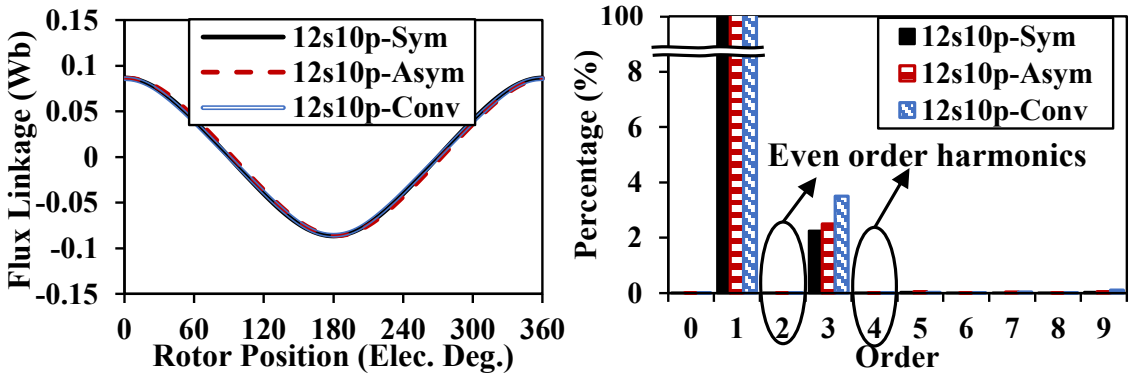

(a) 12s10p

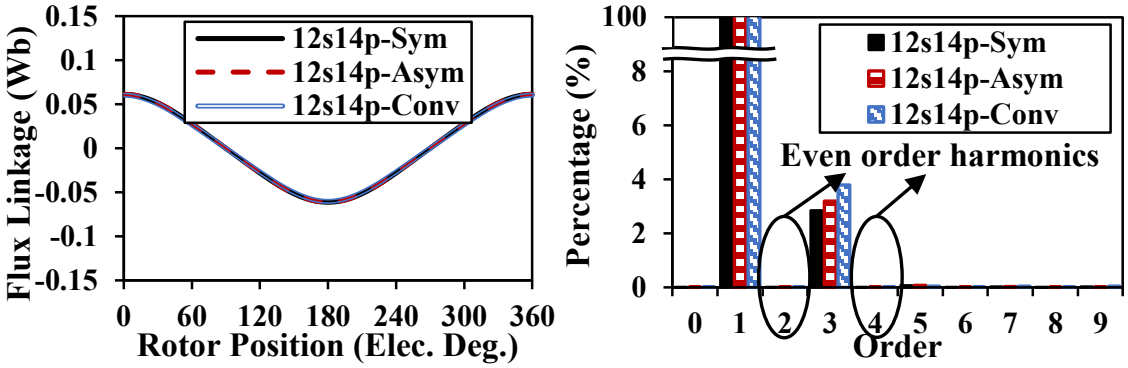

(b) 12s14p

Fig. 5.24 Open-circuit flux linkages for one phase winding.

5.4.2.2 Inductance

Obviously, due to iron saliency in CPPM rotor, the odd order harmonics exist in all the coil inductances for all machines, Fig. 5.25. However, in the phase winding inductances, the odd order harmonics are canceled, Fig. 5.26, which confirms the foregoing analyses.

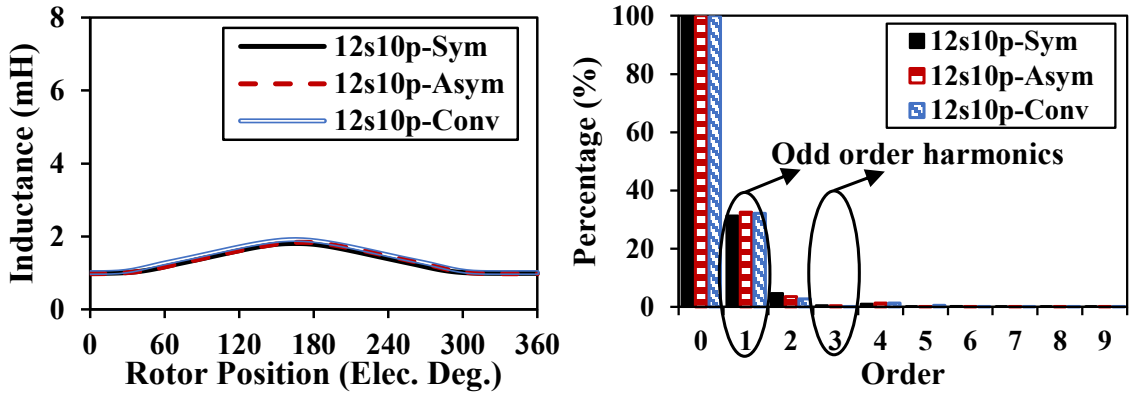

(a) 12s10p

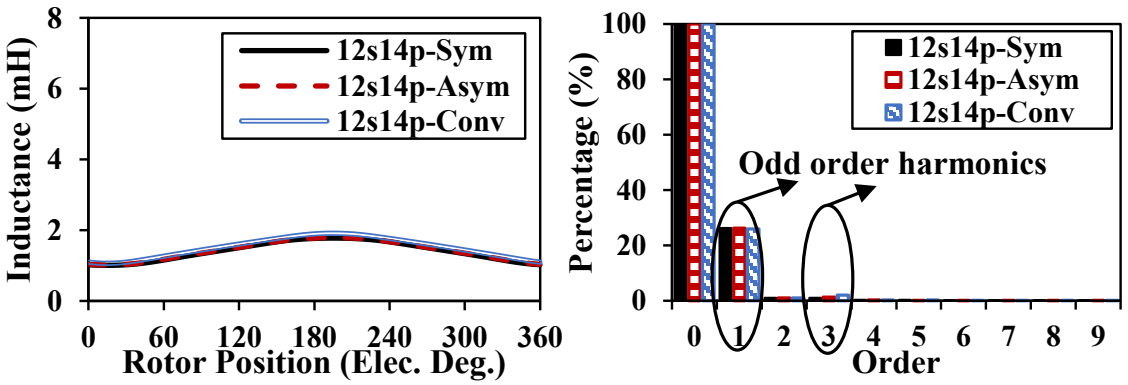

(b) 12s14p

Fig. 5.25 Inductances for one coil.

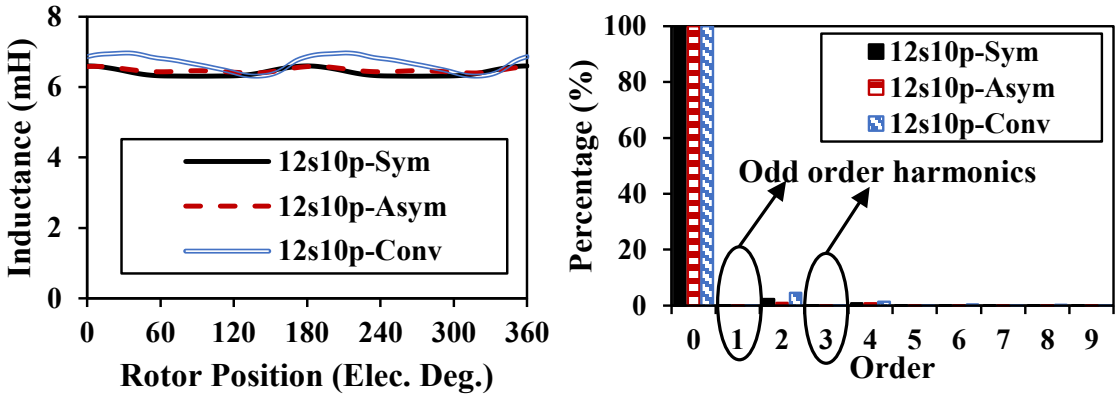

(a) 12s10p

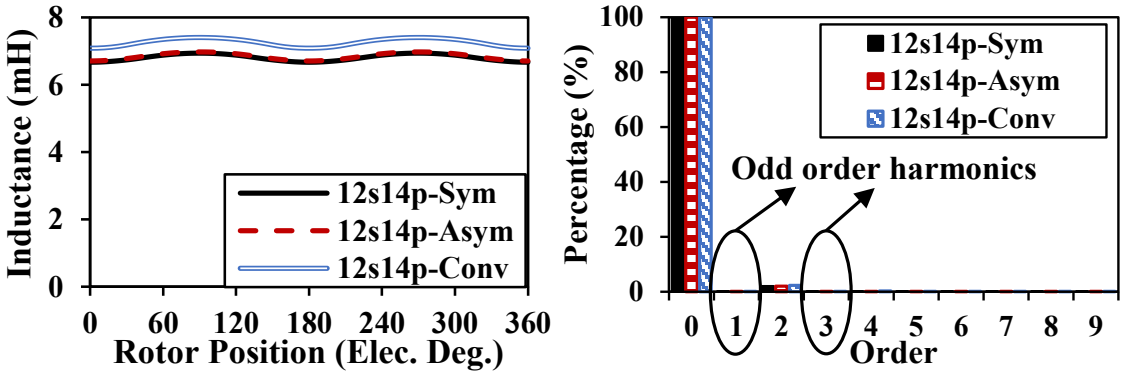

(b) 12s14p

Fig. 5.26 Inductances for one phase winding.

5.4.2.3 Cogging Torque

Fig. 5.27 demonstrates the cogging torques for 12s10p and 12s14p machines and the peak-to-peak values are shown in Table 5.9. It can be found that the pole-shaped CPPM machines tend to show lower cogging torques than those of their conventional counterparts due to reduction in flux density harmonics.

Table 5.9. Summary of Cogging Torque of Analyzed Machines

Machine	12s10p			12s14p		
	Sym	Asym	Conv.	Sym	Asym	Conv.
$T_{cogging}$ (mNm)	8	113	237	8	17	84

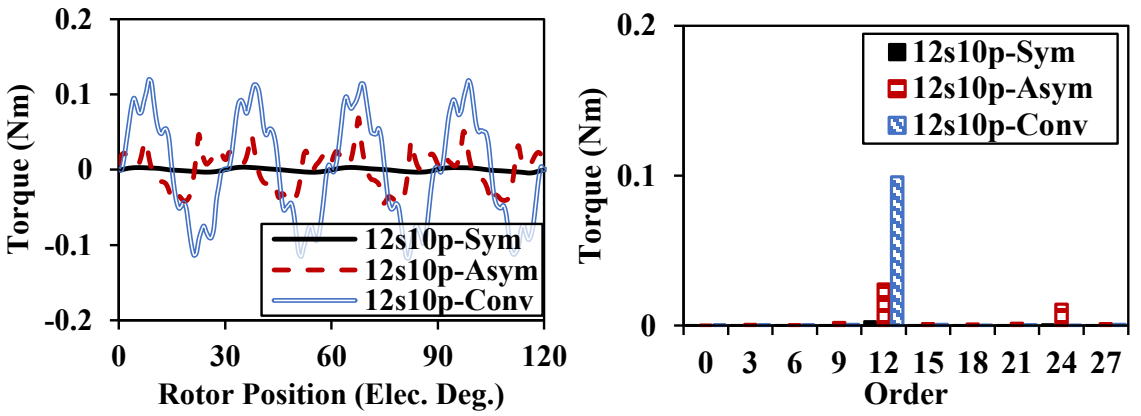

(a) 12s10p

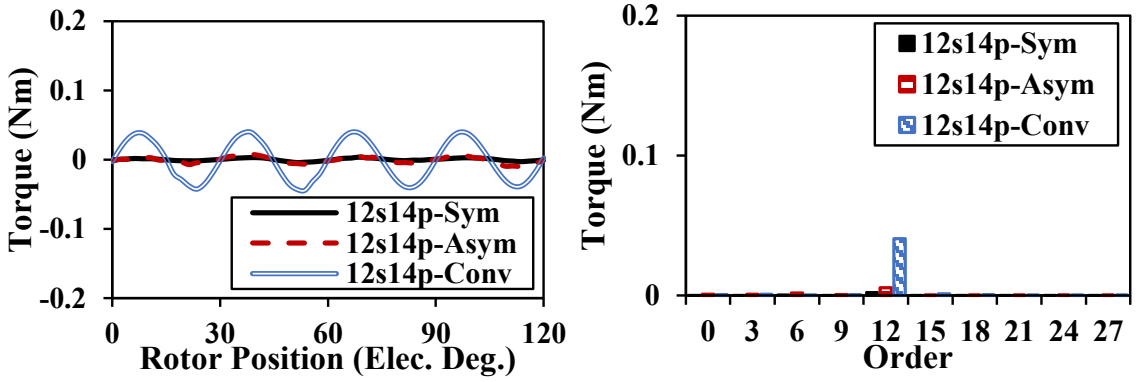

(b) 12s14p

Fig. 5.27 Cogging torque.

5.4.2.4 Torque Characteristics at Rated Load Condition

The torque performances are compared in Table 5.10 and the torque waveforms are shown in Fig. 5.28. With the help of wider PM pole arcs and the air spaces adjacent to the sides of the magnets for reducing flux leakage, the pole-shaped machines can realize even higher average torque than their conventional counterpart and maintain high level PM utilization ratios. In the case of torque ripple, it is evident that all the torque ripple orders for the second group CPPM machines are the multiple of 6 and the symmetrical and asymmetric models have similar levels of torque ripple. The results are consistent with the analysis in section III.

Table 5.10. Torque Characteristics and PM Utilization Ratio Comparison

Parameters	12s10p			12s14p		
	Sym.	Asym.	Conv.	Sym.	Asym.	Conv.
6^{th} (Nm)	0.0359	0.0245	0.0528	0.0219	0.0215	0.037
12^{th} (Nm)	0.004	0.0227	0.144	0.0032	0.0039	0.0434
T_{pp} (Nm)	0.07	0.07	0.36	0.05	0.05	0.16
T_{avg} (Nm)	6.15	6.16	6.07	6.11	6.11	5.97
η_{PM} (Nm/m^3)	4.2×10^5	4.2×10^5	4.1×10^5	4.1×10^5	4.1×10^5	4.1×10^5
T_{ripple} (%)	1.2	1.2	5.9	0.8	0.9	2.6

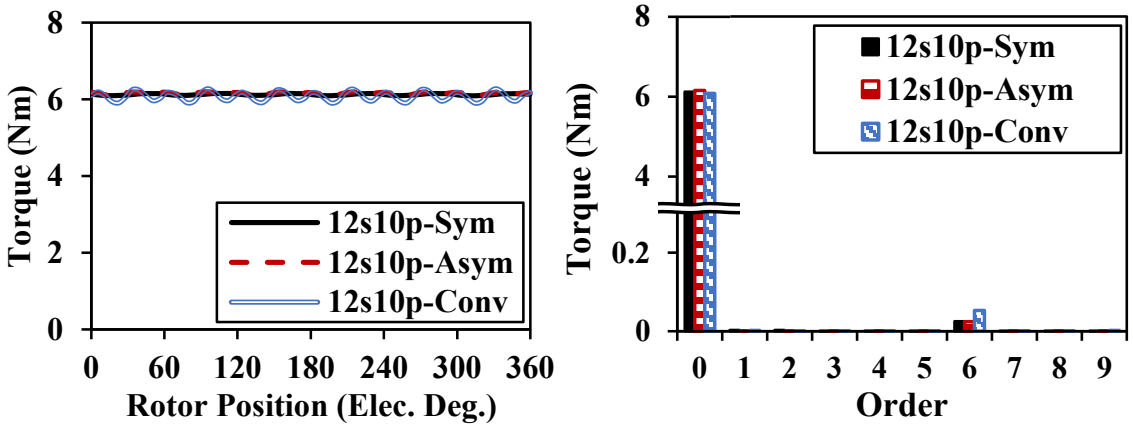

(a) 12s10p

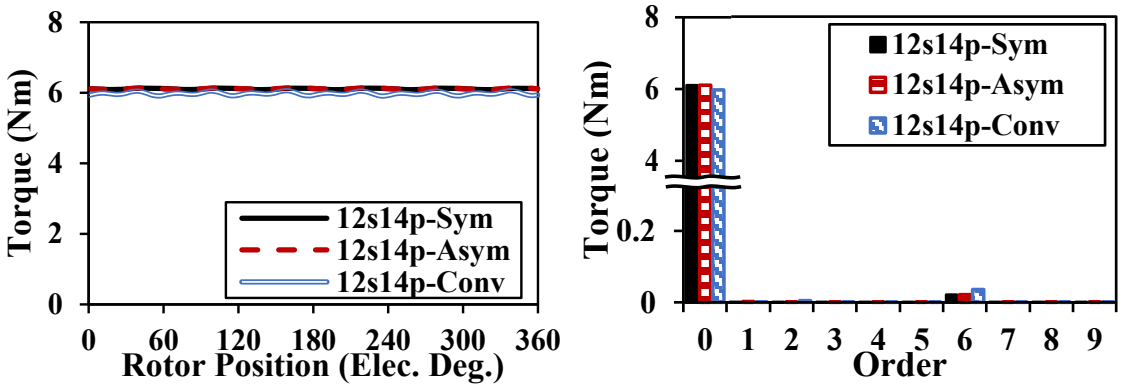

(b) 12s14p

Fig. 5.28 Rated torque.

5.4.2.5 Effect of Load

Torque performances under different operating conditions are presented in Fig. 5.29. It can be observed that with increasing current (particularly beyond 10A), the torque ripples of all the pole-shaped designs tend to maintain a low level. When the injected current is close to 0, the torque ripples for symmetrical pole-shaped machines are still low which is mainly because of their low cogging torques.

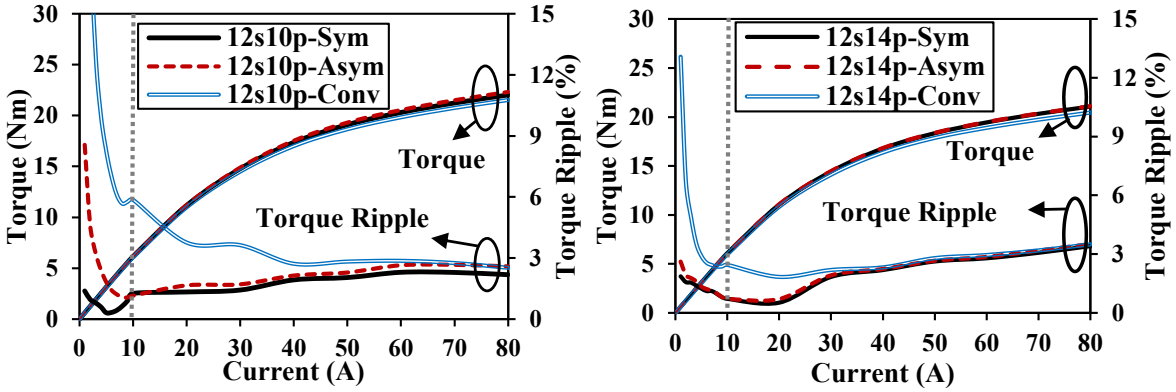

(a) 12s10p (b) 12s14p

Fig. 5.29 Torque characteristics under different loads.

5.4.3 Comparison

From the previous analyses, the characteristics of basic performances as well as the pole-shaped models for two groups of CPPM machines can be summarized and compared in Table 5.11 and Table 5.12.

5.5 Comparison and Analysis of Performances of SPM Machines

5.5.1 Comparison and Analysis of Performances in Group 1 - SPM Machines Having Odd Coil Number per Phase per Submachine

For the first group SPM machines, four typical machines, which are denoted as 12s8p-Sym, 12s8p-Asym, 9s6p-Sym, and 9s6p-Asym, are selected as illustrated in green points in Fig. 5.10. For comparison, conventional SPM machines with plain PM profiles without shaping and equal north and south pole widths are also analyzed, which are denoted as 12s8p-Conv and 9s6p-Conv. The rotor geometry parameters for these machines are listed in Table 5.13 and the structures are presented in Fig. 5.30. It is evident that the GA optimization process has led to almost equal north and south pole widths.

Table 5.11. Characteristics of Basic Performance For Two Groups of CPPM Machines

Machine	Group 1 e.g. 12s8p, 9s6p, 9s8p etc.	Group 2 e.g. 12s10p, 12s14p, 6s10p etc.
Flux density in air-gap	With even order harmonics.	
Coil flux linkage	With even order harmonics.	
Phase winding flux linkage	With even order harmonics.	Without even order harmonics.
Coil inductance	With odd order harmonics	
Winding inductance	With odd order harmonics	Without odd order harmonics.
Torque ripple	Harmonics orders are multiples of 3.	Harmonics orders are multiples of 6.

Table 5.12. Characteristics of Pole-Shaped Models for Two Groups of CPPM Machines

Machine	Group 1 e.g. 12s8p, 9s6p, 9s8p etc.	Group 2 e.g. 12s10p, 12s14p, 6s10p etc.
Pole shaping method	Asymmetric pole shaping can result in a much lower torque ripple than symmetrical pole shaping.	Symmetrical pole shaping method can achieve a similar level of torque ripple as that of asymmetric method but with lower optimization complexity.
Pole arc width	PM and iron pole arcs need to be almost identical.	PM pole arc should be larger than iron pole arc.
Overload capability	Overload capabilities for shaped machines are all improved slightly.	

The flux densities, flux linkages, inductances, and torque performances for these six machines are shown in Fig. 5.31 to Fig. 5.38, Table 5.14, and Table 5.15. It is obvious that the conventional SPM machine with equal north and south pole widths can eliminate the additional harmonics in flux densities, flux linkages, and inductances, while the pole-shaped machines tend to have those harmonics. Similar to CPPM counterparts, the even order harmonics in air-gap flux densities can produce corresponding harmonics in winding flux linkages, which will lead to odd order torque ripples. However, due to the objective of low torque ripple in optimization, all the harmonics are low enough. In addition, symmetrical and asymmetric pole-shaped machines have similar torque ripple levels, which confirms the analysis in section III.

Table 5.13. Rotor Parameters for 4 Pole-Shaped SPM Models

12s8p-Sym (mm)		12s8p-Asym (mm)				9s6p-Sym (mm)		9s6p-Asym (mm)			
Rm_1	23.86	Rm_1	23.19	Ri_1	24.19	Rm_1	22.96	Rm_1	24.12	Ri_1	21.58
Rm_2	26.89	Rm_2	26.39	Ri_2	27.15	Rm_2	25.31	Rm_2	25.43	Ri_2	25.00
Rm_3	27.47	Rm_3	27.46	Ri_3	27.47	Rm_3	27.39	Rm_3	27.12	Ri_3	27.20
Rm_4	27.27	Rm_4	27.12	Ri_4	27.33	Rm_4	27.25	Rm_4	27.20	Ri_4	27.01
Ri_1	23.71	Rm_5	27.37	Ri_5	27.45	Ri_1	22.95	Rm_5	27.16	Ri_5	27.42
Ri_2	27.03	Rm_6	27.24	Ri_6	26.90	Ri_2	25.14	Rm_6	25.37	Ri_6	25.83
Ri_3	27.46	Rm_7	25.04	Ri_7	25.95	Ri_3	27.38	Rm_7	23.50	Ri_7	22.73
Ri_4	27.35	θm_p	44.44			Ri_4	27.22	θm_p	60.42		
θm_p	44.81					θm_p	60.58				

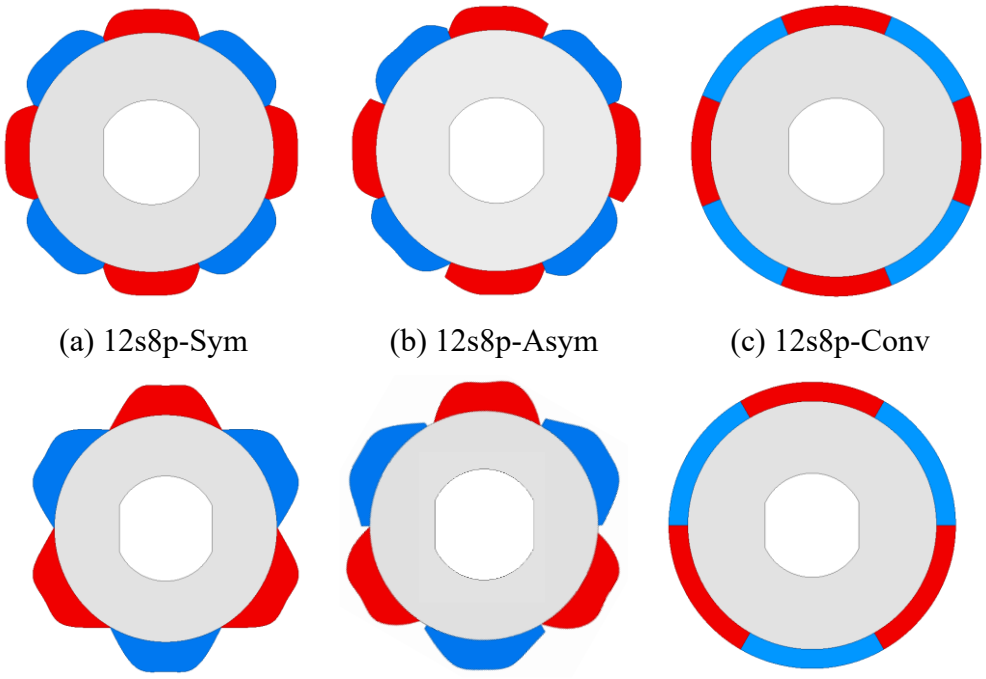

(a) 12s8p-Sym (b) 12s8p-Asym (c) 12s8p-Conv

(d) 9s6p-Sym (e) 9s6p-Asym (f) 9s6p-Conv

Fig. 5.30 Optimized models for Group 1 - SPM machines.

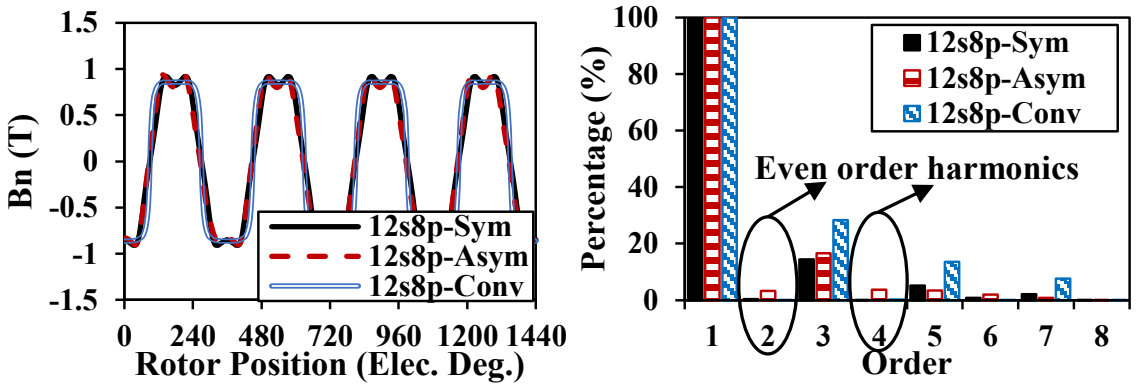

(a) 12s8p

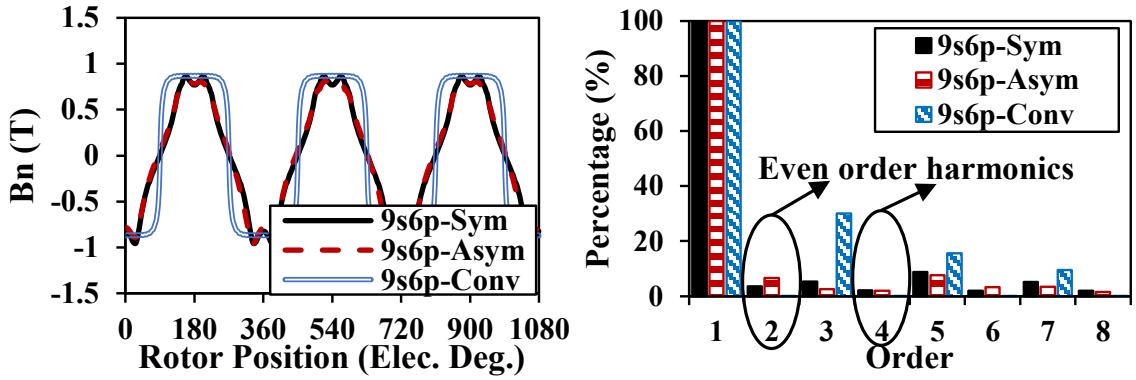

(b) 9s6p

Fig. 5.31 Air-gap flux density.

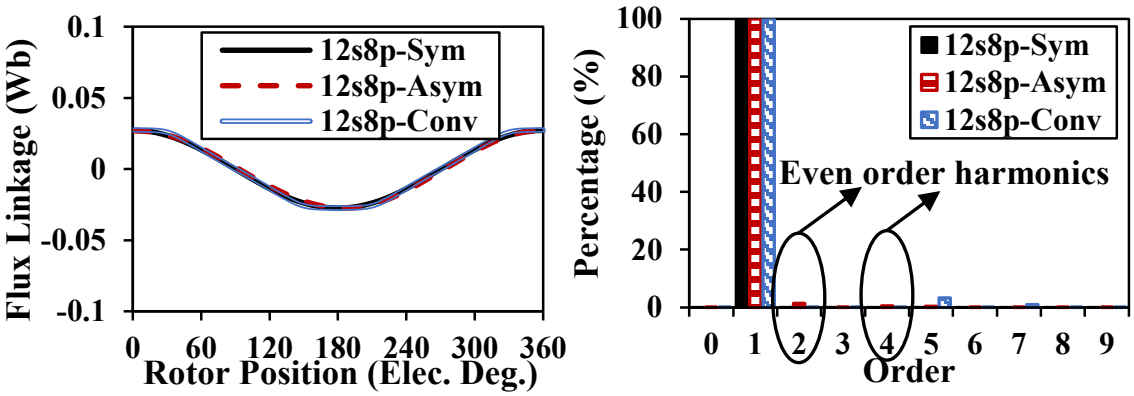

(a) 12s8p

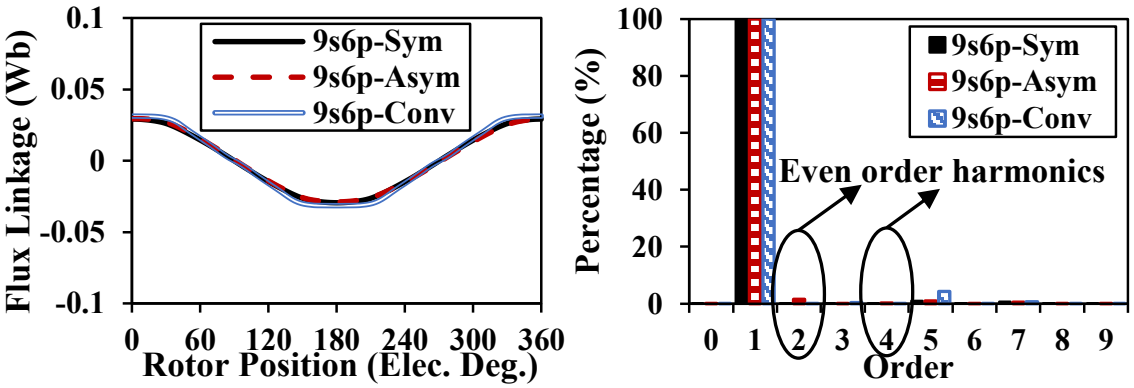

(b) 9s6p

Fig. 5.32 Open-circuit flux linkages for one coil.

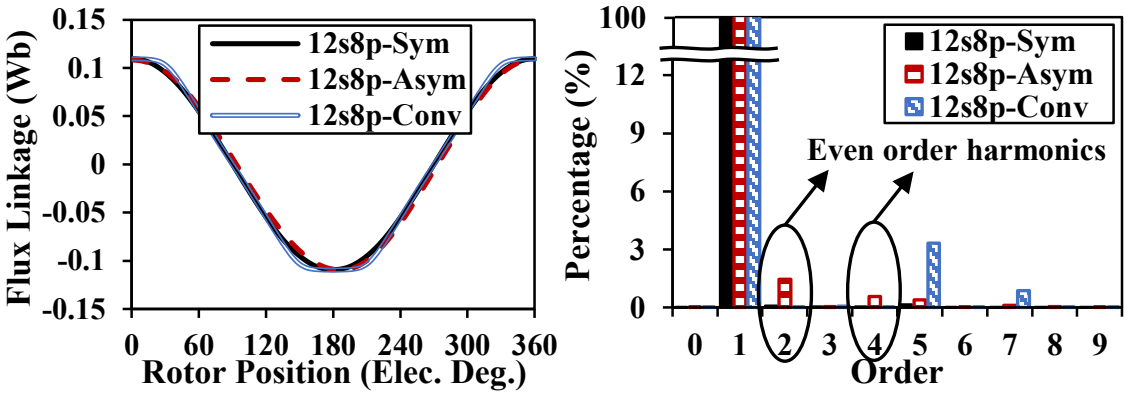

(a) 12s8p

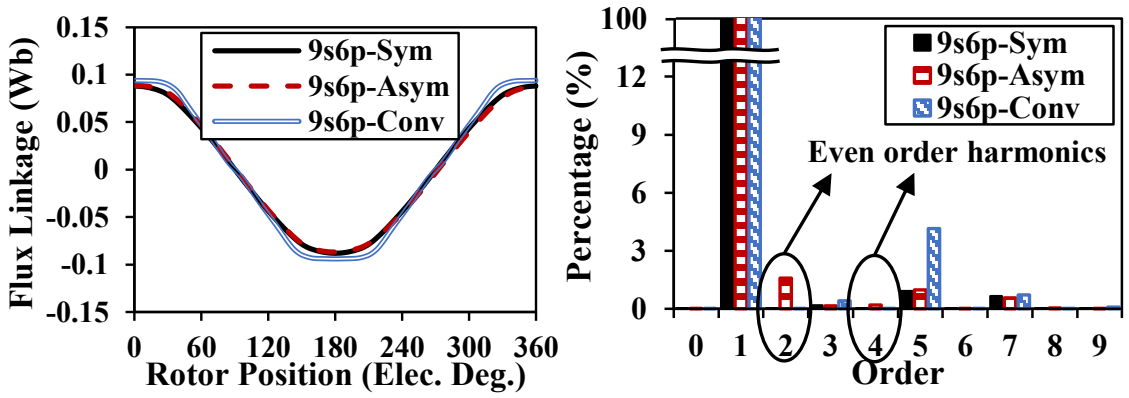

(b) 9s6p

Fig. 5.33 Open-circuit flux linkages for one phase winding.

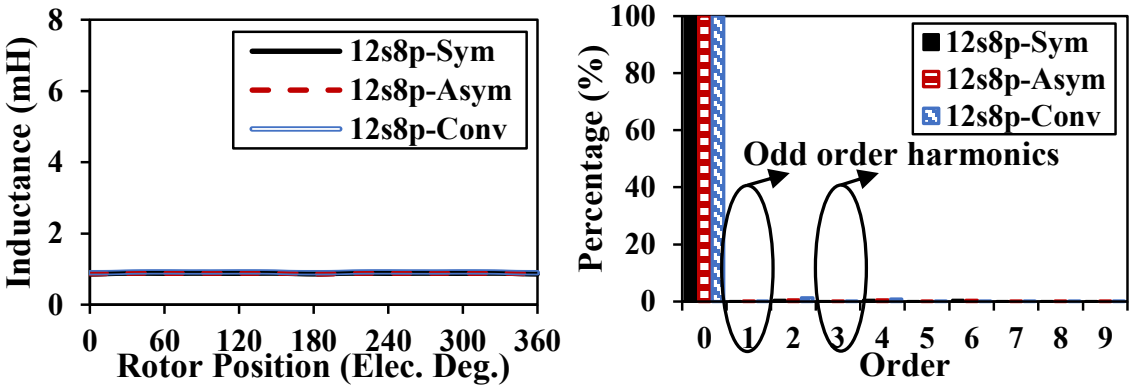

(a) 12s8p

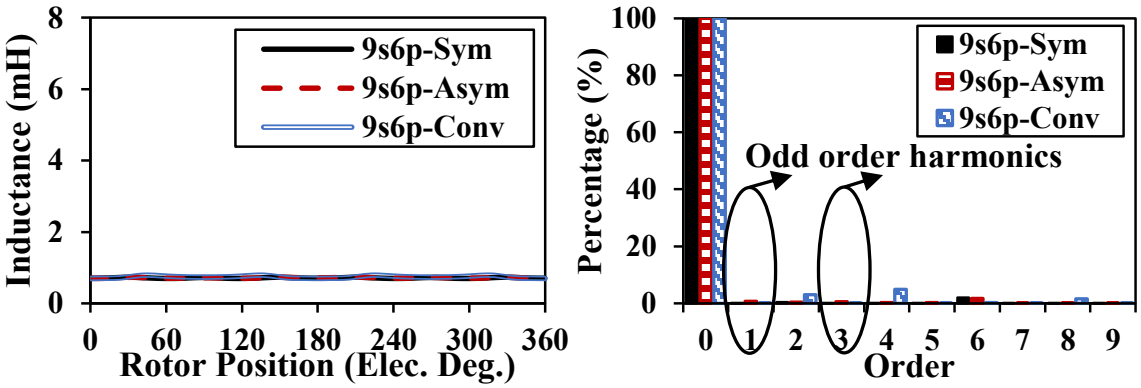

(b) 9s6p

Fig. 5.34 Inductances for one coil.

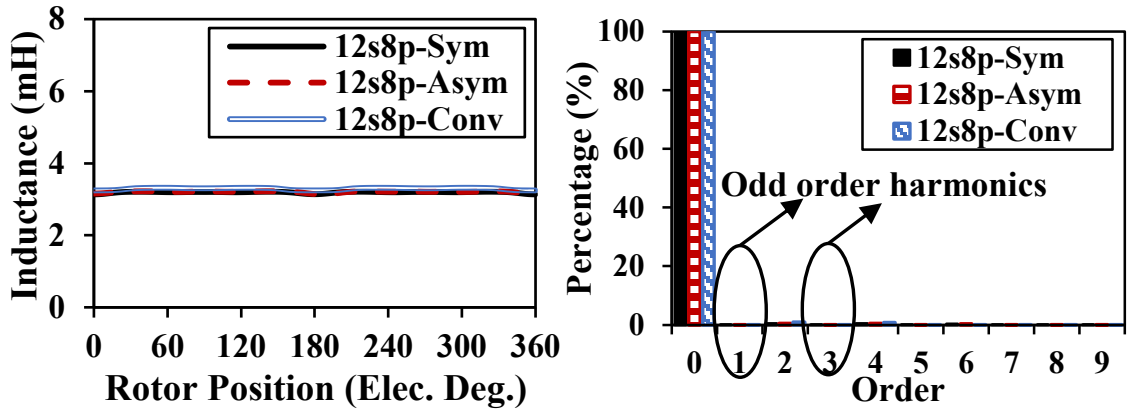

(a) 12s8p

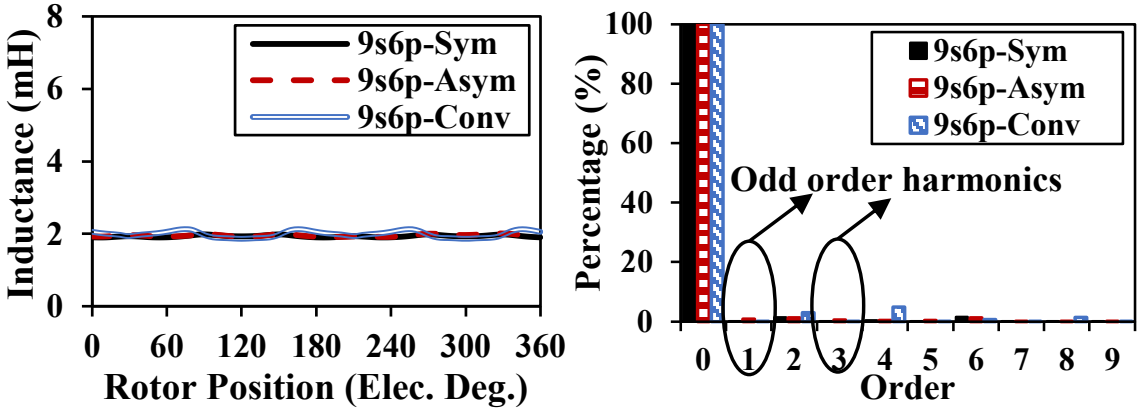

(b) 9s6p

Fig. 5.35 Inductances for one phase winding.

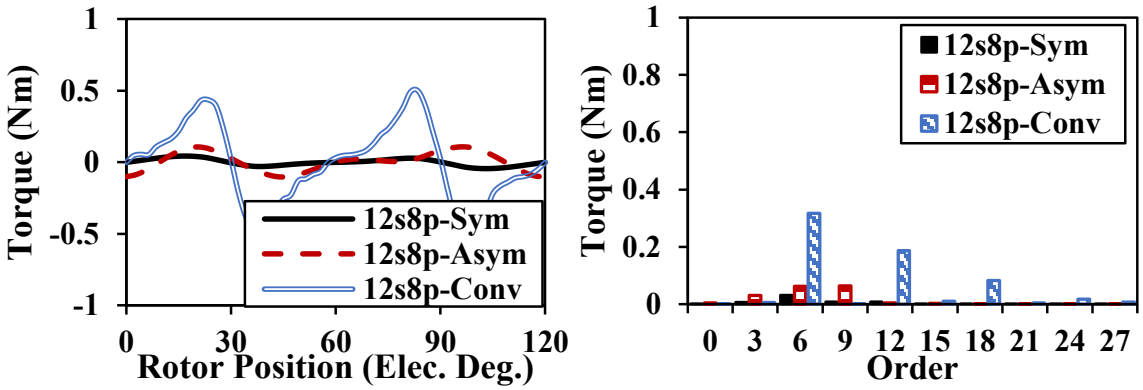

(a) 12s8p

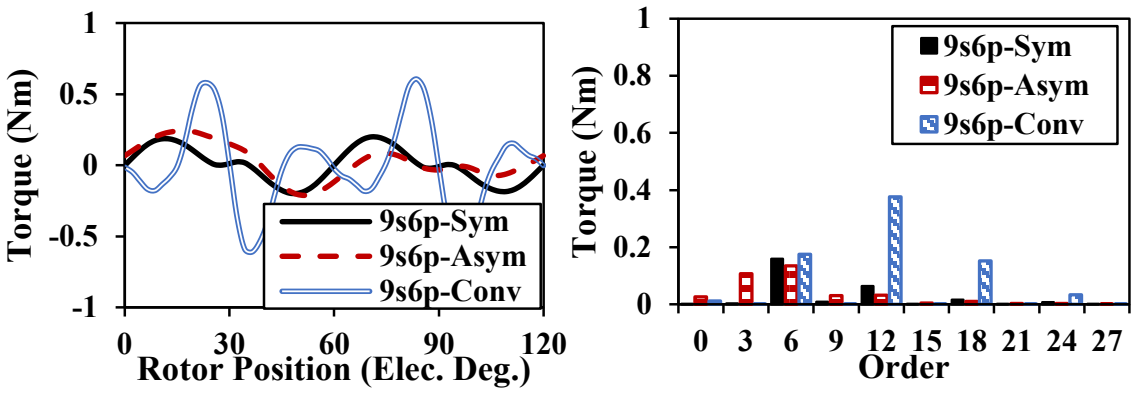

(b) 9s6p

Fig. 5.36 Cogging torque.

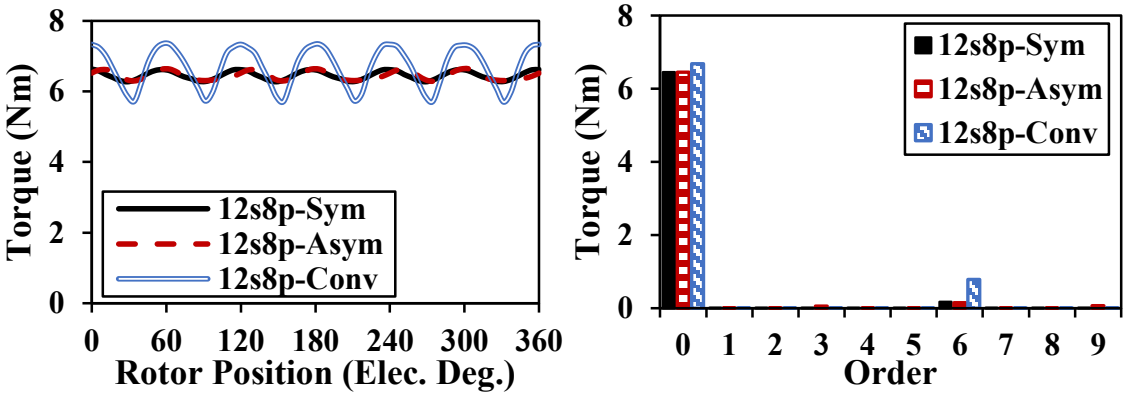

(a) 12s8p

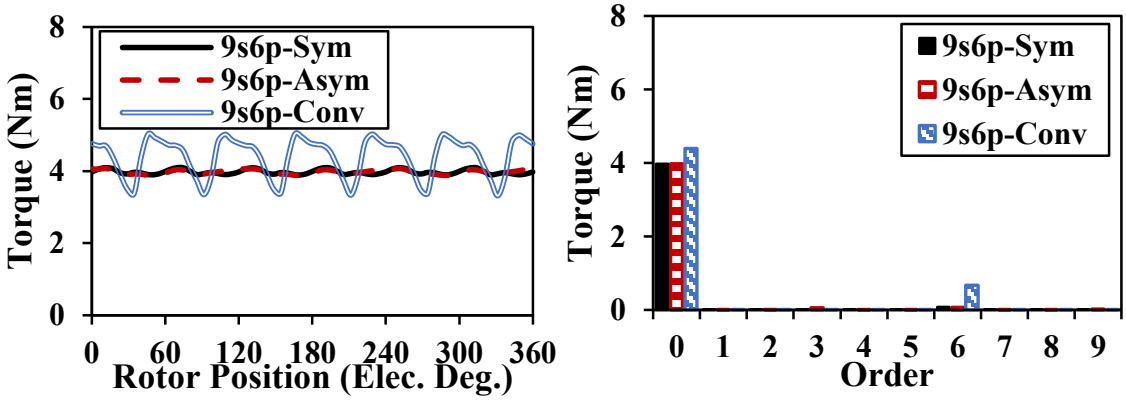

(b) 9s6p

Fig. 5.37 Rated torque.

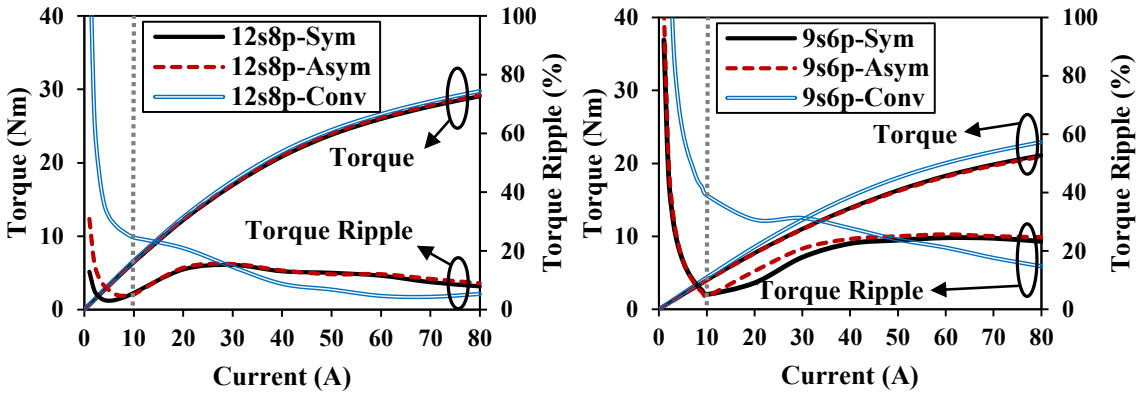

(a) 12s8p (b) 9s6p

Fig. 5.38 Torque characteristics under different loads.

Table 5.14. Summary of Cogging Torque of Analyzed Machines

Machine	12s8p			9s6p		
	Sym	Asym	Conv.	Sym	Asym	Conv.
$T_{cogging}$ (mNm)	88	210	965	397	453	1241

Table 5.15. Torque Characteristics and PM Utilization Ratio Comparison

Parameters	12s8p			9s6p		
	Sym.	Asym.	Conv.	Sym.	Asym.	Conv.
3rd (Nm)	0.0088	0.0492	0.006	0.0023	0.0514	0.0024
6th (Nm)	0.1708	0.1452	0.7784	0.0751	0.0594	0.6686
9th (Nm)	0.0121	0.0607	0.0045	0.0056	0.0186	0.0039
12th (Nm)	0.0074	0.0068	0.1495	0.0474	0.0216	0.338
T_{pp} (Nm)	0.36	0.35	1.66	0.19	0.19	1.71
T_{avg} (Nm)	6.46	6.45	6.69	3.97	3.98	4.40
η_{PM} (Nm/m^3)	3.7×105	3.7×105	3.8×105	2.5×105	2.5×105	2.6×105
T_{ripple} (%)	5.6	5.5	24.7	4.9	4.7	38.9

5.5.2 Comparison and Analysis of Performances in Group 2 - SPM Machines Having Even Coil Number per Phase per Submachine

For the second group SPM machines, four typical machines as shown in green points in Fig. 5.11 are selected with their structures and parameters demonstrated in Fig. 5.39 and Table 5.16. Similar to the first group SPM machines, the optimized models have almost same north and south pole widths, which can reduce the unbalance between two poles. Also, conventional SPM with equal north and south pole arc widths are also selected for comparison.

The flux densities, flux linkages, inductances, and torque performances for these six machines are shown in Fig. 5.40 to Fig. 5.47, Table 5.17, and Table 5.18. Similar to the first group SPM machines, the pole-shaped machines tend to have additional flux density harmonics. But these harmonics can be eliminated in winding flux linkages, which will not lead to odd order torque ripples. In addition, symmetrical and asymmetric pole-shaped machines have similar torque ripple levels, which confirms the analysis in section III.

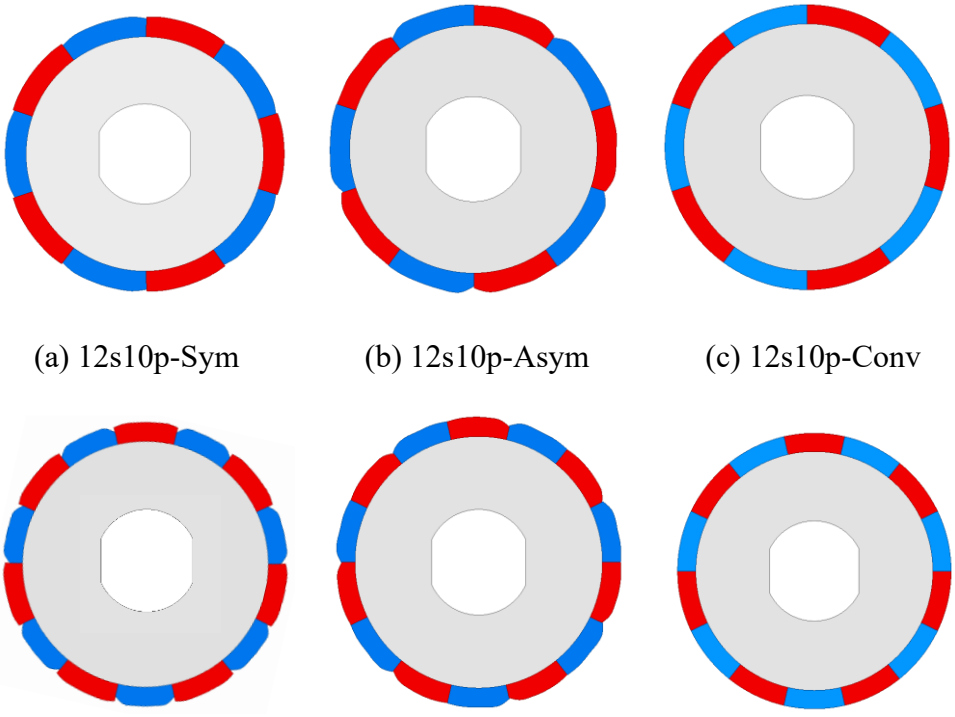

(a) 12s10p-Sym (b) 12s10p-Asym (c) 12s10p-Conv

(d) 12s14p-Sym (e) 12s14p-Asym (f) 12s14p-Conv

Fig. 5.39 Optimized models for Group 2 - SPM machines.

Table 5.16. Rotor Parameters for 4 Pole-Shaped SPM Models

12s10p-Sym (mm)		12s10p-Asym (mm)				12s14p-Sym (mm)		12s14p-Asym (mm)			
Rm_1	27.05	Rm_1	26.09	Ri_1	27.40	Rm_1	26.22	Rm_1	26.49	Ri_1	27.26
Rm_2	27.48	Rm_2	27.43	Ri_2	27.35	Rm_2	27.43	Rm_2	27.38	Ri_2	27.43
Rm_3	27.49	Rm_3	27.41	Ri_3	27.45	Rm_3	27.45	Rm_3	27.50	Ri_3	27.49
Rm_4	27.49	Rm_4	27.34	Ri_4	27.26	Rm_4	27.48	Rm_4	27.37	Ri_4	27.48
Ri_1	27.40	Rm_5	27.36	Ri_5	27.37	Ri_1	27.15	Rm_5	27.44	Ri_5	27.39
Ri_2	27.50	Rm_6	27.48	Ri_6	27.34	Ri_2	27.50	Rm_6	27.43	Ri_6	27.21
Ri_3	27.49	Rm_7	27.47	Ri_7	26.44	Ri_3	27.47	Rm_7	27.31	Ri_7	26.29
Ri_4	27.50	θm_p	35.43			Ri_4	27.48	θm_p	25.84		
θm_p	34.52					θm_p	26.42				

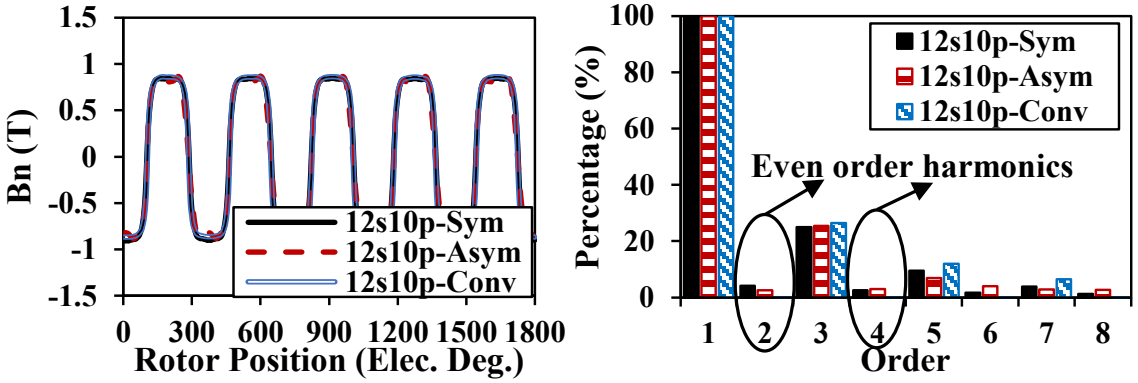

(a) 12s10p

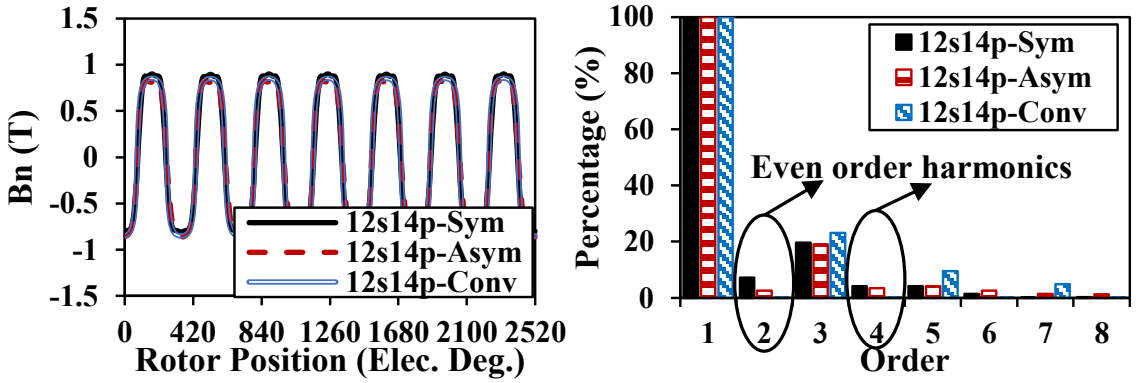

(b) 12s14p

Fig. 5.40 Air-gap flux density.

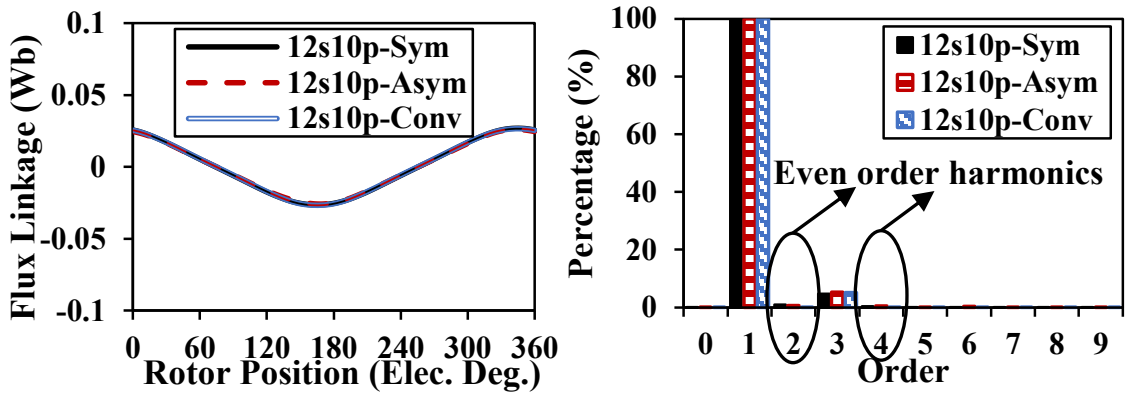

(a) 12s10p

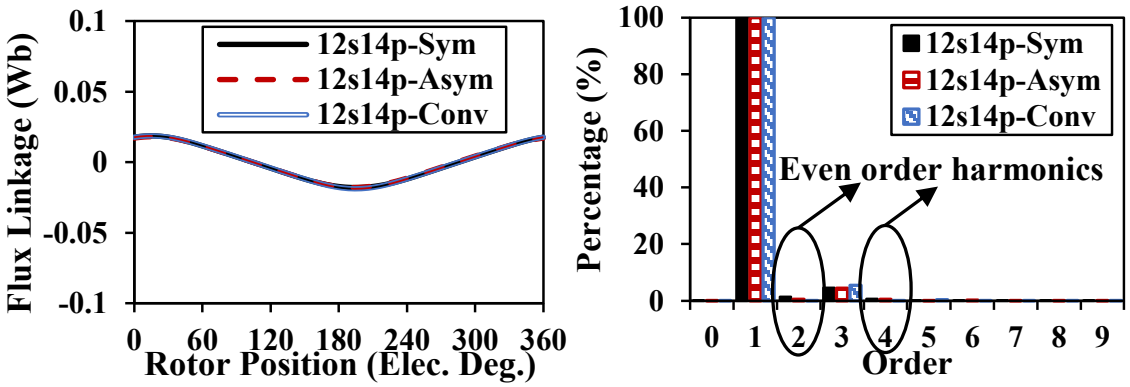

(b) 12s14p

Fig. 5.41 Open-circuit flux linkages for one coil.

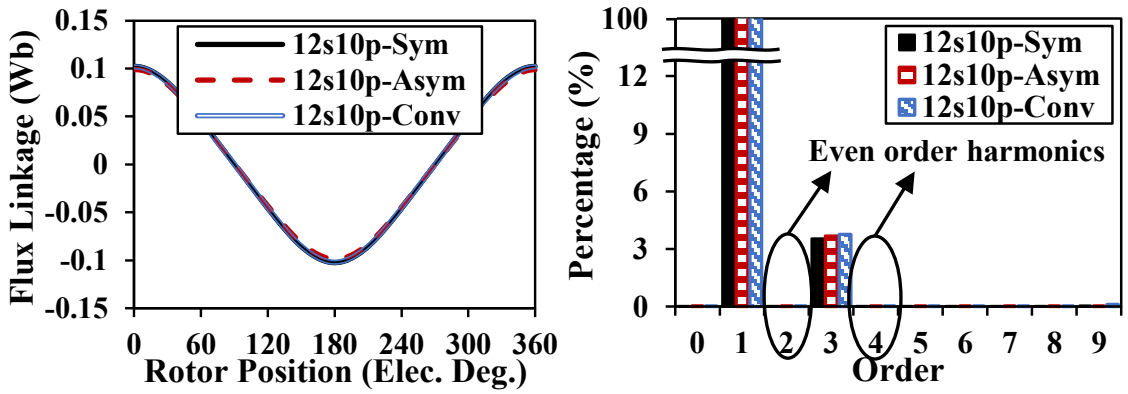

(a) 12s10p

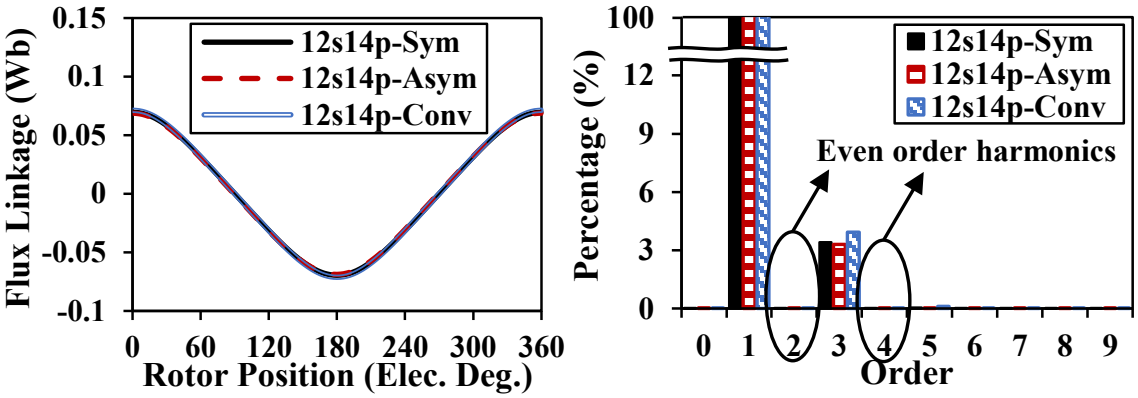

(b) 12s14p

Fig. 5.42 Open-circuit flux linkages for one phase winding.

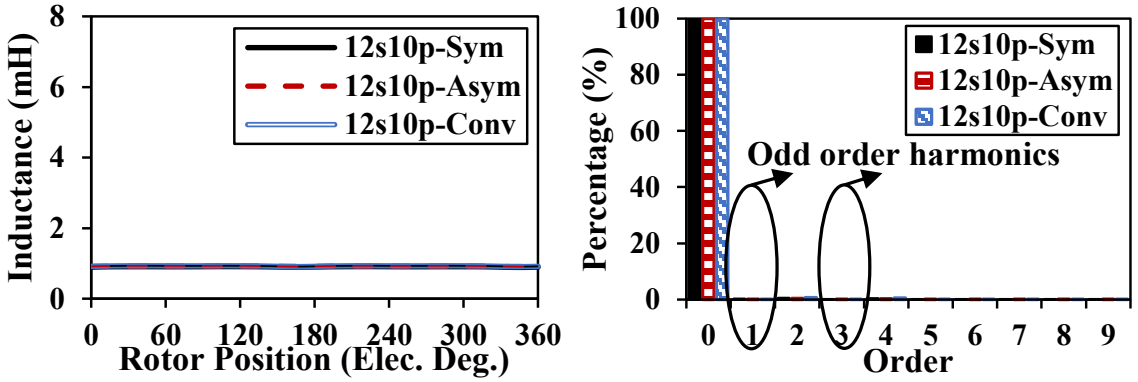

(a) 12s10p

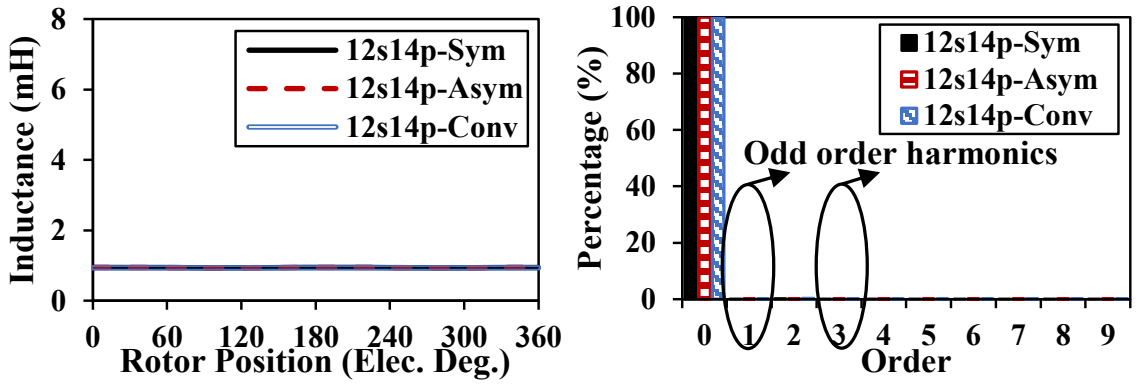

(b) 12s14p

Fig. 5.43 Inductances for one coil.

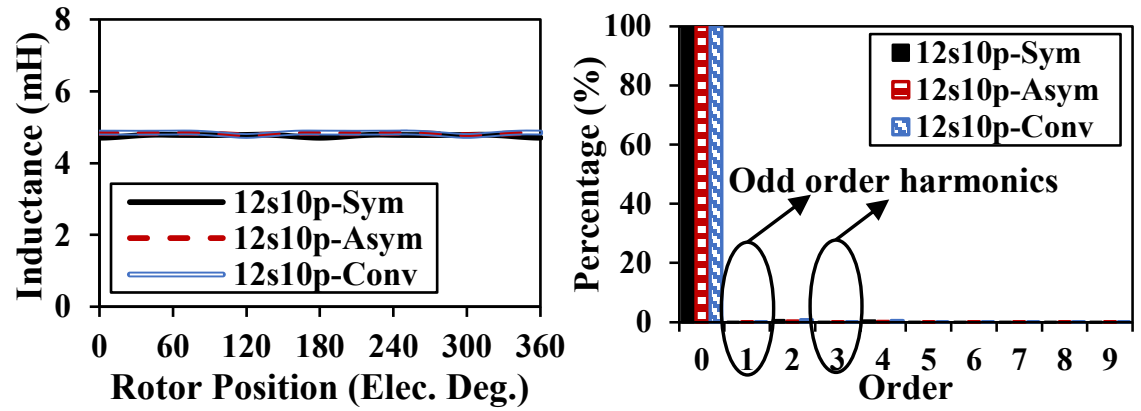

(a) 12s10p

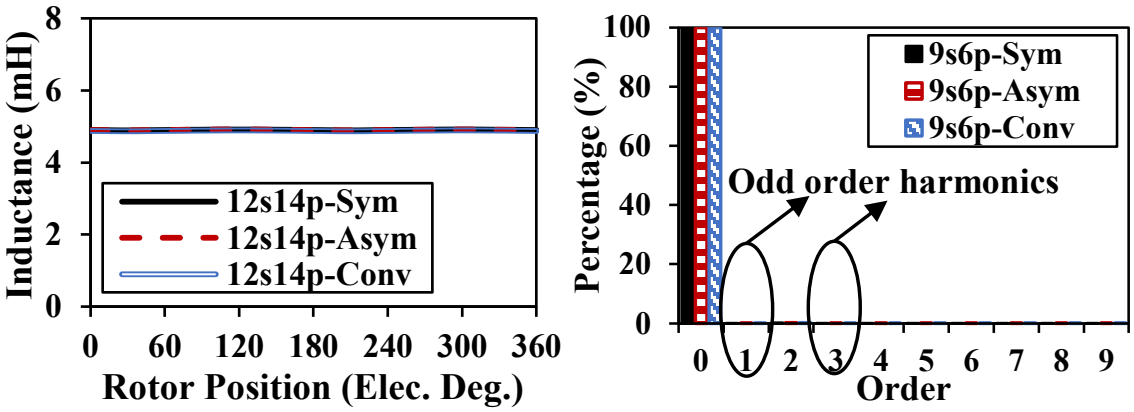

(b) 12s14p

Fig. 5.44 Inductances for one phase winding.

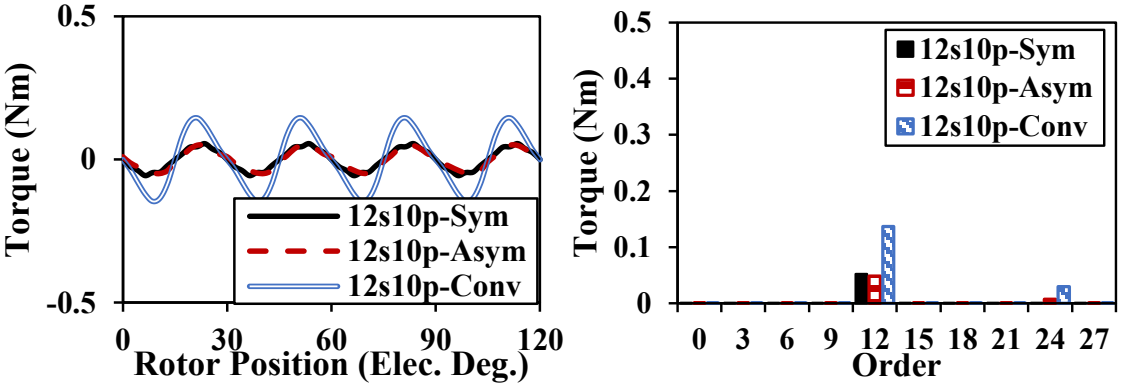

(a) 12s10p

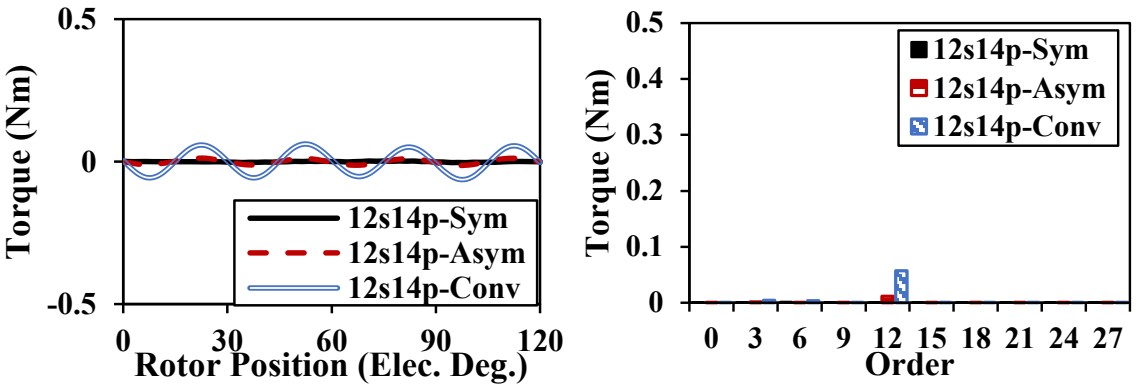

(b) 12s14p

Fig. 5.45 Cogging torque.

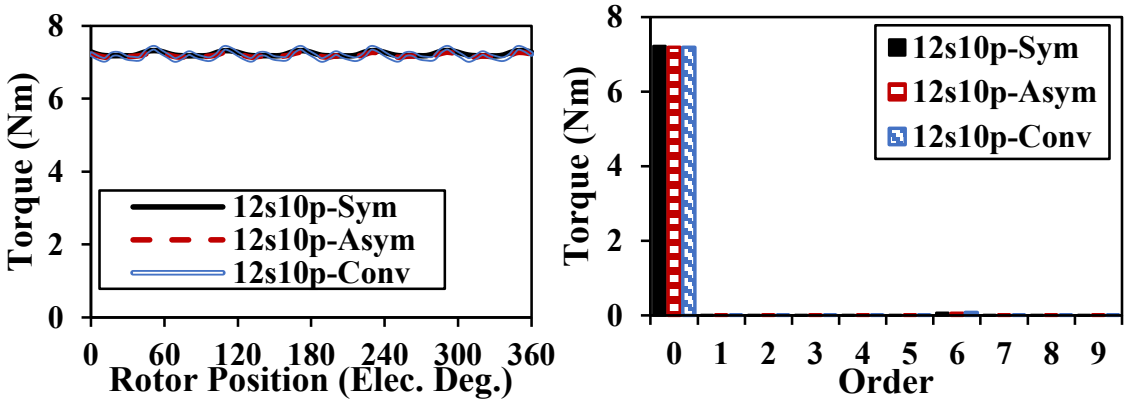

(a) 12s10p

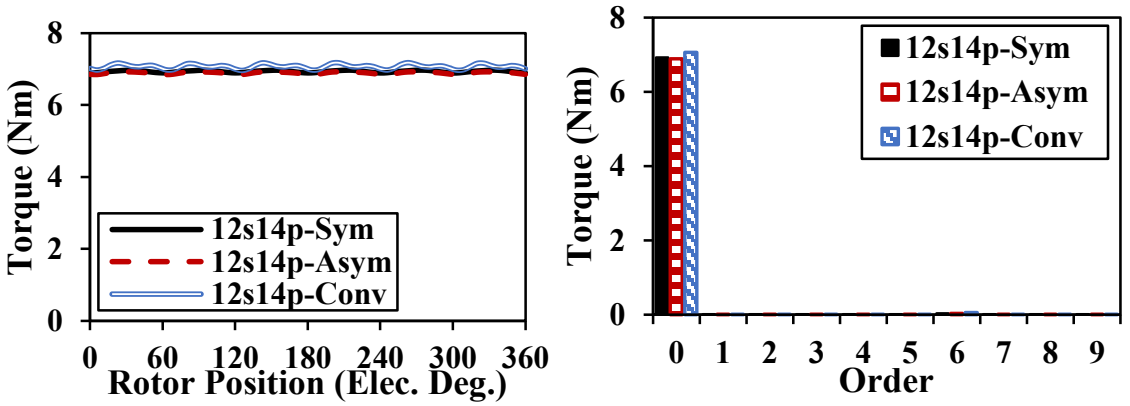

(b) 12s14p

Fig. 5.46 Rated torque.

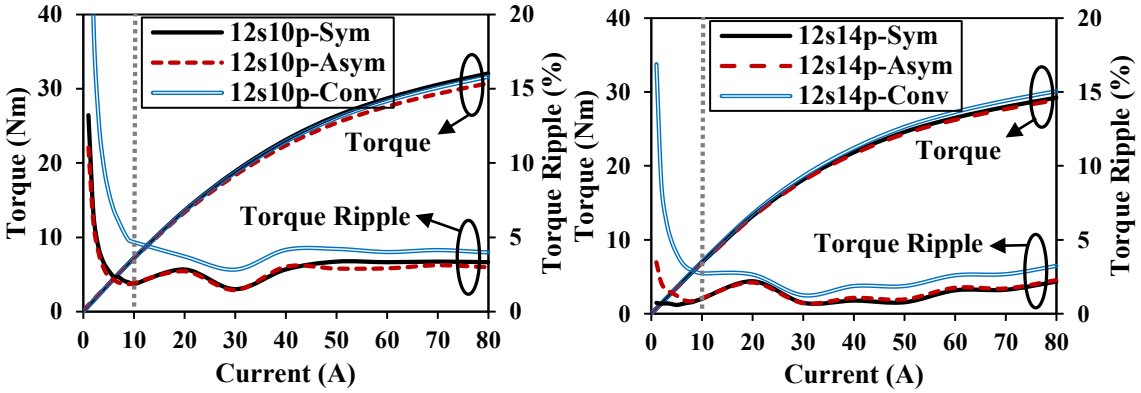

(a) 12s10p (b) 12s14p

Fig. 5.47 Torque characteristics under different loads.

Table 5.17. Summary of Cogging Torque of Analyzed Machines

Machine	12s10p			12s14p		
	Sym	Asym	Conv.	Sym	Asym	Conv.
$T_{cogging}$ (mNm)	112	100	292	5	26	123

Table 5.18. Torque Characteristics and PM Utilization Ratio Comparison

Parameters	12s10p			12s14p		
	Sym.	Asym.	Conv.	Sym.	Asym.	Conv.
6^{th} (Nm)	0.0678	0.0522	0.0783	0.0343	0.0344	0.0582
12^{th} (Nm)	0.0219	0.027	0.1101	0.004	0.009	0.0551
T_{pp} (Nm)	0.14	0.14	0.34	0.07	0.08	0.22
T_{avg} (Nm)	7.23	7.19	7.20	6.93	6.89	7.07
η_{PM} (Nm/m^3)	2.3×105	2.4×105	2.4×105	2.4×105	2.4×10^5	2.4×10^5
T_{ripple} (%)	1.9	1.9	4.7	1.1	1.1	3.0

5.5.3 Comparison

From the previous analysis, the characteristics of basic performances as well as the pole-shaped models for two groups of SPM machines can be summarized in Table 5.19 and Table 5.20.

Table 5.19. Characteristics of Basic Performance For SPM Machines

	With Unequal Pole Widths		With Equal Pole Widths	
Machine	Group 1	Group 2	Group 1	Group 2
Flux density in air-gap	With even order harmonics.		Without even order harmonics.	
Coil flux linkage	With even order harmonics.		Without even order harmonics.	
Winding flux linkage	With even order harmonics.	Without even order harmonics.	Without even order harmonics.	
Coil inductance	Without odd order harmonics		Without odd order harmonics	
Winding inductance	Without odd order harmonics.		Without odd order harmonics	
Torque ripple	Harmonics orders are multiples of 3.	Harmonics orders are multiples of 6.	Harmonics orders are multiples of 6.	

Table 5.20. Characteristics of Pole-Shaped Models for Two Groups of SPM Machines

Machine	First group e.g. 12s8p, 9s6p, 9s8p etc.	Second group e.g. 12s10p, 12s14p, 6s10p etc.
Pole shaping method	Symmetrical pole shaping method can achieve a similar level of torque ripple as that of asymmetric method but with lower optimization complexity.	
Pole arc width	North and south pole arc need to be almost identical.	

5.6 Comparisons Between CPPM and SPM Machines

Based on the above analyses, the characteristics of CPPM and SPM machines in terms of air-gap flux density, winding flux linkage, inductance, torque ripples, and effects of pole shaping machines are compared in Table 5.21.

Table 5.21. Characteristics Comparison of CPPM and SPM Machines

Machine	CPPM	SPM
First group	• Even order harmonics in air-gap flux density can produce corresponding harmonics in winding flux linkage. • Odd order harmonics in inductance cannot be eliminated. • Torque ripple harmonics orders are multiples of 3. • Compared with symmetrical pole shaping method, asymmetric pole shaping method can contribute to lower torque ripple.	• Even order harmonics in air-gap flux density can produce corresponding harmonics in winding flux linkage. • There are no harmonics in inductance. • Torque ripple harmonics orders are multiples of 3 with unequal north and south pole widths, while they are 6 with equal pole widths. • Symmetrical and asymmetric pole shaping methods have similar capabilities in torque ripple reduction.
Second group	• Even order harmonics in winding flux linkage can be eliminated due to cancellation effect of coil connections. • There are no odd order harmonics in inductance. • Torque ripple harmonics orders are multiples of 6. • Symmetrical and asymmetric pole shaping methods have similar capabilities in torque ripple reduction.	

5.7 Experimental Verification and Discussion

Two stators with 12-slot and 6 CPPM rotors with both 8-pole and 10-pole are manufactured as shown in Fig. 5.48. The on-load torque is tested on the dynamic platform, Fig. 3.18, while the inductances are measured on the static platform, Fig. 4.24.

Although the manufacturing cost will be relatively higher for the low volume prototyping of pole-shaped CPPM machines, the cost will be almost the same as conventional CPPM machines in mass production since the increased cost of mold can be minor [Du19].

(a) Stators

(b) Rotors

Fig. 5.48 Manufactured prototypes with and without shaping (the left is 8-pole and the right is 10-pole).

5.7.1 Back EMF

For the phase back EMF tests, a dc motor is used to drive the rotor of the prototype machine. Fig. 5.49 shows the measured and predicted phase back EMFs with the rotor position at 400rpm, whereas Fig. 5.50 presents the dominant harmonics of measured back EMF. It can be observed that 12s8p CPPM machines have even order harmonics while 12s10p CPPM machines only have odd order harmonics, which validates the theoretical and FEM analyses.

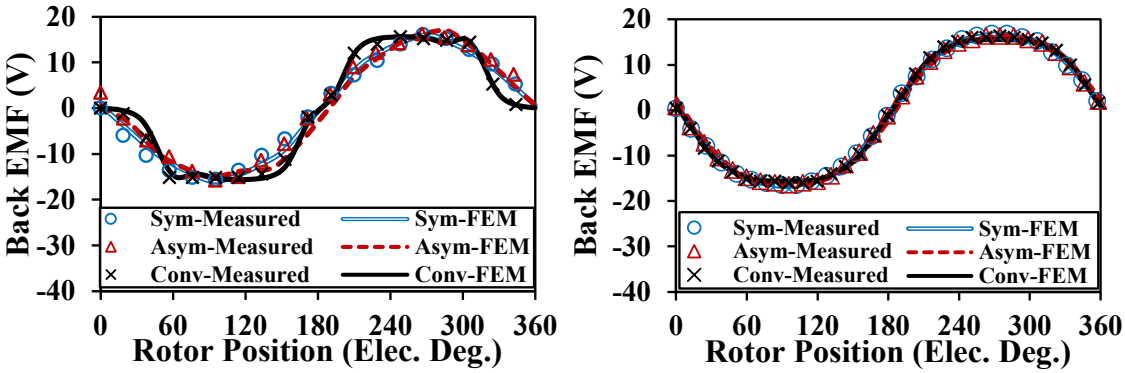

(a) 12s8p machines (b) 12s10p machines

Fig. 5.49 Measured and FEM predicted back EMFs at 400 rpm.

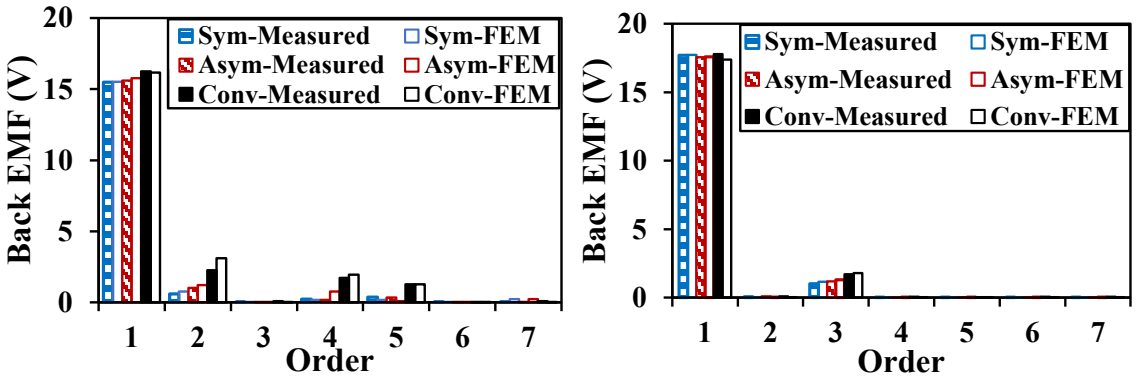

(a) 12s8p (b) 12s10p

Fig. 5.50 Spectrum comparisons of measured and predicted back EMFs.

5.7.2 Inductances

Fig. 5.51 and Fig. 5.52 compare the measured and FEM predicted phase inductance waveforms and spectra. It can be seen that the periods of the experimental results agree well with the predicted ones. The small odd order harmonics in 12s10p machines are caused by the asymmetric coil features in the winding process.

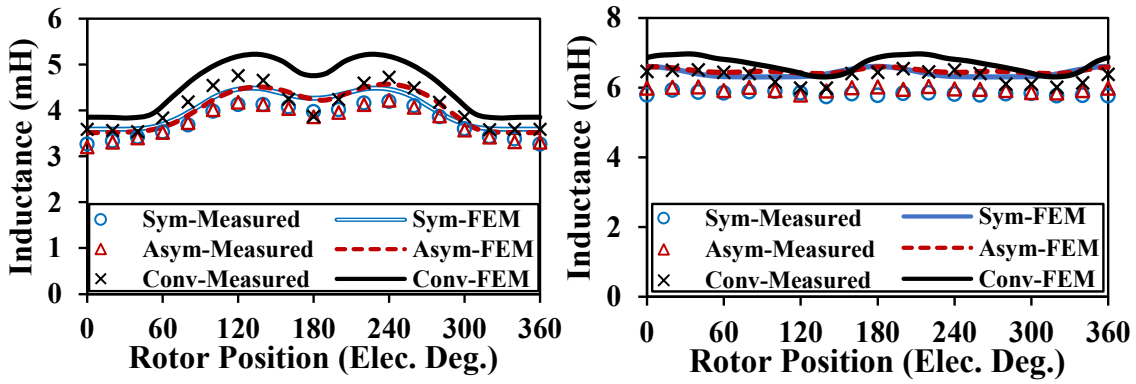

(a) 12s8p machines (b) 12s10p machines

Fig. 5.51 Measured and FEM predicted self-inductances.

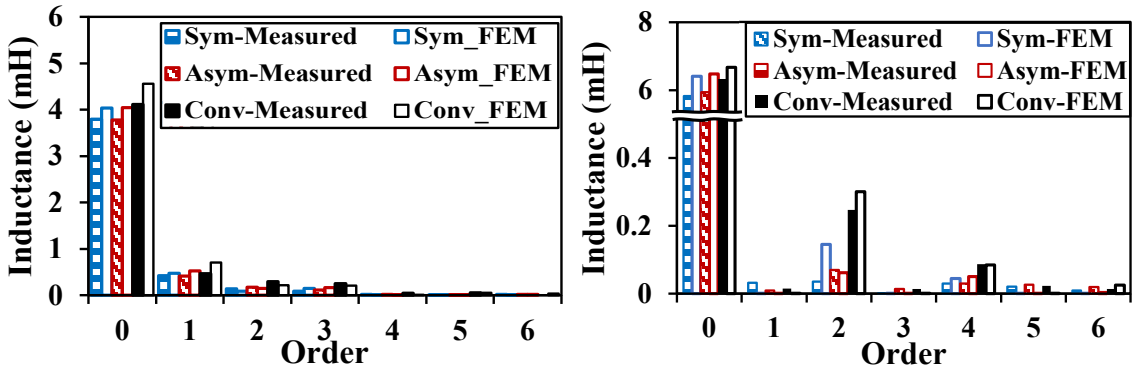

(a) 12s8p (b) 12s10p

Fig. 5.52 Spectrum comparisons of measured and predicted inductances.

5.7.3 Torque Waveform

By utilizing the online torque transducer, the measured and predicted rated torques under I_q=10A are compared in Fig. 5.53 and Fig. 5.54. It is obvious that the 12s8p-Asym has the lowest torque ripple among all the 12s8p CPPM machines while both the 12s10p-Sym and 12s10p-Asym machines have lower torque ripple than the 12s10p-Conv machine, which confirms the FEM results.

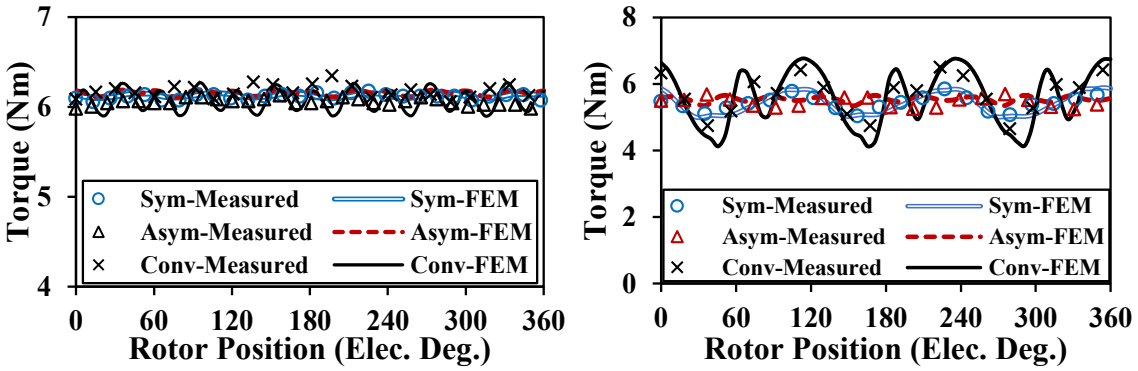

(a) 12s8p machines (b) 12s10p machines

Fig. 5.53 Measured and FEM predicted torque waveforms for prototypes (I_q=10A).

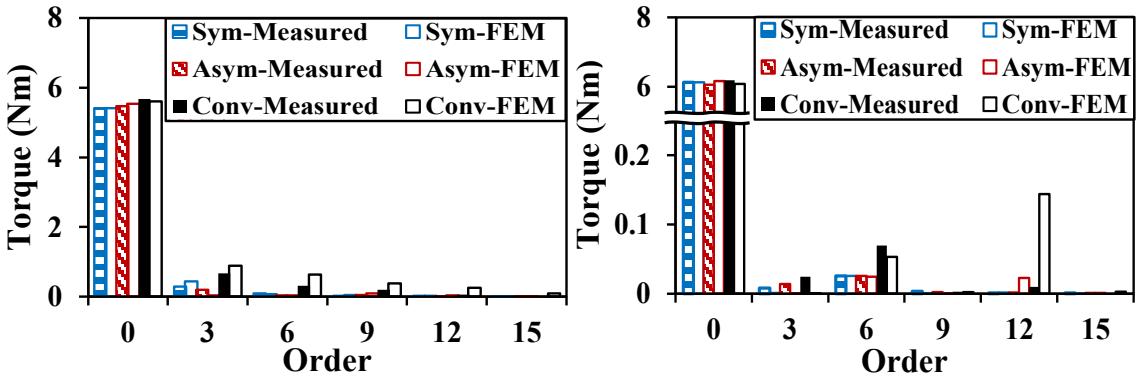

(a) 12s8p (b) 12s10p

Fig. 5.54 Spectrum comparisons of measured and predicted torques.

In general, good agreements can be obtained in back EMFs, inductances, and torque waveforms. There are slight differences between the measured and predicted values since the 2-dimensional FEM models are used and also the perfect manufacture and assembly of the prototype machines are assumed.

5.8 Conclusion

This chapter has investigated the effects of slot/pole number combinations on various electromagnetic performances and effect of symmetrical and asymmetric pole shaping methods of machines with unequal north and south poles, including both CPPM and SPM machines.

For CPPM machines, when the number of coils per phase in a submachine $N_s/m/\mathrm{GCD}(N_s, p)$ is odd, i.e. the first group (e.g. 12s8p, 9s6p, 9s8p, etc.), even order flux linkages and odd order inductances can be produced in windings. On the contrary, when $N_s/m/\mathrm{GCD}(N_s, p)$ is even, i.e. the second group (e.g. 12s10p, 12s14p, 6s10p, etc.), the effect of unbalanced pole behaviors on windings can be eliminated, as is the same case of conventional SPM machines with equal pole widths. For SPM machines, the performances, including flux linkage harmonics and torque ripples, are the same as CPPM machines, except that the harmonics of inductance for SPM machines are always 0.

For all the SPM machines and the second group CPPM machines, symmetrical pole shaping method can achieve a similar on-load torque ripple as asymmetric pole shaping method but

with lower optimization complexity. However, for the first group CPPM machines, asymmetric pole shaping method shows a better effect on torque ripple reduction, compared with symmetrical pole shaping method.

CHAPTER 6
INFLUENCE OF ARMATURE REACTION ON ELECTROMAGNETIC PERFORMANCE AND POLE SHAPING EFFECT IN CONSEQUENT POLE PM MACHINES

CPPM machines can improve the ratio of average torque to PM volume, but suffer from more serious armature reactions. In this chapter, the variations of electromagnetic performance of SPM, conventional CPPM machines, and pole-shaped CPPM machines with armature reaction at currents up to 5 times overload are analyzed and compared. The flux densities, flux linkages, back EMFs, inductances, torque characteristics, and demagnetization withstand capabilities are analyzed by the FEM and frozen permeability method. It is validated that the third order harmonics in inductances for CPPM machines tend to be reduced as current rises since the saturation in iron pole is prone to reducing the saliency effect. But the armature reaction tends to result in the increase of torque ripple components for all the machines. It is also found that the overall torque ripple of the asymmetric pole-shaped machine tends to increase significantly under overload conditions. On the contrary, the symmetrical pole-shaped machine can maintain a relatively stable torque ripple under overload conditions which is similar to the SPM counterpart. Additionally, due to the large armature reactions, CPPM machines suffer from weaker demagnetization withstand capabilities and weaker overload capabilities than their SPM counterparts. Four CPPM prototypes with and without pole shaping are tested to confirm the FEM analysis.

This chapter has been published on Energies [Qi23]:

[Qi23] J. Qi, Z.Q. Zhu, L. Yan, G.W. Jewell, C.W. Gan, Y. Ren, S. Brockway, and C. Hilton, "Influence of armature reaction on electromagnetic performance and pole shaping effect in consequent pole PM machines," *Energies*, vol. 16, no. 4, pp. 1982, Jan. 2023.

6.1 Introduction

CPPM machines can save the magnet cost, albeit with some problems, including high armature reaction and large torque ripple.

Due to lower flux reluctance along the PM flux path and thus higher inductance, the armature reactions in CPPM machines are more serious than those in conventional SPM counterparts, which will inevitably lead to saturation problems and result in performance variations. [Wu14] [Hu18] found that consequent pole interior PM machines have lower overload capacity than conventional pole IPM machines but without deep analysis. In [Bor21], the influence of armature current on the radial force in eccentric CPPM machines was investigated. A subdomain model was developed in [Zhu19] to predict the armature reaction field in dual-stator CPPM machines. But the saturation is ignored in the analytical model. Obviously, a high armature reaction will inevitably affect the torque ripples for CPPM machines but hitherto without any comprehensive studies.

As for the suppression of torque ripple, pole shaping methods have been analyzed in literatures. Based on an outer rotor CPPM machine with high pole numbers, [Chu16] proposed a non-uniform air-gap profiling method that can reduce the torque ripple. A six-phase machine was optimized to improve torque performance in [Dhu21]. However, the torque ripple of the optimized machine is still larger than that of its SPM counterpart. The pole-end barrier shape can also be optimized to reduce torque ripple as reported in [Wat18] and [Hu18]. The 3rd order harmonic is utilized in the magnet pole shaping in CPPM machines [Zha20a] and the torque ripple can be suppressed. [Qi22a] and [Qi22b] in Chapters 3 and 4 validated that the asymmetric pole shaping method is effective in suppressing the torque ripple for a 12-slot/8-pole (12s8p) CPPM machine. This is followed by the investigation of the influence of slot/pole number combinations as demonstrated in chapter 5, where the CPPM machines are divided into two groups according to the odd/even slot number for one phase in a submachine. It has been validated that the asymmetric pole shaping is more suitable for CPPM machines with odd slot number per phase in a submachine while the symmetrical pole shaping is more suitable for CPPM machines with even slot number per phase in a submachine. However, the influences of

armature reaction on pole-shaped CPPM machines are not fully investigated in all of these literature.

In this chapter, the performances, including flux density, flux linkage, back EMF, inductance, torque, and demagnetization withstand capability under different currents will be analyzed with the FEM. Frozen permeability method will be used to obtain the on-load performances and torque components. The variation of waveforms, harmonics, and contour in these performances will be investigated. In addition, the influence of armature reaction on pole-shaped machines will be analyzed, which shows that the torque ripple of the asymmetric pole-shaped machine will rise significantly as current increases, while that of the symmetrical pole-shaped machine can be relatively stable.

This chapter is arranged as follows. Firstly, the analyzed models, including conventional SPM, conventional CPPM (CCPPM), and pole-shaped CPPM (PSCPPM) machines, will be introduced in section 6.2. Machines with 12s8p and 12s10p are selected in this chapter for analysis, which covers two groups of CPPM machines that have different performances as has been clarified in chapter 5. In section 6.3, the influences of armature reaction on CCPPM are analyzed and compared with their SPM counterparts. Then, the performances of PSCPPM machines will be investigated and discussed in section 6.4. This is followed by the experimental verification with four prototypes, i.e. 12s8p-CCPPM, 12s8p-PSCPPM, 12s10p-CCPPM, and 12s10p-PSCPPM machines in section 6.5. Finally, important conclusions will be highlighted in section 6.6.

6.2 CPPM Model and Machine Topologies

6.2.1 CPPM Model

As shown in Fig. 6.1, the flux circuits for SPM and CPPM machines are demonstrated. Thus, the magnet fluxes for SPM machine φ_{SPM} and CPPM machine φ_{CPPM} can be obtained:

$$\varphi_{SPM} = \frac{2Fc_{PM}}{2R_{PM} + 2R_{AG} + R_{stator} + R_{rotor}} \tag{6.1}$$

$$\varphi_{CPPM} = \frac{Fc_{PM}}{R_{PM}' + 2R_{AG} + R_{stator} + R_{rotor}'} \tag{6.2}$$

where Fc_{PM} is the magnetic MMF of PMs, R_{AG} and R_{stator} are the flux reluctances in air-gap and stator, R_{PM} and R_{PM}' are the flux reluctances in the magnet for SPM and CPPM machines, respectively, and R_{rotor} and R_{rotor}' are the flux reluctances in the rotor core for SPM and CPPM machines, respectively.

Commonly, the flux reluctances in stator and rotor iron can be treated as 0 in the flux circuit models since the saturation can be neglected. It has been proven that although the magnetic MMF for CPPM machines is half of that for SPM machines, the flux reluctance is also almost halved. Consequently, the magnet fluxes for SPM machine φ_{SPM} and CPPM machine φ_{CPPM} are almost the same. However, when the saturation cannot be neglected, the flux reluctances in stator and rotor iron need to be considered, which will inevitably result in the drop of magnetic flux for both SPM and CPPM machines. Depending on the saturation level, the characteristics of the flux linkages under different load conditions will be different for SPM and CPPM machines. Generally, the saturation levels for CPPM machines are higher due to the higher armature reaction and inductance.

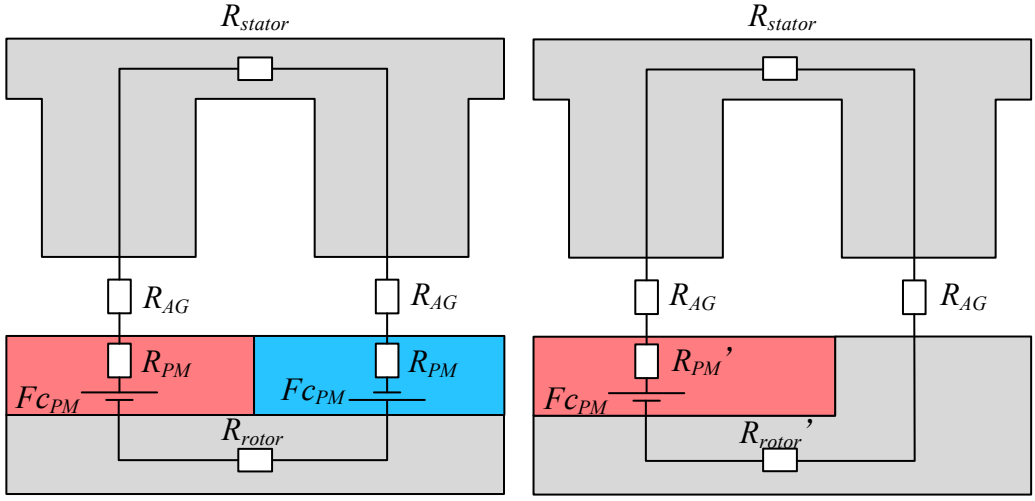

(a) SPM (b) CPPM

Fig. 6.1 Flux circuit models for SPM and CPPM machines.

Apart from the fluxes produced by PMs, the inductances for CPPM machines are also different from those of SPM machines. The average inductance value for CPPM machine L_{CPPM} is also larger than that of SPM counterpart L_{SPM}, which can be explained by the following equations:

$$L_{SPM} = \frac{{N_c}^2}{2R_{PM} + 2R_{AG} + R_{stator} + R_{rotor}} \tag{6.3}$$

$$L_{CPPM} = \frac{{N_c}^2}{{R_{PM}}' + 2R_{AG} + R_{stator} + {R_{rotor}}'} \tag{6.4}$$

where N_c is the number of turns per winding. Obviously, due to the lower flux reluctance for CPPM machines, the inductance value is higher, which will lead to a larger armature reaction and in turn lead to a relatively large variation range in inductance.

In addition, it has been validated in chapter 5 that the harmonic components in winding inductance for CPPM machines are highly dependent on the slot/pole number combination, namely, the inductance contains odd order harmonics when there is an odd slot number for one phase in a submachine, while the inductance only contains even order harmonics when there is an even slot number for one phase in a submachine.

Since saturation due to armature reaction will lead to changes in flux and inductance, the output torque will also be affected. The overall output torque T_e can be considered as being made up of three components: PM excitation torque T_{PM}, reluctance torque T_r, and cogging torque T_{cog} and can be expressed by [Liu05] [Chu98] [Yan19a]:

$$\begin{cases} T_e = T_{PM} + T_r + T_{cog} \\ T_{PM} = \dfrac{3}{2} p i_q \left(\psi_d^{PM} + \dfrac{d\psi_q^{PM}}{d\theta} \right) - \dfrac{3}{2} p i_d \left(\psi_q^{PM} - \dfrac{d\psi_d^{PM}}{d\theta} \right) \\ T_r = \dfrac{3}{2} p i_q i_d \left(L_d - L_q \right) + \dfrac{3}{4} p \left({i_d}^2 \dfrac{dL_d}{d\theta} + {i_q}^2 \dfrac{dL_q}{d\theta} \right) \end{cases} \tag{6.5}$$

where ψ_d^{PM} and ψ_q^{PM} are the dq-axes PM fluxes, i_d and i_q are the dq-axes currents, L_d and L_q are the dq-axes inductances and p is the pole pair number. It is clear that the PM flux linkage will affect the PM torque T_{PM} and the inductance will affect the reluctance torque T_r. The saturation will also influence on-load cogging torque [Aza12]. It is worth noting that although (6.5) is complex enough, it still cannot predict the on-load torque ripple precisely even with on-load values of flux linkages and inductances. This is because the d-/q- axis flux linkages and inductances are calculated from the integral of flux densities under wound teeth area

produced by PMs and unit current, respectively, which cannot describe the influence of local saturations completely. However, local saturations will definitely lead to torque ripples and are quite common under on-load conditions. Therefore, the influences of armature reaction on magnetic flux, inductance, and torque will be comprehensively analyzed by FEM with the frozen permeability method in the following text.

6.2.2 Machine Topologies

It has been pointed out in chapter 5 that the CPPM machines can be divided into two groups according to the slot/pole number combinations. Therefore, in this chapter, a CPPM machine with an odd slot number for one phase in a submachine, 12-slot/8-pole (12s8p), and a CPPM machine with an even slot number for one phase in a submachine, 12s10p, are selected for demonstration, which is denoted as CCPPM machines, i.e. 12s8p-CCPPM and 12s10p-CCPPM machines. As shown in Fig. 6.2, to obtain the maximum average torque, the PM pole arc ratios, i.e. the ratio of PM pole arc to pole pitch, for both 12s8p and 12s10p machines are changed under a fixed amount of magnet and finally set as 1.2. For comparison, the corresponding SPM machines will also be analyzed, namely 12s8p-SPM and 12s10p-SPM machines. To further investigate the influence of armature reaction on pole shaping effect, the 12s8p CPPM machine with asymmetric pole shape and the 12s10p CPPM machine with symmetrical pole shape are also selected for investigation, which show the best performances in the analysis of previous chapters and are denoted as PSCPPM machines, i.e. 12s8p-PSCPPM and 12s10p-PSCPPM machines. With the key parameters summarized in Table 3.1, the relationships for these models are illustrated in Fig. 6.3. It is worth noting that the magnet volumes for CPPM machines are the same and are half of SPM machines. Besides, the temperature of PM is set at 80^{o}C in analysis of demagnetization performances while it is 20^{o}C for other performances.

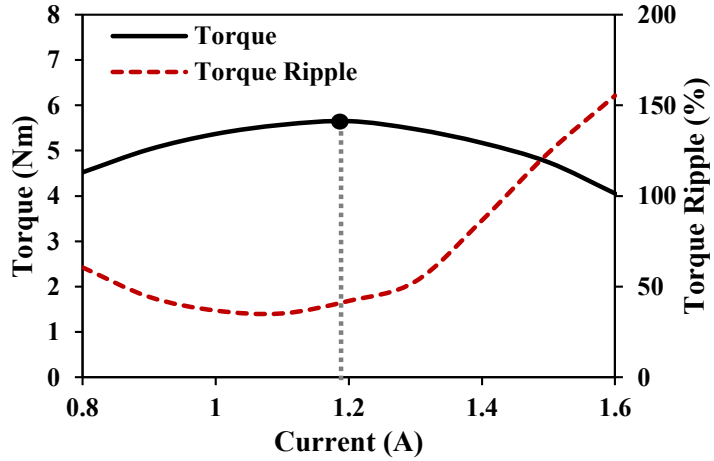

(a) Torque characteristics for 12s8p CCPPM machine

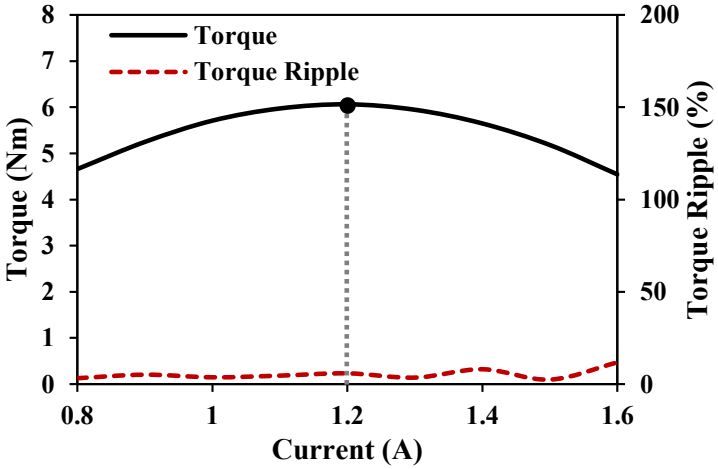

(b) Torque characteristics for 12s10p CCPPM machine

Fig. 6.2 Models for analysis in this chapter.

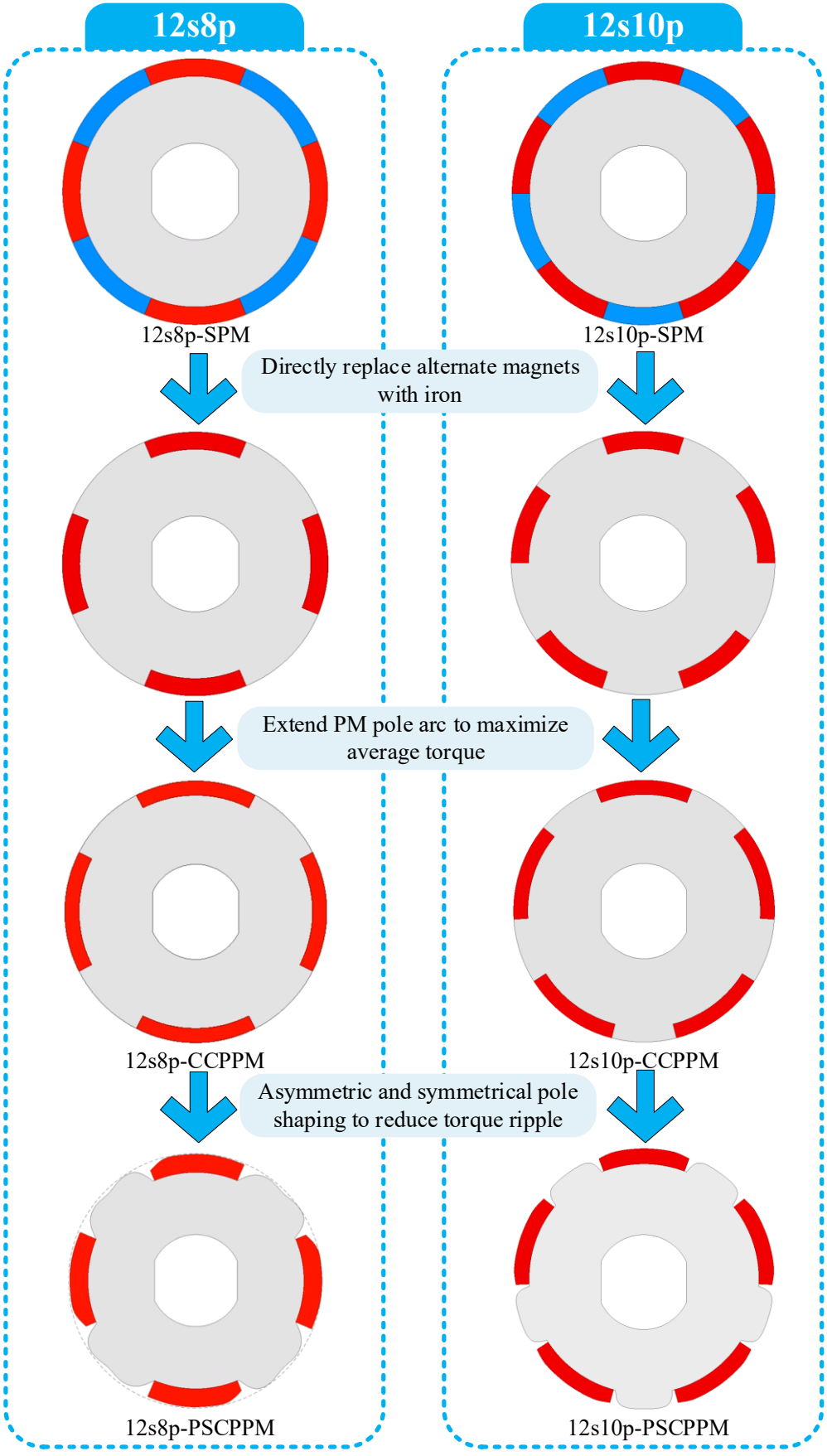

Fig. 6.3 Models for analysis in this chapter.

6.3 Influence of Armature Reaction on CPPM Machines

In this section, the focus is on the influence of armature reaction on CCPPM and SPM machines. Therefore, 12s8p-SPM, 12s8p-CCPPM, 12s10p-SPM, and 12s10p-CCPPM are analyzed and compared, while the 12s8p-PSCPPM and 12s10p-PSCPPM will be analyzed in the next section to demonstrate the influence of armature reaction on pole shaping effect.

The frozen permeability method in JMAG is employed to obtain the on-load performances, including flux density, flux linkage, back EMF, inductance, and torque components. The calculation process can be briefly described as follows:

(1) The model runs under the load condition, and the permeability of iron part at each step in each step is recorded.

(2) Then, the materials with those recorded permeabilities can be treated as linear at each step and the model will be run again without current to obtain the on-load cogging torque, flux density, PM flux linkage, and back EMF.

(3) With the same recorded permeabilities, the model will be run without magnets to obtain the on-load reluctance torque. After that, the on-load PM torque can be obtained by making the difference between the total torque and the other two components.

(4) With the same recorded permeabilities, unit direct current in one phase winding is injected to obtain the flux linkage in each phase. Then, the inductances can be obtained from (6.6) in *abc*-frame. Finally, the inductances in *abc*-frame will be transferred to *dq*-axes in Matlab.

$$L = \frac{\Psi}{I_{unit}} \tag{6.6}$$

where I_{unit} is the unit current, namely 1A, Ψ and L are the corresponding flux linkage and inductance.

Several armature reaction conditions are selected as given in Table 6.1. Since the reluctance torques for CPPM machines are too small to be utilized, as verified in chapter 3, the current advanced angle is set as 0 for all the conditions.

Table 6.1 Key Design Parameters of Analyzed Machines

Case	Speed (rpm)	Peak Current (A)
Open Circuit	400	0
On-load		10 (Rated)
		20
		30
		40
		50

6.3.1 Magnetic Flux Density Characteristics

With the frozen permeability method, the PM magnetic flux density in air-gap under open circuit and on-load conditions are obtained as shown in Fig. 6.4 and Fig. 6.5. Clearly, as the current increases, the deformation of the waveform becomes more severe and the amplitudes of fundamental flux densities show a decreasing trend. It can also be found that the decrease of CCPPM is more pronounced than that of SPM, which is due to the larger armature reaction that caused saturation for CCPPM machines.

The equal potential distributions for these machines under different current conditions are demonstrated in Fig. 6.6 to Fig. 6.9. It can be found that the PM fluxes can be shifted with the current increase for all machines. Additionally, the fluxes of armature currents are mainly concentrated on several teeth under light load conditions and tend to distribute on more teeth as the current rises.

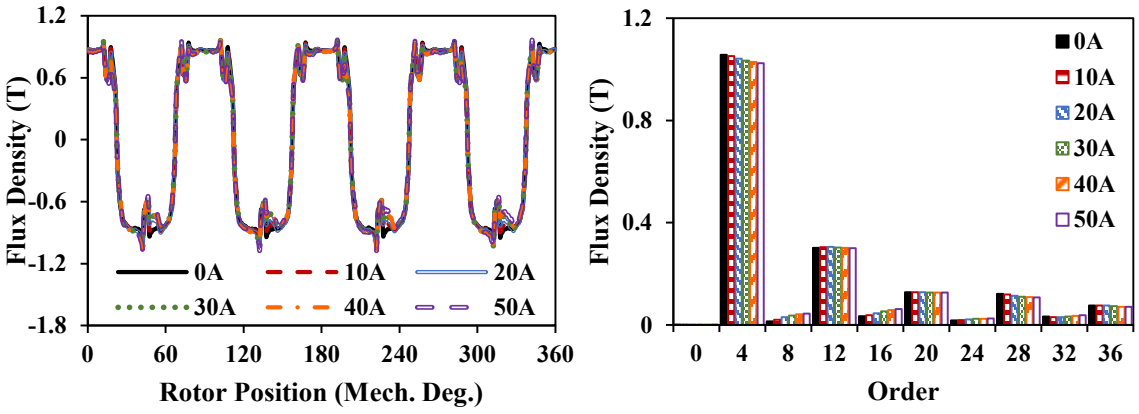

(a) 12s8p-SPM

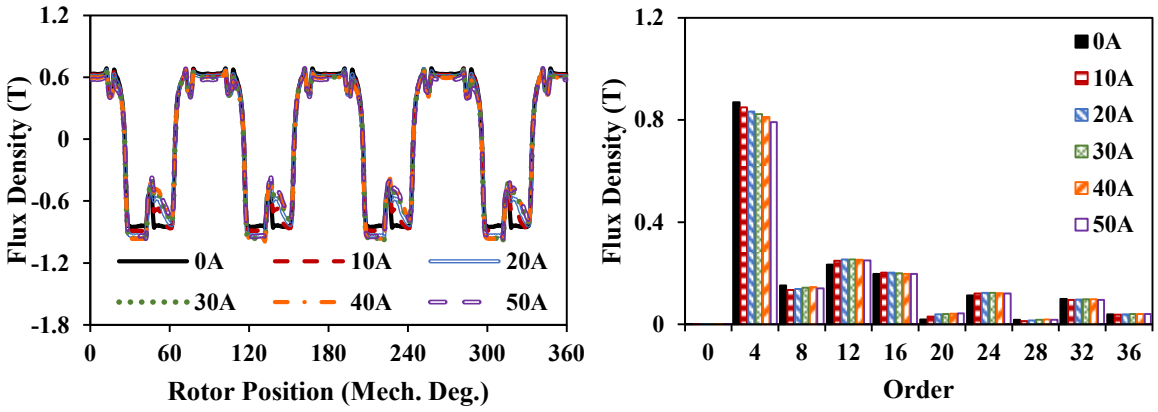

(b) 12s8p-CCPPM

Fig. 6.4 Air-gap flux densities and spectra for 12s8p machines.

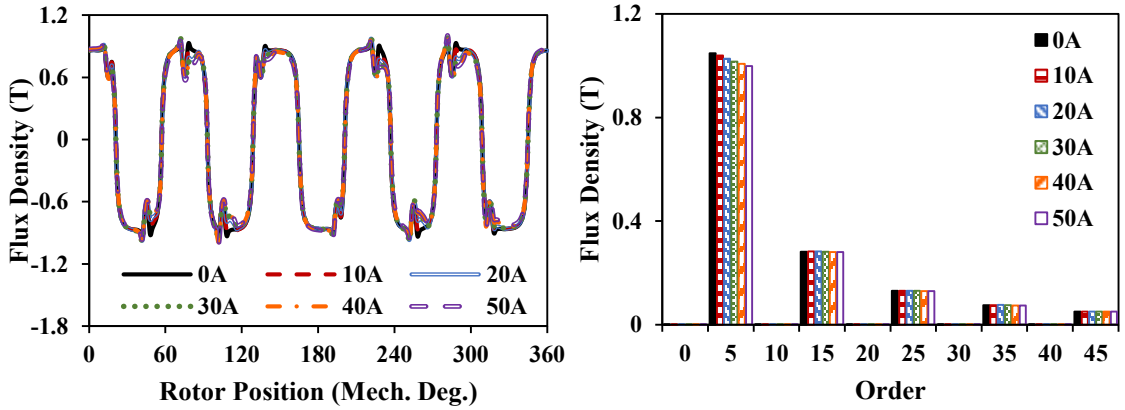

(a) 12s10p-SPM

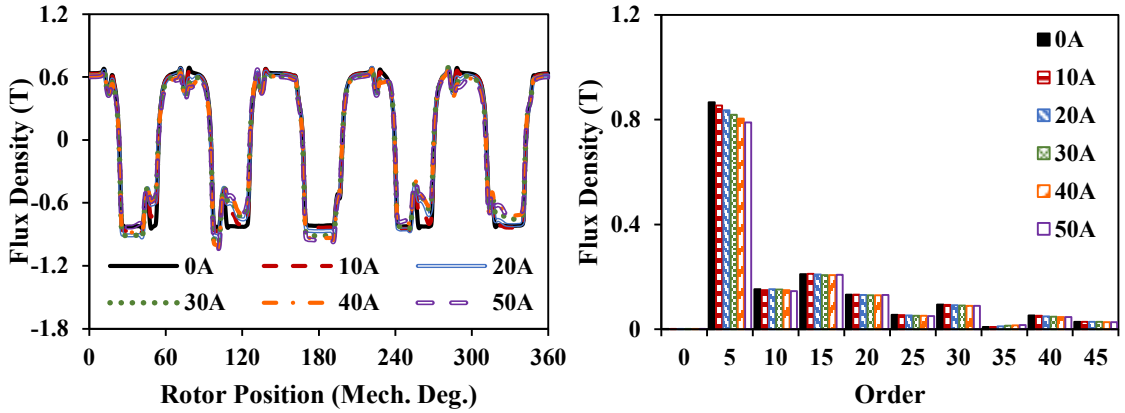

(b) 12s10p-CCPPM

Fig. 6.5 Air-gap flux densities and spectra for 12s8p machines.

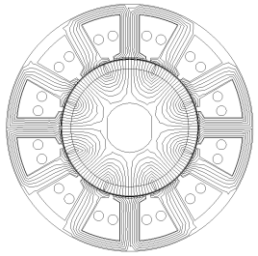

(a) 0A

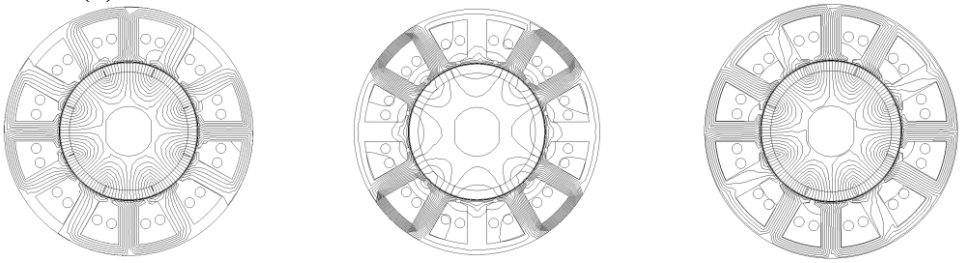

(b) 10A

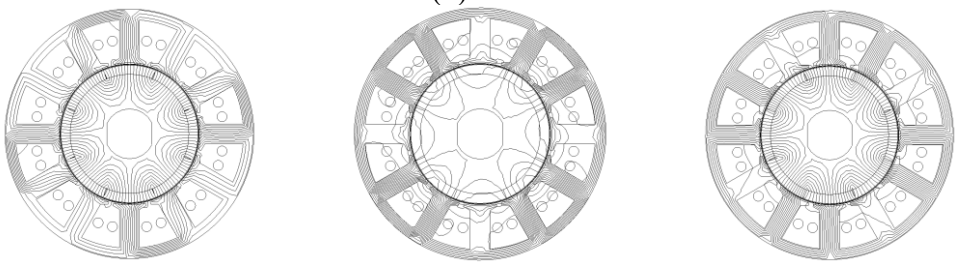

(c) 20A

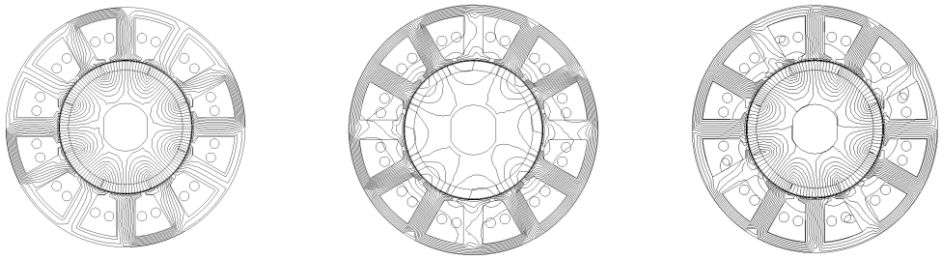

(d) 30A

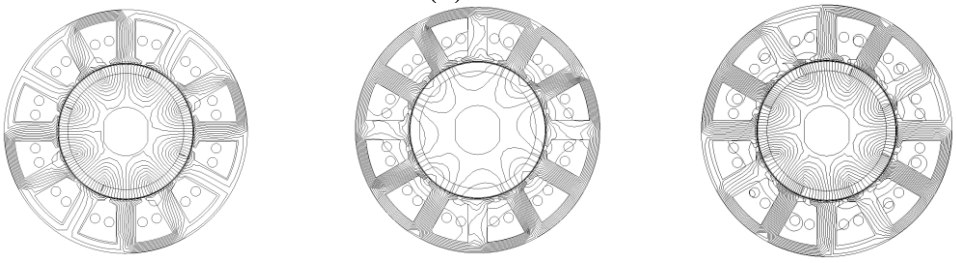

(e) 40A

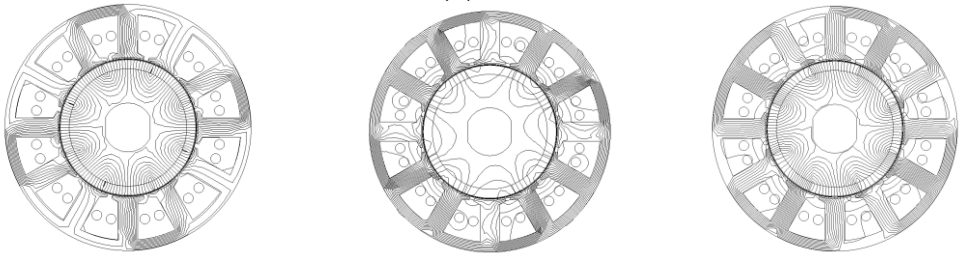

(f) 50A

Fig. 6.6 Equal potential distributions for 12s8p-SPM. (from left to right: PM only, armature current only, overall)

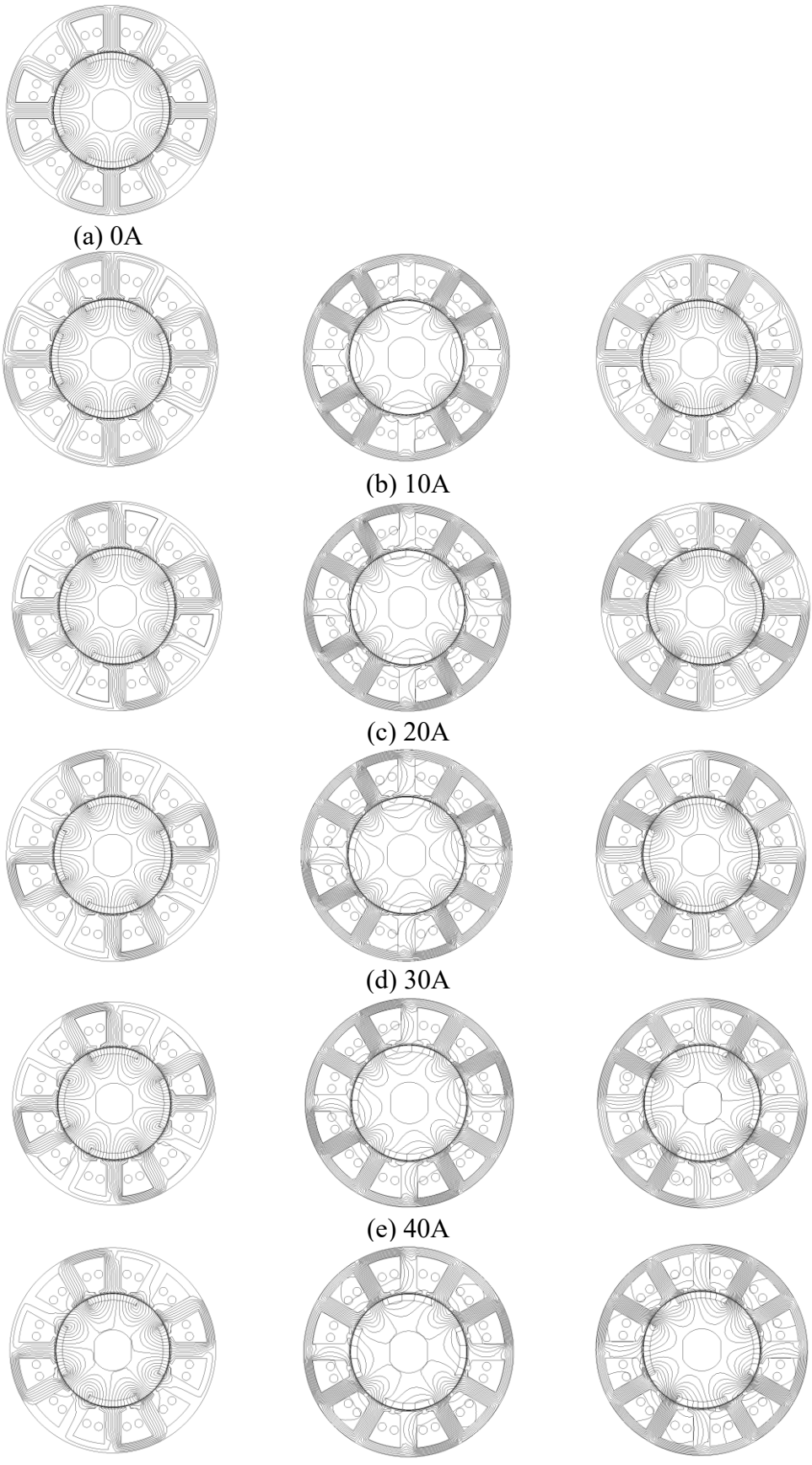

(a) 0A

(b) 10A

(c) 20A

(d) 30A

(e) 40A

(f) 50A

Fig. 6.7 Equal potential distributions for 12s8p-CCPPM. (from left to right: PM only, armature current only, overall)

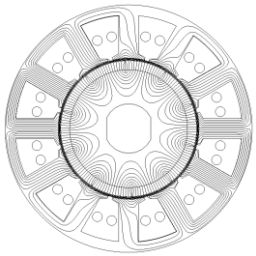

(a) 0A

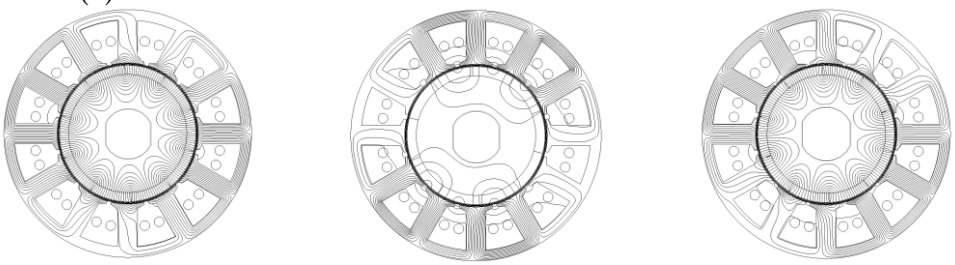

(b) 10A

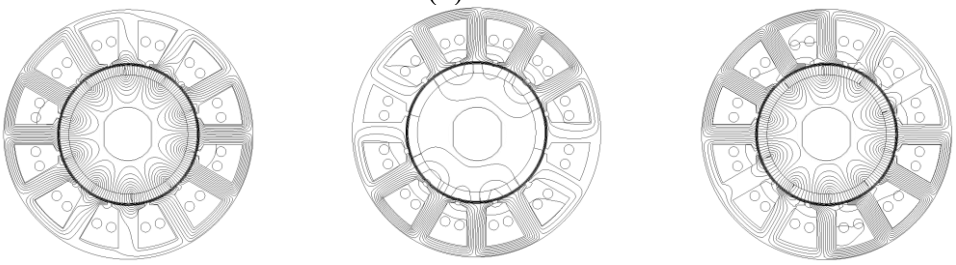

(c) 20A

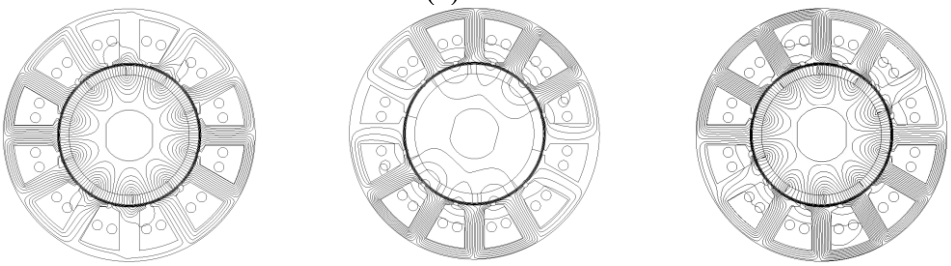

(d) 30A

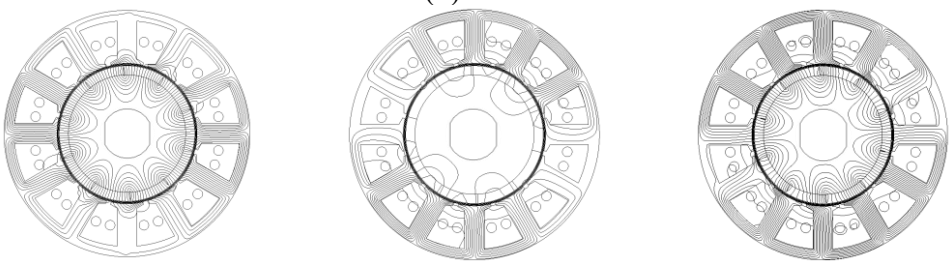

(e) 40A

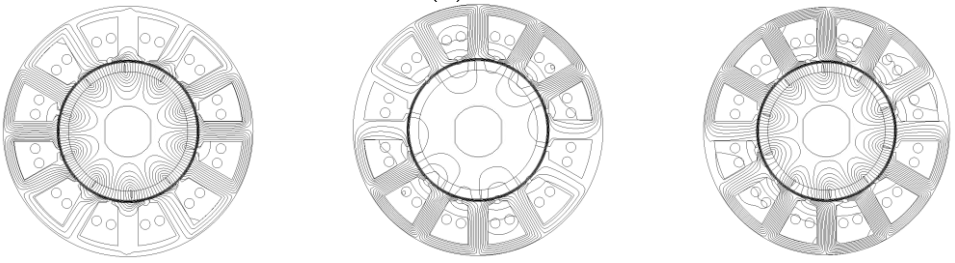

(f) 50A

Fig. 6.8 Equal potential distributions for 12s10p-SPM. (from left to right: PM only, armature current only, overall)

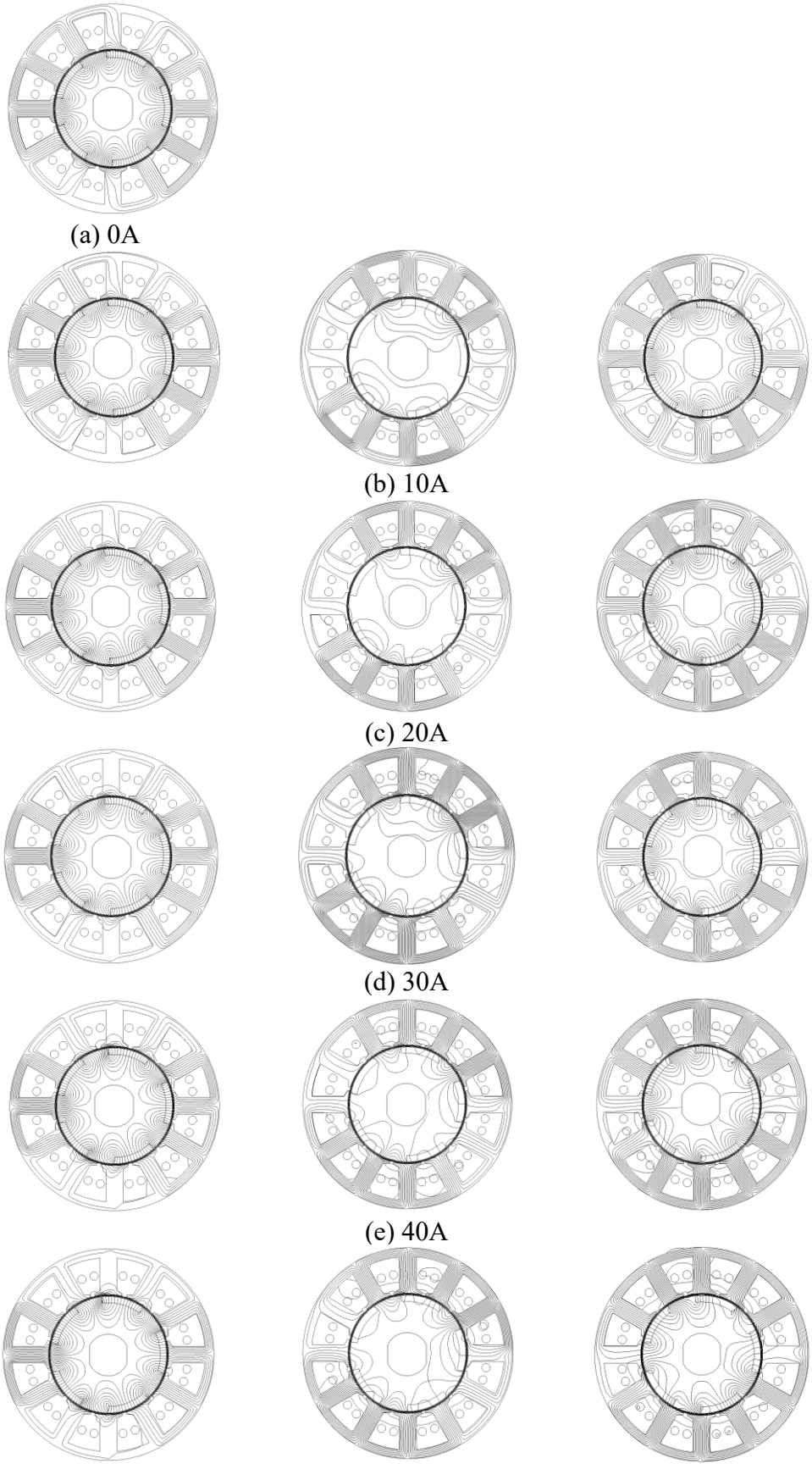

(a) 0A

(b) 10A

(c) 20A

(d) 30A

(e) 40A

(f) 50A

Fig. 6.9 Equal potential distributions for 12s10p-CCPPM. (from left to right: PM only, armature current only, overall)

6.3.2 PM Flux-linkage and Back EMF Characteristics

Fig. 6.10 and Fig. 6.11 show the amplitude variation of fundamental components (fundamental torque production harmonics) in phase A under different currents. Obviously, armature reaction has a negative influence on the amplitudes of PM flux-linkage and corresponding back-EMF for both SPM and CCPPM machines. Besides, the effects in the CPPM machines are more significant as proved by the larger variation range in both PM flux linkages and back EMFs. Fig. 6.12 to Fig. 6.15 show the *d*-/*q*-axis flux linkages and back-EMFs. It is clear that as the current rises, the amplitudes of harmonics are prone to increase, which can result in larger PM torque ripples. It can also be seen that the *q*-axis PM flux linkages and back-EMFs increase with the current increase, which means that the phase angles of PM fluxes can be shifted by the saturation produced by the armature reaction.

It should be noted that there exist 3rd order harmonics in 12s8p-CCPPM machine, while there are no 3rd order harmonics in 12s8p-SPM machine, which is because of the unbalance in CPPM rotor. However, there are no 3rd order harmonics in both 12s10p-CCPPM and 12s10p-SPM machines, which is due to the compensation effect in 12s10p-CCPPM.

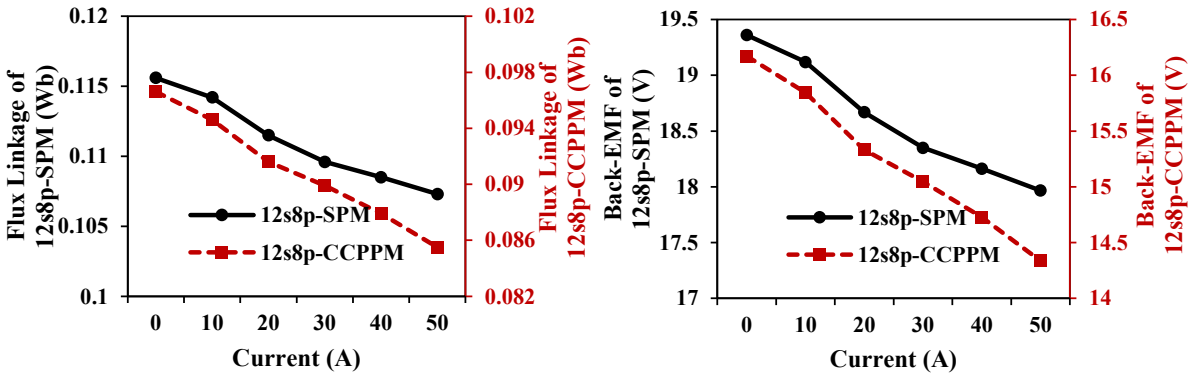

Fig. 6.10 Amplitudes of fundamental harmonics in phase-A for 12s8p machines.

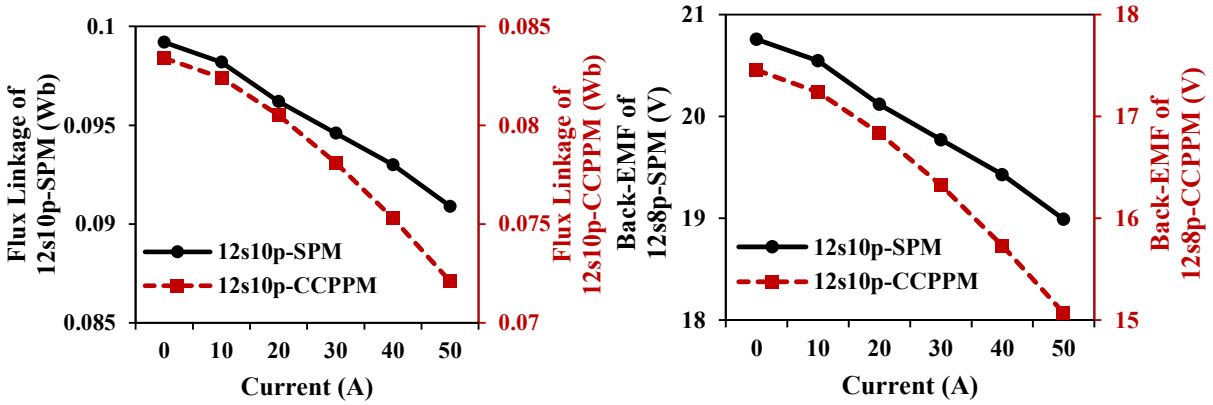

Fig. 6.11 Amplitudes of fundamental harmonics in phase-A for 12s10p machines.

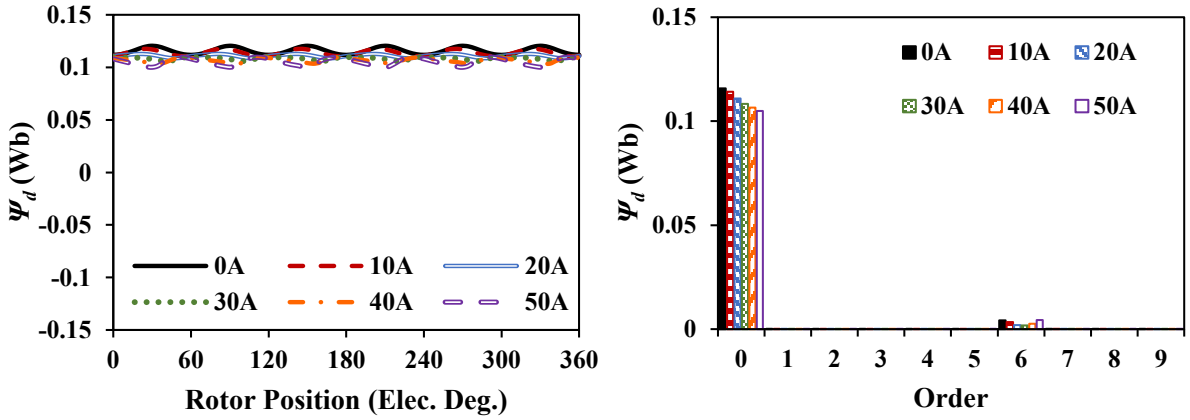

(a) D-axis flux linkage of 12s8p-SPM

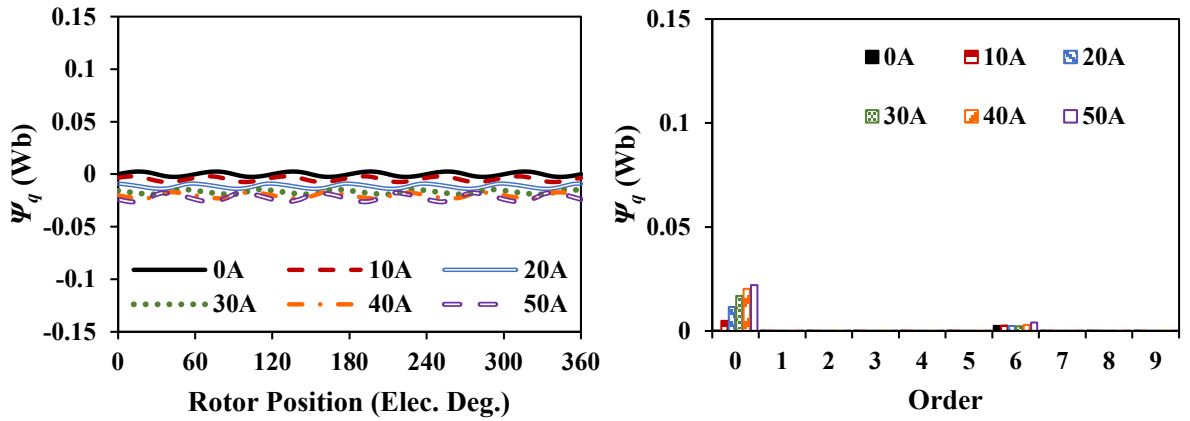

(b) Q-axis flux linkage of 12s8p-SPM

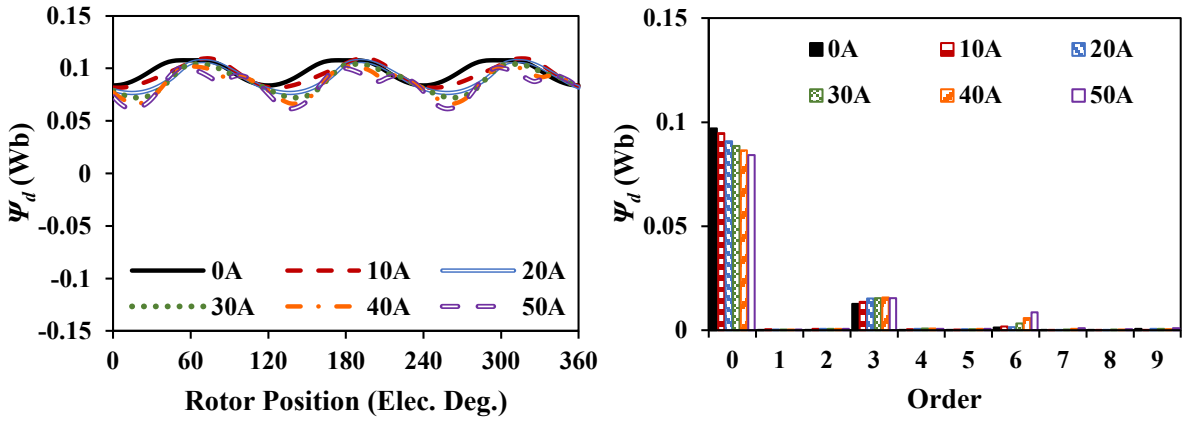

(c) D-axis flux linkage of 12s8p-CCPPM

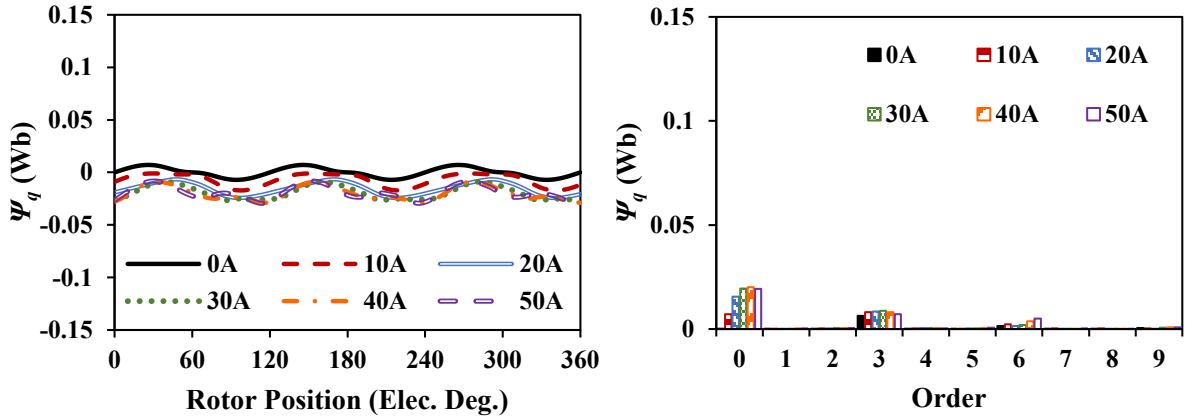

(d) Q-axis flux linkage of 12s8p-CCPPM

Fig. 6.12 Flux linkages and spectra for 12s8p machines.

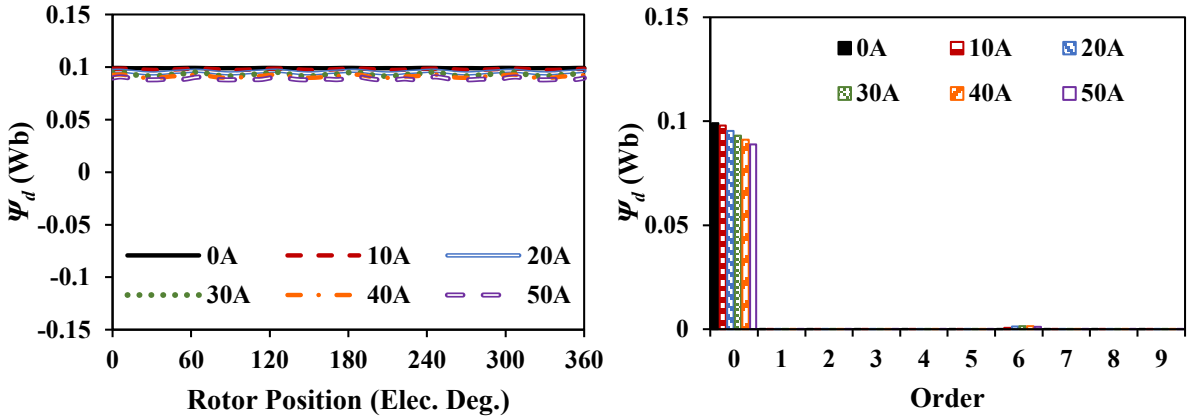

(a) D-axis flux linkage of 12s10p-SPM

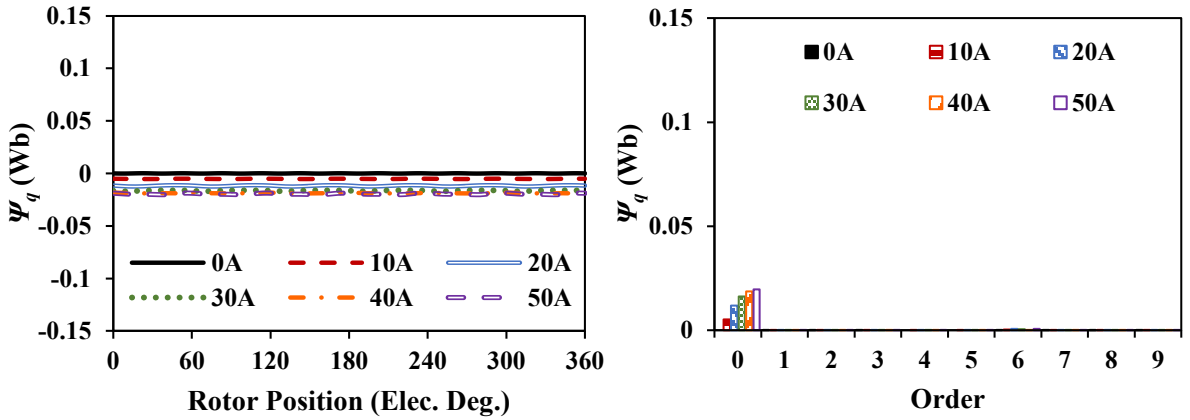

(b) Q-axis flux linkage of 12s10p-SPM

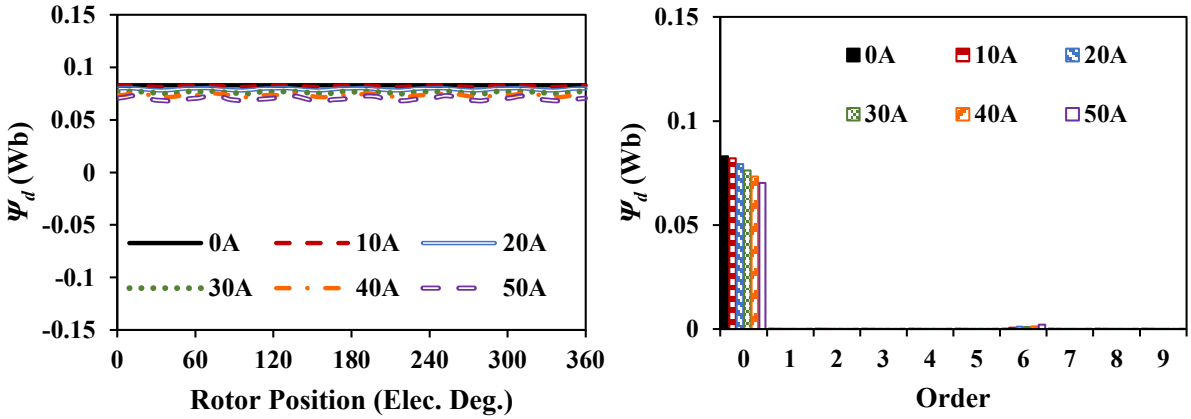

(c) D-axis flux linkage of 12s10p-CCPPM

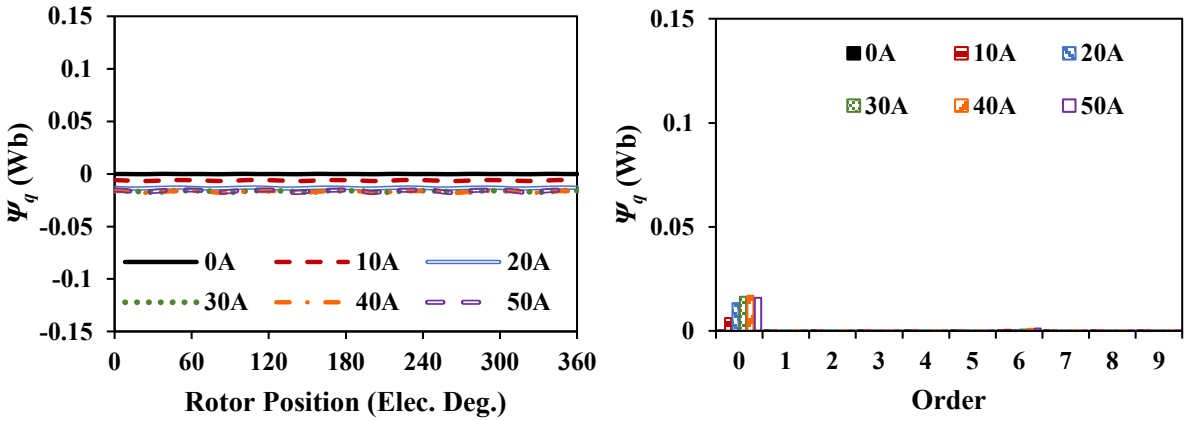

(d) Q-axis flux linkage of 12s10p-CCPPM

Fig. 6.13 Flux linkages and spectra for 12s10p machines.

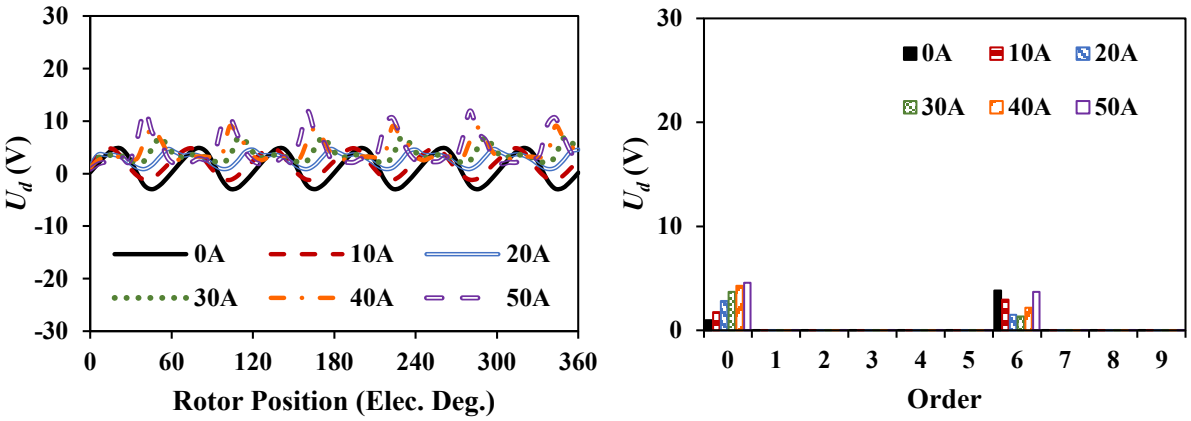

(a) D-axis back-EMF of 12s8p-SPM

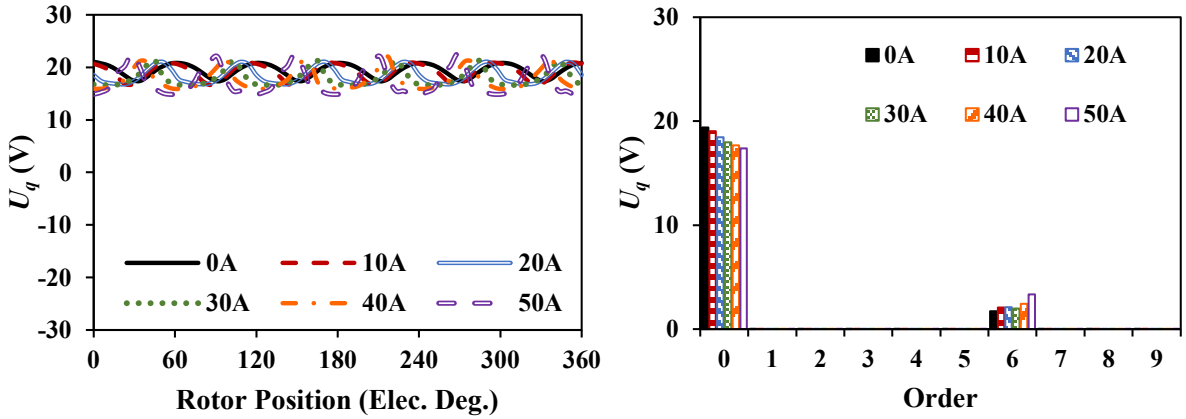

(b) Q-axis back-EMF of 12s8p-SPM

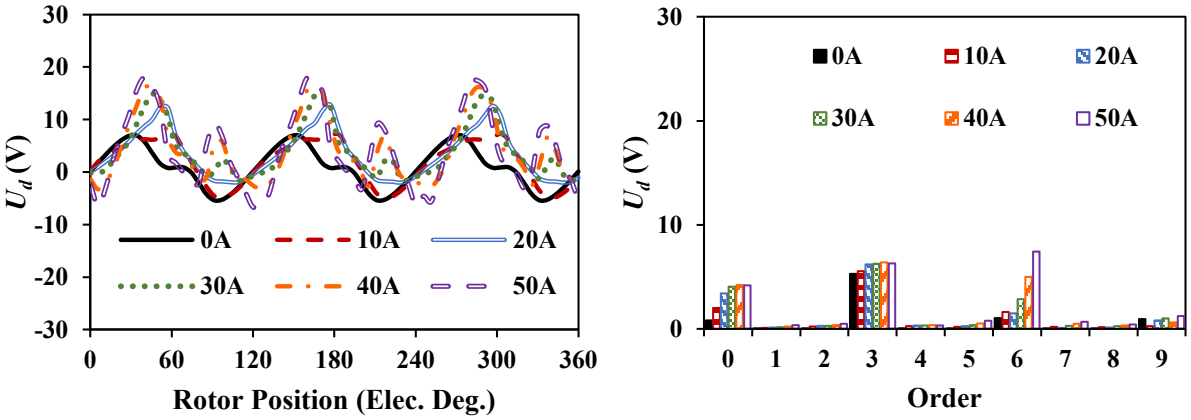

(c) D-axis back-EMF of 12s8p-CCPPM

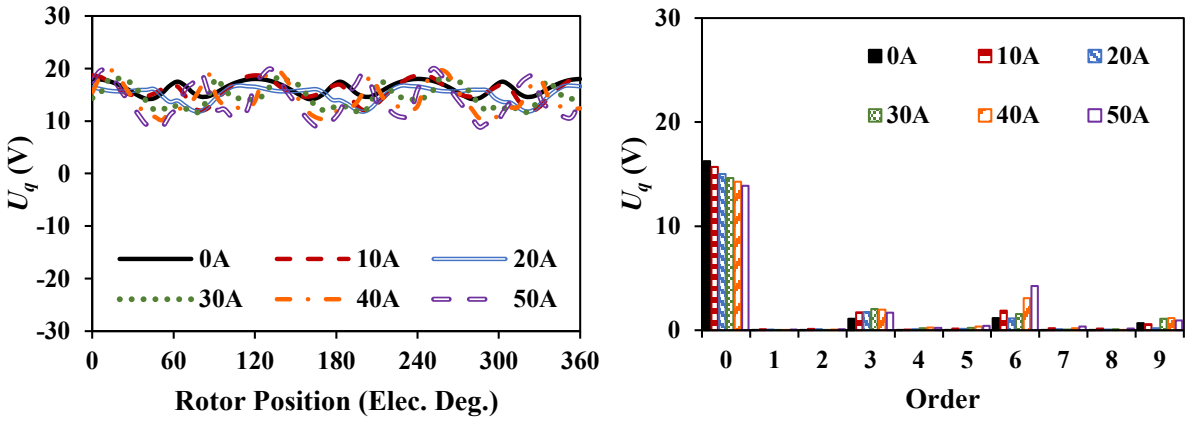

(d) Q-axis back-EMF of 12s8p-CCPPM

Fig. 6.14 Back-EMFs and spectra for 12s8p machines.

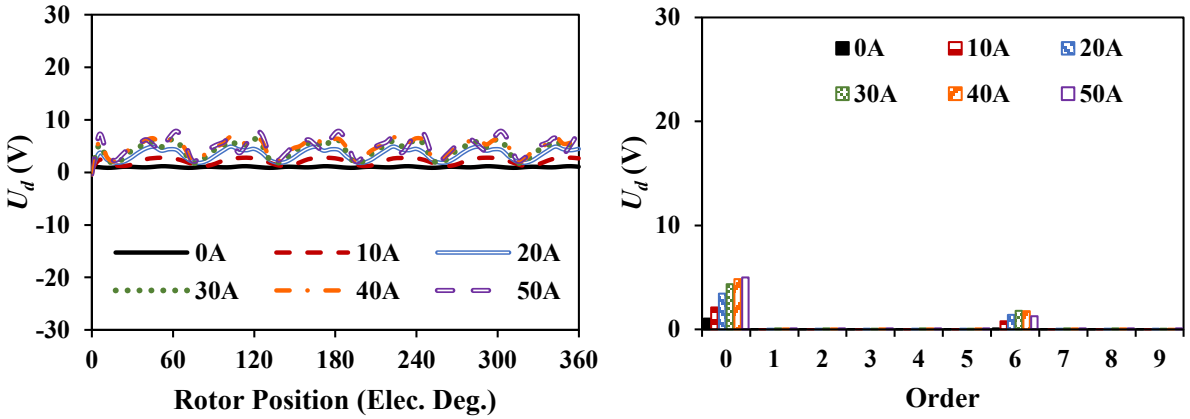

(a) D-axis back-EMF of 12s10p-SPM

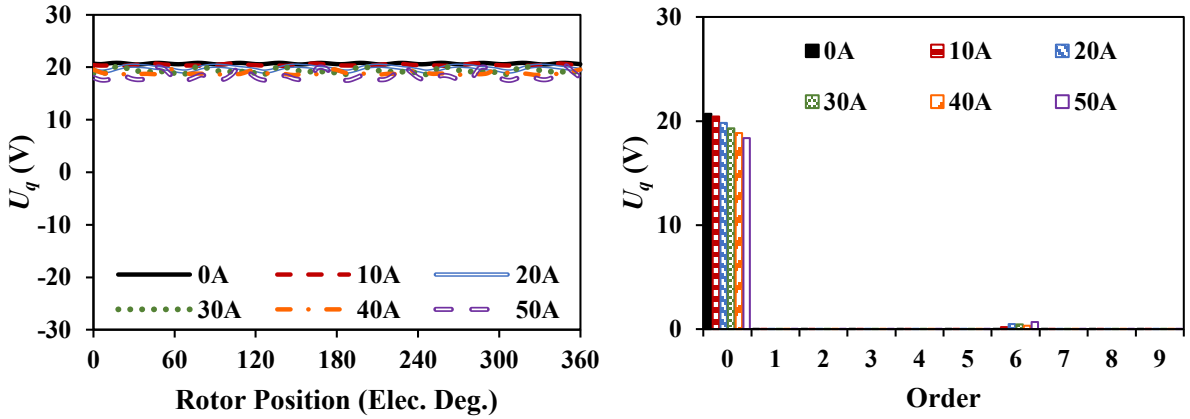

(b) Q-axis back-EMF of 12s10p-SPM

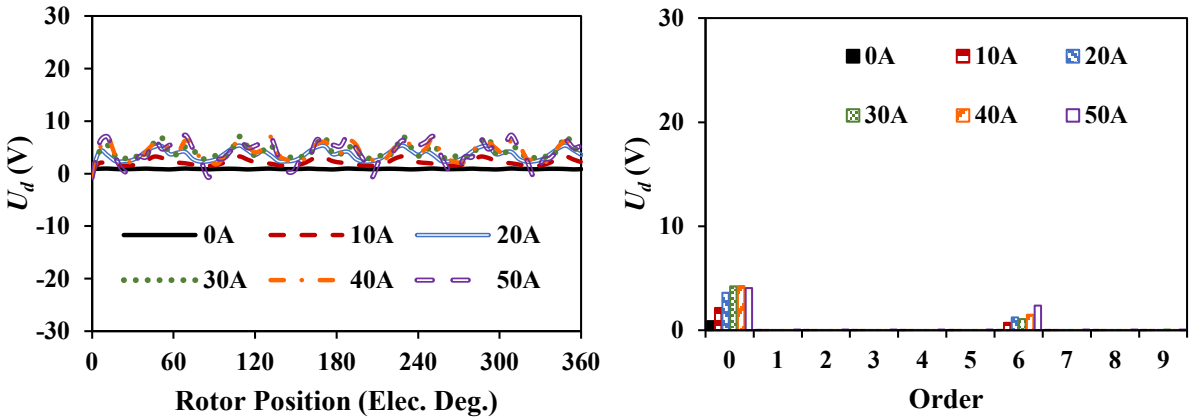

(c) D-axis back-EMF of 12s10p-CCPPM

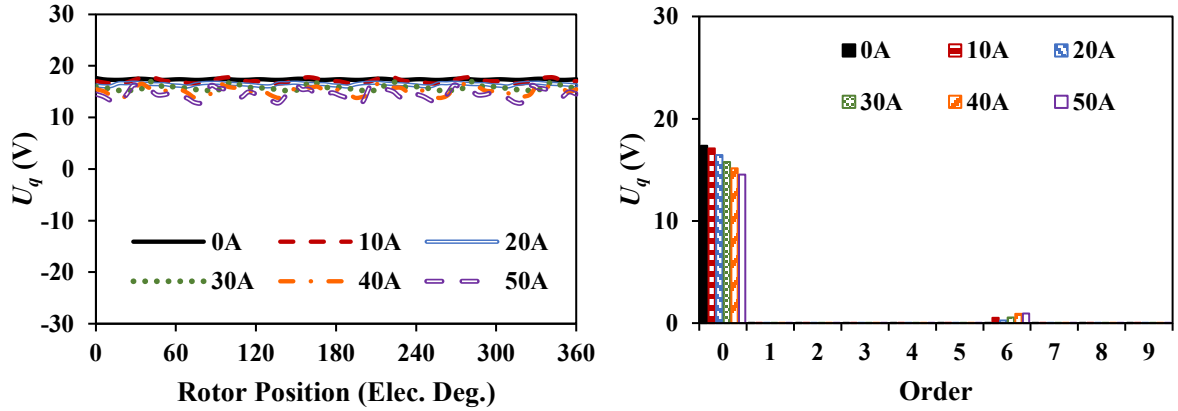

(d) Q-axis back-EMF of 12s10p-CCPPM

Fig. 6.15 Back-EMFs and spectra for 12s10p machines.

6.3.3 Inductance Characteristics

Fig. 6.16 - Fig. 6.19 show the inductance characteristics for 12s8p and 12s10p machines. Obviously, with the increase of current, the average values for all of these four machines decrease and for each machine, L_q has a larger variation range than L_d since the armature reaction mainly acts on the q-axis. Since the unbalanced features between north and south poles can be linked to windings for 12s8p-CCPPM machine, there exist harmonics in multiples of three. On the contrary, the 12s10p-CCPPM can overcome the unbalanced feature in CPPM rotor and it has the same harmonic contents as the 12s10p-SPM machine.

Commonly, a higher armature reaction tends to result in higher pulsation in inductance, which can be seen in the amplitudes of 6^{th} order harmonics in L_d and L_q for all the machines. However,

the dominant 3rd order harmonics for 12s8p-CCPPM machine are smaller with the current increase, which leads to its decreasing trend of the overall fluctuation in inductance waveforms. This is because the saturation in iron pole can reduce the unbalance permeability between PM and iron poles in the rotor, which is the source of the dominant third-order harmonics in L_d and L_q. Consequently, the overall fluctuation in differences between L_d and L_q for 12s8p-CCPPM machine shows a decreasing trend while an increasing trend can be seen in other machines. However, the reluctance torque is proportional to the square of the current. Therefore, the overall reluctance torque ripple still shows a rising trend with the current increase.

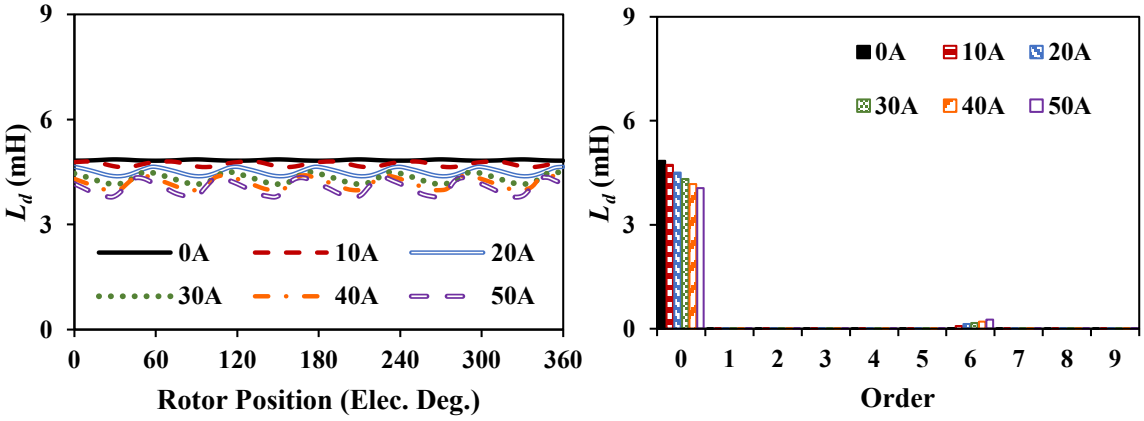

(a) L_d

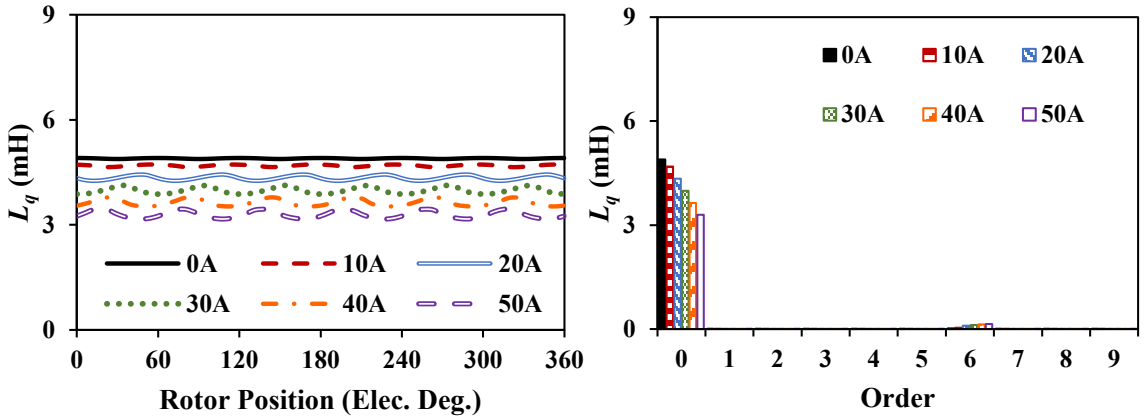

(b) L_q

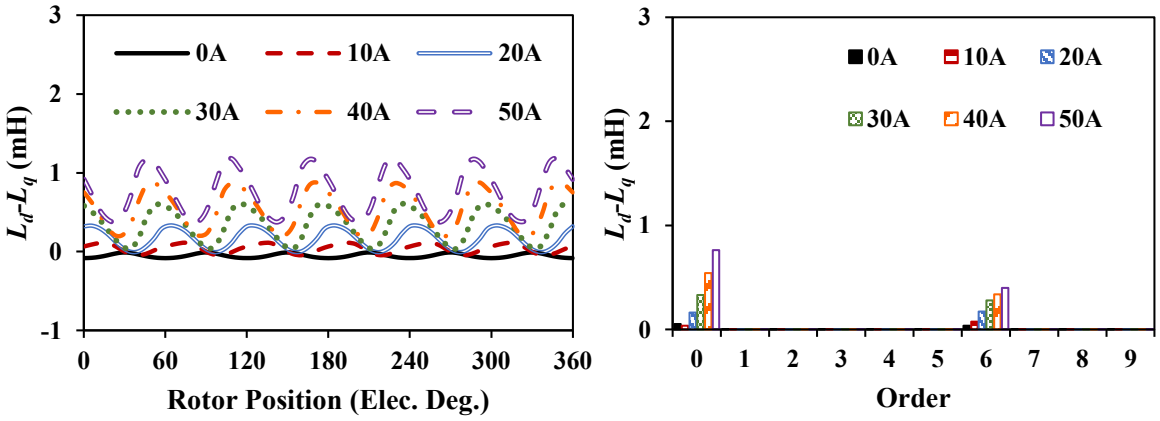

(c) L_d - L_q

Fig. 6.16 Inductances and spectra for 12s8p SPM machine.

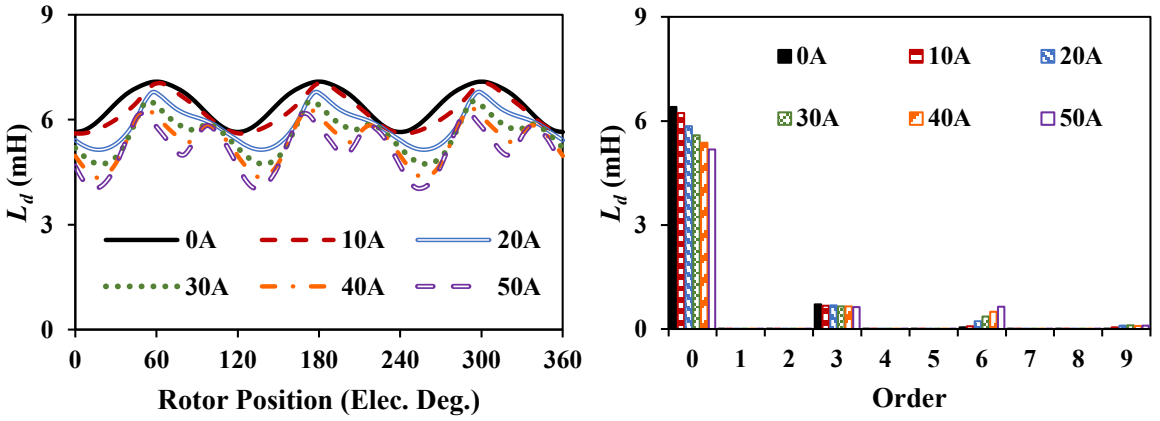

(a) L_d

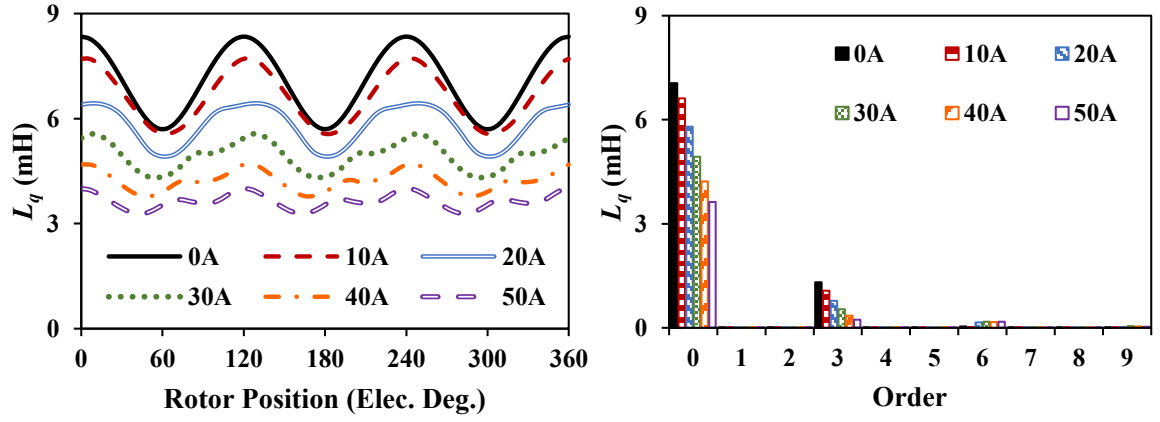

(b) L_q

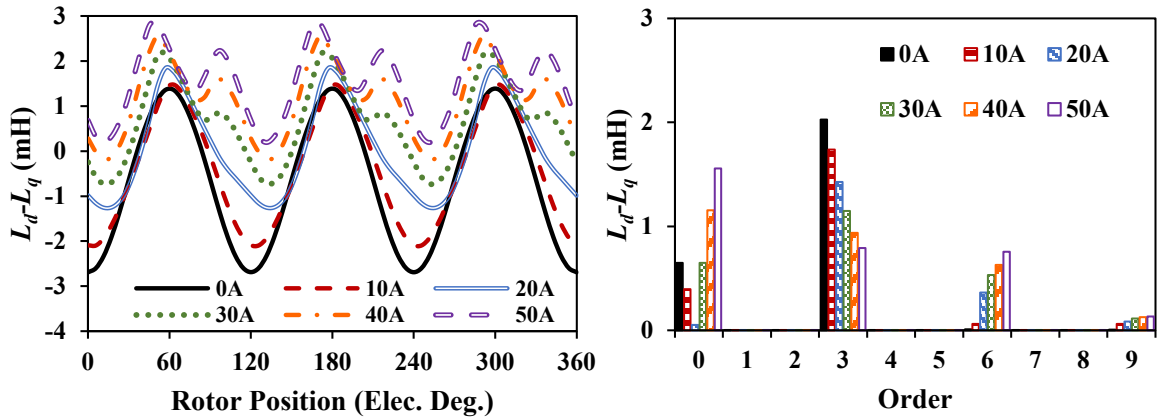

(c) L_d - L_q

Fig. 6.17 Inductances and spectra for 12s8p CCPPM machine.

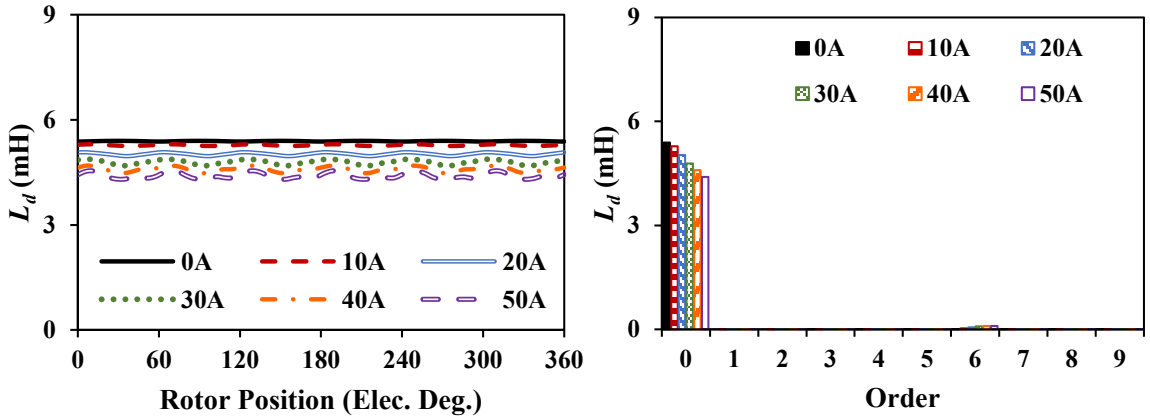

(a) L_d

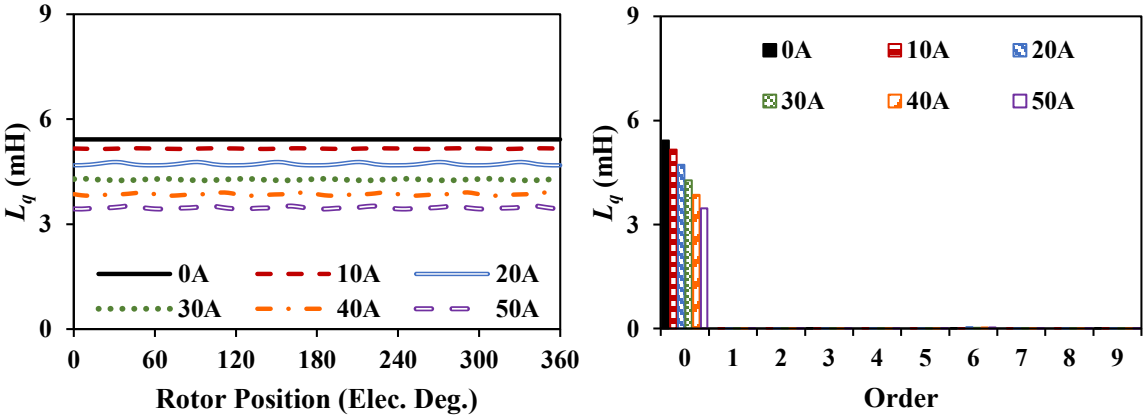

(b) L_q

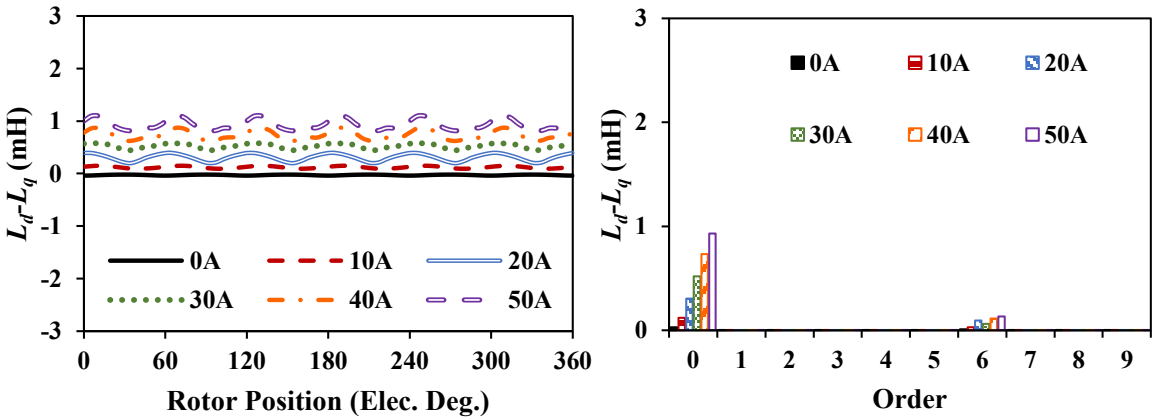

(c) L_d - L_q

Fig. 6.18 Inductances and spectra for 12s10p SPM machine.

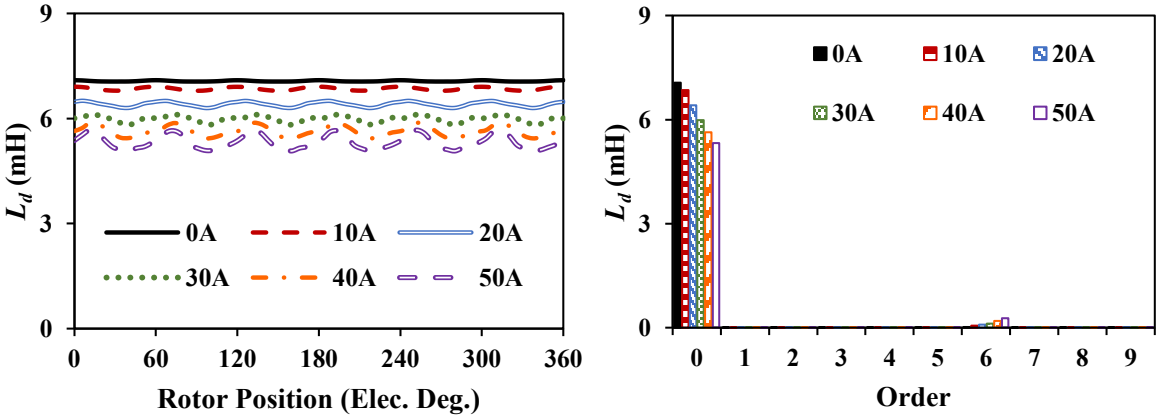

(a) L_d

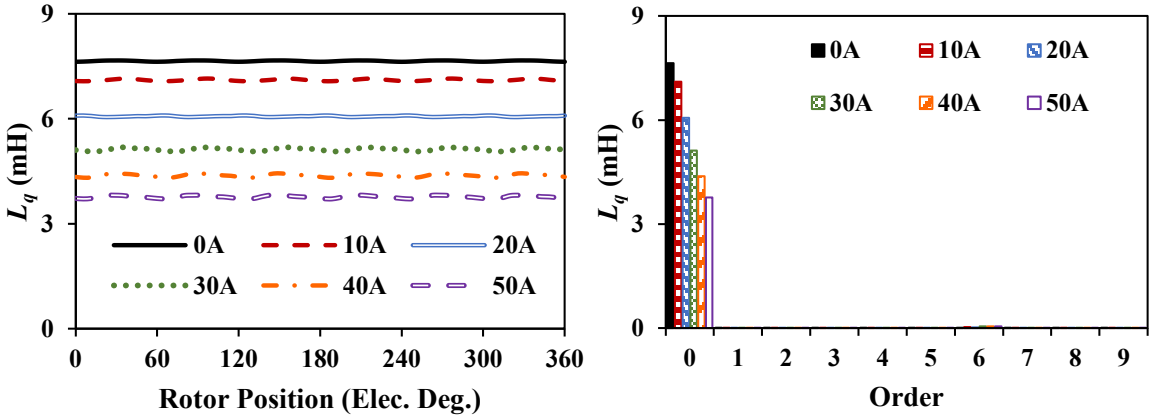

(b) L_q

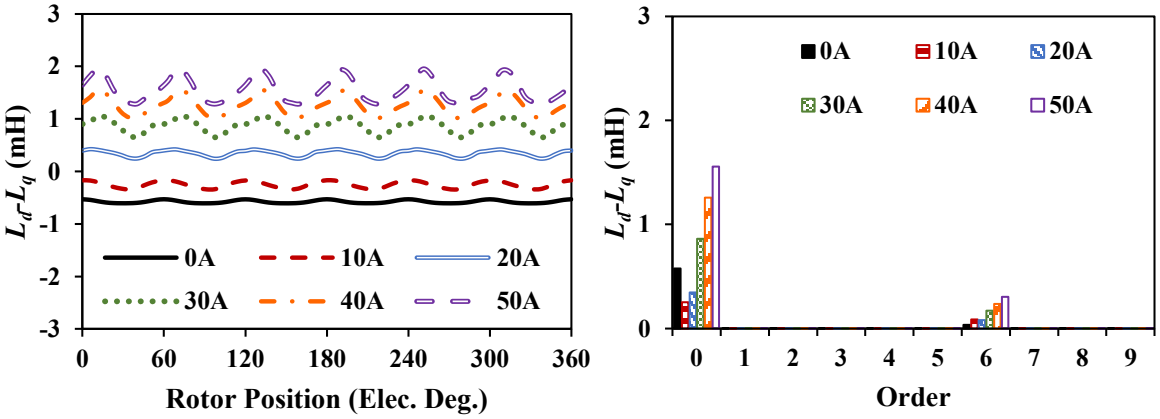

(c) L_d - L_q

Fig. 6.19 Inductances and spectra for 12s10p CCPPM machine.

6.3.4 Torque Characteristics

Supposing the torque ripple T_{ripple} is the ratio of peak to peak value to average value, the average torque and torque ripples are shown in Fig. 6.20. Clearly, the differences between the average torques of SPM machines and those of CCPPM machines become larger with the increase of current, which indicates that CCPPM machines suffer from higher armature reactions and thus higher saturation levels. Fig. 6.21 shows the torque ripple spectra for these machines. It can be found that only 12s8p-CCPPM has the 3rd order torque ripple and the dominant 3rd order torque ripple increases significantly as the current rises.

To analyze the torque ripple, Fig. 6.22 shows the peak to peak values of torque components under different current conditions. Generally, all of the PM torque ripples, reluctance torque ripples, and cogging torque ripples increase as the current rises for all the machines. The unevenly distributed local saturation leads to fluctuating growth. Besides, the phase differences between torque ripple components result in the uneven growth of peak to peak value of overall torque. Considering the increased average torque, T_{ripple} for different machines have different trends as shown in Fig. 6.20.

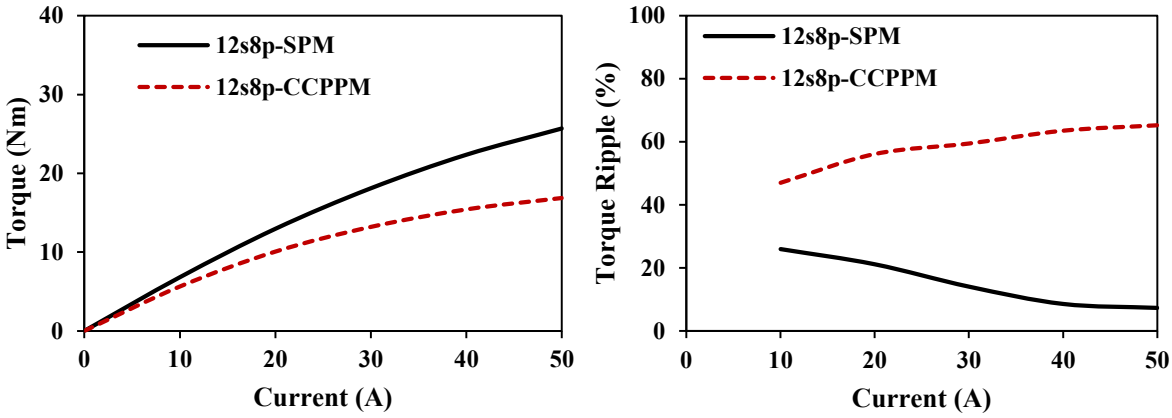

(a) 12s8p machines

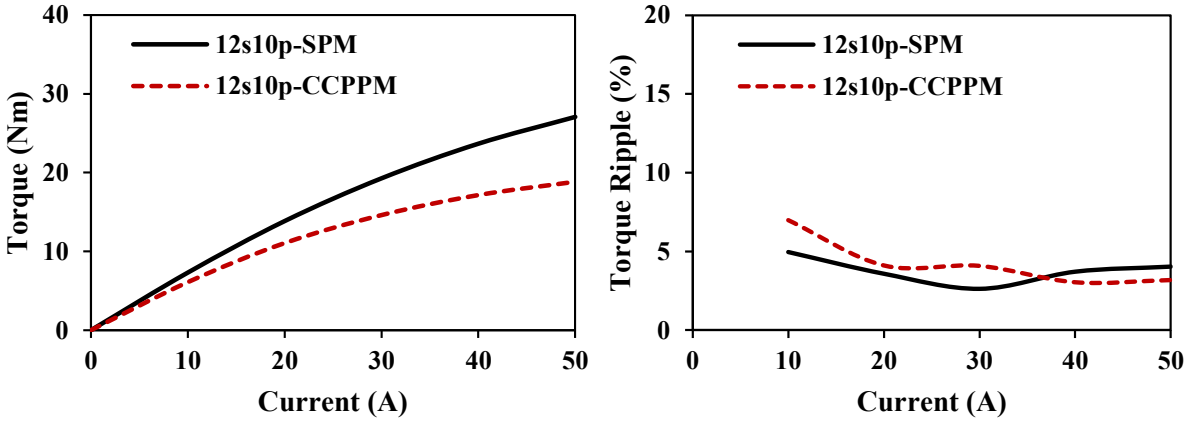

(b) 12s10p machines

Fig. 6.20 Average torques and torque ripples for SPM and CCPPM machines.

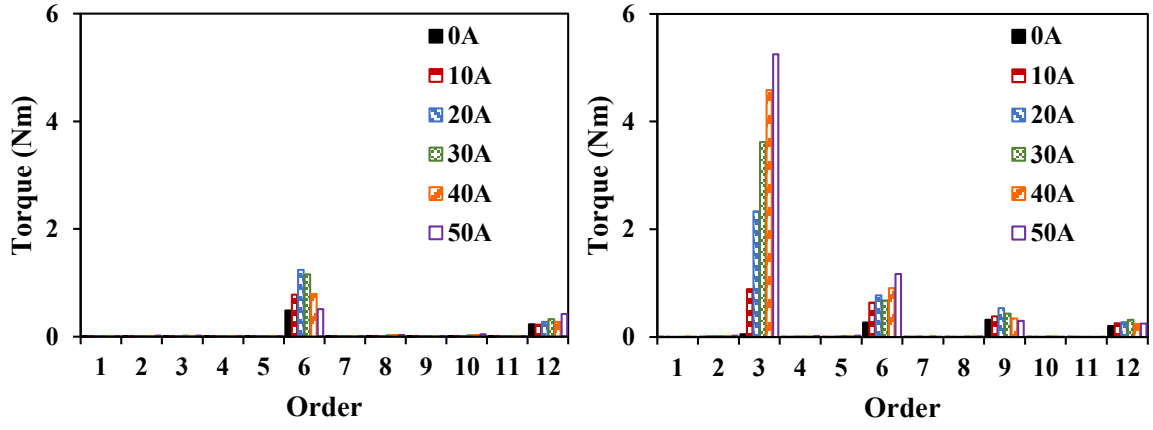

(a) 12s8p-SPM (b) 12s8p-CCPPM

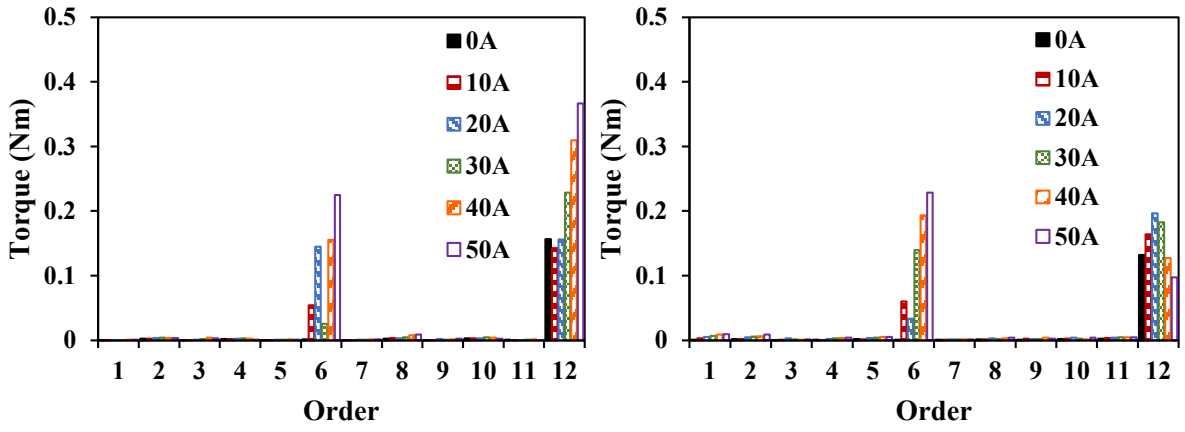

(c) 12s10p-SPM (d) 12s10p-CCPPM

Fig. 6.21 Torque ripple spectra for SPM and CCPPM machines.

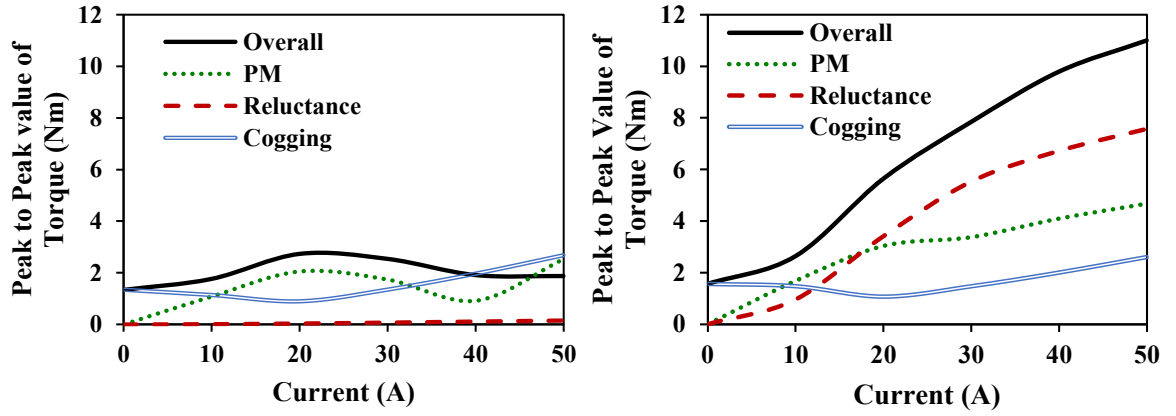

(a) 12s8p-SPM (b) 12s8p-CCPPM

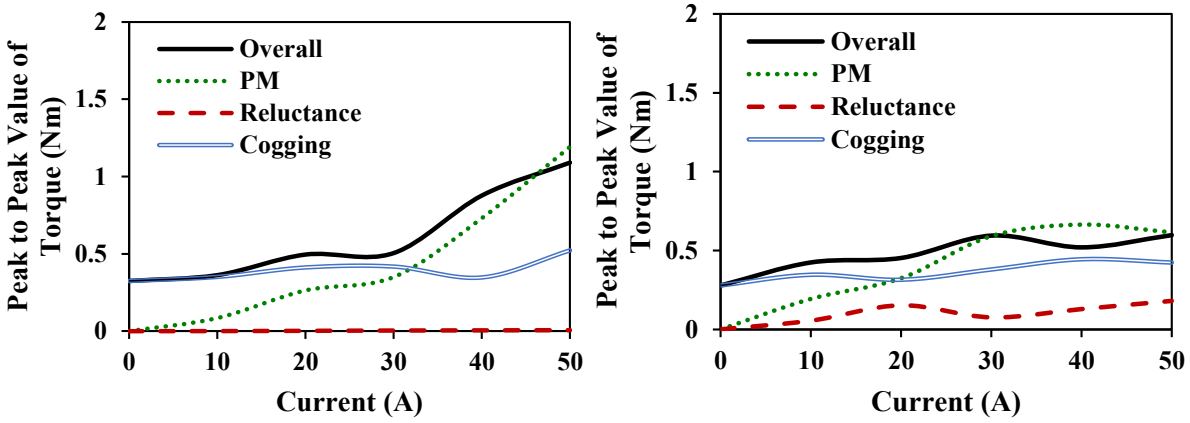

(c) 12s10p-SPM (d) 12s10p-CCPPM

Fig. 6.22 Peak to peak values of torque ripples for SPM and CCPPM machines.

6.3.5 Demagnetization Analysis

Due to the larger armature reaction for CPPM machines, the demagnetization withstand capabilities of CPPM machines are weaker than those of SPM counterparts. Since the electrical machines for electric vehicles are approximately cooling at 65ºC water, to analyze the demagnetization withstand performances under the worst scenario, the temperatures of magnets are set at 80ºC in this part with the B-H curve presented in Fig. 6.23. The analyses are conducted under a negative *d*-axis current and the flux density in magnets is saved at the position that magnets align to the winding of phase A. 0.3T in the normal B-H curve is set as the knee point, which means that the areas can be treated as demagnetized when their flux density is below 0.3T.

Supposing the demagnetization area ratio is defined as the demagnetized PM area to the whole PM area, the magnetic fields along the magnetization direction, namely the radial direction, in PMs for four machines are analyzed as the results shown in Fig. 6.24 and Fig. 6.25. It can be seen that under light load conditions, the demagnetization area ratios for both SPM and CCPPM machines are 0. However, when the current is larger, the demagnetization area ratios for CCPPM machines increase significantly while those for SPM machines still maintain a low level. This indicates that the CCPPM machines suffer from weaker demagnetization withstand capabilities. It should be noted that the repetitive overloading will lead to the creeping effect of demagnetization. Thus, under I_d=-50A, the progressions of demagnetization are analyzed with the results shown in Fig. 6.26. It is clear that for all the machines, with the increase of operation time, the demagnetization area ratio first increases and then keeps stable. This means that in practical applications, creep effects that cause demagnetization must be considered.

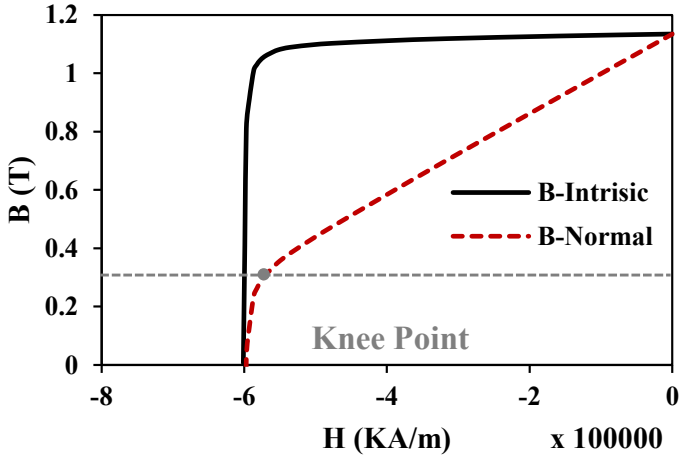

Fig. 6.23 B-H curve for N35 under 80°C.

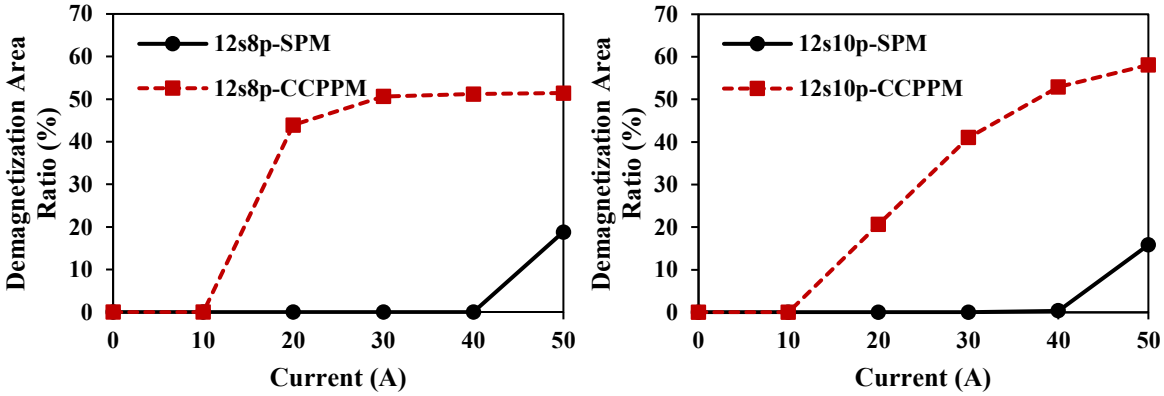

(a) 12s8p machines (b) 12s10p machines

Fig. 6.24 Demagnetization area ratios with negative *d*-axis current.

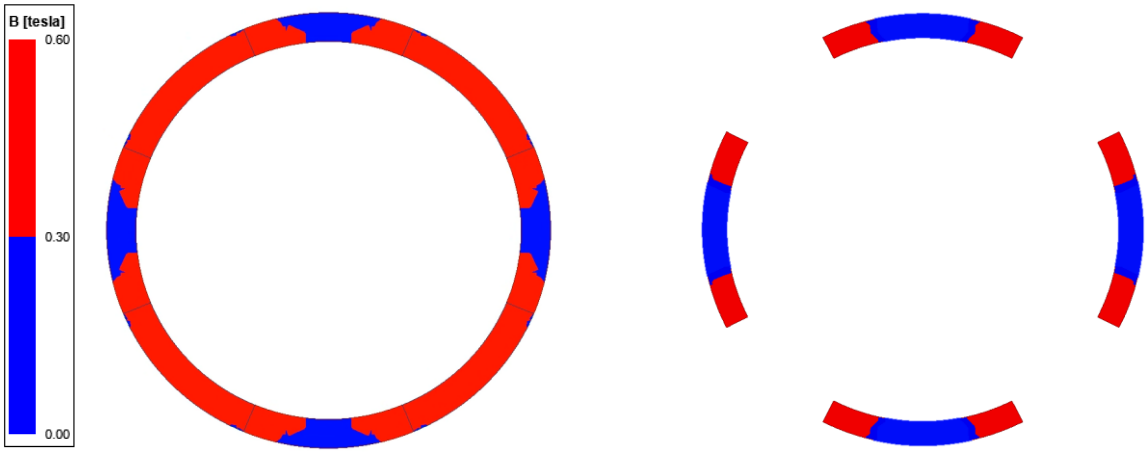

(a) 12s8p-SPM (b) 12s8p-CCPPM

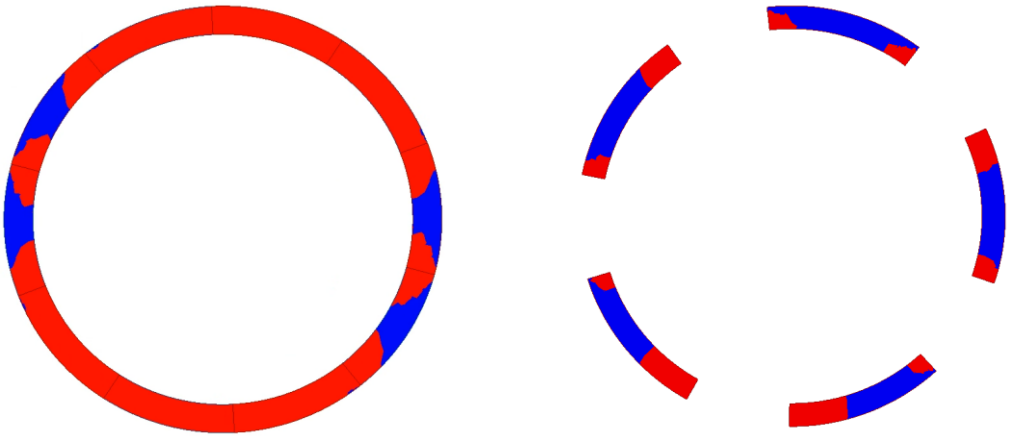

(c) 12s10p-SPM (d) 12s10p-CCPPM

Fig. 6.25 Demagnetization area distribution in magnets under I_d=-50A.

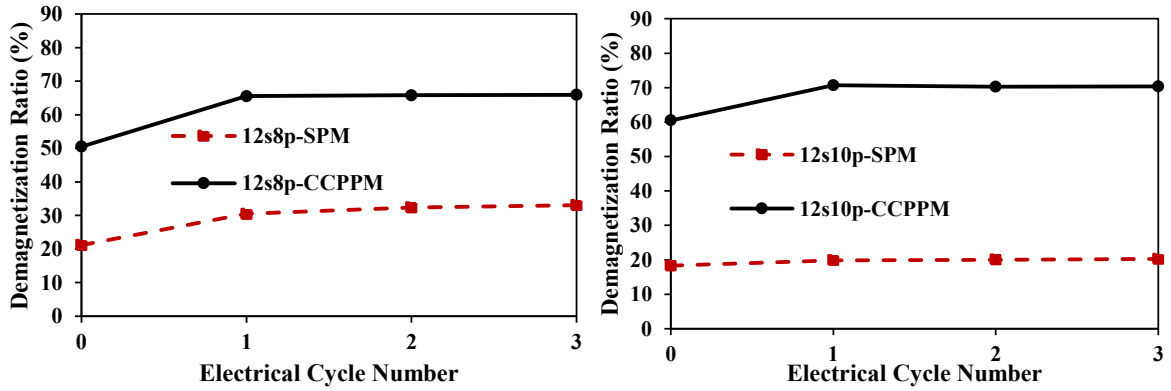

(a) 12s8p machines (b) 12s10p machines

Fig. 6.26 Creeping effect of demagnetization with I_d=-50A.

6.4 Influence of Armature Reaction on Pole Shaping Effect for CPPM Machines

6.4.1 Magnetic Flux Density Characteristics

In this section, the asymmetric pole-shaped 12s8p CPPM machine and the symmetrical pole-shaped 12s10p CPPM machine are analyzed. As shown in Fig. 6.27, the flux density waveforms deform with higher current injected although it is not so obvious. As for the spectra, it is obvious that the amplitudes of fundamental harmonics drop with the increase of current, while the amplitudes of harmonics show different trends, which are caused by various local saturation conditions under different currents. Besides, the equal potential distributions are demonstrated

in Fig. 6.28 and Fig. 6.29. Similar to CCPPM machines, PM fluxes and armature current fluxes will be shifted as the current increases.

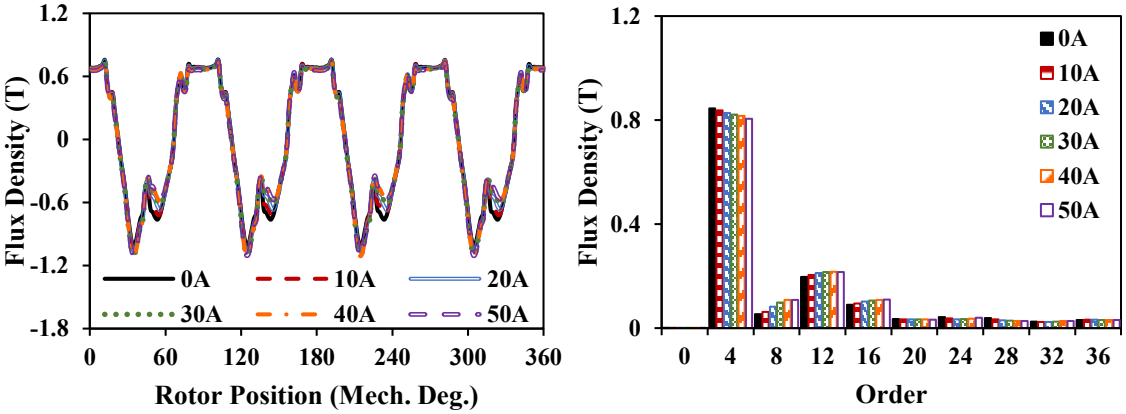

(a) 12s8p-PSCPPM

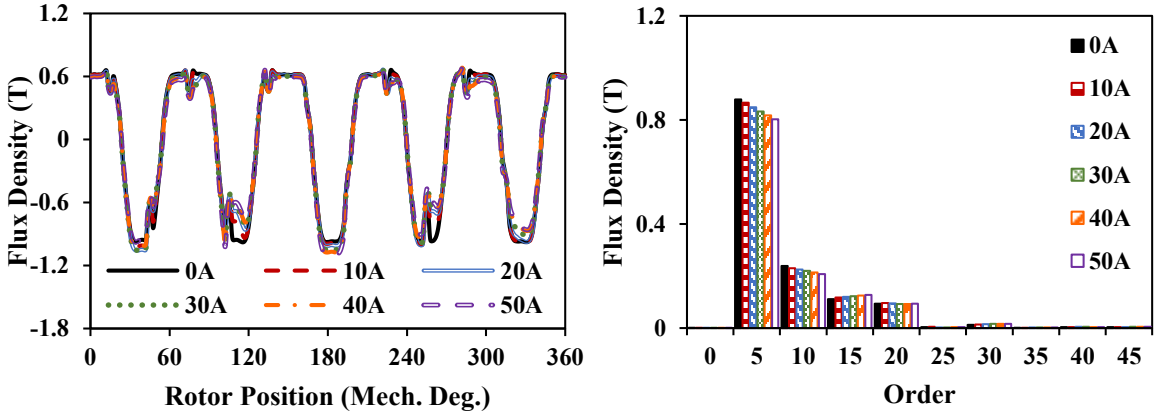

(b) 12s10p-PSCPPM

Fig. 6.27 Flux densities and spectra of two PSCPPM machines.

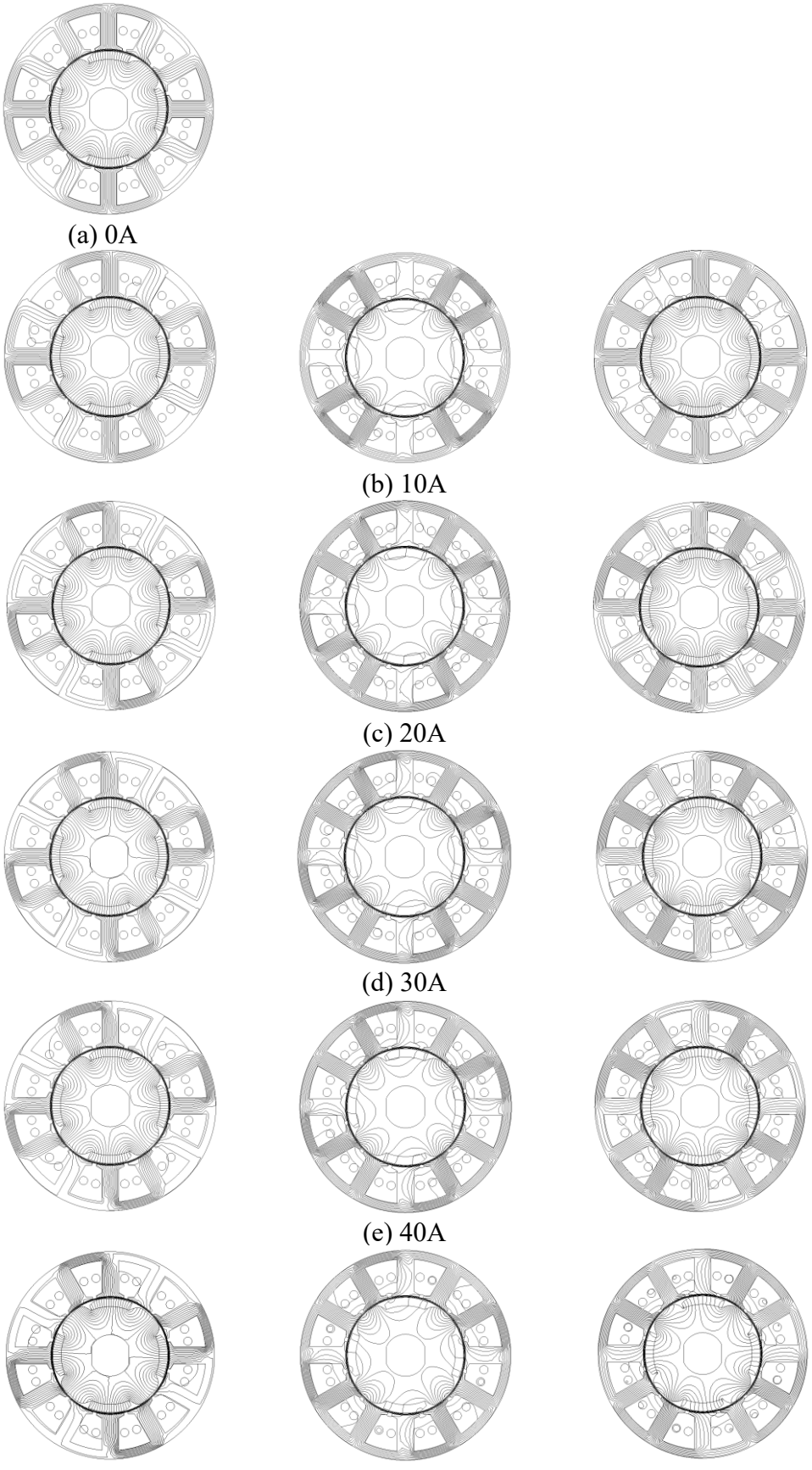

(a) 0A

(b) 10A

(c) 20A

(d) 30A

(e) 40A

(f) 50A

Fig. 6.28 Equal potential distributions for 12s8p-PSCPPM. (from left to right: PM only, armature current only, overall)

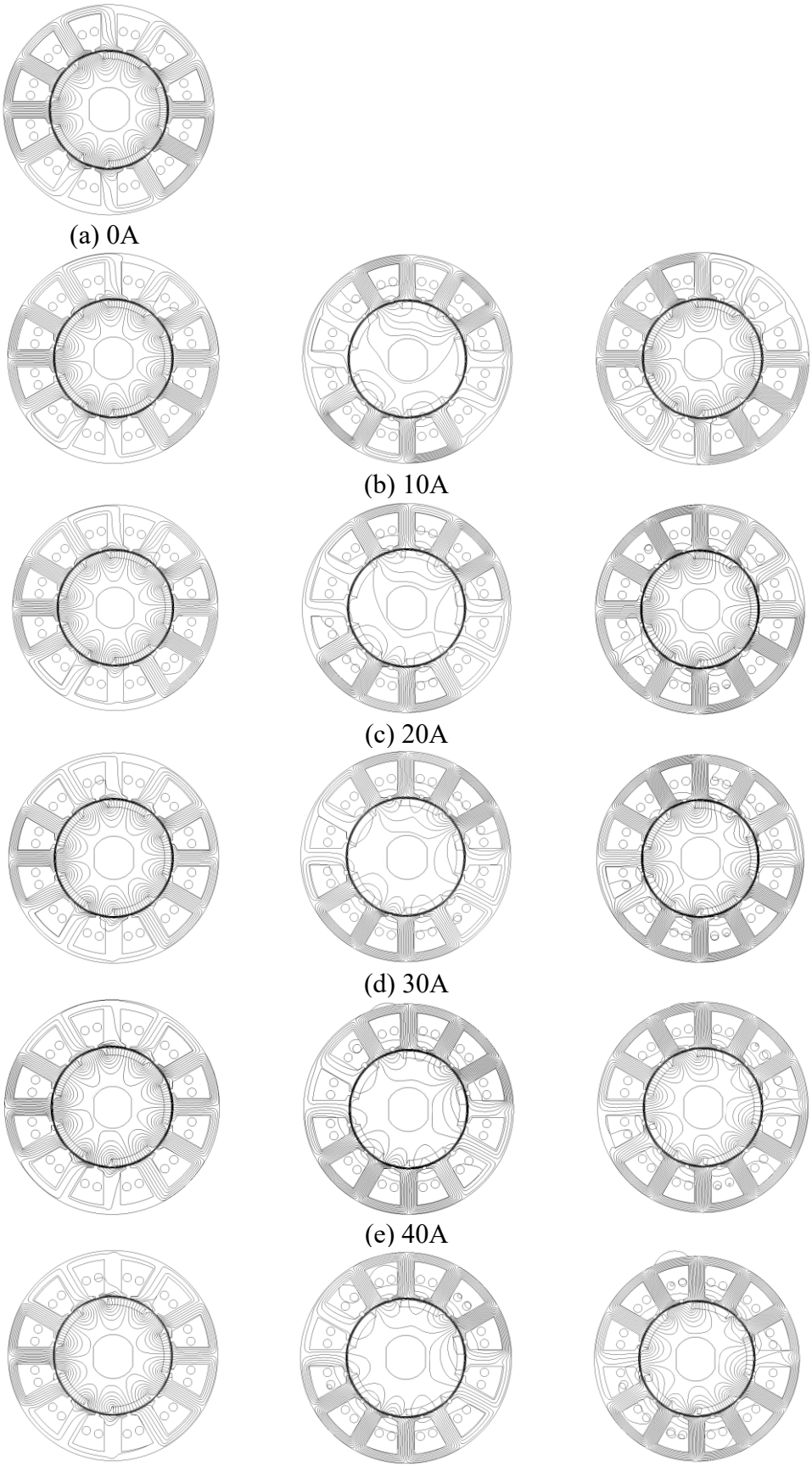

(a) 0A

(b) 10A

(c) 20A

(d) 30A

(e) 40A

(f) 50A

Fig. 6.29 Equal potential distributions for 12s10p-PSCPPM. (from left to right: PM only, armature current only, overall)

6.4.2 PM Flux-linkage and Back EMF Characteristics

Fig. 6.30 and Fig. 6.31 present the flux linkages and back EMFs for two PSCPPM machines, respectively. Obviously, a larger injected current can lead to larger deformation in flux linkage and back EMF waveforms, which means higher harmonic amplitudes. The same as SPM and CCPPM machines, the drop and rise trends of amplitudes in d-/q- axis average values indicate the phase shift of magnet flux due to the armature reaction.

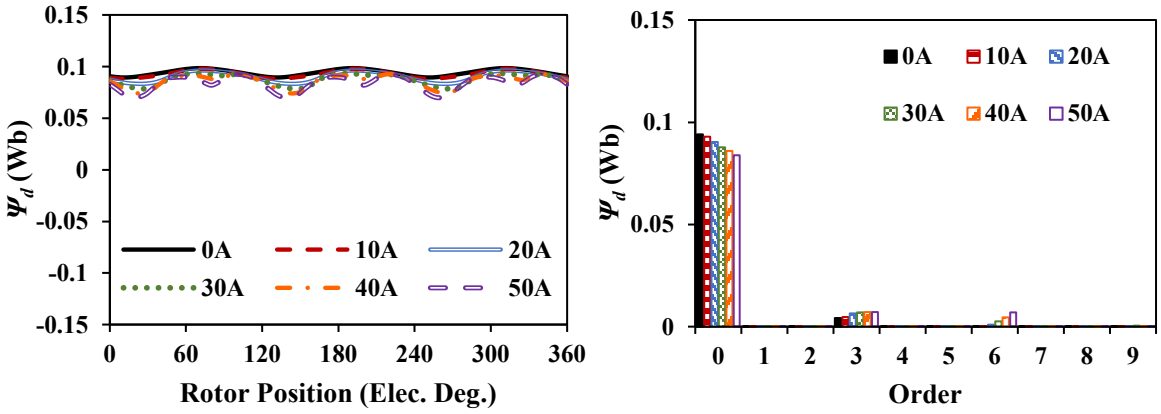

(a) D-axis flux linkage of 12s8p-PSCPPM

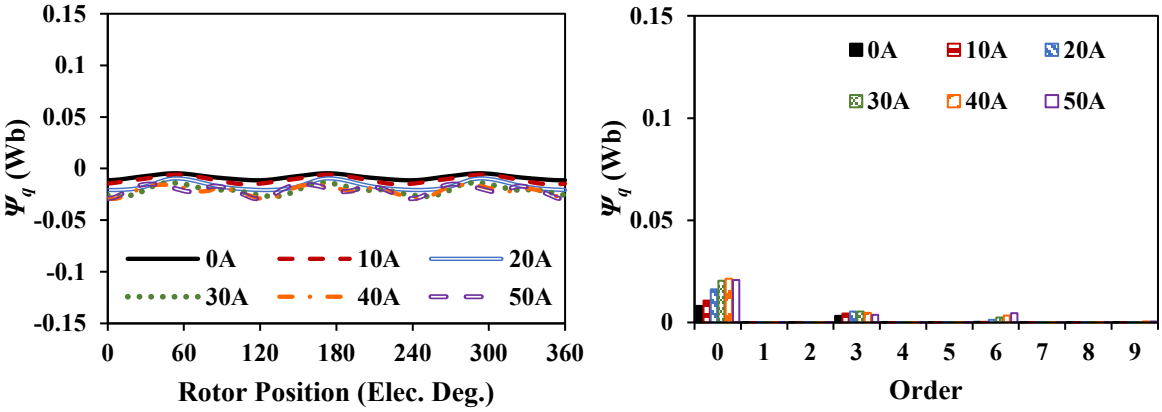

(b) Q-axis flux linkage of 12s8p-PSCPPM

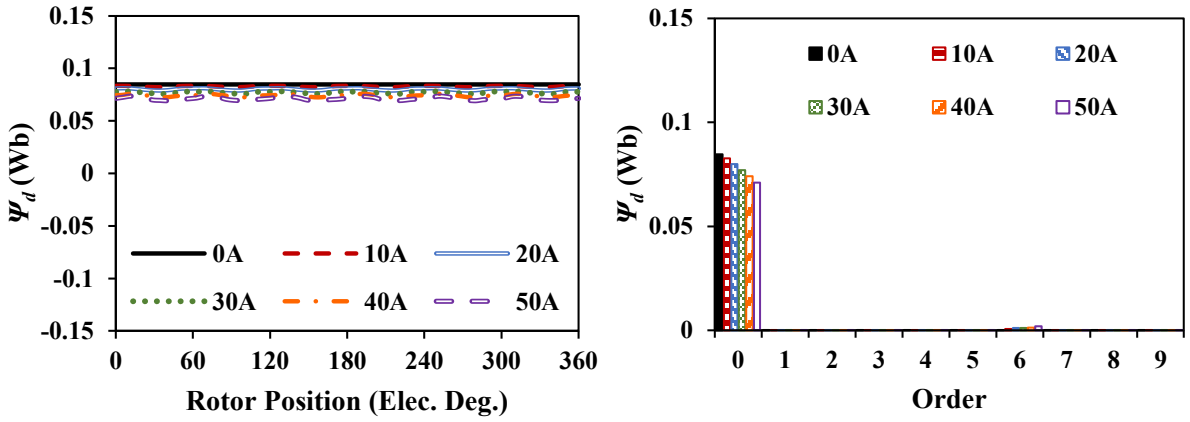

(c) D-axis flux linkage of 12s10p-PSCPPM

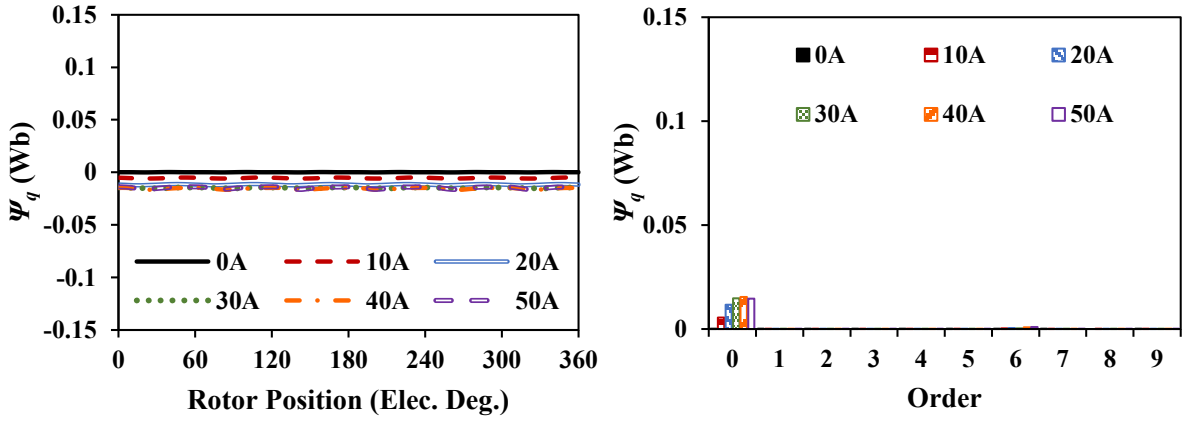

(d) Q-axis flux linkage of 12s10p-PSCPPM

Fig. 6.30 Flux linkages and spectra of two PSCPPM machines.

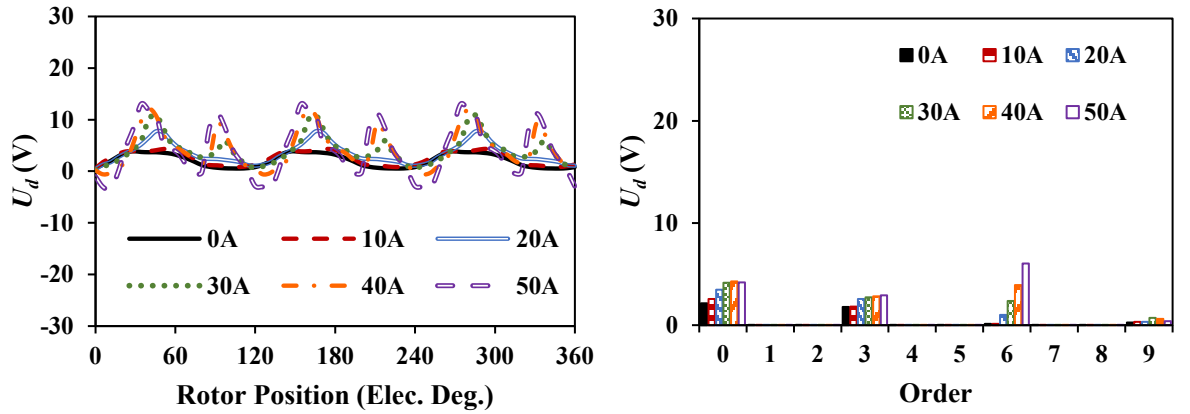

(a) D-axis back-EMF of 12s8p-PSCPPM

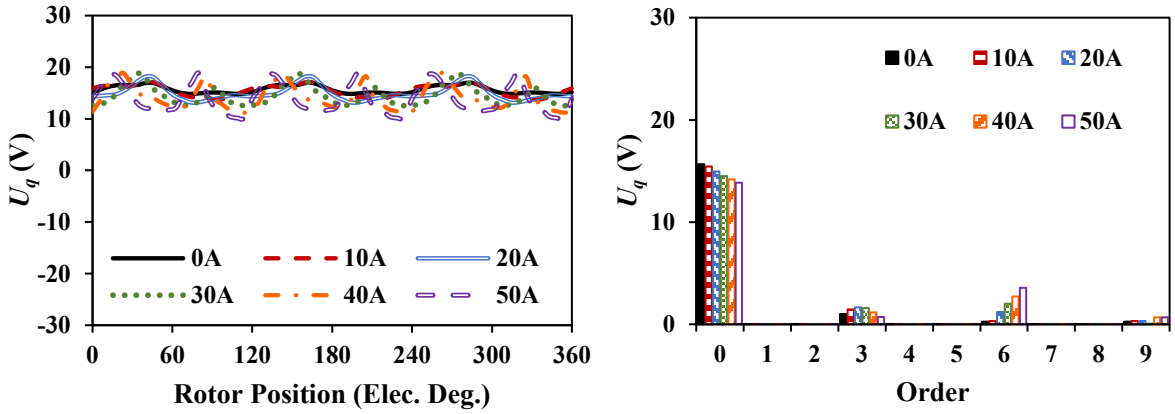

(b) Q-axis back-EMF of 12s8p-PSCPPM

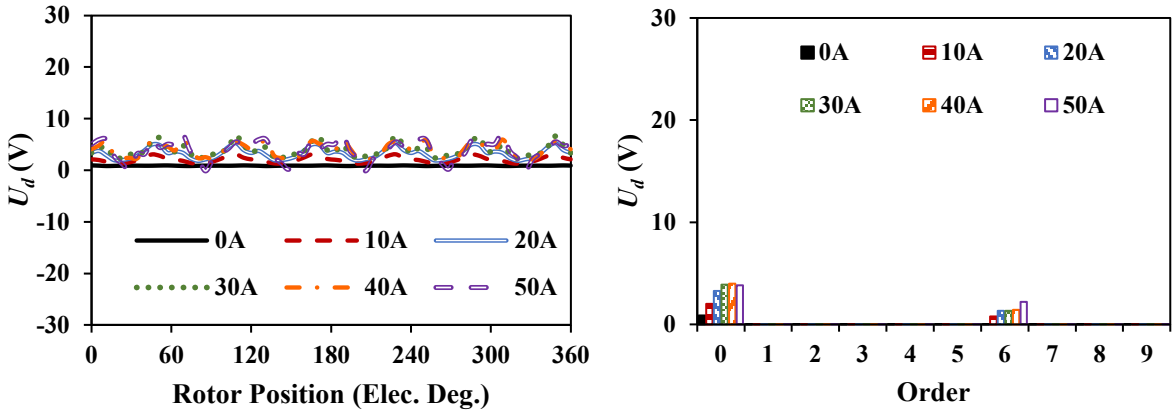

(c) D-axis back-EMF of 12s10p-PSCPPM

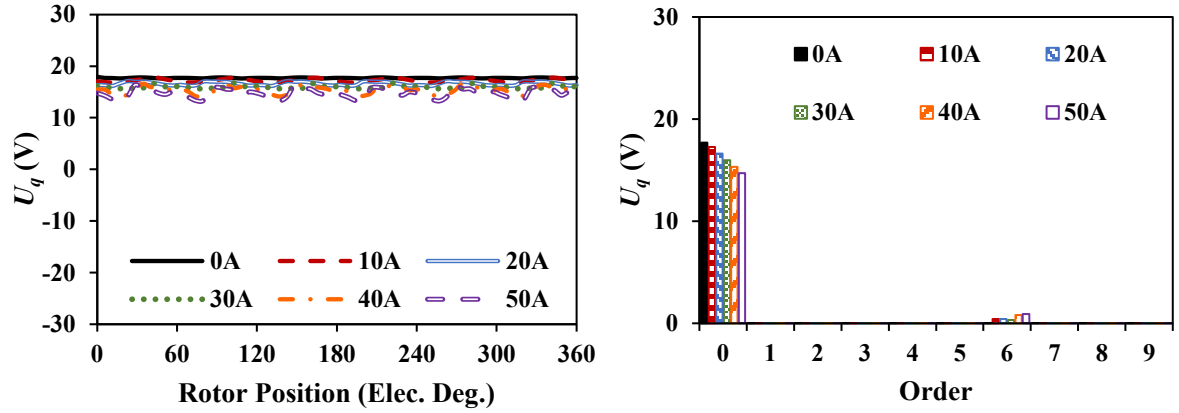

(d) Q-axis back-EMF of 12s10p-PSCPPM

Fig. 6.31 Back EMFs and spectra of two PSCPPM machines.

6.4.3 Inductance Characteristics

Similar to CCPPM machines, the increase in current will result in drops in average and 3rd order harmonic amplitudes, while increases in the 6th order harmonic amplitudes as illustrated in Fig. 6.32 and Fig. 6.33. Such harmonics will lead to different characteristics in reluctance torque ripples for these machines.

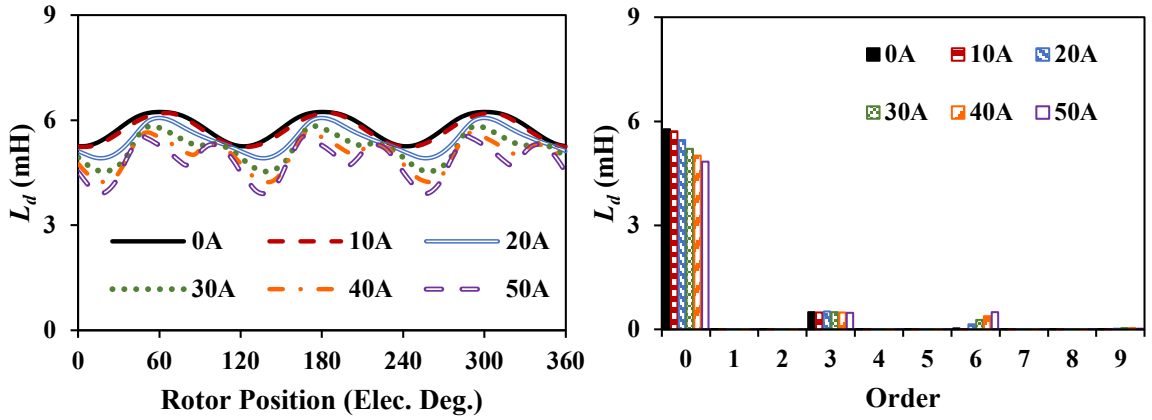

(a) L_d

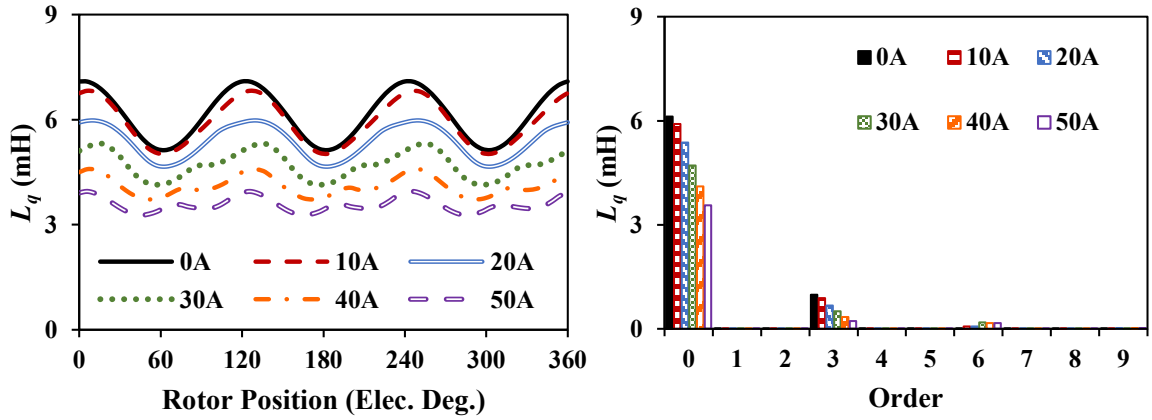

(b) L_q

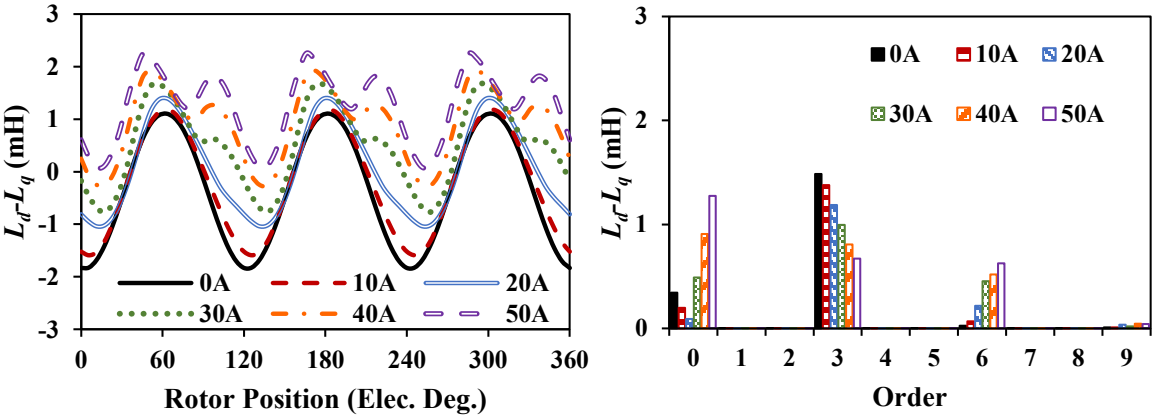

(c) L_d - L_q

Fig. 6.32 Inductances and spectra of 12s8p-PSCPPM machines.

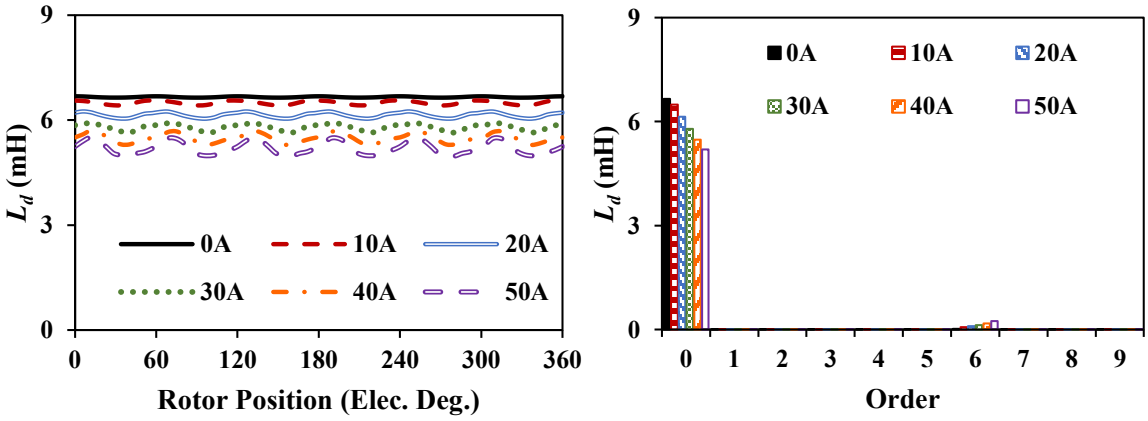

(a) L_d

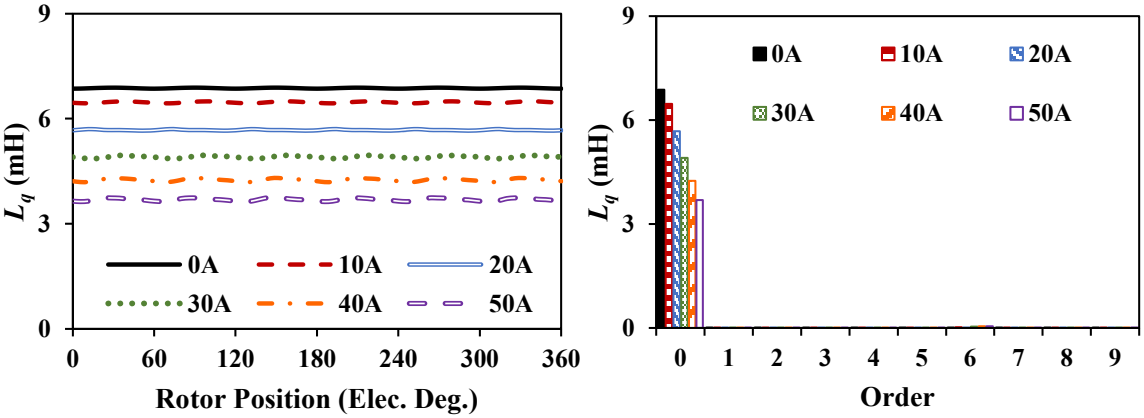

(b) L_q

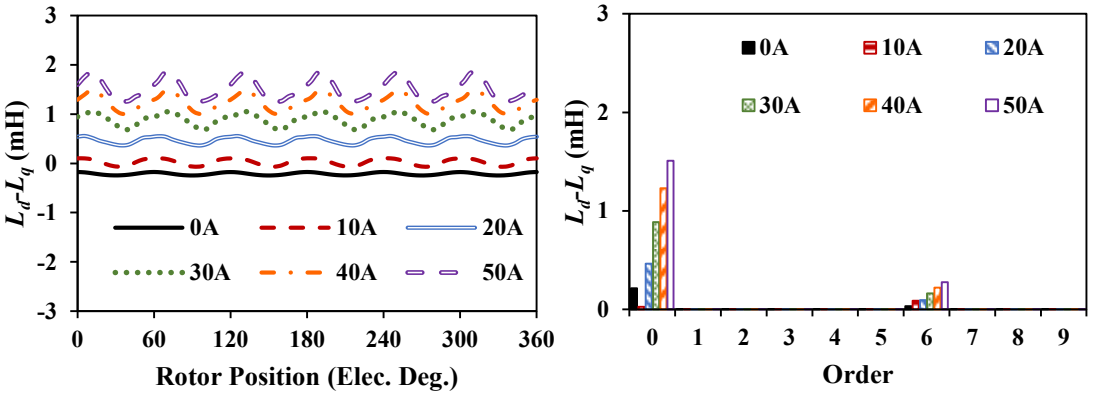

(c) L_d - L_q

Fig. 6.33 Inductances and spectra of 12s10p-PSCPPM machines.

6.4.4 Torque Characteristics

For the 12s8p-PSCPPM machine, ideally, reluctance torque is proportional to the square of the current, while PM torque is proportional to the current, as can be seen in Fig. 6.34 (b) with

current under 20A. When the current is higher than 20A, saturation will suppress the improvement of both reluctance and PM torques. Since the 12s8p-PSCPPM machine is optimized under rated condition (10A) and torque ripple components can counteract each other at this condition, the different variations of amplitudes and phase angle for PM, reluctance, and cogging torques will inevitably lead to the fact that the torque ripple components cannot be completely canceled. Therefore, when the current is higher than 10A, the torque ripple increases significantly, Fig. 6.34.

However, for the 12s10p-PSCPPM machine, the unbalance of CPPM rotor can be eliminated and the performance is quite similar to the 12s10p-SPM counterpart. Therefore, the reluctance torque ripple is small and does not need to be considered under light load conditions. But under heavy load conditions, there is still small reluctance torque as shown in Fig. 6.35 (b), which origins from the saturation caused by the armature reaction. Overall, as shown in Fig. 6.35, the variations of peak to peak values for torques are much smaller and the torque ripple T_{ripple} is relatively stable with the current increase.

Generally, the higher current will cause the increase of all the torque ripple components, including PM torque, reluctance torque, and cogging torque, which in turn contribute to the increase of overall torque ripple.

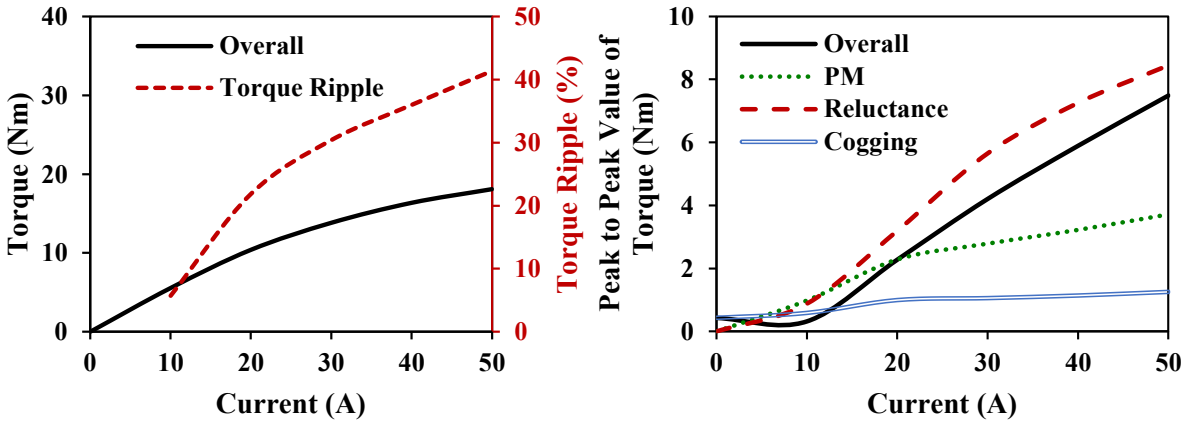

(a) Average torque and torque ripple

(b) Peak to peak value of torque components

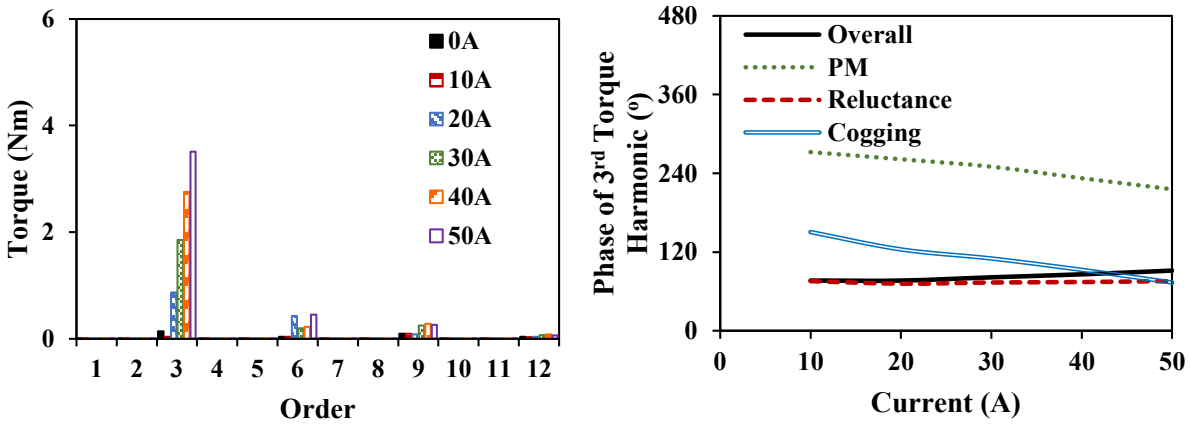

(c) Overall torque ripple spectra (d) Phases of dominant 3rd order torque harmonics

Fig. 6.34 Torque characteristics of 12s8p-PSCPPM machine.

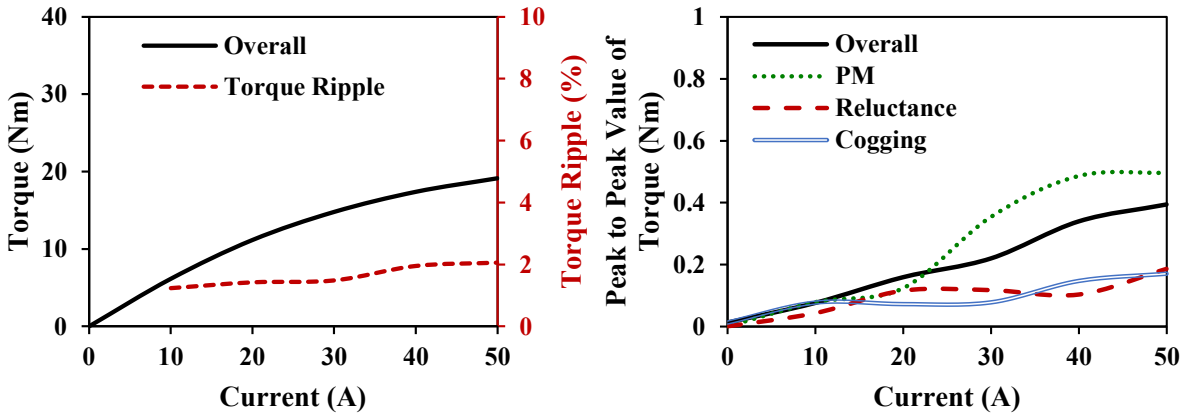

(a) Average torque and torque ripple (b) Peak to peak value of torque components

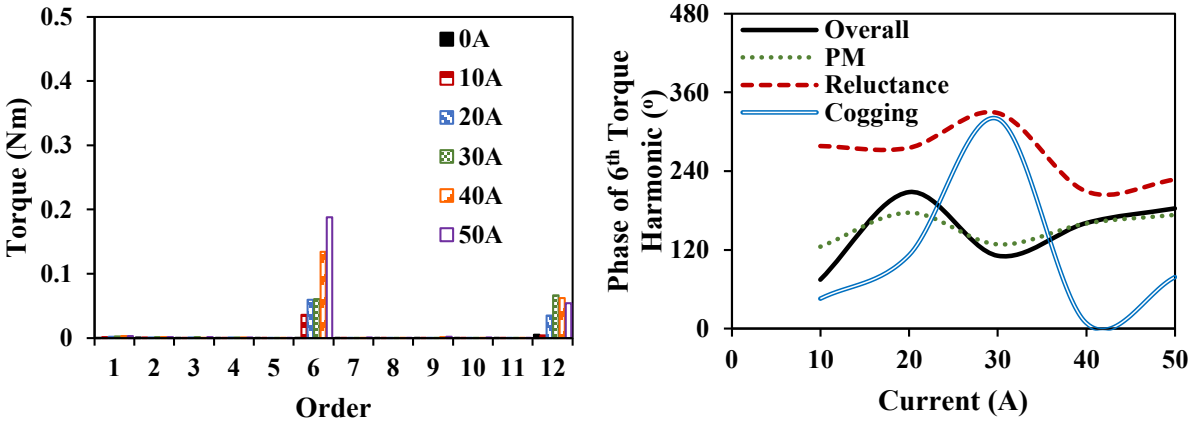

(c) Overall torque ripple spectra (d) Phases of dominant 3rd order torque harmonics

Fig. 6.35 Torque characteristics of 12s10p-PSCPPM machine.

6.4.5 Demagnetization Analysis

With 80ºC and negative *d*-axis current, the demagnetization performances for two PSCPPM machines are demonstrated in Fig. 6.36 where the magnetic fields along the magnetization direction in PMs are analyzed. Although the PSCPPM machines have larger equivalent air-gap lengths, the armature reaction is hardly affected. Therefore, as shown in Fig. 6.37, it is evident that for two PSCPPM machines, the demagnetization areas are quite large, which means the weaker demagnetization withstand capabilities, compared with the SPM counterparts shown in Fig. 6.25. In fact, it is very hard to quantify typical limits on overload since there are many influence factors, such as the machine topology, geometry parameters, current amplitude, and so on. But for the CPPM machines analyzed in this chapter, they are only suitable for working within the rated current, and they all suffer from irreversible demagnetization risks under the overload demagnetization current. Under I_d=-50A, the progressions of demagnetization are analyzed with the results shown in Fig. 6.38. It is clear that for all the PSCPPM machines, the creeping effect will lead to an increase in demagnetization area.

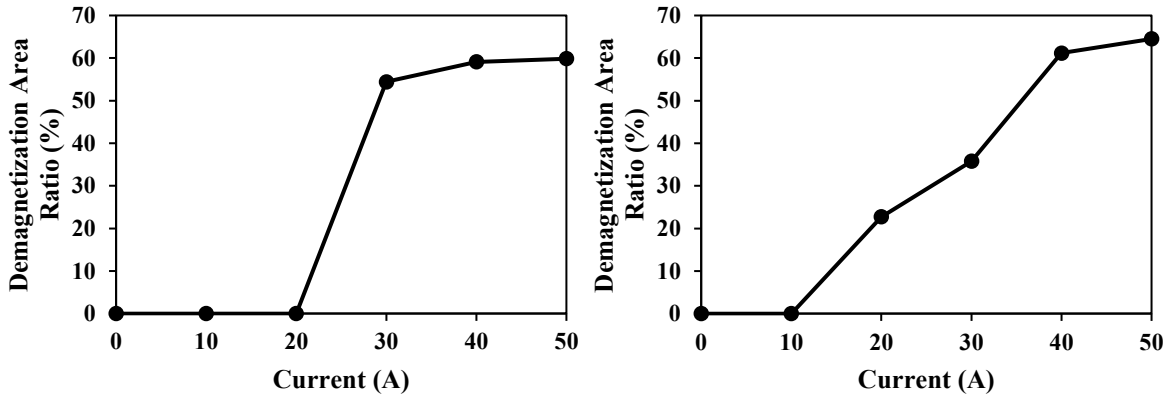

(a) 12s8p-PSCPPM (b) 12s10p-PSCPPM

Fig. 6.36 Demagnetization area ratios negative *d*-axis current.

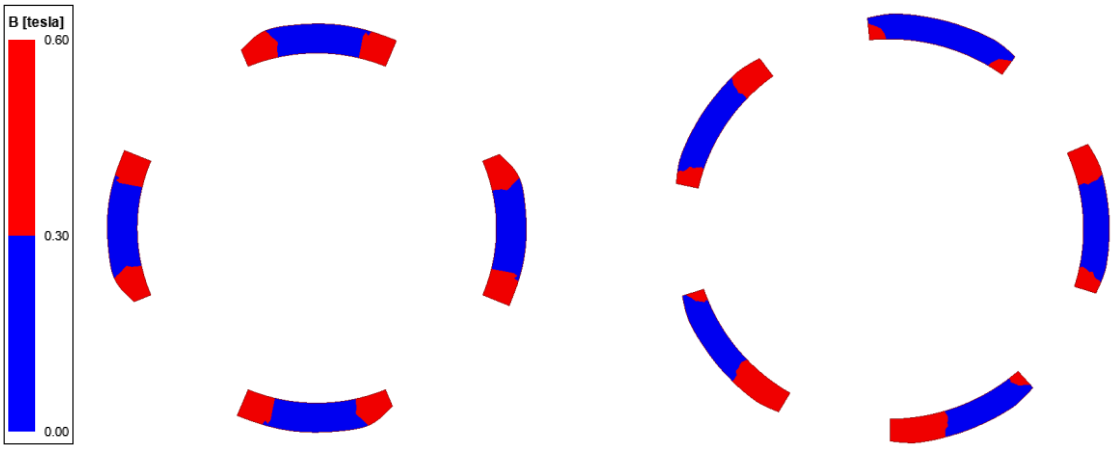

(a) 12s8p-PSCPPM (b) 12s10p-PSCPPM

Fig. 6.37 Demagnetization area distribution under I_d=-50A.

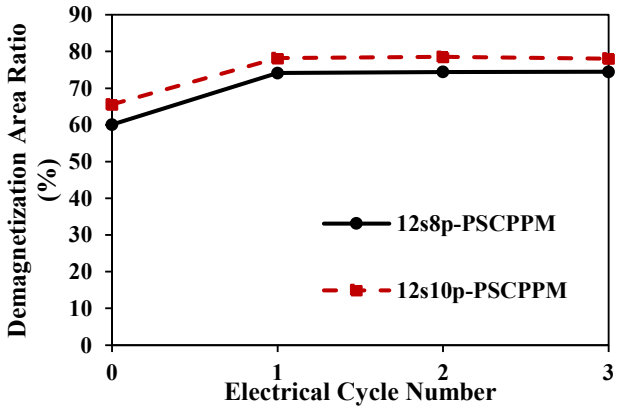

Fig. 6.38 Creeping effect of demagnetization with I_d=-50A.

6.5 Experimental Results

To validate the FEM analysis results, four prototypes, namely 12s8p-CCPPM, 12s8p-PSCPPM, 12s10p-CCPPM, and 12s10p-PSCPPM, are manufactured and tested, Fig. 6.39. The experiment test rigs are demonstrated in Fig. 3.18, Fig. 2.24 (b), and Fig. 4.24 where the dynamic platform is used for testing on-load torques and back EMFs, while the static platform is used for testing cogging torques and inductances.

(a) 12s8p (left) and 12s10p (right) stators

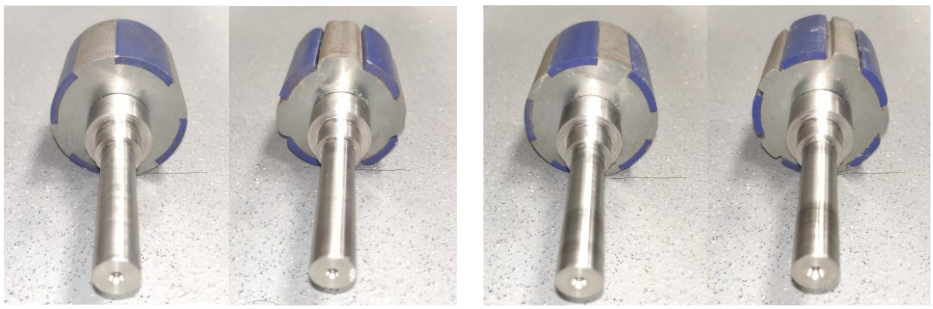

(b) Rotors (from left to right: 12s8p-CCPPM, 12s8p-PSCPPM, 12s10p-CCPPM, 12s10p-PSCPPM)

Fig. 6.39 Manufactured prototypes.

6.5.1 Test with Static Platform

The method proposed in [Zhu09b] is employed to test the cogging torques. Fig. 6.40 to Fig. 6.43 compare the experimental and FEM results under open circuit condition. Since the prototype is handmade and the test rig will cause noise in the transient torque, there are small errors in cogging torques and inductances but the waveform shape is consistent. Overall, the experimental results agree well with FEM results, which validates the effectiveness of FEM results.

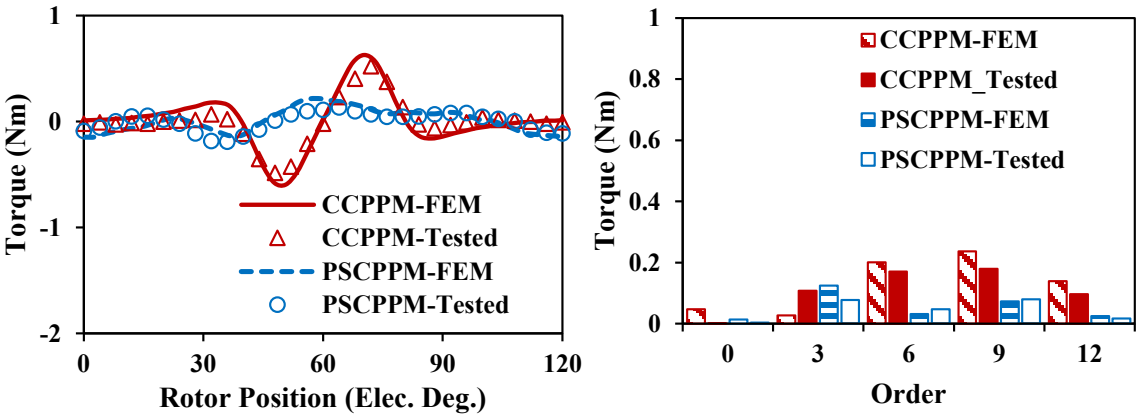

Fig. 6.40 Cogging torque waveforms and spectra of 12s8p machines.

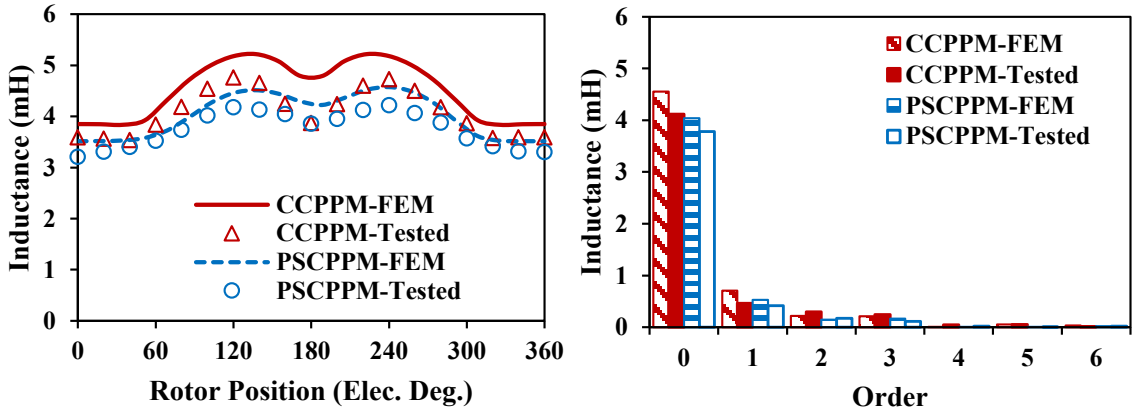

Fig. 6.41 Inductance waveforms and spectra of 12s8p machines.

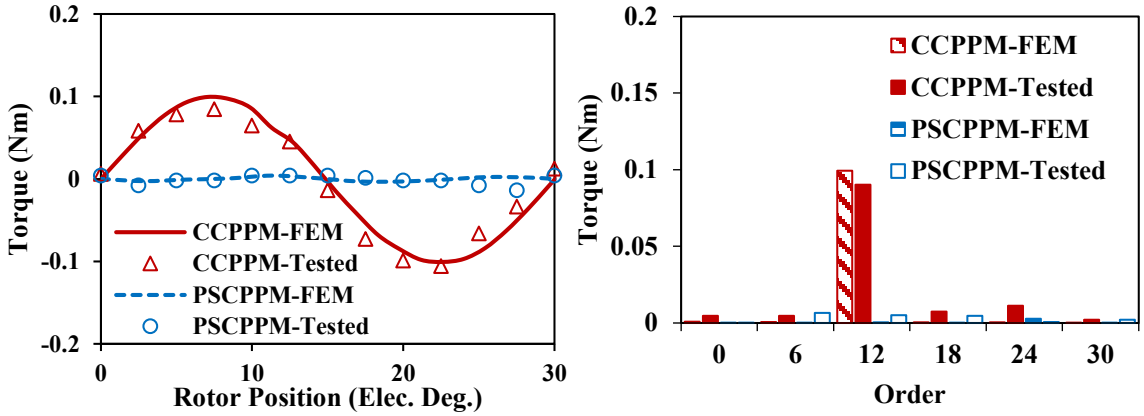

Fig. 6.42 Cogging torque waveforms and spectra of 12s10p machines.

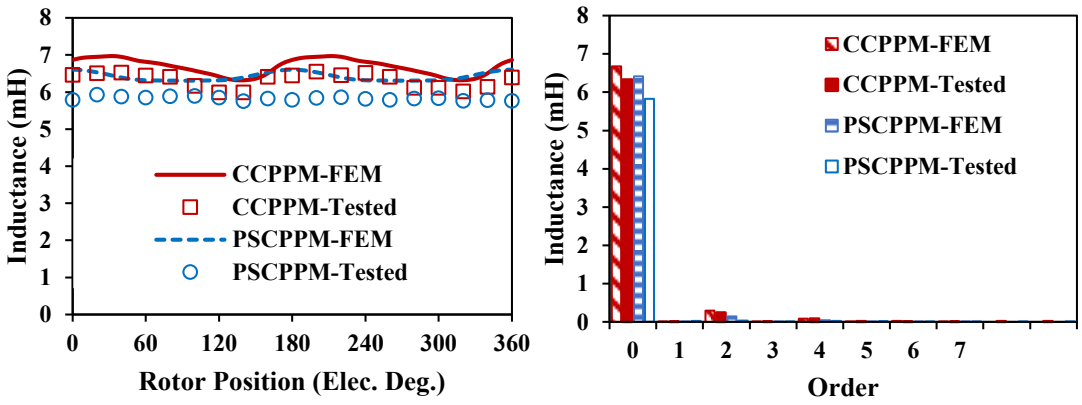

Fig. 6.43 Inductance waveforms and spectra of 12s10p machines.

6.5.2 Test with Dynamic Platform

With torque transducer and reader in the dynamic platform, the on-load torque waveforms for these four machines can be obtained as demonstrated in Fig. 6.44 and Fig. 6.45. It can be found that the tested torque ripples for two PSCPPM machines are a little larger than the FEM results due to assembly deficiencies and measurement error, but the trend is in good agreement with the FEM results.

Limited by the controller and the test rig, the prototype machines can only work with a maximum current of 10A. Consequently, Fig. 6.44 (c) and Fig. 6.45 (c) only show the torque performances under 10A. Obviously, with these conditions, the saturation caused by armature reaction is not serious thus leading to almost linear torque-current relationships. Generally, good agreement between experimental and FEM results can be witnessed, which confirms the analysis.

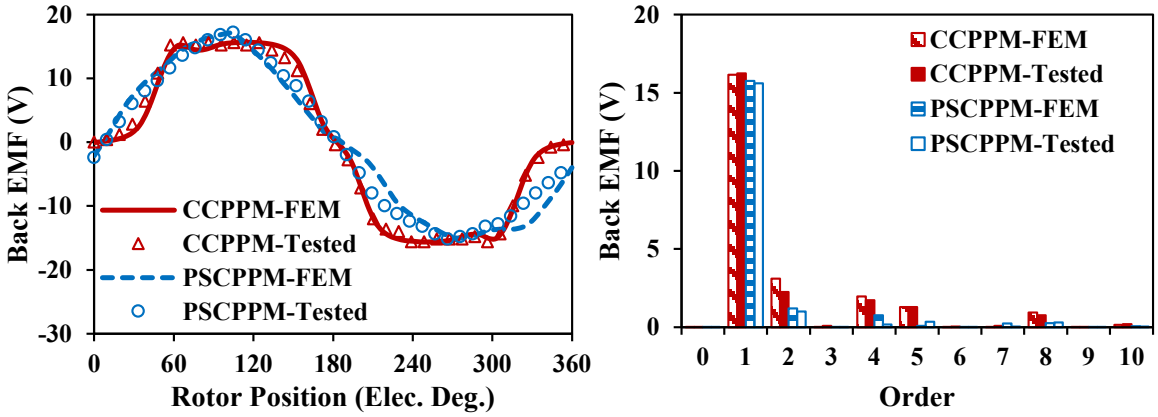

(a) Back EMFs

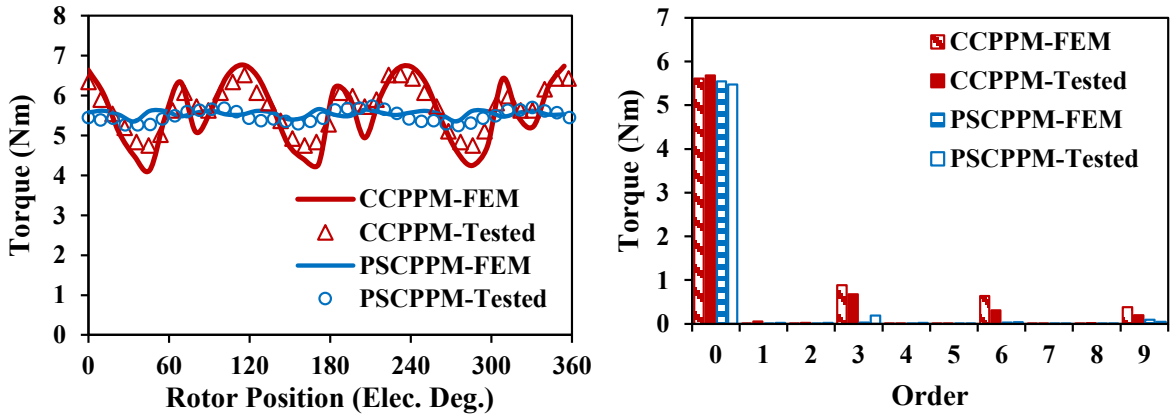

(b) Rated torques (10A)

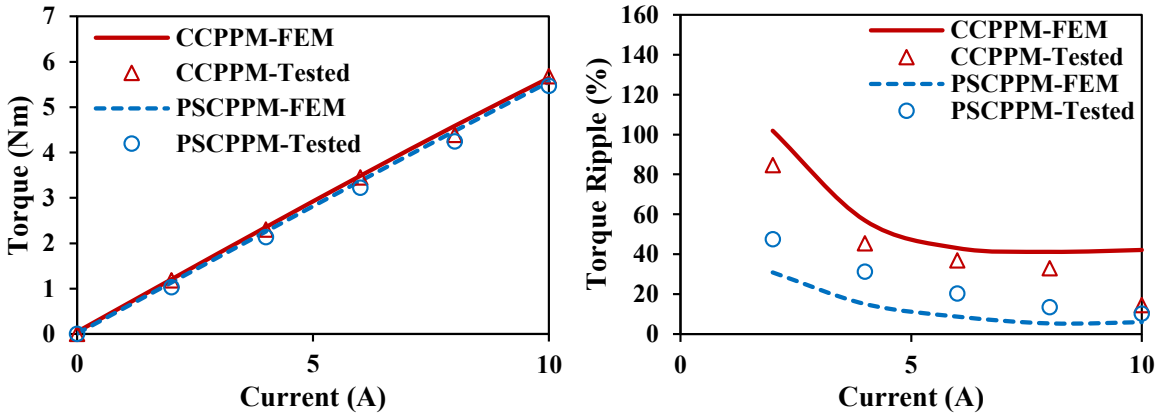

(c) Torque performances under different current

Fig. 6.44 On load performances of 12s8p machines.

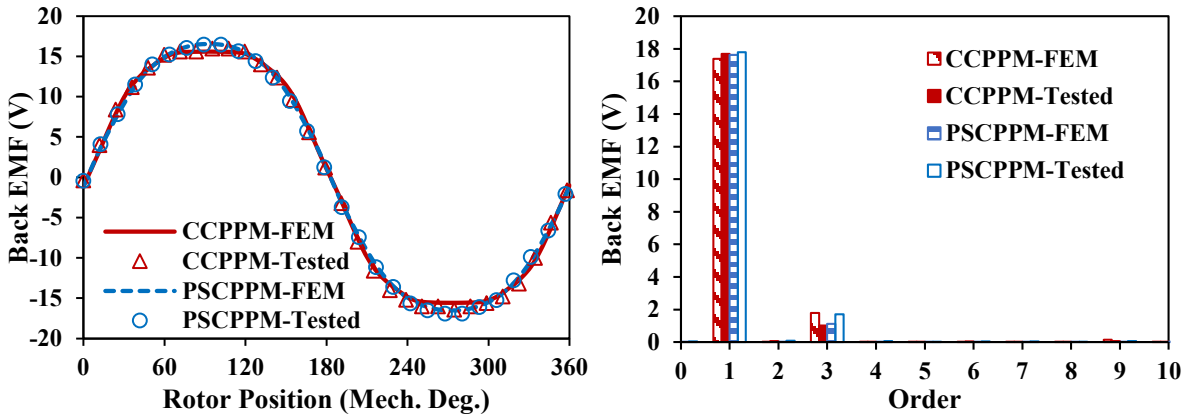

(a) Back EMFs

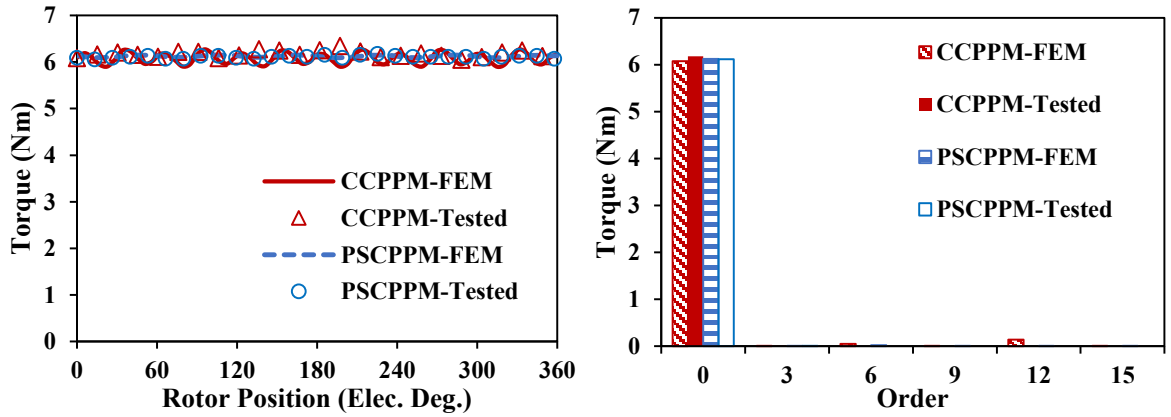

(b) Rated torques (10A)

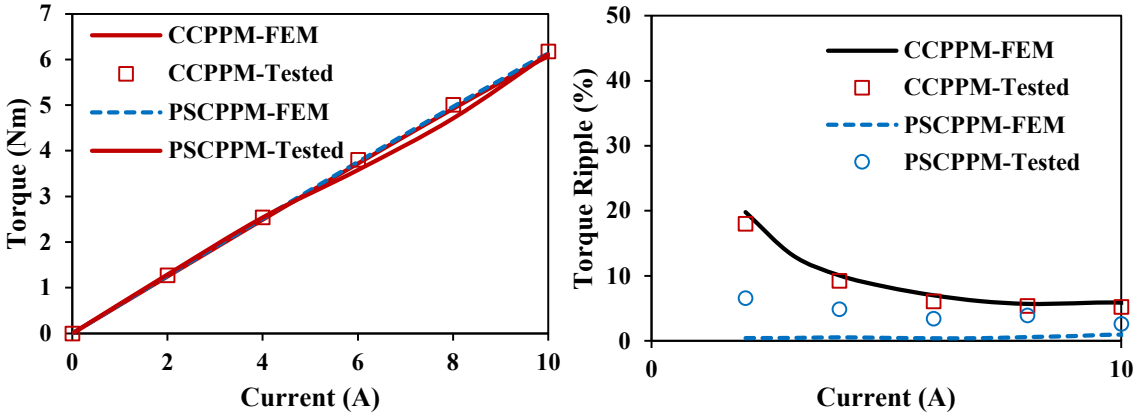

(c) Torque performances under different current

Fig. 6.45 On load performances of 12s10p machines.

6.6 Summary

This chapter focuses on the influence of armature reaction in CPPM machines. Six machines with 12s8p and 12s10p are selected to demonstrate the influence of armature reaction. Firstly, SPM and CCPPM machines are compared to show the general influence of armature reaction on CPPM machines. It is found that the amplitudes of the 3rd order inductance harmonics reduce in 12s8p-CCPPM machine with the increase of current, but the overall torque ripples still show an increasing trend. Then, the influences of armature reaction on pole-shaped machines are analyzed, which shows that the 12s8p-PSCPPM machine can only achieve low torque ripple in a small range around the rated working condition, while the 12s10p-PSCPPM machine can achieve much lower torque ripple in a wide range. In addition, it is also found that CPPM machines suffer from weaker demagnetization withstand capabilities and weaker

overload capabilities than SPM counterparts due to the large armature reactions. The FEM results are validated by experimental results with four prototypes.

CHAPTER 7
GENERAL CONCLUSION AND FUTURE WORK

7.1 General Conclusion

7.1.1 Research Scope

In this thesis, a novel analytical method for analyzing cogging torque has been developed accounting for unbalanced features in CPPM machines and conventional SPM machines; symmetrical and asymmetric pole shaping methods are utilized for reducing torque ripple in CPPM machines, in which the torque ripple components, i.e. cogging, PM, and reluctance torque ripples, are counteracted; and the influence of slot/pole number combinations and armature reaction are investigated. It is found that the asymmetric pole shaping method can always achieve the lowest torque ripple, while the symmetrical pole shaping method saves computation time due to fewer variables. Concrete summaries and comparisons will be given in the following text.

In Chapter 2, a novel analytical method has been developed for analyzing cogging torque in CPPM machines. It can account for unbalanced features in CPPM machines and conventional SPM machines. Consequently, similarities and differences in fundamental orders of cogging torque between CPPM and conventional SPM machines have been identified. The cogging torque can be minimized from the developed analytical model by employing analytically derived optimum design parameters, including slot opening width and pole arc width. To further reduce on-load torque ripple, in Chapter 3, symmetrical pole shaping method is proposed with both cogging torque and PM torque considered. This is followed by Chapter 4, where the torque ripple components, i.e. cogging, PM, and reluctance torque ripples, are counteracted each other by asymmetric pole shaping method. It is found that the asymmetric pole shaping method can achieve a much smaller torque ripple than the symmetrical pole shaping method in a 12s8p CPPM machine. However, it is also found that both slot/pole number combination and armature reaction will affect the performances of torque ripple. For torque ripple counteraction capability, asymmetric pole shaping method can only have the

benefits with CPPM machines that have odd number of slots per phase per submachine since the unbalanced north and south pole features can produce additional harmonics in winding flux linkage and winding inductance in these machines, as analyzed in Chapter 5. In addition, the influence of armature reaction is researched in Chapter 6. It is shown that the harmonics in flux density, flux linkage, back EMF, inductance, and torque ripple can be affected for all the CPPM machines. The relationship between chapters is summarized in Fig. 7.1.

As shown in Fig. 7.2, the contents of this thesis can be concluded in three aspects:

1) Research methodology.

2) Features of torque ripple reduction solutions.

3) Influencing factors.

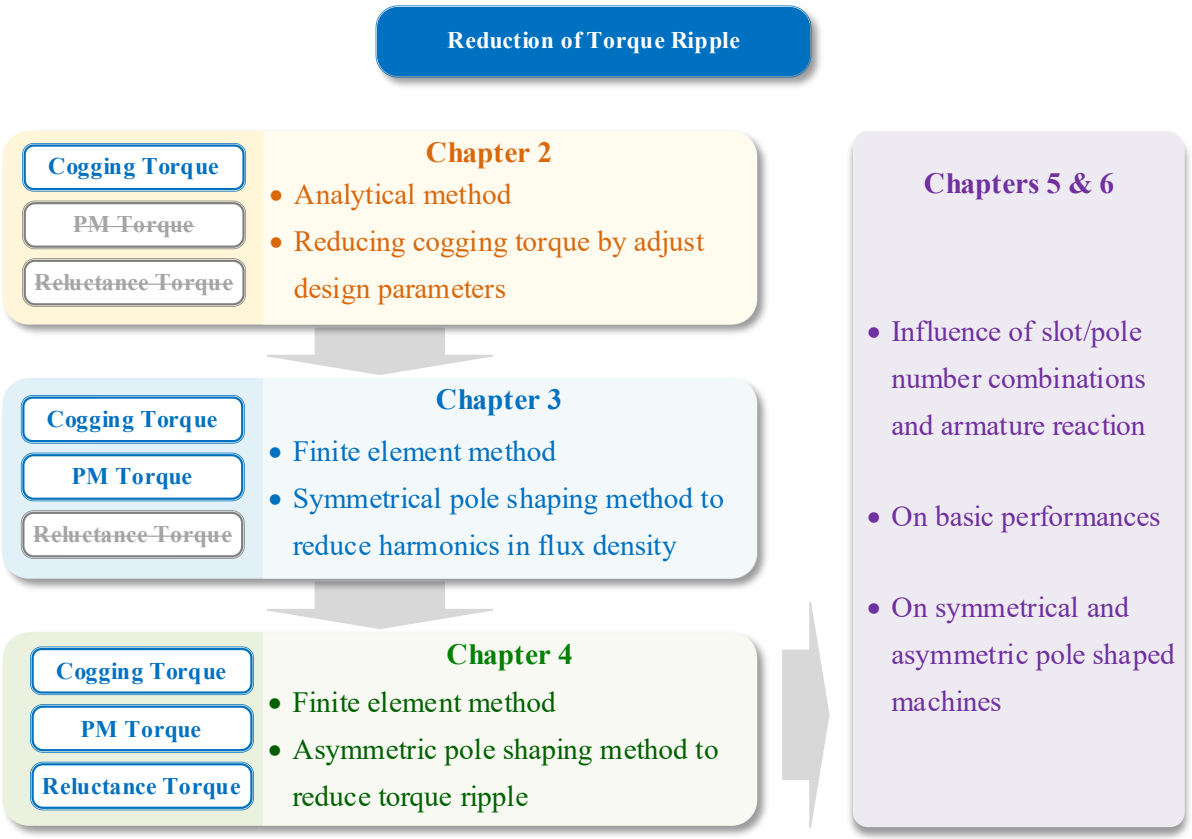

Fig. 7.1 Relationship between different Chapters.

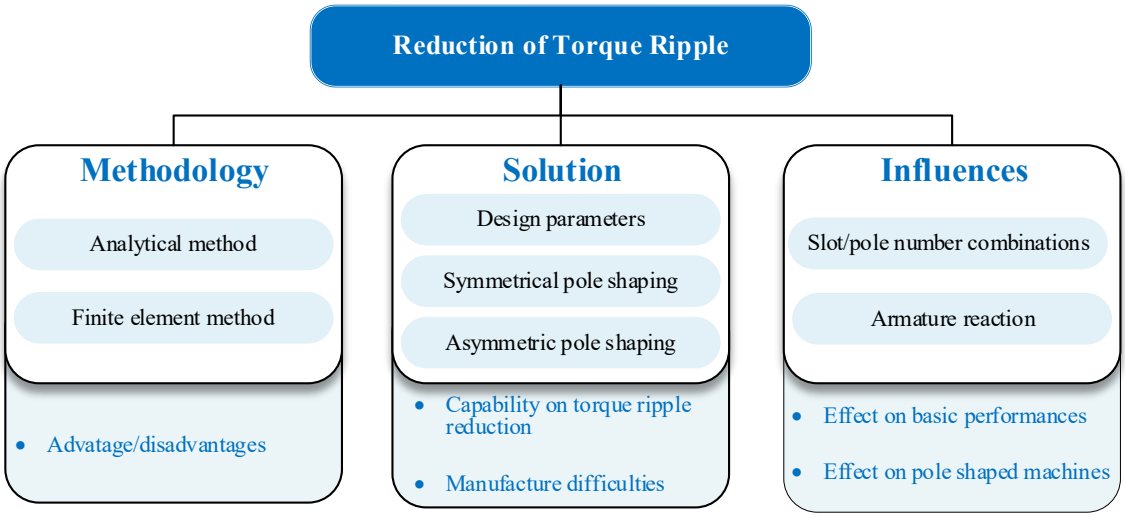

Fig. 7.2 Structure of Chapter 7.

7.1.2 Research Methodologies

Both analytical and FEM are employed in this thesis.

For analytical methods, magnetic circuit method and energy method are used in Chapter 1 and Chapter 2, respectively.

In Chapter 1, the magnetic circuit method is used to introduce the general performance of CPPM machines.

In Chapter 2, the energy method is adopted to obtain the relationship between design parameters and no-load cogging torque, which can be applied to both CPPM and SPM machines. Based on the developed analytical model, the characteristics of cogging torque in the machines with unequal north and south pole widths, particularly the fundamental cogging torque order, are analytically derived and general methodologies for minimizing the cogging torque are obtained, accounting for the influences of design parameters, including the slot opening ratio, the rotor pole ratio, and the rotor pole shifting, etc. The contributions can be summarized as follows:

1) When the north and south pole widths are unequal, no matter whether they are CPPM machines or SPM machines, the fundamental cogging torque order is the LCM between N_s and p, while it is the LCM between N_s and $2p$ when the machine has equal north and south pole widths.

2) Even if the north and south pole widths are equal, as long as the north and south poles are physically not identical, as often the case in CPPM machines, the fundamental cogging torque order is the LCM between N_s and p.

3) When there is an even number of slots in one submachine, LCM(N_s, p)=LCM(N_s, 2p). On the contrary, when there is an odd number of slots in one submachine, LCM(N_s, p)=LCM(N_s, 2p)/2.

4) The cogging torque in CPPM machines can be minimized by selecting proper slot opening width, PM and iron pole widths.

5) North or south pole shifting is prone to change the optimum PM and iron pole widths combinations. However, it is verified that the pole shifting will not affect the minimum cogging torque under some specific pole-arc widths combinations.

However, the saturation and different features between PM and iron poles for CPPM machines are neglected in analytical methods.

To analyze the torque ripple comprehensively and improve the accuracy of calculation, FEM without and with frozen permeability (FP) method is adopted in Chapter 3 and Chapters 4-6, respectively. In Chapter 3, FEM can obtain the performances by considering the saturation and different features between PM and iron poles. In this chapter, the harmonics in air-gap flux density are suppressed by symmetrical pole shaping method. To further separate the on-load performances, including the on-load torque components, on-load flux linkages, on-load inductances, etc., the FEM with FP is adopted in Chapters 4-6, where an asymmetric pole shaping method is proposed to further reduce the on-load torque ripple and the influences of slot/pole number combinations as well as armature reaction are analyzed.

These are concluded in Table 7.1.

Table 7.1. Comparisons of Research Methodologies

Analysis method		Chapter	Description
Analytical	Magnetic circuit	1	• General performance analysis. • Not accurate enough.
	Energy	2	• Reveal the relationships between design parameters and cogging torque. • Ignore magnetic saturation and different features between PM and iron poles.
FEM	Without FP	3	• Obtain the performances by considering the saturation and different features between PM and iron poles. • Cannot separate the on-load performances.
	With FP	4-6	• Separate the on-load performances, including torque components and on-load back EMF.

7.1.3 Features of Torque Ripple Reduction Solutions

In this thesis, there are three methods investigated to reduce torque ripples:

1) Optimizing design parameters;

2) Symmetrical pole shaping method;

3) Asymmetric pole shaping method.

Their different features are summarized in Table 7.2.

The first two methods, namely optimizing design parameters and symmetrical pole shaping method can reduce the no-load cogging torque effectively, while asymmetric pole shaping method can result in minimum onload torque ripple although the cogging torque is relatively larger. This is because the harmonics in air-gap flux densities in CPPM machines with the first two methods can be minimized. On the other hand, in asymmetric pole shaping method, in order to minimize onload torque ripple, extra torque ripple components are introduced to

counteract each other, which means that the extra harmonics in air-gap flux densities are also introduced and the cogging torque cannot be minimized. Nevertheless, the cogging torque in CPPM machines with this method can still be much lower than that in conventional CPPM machines with plain pole shapes. Therefore, for three methods, the effectiveness of torque ripple reduction under light load conditions, which is highly related to the cogging torque, exhibits a similar trend as cogging torque suppression.

Although the cogging torque can be reduced by optimizing design parameters, the onload torque ripple under heavy load condition is still large since the PM and reluctance torque ripples caused by armature reaction are very large and need to be considered. Symmetrical pole shaping method can only suppress the PM torque ripple by reducing amplitudes of harmonics in flux linkage. On the contrary, the asymmetric pole shaping method can not only suppress the PM torque ripple, but also manipulate the phasors of torque harmonics, including PM, reluctance, and cogging torques, which contribute to the lowest overall torque ripple. But due to the number of variables are the highest for asymmetric pole shaping method, it takes the highest computational cost, while the first method is the easiest in design process. In terms of manufacturing process, last two methods with pole shaping are relatively harder than the first method.

These characteristics are summarized and compared in Table 7.2.

7.1.4 Influencing Factors

Two influencing factors, namely, slot/pole number combinations and armature reaction, are investigated in this thesis.

Cogging torque can always be minimized when the pole arc ratio is $2kp/N_c$ regardless the slot/pole number combinations for CPPM machines, where k is any positive integer, and N_c is the LCM between slot number N_s and rotor pole-pair number p. Besides, the torque ripple can always be reduced with asymmetric pole shaping method. However, for CPPM machines with even slot number for one phase in a submachine, the symmetrical pole shaping method can achieve a similar level of torque ripple as that of asymmetric method but with lower optimization complexity. In addition, for this type of CPPM machines, wider PM pole arc than

iron pole arc can be applied to improve average torque without leading to large torque ripple since the effect of unbalanced PM and iron features can be eliminated by the winding connection. On the contrary, for other CPPM machines, PM pole arc and iron pole arc need to be almost identical to reduce torque ripple, which affect the average torque.

CPPM machines always suffer from high saturation problems due to high winding inductance and high armature reaction. Both amplitude and phase angles of harmonics in cogging torque and torque ripple can be affected by the armature reaction. Besides, the armature reaction will affect the linearity of average torque against current.

All of these are summarized in Table 7.3.

Table 7.2. Comparison of Features of Torque Ripple Reduction Solutions

	Design parameters (slot opening width, north and south pole widths, etc.)	**Symmetrical pole shaping**	**Asymmetric pole shaping**
Capability of cogging torque reduction	Good	Good	Middle
Capability of torque ripple reduction under light load conditions	Good	Good	Middle
Capability of torque ripple reduction under heavy load conditions	Poor	Middle	Good
Design difficulties	Easy	Middle	Hard
Manufacture difficulties	Easy	Hard	Hard

Table 7.3. Comparison of Influencing Factors

	Slot/Pole number combination		**Armature reaction**
	Odd slot number per phase per submachine	**Even slot number per phase per submachine**	
Cogging torque minimization	Cogging torque can always be minimized when pole arc ratio is $2kp/N_c$.		Both amplitude and phase angles of harmonics are affected.
Torque ripple reduction	Asymmetric pole shaping can result in a much lower torque ripple than symmetrical pole shaping.	Symmetrical pole shaping method can achieve a similar level of torque ripple as that of asymmetric method but with lower optimization complexity.	
Average torque	PM pole arc and iron pole arc need to be almost identical to reduce torque ripple, which affect the average torque.	Wider PM pole arc than iron pole arc can be applied to improve average torque.	Linearity is affected.

7.2 Future Work

Based on the above analyses and conclusions, some future work are summarized as follows:

(1) Investigating the influences of parallel winding branches on performances, including flux density, flux linkage, inductance, back EMF, torque ripple, etc.

(2) Investigating parasitic effects, e.g. acoustic noise and vibration, for symmetrical and asymmetric pole shaped CPPM machines.

(3) Investigating the torque ripple reduction methods in vernier CPPM machines with high pole number where the magnetic gearing effect is relatively large.

(4) Investigation of symmetrical and asymmetric pole shaping methods with other rotor CPPM structures, such as IPM, IPM spoke-type, combined CPPM and spoke-type machine structures [Daj19], with FEM frozen permeability method.

(5) Investigation of the torque performances in stator CPPM machines and the influence of slot/pole number combinations.

(6) Applying the counteraction effect of torque components in other kinds of machine structures to reduce the overall torque ripple.

(7) Sensitivity analysis of torque performances of CPPM machines to manufacturing and assembly errors.

Appendix: Expansion of $G^2(\theta)$, $B^2(\theta, \alpha)$ Expressions in Chapter 2

To aid the expansion of the $G^2(\theta)$, $B^2(\theta, \alpha)$ expressions in chapter 2, the Fourier series of a standard square wave function $Sq(\theta)$, Fig. A.1, can be given by

$$Sq(\theta) = k_d + \frac{2}{\pi}\sum_{n=1}^{\infty}\frac{\sin(k_d n\pi)}{n}\cos\left(n\frac{2\pi}{T}\theta\right) \tag{A.1}$$

where T is the periodicity period and k_d is the ratio of high amplitude region to T, which can be simply expressed by the ratio of slot opening to slot pitch or the ratios of pole-arcs to pole-pitch in deriving $G^2(\theta)$ and $B^2(\theta,\alpha)$.

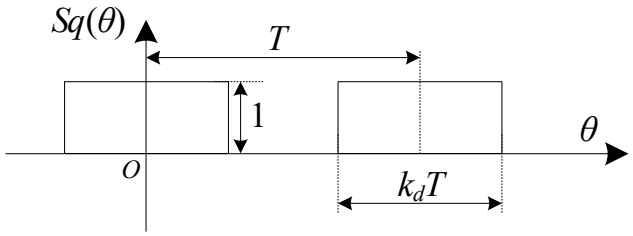

Fig. A.1 Square waveform used for deriving $G^2(\theta)$ and $B^2(\theta,\alpha)$.

A.1 Derivation of Permanence Coefficients G_{a0}, G_{akNs}, and G_{bkNs}

Assuming the depth of stator slots is infinite, the simplified permeance function can be obtained in Fig. 2.2 (a). Supposing γ_0 is the slot opening angle, the ratio of slot opening to slot pitch, k_{so}, can be defined as:

$$k_{so} = \frac{\gamma_0}{2\pi/N_s} \tag{A.2}$$

Thus, the waveform of $G^2(\theta)$ can be expressed as:

$$G^2(\theta) = G_{atooth}Sq(\theta) \tag{A.3}$$

Based on (A.3), the Fourier coefficients in (2.2), G_{a0} and G_{akNs}, can be given by:

$$G_{a0} = (1 - k_{so})G_{atooth} \tag{A.4}$$

$$G_{akN_s} = \frac{2G_{atooth}}{k\pi}\sin\big((1-k_{so})k\pi\big) = \frac{2N_sG_{atooth}}{nN_C\pi}\sin\left((1-k_{so})\frac{nN_C}{N_s}\pi\right) \quad \text{(A.5)}$$

Due to symmetrically distributed stator slots, G_{bkNs} is zero. If the slots are asymmetrically distributed, G_{bkNs} can also be derived similarly.

B.1 Derivation of Flux Density Coefficients B_{a0}, B_{aqp}, and B_{bqp}

Albeit the north and the south pole-arc widths are different, Fig. 2.2 (b), the fluxes under the north pole (PM pole) and the south pole (iron pole) should be the same, i.e.:

$$B_{anorth}S_{north} = B_{asouth}S_{south} \quad \text{(A.6)}$$

where B_{north} and B_{south} are the amplitudes of flux densities under the north and south poles, respectively, and S_{north} and S_{south} are the corresponding cross-section areas. Since the stack axial lengths for PM pole and iron pole are the same and the radius of the outer surfaces for north and south poles are also the same, the above formula can be rewritten as:

$$B_{anorth}k_{north} = B_{asouth}k_{south} \quad \text{(A.7)}$$

Neglecting the axial flux leakage and magnet fringing effect, the air-gap B^2 waveform can be considered as constant over the pole-arc and zero between inter-poles. Therefore, similar to $G^2(\theta)$ in (A.3), the waveform of $B^2(\theta,\alpha)$ distribution can be considered as a combination of two square waves with different north and south pole-arc ratios and different amplitudes, i.e.:

$$B^2(\theta,\alpha) = B_{anorth}Sq(p\theta,\alpha) + B_{asouth}Sq(p\theta-\pi-\beta,\alpha) \quad \text{(A.8)}$$

Substituting (A.1) into (A.8), the Fourier coefficient B_{a0}, and q-th order harmonic in $B^2(\theta,\alpha)$, $B_q{}^2(\theta,\alpha)$, can be derived as:

$$B_{a0} = B_{anorth}\frac{k_{north}}{2} + B_{asouth}\frac{k_{south}}{2} \quad \text{(A.9)}$$

$$
\begin{aligned}
&{B_q}^2(\theta,\alpha)\\
&=\frac{2B_{anorth}}{\pi}\frac{\sin\left(q\frac{k_{north}}{2}\pi\right)}{q}\cos(qp\theta-qp\alpha)\\
&+\frac{2B_{asouth}}{\pi}\frac{\sin\left(q\frac{k_{south}}{2}\pi\right)}{q}\cos(q(p\theta-\pi-\beta)-qp\alpha)\\
&=\frac{2B_{anorth}}{q\pi}\sin\left(\frac{qk_{north}}{2}\pi\right)\cos(qp\theta-qp\alpha)\\
&+(-1)^q\frac{2B_{asouth}\sin\left(q\frac{k_{south}}{2}\pi\right)}{q\pi}\cos(qp\theta-qp\alpha)\cos(q\beta)\\
&+(-1)^q\frac{2B_{asouth}\sin\left(q\frac{k_{south}}{2}\pi\right)}{q\pi}\sin(qp\theta-qp\alpha)\sin(q\beta)
\end{aligned}
\tag{A.10}
$$

Consequently, substituting (2.6) into (A.10), the Fourier coefficients B_{aqp} and B_{bqp} can be given by:

$$
\begin{aligned}
B_{aqp} &= \frac{2pB_{anorth}}{nN_C\pi}\sin\left(\frac{nN_Ck_{north}}{2p}\pi\right)\\
&\quad+(-1)^{\frac{nN_C}{p}}\frac{2pB_{asouth}\sin\left(\frac{nN_Ck_{iron}}{2p}\pi\right)}{nN_C\pi}\cos\left(\frac{nN_C}{p}\beta\right)
\end{aligned}
\tag{A.11}
$$

$$
B_{bqp}=(-1)^{\frac{nN_C}{p}}\frac{2pB_{asouth}\sin\left(\frac{nN_Ck_{iron}}{2p}\pi\right)}{nN_C\pi}\sin\left(\frac{nN_C}{p}\beta\right)
\tag{A.12}
$$

Considering the relation between B_{north} and B_{south} in (A.7), (A.11) and (A.12) can be rewritten as:

$$
\begin{aligned}
B_{aqp} &= \frac{2pB_{anorth}}{nN_C\pi}\left[\sin\left(\frac{nN_Ck_{north}}{2p}\pi\right)\right.\\
&\quad\left.+(-1)^{\frac{nN_C}{p}}\left(\frac{k_{north}}{k_{south}}\right)^2\sin\left(\frac{nN_Ck_{south}}{2p}\frac{k_{south}}{2}\pi\right)\cos\left(\frac{nN_C}{p}\beta\right)\right]
\end{aligned}
\tag{A.13}
$$

$$
B_{bqp}=(-1)^{\frac{nN_C}{p}}\frac{2pB_{anorth}}{nN_C\pi}\left(\frac{k_{north}}{k_{south}}\right)^2\cdot\sin\left(\frac{nN_Ck_{south}}{2p}\pi\right)\sin\left(\frac{nN_C}{p}\beta\right)
\tag{A.14}
$$

REFERENCES

[All20]	A. Allahyari and H. Torkaman, "A novel high-performance consequent pole dual rotor permanent magnet vernier machine," *IEEE Trans. Energy Convers.*, vol. 35, no. 3, pp. 1238-1246, Sept. 2020.
[Asa09]	Y. Asano, A. Mizuguchi, M. Amada, J. Asama, A. Chiba, M. Ooshima, M. Takemoto, T. Fukao, O. Ichikawa, and D. G. Dorrell, "Development of a four-axis actively controlled consequent-pole-type bearingless motor," *IEEE Trans. Ind. Appl.*, vol. 45, no. 4, pp. 1378-1386, July-Aug. 2009.
[Asa13]	J. Asama, D. Kanehara, T. Oiwa, and A. Chiba, “Suspension performance of a two-axis actively regulated consequent-pole bearingless motor,” *IEEE Trans. Energy Convers.*, vol. 28, no. 4, pp. 894-901, Dec. 2013.
[Asa14]	J. Asama, D. Kanehara, T. Oiwa, and A. Chiba, “Development of a compact centrifugal pump with a two-axis actively positioned consequent-pole bearingless motor,” *IEEE Trans. Ind. Appl.*, vol. 50, no. 1, pp. 288-295, Jan.-Feb. 2014.
[Asa15]	J. Asama, A. Mouri, T. Oiwa, and A. Chiba, “Suspension force investigation for consequent-pole and surface-mounted permanent magnet bearingless motors with concentrated winding,” *Proc. IEEE Int. Electr. Mach. Drives Conf. (IEMDC)*, May 2015, pp. 780-785.
[Aza12]	Z. Azar, Z. Q. Zhu, and G. Ombach, "Influence of electric loading and magnetic saturation on cogging torque, back-EMF, and torque ripple of PM machines," *IEEE Trans. Magn.*, vol. 48, no. 10, pp. 2650-2658, Oct. 2012.
[Bai15]	G. Bailey, N. Mancheri, and K. V. Acker, “Sustainability of permanent rare earth magnet motors in (H)EV industry,” *J. Sustain. Metall.*, vol. 1, no. 1, 2015.
[Bai18]	J. Bai, J. Liu, M. Wang, P. Zheng, Y. Liu, H. Gao, and L. Xiao, "Investigation of a less rare-earth permanent-magnet machine with the consequent pole rotor," *AIP Adv.*, vol. 8, no. 5, pp. 056626.1- 056626.6, Nov. 2018.
[Bal18]	N. Baloch, B.-I. Kwon, and Y. Gao, “Low-cost high-torque-density dual-stator consequent-pole permanent magnet Vernier machine,” *IEEE Trans. Magn.*, vol. 54, no. 11, Nov. 2018.
[Bia02]	N. Bianchi and S. Bolognani, "Design techniques for reducing the cogging torque in surface-mounted PM motors," *IEEE Trans. Ind. Appl.*, vol. 38, no. 5, pp. 1259-1265, Sept.-Oct. 2002.
[Bor21]	S. T. Boroujeni, S. P. Emami, N. Takorabet, and A.Mahmoudi, "Analytical investigation of the armature current influence on the torque and radial force in eccentric consequent-pole PM machines," *IET Electr. Power Appl.*, vol. 15, no. 4, pp. 1751-8660, 2021.

[Bot20]	C.D. Botha, M.J. Kamper, R.-J. Wang, and A.J. Sorgdrager, "Force ripple and cogging force minimisation criteria of single-sided consequent-pole linear vernier hybrid machines," *Int. Conf. Electr. Mach. (ICEM)*, 2020, pp. 469-475.
[Bre00]	C. Breton, J. Bartolome, J.A. Benito, G. Tassinario, I. Flotats, C.W. Lu, and B.J. Chalmers, "Influence of machine symmetry on reduction of cogging torque in permanent-magnet brushless motors," *IEEE Trans. Magn.*, vol. 36, no. 5, pp. 3819-3823, Sept 2000.
[Cai20]	S. Cai, Z. Q. Zhu, C. Wang, J. C. Mipo, and S. Personnaz, "A novel fractional slot non-overlapping winding hybrid excited machine with consequent-pole pm rotor," *IEEE Trans. Energy Convers.*, vol. 35, no. 3, pp. 1628-1637, Sept. 2020.
[Cai21]	S. Cai, Z. Q. Zhu, S. Mallampalli, J. C. Mipo, and S. Personnaz, "Investigation of novel fractional slot nonoverlapping winding hybrid excited machines with different rotor topologies," *IEEE Trans. Ind. Appl.*, vol. 57, no. 1, pp. 468-480, Jan. /Feb. 2021.
[Cha20]	W. Chai, Z. Cai, B. -I. Kwon, and J. -W. Kwon, "Design of a novel low-cost consequent-pole permanent magnet synchronous machine," *IEEE Access*, vol. 8, pp. 194251-194259, 2020.
[Che21]	B. Chen, Y. Xiao, Y. Hu, M. Liu, and L. Li, "Radial force characteristics of a consequent-pole permanent magnet synchronous motor," *24th Int. Conf. Electr. Mach. Syst. (ICEMS)*, 2021, pp. 1162-1166.
[Chi18]	M. T. Chiu, J. A. Chiang, and C. H. Lin, "Design and optimization of a novel V-type consequent-pole interior permanent magnet synchronous motor for applying to refrigerant compressor," *Proc. 21st Int. Conf. Electri. Sys. (ICEMS)*, 2018, pp. 413-418.
[Chu10]	S. Chung, H. Lee, B. Woo, J. Kim, J. Lee, S. Moon, and S. Hwang, "A feasibility study on a new doubly salient permanent magnet linear synchronous machine," *IEEE Trans. Magn.*, vol. 46, no. 6, pp. 1572-1575, June 2010.
[Chu11]	S. Chung, J. Kim, B. Woo, D. Hong, J. Lee, and D. Koo, “A novel design of modular three-phase permanent magnet vernier machine with consequent pole rotor,” *IEEE Trans. Magn.*, vol. 47, no. 10, pp. 4215-4218, Oct. 2011.
[Chu12]	S. Chung, J. Kim, D. Koo, B. Woo, D. Hong, and J. Lee, "Fractional slot concentrated winding permanent magnet synchronous machine with consequent pole rotor for low speed direct drive," *IEEE Trans. Magn.*, vol. 48, no. 11, pp. 2965-2968, Nov. 2012.
[Chu13]	W. Q. Chu and Z. Q. Zhu, "On-load cogging torque calculation in permanent magnet machines," *IEEE Trans. Magn.*, vol. 49, no. 6, pp. 2982-2989, June 2013.

[Chu15]	S. U. Chung, J. W. Kim, Y. D. Chun, B. C. Woo, and D. K. Hong, “Fractional slot concentrated winding PMSM with consequent-pole rotor for a low-speed direct drive: reduction of rare earth permanent magnet,” *IEEE Trans. Energy Convers.*, vol. 30, no. 1, pp. 103–109, Mar. 2015.
[Chu16]	S. Chung, S. Moon, D. Kim, and J. Kim, "Development of a 20-pole–24-slot SPMSM with consequent pole rotor for in-wheel direct drive," *IEEE Trans. Ind. Electron.*, vol. 63, no. 1, pp. 302-309, Jan. 2016.
[Chu98]	S. Chung, H. Kim, C. Kim, and M. Youn, "A new instantaneous torque control of PM synchronous motor for high-performance direct-drive applications," *IEEE Trans. Power Electron.*, vol. 13, no. 3, pp. 388-400, May 1998.
[Daj18]	G. Dajaku, “Rotor for permanent magnet machines,” DE Patent Appl. 102 018 127 127.1, Oct. 30, 2018.
[Daj19]	G. Dajaku, H. Zhou, X. Dajaku, and D. Gerling, "Novel rotor design with reduced rare-earth material for PM machines," *IEEE Int. Electr. Mach. Drives Conf. (IEMDC)*, San Diego, CA, USA, 2019, pp. 1-7.
[Daj20]	G. Dajaku, "Open-circuit air-gap field calculation of a new PM machine having a combined SPM and spoke-type magnets," *IEEE Trans. Magn.*, vol. 56, no. 6, pp. 1-9, June 2020.
[Daj21]	G. Dajaku, "Analytical analysis of electromagnetic torque and magnet utilization factor for two different PM machines with SPM and HUPM rotor topologies," *IEEE Trans. Magn.*, vol. 57, no. 6, pp. 1-9, June 2021.
[Daj22]	G. Dajaku, "Comparison study of permanent magnet synchronous machines with consequent pole and HUPM rotor," *IEEE Trans. Magn.*, vol. 58, no. 3, pp. 1-10, March 2022.
[De89]	J. De La Ree and N. Boules, “Torque production in permanent-magnet synchronous motors,” *IEEE Trans. Ind. Appl.*, vol. 25, no. 1, pp. 107–112, 1989.
[Dhu21]	H. Dhulipati, S. Mukundan, Z. Li, E. Ghosh, J. Tjong, and N. C. Kar, “Torque performance enhancement in consequent pole PMSM based on magnet pole shape optimization for direct-drive EV,” *IEEE Trans. Magn.*, vol. 57, no. 2, pp. 1-7, Feb. 2021.
[Dhu21]	H. Dhulipati, S. Mukundan, Z. Li, E. Ghosh, J. Tjong, and N. C. Kar, “Torque performance enhancement in consequent pole PMSM based on magnet pole shape optimization for direct-drive EV,” *IEEE Trans. Magn.*, vol. 57, no. 2, pp. 1-7, Feb. 2021.
[Dor10]	D. G. Dorrell, M. Popescu, and D. M. Ionel, "Unbalanced magnetic pull due to asymmetry and low-level static rotor eccentricity in fractional-slot brushless permanent-magnet motors with surface-magnet and consequent-pole rotors," *IEEE Trans. Magn.*, vol. 46, no. 7, pp. 2675-2685, July 2010.

[Du19]	Z. S. Du and T. A. Lipo, "High torque density and low torque ripple shaped-magnet machines using sinusoidal plus third harmonic shaped magnets," *IEEE Trans. Ind. Appl.*, vol. 55, no. 3, pp. 2601-2610, May-June 2019.
[EIA20]	US EIA, “Manufacturing energy consumption survey.” IEA, Energy Efficiency Indicators, 2020.
[Eva10]	S. A. Evans, "Salient pole shoe shapes of interior permanent magnet synchronous machines," *The XIX Int. Conf. Electr. Mach. (ICEM)*, Rome, 2010, pp. 1-6.
[Fan20]	Y. Fan, Y. Mei, and Q. Zhang, " Torque ripple reduction of outer rotor permanent magnet vernier machine with concentrated winding," *Int. Conf. Electr. Mach. (ICEM)*, 2020, pp. 543-549.
[Gao16]	Y. Gao, R. Qu, D. Li, J. Li, and G. Zhou, “Consequent-pole flux-reversal permanent-magnet machine for electric vehicle propulsion,” *IEEE Trans. Appl. Supercond.*, vol. 26, no. 4, Jun. 2016.
[Gao18]	Y. Gao, D. Li, R. Qu, H. Fang, H. Ding, and L. Jing, "Analysis of a novel consequent-pole flux switching permanent magnet machine with flux bridges in stator core," *IEEE Trans. Energy Convers.*, vol. 33, no. 4, pp. 2153-2162, Dec. 2018.
[Gao20]	Y. Gao and M. Doppelbauer, "Comparative analysis of double flux modulation flux reversal machines with pms on both stator and rotor," *Int. Conf. Electr. Mach. (ICEM)*, 2020, pp. 1964-1970.
[Ge16]	X. Ge, Z. Q. Zhu, J. Li, and J. Chen, “A spoke-type IPM machine with novel alternate airspace barriers and reduction of unipolar leakage flux by step-staggered rotor,” *IEEE Trans. Ind. Appl.*, vol. 52, no. 6, pp. 4789-4797, Nov./Dec. 2016.
[Gha19]	A. Ghaffari, A. Rahideh, H. Moayed-Jahromi, A. Vahaj, A. Mahmoudi, and W. L. Soong, "2-D analytical model for outer-rotor consequent-pole brushless PM machines," *IEEE Trans. Energy Convers.*, vol. 34, no. 4, pp. 2226-2234, Dec. 2019.
[Gua14]	Y. Guan, Z. Q. Zhu, I. A. A. Afinowi, J. C. Mipo, and P. Farah, "Comparison between induction machine and interior permanent magnet machine for electric vehicle application," 17*th Int. Conf. Electr. Mach. Syst. (ICEMS)*, Hangzhou, 2014, pp. 144-150.
[Hen94]	J. R. Hendershot and T. J. E. Miller, Design of brushless permanent magnet motors. New York: Oxford Univ. Press, 1994.
[Hu18]	Y. Hu, Y. Xiao, B. Chen, and Q. Li, “Topology optimization of a consequent-pole rotor with V-shaped magnet placement,” *21st Int. Conf. Electr. Mach. Syst. (ICEMS)*, Jeju, 2018, pp. 234-239.

[Hua16]	H. Hua, Z. Q. Zhu, and H. L. Zhan, “Novel consequent-pole hybrid excited machine with separated excitation stator,” *IEEE Trans. Ind. Electron.*, vol. 63, no. 8, pp. 4718-4728, Aug. 2016.
[Hua18]	L. R. Huang, J. H. Feng, S. Y. Guo, Y. F. Li, J. X. Shi, and Z. Q. Zhu, "Rotor shaping method for torque ripple mitigation in variable flux reluctance machines," *IEEE Trans. on Energy Conversion*, vol. 33, no. 3, pp. 1579-1589, Sept. 2018.
[Hua20]	H. Huang, D. Li, R. Qu, and B. Han, "A dual consequent-pole split-tooth vernier machine with enhanced modulation effect," *2020 IEEE 1st China Int. Youth Conf. Electr. Eng. (CIYCEE)*, 2020, pp. 1-7.
[Hua21b]	H. Huang, D. Li, X. Ren, and R. Qu, "Analysis and reduction of cogging torque in dual PM vernier machine with irregular split teeth," *IEEE Int. Electr. Mach. Drives Conf. (IEMDC)*, 2021, pp. 1-8.
[Hua21c]	H. Huang, D. Li, R. Qu, X. Gao, and B. Han, "Design and analysis of T-shape consequent pole dual PM vernier machines with differential magnetic network method," *IEEE J. Emerg. Sel. Top. Power Electron.*, vol. 10, no. 4, pp. 4546-4555, Aug. 2022.
[Hwa00]	S. Hwang, J. Eom, G. Hwang, W. Jeong, and Y. Jung, "Cogging torque and acoustic noise reduction in permanent magnet motors by teeth pairing," *IEEE Trans. Magn.*, vol. 36, no. 5, pp. 3144-3146, Sept 2000.
[Hwa01]	S. Hwang, J. Eom, Y. Jung, D. Lee, and B. Kang, "Various design techniques to reduce cogging torque by controlling energy variation in permanent magnet motors," *IEEE Trans. Magn.*, vol. 37, no. 4, pp. 2806-2809, July 2001.
[Hwa14]	C. Hwang, S. Hung, C. Liu, and S. Cheng, "Optimal design of a high speed SPM motor for machine tool applications," *IEEE Trans. Magn.*, vol. 50, no. 1, pp. 1-4, Dec. 2014.
[Ife13]	C. J. Ifedi, B. C. Mecrow, S. T. M. Brockway, G. S. Boast, G. J. Atkinson, and D. Kostic-Perovic, "Fault-tolerant in-wheel motor topologies for high-performance electric vehicles," *IEEE Trans. Ind. Appl.*, vol. 49, no. 3, pp. 1249-1257, May-June 2013.
[Ish95]	A. Ishizaki, T. Tanaka, K. Takasaki, and S. Nishikata, "Theory and optimum design of PM Vernier motor," *7th Int. Conf. Electr. Mach. Drives*, 1995, pp.208-212.
[Jah96]	T. M. Jahns and W. L. Soong, "Pulsating torque minimization techniques for permanent magnet AC motor drives-a review," *IEEE Trans. Ind. Electron.*, vol. 43, no. 2, pp. 321-330, April 1996.
[Jer10]	J. Kolehmainen, "Optimal dovetail permanent magnet rotor solutions for various pole numbers," *IEEE Trans. Ind. Electron.*, vol. 57, no. 1, pp. 70-77, Jan. 2010.

[Jia20]	S. Jia, D. Liang, and Z.Q. Zhu, "Enhanced flux modulation of FSCW consequent pole PM machine employing stator slot Halbach PM," *Int. Conf. Electr. Mach. (ICEM)*, 2020, pp. 1985-1991.
[Jia21]	S. Jia, K. Yan, D. Liang, R. Qu, J. Liu, and J. He, "A novel DC-biased current dual PM vernier machine," *IEEE Trans. Ind. Appl.*, vol. 57, no. 5, pp. 4595-4605, Sept.-Oct. 2021.
[Jia22]	L. Jia, M. Lin, K. Lin, W. Le, and A. Yang, “Design and analysis of dual-rotor modular-stator hybrid-excited axial-flux permanent magnet vernier machine,” *Energies*, vol. 15, no. 4, pp. 1458.1-1458.13, 2022.
[Kol78]	Kollmorgen Technologies Corp., "Rare earth permanent magnet machines," U.K. Patent GB1598257A, Mar. 28, 1978.
[Li17]	F. Li, K. Wang, J. Li, H. Y. Sun, and P. C. Luk, "Electromagnetic performance analysis of PMSM with eccentric consequent pole rotor," *7th Int. Conf. Power Electron. Syst. Appl. Smart Mob. Power Xfer. & Sec. (PESA)*, Hong Kong, 2017, pp. 1-7.
[Li18a]	J. Li, K. Wang, and F. Li, "Analytical prediction of optimal split ratio of consequent-pole permanent magnet machines," *IET Electr. Power Appl.*, vol. 12, no. 3, pp. 365-372, Mar. 2018.
[Li18b]	J. Li and K. Wang, "Analytical determination of optimal PM-arc ratio of consequent-pole permanent magnet machines," *IEEE/ASME Trans. Mechatronics*, vol. 23, no. 5, pp. 2168-2177, Oct. 2018.
[Li18c]	F. Li, K. Wang, J. Li, and H. J. Zhang, "Suppression of even-order harmonics and torque ripple in outer rotor consequent-pole PM machine by multilayer winding," *IEEE Trans. Magn.*, vol. 54, no. 11, pp. 1-5, Nov. 2018.
[Li18d]	J. Li, K. Wang, C. Liu, and B. F. Xu, "Elimination of unipolar leakage flux in consequent-pole PM machines by employing novel pole sequence," *IEEE Trans. Magn.*, vol. 54, no. 11, pp. 1-5, Nov. 2018.
[Li18e]	J. Li, K. Wang, and C. Liu, "Torque improvement and cost reduction of permanent magnet machines with a dovetailed consequent-pole rotor," *IEEE Trans. Energy Convers.*, vol. 33, no. 4, pp. 1628-1640, Dec. 2018.
[Li18f]	H. Y. Li and Z. Q. Zhu, "Analysis of flux-reversal permanent-magnet machines with different consequent-pole pm topologies," *IEEE Trans. Magn.*, vol. 54, no. 11, pp. 1-5, Nov. 2018.
[Li18g]	Y. Li, H. Yang, H. Lin, and S. Lyu, "Analysis of field modulation effect in consequent pole permanent magnet machines with concentrated windings," *The XIII Int. Conf. Electr. Mach. (ICEM)*, Alexandroupoli, 2018, pp. 65-71.
[Li19a]	J. Li, K. Wang, and C. Liu, "Comparative study of consequent-pole and hybrid-pole permanent magnet machines," *IEEE Trans. Energy Convers.*, vol. 34, no. 2, pp. 701-711, June 2019.

[Li19b]	J. Li, K. Wang, and F. Li, "Reduction of torque ripple in consequent-pole permanent magnet machines using staggered rotor," *IEEE Trans. Energy Convers.*, vol. 34, no. 2, pp. 643-651, June 2019.
[Li19c]	J. Li, K. Wang, F. Li, S. S. Zhu, and C. Liu, "Elimination of even-order harmonics and unipolar leakage flux in consequent-pole PM machines by employing N-S-iron–S-N-iron rotor," *IEEE Trans. Ind. Electron.*, vol. 66, no. 3, pp. 1736-1747, March 2019.
[Li19c]	J. Li, K. Wang, F. Li, S. S. Zhu, and C. Liu, "Elimination of even-order harmonics and unipolar leakage flux in consequent-pole PM machines by employing N-S-iron–S-N-iron rotor," *IEEE Trans. Ind. Electron.*, vol. 66, no. 3, pp. 1736-1747, March 2019.
[Li19d]	F. Li, K. Wang, J. Li, and H. Y. Sun, “Electromagnetic performance analysis of consequent-pole PM machine with asymmetric magnetic pole,” *IEEE Trans. Magn.*, vol. 55, no. 6, Jun. 2019.
[Li19e]	F. Li, K. Wang, H. Sun, and J. Kong, "Influence of various magnetic pole on electromagnetic performance of consequent-pole permanent magnet machine," *IEEE Access*, vol. 7, pp. 121853-121862, 2019.
[Li19f]	J. Li, K. Wang, and H. Zhang, “Flux-focusing permanent magnet machines with modular consequent-pole rotor,” *IEEE Trans. Ind. Electron.*, pp. 1-1, Jun. 2019.
[Li19g]	J. Li, and K. Wang, “A parallel hybrid excited machine using consequent pole rotor and AC field winding,” *IEEE Trans. Magn.*, vol. 55, no. 6, pp. 1-5, 2019.
[Li19h]	F. Li, K. Wang, H. Y. Sun, H. Zhang, and L. Zhang, "Quantitative comparison between SPM machine and consequent pole PM machines with different rotor topologies," *IEEE Int. Electr. Mach. Drives Conf. (IEMDC)*, San Diego, CA, USA, 2019, pp. 127-134.
[Li19i]	H. Li and Z. Q. Zhu, "Investigation of stator slot/rotor pole combination of flux reversal permanent magnet machine with consequent-pole PM structure," *J. Eng.*, vol. 2019, no. 17, pp. 4267-4272, 2019.
[Li19j]	J. Li and K. Wang, “A novel spoke-type PM machine employing asymmetric modular consequent-pole rotor,” *IEEE ASME Trans. Mechatron.*, pp. 1-1, Jul. 2019.
[Li19k]	Y. Li, H. Yang, H. Lin, W. Liu, and S. Lyu, "A novel dual-sided PM machine with stator spoke-type PM structure," 2019 *IEEE Energy Convers. Congr. Expo. (ECCE)*, 2019, pp. 1721-1728.
[Li20a]	J. Li, K. Wang, and H. Zhang, “Comparative analysis of spoke-type, consequent-pole and hybrid-pole permanent magnet machines,” *IET Electr. Power Appl.*, vol. 14, no. 4, pp. 648-657, April 2020.

[Li20b]	F. Li, K. Wang, J. Zhang, and F. Zeng, "Effect of angle displacements on electromagnetic performance of dual three-phase consequent-pole permanent magnet machine," *IET Electr. Power Appl.*, vol. 14, no. 7, pp. 1177-1185, July. 2020.
[Li20c]	Y. Li, H. Yang, H. Lin, L. Qin, and S. Lyu, "Investigation of double-side field modulation mechanism in consequent-pole PM machines with concentrated windings," *IEEE Trans. Energy Convers.*, vol. 36, no. 3, pp. 1635-1648, Sept. 2021.
[Li22a]	Y. Li, H. Yang, H. Lin, S. Ding, J. Hang and W. Li, "Influences of magnet arrangements on air-gap field modulation effects in interior consequent-pole PM machines," *IEEE Trans. Transp. Electrif.*, 2022. (Early Access)
[Li22b]	Y. Li, Q. Zhou, S. Ding, W. Li, and J. Hang, "Design and evaluation of reduced-rare-earth interior consequent-pole permanent magnet machines for automotive applications," *IEEE Trans. Ind. Appl.*, 2022.
[Lin20]	Q. Lin, S. Niu, F. Cai, W. Fu, and L. Shang, "Design and optimization of a novel dual-PM machine for electric vehicle applications," *IEEE Trans. Veh. Technol.*, vol. 69, no. 12, pp. 14391-14400, Dec. 2020.
[Liu05]	Y. Liu, Z. Q. Zhu, and D. Howe, "Direct torque control of brushless DC drives with reduced torque ripple," *IEEE Trans. Ind. Appl.*, vol. 41, no. 2, pp. 599-608, March-April 2005.
[Liu13]	G. Liu, X. Du, W. Zhao, and Q. Chen, "Reduction of torque ripple in inset permanent magnet synchronous motor by magnets shifting," *IEEE IEEE Trans. Magn.*, vol. 53, no. 2, pp. 1-13, Feb. 2017, Art no. 8100713.
[Liu18]	W. Liu and T. A. Lipo, "Analysis of consequent pole spoke type vernier permanent magnet machine with alternating flux barrier design," *IEEE Trans. Ind. Appl.*, vol. 54, no. 6, pp. 5918-5929, Nov. /Dec. 2018.
[Liu20]	D. Liu, G. Kan, and Y. Mu, "Analysis of a consequent-pole permanent magnet machine for electric vehicle propulsion," *23rd Int. Conf. Electr. Mach. Syst. (ICEMS)*, 2020, pp. 1615-1618.
[Liu21]	F. Liu, X. Wang, Z. Xing, A. Yu, and C. Li, "Reduction of cogging torque and electromagnetic vibration based on different combination of pole arc coefficient for interior permanent magnet synchronous machine," *CES Trans. Electr. Mach. Syst.*, vol. 5, no. 4, pp. 291-300, Dec. 2021.
[Liu22]	W. Liu, J. Wang, and T. A. Lipo, "A consequent pole single rotor single stator vernier design to effectively improve torque density of an industrial PM drive," *IEEE Trans. Ind. Electron*., vol. 70, no. 1, pp. 255-264, Jan. 2023.
[Ma18]	G. Ma, X. Qiu, J. Yang, F. Bu, Y. Dou, and W. Cao, "Structural parameter optimization to reduce cogging torque of the consequent pole in-wheel motor," *IEEE* 18*th Int. Power Electron. Mot. Contrl. Conf. (PEMC)*, Budapest, 2018, pp. 170-175.

[Ma19]	H. Ma, W. Wang, X. Qiu, and J. Yang, "Inductance characteristic analysis of consequent-pole permanent magnet in-wheel motor," *IEEE Access*, vol. 7, pp. 90507-90516, 2019.
[Mai87]	A. Mailfert, H. Kubler, and J. Zhou, "Hybrid stepping motors comparative experimental results," *Int. Conf. Electr. Mach.*, 1987, pp. 781-783.
[Mcc86]	F. B. McCarty, "Consequent pole permanent magnet rotor," U.S. Patent US4631435A, Dec. 23, 1986.
[Mit22]	H. Mitsuda, T. Fukami, M. Koyama, and K. Ito, "Performance analysis of flux-modulating consequent pole motors," *2022 Int. Power Electron. Conf. (IPEC-Himeji 2022- ECCE Asia)*, 2022, pp. 1253-1260.
[Miz94]	T. Mizuno, "Basic principles and design of hybrid excitation synchronous machine," *Nat. Conf. IEE, Japan Ind. Appl.*, Japan, 1994, pp 25.
[Ons17]	M. Onsal, Y. Demir, and M. Aydin, "A new nine-phase permanent magnet synchronous motor with consequent pole rotor for high-power traction applications," *IEEE Trans. Magn.*, vol. 53, no. 11, pp. 1-6, Nov. 2017.
[Ons18]	M. Onsal, B. Cumhur, Y. Demir, E. Yolacan, and M. Aydin, "Rotor design optimization of a new flux-assisted consequent pole spoke-type permanent magnet torque motor for low-speed applications," *IEEE Trans. Magn.*, vol. 54, no. 11, pp. 1-5, Nov. 2018.
[Pap17]	L. Papini, F. Papini, P. Bolognesi, and C. Gerada, “Comparison of surface mounted and uneven consequent-pole PM high-speed machines,” *Proc. IEEE Workshop Electr. Mach. Des. Control Diagnosis*, pp. 52-57, 2017.
[Pu20]	W. Pu, Z. Xiang, X. Zhu, L. Quan, and Y. Zuo, "Design and analysis of a dual-PM-excited motor considering harmonic characteristics," *2020 IEEE Int. Conf. Appl. Supercond. Electromagn. Dev. (ASEMD)*, 2020, pp. 1-2.
[Pu21]	W. Pu, Z. Xiang, X. Zhu, L. Quan, and D. Fan, "Research on enhanced harmonic effect of a dual-PM-excited flux-modulated motor," *IEEE Trans. Appl. Supercond.*, vol. 31, no. 8, pp. 1-6, Nov. 2021.
[Qi19]	J. Qi, W. Hua, and H. Zhang, "Thermal analysis of modular-spoke-type permanent-magnet machines based on thermal network and FEA method," *IEEE Trans. Magn.*, vol. 55, no. 7, pp. 1-5, July 2019.
[Qi22a]	J. Qi, Z.Q. Zhu, L. Yan, G.W. Jewell, C.W. Gan, Y. Ren, S. Brockway, and C. Hilton, "Effect of pole shaping on torque characteristics of consequent pole PM machines," *IEEE Trans. Ind. Appl.*, vol. 58, no. 3, pp. 3511-3521, May-June 2022.
[Qi22b]	J. Qi, Z.Q. Zhu, L. Yan, G.W. Jewell, C.W. Gan, Y. Ren, S. Brockway, and C. Hilton, "Suppression of torque ripple for consequent pole PM machine by asymmetric pole shaping method," *IEEE Trans. Ind. Appl*, vol. 58, no. 3, pp. 3545-3557, May-June 2022.

[Qi22c]	J. Qi, Z.Q. Zhu, L. Yan, G.W. Jewell, C.W. Gan, Y. Ren, S. Brockway, and C. Hilton, "Analytical analysis of cogging torque in permanent magnet machines with unequal north and south poles, with particular reference to consequent pole machines," *IEEE Trans. Energy Convers.*, 2022. (Early Access)
[Qi22d]	J. Qi, Z.Q. Zhu, G.W. Jewell, L. Yan, C.W. Gan, Y. Ren, S. Brockway, and C. Hilton, "Influence of slot/pole number combinations and pole shaping on electromagnetic performance of permanent magnet machines with unbalanced north and south poles," *IET Electr. Power Appl.*, pp.1–28, 2023. DOI: https://doi.org/10.1049/elp2.12293
[Qi23]	J. Qi, Z.Q. Zhu, L. Yan, G.W. Jewell, C.W. Gan, Y. Ren, S. Brockway, and C. Hilton, "Influence of armature reaction on electromagnetic performance and pole shaping effect in consequent pole PM machines," *Energies*, vol. 16, no. 4, pp. 1982, Jan. 2023.
[Qu19]	G. Qu, Y. Fan, and Z. Wu, "Design and analysis of a new hybrid-excited permanent magnet machine with unequal teeth," *IEEE Trans. Magn.*, vol. 55, no. 7, pp. 1-5, July 2019.
[Qu21]	H. Qu, Z. Q. Zhu, and H. Li, "Analysis of novel consequent pole flux reversal permanent magnet machines," *IEEE Trans. Ind. Appl.*, vol. 57, no. 1, pp. 382-396, Jan.-Feb. 2021.
[Qu22]	G. Qu, Y. Fan, and Q. Chen, "Suppression of torque ripple in a new consequent-pole permanent magnet machine by segmented structure," *IEEE Trans. Magn.*, vol. 58, no. 8, pp. 1-6, Aug. 2022.
[Ren19]	B. Ren, G. Li, Z. Zhu, M. Foster, and D. Stone, "Performance comparison between consequent-pole and inset modular permanent magnet machines," *J. Eng.*, vol. 2019, no. 17, pp. 3951-3955, Jun. 2019.
[Sha20]	S. Shastri, U. Sharma, and B. Singh, "Design of fractional-slot concentrated winding consequent pole motor for ceiling fans," *IEEE 5th Int. Conf. Comput. Comms. Autom. (ICCCA)*, 2020, pp. 390-395.
[Sha21]	Y. Shang, D. Liang, S. Jia, and Y. Liang, "Optimization of a consequent-pole PMSM with a sobol sequence based multi-objective hybrid optimization algorithm," *24th Int. Conf. Electr. Mach. Syst. (ICEMS)*, 2021, pp. 1650-1653, 2021.
[She17]	J. Shen, H. Li, H. Hao, and M. Jin, "A coaxial magnetic gear with consequent-pole rotors," *IEEE Trans. Energy Convers.*, vol. 32, no. 1, pp. 267-275, March 2017.
[Shi19]	C. J. Shi, R. H. Qu, D. W. Li, Y. T. Gao, and R. Li, "Comparative study on a novel consequent-pole modular linear vernier machine with PMs on both mover and stator iron cores," *IEEE Energy Convers. Congr. Expo. (ECCE)*, Sept.-Oct. 2019, pp. 712-716.

[Shi21]	Y. Shi, Z. Cheng, and L. Jian, "Comparative analysis of two typical field modulated permanent-magnet machines," *Trans. China Electrotech. Soc.*, vol. 36, no. 1, pp. 120-130, 2021.
[Tap03]	J. A. Tapia, F. Leonardi, and T. A. Lipo, "Consequent-pole permanent-magnet machine with extended field-weakening capability," *IEEE Trans. Ind. Appl.*, vol. 39, no. 6, pp. 1704-1709, Nov.-Dec. 2003.
[Tey16]	S. Teymoori, A. Rahideh, H. Moayed-Jahromi, and M. Mardaneh, "2-D analytical magnetic field prediction for consequent-pole permanent magnet synchronous machines," *IEEE Trans. Magn.*, vol. 52, no. 6, pp. 1-14, June 2016.
[Too16]	F. Tootoonchian and Z. Nasiri-Gheidari, "Cogging force mitigation techniques in a modular linear permanent magnet motor," *IET Electr. Power Appl.*, vol. 10, no. 7, pp. 667-674, Aug. 2016.
[Ull19]	W. Ullah, F. Khan, N. Ullah, M. Umair, B. Khan, and H. A. Khan, "Comparative study between C-core/E-core SFPMM with consequent pole SFPMM," *2019 Int. Symp. Recent Adv. Electr. Eng. (RAEE)*, 2019, pp. 1-6.
[Ull20a]	W. Ullah, F. Khan, E. Sulaiman, and M. Umair, "Torque characteristics of high torque density partitioned PM consequent pole flux switching machines with flux barriers," *CES Trans. Electr. Mach. Syst.*, vol. 4, no. 2, pp. 130-141, June 2020.
[Ull20b]	W. Ullah, F. Khan, and M. Umair, "Design and optimization of segmented PM consequent pole hybrid excited flux switching machine for EV/HEV application," *CES Trans. Electr. Mach. Syst.*, vol. 4, no. 3, pp. 206-214, Sept. 2020.
[Ull20c]	W. Ullah and F. Khan, "Sub-domain modelling and multi-variable optimisation of partitioned PM consequent pole flux switching machines," *IET Electr. Power Appl.*, vol. 14, no. 8, pp. 1360-1369, 2020.
[Ull21c]	W. Ullah, F. Khan, and M. Umair, "Multi-objective optimization of high torque density segmented PM consequent pole flux switching machine with flux bridge," *CES Trans. Electr. Mach. Syst*., vol. 5, no. 1, pp. 30-40, March 2021.
[Ull21d]	W. Ullah, F. Khan, and M. Umair, "Optimal rotor poles and structure for design of consequent pole permanent magnet flux switching machine," *Chin. J. Electr. Eng.*, vol. 7, no. 1, pp. 118-127, March 2021.
[Ull21e]	W. Ullah, F. Khan, M. Umair, and E. Sulaiman, "Coupled electromagnetic-thermal analysis of segmented PM consequent pole flux switching machine," *Chin. J. Electr. Eng.*, vol. 7, no. 2, pp. 50-60, June 2021.
[Ull22a]	W. Ullah, F. Khan, S. Hussain, F. Alturise, M. Yousuf, and S. Akbar, "Consequences of flux gap on intriguing features of modular stator inset permanent magnet consequent pole synchronous machine," *IEEE Access*, vol. 10, pp. 49551-49565, 2022.

[Ull22b]	W. Ullah, F. Khan, N. Ullah, and A. Majid, “Investigation of third harmonic utilization for torque performance improvement in novel H-type modular stator consequent pole machine,” *Electr. Eng.*, pp. 1-13, 2022.
[Wan06]	Xiuhe Wang, Tingting Ding, Ning Shen, Shiyong Liu, and Shiyou Yang, "Optimization of the different pole arc combination to reduce the cogging torque in PMDC motors," *12th Bienn. IEEE Conf. Electromagn. Field Comput.*, 2006, pp. 367-367.
[Wan10]	D. Wang, X. Wang, Y. Yang, and R. Zhang, "Optimization of magnetic pole shifting to reduce cogging torque in solid-rotor permanent-magnet synchronous motors," *IEEE Trans. Magn.*, vol. 46, no. 5, pp. 1228-1234, May 2010.
[Wan13]	D. Wang, X. Wang, and S. Jung, "Cogging torque minimization and torque ripple suppression in surface-mounted permanent magnet synchronous machines using different magnet widths," *IEEE Trans. Magn.*, vol. 49, no. 5, pp. 2295-2298, May 2013.
[Wan14a]	K. Wang, Z. Q. Zhu, and G. Ombach, "Torque enhancement of surface-mounted permanent magnet machine using third-order harmonic," *IEEE Trans. Magn.*, vol. 50, no. 3, pp. 104-113, March 2014.
[Wan14b]	K. Wang, Z. Q. Zhu, G. Ombach, and W. Chlebosz, "Average torque improvement of interior permanent-magnet machine using third harmonic in rotor shape," *IEEE Trans. Ind. Electron.*, vol. 61, no. 9, pp. 5047-5057, Sept. 2014.
[Wan17a]	H. Wang, S. Fang, H. Yang, H. Lin, Y. Li, and J. Jiang, “A novel consequent-pole hybrid excited vernier permanent-magnet machine for EV/HEV applications,” *2017 IEEE Int Magn. Conf. (INTERMAG)*, April 2017, pp. 24–28.
[Wan17b]	K. Wang, Z. Y. Gu, Z. Q. Zhu, and Z. Z. Wu, "Optimum injected harmonics into magnet shape in multiphase surface-mounted PM machine for maximum output torque," *IEEE Trans. Ind. Electron*., vol. 64, no. 6, pp. 4434-4443, June 2017.
[Wan17c]	Q. Wang, S. Niu, and X. Luo, "A novel hybrid dual-pm machine excited by AC with DC bias for electric vehicle propulsion," *IEEE Trans. Ind. Electron*., vol. 64, no. 9, pp. 6908-6919, Sept. 2017.
[Wan19a]	K. Wang and Z. Q. Zhu, Third harmonic utilization in permanent magnet machines, Springer Singapore, 2019, pp. 13-61.
[Wan19b]	K. Wang, J. Li, S. S. Zhu, and C. Liu, “Novel hybrid-pole rotors for consequent-pole PM machines without unipolar leakage flux,” *IEEE Trans. Ind. Electron.*, vol. 66, no. 9, pp. 302-309, Jan. 2019.
[Wan20]	K. Wang, F. Li, H. Y. Sun, and X. D. Sun, "Consequent pole permanent magnet machine with modular stator," *IEEE Trans. Veh. Technol.*, vol. 69, no. 7, pp. 7054-7063, July 2020.

[Wan21]	H. Wang, K. T. Chau, C. H. T. Lee, C. C. Chan, and T. Yang, “Nonlinear varying-network magnetic circuit analysis of consequent-pole permanent-magnet motor for electric vehicles,” *World Electr. Veh. J.*, vol.12, no. 4, pp. 254, 2021.
[Wat18]	T. Watahiki, Y. Toriumi, and I. Miki, "A consequent pole motor with novel pole structure," *Int. Symp. Power Electron., Electr. Drives, Autom. Mot. (SPEEDAM)*, Amalfi, 2018, pp. 1136-1140.
[Wei20a]	L. Wei and T. Nakamura, "Optimization design of a dual-stator switched flux consequent pole permanent magnet machine with unequal length teeth," *IEEE Trans. Magn.*, vol. 56, no. 2, pp. 1-5, Feb. 2020.
[Wei20b]	L. Wei and T. Nakamura, "A novel dual stator hybrid excited permanent magnet vernier machine with Halbach-array PMs," *IEEE Trans. Magn.*, vol. 57, no. 2, pp. 1-5, Feb. 2021.
[Wei22a]	F. Wei, Z. Q. Zhu, X. Sun, L. Yan, and J. Qi, "Investigation of asymmetric consequent-pole hybrid excited flux reversal machines," *IEEE Trans. Ind. Appl.*, vol. 58, no. 3, pp. 3434-3446, May-June 2022.
[Wei22b]	F. Wei, Z. Q. Zhu, L. Yan, and J. Qi, "Investigation of stator/rotor pole number combinations and PM numbers in consequent-pole hybrid excited flux reversal machine," *IEEE Trans. Energy Convers.* (Early Access).
[Wu14]	L. Wu, and R. Qu, “Comparison of conventional and consequent pole interior permanent magnet machines for electric vehicle application,” *17th Int. Conf. Electr. Mach. Syst. (ICEMS)*, Oct. 2014, pp. 70-74.
[Wu15]	Z. Z. Wu and Z. Q. Zhu, "Partitioned stator flux reversal machine with consequent-pole PM stator," *IEEE Trans. Energy Convers.*, vol. 30, no. 4, pp. 1472-1482, Dec. 2015.
[Wu19a]	Z. Wu, Y. Fan, Q. Zhang, and D. Gao. "Comparison and analysis of permanent magnet vernier motors for low-noise in-wheel motor application," *IET Electr. Power Appl.*, vol. 14, no. 2, pp. 274-281, 2019.
[Wu19b]	L. Wu, M. Zhu, D. Wang, and Y. Fang, "A subdomain model for open-circuit field prediction in dual-stator consequent-pole permanent magnet machines," *IEEE Trans. Magn.*, vol. 55, no. 8, pp. 1-12, Aug. 2019.
[Xu01]	Y. Xu, J. Xu, W. Wan, and R. Tang, "Development of permanent magnet synchronous motor used in electric vehicle," *The Fifth Int. Conf. Electr. Mach. Syst. (ICEMS)*, Shenyang, China, 2001, pp. 884-887.
[Xu19]	X. Xu, Z. Sun, B. Du, H. Feng, H. Du, and J. Lu, "Magnetic unbalance and thrust ripple reduction design for novel PMLSM with Halbach consequent pole," *22nd Int. Conf. Electr. Mach. Syst. (ICEMS)*, Harbin, China, 2019, pp. 1-5.

[Xu20]	X. Xu, Z. Sun, B. Du, and L. Ai, "Pole optimization and thrust ripple suppression of new Halbach consequent-pole PMLSM for ropeless elevator propulsion," *IEEE Access*, vol. 8, pp. 62042-62052, 2020.
[Xu20a]	G. Xu, W. Zhao, G. Liu, F. Zhai, and Q. Chen, "Torque performance improvement of consequent-pole PM motors with hybrid rotor configuration," *IEEE Trans. Transp. Electrif.*, vol. 7, no. 3, pp. 1561-1572, Sept. 2021.
[Xu22]	B. Xu, Q. Wu, J. Ma, L. Wu, L. Qiu, X. Liu, and Y. Fang, "Research on the influence of end turn length on consequent-pole vernier permanent-magnet machines," *IEEE Trans. Magn.*, no. 8, pp. 1-9, Aug. 2022.
[Yan19a]	L.C. Yan, Y. Liao, H. Lin, and J. Sun, "Torque ripple suppression of permanent magnet synchronous machines by minimal harmonic current injection," *IET Power Electron.*, vol. 12, no. 6, pp. 1368-1375, 2019.
[Yan19b]	H. Yang, Y. Li, H. Lin, W. Liu, and X. Zhao, "Novel dual-sided permanent magnet machines with different stator magnet arrangements," *2019 IEEE Energy Convers. Congr. Expo. (ECCE)*, 2019, pp. 6114-6121.
[Yan20a]	L. Yan, Z. Q. Zhu, J. Qi, Y. Ren, C. Gan, S. Brockway, and C. Hilton, “Enhancement of disturbance rejection capability in dual three phase PMSM system by using virtual impedance,” *IEEE Energy Convers. Congr. Expo. (ECCE)*, Detroit, USA, 2020, pp. 6104-6110.
[Yan20b]	X. Yang, B. Kou, J. Luo, and H. Zhang, "Electromagnetic design of a dual-consequent-pole transverse flux motor," *IEEE Trans. Energy Convers.*, vol. 35, no. 3, pp. 1547-1558, Sept. 2020.
[Yan21a]	K. Yang, F. Zhao, Y. Wang, and Z. Bao, "Consequent-pole flux reversal permanent magnet machine with Halbach array magnets in rotor slot," *IEEE Trans. Magn.*, vol. 57, no. 2, pp. 1-5, Feb. 2021.
[Yan21b]	K. Yang, F. Zhao, and Y. Wang, "Analysis of double-layer permanent-magnet flux reversal machines with different permanent magnet arrangements in stator," *IEEE Trans. Magn.*, vol. 57, no. 2, pp. 1-5, Feb. 2021.
[Yu19]	Y. Yu, Y. Pei, L. Chen, F. Chai, and G. Han, "Design and comparative analysis of consequent pole rotor configurations in PM vernier motors for in-wheel drive application," *22nd Int. Conf. Electr. Mach. Syst. (ICEMS)*, Harbin, China, 2019, pp. 1-6.
[Zha18a]	H. L. Zhang and W. Hua, “The influence of magnetization on modular spoke-type permanent-magnet machine for in-wheel traction applications,” *IEEE Trans. Magn.*, vol. 54, no. 11, Nov. 2018.
[Zha18b]	H. Zhang, W. Hua, Z. Wu, and X. Zhu, “Design considerations of novel modular-spoke-type permanent magnet machines,” *IEEE Trans. Ind. Appl.*, vol. 54, no. 5, pp. 4236-4245, May. 2018.

[Zha18c]	H. Zhang, W. Hua, and Z. Wu, “Modular spoke-type permanent-magnet machine for in-wheel traction applications,” *IEEE Trans. Ind. Electron*., vol. 65, no. 10, pp. 7648-7659, Oct. 2018.
[Zha19a]	L. Zhang, K. Wang, J. Li, and F. Li, "Comparison study of interior permanent magnet synchronous machine with conventional and consequent pole rotor," 22*nd Int. Conf. Electr. Mach. Syst. (ICEMS)*, Harbin, China, 2019, pp. 1-5.
[Zha19b]	G. H. Zhang, K. Wang, and J. Li, "Torque ripple suppression of consequent-pole permanent magnet machine by magnet shifting," 22*nd Int. Conf. Electr. Mach. Syst. (ICEMS)*, Harbin, China, 2019.
[Zha19c]	H. Zhang, W. Hua, D. Gerada, C. Gerada, Y. Li, and G. Zhang, “Comparative study on two modular spoke-type PM machines for in-wheel traction applications,” *IEEE Trans. Energy Convers.*, vol. 34, no. 4, pp. 1-1, 2019.
[Zha19d]	X. Zhao, S. Niu, and W. Fu, "Design of a novel parallel-hybrid-excited dual-PM machine based on armature harmonics diversity for electric vehicle propulsion," *IEEE Trans. Ind. Electron*., vol. 66, no. 6, pp. 4209-4219, June 2019.
[Zha20a]	G. Zhang, K. Wang, J. Li, R. Zheng, and J. Kong, "Torque ripple reduction of consequent-pole permanent magnet machine by shaped rotor," *IEEE 9th Int. Power Electron. Mot. Contrl. Conf. (IPEMC2020-ECCE Asia)*, 2020, pp. 1962-1966.
[Zha20b]	J. Zhao, X. Quan, X. Sun, J. Li, and M. Lin, "Design of a novel axial flux rotor consequent-pole permanent magnet machine," *IEEE Trans. Appl. Supercond.*, vol. 30, no. 4, pp. 1-6, June 2020.
[Zha20c]	Z. Zhang, "Consequent pole toroidal winding dual rotor permanent magnet synchronous machines," 2020 *IEEE Energy Convers. Congr. Expo. (ECCE)*, Detroit, MI, USA, 2020, pp. 2034-2041.
[Zha22]	Z. Zhang, M. Zhang, J. Yin, J. Wu, C. Yang, “An analytical method for calculating the cogging torque of a consequent pole hybrid excitation synchronous machine based on spatial 3D field simplification,” *Energies*, vol. 15, no. 3, pp. 878, 2022.
[Zho19a]	R. Zhou, G. J. Li, Z. Q. Zhu, Y. X. Li, M. P. Foster, and D. A. Stone, "Investigation of integer/fractional slot consequent pole PM machines with different rotor structures," *IEEE Int. Electr. Mach. Drives Conf. (IEMDC)*, San Diego, CA, USA, 2019, pp. 119-126.
[Zho19b]	R. Zhou, G. J. Li, Z. Q. Zhu, Y. X. Li, M. P. Foster, and D. A. Stone, "Comparative studies of fractional/integer-slot consequent pole permanent magnet machines," *IEEE Int. Electr. Mach. Drives Conf. (IEMDC)*, San Diego, CA, USA, 2019, pp. 104-111.

[Zho19c]	R. Zhou, G. J. Li, K. Zhang, Z. Q. Zhu, M. Foster, and D. Stone, "Performance investigation of consequent-pole PM machines with E-core and C-core modular stators," *IEEE Trans. Energy Convers.*, vol. 36, no. 2, pp. 1169 - 1179, June 2020.
[Zho20]	R. Zhou, G. J. Li, Z. Q. Zhu, M. P. Foster, and D. A. Stone, "Improved cooling in modular consequent pole pm machine utilizing flux gaps," 2020 *IEEE Energy Convers. Congr. Expo. (ECCE)*, Detroit, MI, USA, 2020, pp. 4253-4260.
[Zho22]	H. Zhou, W. Tao, G. Jiang, G. -J. Li, and G. Liu, "Reduction of saturation and unipolar leakage flux in consequent-pole PMV machine," *IEEE J. Emerg. Sel. Top. Power Electron.*, vol. 10, no. 2, pp. 1870-1880, April 2022.
[Zhu00]	Z. Q. Zhu and D. Howe, "Influence of design parameters on cogging torque in permanent magnet machines," *IEEE Trans. Energy Convers.*, vol. 15, no. 4, pp. 407-412, Dec. 2000.
[Zhu03]	Z. Q. Zhu, Z. P. Xia, Y. F. Shi, D. Howe, A. Pride, and X. J. Chen, "Performance of Halbach magnetized brushless AC motors," *IEEE Trans. Magn.*, vol. 39, no. 5, pp. 2992-2994, Sep. 2003.
[Zhu07]	Z. Q. Zhu and D. Howe, "Electrical machines and drives for electric, hybrid, and fuel cell vehicles," *Proc. of the IEEE*, vol. 95, no. 4, pp. 746-765, Apr. 2007.
[Zhu09a]	L. Zhu, S. Z. Jiang, Z. Q. Zhu, and C. C. Chan, "Analytical methods for minimizing cogging torque in permanent-magnet machines," *IEEE Trans. Magn.*, vol. 45, no. 4, pp. 2023-2031, April 2009.
[Zhu09b]	Z. Q. Zhu, "A simple method for measuring cogging torque in permanent magnet machines," *2009 IEEE Power Energy Soc. Gen. Meet.*, 2009, pp. 1-4.
[Zhu16]	Z.Q. Zhu and W.Q. Chu, "Advanced frozen permeability technique and applications in developing high performance electrical machines," *Trans. China Electrotech. Soc.*, vol.31, no.20, pp.13-29, Oct. 2016.
[Zhu18a]	Z. Q. Zhu and Y. X. Li, "Modularity techniques in high performance permanent magnet machines and applications," *CES Trans. Electr. Mach. Syst.*, vol. 2, no. 1, pp. 93-103, March 2018.
[Zhu19]	M. Zhu, L. Wu, Y. Fang, and T. Lubin, "Subdomain model for predicting armature reaction field of dual-stator consequent-pole PM machines accounting for tooth-tips," *CES Trans. on Electr. Mach. Syst.*, vol. 3, no. 2, pp. 143-150, June 2019.
[Zhu23]	S. Zhu, J. Ji, W. Zhao, G. Liu, and C. H. T. Lee, "Vibration reduction design of consequent pole PM machine by symmetrizing local and global magnetic field," *IEEE Trans. Ind. Electron*., vol. 70, no. 1, pp. 243-254, Jan. 2023.